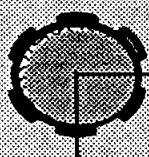


**Texas A&M University  
Mechanical Engineering Department**



**Thermohydrodynamic Analysis of  
Cryogenic Liquid Turbulent Flow  
Fluid Film Bearings**

**Luis San Andres  
Associate Professor  
December 1996**

**FINAL REPORT**

**to**

**NASA Lewis Research Center  
NASA Grant NAG3-1434  
Contract Monitor: Mr. James Walker**

**Period of performance: January 1, 1993 to December 31, 1996**

# **THERMOHYDRODYNAMIC ANALYSIS OF CRYOGENIC LIQUID TURBULENT FLOW FLUID FILM BEARINGS**

Dr. Luis San Andres, P.I.

Associate Professor

Texas A&M University

Period of Performance: January 1, 1993 - December 31, 1996

<b>INDEX</b>	<b><u>Page</u></b>
<b>EXECUTIVE SUMMARY</b>	
<b>WORK COMPLETED ON PHASE I OF THE RESEARCH PROGRAM</b> Description of program <i>hydrosealt</i>	3
<b>WORK COMPLETED ON PHASE II OF THE RESEARCH PROGRAM</b> Description of program <i>hydroflect</i> Description of program <i>hydrotran</i>	5
<b>SURVEY ON REQUIRED ADVANCES ON FLUID FILM BEARING ANALYSIS</b>	6
<b>WORK COMPLETED ON PHASE III OF THE RESEARCH PROGRAM</b> Description of program <i>hydrojet</i> Analysis of two-phase flow in annular pressure seals Description of program <i>hseal2p</i>	3
<b>SCHEDULE OF PROGRAM RELEASES FROM NASA NAG3-1434 PROJECT</b>	12
<b>LIST OF PUBLICATIONS RELATED TO THE RESEARCH</b> <b>JOURNAL PUBLICATIONS</b>	12
1. Angled Injection - Hydrostatic Bearings, Analysis and Comparison to Test Results, <i>ASME paper 96-TRIB-10</i> , 1996.	
2. Transient Response of Externally Pressurized Fluid Film Bearings, <i>STLE Paper96-TC-3A-1</i> , 1996.	
3. Bulk-Flow Model for the Transition to Turbulence Regime in Annular Seals, <i>STLE Tribology Transactions</i> , Vol. 39, 4, pp. 835-84, 1996.	
4. Thermal Effects in Liquid Oxygen Hybrid Bearings, , <i>STLE Tribology Transactions</i> , Vol. 39, 3, pp. 654-662, 1996.	
5. Turbulent Flow, Flexure-Pivot Hybrid Bearings for Cryogenic Applications, <i>ASME Journal of Tribology</i> , Vol. 118, 1, pp. 100-200, 1996.	
6. Turbulent Flow Hydrostatic Bearings: Analysis and Experimental Results, <i>International Journal of Mechanical Sciences</i> , Vol. 37, 8, pp. 815-829, 1995.	

## INDEX

## Page

7. a) Thermohydrodynamic Analysis of Process Liquid Hydrostatic Bearings in Turbulent Regime, Part I: The Model and Perturbation Analysis, *ASME Journal of Applied Mechanics*, Vol. 62, 3, pp. 674-678, 1995.
7. b) Thermohydrodynamic Analysis of Process Liquid Hydrostatic Bearings in Turbulent Regime, Part II: Numerical Solution and Results, *ASME Journal of Applied Mechanics*, Vol. 62, 3, pp. 679-684, 1995.
8. Thermohydrodynamic Analysis of Fluid Film Bearings for Cryogenic Applications, *AIAA Journal of Propulsion and Power*, Vol. 11, 5, pp. 964-972, 1995.
9. Inertia Effects in a Hybrid Bearing with a 45 degree Entrance Region, *ASME Journal of Tribology*, Vol. 117, 3, pp. 498-505, 1995.
10. Turbulent Flow Foil Bearings for Cryogenic Applications, *ASME Journal of Tribology*, Vol. 117, 1, pp. 185-195, 1995.

## CONFERENCE PROCEEDINGS PUBLICATIONS

11. Angled Injection, Turbulent Flow Hybrid Bearings, Comparison to Test Results, *Proceedings of the 8<sup>th</sup> Workshop on Instability Problems in Rotating Machinery*, Texas A&M University, May 1996.
12. Process Liquid Turbulent Flow Hydrostatic Bearings: Analysis and Tests for Rotordynamic Coefficients, *Proceedings of the 4<sup>th</sup> International IFToMM Rotordynamics Conference*, pp. 233-242, Chicago, September, 1994.
13. Thermohydrodynamic Analysis of Fluid Film Bearings for Cryogenic Applications, *Proceedings of the 6<sup>th</sup> NASA Conference on Advanced Earth-to-Orbit Propulsion Technology*, Huntsville, ALA, NASA CP 3282, Vol. II, pp. 421-430, May 1994.
14. Analysis of Arbitrary Recess Geometry Hydrostatic Bearings, *Proceedings of the 6<sup>th</sup> NASA Conference on Advanced Earth-to-Orbit Propulsion Technology*, Huntsville, ALA, NASA CP 3282, Vol. II, pp. 431-441. May 1994.

## MANUSCRIPTS IN REVIEW:

15. Analysis of Two Phase Flow in Cryogenic Damper Seals. Part I: Theoretical Model, *submitted to ASME Journal of Tribology*, November, 1996.
16. Analysis of Two Phase Flow in Cryogenic Damper Seals. Part II: Model Validation and Predictions, *submitted to ASME Journal of Tribology*, November, 1996.

# THERMOHYDRODYNAMIC ANALYSIS OF CRYOGENIC LIQUID TURBULENT FLOW FLUID FILM BEARINGS

Dr. Luis San Andres, P.I.

Associate Professor

Texas A&M University

Period of Performance: Jan. 1, 1993 - December 31, 1996

## EXECUTIVE SUMMARY

Research was conducted to develop a thermohydrodynamic analysis and computer programs for prediction of the static and dynamic force response of fluid film bearings for cryogenic applications. The importance of hybrid (combination hydrostatic and hydrodynamic) journal bearings and damping seal bearings as support elements in cryogenic turbomachinery has steadily grown over the past few years. Fluid film bearings enable smaller and lighter turbopumps through no bearing DN life limitation and no sub-critical rotor operation. These mechanical elements have durability, low friction and wear, accuracy of positioning, and large direct stiffness and damping force coefficients. The growth of an "all-fluid-film-bearing" technology for advanced and less expensive (per launching cost) turbopumps demands the development of analytical models and design tools, the testing of components, and the implementation of the technology. The research performed addressed effectively the most important theoretical and practical issues related to the operation and performance of cryogenic fluid film bearings. Bearing configurations and operating conditions, flow turbulence, fluid inertia, liquid compressibility, thermal effects, and two-phase flow phenomena have been considered in detail.

The research program has been successful in terms of the products (computer programs) released to NASA as well as in the number of accepted technical publications. Five computer codes (*hydrosealt*, *hydroflect*, *hydrotran*, *hydrojet* and *hseal2p*) have been licensed by The Texas A&M University System (TAMUS) to NASA centers and contractors, US Air Force, Rockwell International, Pratt & Whitney, and two US universities. A total of 14 technical papers (10 peer reviewed for journals and 4 conference proceedings) have been published on the archival literature. Most papers were also delivered at prestigious technical meetings like the ASME/STLE Tribology Conferences. In January 1997, Pratt & Whitney will support further work to develop a computational bulk-flow analysis for prediction of the static and dynamic force characteristics of cryogenic fluid hybrid **thrust bearings**.

The computer programs generated are not restricted in their application to cryogenic fluid film bearings and seals. The codes have been validated and tested for analysis of *process fluid* film bearings with mineral oils, water and air (perfect gas) in regimes of operation ranging from laminar flow to turbulent flows, and including the transition zone to fully developed turbulence. The industrial members of the TAMU Turbomachinery Research Consortium have found the programs to be of immediate use for their specific needs in rotordynamic analysis and troubleshooting of rotor-bearing systems.

The motion of a cryogenic fluid within the thin film annular region of a fluid film bearing is described by a set of two-dimensional mass and momentum conservation, and energy transport equations for the bulk-flow fluid velocities, pressure and temperature (or enthalpy), and accompanied by thermophysical state equations for evaluation of the fluid material properties. A perturbation analysis is carried out to separate the flow into equilibrium (zeroth-order) and perturbed (first-order) fields. Zeroth-order equations describe the fluid flow field for a journal static equilibrium position, while first-order linear equations govern the fluid flow for small amplitude journal center radial motions and journal axis conical motions. Solution to the zeroth-order flow field equations provides the bearing flow rate, load capacity, restoring moments, drag torque and power dissipation for a given journal static position. Solution to the first-order equations determines the rotordynamic force and moment coefficients due to journal lateral and angular motions. The analysis and computer codes constitute advanced tools for the design and prediction of cryogenic fluid film hydrostatic journal bearings, damping bearing seals, and cylindrical (rigid and tilting) pad journal bearings with a simple compliant bearing surface.



The thermohydrodynamic analysis for prediction of the static and dynamic force response of variable properties - cryogenic fluid film bearings considers:

**Governing Equations on film lands of bearing:**

- Mass conservation,
- Bulk-Flow momentum in circumferential and axial directions,
- Energy transport equation for mean flow temperature or enthalpy
- Adiabatic or isothermal journal (shaft) and bearing (stator) boundaries, or specified radial heat flow through the bearing shell.
- Realistic boundary conditions including fluid inertia effects at entrance and exit flow regions.

**Governing Equations at rectangular recesses of a hydrostatic bearing:**

- Global mass conservation relating the orifice inlet flow, the flow from recess closure towards or from the film lands, and the rate of accumulation of fluid within the recess volume,
- Global momentum in circumferential direction relating the momentum fluxes from film lands towards or from the recess closure and the inlet momentum flux due to the angled injection.
- Global energy transport equation at bearing recesses with adiabatic heat flow surfaces and mechanical energy dissipation due to journal rotation.

Laminar, laminar to turbulent transition, and fully developed turbulent bulk-flow model on thin film flow configurations.

Turbulent flow closure model: bulk-flow with friction parameters based on Moody's friction factor equations including surface roughness.

Fluid of variable properties, functions of pressure and temperature, with realistic thermophysical equations of state ( NIST standard data base - *miprops*).

**On Phase I (1993)**, the research effort focused on the analysis of single-row, rectangular recess hydrostatic bearings and annular pressure seals. Thermal effects were considered in the fluid film bearing with thermally adiabatic solid surfaces bounding the annular flow region.

**On Phase II (1994)**, the research concentrated on the analysis of single-row and side-by-side two recess row hydrostatic bearings, damping bearing seals, and cylindrical tilting pad and flexure pivot journal bearings. Thermal effects were extended to include radial heat flow through a solid cylinder bearing and an average journal (shaft) temperature. Additionally, the analysis also incorporated a simple bearing elastic structure for the modeling of bending dominated foil film bearings.

The dynamic response of a point mass supported on cryogenic fluid film bearings motions due to specified time-load histories was analyzed. This model provides useful information for prediction of rotor liftoff, synchronous whirl imbalance response, and abnormal shock and maneuvering load transient responses in a cryogenic turbopump supported on fluid film bearings

**On Phase III (1995)**, a bulk-flow analysis and computer program for prediction of the load performance and force coefficients in orifice-compensated hydrostatic bearings with angled injection against shaft rotation were completed. Numerical predictions have been validated with experimental data available from the TAMU Hydrostatic Bearing Test Facility.

**On Phase III - extended (1996)**, the analysis and computer program for two-phase flow in cryogenic fluid damper seals were completed. The computational model predictions have been validated with existing test data from a liquid nitrogen seal which shows two-phase at the seal discharge plane.

The computer programs (products of the research) have been released through the TAMUS Technology Licensing Office. These are briefly listed as:

- a) **hydrosealt** (December, 1993): analysis of annular seals and hydrostatic bearings with rectangular recesses distributed circumferentially on a single-row or a side-by-side double-row. The thermal models include isothermal journal(rotor) and bearing(stator) surfaces, and adiabatic flow through journal(rotor) and bearing(stator) surfaces.
- b) **hydroflect** and **hydrotran** (December, 1994): analysis of single-row or side-by-side, rectangular recess hybrid (hydrostatic / hydrodynamic) bearings, damping bearing seals, and flexure pivot, tilting pad journal bearings. The thermal models include isothermal or adiabatic bearing surfaces, or specified radial heat flow through bearing pad shells. Transient bearing reaction forces, unsteady bulk-flow and the dynamic response of a point mass supported on fluid film bearings are considered on the **hydrotran** code.
- c) **hydrojet** (December, 1995): analysis of rectangular recess hybrid (hydrostatic / hydrodynamic) bearings with angled (from radial to tangential) fluid flow injection.
- d) **hseal2p** (December, 1996): analysis of centered annular damper (seals) with two-phase flow conditions for cryogenic fluids.

The computer programs are supplied with an extensive documentation including a *User's Manual*, a *User's Tutorial*, and an *Examples Handbook* detailing numerical comparisons to available experimental data.

## WORK COMPLETED ON PHASE I OF THE RESEARCH PROGRAM

On Phase I (1993), the thermohydrodynamic analysis of rectangular recess, orifice compensated hydrostatic bearings and annular pressure seals was completed. In addition, the two-dimensional computational flow analysis of a bearing recess with angled injection was undertaken with the collaboration of Dr. D. Hill and Dr. E. Baskharone of Texas A&M University.

Level of completion of research objectives: +100%

### Description of the program **hydrosealt**:

The code includes the following thermal models:

- adiabatic model, i.e. insulated journal and bearing surfaces.
- isothermal journal at specified temperature and insulated (adiabatic) bearing.
- isothermal bearing at specified temperature and insulated journal.
- isothermal journal and bearing surfaces.

The program includes the prediction of the static and dynamic force performance of cylindrical pad journal bearings and pad hydrostatic bearings of arbitrary circumferential arc length and bearing preload. It is noted that this early development was contemplated as an objective for Phase II of the original research proposal. Full details on the analysis and comparison of numerical predictions with experimental results are given on the Annual Research Progress Report (San Andres, 1993).

Fortran 77 program **hydrosealt** calculates

- 1) bearing flowrate or seal leakage,
- 2) friction torque, power dissipation and temperature rise,
- 3) load capacity (fluid film forces and restoring moments),
- 4) 16 complex impedance force coefficients due to dynamic journal center displacements and journal axis rotations. The real and imaginary parts of the impedances correspond to the stiffness and damping coefficients evaluated at a specified excitation frequency,
- 5) stability indicator or whirl frequency ratio for lateral journal motions and equivalent stiffness at threshold speed of instability,

- 6) pressure and temperature fields on the bearing surface, and density and viscosity field variations, within ranges of fluid flow Reynolds numbers and Mach numbers.

for

- isothermal flow with barotropic fluid,
- thermohydrodynamic adiabatic flow and/or isothermal journal and bearing surfaces in the single phase flow regime.

as a function of

- a) rotor (journal) center eccentricity and journal axis misalignment,
- b) inlet specified circumferential pre-swirl velocity distribution.

and the following fluids:

- |                  |  |
|------------------|--|
| 1) parahydrogen, | 2) nitrogen,   |
| 3) oxygen,       | 4) methane,  |
| 5) water,        | 6) oil,  |
| 7) air,          | 12) barotropic liquid (properties a function of pressure solely) |

The *miprops* program from *NIST Standard Reference Database 12* is used to evaluate the material properties of the cryogenic fluids (liquid, vapor or supercritical conditions).

The computer program *hydrosealt* is supplied with an extensive documentation including a *User's Manual*, a *User's Tutorial*, and an *Examples Handbook* detailing numerical comparisons to available experimental data as reported on the Annual Progress Report.

At the NASA Advanced Earth-to-Orbit Propulsion Technology Conference (Huntsville, May, 1994), several technical presentations from Pratt & Whitney, Rockwell Int., SRS, Inc., and Sverdup, referred to *hydrosealt* as a reliable and efficient code for numerical prediction of cryogenic fluid film bearing performance.

## WORK COMPLETED ON PHASE II OF THE RESEARCH PROGRAM

On Phase II (1994), the analysis of cryogenic fluid bearings continued successfully and the following tasks were completed:

- (a) Extension of the thermohydrodynamic analysis and computer program *hydrosealt* to model the following bearing types: tilting-pad hydrodynamic journal bearings, flexure-pivot tilting pad cylindrical bearings (hydrostatic and hydrodynamic, and cylindrical pad bearings with a simple elastic matrix (ideal foil bearing).
- (b) Enhanced thermal model to include radial heat transfer through the bearing (stator).
- (c) Calculation of the unsteady bulk-flow field and fluid film bearing forces, and the transient response of a point mass rotor supported on fluid film bearings.
- (d) Preparation of a literature survey on the subject of two-phase flows and homogeneous - mixture flows in thin-film flow geometries.

Level of completion of research objectives: +100%

The programs released at the end of 1994 are named *hydroflex* and *hydrotran*. Both codes are fully compatible with the *hydrosealt* program. The 1994 programs retain the same calculating options of *hydrosealt* plus the added bearing geometries, and unsteady flow and transient forced bearing response. The analysis and comparison of numerical predictions with experimental results are given on an Annual Research Progress Report (San Andres, 1994).

### Description of the program *hydroflex*

This fortran F77 program calculates the static load and dynamic force coefficients for the following bearing types:

1. hydrostatic bearings with orifice compensation and rectangular recesses (single recess row or side-to-side double recess row),
2. annular pressure seals (damping bearing seals) (cylindrical and multiple-lobe),
3. plain cylindrical hydrodynamic bearings (cylindrical and multiple-lobe),
4. fixed arc hydrodynamic bearings with arbitrary pre-load,
5. tilting-pad journal bearings,
6. flexure-pivot tilting-pad journal bearings (hydrostatic and hydrodynamic),
7. cylindrical pad bearings with a simple elastic matrix (ideal foil bearing).

*hydroflex* includes the following thermal models:

- adiabatic surfaces, i.e. insulated journal and bearing surfaces,
- isothermal journal at specified temperature and insulated (adiabatic) bearing,
- isothermal bearing at specified temperature and insulated (adiabatic) journal,
- isothermal journal and bearing surfaces,
- isothermal journal and radial heat flow through bearing (stator),
- adiabatic journal and radial heat flow through bearing (stator).

Fortran 77 program *hydroflex* calculates

- 1) bearing flowrate or seal leakage,
- 2) friction torque, power dissipation and temperature rise,
- 3) load capacity (fluid film forces and restoring moments),
- 4) 16 complex impedance force coefficients due to dynamic journal center displacements and journal axis rotations. The real and imaginary parts of the impedances correspond to the stiffness and damping coefficients evaluated at a specified excitation frequency,
- 5) stability indicator or whirl frequency ratio for lateral journal motions and equivalent stiffness at threshold speed of instability,
- 6) pressure and temperature fields on the bearing surface, and density and viscosity field variations, within ranges of fluid flow Reynolds numbers and Mach numbers.

for

- isothermal flow with barotropic fluid,
- thermohydrodynamic adiabatic flow and/or isothermal journal and bearing surfaces in the single phase flow regime.

as a function of

- a) rotor (journal) center eccentricity and journal axis misalignment, OR
- b) applied external load to bearing,
- c) inlet specified circumferential pre-swirl velocity distribution.

and the following fluids:

- |                         |                         |
|-------------------------|-------------------------|
| 1) liquid/gas hydrogen, | 2) liquid/gas nitrogen, |
| 3) liquid/gas oxygen,   | 4) liquid/gas methane,  |
| 5) liquid water,        | 6) oil,                 |
| 7) air,                 | 12) barotropic fluid.   |

The program handles the following boundary conditions at the bearing exit planes:

- (1) periodic pressure asymmetry in the axial direction,
- (2) local discharge end seal effects via an orifice like model to simulate wear-ring hydrostatic bearings or annular seals,
- (3) inlet specified circumferential pre-swirl velocity distribution.

The axial clearance functions included are of the type:

- a) uniform,    b) tapered,
- c) stepped, or,    d) arbitrary via spline interpolation.

Cylindrical bearings may be specified as multiple lobe geometries, and bearing pads may have an assembly preload. For (flexure-pivot) tilting-pad journal bearings, pads' mass moment of inertia, flexure web rotational stiffness and damping coefficients are needed for full specification of the bearing geometry.

### Description of program *hydrotran*

The extended Fortran F77 program *hydrotran* predicts the dynamic (transient) force response of a rigid rotor supported on fluid film bearings. The code calculates at each time step of numerical integration the unsteady bulk-flow field and the bearing reaction forces due to prescribed time-varying external loads The transient analysis is restricted to isothermal flows and rigid pad bearings, i.e., the model does not account for transient thermal effects and can not handle the transient dynamics of tilting pad bearings. These restrictions on the code are due to the large computational times required to determine a transient solution with sufficiently small time steps.

The equations of motion solved with appropriate initial conditions are:

$$\mathbf{M} \mathbf{A}_X = \mathbf{F}_X + \mathbf{W}_X(t) \quad \mathbf{M} \mathbf{A}_Y = \mathbf{F}_Y + \mathbf{W}_Y(t) \quad (1)$$

where  $\mathbf{M}$ : rotor point mass [kg],  $\mathbf{W}_X, \mathbf{W}_Y$ : external time dependent loads [N],  $\mathbf{A}_X, \mathbf{A}_Y(t)$ : rotor accelerations [m/s<sup>2</sup>], and  $\mathbf{F}_X, \mathbf{F}_Y$ : fluid film bearing reaction forces [N], functions of the instantaneous journal position and velocity.

The external load cases considered are:

- (1) periodic forcing function,

$$W_X = F_{\text{mag}} \cos(\omega t), \quad W_Y = F_{\text{mag}} \sin(t), \quad \omega \text{ is an excitation frequency [rad/s],}$$

- (2) ramp loading along X direction,

$$W_X = F_{\text{mag}} (t/T) \quad \text{if } 0 < t < T \quad \text{or} \quad W_X = F_{\text{mag}} \text{ if } t \geq T; \quad W_Y = 0$$

- (3) step loading along X direction,

$$W_X = F_{\text{mag}} \text{ for } t \geq 0; \quad W_Y = 0.$$

- (4) rotor weight along X + sudden unbalance forcing function (blade loss simulation),

$$W_X = M \cdot g + F_{\text{unbal}} \cos(\omega t); \quad W_Y = 0 + F_{\text{unbal}} \sin(\omega t), \quad \text{with } F_{\text{unbal}} = M \text{ UNB}_{\text{mag}} [\text{m}] \omega^2$$

- (5) impulse load along Y direction applied over  $t_0$  (secs),

$$W_X = M \cdot g, \quad W_Y = F_{\text{impulse}} e^{-0.5(t/t_0)^2}$$

The Wilson- $\theta$  method is used to perform the numerical integration of the equations of motion (1). A short program (*TWOdof*) uses the (linear) rotordynamic force coefficients at an equilibrium position and calculates an approximate transient response. This program executes much faster than the full numerical nonlinear solution and can be used efficiently for rotors supported on externally pressurized bearings, i.e. bearings which do not show great variation of their force coefficients with the applied load or journal position.

The computer program *hydroflex* and *hydrotran* are supplied with a *User's Manual*, a *User's Tutorial*, and an *Examples Handbook* detailing numerical comparisons to available experimental data as reported on the Annual Progress Report (San Andres, 1994).

## SURVEY ON REQUIRED ADVANCES ON FLUID FILM BEARING ANALYSIS

From September to October, 1994, a survey was carried out to determine appropriate directions for further research on the analysis of fluid film bearings for cryogenic applications. The topics identified were:

- 1) Thermohydrodynamics of two-phase flows in damping bearing seals,
- 2) Hydrodynamics of sonic flow operation,
- 3) Fluid injection opposite to journal rotation in hybrid journal bearings,
- 4) Code for design of hybrid thrust bearings,
- 5) Improved bulk-flow model for internally fed damping bearings

The results of the survey are listed below as:

TOPIC	#1	#2	#3	#4	#5
<u>NASA Marshall SFC</u>					
Pat Valley	1	3	2	6	6
Henry Stenson	2	4	3	1	5
Eric Earhart	3	1	2	4	5
Gary Genge	3	1	2	4	5
Robert Thom / SRS	1	2	1	3	4
<u>NASA Lewis RC</u>					
James Walker	2	4	1	3	5
Robert Hendricks	1	2	-	-	-
<u>US Air Force</u>					
Phillips Lab	1	2	3	6	6
<u>Rockwell Int.,</u>					
Robert Beatty	1	2	4	3	6
<u>Pratt &amp; Whitney</u>					
Phil Pelfrey	3	4	1	2	5
<u>Texas A&amp;M University</u>					
Dara Childs	1	4	2	3	6
Luis San Andres	3	2	1	5	4
<b>RANKING TOTAL</b>	<b>22</b>	<b>31</b>	<b>22</b>	<b>40</b>	<b>57</b>
TOPIC	#1	#2	#3	#4	#5

[lowest ranking (1) indicates greatest interest on the suggested topic while (6) indicates no interest at all].

The results of the survey indicated that the analysis of two-phase flow in damping bearings and the analysis of angled fluid injection against shaft rotation in hydrostatic bearings were the most important to advance the state-of-the-art in the analysis of cryogenic fluid film bearings as reliable mechanical support elements under dynamic operating conditions. It is important to note that the survey was motivated solely by the intention to generate useful research products addressing to the actual (and current) needs of fluid film bearing technology for cryogenic applications.

## WORK COMPLETED ON PHASE III OF THE RESEARCH PROGRAM

On Phase III (1995), the analysis of cryogenic fluid film bearings continued and the following objectives were completed:

- (a) Bulk-flow analysis and computer program for prediction of the dynamic force response of orifice-compensated hydrostatic bearings with angled injection against shaft rotation.
- (b) Analysis and computer program for prediction of the dynamic force response in damper bearings (annular seals) operating under two-phase flow conditions.
- (c) Enhanced friction factor model to include the transition zone from laminar flow to the fully developed turbulent flow regime.

The last objective was not originally established on the statement of work but carried out for completeness in the research.

Level of completion of research objectives: +60%

### **Description of program *hydrojet***

The computer program released at the end of 1995 is named *hydrojet*, and it is fully compatible with the *hydroflex* code. The analysis and comparison of numerical predictions with experimental results are given on the 1995 Annual Research Progress Report (San Andres, 1995). A detailed description of program *hydrojet* is not necessary since (except for the angled injection capability) it is virtually identical to the *hydroflex* program. The motivation for the research follows.

Hydrostatic/hydrodynamic (hybrid) journal bearings handling process fluids have limited dynamic stability characteristics and their application as support elements to high speed flexible rotating systems is severely restricted. Measurements on water hybrid bearings with angled orifice injection have demonstrated improved rotordynamic performance with virtual elimination of cross-coupled stiffness coefficients and null or negative whirl frequency ratios. A bulk-flow model for prediction of the static performance and force coefficients of hybrid bearings with angled orifice injection was advanced in 1995. The analysis reveals that the fluid momentum exchange at the orifice discharge produces a pressure rise in the hydrostatic recess which retards the shear flow induced by journal rotation, and thus, reduces cross-coupling forces. The computational predictions from *hydrojet* are compared with experimental measurements for a 45° angled orifice injection, 5 recess water hydrostatic bearing operating at 10.2, 17.4 and 24.6 krpm and with supply pressures of 4, 5.5 and 7 MPa. The correlations include recess pressures, flow rates, and rotordynamic force coefficients at the journal centered position. An application example for a liquid oxygen hybrid bearing also demonstrates the advantages of tangential orifice injection on the rotordynamic coefficients and stability indicator for forward whirl motions, and without performance degradation on direct stiffness and damping coefficients

### **Analysis of two-phase flow in annular pressure (damper) seals**

Cryogenic fluid damper seals operating close to the liquid-vapor region (near the critical point or slightly sub-cooled) are likely to operate in a two-phase flow region which affects the seal overall performance and reliability. A no-cost extension on the Project until December 1996 allowed the completion of a bulk-flow analysis and computer program for prediction of the dynamic force response in damper bearings (annular seals) operating under two-phase flow conditions.

The analysis of two-phase flow in thin fluid film bearings and seals is complicated due to

- the lack of firm experimental evidence for turbulence closure models in multiple phase flows,
- the existing literature is contradictory and available results depend greatly on the type of flow model used: homogeneous mixture, frothy flow, annular flow, stratified flow, or bubbly mixture,
- very limited theoretical progress on the interaction between phases or mixture components in terms of shear interface stresses and energy transport.

A concentric seal model is considered since it is well known that single phase - seal force coefficients do not vary greatly with the static rotor position. The analysis studies flow regions like all liquid, all vapor, liquid→two phase saturated mixture, vapor→two phase saturated mixture; and including specified two-phase flow conditions at the seal supply. A perturbation analysis for small amplitude rotor motions about the seal centered position renders zeroth and first order bulk-flow equations describing the equilibrium flow and perturbed flow fields. Solution to the zeroth-order equations determines the seal flow rate, drag torque, and mechanical power dissipation. Solution to the first-order equations provides the linear force coefficients due to rotor lateral motions at a specified whirl frequency.

The treatment of the energy transport equation followed two paths leading to two computational models. The first program (and early analysis) solves the energy transport equation given in terms of (a) temperature in the single-phase (all liquid or vapor) regions, and (b) the mixture quality in the two-phase

flow region. The second program solves the energy transport equation in terms of enthalpy in all flow regions (liquid, vapor or two-phase), and determines the fluid temperature or mixture quality as secondary parameters. The results from both zeroth-order programs give nearly identical flow fields, leakage and torque. The two phase region onset and extent within the seal, and as given by the mixture quality field, depends greatly on the grid density and on the accurate satisfaction of inter-phase conditions.

Two programs for solution of perturbed fields and based on energy transport defined by (a) mixture quality and pressure, and (b) enthalpy and pressure were also generated. The programs provide identical force coefficients for the all-liquid or all-vapor seal cases. However, the calculated force coefficients for seals with two-phase conditions show great differences and even opposite trends, with extreme sensitivity to the flow properties (density and viscosity) in two-phase regions with very low (vapor mass content) qualities. Later, the program based on transport of mixture quality was abandoned since it was clear that the discontinuities in this field were the cause for unreliable numerical predictions.

Arauz (1997) in his Ph.D. dissertation details the analysis and computer method (*hseal2p*) for prediction of the forced response of cryogenic fluid damper seals operating under two-phase flow conditions. Computed predictions for leakage and pressure drop have been validated with existing experimental results, from Hendricks (1987) at NASA LeRC, for a nitrogen seal which shows two-phase flow conditions at the exit plane. Flow rates and mixture quality predictions agree with the results given in the literature for a liquid oxygen seal operating over a full range of two-phase flow conditions. The most important effect of two-phase flow on the dynamic forced response of the seals studied occurs when the transition from liquid to mixture takes place within the seal. The large variations in fluid compressibility (and mixture sonic speed) as the transition evolves from all-liquid to a low quality mixture within a short physical zone induce a dramatic change in the rotordynamic force coefficients, namely a rise in direct stiffness and a drop in cross-coupled stiffness. This notable phenomena has been reported earlier in the literature from an experimental seal with a mixture of low gaseous mass content (air in water). Two journal publications have been prepared on the model and are currently under peer review.

### **Description of the program *hseal2p*:**

The flow model includes

- Homogeneous two-phase flow in thermodynamic equilibrium
- Continuous vaporization model, i.e., all-liquid, liquid-vapor, and all-vapor regions within seal.
- Fully developed, turbulent bulk-flow model,
- Centered shaft, i.e. concentric rotor static operation,
- Cryogenic fluids with thermophysical equations of state,
- A mixture viscosity model with rise in viscosity for low quality (small vapor mass content) mixtures,
- Governing Equations at film lands for a saturated homogeneous mixture:
  - Mass conservation,
  - Bulk-Flow momentum in axial and circumferential directions.
  - Energy (enthalpy) transport for mixture with adiabatic wall boundaries (shaft and stator surfaces).
- Turbulence closure model: bulk-flow with friction parameters based on Moody's friction factor equations.

Fortran 77 program *hseal2p* calculates

- 1) seal leakage (flow rate),
- 2) friction torque, power dissipation and discharge temperature rise,
- 3) fluid properties for (two-phase) mixture,
- 4) 4 complex impedance force coefficients due to rotor displacements at the centered position for a set of excitation frequencies,
- 5) pressure, temperature, and mixture quality fields on the seal surface, and mixture sonic speed, density and viscosity variations.



for adiabatic flows in thermodynamic equilibrium, and as a function of the seal geometry, operating conditions and specified circumferential pre-swirl velocity. The program handles seals with the following fluids:

- 1) parahydrogen,
- 2) nitrogen,
- 3) loxygen,
- 4) methane,

## **SCHEDULE OF PROGRAM RELEASES FROM NASA NAG3-1434 PROJECT**

Author of all programs: Dr. Luis San Andres, Texas A&M University System.

The following list is accurate as of December 31, 1996.

<b>Code</b>	<b>Release Date</b>	<b>COMPANY</b>	<b>released to the attention of</b>
hydroseal	6/93	NASA Lewis RC	Mr. James Walker, Space Propulsion Technology
hydroseal	8/93	NASA Marshall SFC	Mr. Robert Thom, Tribology Research
hydroseal	9/93	NASA Marshall SFC	Mr. Mark Darden, Structures & Dynamics
hydroseal	9/93	Edwards Air Force Base	Cpt. Mark Miller, Phillips Laboratory
hydrosealt	02/94	NASA Lewis RC	Mr. James Walker, Space Propulsion Technology
hydrosealt	04/94	NASA Marshall SFC	Mr. Robert Thom, Tribology Research
hydrosealt	04/94	NASA Marshall SFC	Mr. Wayne Bordelon, CFD Research
hydrosealt	06/94	NASA Marshall SFC	Mr. Shawn Fears, CFD Research
hydrosealt	09/94	Edwards Air Force Base	Mr. Eric Schmidt, Phillips Laboratory
hydrosealt	09/94	Pratt & Whitney	Mr. Philip Pelfrey, P&W Government Engines
hydrosealt	10/94	Rockwell, Inc.	Mr. Dave Becht, Rocketdyne
hydroflect/tran	01/95	NASA Lewis RC	Mr. James Walker, Space Propulsion Technology
hydroflect/tran	02/95	Edwards Air Force Base	Mr. Eric Schmidt, Phillips Laboratory
hydroflect/tran	03/95	NASA Marshall SFC	Mr. Robert Thom, Tribology Research
hydroflect/tran	04/95	Pratt & Whitney	Mr. Philip Pelfrey, P&W Government Engines
hydroflect/tran	04/95	Rockwell, Inc.	Mr. Dave Becht, Rocketdyne
hydroflect/tran	08/95	Cleveland State Univ.	Dr. Jerzy Sawicki, Cleveland State University
hydroflect/tran	11/95	MIT	Dr. Kenny Breuer
hydrojet	01/96	NASA Lewis RC	Mr. James Walker, Space Propulsion Technology
hydrojet	03/96	NASA Marshall SFC	Mr. Robert Thom, Tribology Research
hydrojet	08/96	Rockwell	Mr. John Keba, Rocketdyne
hydrojet	10/96	Pratt&WHitney	Mr. Philip Pelfrey, P&W Government Engines
hydroflex PC	11/96	Cleveland State Univ.	Dr. Jerzy Sawicki, Cleveland State University

All program have been transfered via ftp, except those of 1993 (magnetic tape)

## **LIST OF PUBLICATIONS RELATED TO THE RESEARCH**

### **Ph.D. Dissertations**

Arauz, G., "Analysis of Two-Phase Flows in Damper Seals for Cryogenic Turbopumps," Texas A&M University, May 1997.

### **Annual Research Progress Reports**

San Andres, L., "Angled Injection - Hybrid Fluid Film Bearings for Cryogenic Applications, Phase III" Technical Report to NASA Lewis Research Center, NASA Grant NAG3-1434, December 1995.

San Andres, L., "Thermohydrodynamic Analysis of Cryogenic Liquid, Turbulent Flow Fluid Film Bearings, Phase II" Technical Report to NASA Lewis Research Center, NASA Grant NAG3-1434, December 1994.

San Andres, L., "Thermohydrodynamic Analysis of Cryogenic Liquid, Turbulent Flow Fluid Film Bearings," Technical Report to NASA Lewis Research Center, NASA Grant NAG3-1434, December 1993.

#### **Peer reviewed journal publications**

San Andres, L., and D. Childs, 1996, "Angled Injection - Hydrostatic Bearings, Analysis and Comparison to Test Results," accepted for publication at *ASME Journal Of Tribology*, ASME Paper 96-TRIB-10

San Andres, L., 1996, "Transient Response of Externally Pressurized Fluid Film Bearings," accepted for publication at *STLE Tribology Transactions*, Preprint 96-TC-3A-1.

Zirkelback, N., and L. San Andres, 1996, "Bulk-Flow Model for the Transition to Turbulence Regime in Annular Seals," *STLE Tribology Transactions*, Vol. 39, 4, pp. 835-842.

San Andres, L., Yang, Z., and D. Childs, 1996, "Thermal Effects in Liquid Oxygen Hybrid Bearings," *STLE Tribology Transactions*, Vol. 39, 3, pp. 654-662, ( Preprint 95-TC-3A-1).

San Andres, L., "Turbulent Flow, Flexure-Pivot Hybrid Bearings for Cryogenic Applications," 1996 *ASME Journal of Tribology*, Vol. 118, 1, pp. 190-200, (ASME Paper 95-TRIB-14).

San Andres, L., Yang, Z., and D. Childs, 1995, "Turbulent Flow Hydrostatic Bearings: Analysis and Experimental Results," *International Journal of Mechanical Sciences*, Vol. 37, 8, pp. 815-829.

Yang, Z., L. San Andres and D. Childs, 1995, "Thermohydrodynamic Analysis of Process Liquid Hydrostatic Bearings in Turbulent Regime, Part I: The Model and Perturbation Analysis," *ASME Journal of Applied Mechanics*, Vol. 62, 3, pp. 674-678.

Yang, Z., L. San Andres and D. Childs, 1995, "Thermohydrodynamic Analysis of Process Liquid Hydrostatic Bearings in Turbulent Regime, Part II: Numerical Solution and Results," *ASME Journal of Applied Mechanics*, Vol. 62, 3, pp. 679-684.

San Andres, L., 1995, "Thermohydrodynamic Analysis of Fluid Film Bearings for Cryogenic Applications," *AIAA Journal of Propulsion and Power*, Vol. 11, 5, pp. 964-972.

Hill., D., E. Baskharone, and L. San Andres, 1995, "Inertia Effects in a Hybrid Bearing with a 45 degree Entrance Region," *ASME Journal of Tribology*, Vol. 117, 3, pp. 498-505.

San Andres, L., 1995, "Turbulent Flow Foil Bearings for Cryogenic Applications", *ASME Journal of Tribology*, Vol. 117, 1, pp. 185-195, (ASME Paper 94-TRIB-33).

#### **Conference Proceedings - Not reviewed**

San Andres, L., and D. Childs, 1996, "Angled Injection, Turbulent Flow Hybrid Bearings, Comparison to Test Results," Proceedings of the 8<sup>th</sup> Workshop on Instability Problems in Rotating Machinery, Texas A&M University, May.

Yang, Z., L. San Andres, and D. Childs, 1994, "Process Liquid Turbulent Flow Hydrostatic Bearings: Analysis and Tests for Rotordynamic Coefficients," Proceedings of the 4th International IFToMM Rotordynamics Conference, pp. 233-242, Chicago, September.

San Andres, L., and Yang, Z., 1994, "Thermohydrodynamic Analysis of Fluid Film Bearings for Cryogenic Applications," Proceedings of the 6th NASA Conference on Advanced Earth-to-Orbit Propulsion Technology, Huntsville, Alabama, May, NASA CP 3282, Vol. II, pp. 421-430.

San Andres, L., 1994, "Analysis of Arbitrary Recess Geometry Hydrostatic Bearings," Proceedings. of the 6th NASA Conference on Advanced Earth-to-Orbit Propulsion Technology, Huntsville, Alabama, May, NASA CP 3282, Vol. II, pp. 431-441.

**Papers under peer review** (as of December 1996)

Arauz, G., and L. San Andres, "Analysis of Two Phase Flow in Cryogenic Damper Seals. Part I: Theoretical Model," submitted for peer review to *ASME Journal of Tribology*, November, 1996.

Arauz, G., and L. San Andres, "Analysis of Two Phase Flow in Cryogenic Damper Seals. Part II: Model Validation and Predictions," submitted for peer review to *ASME Journal of Tribology*, November, 1996.

**1. "Angled Injection - Hydrostatic Bearings, Analysis and Comparison to Test Results," San Andres, L., and D. Childs, 1996, accepted for publication at ASME *Journal Of Tribology* , ASME Paper 96-TRIB-10**



The Society shall not be responsible for statements or opinions advanced in papers or discussion at meetings of the Society or of its Divisions or Sections, or printed in its publications. Discussion is printed only if the paper is published in an ASME Journal. Authorization to photocopy material for internal or personal use, under circumstance not falling within the fair use provisions of the Copyright Act is granted by ASME to libraries and other users registered with the Copyright Clearance Center (CCC) Transactional Reporting Service provided that the base fee of \$0.30 per page is paid directly to the CCC, 27 Congress Street, Salem, MA 01970. Requests for special permission or bulk reproduction should be addressed to the ASME Technical Publishing Department.

Copyright © 1996 by ASME

All Rights Reserved

Printed in U.S.A.

# Angled Injection—Hydrostatic Bearings Analysis and Comparison to Test Results<sup>1</sup>

Luis San Andres  
Associate Professor.

Dara Childs  
Leland T. Jordan Professor.

Mechanical Engineering Department,  
Texas A&M University,  
College Station, TX 77843

*Hydrostatic/hydrodynamic (hybrid) journal bearings handling process liquids have limited dynamic stability characteristics and their application as support elements to high speed flexible rotating systems is severely restricted. Measurements on water hybrid bearings with angled orifice injection have demonstrated improved rotordynamic performance with virtual elimination of cross-coupled stiffness coefficients and null or negative whirl frequency ratios. A bulk-flow model for prediction of the static performance and force coefficients of hybrid bearings with angled orifice injection is advanced. The analysis reveals that the fluid momentum exchange at the orifice discharge produces a pressure rise in the hydrostatic recess which retards the shear flow induced by journal rotation, and thus, reduces cross-coupling forces. The predictions from the model are compared with experimental measurements for a 45 deg angled orifice injection, 5 recess, water hydrostatic bearing operating at 10.2, 17.4, and 24.6 krpm and with supply pressures of 4, 5.5 and 7 MPa. The correlations include recess pressures, flow rates, and rotordynamic force coefficients at the journal centered position. An application example for a liquid oxygen hybrid bearing also demonstrates the advantages of tangential orifice injection on the rotordynamic coefficients and stability indicator for forward whirl motions, and without performance degradation on direct stiffness and damping coefficients.*

## Introduction

The importance of hybrid (combination hydrostatic and hydrodynamic) journal bearings as support elements in cryogenic turbomachinery has steadily grown over the past few years. Hybrid journal bearings (HJBs) enable smaller and lighter turbopumps through no bearing DN life limitation and no sub-critical rotor operation. HJBs have durability, low friction and wear, accuracy of positioning, and large direct stiffness and damping force coefficients. The growth of an "all-fluid-film-bearing" technology for advanced and less expensive (per launching cost) turbopumps demands the development of analytical models and design tools, the testing of components, and the implementation of the technology (Pelfrey, 1995).

Primary power cryogenic turbomachinery operates at high speeds and produces large fluid pressure rises (max. 30 MPa). These typical operating conditions determine the flow in the supporting fluid film bearings to be fully turbulent with dominance of fluid inertia and thermal transport effects. San Andres (1990–5) provides bulk-flow analyses and computational pro-

grams for the calculation of cryogenic bearing performance and rotordynamic force coefficients. Measurements of bearing rotordynamic force coefficients and load performance are routinely performed at a high-speed Hydrostatic Bearing Test Facility (HBTF) (Childs and Hale, 1994). Tests have been conducted with water on over 30 hybrid journal bearings and damper seals with rotational speeds ranging from 10 to 25 krpm and pressure differentials from 4 to 7 MPa (Childs and Hale, 1994), Kurtin et al. (1993), Franchek et al. (1994–5), Mosher and Childs (1995), and Yang et al. (1995) report extensive experimental data for the static performance characteristics of a 5 recess HJB for the operating conditions noted and three different bearing clearances (76 to 127  $\mu\text{m}$ ). These studies show bulk-flow model calculations to correlate favorably with the experimental results. Accurate predictions depend greatly on the knowledge of the bearing operating clearances, and most importantly, on the orifice discharge coefficients. The references cited along with San Andres (1995a) also discuss the sensitivity of the computed predictions to variations in the input empirical parameters.

Despite the many advantages offered by HJBs, hydrodynamic and "pneumatic hammer" stability limits and two-phase flow operation are issues of primary concern for high speed operation with large pressure differentials. Fluid vaporization is possible since the cryogenic liquid enters the bearing (or seal) at conditions close to its saturation temperature. "Pneumatic hammer" effects are avoided by appropriate selection of the flow restrictor, by designing bearing recesses with small volumes, and

<sup>1</sup> This work was funded by grant NAG3-1434 from NASA Lewis Research Center, Project Thermohydrodynamic Analysis of Cryogenic Liquid Turbulent Flow Fluid Film Bearings, Mr. James Walker—Contract Monitor.

Contributed by the Tribology Division of THE AMERICAN SOCIETY OF MECHANICAL ENGINEERS for presentation at the ASME/STLE Joint Tribology Conference, San Francisco, Calif., October 13–17, 1996. Manuscript received by the Tribology Division January 5, 1996; revised manuscript received May 20, 1996. Paper No. 96-Trib-10. Associate Technical Editor: J. Frenc.

Copies will be available until March 1998.

by restricting bearing operation to flow conditions where the pressure differential is a small fraction of the liquid bulk modulus (Redecliff and Vohr, 1969).

The stability of a simple rotor-bearing system is defined by its threshold speed and the whirl frequency ratio (WFR). This instability is due to the effect of journal rotational speed on the bearing flow field. The threshold speed corresponds to the rotor speed at which a bearing is deprived from its effective damping and any small perturbation from an equilibrium position will determine unbounded rotor motions. The WFR denotes the ratio between the onset whirl frequency (typically the system first critical speed) and the threshold speed of instability. Plain journal bearings show a WFR equal to 0.50 for small to moderate operating eccentricities (light loads), and thus instability at a rotational speed equal to twice the system first critical speed is likely to occur. Measurements in hybrid bearings verify closely the theoretical WFR prediction. In some circumstances the WFR even increases above 0.50, in particular for low rotational speeds and large supply pressures (Franchek, 1992; Franchek et al., 1995).

The WFR = 0.50 condition limits severely the application of HJBs to high speed, light weight turbomachinery, and thus, the research has concentrated on conceiving hybrid bearings with improved stability and without loss in centering stiffness and damping ability. Some of the technological advances have been the natural outcome of analysis and engineering design, while others follow empirical evidence and past experience when a mathematical model is yet to be crafted. Other recommended fixes to improve the hydrodynamic stability of hybrid bearings by reducing or eliminating the WFR are the following:

- Use of machine roughened bearing surfaces to decrease the cross-coupled stiffness coefficients. Test results show a rough knurled-pattern HJB to have WFR as low as 0.30 but with a reduced load capacity and direct stiffness when compared to a smooth surface HJB (Franchek, 1992).
- Use of circumferentially asymmetric pad bearings and recesses to produce enough anisotropy on the rotordynamic force coefficients. Measurements and analysis for an engineered two pad HJB validated the concept (San Andres, 1995b). However, this bearing configuration is highly sensitive to the direction of applied static loads.
- Use of flexure-pivot, tilting pad HJBs or compliant surface (foil) journal bearings due to their inherent stability. San Andres (1995c, 1996) discusses at length these concepts and evaluates their potential for cryogenic uses. Flexure-pivot HJBs constitute a novel alternative and full-scale testing is being planned. Foil bearings have also demonstrated their performance in cryogenic turbomachinery (Genge et al., 1993). The current foil bearing technology allows only for specific loads applicable to secondary power cryogenic turbopumps. The interested reader should recall the cited references for further details.
- Use of hybrid bearings with angled liquid injection opposing journal rotation to reduce the development of the circumferential flow velocity and with virtual elimination of cross-coupled stiffness coefficients. This concept has lacked firm theoretical modeling though it has proved successful in some applications (Tondl, 1967; Brown

## Nomenclature

$A_n = C_d \pi d_n^2 / 4$ . Effective orifice area [m<sup>2</sup>]  
 $b$  = recess circumferential length [m]  
 $C$  = radial clearance function [m]  
 $C_p$  = fluid specific heat [J/kg·°K]  
 $C_{xx}, C_{xy}, C_{yx}, C_{yy}$  = damping force coefficients [Ns/m]  
 $C_d$  = orifice discharge coefficient  
 $D = 2 \cdot R$ . Bearing diameter [m]  
 $d_n$  = orifice diameter [m]  
 $f_{j,b} = a_M \{ 1 + [c_M(r_{j,b}/H) + (b_M/R_{j,b})]^{e_M} \}$ ;  $a_M = 0.001375$   $b_M = 500,000$ ;  $c_M = 10,000$   $e_M = 1/3.00$  turbulent flow friction factors at journal and bearing surfaces  
 $e_x, e_y$  = journal center eccentricity components [m]  
 $F_x, F_y$  = bearing fluid film forces along {X, Y} axes [N]  
 $h_x, h_y = \cos(\Theta), \sin(\Theta)$   
 $H = C + e_x(t) \cos(\Theta) + e_y(t) \sin(\Theta)$ . Film thickness [m]  
 $H_r$  = recess depth [m]  
 $H_e$  = effective film depth for rough surface bearing [m]

$K_{xx}, K_{xy}, K_{yx}, K_{yy}$  = bearing force stiffness coefficients [N/m]  
 $L, l$  = bearing axial length, recess axial length [m]  
 $M_{xx}, M_{xy}, M_{yx}, M_{yy}$  = bearing inertia force coefficients [kg]  
 $P, P_r, P_s$  = fluid pressure, recess pressure, supply pressure [N/m<sup>2</sup>]  
 $Q_m = (\rho V_n A_n)$ . Flow rate across orifice [kg/s]  
 $Re = (\rho \cdot \Omega \cdot C \cdot R / \mu)_n$ . Nominal circumferential flow Reynolds number  
 $R_j, R_b = (\rho / \mu) H \times \sqrt{[(U_x - \Omega \cdot R)^2 + U_y^2]} / (\rho / \mu) H \times \sqrt{[U_x^2 + U_y^2]}$ ; flow Reynolds numbers relative to journal and bearing surfaces  
 $r_j, r_b$  = roughness depths at journal and bearing surfaces [m]  
 $t$  = time [s]  
 $T, T_s$  = temperature, supply temperature [°K]  
 $U_x, U_y$  = bulk-flow velocities in circ. (x) and axial (y) directions [m/s]  
 $V_n$  = fluid velocity through recess orifice [m/s]

$V_r$  = recess volume including supply line [m<sup>3</sup>]  
 $W_x, W_y$  = external loads applied on journal [N]  
 $x, y$  = coordinate system on plane of bearing [m]  
 $X, Y$  = inertial coordinate system [m]  
 $\beta_p = (1/\rho)(\partial \rho / \partial P)$ . Liquid compressibility coefficient [m<sup>2</sup>/N]  
 $\beta_T = -(1/\rho)(\partial \rho / \partial T)$ . Liquid volumetric expansion coefficient [1/°K]  
 $\delta$  = angle of injection on orifice of recess [rad]  
 $\Delta p_n$  = hydrodynamic pressure rise within recess [N/m<sup>2</sup>]  
 $\Delta p_m$  = recess pressure drop due to momentum exchange [N/m<sup>2</sup>]  
 $\Theta = x/R$ . Circumferential or angular coordinate  
 $\kappa_y = \kappa_x = \frac{1}{2}(\kappa_j + \kappa_b)$ . Turbulence shear factors in (y, x) flow directions  
 $\kappa_j, \kappa_b = f_j \cdot R_j, f_b \cdot R_b$ . Turbulent shear parameters at journal and bearing surfaces  
 $\rho, \mu$  = fluid density [kg/m<sup>3</sup>], viscosity [Ns/m<sup>2</sup>]

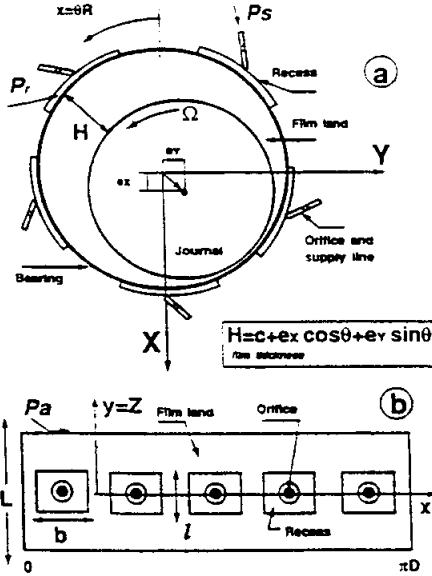


Fig. 1 Geometry of an orifice compensated—angled injection hybrid bearing (HJB)

and Hart, 1986). Experimental measurements for a 5 recess water HJB demonstrate that angled injection aids in reducing the whirl frequency ratio without decreasing the bearing centering stiffness and load capacity (Franchek, 1992; Franchek and Childs, 1995).

The thermohydrodynamic analysis of real properties, hybrid bearings with angled orifice injection is advanced. The objective is to develop a model able to predict reliably the performance of angled injection HJBs in lieu of their favorable (measured) rotordynamic performance. The motion of a fluid through the thin film lands is governed by mass, momentum and energy transport equations for the bulk-flow velocities, pressure and temperature, along with thermophysical state equations for evaluation of the cryogen material properties. The turbulent bulk-flow is modeled with simple friction coefficients and include effective film depths to accommodate for macroscopic surface roughness. A simple analysis for the angled injection— orifice flow reveals that the fluid momentum exchange produces a pressure rise in the recess which retards the shear flow induced by journal rotation. The numerical predictions from the model are correlated extensively with the experimental data of Franchek (1992).

### Analysis

Figure 1 shows the geometry of a hybrid (combination hydrostatic/hydrodynamic) journal bearing and the relevant nomenclature. A liquid at high pressure ( $P_s$ ) and inlet temperature ( $T_s$ ) is supplied (radially or angled) through orifice restrictors and impinges into the bearing recesses with a mean pressure

( $P_r$ ). The pressure field within the recesses is determined from flow continuity with the film lands, momentum exchange at the orifice plane and a viscous rise due to journal rotation. At the recess edges, an inertial pressure drop also occurs due to the sudden transition from the recess of depth ( $H_r$ ) into the film lands of thickness ( $H$ ). Past the recesses, the liquid then flows through the film lands and the pressure drops to the discharge value ( $P_a$ ).

**Equations of Flow on the Bearing Film Lands.** On the thin film lands flow turbulence, fluid inertia and compressibility effects are important. The model then assumes a fully developed turbulent bulk-flow of a fluid whose material properties depend on its local thermophysical state of pressure and temperature. The equations of mass, axial and circumferential momentum, and adiabatic-flow energy transport for the bulk-flow velocities, pressure and temperature in the bearing film lands are given as (Yang et al., 1995; Kleynhans and Childs, 1995):

$$\frac{\partial}{\partial t}(\rho H_r) + \frac{\partial}{\partial y}(\rho H U_y) + \frac{\partial}{\partial x}(\rho H U_x) = 0 \quad (1)$$

$$-H \frac{\partial P}{\partial y} = \frac{\mu}{H} \left\{ \kappa_y U_y \right\} + \frac{\partial(\rho H_r U_y)}{\partial t} + \left\{ \frac{\partial(\rho H U_y U_y)}{\partial y} + \frac{\partial(\rho H U_y U_x)}{\partial x} \right\} \quad (2)$$

$$-H \frac{\partial P}{\partial x} = \frac{\mu}{H} \left\{ \kappa_x U_x - \kappa_r \frac{\Omega R}{2} \right\} + \frac{\partial(\rho H_r U_x)}{\partial t} + \left\{ \frac{\partial(\rho H U_x U_y)}{\partial y} + \frac{\partial(\rho H U_x U_x)}{\partial x} \right\} \quad (3)$$

$$C_p \left\{ \frac{\partial}{\partial t}(\rho H_r T) + \frac{\partial}{\partial x}(\rho H U_x T) \right\} = \beta_r H T \left\{ \frac{\partial P}{\partial t} + U_x \frac{\partial P}{\partial x} \right\} + \Omega \cdot R \frac{H}{2} \frac{\partial P}{\partial x} + \frac{\mu}{H} \left\{ \kappa_x \left( U_x^2 + U_y^2 + \frac{1}{2} \Omega \cdot R \cdot U_x \right) + \kappa_r \Omega R \left( \frac{1}{4} \Omega R - U_x \right) \right\}_{\sigma=x,y} \quad (4)$$

Please refer to the Nomenclature for a description of all variables.  $\kappa_x = \kappa_r = (k_f + k_g)/2$  are the wall shear stress parameters determined as local functions of turbulent friction factors which depend on the bearing and journal surface conditions and the flow Reynolds numbers relative to the rotating ( $R_j$ ) and stationary ( $R_s$ ) surfaces, i.e.  $\kappa_f = f_f \cdot R_j$ ,  $\kappa_g = f_g \cdot R_s$  (Hirs, 1973). The cryogenic liquid properties are extracted from the Benedict-Web-Rubin equation of state as given in the standard data base of McCarty (1986).

The fluid pressure at the sides of the bearing ( $y = \pm L/2$ ) equals the discharge or ambient pressure ( $P_a$ ). At the interface

### Nomenclature (cont.)

$\xi_{in}, \xi_{ed}$  = empirical recess-edge entrance loss coefficients in circumferential (upstream, downstream) direction

$\xi_v$  = empirical recess-edge entrance loss coefficients in axial direction

$\Omega, \omega$  = rotational speed of journal, excitation or whirl frequency [1/s]

### Subscripts

$x, y$  = in direction of local circumferential and axial coordinates inplane of bearing

$o$  = orifice

$r, e$  = bearing recesses and edges (entrance)

$u, d$  = upstream and downstream of recess

$B, J$  = refer to bearing and journal surfaces

with the bearing recesses, continuity of flow and pressure must be attained as detailed below.

**Angled Injection—Recess Flow and Pressure Equations.** Figure 2(a) depicts a hydrostatic bearing recess (or pocket) with axial length ( $l$ ) and circumferential extent ( $b$ ). The figure shows the direction of the journal surface speed ( $\Omega \cdot R$ ), and relative to this velocity the recess is divided into upstream ( $u$ ) and downstream ( $d$ ) regions. The fluid supply orifice port with injection angle ( $\delta$ ) is located at a distance  $b_u$  from the upstream recess edge. The orifice has an effective area  $A_o$ , normal to the feed speed  $V_o$ . Radial fluid supply is indicated by  $\delta = 0$  while a tangential feed opposite to journal rotation is given by  $\delta = \pi/2$  (90 deg).

Conventional analysis of hydrostatic bearings do not calculate the flow field within the recess since these are typically deep and enclose large and nearly stagnant fluid volumes. Analysis then accounts only for flow continuity with the film lands and determines a (uniform) recess pressure using the standard orifice equation with a discharge coefficient. The complexity of the flow field in hydrostatic pockets has been discussed by Hill et al. (1995) and Braun et al. (1993, 1995) with the aid of two-dimensional computational fluid mechanics analyses. Numerical results reveal the generation of hydrodynamic pressures within the pocket and followed by sharp inertial pressure drops at the recess edges. This field of study is of utmost importance for the development of a mature technology on hybrid bearings for cryogenic applications.

The analysis of angled injection—hydrostatic pockets follows here a simplified approach which intends to be of practical use without resorting to computationally intensive three dimensional flow calculations. The flow model is evidently crude yet it grasps the fundamental mechanisms of pressure generation within the bearing pockets. The favorable correlation with hybrid bearing experimental performance characteristics given later justifies the method used.

A mass conservation equation at each bearing recess of area ( $l \cdot b$ ) and depth  $H$ , is defined by the global balance between the mass flow through the orifice restrictor ( $Q_m$ ), the mass flow into the film lands and the time rate of change of liquid mass within the recess and supply line volume ( $V_r$ ), i.e.,

$$Q_m = \rho_r A_o V_o = \int_{\Gamma_r} [\rho H \vec{U} \cdot \vec{n}] d\Gamma_r + \frac{\partial}{\partial t} (\rho_r V_r) \quad \text{for } r = 1, 2, \dots, N_{\text{recess}} \quad (5)$$

where  $A_o = C_d \pi d_o^2 / 4$  is the effective orifice area with  $C_d$  as an empirical discharge coefficient.  $\Gamma_r$  denotes the closure of the recess with the film lands and has a normal  $\vec{n}$  along the boundary line. At the orifice discharge plane, the mean recess pressure is denoted by  $P_r$  (see Fig. 2(b)) and given from Bernoulli's equation as:

$$(P_r - P_s) = \left(\frac{1}{2}\right) \rho_r V_o^2 \quad (6)$$

Computational fluid mechanics analysis reveals that the axial pressure within the recess is (to a first approximation) practically uniform. Hence, modeling of the flow in the pocket as a one-dimensional bulk-flow bearing determines that the pressure difference (downstream-upstream) on a recesses is given by two contributions:

(a) a viscous pressure rise ( $\Delta P_v$ ) due to shear flow induced by journal rotation (San Andres, 1992):

$$\Delta P_v = [P_d - P_u]_v = \mu_r \kappa_r \frac{b}{H_r^2} \left( \frac{\Omega \cdot R}{2} - U_{rx} \right) \quad (7)$$

(b) a pressure drop ( $\Delta P_m$ ) at the orifice injection plane

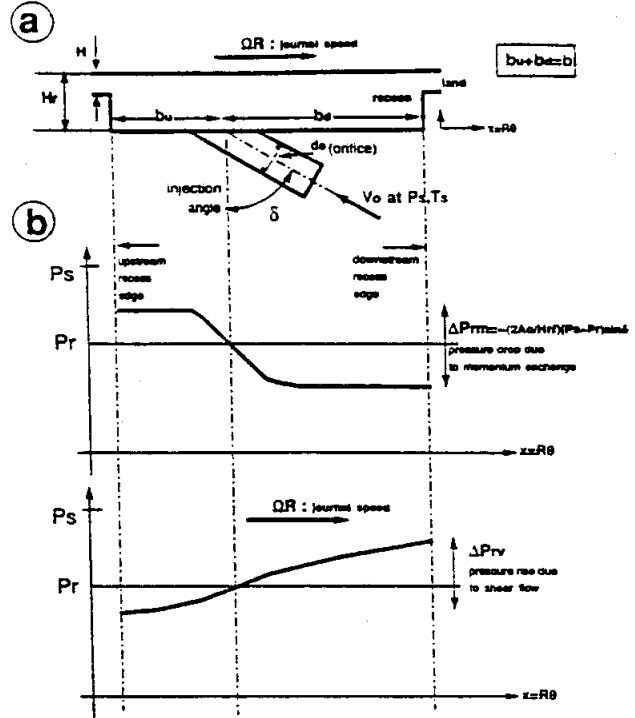


Fig. 2 (a) Description of hydrostatic recess with angled injection (b) Assumed pressure field within hydrostatic recess

and due to the exchange of fluid momentum, and simply stated as:

$$\begin{aligned} \Delta P_m &= [P_d - P_u]_m = - \frac{Q_m V_o \sin(\delta)}{H_r \cdot l} \\ &= - \frac{2 A_o}{H_r \cdot l} (P_s - P_r) \sin(\delta) \end{aligned} \quad (8)$$

where the orifice equation (6) has been used on the right hand side of Eq. (8). Note that for radial injection ( $\delta = 0$ ) there is no momentum pressure drop at the supply port, while the largest pressure drop occurs for large pressure differentials ( $P_s - P_r$ ) and tangential injection ( $\delta = 90$  deg). For simplicity the pressure field within the hydrostatic pocket is then taken as linear and combines the two pressure differences as shown pictorially in Fig. 2(b). Note that this simplification avoids the calculation of the complex flow field on the entire bearing recess.

Finally, the entrance pressures ( $P_e$ ) to the film lands in the circumferential (upstream and downstream) and axial directions are given by (San Andres, 1992):

$$[P_e]_{u,d} = \left[ P_r - \frac{\rho_r}{2} (1 + \xi_{u,d}) U_{rx}^2 \right]_{u,d} \quad (9a)$$

$$P_e = P_r - \frac{\rho_r}{2} (1 + \xi_u) U_{rx}^2 \quad (9b)$$

These equations are used only when fluid flows from the recess towards the film lands. Details of energy transport at the recesses are given by Yang et al. (1995).

**Perturbation Analysis.** Consider the motion of the journal as the superposition of small amplitude periodic motions of frequency ( $\omega$ ) around a static equilibrium position. That is, the journal center displacements are given as

$$e_x(t) = e_{x_0} + \Delta e_x e^{i\omega t}, \quad e_y(t) = e_{y_0} + \Delta e_y e^{i\omega t}; \quad i = \sqrt{-1} \quad (10)$$



The magnitudes of the dynamic perturbations in journal displacements are small, i.e.,  $|\{\Delta e_x, \Delta e_y\}| \ll C$ . The film thickness ( $H$ ) can then be regarded as the superposition of a steady-state ( $H_s$ ) and dynamic components given by the real part of the following expression:

$$H = H_s + \{\Delta e_x h_x + \Delta e_y h_y\} e^{i\omega t} \quad (11)$$

where  $H_s = C(y) + e_{x0} h_x + e_{y0} h_y$ ; and  $h_x = \cos(\theta)$ ,  $h_y = \sin(\theta)$ .

The flow field variables ( $U$ ,  $U$ ,  $P$ ,  $T$ ), as well as the fluid properties ( $\rho$ ,  $\mu$ ) and the shear parameters ( $\kappa_x$ ,  $\kappa_y$ ) are also formulated as the superposition of zeroth-order and first-order complex fields describing an equilibrium for steady-state flow, and the perturbed condition for small amplitude dynamic journal motions, respectively. In general, these fields are expressed as:

$$\Psi = \Psi_s + \{\Delta e_x \Psi_x + \Delta e_y \Psi_y\} e^{i\omega t} \quad (12)$$

Substitution of Eqs. (11) and (12) into the flow Eqs. (1)–(9) renders zeroth- and first-order equations for determination of the steady-state and perturbed flow-fields. These equations are not reproduced here for brevity but can be found in their full extent in the reference of San Andres (1993). The bearing static and dynamic force characteristics are evaluated once a solution to the flow equations is obtained. Fluid film forces ( $F_x$ ,  $F_y$ ) and force coefficients (stiffness  $K_{\alpha\beta}$ , damping  $C_{\alpha\beta}$  and inertia  $M_{\alpha\beta}$ ) are calculated by integration of the pressure fields over the journal surface. The appropriate formulas are:

$$F_\alpha = \int_0^L \int_0^{2\pi} P_\alpha h_\alpha R \cdot d\Theta \cdot dy; \alpha = X, Y \quad (13)$$

$$K_{\alpha\beta} - \omega^2 M_{\alpha\beta} + i\omega C_{\alpha\beta} = \int_0^L \int_0^{2\pi} P_\beta h_\alpha R \cdot d\Theta \cdot dy; \alpha, \beta = X, Y \quad (14)$$

**Numerical Method of Solution.** The control-volume method of Launder and Leschziner (1978) is used to solve the differential equations of motion. Staggered grids containing control volumes for the primitive flow variables (circumferential and axial velocity, pressure and temperature) cover the flow domain. Algebraic difference equations are derived on each control volume for the conservation of mass, axial and circumferential momentum, and balance of energy. A pressure correction equation is derived using the SIMPLEC procedure of Van Doormaal and Raithby (1984). A Newton-Raphson scheme is also used for satisfaction of the recess mass flow constraint. Full descriptions on the accuracy and parameter sensitivity of the method as applied to hybrid bearings and annular pressure seals are given in past publications (San Andres, 1990–1995). The interested reader should consult the cited references for a detailed exposition of the numerical method used.

### Comparisons to Test Results From a Water 5-Recess Hybrid Bearing

Franchek (1992) presents an experimental study of five hybrid bearings with distinctive geometrical configurations. These are namely, smooth bearings with radial injection and rectangular (baseline), triangular and circular recesses, a knurled rough-surface bearing with rectangular recesses, and a smooth surface bearing with rectangular recesses and a 45 deg angled orifice injection. The tests consisted of the measurement of load versus journal eccentricity, torque and flow rate, and the identification of rotordynamic force coefficients. Childs and Hale (1994) provide a full description of the test apparatus and the experimental procedure. The nominal test conditions include:

- (a) 3 rotational speeds: 10.0, 17.4 and 24.6 krpm
- (b) 3 supply pressures: 4.0, 4.5 and 7.0 MPa (600, 800 and 1000 psig)

- (c) 6 journal eccentricity ratios ( $e/c$ ): 0.0 to 0.5 at a fluid supply temperature of 55°C (130°F).

Franchek and Childs (1994) and Franchek et al. (1995) report the measurements with comparisons to predictions for the radial injection bearing (conventional design). These references also include the precision and experimental uncertainty of the measured flow rates, recess pressures and identified rotordynamic coefficients. Details of these studies are omitted for brevity. Table 1 describes the geometry of the test bearing with angled (45 deg) injection. At the journal centered position the measured data for flow rate, supply and average recess pressures and operating clearance is also given. From these values, empirical orifice loss coefficients ( $C_d$ ) are estimated for each test condition and used in all computations including journal off-centered operations. The values of circumferential ( $Re_c$ ) and axial flow Reynolds ( $Re_a$ ) numbers demonstrate the character of the flow within the test bearing. San Andres (1995d) reports detailed comparisons of predictions and test results for both radial and angled (45 deg) injection hybrid bearings. Selected experimental measurements along with predictions from the model follow.

Franchek et al. (1995) and San Andres (1995a) give sensitivity analysis of the numerical predictions to changes in the empirical factors, namely the orifice discharge coefficient ( $C_d$ ) and the entrance loss coefficients ( $\xi_{e,x}$ ). The analysis involved changing an input parameter by  $\pm 10\%$  from its estimated experimental value for each operating condition while the other parameters were kept invariant. The maximum difference between the numerical prediction and experimental value for each case was then compared with the maximum difference from the original results. A relative sensitivity of 1.0 then indicates a 10% change in maximum error associated with the 10 percent change in the input parameter. The studies determined the flow rate and direct stiffness coefficients to be particularly sensitive to changes in the orifice discharge coefficient ( $C_d$ ) and much less sensitive to variations in the entrance loss coefficients. Maximum sensitivities for the rotordynamic coefficients are 1.9 for direct stiffness, 0.4 for cross-coupled stiffness, 0.1 for direct damping, and 0.4 for whirl frequency ratio. These results then suggest the need to extract close estimates for the  $C_d$  coefficient based on actual measurements of bearing flow rate and pressure drop across the orifice restrictors.

**Static Performance Characteristics of Angled Injection Bearing.** Figure 3 depicts the journal eccentricity versus applied load ( $W_x$ ) at a nominal supply pressure of 7.0 MPa and three rotational speeds. The journal eccentricity increases linearly with the applied load as is typical in externally pressurized bearings. The predictions correlate very well with the measurements and also demonstrate that the stiffness coefficients for the bearing will not vary (greatly) with the journal center position. Figure 4 shows the predicted journal center loci as the load increases. Note the negative attitude angle at the lowest speed (10.2 krpm), an almost null angle at the medium speed (17.4 krpm), and a positive angle at the highest speed (24.6 krpm). Test results are not shown since these were not included by Franchek (1992). The predictions reveal the fundamental effect of angled injection on the bearing static load performance. Engineering design could then lead to a hybrid bearing free of cross-coupling effects with the appropriate combination of injection angle, supply pressure and operating speed.

Figure 5 depicts the recess pressure ratios  $\{(P_r - P_a)/(P_s - P_a)\}$  at the journal concentric position for the three nominal supply pressures and speeds. Recess pressure ratios rise with the journal speed and decrease with supply pressures since land flow resistance and turbulence are greater. The correlations with the model predictions are good except at the largest speed and lowest supply pressure and at the lowest speed with largest pressure supply. Note that the comparisons have been made with averaged test recesses pressures. Actual measured recess

**Table 1 Description of water lubricated orifice compensated hybrid bearing tested by Franchek and Childs (1994)**

No of recesses (Nrec)	5
Clearance nominal ( $C$ )	125.4 $\mu\text{m}$ (0.005 in)
Diameter ( $D$ )	76.2 mm (3 in)
Length ( $L$ )	76.2 mm (3 in)
Land roughness (peak-peak)	0.33 $\mu\text{m}$ (13 $\mu\text{in}$ )

Recess dimensions: square ( $l$ ) 27 mm  $\times$  ( $b$ ) 27 mm  $\times$  254  $\mu\text{m}$  (depth); Supply volume  $V_s = 0.1289 \text{ dm}^3$

Orifice at midplane of recess: diameter  $d = 2.49 \text{ mm}$ , angled injection ( $\delta = \pi/4$  [45°])

Lubricant: water at  $T_s = 328.3^\circ \text{K}$

Viscosity ( $\mu$ ) 0.4929E-3 Pa.s

Density ( $\rho$ ) 986.26 kg/m<sup>3</sup>

Discharge pressure  $P_a$ : 0.0 MPa (0 psig)

Empirical parameters:

Entrance loss factors  $\xi_r, \xi_s = 0.0$

**Test conditions and estimated parameters at centered operation**

Speed Kcpm	$P_s$ MPa	$C$ $\mu\text{m}$	Flow lt/min	$P_{r_{ave}}$ MPa	$C_d$	$Re_c$ ( $\rho\Omega R c/\mu$ )	$Re_a$ ( $Q_0/\rho D\mu$ )
10.2	4.133	122.8	79.94	1.128	0.700	9,988.0	11,136.0
	5.519	124.4	92.21	1.252	0.680	10,129.1	12,845.6
	6.877	124.9	102.29	1.434	0.660	10,169.8	14,249.9
17.4	4.154	120.5	79.60	1.866	0.800	16,737.3	11,088.3
	5.521	121.5	91.67	2.148	0.763	16,876.2	11,088.9
	6.846	122.7	101.75	2.316	0.726	17,042.0	14,174.0
24.6	4.135	119.4	78.07	2.424	0.907	23,447.2	10,875.8
	5.532	120.8	92.21	2.870	0.859	23,722.0	12,942.4
	6.844	117.1	101.38	3.206	0.808	23,000.0	14,123.0

(\*)  $C_d$  values estimated from measured flow rate and average recess pressures.

pressures vary as much as thirteen percent from the calculated (experimental) average. Figure 6 shows the predicted flow rates to agree with the measurements at the medium speeds (17.4 krpm). The discrepancies at the lowest and highest speeds are attributed to the larger predicted recess pressures.

**Dynamic Performance Characteristics at Journal Centered Position.** The test results and numerical predictions demonstrate that the rotordynamic force coefficients are practically insensitive to the applied load for journal eccentricities to 50 percent of the bearing clearance. Hence, in the following, only force coefficients at the concentric position are presented.

The whirl frequency ratio (WFR), a stability indicator of paramount importance for the application of hybrid bearings to high speed applications, is depicted in Fig. 7. Although not shown here, the radial bearing presents a (measured) WFR ranging from 0.60 to 0.48 for most operating conditions (Franchek, 1992). On the other hand, the angled (45 deg) injection bearing shows a (large) negative WFR at the lowest

speed and raising to the 0.5 limit as the rotational speed increases. The numerical predictions agree well with the measurements at the middle and high speeds, i.e. 17.4 and 24.6 krpm. Note that the advantages of angled injection are then lost as the journal speed increases and determines dominance of hydrodynamic effects over hydrostatic effects.

Figure 8 depicts the cross-coupled stiffness coefficients ( $K_{xy} = -K_{yx}$ ) as the journal speed increases for the three nominal supply pressures. In the radial injection bearing, the cross-coupled stiffness are always positive and increase with the journal speed (Franchek et al., 1995). On the other hand, the angled injection bearing presents negative cross-coupled coefficient at the lowest speed. From a rotordynamics point of view this is a desirable occurrence since then these coefficients render forces opposing the development of forward whirl motions. The numerical predictions show the same trends as the measurements but do not agree well with the measurements.

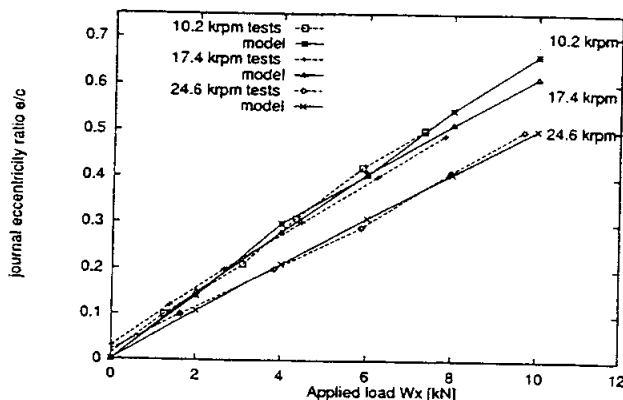


**Fig. 3 Journal eccentricity versus applied load  $W_x$  for angled injection HJB,  $P_s = 7.0 \text{ MPa}$**

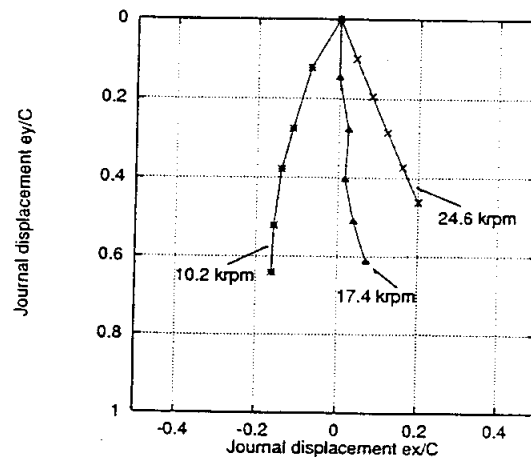


**Fig. 4 Journal center locus for angled injection HJB,  $P_s = 7.0 \text{ MPa}$ , Load  $W_x$ : 0 to 10 kN**

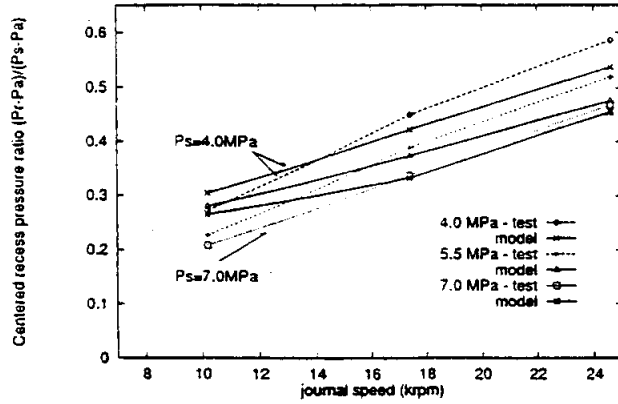


Fig. 5 Centered recess pressure ratio for angled injection HJB vs. journal speed and increasing pressure supplies  $P_s = 4, 5.5, 7$  MPa

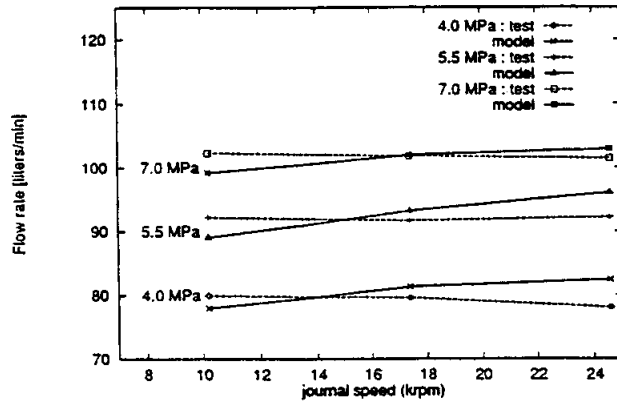


Fig. 6 Flow rate for angled injection HJB versus journal speed and increasing pressure supplies  $P_s = 4, 5.5, 7$  MPa

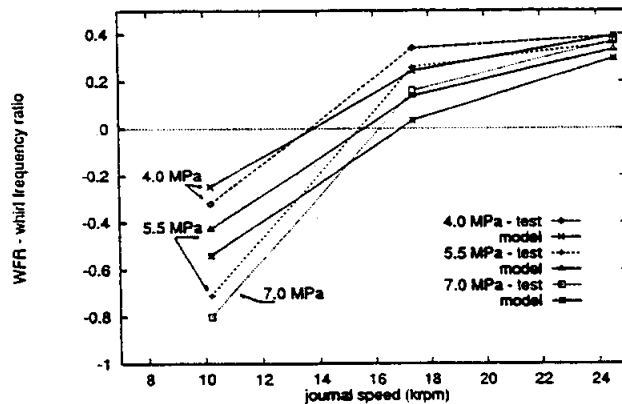


Fig. 7 Whirl frequency ratio for angled injection HJB versus journal speed and increasing pressure supplies  $P_s = 4, 5.5, 7$  MPa

Figure 9 presents the direct stiffness coefficients ( $K_{xx} = K_{yy}$ ) versus the journal speed and nominal supply pressures. The experimental results show significant discrepancies between  $K_{xx}$  and  $K_{yy}$  and attributed to minute differences in the diameters of the feeding orifices. The numerical predictions agree well with the measurements except at the lowest speed and highest pressure where the tests show an unexpected behavior.

The direct damping coefficients ( $C_{xx} = C_{yy}$ ) are depicted in Figure 10. The predictions and measurements show direct damping to increase with journal speed and supply pressure. Correlation test and model is best at the lowest (10.2 krpm) speed. However, direct damping is underpredicted by as much as 25 percent at 24.6 krpm.

Figure 11 shows the predicted cross-coupled damping coefficients ( $C_{xy} = -C_{yx}$ ) to increase with journal speed and with little influence of the external supply pressure. On the other hand, the test results show a different behavior with cross-damping coefficients being the largest at the middle test speed (17.4 krpm). No conclusive remark can be made in regard to the correlation of prediction and identified test coefficients.

Comparisons to inertia force coefficients are given by San Andres (1995d) and not reported here for brevity. The predictions show added mass coefficients independent of external supply pressure and with a slow variation as the journal speed increases. The experimentally identified inertia coefficients are

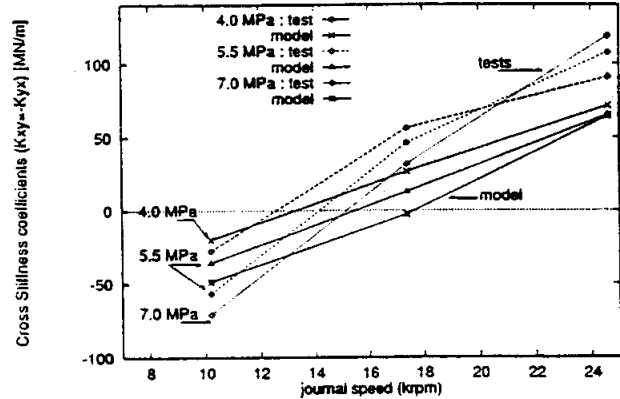


Fig. 8 Cross-stiffness coefficients for angled injection HJB versus journal speed and increasing pressure supplies  $P_s = 4, 5.5, 7$  MPa

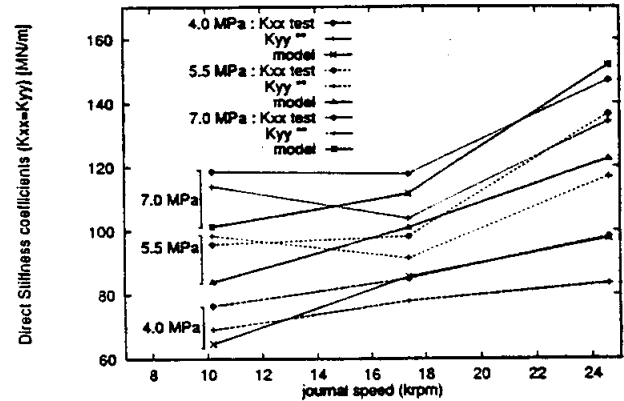


Fig. 9 Direct-stiffness coefficients for angled injection HJB versus journal speed and increasing pressure supplies  $P_s = 4, 5.5, 7$  MPa

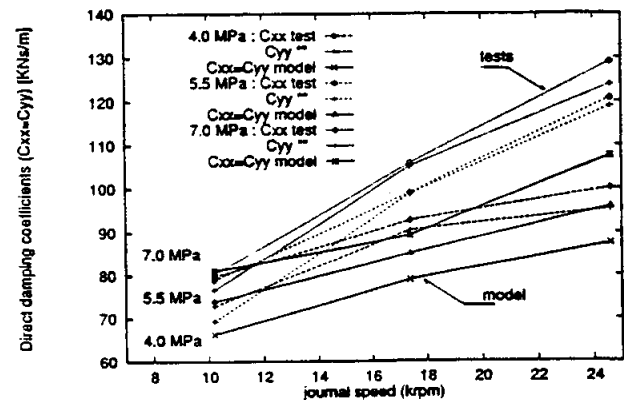


Fig. 10 Direct damping coefficients for angled injection HJB versus journal speed and increasing pressure supplies  $P_s = 4, 5.5, 7$  MPa

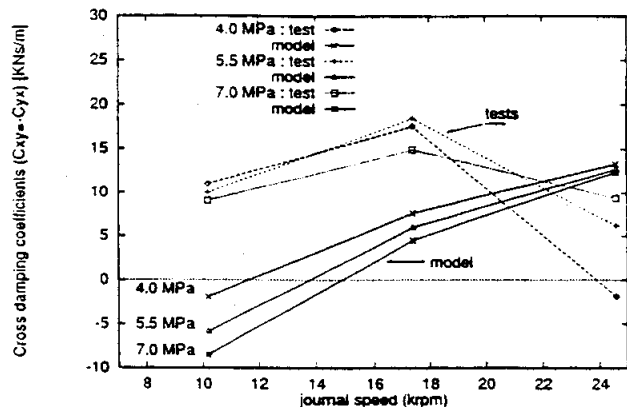


Fig. 11 Cross-damping coefficients for angled injection HJB versus journal speed and increasing pressure supplies  $P_s = 4, 5.5, 7$  MPa

of the same order of magnitude as the predictions but present an erratic behavior. Franchek and Childs (1994) indicate the test inertia coefficients have average uncertainties of 53 percent.

### Hybrid Bearing Example for a Liquid Oxygen Application

Table 2 contains design data for a liquid oxygen ( $T_s = 90^\circ\text{K}$ ), 6 recess hybrid bearing operating at 25 krpm and with a pressure drop ( $P_s - P_a$ ) equal to 17.9 MPa. The application corresponds to an Advanced Launching System (ALS) turbopump configuration (San Andres, 1995c). The analysis for journal centered operation investigates the effects of the angle of fluid injection on the performance characteristics of the bearing.

Figure 12 presents the bearing whirl frequency ratio (WFR), flow rate, mean recess pressure ratio  $[(P_r - P_s)/(P_s - P_a)]$  and maximum pressure ( $P_{\max}$ ) within the recess versus increasing values of the injection angle ( $\delta$ ). The flow rate and recess pressure ratio remain practically constant for all injection angles while the maximum (upstream) recess pressure retarding the development of journal rotation steadily increases and becomes a maximum for tangential injection. The most important result

Table 2 Description of 6 recess liquid oxygen hybrid bearing with angled injection

No of recesses ( $N_{\text{rec}}$ )	6
Clearance nominal ( $C$ )	76.2 $\mu\text{m}$ (0.003 in)
Diameter ( $D$ )	92.7 mm (3.65 in)
Length ( $L$ )	37.1 mm (1.46 in)
Land roughness (peak-peak):	smooth
Recess dimensions: square ( $l$ )	19 mm $\times$ (b) 19 mm $\times$ 228 $\mu\text{m}$ (depth). Supply volume $V_s = 0.0 \text{ dm}^3$
Orifice at midplane of recess.	diameter $d = 2.328 \text{ mm}$ , $C_d = 1.0$ , angle of injection ( $-10^\circ$ to $90^\circ$ )
Rotational speed:	25,000 rpm (2,618 rad/s)
Lubricant: liquid oxygen at $T_s = 90^\circ\text{K}$ (supercritical conditions)	
Supply pressure $P_s$	26.71 MPa (3,874 psi)
Exit pressure $P_a$	8.81 MPa (1,278 psi)

	Supply	Exit
Viscosity ( $\mu$ )	0.2459E-3	0.2125E-3 Pa.s
Density ( $\rho$ )	1,192	1,160 kg/m <sup>3</sup>

Empirical parameters:  
Entrance loss factors  $\xi_s, \xi_e = 0.0$ ,  $C_d = 1.0$

Circumferential flow Reynolds number,  $Re_c = \rho \Omega R c / \mu = 44,822$

Nominal axial flow Reynolds number,  $Re_a = Q / \pi D \mu = 48,972$

Maximum predicted fluid exit temperature = 101.5° K

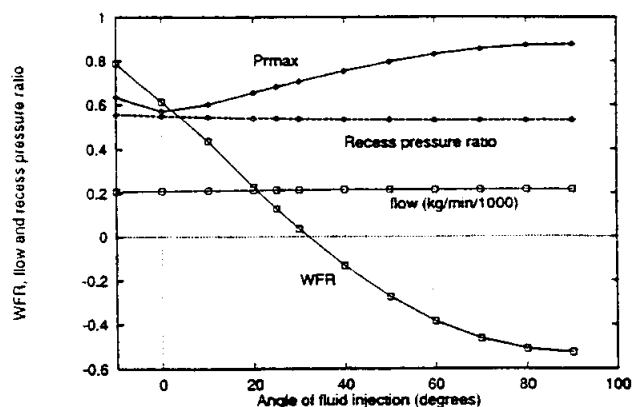


Fig. 12 Whirl frequency, flow rate and recess pressure ratios versus angle of fluid injection for 6 recess LO2 HJB, ( $P_s - P_a = 17.9$  MPa,  $T_s = 90$  K, 25 krpm)

concerns the whirl frequency ratio which decreases from a value close to 0.60 for radial injection to approximately -0.53 for tangential injection.

Figures 13 and 14 show the stiffness ( $K_{\alpha\beta}$ ) $_{\alpha\beta=x,y}$  and damping ( $C_{\alpha\beta}$ ) $_{\alpha\beta=x,y}$  coefficients versus increasing values of the angle of injection. The subindex ( $\alpha$ ) on the stiffness coefficients denotes values at zero frequency ( $\omega = 0$ ), while the others are evaluated at a synchronous frequency, i.e., they contain the inertia coefficients and could be thought as *dynamic stiffnesses* equal to  $K_{\alpha\beta} - \omega^2 M_{\alpha\beta}$ . Note that direct stiffness and damping coefficients vary little with the angle of fluid injection. On the other hand,

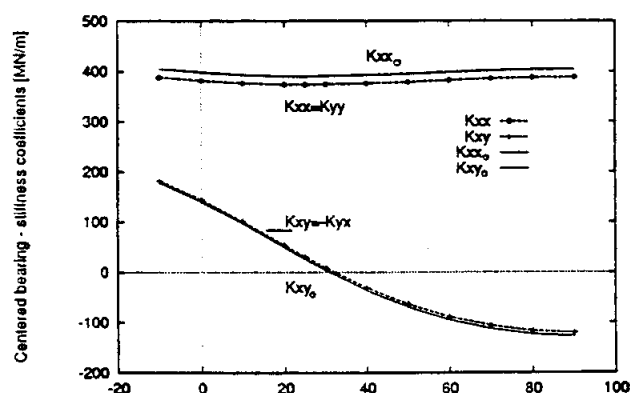


Fig. 13 Stiffness coefficients ( $K_{xx} = K_{yy}$ ), ( $K_{xy} = -K_{yx}$ ) versus angle of fluid injection for 6 recess LO2 HJB, ( $P_s - P_a = 17.9$  MPa,  $T_s = 90$  K, 25 krpm)

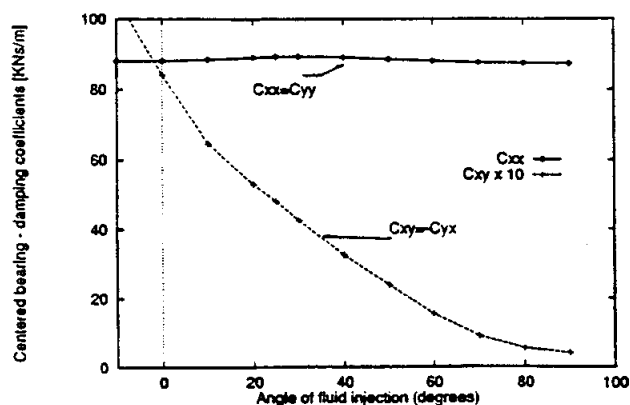


Fig. 14 Damping coefficients ( $C_{xx} = C_{yy}$ ), ( $C_{xy} = -C_{yx}$ ) versus angle of fluid injection for 6 recess LO2 HJB, ( $P_s - P_a = 17.9$  MPa,  $T_s = 90$  K, 25 krpm)

the cross-coupled coefficients decrease steadily as the orifice supply angle increases with minimum values for tangential injection. For injection angles greater than 25 deg the WFR is zero and then negative indicating a bearing with unlimited stability for forward whirl motions.

## Conclusions

The growth of an "all-fluid-film-bearing" technology for support of advanced cryogenic turbopumps demands the development of models and design tools, the testing of components, and the implementation of the technology on actual hardware. Conventional hybrid fluid film bearings have demonstrated adequate load support, direct stiffness and damping, but suffer from limited hydrodynamic stability which deters their use to high speed applications and flexible rotating structural systems. On the other hand, experiments on hybrid bearings with angled orifice injection have shown virtual elimination of cross-coupled stiffness coefficients and null or negative whirl frequency ratios. No firm analysis was available at the time of the measurements, and hence, further technological developments since then were prevented.

A bulk-flow analysis for prediction of the static load and force coefficients of hybrid bearings with angled orifice injection is advanced. A simple model reveals that the fluid momentum exchange at the orifice discharge produces a pressure rise in the recess which retards the shear flow induced by journal rotation, and consequently, reduces cross-coupling forces. The predictions from the model are compared with measurements for a hybrid bearing with a 45 deg angled injection. The test bearing nominal clearance is 125  $\mu\text{m}$  and operates with water from 10.2 krpm to 24.6 krpm and with supply pressures from 4 to 7 MPa. Comparison of experiments and model calculations for load, flow rate and recess pressures are good and verify the soundness of the bulk-flow model. Correlations of model and test direct stiffness and damping coefficients are also favorable. The predictions show the same trends as the test values for the whirl frequency ratio and cross-coupled stiffness coefficients but large differences are apparent. Inertia force coefficients do not agree with the experimental values perhaps due to the large uncertainty in the test coefficients. The predictions as well as the measurements demonstrate that the advantages of angled injection in hybrid bearings are lost as the journal speed increases and brings dominance of hydrodynamic over hydrostatic effects.

An application example for a liquid oxygen 6-recess hybrid bearing also verifies that a tangential angled orifice injection produces the lowest (negative) whirl frequency ratio and induces the largest cross-coupled stiffnesses which retard the development of forward whirl journal motions.

## Acknowledgments

The support of NASA Lewis Research Center under NASA Grant NAG-1434 is gratefully acknowledged. Thanks to Mr. James Walker of NASA LeRC for his interest on this work. Thanks to my daughter, Maria Jose (12), who helped on the graphical art.

## References

Braun, M. J., Choy, F. K., and Zhou, Y. M., 1993, "The Effects of a Hydrostatic Pocket Aspect Ratio, Supply Orifice Position and Attack Angle on Steady-State Flow Patterns, Pressure and Shear Characteristics," *ASME JOURNAL OF TRIBOLOGY*, Vol. 115, pp. 678-685.

- Braun, M. J., Dzodzo, M., 1995, "Effects of the Feedline and the Hydrostatic Pocket Depth on the Flow Patterns and Pressure Distribution," *ASME JOURNAL OF TRIBOLOGY*, Vol. 117, pp. 224-233.
- Brown, R. D., Hart, J. A., 1986, "A Novel Form of Damper for Turbomachinery," *Proceedings of the Workshop on Rotordynamic Instability Problems in High Performance Turbomachinery*, Texas A&M University, pp. 325-348, NASA CP 2443.
- Childs, D., and Hale, K., 1994, "A Test Apparatus and Facility to Identify the Rotordynamic Coefficients of High Speed Hydrostatic Bearings," *ASME JOURNAL OF TRIBOLOGY*, Vol. 116, pp. 337-344.
- Franchek, N., 1992, "Theory Versus Experimental Results and Comparisons for Five Recessed, Orifice Compensated, Hybrid Bearing Configurations," Texas A&M University, M.S. Thesis, TAMU Turbomachinery Laboratories, Aug.
- Franchek, N., and Childs, D., 1994, "Experimental Test Results for Four High-Speed, High-Pressure, Orifice-Compensated Hybrid Bearings," *ASME JOURNAL OF TRIBOLOGY*, Vol. 116, 2, pp. 285-290.
- Franchek, N., Childs, D., and San Andres, L., 1995, "Theoretical and Experimental Comparisons for Rotordynamic Coefficients of a High-Speed, High-Pressure, Orifice-Compensated Hybrid Bearings," *ASME JOURNAL OF TRIBOLOGY*, Vol. 117, 2, pp. 285-290.
- Genge, G. G., Saville, M., and Gu, A., 1993, "Foil Bearing Performance in Liquid Nitrogen and Liquid Oxygen," *AIAA/SAE/ASME/ASCE 29th Joint Propulsion Conference and Exhibit*, Monterey, CA, June, Paper AIAA-93-2537.
- Hill, D., Baskharone, E., and San Andres, L., 1995, "Inertia Effects in a Hybrid Bearing with a 45 Degree Entrance Region," *ASME JOURNAL OF TRIBOLOGY*, Vol. 117, 3, pp. 498-505.
- Hirs, G. G., 1973, "A Bulk-Flow Theory for Turbulence in Lubricating Films," *ASME JOURNAL OF LUBRICATION TECHNOLOGY*, Vol. 95, pp. 135-146.
- Kleynhans, G., and Childs, D., 1995, "The Acoustic Influence of Cell Depth on the Rotordynamic Characteristics of Smooth-Rotor/Honeycomb-Stator Annular Gas Seals," *Seals Code Development Workshop*, NASA Lewis Research Center, Cleveland, OH, June 15, 1995.
- Kurtin, K., Childs, D., San Andres, L., and Hale, K., 1993, "Experimental versus Theoretical Characteristics of a High Speed Hybrid (combination Hydrostatic and Hydrodynamic) Bearing," *ASME JOURNAL OF TRIBOLOGY*, Vol. 115, 1, pp. 160-169.
- Lauder, B., and Leschziner, M., 1978, "Flow in Finite Width Thrust Bearings Including Inertial Effects," *ASME JOURNAL OF LUBRICATION TECHNOLOGY*, Vol. 100, pp. 330-345.
- McCarty, R. D., 1986, *NBS Standard Reference Data Base 12, Thermophysical Properties of Fluids*, MIPROPS 86, Thermophysics Division, Center for Chemical Engineering, National Bureau of Standards, Colorado.
- Mosher, P., and Childs, D., 1995, "Theory Versus Experiment for the Effect of Pressure Ratio on the Performance of an Orifice-Compensated Hybrid Bearing," 1995 ASME Design Engineering Technical Conference, DE-Vol 84-2, Vol. 3-Part B, pp. 1119-1129.
- Pelfrey, P., 1995, "Pratt & Whitney Fluid-Film Bearing and Seal Technology Development and Implementation," *Seals Code Development Workshop*, NASA Lewis Research Center, Cleveland, OH, June 15, 1995.
- Redcliffe, J. M., and Vohr, J. H., 1969, "Hydrostatic Bearings for Cryogenic Rocket Engine Pumps," *ASME JOURNAL OF LUBRICATION TECHNOLOGY*, pp. 557-575.
- San Andres, L. A., 1990, "Turbulent Hybrid Bearings with Fluid Inertia Effects," *ASME JOURNAL OF TRIBOLOGY*, Vol. 112, pp. 699-707.
- San Andres, L., 1992, "Analysis of Turbulent Hydrostatic Bearings with a Barotropic Fluid," *ASME JOURNAL OF TRIBOLOGY*, Vol. 114, 4, pp. 755-765.
- San Andres, L., 1993, "Thermohydrodynamic Analysis of Cryogenic Liquid Turbulent Film Bearings for Cryogenic Applications," *Research Progress Report to NASA Lewis Research Center*, NASA Grant NAG3-1434, Dec.
- San Andres, L., 1995a, "Thermohydrodynamic Analysis of Fluid Film Bearings for Cryogenic Applications," *AIAA Journal of Propulsion and Power*, Vol. 11, 5, pp. 964-972.
- San Andres, L., 1995b, "Two Pad Axially Grooved Hydrostatic Bearing," U.S. Patent 5,433,528, July, 18.
- San Andres, L., 1995c, "Turbulent Flow Foil Bearings for Cryogenic Applications," *ASME JOURNAL OF TRIBOLOGY*, Vol. 117, 1, pp. 185-195.
- San Andres, L., 1995d, "Angled Injection—Hybrid Fluid Film Bearings for Cryogenic Applications," *Annual Research Progress Report to NASA Lewis Research Center*, NASA Grant NAG3-1434, December.
- San Andres, L., 1996, "Turbulent Flow, Flexure-Pivot Hybrid Bearings for Cryogenic Applications," *ASME JOURNAL OF TRIBOLOGY*, Vol. 118, No. 1, pp. 190, 200.
- Tondl, A., 1967, "Bearings with a Tangential Gas Supply," *Gas Bearing Symposium*, University of Southampton, Dept. of Mechanical Engineering.
- Van Doormaal, J. P., and Raithby, D., 1984, "Enhancements of the SIMPLE Method for Predicting Incompressible Fluid Flows," *Numerical Heat Transfer*, Vol. 7, pp. 147-163.
- Yang, Z., San Andres, L., and Childs, D., 1995, "Thermohydrodynamic Analysis of Process Liquid Hydrostatic Bearings in Turbulent Regime, Part I: The Model and Perturbation Analysis, Part II: Numerical Solution and Results," *ASME JOURNAL OF APPLIED MECHANICS*, Vol. 62, 3, pp. 674-684.

2. "Transient Response of Externally Pressurized Fluid Film Bearings," 1996, SanAndres, L., accepted for publication at *STLE Tribology Transactions*, Preprint 96-TC-3A-1.



# Transient Response of Externally Pressurized Fluid Film Bearings<sup>©</sup>

LUIS SAN ANDRES  
Texas A&M University  
Mechanical Engineering Department  
College Station, Texas 77843-3123

The transient response of a point-mass rotor supported in turbulent flow, externally pressurized fluid film bearings is presented. The equations of motion are solved numerically with local linearization at each integration time step. The bearing reaction forces are calculated from the numerical solution of unsteady bulk-flow equations including fluid inertia, turbulence, variable fluid properties and thermal energy transport. Examples for the transient response of damper seals

and hydrostatic bearings under a variety of external loads are presented. Transient responses based on an approximate model which uses constant rotordynamic force coefficients are also included and shown to compare well with the full nonlinear responses. The nonlinear model needs small time steps with large execution times, while the simple linear model provides reliable results in a minute fraction of time.

Presented as a Society of Tribologists and Lubrication Engineers paper at the ASME/STLE Tribology Conference in San Francisco, California, October 13-17, 1996  
Final manuscript approved June 3, 1996

## KEY WORDS

Fluid Film Bearings, Dynamic Modelling

## NOMENCLATURE

$A_X, A_Y$	= rotor accelerations [m/s <sup>2</sup> ]
$C$	= radial clearance function [m]
$C_p$	= fluid specific heat [J/kg °K]
$C_{XX}, C_{XY}, C_{YX}, C_{YY}$	= damping force (linear) coefficients [Ns/m]
$C_d$	= orifice discharge coefficient
$D$	= 2 R; bearing diameter [m]
$D_{X(t)}, D_{Y(t)}$	= journal (rotor) center displacements in inertial coordinates [m]
$d_o$	= orifice diameter [m]
$f_{j,B}$	= turbulent flow friction factors at journal and bearing surfaces
	$f_{j,B} = a_M \left\{ 1 + \left( \frac{C_M r_{j,B}}{H} + \frac{b_M}{R_{j,B}} \right)^{1/\epsilon_M} \right\}$
	$a_M = 0.001375$
	$b_M = 500,000, C_M = 10^4$
	$\epsilon_M = 3.0$
$F_X, F_Y$	= bearing fluid film forces along {X,Y} axes [N]
$H$	= $C + D_X(t) \cos \theta + D_Y(t) \sin \theta$ ; film thickness [m]
$H_r$	= recess depth [m]
$K_{XX}, K_{XY}, K_{YX}, K_{YY}$	= bearing (linear) force stiffness coefficients [N/m]

$L, l$	= bearing axial length, recess axial length [m]
$M$	= point rotor mass [kg]
$M_{XX}, M_{XY}, M_{YX}, M_{YY}$	= bearing (linear) inertia force coefficients [kg]
$P, P_r$	= fluid pressure, recess pressure [N/m <sup>2</sup> ]
$P_s$	= external supply pressure [N/m <sup>2</sup> ]
$Re$	= $(RC/\mu)^*$ ; nominal circumferential flow Reynolds number
$R_j, R_B$	= flow Reynolds numbers relative to journal and bearing surfaces
	$\frac{\rho H}{\mu} [(U_x - \Omega R)^2 + U_y^2]^{1/2}$
	$\frac{\rho H}{\mu} [U_x^2 + U_y^2]^{1/2}$
$r_j, r_B$	= roughness depths at journal and bearing surfaces [m]
$x, y$	= (Rθ, Z) circumferential and axial flow coordinates
$t, t_o$	= time coordinate [s], initial time [s]
$T, T_s$	= temperature, supply temperature [°K]
$u$	= rotor imbalance displacement [m]
$U_x, U_y$	= bulk-flow velocities in circumferential (x) and axial (y) directions [m/s]
$V_X, V_Y$	= journal (rotor) velocity components [m/s]
$W_{X(t)}, W_{Y(t)}$	= external loads applied on rotor [N]

$\beta_T$	$= -(1/\rho)(\partial\rho/\partial T)$ ; liquid volumetric expansion coefficient [ $1/^\circ\text{K}$ ]	$\Omega, \omega$	$=$ rotational speed of journal, excitation or whirl frequency [ $1/\text{s}$ ]
$\bar{t}$	$=$ time integration parameter, $\text{typ} = 1.42$	$\Lambda_x$	$= \Omega R$ ; journal surface velocity [ $\text{m/s}$ ]
$\kappa_\gamma = \kappa_x$	$= 1/2(\kappa_J + \kappa_B)$ ; turbulence shear factors in $(\gamma, x)$ flow directions	$\Delta t$	$= t_{i+1} - t_i$ ; time step [ $\text{s}$ ]
$\kappa_J, \kappa_B$	$= f_J \cdot R_J, f_B \cdot R_B$ ; turbulent shear parameters at journal and bearing surfaces	Subscripts	
$\rho, \mu$	$=$ fluid density [ $\text{Kg/m}^3$ ], viscosity [ $\text{Ns/m}^2$ ]	$x, y$	$=$ local circumferential and axial coordinates in plane of bearing
$\xi_{xH}, \xi_{xU}$	$=$ empirical recess-edge entrance loss coefficients in circumferential (upstream, downstream) direction	$r, e$	$=$ bearing recesses and edges (entrance)
$\xi_y$	$=$ empirical recess-edge entrance loss coefficients in axial direction	$i, j$	$=$ refer to discrete times $t_i$ and $t_j$
		$B, J$	$=$ refer to bearing and journal surfaces

## INTRODUCTION

The transient response of rotor-bearing systems is of importance to determine safe operation and dynamic performance under extreme loading conditions. Some fluid film bearing elements and, most notably, plain journal bearings and squeeze film dampers, are known to be highly nonlinear, and rotordynamic studies based on linear force coefficients are (generally) not able to predict system time responses for realistic levels of external dynamic loads. Advanced analytical techniques are then needed to study aperiodic responses, jump-phenomena, bifurcation and even "chaotic" responses in certain regimes of operation (1).

The development of an all-fluid bearing technology for cryogenic turbopumps has advanced steadily over the past few years. Low cost, reliable fluid film bearings will provide maximum operating life with optimum and predictable rotordynamic characteristics. San Andres (2)-(4) presents the computational analysis for the calculation of equilibrium and rotordynamic force coefficients in turbulent flow externally pressurized bearings and seals. Tests from a high speed/high pressure bearing apparatus have validated the numerical predictions (5), (6). Theoretical and experimental studies currently address the effects of fluid compressibility and limited stability in conventional (fixed geometry) bearing designs.

This paper presents the computation of the unsteady bulk-flow and transient-forced response of a rigid rotor supported on turbulent flow, externally pressurized bearings. The objective is to provide a sound computational tool for the prediction of synchronous unbalance response, rotor liftoff, and response to abnormal shock and maneuvering loads in cryogenic turbomachinery.

## Literature Review

The literature on transient dynamics of rotor-bearing systems is extensive. The impedance formulation of Childs et al. (7) allows very rapid calculation of the transient dynamics of rotors supported on plain journal bearings with constant fluid viscosity. This impedance simply defines the instantaneous bearing reaction force vector as a function of the relative displacement and velocity vectors of the journal relative to the bearing. Kirk and Gunter (8), (9) and Barrett et al. (10) pioneered the numerical study of transient dynamics of simple rigid and flexible rotors supported on short length journal bearings. The studies confirm the findings of the clas-

sical linear stability analysis of Lund (11) and detail the severity of a sudden blade loss in rotor-bearing systems.

Choy et al. (12), (13) present computational studies on nonlinear effects in plain journal bearings due to journal misalignment, levels of loading and thermal conditions. Most importantly, the authors develop transfer functions for the response of a simple rotor-journal bearing system due to impulse loadings and compare them with transfer functions obtained from the linearized bearing force coefficients. The numerical results show the importance of nonlinear behavior for journal operation at low eccentricities where nonlinearities increase as the journal is suddenly displaced to a larger eccentric operating point. Adams et al. (14), (15) present transient studies of point-mass rotors supported on cylindrical journal bearings and tilting-pad bearings which address the phenomena of pad flutter at subsynchronous frequencies and the appearance of chaotic phenomena under particular operating and loading conditions.

Hashimoto et al. (16) and Tichy and Bou-Said (17) report on the importance of turbulence and inertia effects on the dynamic response of simple rotors supported in journal bearings and acted upon by large impulsive loads and rotating imbalance forces. The methods used extend and validate (18) the application of the film-averaged momentum equations (bulk-flow methods) to analyze unsteady flows in fluid film bearings.

Paranjpe et al. (19), (20) have steadily advanced the thermohydrodynamic (THD) analysis of dynamically loaded journal bearings for automotive applications. These works describe the complexity of current THD models and provide a lucid explanation on the time scales for thermal effects in a fluid film bearing and its bounding solids. Desbordes et al. (21) and Gadangi and Palazzolo (22) include the effects of film temperature and pivot flexibility on the transient response to suddenly applied unbalanced loads in rotors supported on tilting-pad bearings. The authors bring to attention a rotor-bearing highly nonlinear behavior for large levels of unbalance with hydrodynamic pressures of great magnitude. The results do not question the likelihood of babbit plastic deformations for such extreme regimes of operation.

Padavala (23) completed a time-dependent analysis for a rigid rotor supported on turbulent flow annular pressure seals. The numerical integration of the unsteady bulk-flow



equations is performed in explicit form and, thus, the method requires very small time steps to assure stability of the calculated solution. Padavala concludes that, for most loading cases of interest, annular pressure seals in cryogenic turbomachinery behave as linear elements even for large amplitude rotor motions away from the static equilibrium position.

## ANALYSIS

### The Equations of Motion

The dynamics of a point mass rotor supported on fluid film bearings are described by Eqs. [1a] and [1b].

$$MA_X = F_X(t) + W_X(t) + M \cdot g \quad [1a]$$

$$MA_Y = F_Y(t) + W_Y(t) \quad [1b]$$

where  $\{A_X, A_Y\}$  are the rotor accelerations in the  $X$  and  $Y$  inertial coordinates, and  $\{F_i, W_i\}_{i=X,Y}$  correspond to the time-dependent fluid film bearing reaction forces and applied external loads, respectively. The solution of Eqs. [1a] and [1b] requires the specification of displacements  $\{D_{X0}, D_{Y0}\}$  and velocities  $\{V_{X0}, V_{Y0}\}$  at the initial time ( $t_0$ ). In general, the bearing forces depend on the bearing geometry, operating speed and fluid properties, and the journal (rotor) center displacements and velocities.

Figures 1 and 2 show the geometry and nomenclature for the externally pressurized bearings considered in the analysis, namely a hydrostatic bearing and a damper seal. The local coordinate system  $\{x = \theta R, y = Z\}$  rests on the plane of the fluid flow, and the film thickness and its time derivative are given by

$$H(\theta, y, t) = C(\theta, y) + D_X(t) \cos(\theta) + D_Y(t) \sin(\theta) \quad [2]$$

$$dH/dt = V_X \cos(\theta) + V_Y \sin(\theta)$$

where  $C$  is the film radial clearance. In Eq. [2], the journal center displacements  $(D_X, D_Y)$  and velocities  $(V_X, V_Y)$  are functions of time and determined by solution of the motion equations, Eqs. [1a] and [1b].

The unsteady fluid flow on the film lands of a bearing is considered as fully developed and turbulent due to the large axial pressure drop, high rotor surface speed and the low viscosity typical of process liquids. Here, "average fluid inertia" equations of mass conservation, momentum and energy transport are used to describe the bulk-flow motion in thin film geometries (17), (18). For turbulent flows with no heat conduction through the bearing and journal surfaces, these equations are (4)

$$\frac{\partial}{\partial x_i}(\rho H U_i) + \frac{\partial}{\partial t}(\rho H) = 0; \quad i = x, y \quad [3]$$

$$-H \frac{\partial P}{\partial x_i} = \frac{\mu}{H} \left( k_i - \frac{1}{2} k_j \Lambda_j \right) + \quad [4]$$

$$\frac{\partial}{\partial x_j}(\rho H U_i \cdot U_j) + \frac{\partial}{\partial t}(\rho H U_i); \quad i, j = x, y$$

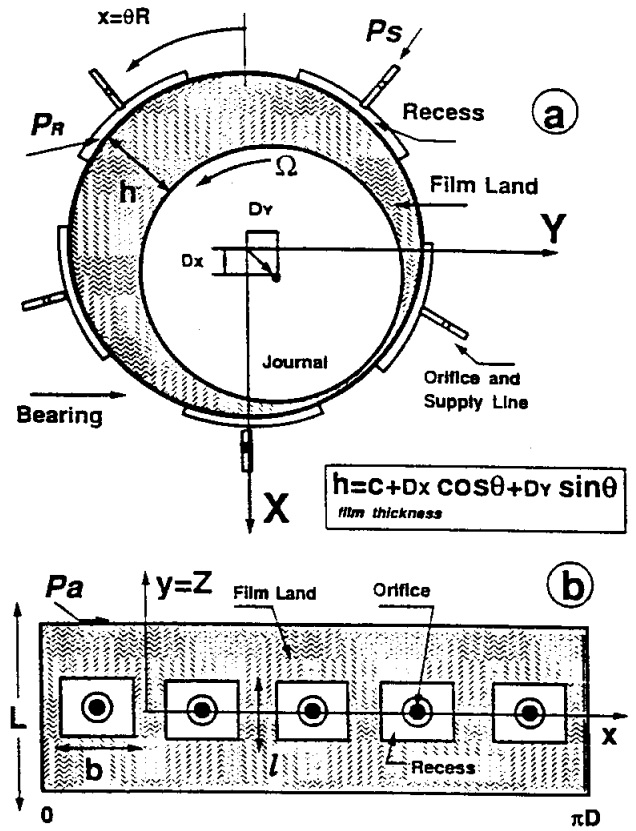


Fig. 1—Geometry of an orifice-compensated hydrostatic bearing.  
(a) axial view and coordinate system  
(b) unwrapped bearing surface

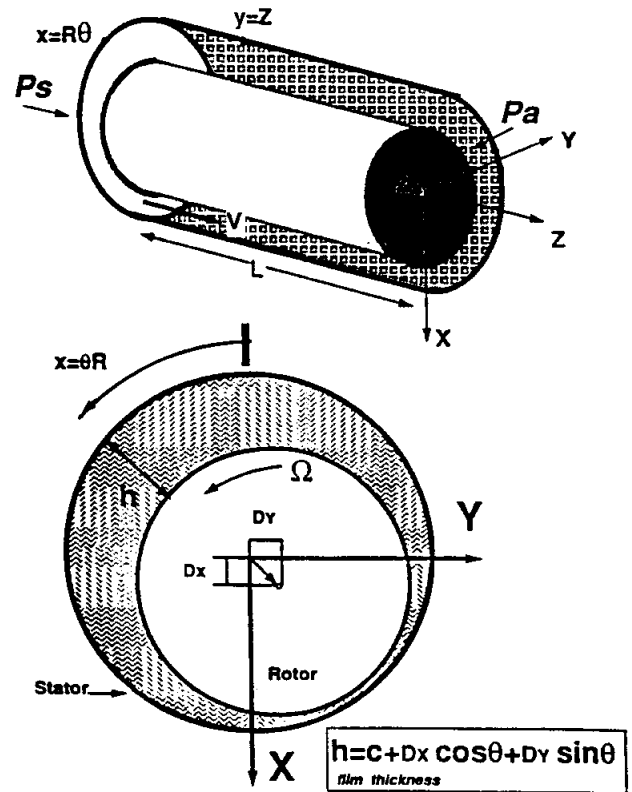


Fig. 2—Geometry of an annular pressure seal.

$$C_p \left\{ \frac{\partial}{\partial t} (\rho HT) + \frac{\partial}{\partial x_i} (\rho H U_i \cdot T) \right\} = \beta_T HT \left\{ \frac{\partial P}{\partial t} + U_i \frac{\partial P}{\partial x_i} \right\} \\ + \Lambda_x H \frac{\partial P}{\partial x} + \frac{\mu}{H} \left\{ \kappa_x \left( U_x^2 + U_y^2 + \frac{1}{2} \Lambda_x \cdot U_x \right) \right. \\ \left. + \kappa_f \Lambda_x \left( \frac{1}{4} \Lambda_x - U_x \right) \right\} \quad i = x, y \quad [5]$$

where  $(U_x, U_y)$  are the bulk-flow velocities in the circumferential and axial directions, and  $P$  and  $T$  are the fluid film pressure and temperature, respectively.  $\Lambda_x = R\Omega$  and  $\Lambda_y = 0$  denote the surface rotor speeds.  $\rho$ ,  $\mu$ ,  $C_p$  and  $\beta_T$  correspond to the fluid density, viscosity, specific heat and volumetric expansion coefficient, respectively.  $\kappa_x = \kappa_y = (\kappa_f + \kappa_b)/2$  denote wall shear stress difference coefficients taken as local functions of journal/bearing surface conditions, and the flow Reynolds numbers relative to the rotating and stationary surfaces. The Benedict-Web-Rubin equation of state is used to evaluate cryogenic fluid properties (24). Details of the flow model at the recesses of a hydrostatic bearing and inertial entrance pressure drops have been given in detail before in Refs. (3) and (4) and not repeated here for brevity.

### Numerical Method of Solution

The general nonlinear equations, Eqs. [1a] and [1b], governing the rotor and bearing motion are numerically solved using the Wilson- $\theta$  method ( $\theta = 1.42$ ) as described by Bathe (25). At the discrete times  $t_i$  and  $t_j = t_i + \Delta t$ , Eqs. [1a] and [1b] reduce to the following algebraic expressions:

$$MA_{Xi} = F_{Xi} + W_{Xi} + Mg \quad [6a]$$

$$MA_{Xj} = F_{Xj} + W_{Xj} + Mg \quad [6b]$$

$$MA_{Yi} = F_{Yi} + W_{Yi} \quad [6c]$$

$$MA_{Yj} = F_{Yj} + W_{Yj} \quad [6d]$$

where  $A_{Xi} = A_{X(i)}$ ,  $W_{Xi} = W_{X(i)}$ , and  $F_{Xi} \sim F_X(D_{Xi}, D_{Yi}, V_{Xi}, V_{Yi})$  are the  $X$ -direction acceleration, external load and bearing force calculated at time  $t_i$ . In the equations above, the journal position and velocity and the fluid film forces are to be determined at time  $t_j$ , and henceforth all quantities at time  $t_i$  are known. Substitution of the algebraic equations in Eqs. [6a]–[6d] renders:

$$\begin{bmatrix} M & 0 \\ 0 & M \end{bmatrix} \begin{bmatrix} \Delta A_{Xi} \\ \Delta A_{Yi} \end{bmatrix} + \begin{bmatrix} K_{XX} & K_{XY} \\ K_{YX} & K_{YY} \end{bmatrix} \begin{bmatrix} \Delta V_{Xi} \\ \Delta V_{Yi} \end{bmatrix} \\ + \begin{bmatrix} C_{XX} & C_{XY} \\ C_{YX} & C_{YY} \end{bmatrix} \begin{bmatrix} \Delta D_{Xi} \\ \Delta D_{Yi} \end{bmatrix} = \begin{bmatrix} \Delta W_{Xi} \\ \Delta W_{Yi} \end{bmatrix} \quad [7]$$

where  $\Delta A_{Xi} = A_{Xj} - A_{Xi}$ ,  $\Delta W_{Xi} = W_{Xj} - W_{Xi}$ ,  $\Delta F_{Xi} = F_{Xj} - F_{Xi}$ , etc. are noted as the incremental changes in accelerations, loads, and bearing forces, respectively. The local (linearized) stiffness and damping force coefficients are defined as

$$K_{\alpha\beta} = - \frac{\partial F_{\alpha}}{\partial D_{\beta}} \bigg|_{D_{X_i}, D_{Y_i}}, \quad C_{\alpha\beta} = - \frac{\partial F_{\alpha}}{\partial V_{\beta}} \bigg|_{D_{X_i}, D_{Y_i}}, \quad [8]$$

$\alpha, \beta = X, Y$

and evaluated from analytical perturbations to the nonlinear flow governing equations. Complete details on the derivation and solution for the flow equations for small perturbations about an operating condition have been given in detail in the past (2)–(4).

The fluid film forces are calculated from the solution of the unsteady flow equations, Eqs. [2]–[5], with the updated values of journal displacements and velocities on the film thickness and its time derivative. The flow equations are discretized using a fully implicit cell finite-difference scheme as given by Launder and Leschziner (26) and Van Doormal and Raithby (27). At a bearing recess, the flow through the supply orifice is coupled to the flow toward the film lands and to the unsteady accumulation of fluid mass within the recess. A Newton-Raphson scheme is then used to update the recess pressures and to satisfy the transient mass continuity constraint at each bearing recess. Details on the accuracy of the algorithm for steady-state problems, evaluation of force coefficients and sensitivity to input parameters are given by Franchek et al. (6) and San Andres (4).

The computational effort required to solve the entire bearing flow field along with evaluation of forces and local force coefficients is intensive. It is noted that time steps need to be kept small if accurate results are to be the natural outcome of the numerical algorithm. The time step selected for calculations is  $\Delta t < 2\pi/\omega^*/60$  where  $\omega^*$  is the largest frequency (in Hz) likely to be excited in the response of the system (7). The less stringent requirement,  $\Delta t < 2/\omega^*$ , guarantees only stability but not necessarily accuracy of the numerical scheme. Note that suddenly applied loads like impulses and step loads contain high frequencies and, henceforth, initial time steps must be small enough to capture with accuracy the response to fast-imposed external actions.

### Approximate (Linear) Transient Solution

Externally pressurized bearings, like hydrostatic bearings and annular pressure seals, have dynamic force coefficients which do not vary greatly with the journal position (or the applied load) at a fixed operating point (2). This is not the case, however, for hydrodynamic journal bearings as the archival literature profusely reports. The uniformity of force coefficients in pressurized bearings and seals allows a dramatic simplification of the general nonlinear equations of motions, Eqs. [1a] and [1b] to render

$$\begin{bmatrix} M + M_{XX} & M_{XY} \\ M_{YX} & M + M_{YY} \end{bmatrix} \begin{bmatrix} \Delta A_X \\ \Delta A_Y \end{bmatrix} + \begin{bmatrix} K_{XX} & K_{XY} \\ K_{YX} & K_{YY} \end{bmatrix} \begin{bmatrix} \Delta V_X \\ \Delta V_Y \end{bmatrix} \\ + \begin{bmatrix} C_{XX} & C_{XY} \\ C_{YX} & C_{YY} \end{bmatrix} \begin{bmatrix} \Delta D_X \\ \Delta D_Y \end{bmatrix} = \begin{bmatrix} W_X(t) \\ W_Y(t) \end{bmatrix} \quad [9]$$

where  $\Delta D_X = D_X - D_{X0}$ ,  $\Delta V_X = V_X$ ,  $\Delta A_X = A_X$ , etc. represent the approximate journal (rotor) center displacements, veloc-

ities and accelerations about the (equilibrium) steady-state position  $(D_{X0}, D_{Y0})$  defined by the static load  $(M \cdot g)$ . The set of coefficients  $\{K_{\alpha\beta}, C_{\alpha\beta}, M_{\alpha\beta}\}$ ,  $\alpha\beta = X, Y$  correspond to the linearized stiffness, damping and inertia force coefficients evaluated at  $\{D_{X0}, D_{Y0}\}$ . The numerical solution of Eqs. [1a] and [1b] above is much faster than for the full nonlinear equations since the inertia, damping and stiffness coefficients are evaluated only once prior to the start of the transient analysis. Furthermore, the method does not even require the solution of the flow equations at each time step. The Wilson- $\theta$  method is also used to solve these linear equations with execution times approximately four orders of magnitude smaller than for the full nonlinear transient solution.

## RESULTS AND DISCUSSION

This section presents results for the transient response of a rigid rotor supported on externally pressurized bearings to impulsive loads and suddenly applied imbalance forces. San Andres (3) includes comparisons with transient responses for point-mass rotors supported on plain journal bearings as given in examples originally reported by Childs et al. (7) and Tichy and Bou-Said (17).

Table 1 presents a description of a rotor-bearing system supported on liquid oxygen tapered damper (annular pressure) seals. Predictions for the static performance and rotor-dynamic force coefficients of this type of seal are given

in detail by San Andres (4). The calculated critical speed based on centered seal force coefficients is 290 Hz and, thus, a rotor speed of 26,000 rpm is 1.5 times above the system resonant speed. The computing time for the nonlinear response is approximately 7 seconds/time step. [Computing times are based on a 30 mhz workstation (12 MIPS, 2.1 MFLOPS).]

Figure 3 depicts the nonlinear and linear transient rotor responses for a step load and a slow ramp load applied in the X-direction. The magnitude of the ramp is 10 kN with a rise time equal to 11.5 msec (3.4 times a rotor natural period). Figure 4 shows the bearing reaction force  $(F_X)$  and the applied external loads. The results predict forced motion with little damping and at a frequency close to the predicted natural frequency for small amplitude motions, i.e., 290 Hz. Note that the approximate (linear) transient solution follows the same trend as the full nonlinear solution but predicts a smaller overshoot and decays faster. For the step load, the initial overshoot is large (approximately 100  $\mu\text{m}$  or 77 percent of the minimum seal clearance). Even for this large amplitude motion, the approximate solution predicts well the system response since the damper seal has force coefficient which vary little with the journal static position.

The time response of the damper seal eccentricity to a suddenly applied synchronous periodic load is shown in Fig. 5. The magnitude of the load is 5 kN and equivalent to a rotor unbalance of 13.5  $\mu\text{m}$ . Figure 6 depicts the magnitude of the

TABLE 1—DESCRIPTION OF ROTOR SUPPORTED ON  $\text{LO}_2$  DAMPER SEAL BEARINGS

### BEARING GEOMETRY

$C(0) = 221.3 \mu\text{m}$ ,  $C(L) = 129.1 \mu\text{m}$ ,  $D = 85.1 \text{ mm}$ ,  $L = 22.2 \text{ mm}$ ,  
stator (bearing) relative roughness = 0.044 (knurled surface)  
Entrance loss factor  $\xi_y = 0.20$ , Inlet swirl = 0.5  $\Omega R$

### LUBRICANT

Liquid oxygen at  $T_s = 110.5^\circ\text{K}$   
Supply pressure  $P_s = 39.6 \text{ MPa}$  (5750 psia)  
Discharge pressure  $P_d = 2.09 \text{ MPa}$  (303 psia)

### ROTOR

Mass  $M = 50 \text{ kg}$ , weight  $Mg = 490 \text{ N}$   
Rotational speed  $\Omega = 2723 \text{ rad/s}$  (26,000 rpm)  
Period of rotational motion: 2.3 msec

### LOAD CASES

- a) Ramp load :  $W_x = 10 \text{ kN}$  ( $t/T^*$ ),  $T^* = 11.5 \text{ msec}$
- b) Step load :  $W_x = 10 \text{ kN}$  for  $t > 0$
- c) Periodic load :  $W_x = 5 \text{ kN} \cdot \cos(\Omega t)$ ,  $W_y = 5 \text{ kN} \cdot \sin(\Omega t)$ ,  
Imbalance =  $\{u\} = 13.5 \mu\text{m}$

### INITIAL CONDITIONS

Equilibrium position due to rotor weight  
 $D_{X0} = 2.45 \mu\text{m}$ ,  $D_{Y0} = 0.53 \mu\text{m}$ ,  $V_{X0} = V_{Y0} = 0 \text{ m/s}$

### AT EQUILIBRIUM POSITION

Natural frequency  $\omega_n = 290 \text{ Hz}$  (17,410 rpm)

### FORCE COEFFICIENTS AT SEAL-CENTERED POSITION

$K_{XX} = K_{YY}$	$K_{XY} = -K_{YX}$	$C_{XX} = C_{YY}$	$C_{XY} = -C_{YX}$	$M_{XX} = M_{YY}$	$M_{XY} = -M_{YX}$
MN/m		KNs/m		kg	
170.0	34.50	26.63	0.94	0.65	0.00

### PARAMETERS FOR TIME INTEGRATION

$\Delta t = 33.3 \mu\text{sec}$ ,  $T_{\text{max}} = 46 \text{ msec}$  (20 rotor revs); 69 time steps per rotor period  
Computing time: 7 sec/time step

Example LOX seal.  $M=50\text{kg}$ ,  $26\text{kcpm}$ ,  $DP=37.5\text{MPa}$ ,  $C^*=129\mu\text{m}$   $T=110\text{K}$

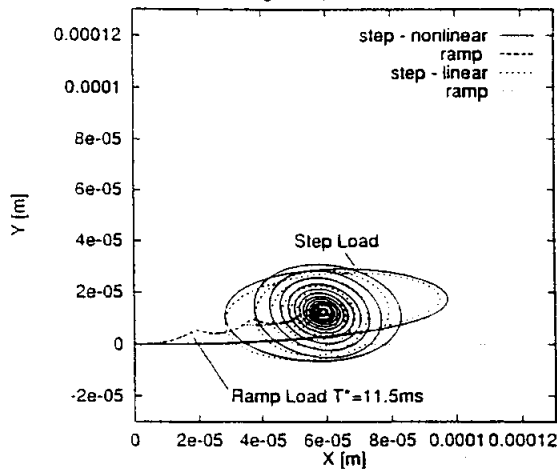


Fig. 3—Transient LO<sub>2</sub> damper seal locus due to ramp and step loads. Static load  $W_x = 10\text{ kN}$ ,  $W_y = 0\text{ N}$ .

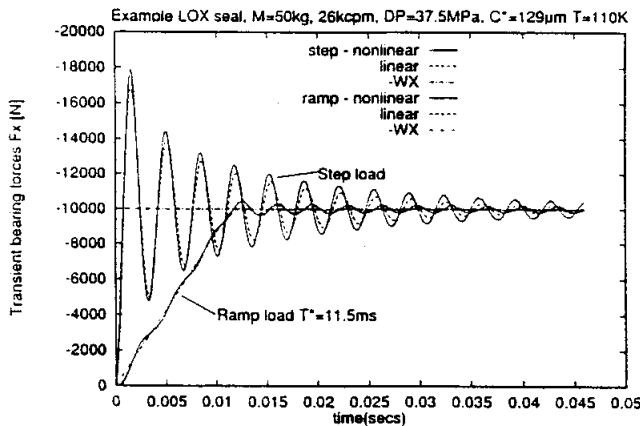


Fig. 4—Transient LO<sub>2</sub> seal force  $F_x$  due to step and ramp loads. Static load  $W_x = 10\text{ kN}$ ,  $W_y = 0\text{ N}$ .

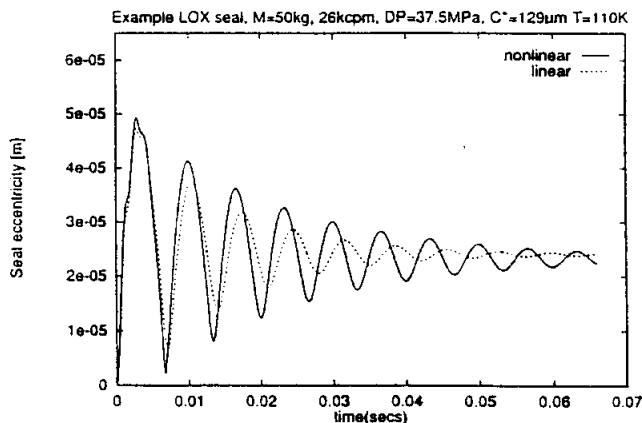


Fig. 5—Transient LO<sub>2</sub> seal eccentricity due to periodic load. Load  $5\text{ kN}$  at synchronous frequency ( $433.3\text{ Hz}$ ).

damper seal reaction force for the linear and nonlinear models. The linear model predicts well the transient response, shows more damping and reaches faster a steady-state which is slightly larger than that of the nonlinear model.

Table 2 presents a description of a rotor supported on water-lubricated hydrostatic bearings (HJBs). The bearings

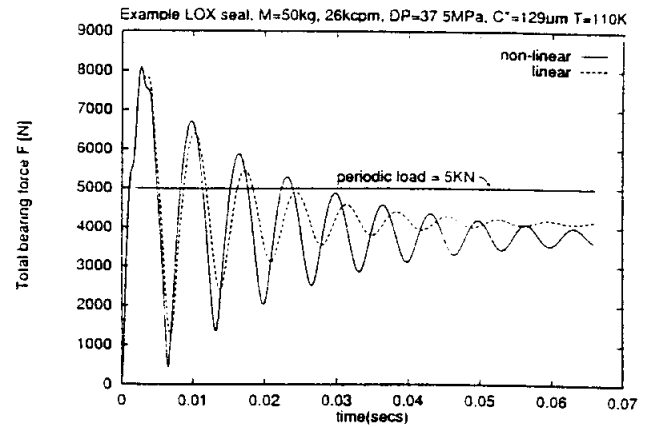


Fig. 6—Transient LO<sub>2</sub> seal force due to periodic load. Load  $5\text{ kN}$  at synchronous frequency ( $433.3\text{ Hz}$ ).

have five rectangular recesses and orifice ports evenly distributed around the bearing circumference (28). Experiments show this bearing to be very stiff at large supply pressures and demonstrate the force coefficients to have a weak dependency on the journal center eccentricity (6). The bearing force coefficients at the centered position are also given in Table 2 and used in the approximate model. These coefficients determine a system critical speed equal to  $15.830\text{ rpm}$  and, hence, the rotor speed is just below twice the critical speed with potential for unstable hydrodynamic operation. The computing time for the nonlinear solution is, on the average, 58 seconds per time step.

Figure 7 shows the bearing transient response to applied ( $5\text{ kN}$ ) ramp loads with rise times equal to  $0.2\text{ msec}$  and  $2\text{ msec}$ , respectively. Note that the rotor period of motion is  $2\text{ msec}$ , and the fast-ramp load reaches its maximum value in  $1/10$  of a rotor full revolution. Figure 8 depicts the bearing reaction force ( $F_x$ ) in the direction of the applied ramp load. The numerical predictions show the system to be highly damped and with similar responses for both the linear and nonlinear transient models.

Figure 9 shows the time response of the rotor-HJB to an impulse load of  $5\text{ kN}$  with a characteristic time of  $0.5\text{ msec}$ . The bearing reaction force ( $F_y$ ) in the direction of the applied impulsive load ( $W_y$ ) is depicted in Figure 10. The linear (approximate) solution shows slightly more damping than the full nonlinear model. The maximum journal center displacements are  $9.8\text{ }\mu\text{m}$  and  $9.5\text{ }\mu\text{m}$  for the nonlinear and linear models, respectively. These values represent motions to just 13 percent of the bearing nominal clearance ( $76.2\text{ }\mu\text{m}$ ).

The time response of the rotor-HJB due to suddenly applied imbalances is also of interest. Rotor center imbalance displacements of  $15.2\text{ }\mu\text{m}$  and  $40\text{ }\mu\text{m}$  determine loads of magnitude equal to  $7520\text{ N}$  and  $19,740\text{ kN}$  at the operating speed, respectively. Figure 11 shows the transient journal eccentricity for 15 rotor revolutions, and Fig. 12 depicts the steady-state rotor orbits. For the largest unbalance ( $u = 40\text{ }\mu\text{m}$ ), the largest rotor displacements reach to 90 percent of the bearing clearance. The steady-state orbit magnitudes for the linear model are slightly different (within four percent of the bearing clearance) to those predicted by the nonlinear model. The predictions demonstrate that the

TABLE 2—DESCRIPTION OF ROTOR SUPPORTED ON HYDROSTATIC BEARINGS

## BEARING TYPE

Orifice-compensated, five-recess hydrostatic bearing

 $C = 76.2 \mu\text{m}$ ,  $D = 76.2 \text{ mm}$ ,  $L = 76.2 \text{ mm}$ Recess dimensions: square  $27 \text{ mm} \times 27 \text{ mm} \times 381 \mu\text{m}$  (depth)orifice diameter  $d_o = 1.49 \text{ mm}$ ,  $C_d = 1.0$ Entrance loss factor  $\xi_v$ ,  $\xi_v = 0.0$ . Inlet swirl  $= 0.5 \Omega R$ 

## LUBRICANT

Water at  $T_f = 330^\circ\text{K}$ Supply pressure  $P_s = 6.55 \text{ MPa}$  (950 psig)Discharge pressure  $P_a = 0.0 \text{ MPa}$  (0 psig)

## ROTOR

Mass  $M = 50 \text{ kg}$ , weight  $Mg = 490 \text{ N}$ Rotational speed  $\Omega = 3.141 \text{ rad/s}$  (30,000 rpm)

Period of rotational motion: 2.0 msec

## LOAD CASES

a) Ramp load :  $W_x = 5 \text{ kN} \cdot (t/T^*)$ ,  $T^* = 2 \text{ msec}$  and  $0.2 \text{ msec}$ b) Impulsive load :  $W_x = M \cdot g = 490 \text{ N}$ ,  $W_y = 5 \text{ kN} \cdot \exp(-t/t_o)$ ,  $t_o = 0.5 \text{ msec}$ c) Periodic load :  $W_x = W_o \cdot \cos(\Omega t)$ ,  $W_y = W_o \cdot \sin(\Omega t)$ : Unbalance  $u = 15.2 \mu\text{m}$ ,  $W_o = 7.320 \text{ N} = M_u \Omega^2$  $u = 40.0 \mu\text{m}$ ,  $W_o = 19.740 \text{ N}$ 

## INITIAL CONDITIONS

Equilibrium position due to rotor weight

 $D_{x0} = 0.91 \mu\text{m}$ ,  $D_{y0} = 1.16 \mu\text{m}$ ,  $V_{x0} = V_{y0} = 0 \text{ m/s}$ 

## AT EQUILIBRIUM POSITION

Natural frequency  $\omega_n = 264 \text{ Hz}$  (15,830 rpm)

## FORCE COEFFICIENTS AT BEARING-CENTERED POSITION

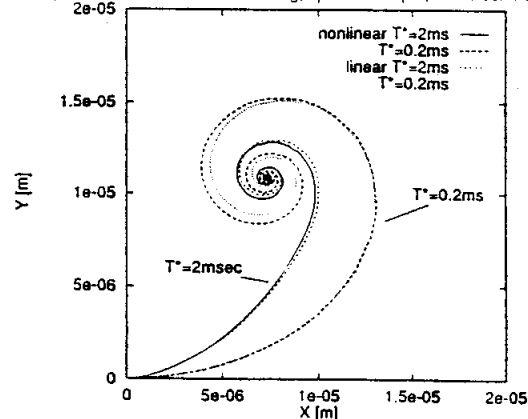
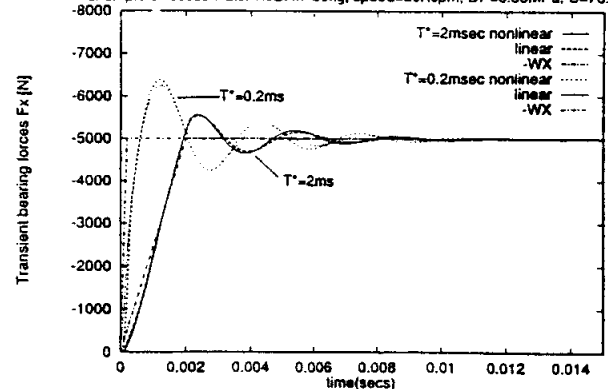
$K_{xx} = K_{yy}$ MN/m	$K_{xy} = -K_{yx}$ MN/m	$C_{xx} = C_{yy}$ KNs/m	$C_{xy} = -C_{yx}$ KNs/m	$M_{xx} = M_{yy}$ kg	$M_{xy} = -M_{yx}$ kg
211.6	315.5	206.5	57.26	16.66	-2.847

## PARAMETERS FOR TIME INTEGRATION

 $\Delta t = 66.6 \mu\text{sec}$ ,  $T_{\max} = 30 \text{ msec}$  (15 rotor revs); 30 time steps per rotor period

Computing time: 58 sec/time step

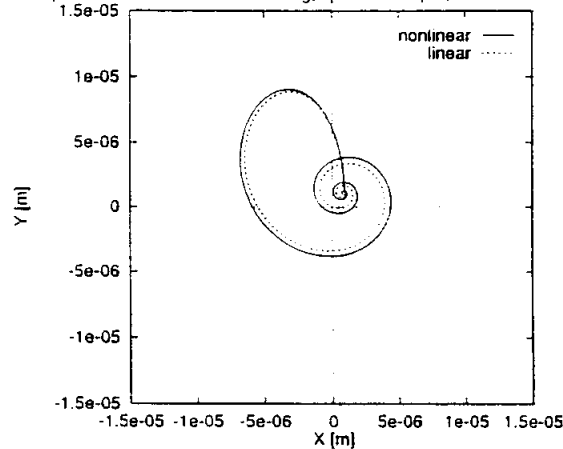
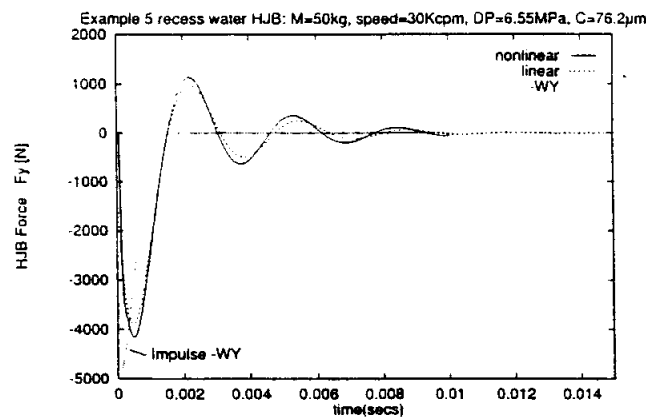
Note: Bearing data from Childs and Hale (28)

Example 5 recess water HJB:  $M=50\text{kg}$ , speed=30Kcpm,  $DP=6.55\text{MPa}$ ,  $C=76.2\mu\text{m}$ Fig. 7—Transient HJB journal center locus due to ramp loads. Load  $W_x = 5 (t/T^*) \text{ kN}$ ,  $T^* = 2 \text{ msec}$ ,  $0.2 \text{ msec}$ ,  $W_y = 0 \text{ N}$ .Example 5 recess water HJB:  $M=50\text{kg}$ , speed=30Kcpm,  $DP=6.55\text{MPa}$ ,  $C=76.2\mu\text{m}$ Fig. 8—Transient HJB force  $F_x$  due to ramp loads. Load  $W_x = 5 (t/T^*) \text{ kN}$ ,  $T^* = 2 \text{ msec}$ ,  $0.2 \text{ msec}$ ,  $W_y = 0 \text{ N}$ .

## CONCLUSIONS

A computational analysis for the prediction of the transient dynamics of a rigid rotor supported in externally pressurized turbulent flow fluid film bearings is presented. The nonlinear equations of motion of the rotor-bearing system are solved numerically with the Wilson- $\theta$  method and using local

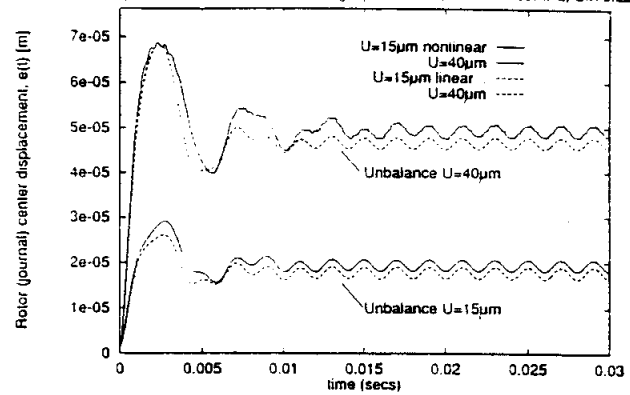
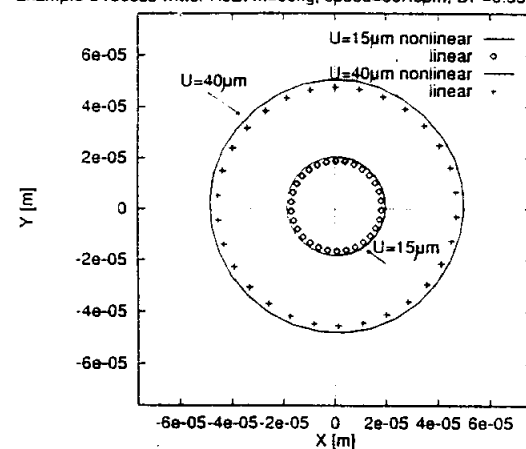
approximate model gives good results when compared to the full nonlinear model. This is due to the linearity in the relationship force versus eccentricity (rotor displacements) and the invariance of the linearized force coefficients to the journal center position.

Example 5 recess water HJB:  $M=50\text{kg}$ , speed= $30\text{Kcpm}$ ,  $DP=6.55\text{MPa}$ ,  $C=76.2\mu\text{m}$ Fig. 9—Transient HJB locus due to impulsive load.  $W_x = Mg = 490\text{ N}$ ,  $W_y = 5\text{ kN.exp}(-t/t_0)$ ,  $t_0 = 0.5\text{ ms}$ .Fig. 10—Transient HJB force  $F_y$  due to impulsive load  $W_y$ .  $W_x = Mg = 490\text{ N}$ ,  $W_y = 5\text{ kN.exp}(-t/t_0)$ ,  $t_0 = 0.5\text{ ms}$ .

spatial linearization at each time step. The bearing reaction forces are evaluated from the numerical solution of the unsteady turbulent bulk-flow equations on the film lands with an implicit control-volume algorithm, and satisfying the time-dependent flow constraints at the recesses of a hydrostatic bearing. Analytical perturbations also render linear bulk-flow equations for calculation of force coefficients at a journal equilibrium position.

Examples for the transient response of point-mass rotors supported on annular pressure seals and hydrostatic bearings under a variety of external loads are presented. Transient responses based on an approximate model which uses constant rotordynamic force coefficients are also included. The full nonlinear model needs small time steps and is computationally very intensive since it demands the solution of the bearing flow equations at each time step.

Externally pressurized bearings generally have rotordynamic force coefficients with a weak dependency on the journal equilibrium position at a constant operating speed. Hence, the linear transient model should be adequate to predict the rotor-bearing system time response due to applied dynamic loads. The numerous comparisons between the linear and nonlinear transient responses support this assertion. Furthermore, the approximate transient model brings dra-

Example 5 recess water HJB:  $M=50\text{kg}$ , speed= $30\text{Kcpm}$ ,  $DP=6.55\text{MPa}$ ,  $C=76.2\mu\text{m}$ Fig. 11—HJB journal eccentricity for unbalance load.  $W_x = Mg + M.u.\omega^2 \cos(\omega t)$ ,  $W_y = M.u.\omega^2 \sin(\omega t)$ ,  $u$  varies.Example 5 recess water HJB:  $M=50\text{kg}$ , speed= $30\text{Kcpm}$ ,  $DP=6.55\text{MPa}$ ,  $C=76.2\mu\text{m}$ Fig. 12—HJB steady-state orbits for unbalance load.  $W_x = Mg + M.u.\omega^2 \cos(\omega t)$ ,  $W_y = M.u.\omega^2 \sin(\omega t)$ ,  $u$  varies.

matic savings on the computing time required to determine the rotor-bearing system time response. Hydrodynamic bearings, on the other hand, are well known to be highly nonlinear and the approximate transient response would be accurate only for small amplitude loads and at operating conditions well below the stability margin of the rotor-bearing system.

## ACKNOWLEDGMENTS

The continued support of NASA Lewis Research Center, Grant NAG3-1434, and the interest of Mr. James Walker are gratefully acknowledged.

## REFERENCES

- (1) Ehrich, F., *Handbook of Rotordynamics*, McGraw-Hill, New York, (1992), p. 4.
- (2) San Andres, L., "Turbulent Hybrid Bearings with Fluid Inertia Effects," *ASME Jour. of Trib.*, 112, pp 699-707, (1990).
- (3) San Andres, L., "Thermohydrodynamic Analysis of Cryogenic Liquid Turbulent Flow Fluid Film Bearings, Phase II," NASA LeRC, NASA Grant No. NAG3-1434, (1994).
- (4) San Andres, L., "Thermohydrodynamic Analysis of Fluid Film Bearings for Cryogenic Applications," *AIAA Jour. of Propulsion and Power*, 11, 5, pp 964-972, (1995).
- (5) Kurin, K., Childs, D., San Andres, L. A. and Hale, K., "Experimental

- Versus Theoretical Characteristics of a High Speed Hybrid (Combination Hydrostatic and Hydrodynamic) Bearing," *ASME Jour. of Trib.*, 115, 2, pp 160-169, (1993).
- (6) Franchek, N., Childs, D. and San Andres, L., "Theoretical and Experimental Comparisons for Rotordynamic Coefficients of a High Speed, High Pressure, Orifice Compensated, Hybrid Bearing," *ASME Jour. of Trib.*, 117, pp 285-290, (1995).
  - (7) Childs, D., Moes, H., and van Leeuwen, H., "Journal Bearing Impedance Descriptions for Rotordynamic Applications," *ASME Jour. of Lubr. Tech.*, 99, 2, pp 198-214, (1977).
  - (8) Kirk, R. G. and Gunter, E. J., "Short Bearing Analysis Applied to Rotordynamics. I: Theory. II: Results of Journal Bearing Response," *ASME Jour. of Lubr. Tech.*, 98, pp 47-56, 319-329, (1976).
  - (9) Kirk, R. G. and Gunter, E. J., "Stability and Transient Motion of a Plain Journal Mounted in Flexible Damper Supports," *ASME Jour. of Eng. for Industry*, 98, 3, pp 376-392, (1976).
  - (10) Barrett, L. E., Allaire, P. E. and Gunter, E. J., "Stability and Dynamic Response of Pressurized Journal Bearings with Nuclear Water Pump Applications," *Annals of Nuclear Energy*, 4, pp 115-126, (1977).
  - (11) Lund, J. W., "The Stability of an Elastic Rotor in Journal Bearings with Flexible, Damped Supports," *ASME Jour. of Appl. Mech.*, 32, 4, pp 911-920, (1965).
  - (12) Choy, F. K., Braun, M. J. and Hu, Y., "Nonlinear Effects in a Plain Journal Bearing," *ASME Jour. of Trib.*, 113, pp 555-570, (1991).
  - (13) Choy, F. K., Braun, M. J. and Hu, Y., "Nonlinear Transient and Frequency Response Analysis of Hydrodynamic Journal Bearings," *ASME Jour. of Trib.*, 114, pp 448-454, (1992).
  - (14) Adams, M. L. and Pavandeh, S., "Self-Excited Vibration of Statically Unloaded Pads in Tilting-Pad Journal Bearings," *ASME Jour. of Lubr. Tech.*, 105, pp 377-384, (1983).
  - (15) Adams, M. L. and Abu-Mahfouz, I. A., "Exploratory Research on Chaos Concepts as Diagnostic Tools for Assessing Rotating Machinery Vibration Signatures," in *Proc. of the IFTOMM 4th Int'l. Conf. on Rotordynamics*, Chicago, IL, pp 29-39, (1994).
  - (16) Hashimoto, H., Wada, S. and Sumitomo, M., "The Effects of Fluid Inertia Forces on the Dynamic Behavior of Short Journal Bearings in Superlaminar Flow Regime," *ASME Jour. of Trib.*, 110, pp 539-547, (1988).
  - (17) Tichy, J. and Bou-Said, B., "Hydrodynamic Lubrication and Bearing Behavior with Impulsive Loads," *Trib. Trans.*, 34, 4, pp 505-512, (1991).
  - (18) Elrod, H. G., Anwar, I. and Colsher, R., "Transient Lubricating Films with Fluid Inertia," *ASME Jour. of Lubr. Tech.*, 105, 3, pp 539-547, (1983).
  - (19) Paranjpe, R. and Han, T., "A Transient Thermohydrodynamic Analysis Including Mass Conserving Cavitation for Dynamically Loaded Journal Bearings," *ASME Jour. of Trib.*, 117, 2, pp 369-378, (1995).
  - (20) Paranjpe, R., "A Study of Dynamically Loaded Engine Bearings Using a Transient Thermohydrodynamic Analysis," STLE/ASME Tribology Conf., Kissimmee, FL, STLE Preprint No. 95-TC-6A-2, (1995).
  - (21) Desbordes, H., Fillon, M., Frene, J. and Chan Hew Wai, C., "The Effects of Three Dimensional Pad Deformations on Tilting-Pad Journal Bearings Under Dynamic Loading," *ASME Jour. of Trib.*, 117, 3, pp 379-384, (1995).
  - (22) Gadangi, R. K. and Palazzolo, A. B., "Transient Analysis of Tilt Pad Journal Bearings Including Effects of Pad Flexibility and Fluid Film Temperature," *ASME Jour. of Trib.*, 117, pp 302-307, (1995).
  - (23) Padavala, S., "Dynamic Analysis of Arbitrary Profile Liquid Annular Seals and Transient Analysis with Large Eccentric Motion," Ph.D. Dissertation, Texas A&M University, College Station, TX, (1993).
  - (24) McCarty, R. D., *Thermophysical Properties of Fluids, MIPROPS 86*, NBS Standard Reference Data Base 12, National Bureau of Standards, CO, (1986).
  - (25) Bathe, K., *Finite Element Procedures in Engineering Analysis*, Prentice-Hall, Englewood Cliffs, NJ, pp 508-511, (1982).
  - (26) Launder, B. E. and Leschziner, M., "Flow in Finite Width Thrust Bearings Including Inertial Effects. I—Laminar Flow. II—Turbulent Flow," *ASME Jour. of Lubr. Tech.*, 100, pp 330-345, (1978).
  - (27) Van Doormal, J. P. and Raithby, G. D., "Enhancements of the SIMPLE Method for Predicting Incompressible Fluid Flows," *Numerical Heat Transfer*, 7, pp 147-163, (1984).
  - (28) Childs, D. and Hale, K., "A Test Apparatus and Facility to Identify the Rotordynamic Coefficients of High Speed Hydrostatic Bearings," *ASME Jour. of Trib.*, 116, 1, pp 337-344, (1994).

3. "Bulk-Flow Model for the Transition to Turbulence Regime in Annular Seals," 1996, Zirkelback, N., and L. San Andres, *STLE Tribology Transactions*, Vol.39, 4, pp. 835-842.





# Bulk-Flow Model for the Transition to Turbulence Regime in Annular Pressure Seals<sup>©</sup>

NICOLE ZIRKELBACK (Member, STLE) and LUIS SAN ANDRES (Member, STLE)  
Texas A&M University

Mechanical Engineering Department  
College Station, Texas 77843-3123

*An analysis for the prediction of the dynamic force response for annular seals in the transition regime to flow turbulence is presented. A heuristic curve fit connects the laminar friction factor to Moody's turbulent friction factor curve in the transition regime from laminar to fully developed turbulent flows. A universal friction factor model*

*is provided and included in the bulk-flow equations (zeroth- and first-order) governing the flow for small amplitude rotor motions about an equilibrium position. General equations are presented for the shear coefficients and their derivatives required in the bulk-flow model. Flow rates, drag torque and rotordynamic force coefficients are compared with those from traditional analyses for an annular seal experiencing wear and increased clearances leading to off-design operating conditions. Predicted seal force coefficients show physically sound, smooth variations while passing through the transition zone and demonstrate a marked improvement over simpler models which predict sharp discontinuities.*

Presented at the 51st Annual Meeting  
in Cincinnati, Ohio  
May 19-23, 1996

Final manuscript approved February 28, 1996

## NOMENCLATURE

$c_s$	= seal nominal clearance (m)	$Re_p$	= $\rho \cdot c_s^3 \Delta P / \mu \cdot R$ , nominal pressure flow Reynolds number
$C_{\alpha\beta}$	= damping force coefficients; $\alpha, \beta = X, Y$ (N · s/m)	$Re_p^*$	= $Re_p(c_s / R)$ , modified pressure flow Reynolds number
$D$	= rotor diameter (m)	$Re_s$	= $\rho \omega c_s^2 / \mu$ , squeeze film Reynolds number
$f_c, f_s$	= friction factors for bulk-flow model	$R_r$	= $(\rho / \mu) H [(U - \Omega R)^2 + V^2]^{1/2}$ , Reynolds number relative to rotor surface
$f_r^*, f_s^*$	= Moody's turbulent flow friction factors at rotor and stator surfaces (Eq. [11])	$R_s$	= $(\rho / \mu) H [U + V]^{1/2}$ , Reynolds number relative to stator surface
$H$	= seal film thickness (m)	$r_s, r_r$	= mean surface roughness at stator and rotor [m]
$h$	= dimensionless film thickness; $h = H/c_s = 1 + \epsilon_X \cos\theta + \epsilon_Y \sin\theta$	$t$	= time (sec)
$h_X, h_Y$	= $\cos\theta, \sin\theta$ , circumferential perturbation functions	$U_s$	= $\Delta P c_s^2 / \mu \cdot R$ , characteristic fluid velocity (m/s)
$k_x, k_y$	= $1/2 (k_r + k_s)$ , dimensionless shear parameters in axial and circumferential directions	$u$	= $U/U_s$ , dimensionless circumferential bulk-flow velocity
$k_r, k_s$	= $f_r R_r, f_s R_s$ , shear parameters at rotor and stator surfaces	$v$	= $V/U_s$ , dimensionless axial bulk-flow velocity
$K_{\alpha\beta}$	= stiffness force coefficients; $\alpha, \beta = X, Y$ (N/m)	$\{X, Y\}$	= inertial coordinate system
$L$	= seal length (m)	$\{x, y\}$	= coordinate system on seal plane; $\{\bar{x}, \bar{y}\} = \{x/R, y/R\}$
$M_{\alpha\beta}$	= inertia force coefficients; $\alpha, \beta = X, Y$ (kg)	$\beta$	= $U_s / \Omega R$ , entrance swirl factor
$P$	= fluid pressure (Pa)	$\theta$	= $x/R$ , circumferential coordinate (radians)
$P_s, P_n$	= external supply and discharge pressures (Pa)	$\gamma$	= first-order perturbed shear coefficients given in Eq. [8] and Table 1
$\Delta P$	= $(P_s - P_n)$ ; pressure drop across seal (Pa)	$\epsilon_X, \epsilon_Y$	= $e_X/c_s, e_Y/c_s$ , dimensionless rotor eccentricities in $X, Y$ directions
$p$	= $(P - P_n) / \Delta P$ , dimensionless pressure	$\Delta\epsilon_X, \Delta\epsilon_Y$	= dimensionless perturbed eccentricities
$p_r$	= $(P_r - P_n) / \Delta P$ , dimensionless pressure at seal entrance	$\Lambda$	= $\Omega R / U_s$ , characteristic dimensionless rotor velocity
$p_X, p_Y$	= dimensionless dynamic pressures for perturbations in the $X, Y$ directions	$\mu, \mu_s, \bar{\mu}$	= fluid absolute viscosity (Pa · s), characteristic viscosity, $\mu / \mu_s$
$R$	= rotor radius (m)	$\xi$	= empirical entrance loss factor
$Re_r$	= $\rho \cdot \Omega R \cdot R / \mu$ , nominal circumferential flow Reynolds number	$\rho, \rho_s, \bar{\rho}$	= fluid density (kg/m <sup>3</sup> ), characteristic density, $\rho / \rho_s$
		$\sigma$	= $\omega R / U_s$ , whirl frequency parameter

$\tau$  =  $\omega t$ , dimensionless time coordinate  
 $\Omega$  = angular velocity of rotor (1/s)  
 $\omega$  = excitation or whirl frequency (1/s)

#### Subscripts

$e$  = entrance

0 = zeroth-order solution  
 $r$  = rotor  
 $s$  = stator  
 $\alpha, \beta$  = first-order perturbations in  $X, Y$  directions  
 $*$  = characteristic value

## KEY WORDS

Hydrodynamic Lubrication, Friction, Turbulent Lubrication, Petrochemical Industry Tribology

## INTRODUCTION

Annular seals are used to block interstage secondary flows in turbomachinery components. In pump applications, seals operating as neck ring or interstage seals lessen leakage of the process fluid from higher pressures to lower pressures. Black (1), Black and Murray (2), and Black and Jenssen (3) first described the paramount effect of liquid annular seals on the rotordynamic behavior of high-performance turbomachinery. Unlike fluid film bearings, high pressure gradients, large clearance-to-radius ratios, and low viscosity process fluids typical in annular seals cause the fluid flow to be turbulent in most cases.

Childs (4) introduced the bulk-flow analysis for prediction of the rotordynamic force coefficients in short-length annular seals. For fully developed turbulent flows in both the axial and circumferential directions, linear zeroth- and first-order perturbed flow equations determine the static and dynamic force characteristics of an annular seal. Childs' model employs Hirs' turbulent bulk-flow theory (5), where the wall shear stresses result from a combination of shear and pressure flow contributions. The friction factor used is based on two constants which depend solely on the flow Reynolds numbers relative to the rotor and stator surfaces.

Von Pragenau (6) first indicated that intentionally roughened stators and smooth rotors reduce undesired cross-coupled stiffness effects and improve seal stability. By using a surface roughness model, Childs and Dressman (7) found that tapered seals decrease leakage while providing an overall increase in the direct damping coefficients. The need for an analysis adequate to model macroscopically rough surfaces led to the realization that Hirs' equation does not contain the physics necessary to represent these situations. Moody's friction factor, adapted from the Moody diagram for pipe flow, is a function of both the Reynolds number for the flow and surface roughness. Nelson and Nguyen (8) show that predictions for smooth seals using Hirs' equation and Moody's equation yield nearly identical results. However, calculations based on Moody's model deviate significantly for roughened surface seals, predicting higher direct and cross-coupled stiffnesses and smaller cross-coupled damping coefficients. Historically, Hirs-based models underpredict direct stiffness compared to experimentally identified values, and this departure increases with increasing surface roughness. Thus, the results from a Moody's equation bulk-flow model indicate an improvement in the prediction of rotordynamic coefficients.

To date, annular seals have been studied in the fully developed turbulent flow regime induced by the high-axial pressure gradients and large clearance-to-radius ratios. However, annular seals and oil seal floating rings used in the petrochemical industry typically operate with high viscosity fluids and relatively low shaft speeds (1800 to 3600 rpm), indicating laminar flow conditions (9). Increased clearances due to normal or unexpected wear cause seals that would normally function in the laminar regime to operate in the transition regime to turbulence. Black and Murray (2) first addressed this issue in a simplified manner when they called attention to the dramatic changes in stiffness associated with the flow regime. Changes in stiffness can be the cause of severe nonlinearities. Incidentally, as the rotor eccentricity increases in turbulent flow seals, flow relaminarization at the minimum film thickness could occur with a sudden change in the seal stiffness which would affect the dynamics of the rotating system.

Transition from laminar to turbulent flow is a complex issue which greatly depends on the nature of the flow and is yet to be completely understood. Singer and Dinavahi (10) present two models for transition regime flow and compare them to existing experiments for seven different flow types. This reference elucidates the complexity of the phenomenon of transition regime flow but, unfortunately, cannot be used within the context of an engineering application.

San Andres (11) and Yang et al. (12) present variable-property thermohydrodynamic bulk-flow analyses for off-centered annular seals. The computational programs provide leakage, static load, power loss, and rotordynamic force coefficients for seals operating in the laminar flow or turbulent flow regimes. Numerical predictions compare favorably with available experimental results and other existing analyses (13), (14). However, the lack of a sound analysis in the transition flow regime leads to discontinuities in predicting the dynamic force coefficients, since the flow is either laminar flow or fully developed turbulent flow with a sharp discontinuity occurring in the friction factor at the onset of the transition zone.

The objective of this paper is to provide a more accurate tool for the design of annular seals. More specifically, the equations which govern the flow within the annulus of the seal are modified by introducing a universal friction factor equation valid for all flow regimes (15). The formulation needed for the transition regime to flow turbulence is discussed within the framework of an isothermal flow analysis (12). Numerical predictions are compared to values obtained from the traditional analysis across the transition flow regime. The model introduced is very simple and does not address the many complexities of the transition flow regime to turbulence since these are yet to be well understood (16). On

the other hand, a successful representation of seal performance depends more on a good characterization of the basic friction laws than on the model of flow turbulence selected.

### ANALYSIS

Figure 1 shows an annular seal at an eccentric position  $(e_x, e_y)$  which denotes the lateral displacement of the rotor from its centered position. The shaft rotates at angular speed  $\Omega$ , and the fluid is confined to the space in the annulus between rotor and stator where  $H$  is the seal film thickness. In the seal annulus, the continuity and momentum bulk-flow equations for isothermal conditions are given for a variable property fluid as (11)

$$\begin{aligned} \frac{\partial}{\partial x}(\rho H U) + \frac{\partial}{\partial y}(\rho H V) + \frac{\partial}{\partial t}(\rho H) &= 0 \\ -H \frac{\partial P}{\partial x} &= \frac{\mu}{H} \left( k_x U - k_r \frac{\Omega R}{2} \right) \\ + \left\{ \frac{\partial}{\partial t}(\rho H U) + \frac{\partial}{\partial x}(\rho H U^2) + \frac{\partial}{\partial y}(\rho H U V) \right\} & \quad [1] \\ -H \frac{\partial P}{\partial y} &= \frac{\mu}{H} k_y V \\ + \left\{ \frac{\partial}{\partial t}(\rho H V) + \frac{\partial}{\partial x}(\rho H U V) + \frac{\partial}{\partial y}(\rho H V^2) \right\} \\ \{0 \leq x \leq 2\pi R, 0 \leq y \leq L\} \end{aligned}$$

The bulk-flow equation, Eq. [1], is widely used for turbulent-flow annular seals. Minor modifications to the advection transport terms are necessary for superlaminar flow conditions where rotational effects are significant. However, these variations are of no consequence to annular pressure seals (13).

Consider the rotor to describe small motions of amplitude  $(\Delta e_x, \Delta e_y)$  at a frequency  $\omega$  about an equilibrium position  $(e_{x0}, e_{y0})$ . Then, the film thickness is given in dimensionless form as

$$h = h_0 + (\Delta e_x h_x + \Delta e_y h_y) e^{i\omega t} \quad [2a]$$

where

$$\begin{aligned} h_0 &= H/r = 1 + \epsilon_{x0} \cos \theta + \epsilon_{y0} \sin \theta; \\ h_x &= \cos \theta; h_y = \sin \theta \end{aligned} \quad [2b]$$

are the equilibrium film thickness and perturbed film functions due to the rotor displacements. For small amplitude motions, the flow variables (pressure and velocities), fluid properties, and shear factors can be expanded in a Taylor series. In dimensionless form, the series expansion is given by

$$\phi = \phi_0 + e^{i\tau} (\Delta \epsilon_x \phi_x + \Delta \epsilon_y \phi_y), \quad i = \sqrt{-1} \quad [3]$$

where  $\phi = \{u, v, p, \bar{\rho}, \mu, k_x, k_y\}$ . Substituting the flow variables, Eqs. [2] and [3], into the governing equations gives

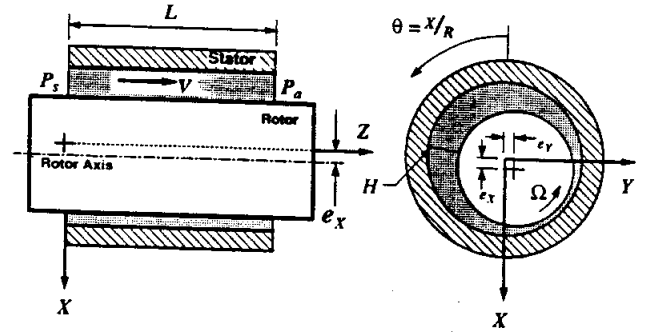


Fig. 1—Geometrical description of an annular pressure seal.

the zeroth-order dimensionless equations (11):

$$\begin{aligned} \frac{\partial}{\partial \bar{x}}(\bar{\rho}_0 h_0 u_0) + \frac{\partial}{\partial \bar{y}}(\bar{\rho}_0 h_0 v_0) &= 0 \\ -h_0 \frac{\partial \bar{p}_0}{\partial \bar{x}} &= \frac{\bar{\mu}_0}{h_0} \left( k_{x0} u_0 - k_{r0} \frac{\Lambda}{2} \right) \\ + Re_p^* \left\{ \frac{\partial}{\partial \bar{x}}(\bar{\rho}_0 h_0 u_0^2) + \frac{\partial}{\partial \bar{y}}(\bar{\rho}_0 h_0 u_0 v_0) \right\} & \quad [4] \\ -h_0 \frac{\partial \bar{p}_0}{\partial \bar{y}} &= \frac{\bar{\mu}_0}{h_0} k_{y0} v_0 \\ + Re_p^* \left\{ \frac{\partial}{\partial \bar{x}}(\bar{\rho}_0 h_0 u_0 v_0) + \frac{\partial}{\partial \bar{y}}(\bar{\rho}_0 h_0 v_0^2) \right\} \\ \{0 \leq \bar{x} \leq 2\pi, 0 < \bar{y} < \frac{L}{R}\} \end{aligned}$$

The entrance pressure and inlet circumferential preswirl velocity are prescribed as (12)

$$p_{r0}|_{\bar{y}=0} = 1 - \frac{(1 + \xi)}{2} \bar{\rho}_0 v_{\theta 0}^2|_{\bar{y}=0}; \quad u_0|_{\bar{y}=0} = \beta \Lambda \quad [5a]$$

while the exit pressure is set to discharge conditions as

$$p_0(\bar{y} = L/R) = 0 \quad [5b]$$

The resulting first-order dimensionless equations are (11)

$$\begin{aligned} \frac{\partial}{\partial \bar{x}}(\bar{\rho}_0 u_{\alpha} h_0) + \bar{\rho}_0 u_0 h_{\alpha} + \bar{\rho}_{\alpha} u_0 h_0 & \\ + \frac{\partial}{\partial \bar{y}}(\bar{\rho}_0 v_{\alpha} h_0) + \bar{\rho}_0 v_0 h_{\alpha} + \bar{\rho}_{\alpha} v_0 h_0 &= -i\sigma(\bar{\rho}_0 h_{\alpha} + \bar{\rho}_{\alpha} h_0) \\ -h_0 \frac{\partial \bar{p}_0}{\partial \bar{x}} &= i\bar{\rho}_0 h_0 Re_{\alpha} u_{\alpha} + \gamma_{xx} u_{\alpha} + \gamma_{xy} v_{\alpha} \\ &+ \gamma_{xh} h_{\alpha} + \gamma_{xp} \bar{p}_{\alpha} + \gamma_{x\mu} \bar{\mu}_{\alpha} \\ + Re_p^* \left\{ \frac{\partial}{\partial \bar{x}}(\bar{\rho}_0 h_0 u_0 u_{\alpha}) + \frac{\partial}{\partial \bar{y}}(\bar{\rho}_0 h_0 v_0 u_{\alpha}) \right. & \\ \left. + \bar{\rho}_0 h_0 \left[ u_{\alpha} \frac{\partial u_0}{\partial \bar{x}} + v_{\alpha} \frac{\partial u_0}{\partial \bar{y}} \right] \right\} & \quad [6] \end{aligned}$$

$$\begin{aligned}
-h_0 \frac{\partial p_0}{\partial y} = & i \bar{\rho}_0 h_0 R e_s v_\alpha + \gamma_{yy} v_\alpha + \gamma_{yx} u_\alpha \\
& + \gamma_{yh} h_\alpha + \gamma_{yp} \bar{p}_\alpha + \gamma_{y\mu} \bar{\mu}_\alpha \\
& + R e_p^* \left\{ \frac{\partial}{\partial x} (\bar{\rho}_0 h_0 u_0 v_\alpha) + \frac{\partial}{\partial y} (\bar{\rho}_0 h_0 v_0 v_\alpha) \right. \\
& \left. + \rho_0 h_0 \left[ u_\alpha \frac{\partial v_0}{\partial x} + v_\alpha \frac{\partial u_0}{\partial y} \right] \right\}
\end{aligned}$$

where the subscript  $\alpha = X, Y$  corresponds to rotor perturbations in the  $X$  and  $Y$  directions, respectively.

The boundary conditions for the perturbed fields are

$$\begin{aligned}
P_\alpha|_{\bar{y}=0} = & \frac{(1 + \xi)}{2} (\bar{p}_\alpha v_0^2 + 2 \bar{\rho}_0 u_0 v_\alpha) ; \\
u_\alpha|_{\bar{y}=0} = & 0, \text{ and } P_\alpha|_{\bar{y}=L/R} = 0
\end{aligned} \quad [7]$$

The zeroth- and first-order dimensionless equations describe the equilibrium rotor position and perturbed dynamic motions, respectively. The perturbed shear coefficients found in the first-order equations ( $\gamma_{xx}$ ,  $\gamma_{xy}$ ,  $\gamma_{xh}$ , etc.) arise from the perturbation of the shear coefficients  $k_x$ ,  $k_y$ , etc. The general form of the perturbed shear coefficients is given by the following relationships:

$$\begin{aligned}
\gamma_{yh} = & \left( -2 \frac{k_y}{h} + \frac{\partial k_y}{\partial h} \right) \frac{\bar{\mu}_0 u_0}{h_0} \\
\gamma_{yy} = & \left( \frac{k_y}{v} + \frac{\partial k_y}{\partial v} \right) \frac{\bar{\mu}_0 u_0}{h_0} \\
\gamma_{yx} = & \left( \frac{\partial k_y}{\partial u} \right) \frac{\bar{\mu}_0 u_0}{h_0} \\
\gamma_{y\mu} = & \left( k_y + \frac{\partial k_y}{\partial \mu} \bar{\mu} \right) \frac{u_0}{h_0} \\
\gamma_{yp} = & \left( -\frac{k_y}{\bar{p}} + \frac{\partial k_y}{\partial \bar{p}} \right) \frac{\bar{\mu}_0 u_0}{h_0} - \frac{h_0}{\bar{\rho}_0} \frac{\partial p_0}{\partial y}
\end{aligned} \quad [8a]$$

$$\begin{aligned}
\gamma_{xh} = & \left( -2 \frac{k_x}{h} + \frac{\partial k_x}{\partial h} \right) \frac{\bar{\mu}_0 u_0}{h_0} + \left( 2 \frac{k_r}{h} - \frac{\partial k_r}{\partial h} \right) \frac{\bar{\mu}_0 \Lambda}{2 h_0} \\
\gamma_{xx} = & \left( \frac{k_x}{u} + \frac{\partial k_x}{\partial u} \right) \frac{\bar{\mu}_0 u_0}{h_0} + \left( -\frac{\partial k_r}{\partial u} \right) \frac{\bar{\mu}_0 \Lambda}{2 h_0} \\
\gamma_{xy} = & \left( \frac{\partial k_x}{\partial v} u - \frac{\partial k_r}{\partial v} \frac{\Lambda}{2} \right) \frac{\bar{\mu}_0}{h_0} \\
\gamma_{x\mu} = & \left( k_x + \frac{\partial k_x}{\partial \mu} \bar{\mu} \right) \frac{u_0}{h_0} - \left( k_r + \frac{\partial k_r}{\partial \mu} \bar{\mu} \right) \frac{\Lambda}{2 h_0} \\
\gamma_{xp} = & \left( -\frac{k_x}{\bar{p}} + \frac{\partial k_x}{\partial \bar{p}} \right) \frac{\bar{\mu}_0 u_0}{h_0} \\
& - \left( -\frac{k_r}{\bar{p}} + \frac{\partial k_r}{\partial \bar{p}} \right) \frac{\bar{\mu}_0 \Lambda}{2 h_0} - \frac{h_0}{\bar{\rho}_0} \frac{\partial p_0}{\partial x}
\end{aligned} \quad [8b]$$

In most bulk-flow models, the shear coefficients at the rotor and stator are described by the following relationship (5):

$$k_{r,s} = f_{r,s} \cdot R_{r,s} \quad [9]$$

For laminar flow, i.e., Reynolds numbers  $R_{r,s} \leq 1000$ , the shear coefficients are  $k_r = k_s = 12(17)$ . In this regime, the friction factor is just defined as

$$f_{r,s} = \frac{12}{R_{r,s}} \quad [10]$$

For turbulent flow ( $R_{r,s} \geq 3000$ ), the friction factor corresponding to Moody's equation (8) is

$$f_{r,s}^* = a_M \left[ 1 + \left\{ c_M \left( \frac{r_{r,s}}{H} \right) + \frac{b_M}{R_{r,s}} \right\}^{e_M} \right] \quad [11]$$

where  $a_M = 0.001375$ ,  $b_M = 5 \times 10^5$ ,  $c_M = 10^4$ , and  $e_M = 1/3$ . Moody's friction factor is based on a large number of experimental observations and is selected due to its simplicity and ability to represent rough surfaces.

Previous bulk-flow analyses have used the friction factor for turbulent flows starting at a Reynolds number of 1000. Figure 2 shows the Moody diagram, a graph of friction factor vs. Reynolds number for increasing values of surface roughness. As shown in the diagram, transition from laminar to turbulent flow is generally accepted to occur at flow Reynolds numbers between 1000 to 3000. For simplicity, past annular seal models extended the turbulent friction factor line through the transition regime until intersection with the laminar friction factor line. To obtain a more physically realistic model, Artiles (15) proposed a curve fit to the Moody diagram connecting the laminar and turbulent friction factor lines in the transition regime. A cubic polynomial most resembles available experimental data, and the relation given in (15) is

$$f_{r,s} = \frac{12}{R_{r,s}} (1 - 3\xi_{r,s}^2 + 2\xi_{r,s}^3) + f_{r,s}^* (3\xi_{r,s}^2 - 2\xi_{r,s}^3) \quad [12]$$

where

$$\xi_{r,s} = \frac{R_{r,s} - A_1}{A_2}, \quad A_1 = 1000, A_2 = 2000 \quad [13]$$

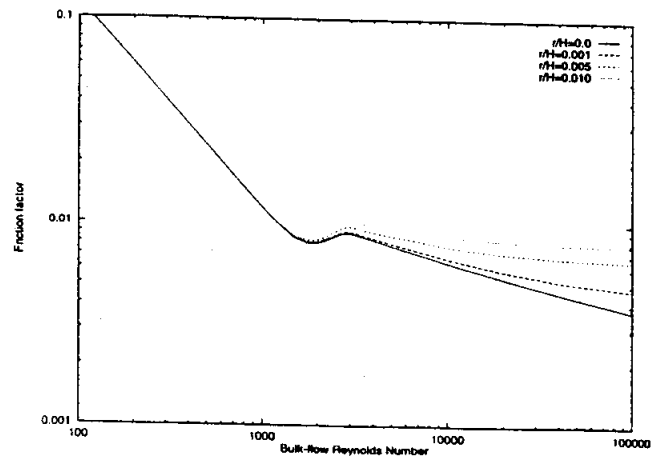


Fig. 2—Friction factor diagram for various surface roughness ratios.

TABLE 1—PERTURBED SHEAR COEFFICIENTS

$\gamma_{yh}$	$\frac{\bar{\mu}_0 v_0}{h_0^2} [-4k_y + t_{1,r}R_r + t_{1,s}R_s + t_{2,r}(2C_{rr} + k_r^*) + t_{2,s}(2C_{rs} + k_s^*)]$
$\gamma_{yy}$	$\bar{\mu}_0 \left\{ \frac{k_y}{h} + \frac{v^2 \left( Re_{\rho} \frac{\bar{\rho}}{\mu} \right)^2 h}{2} \left( \frac{t_{1,r}}{R_r} + \frac{t_{1,s}}{R_s} \right) + t_{2,r}f_{r1}v^2 + t_{2,s}f_{s1}v^2 \right\}_0$
$\gamma_{yx}$	$\bar{\mu}_0 \left\{ \frac{v \left( Re_{\rho} \frac{\bar{\rho}}{\mu} \right)^2 h}{2} \left( \frac{t_{1,r}(u - \Lambda)}{R_r} + \frac{t_{1,s}u}{R_s} \right) + t_{2,r}f_{r1}v(u - \Lambda) + t_{2,s}f_{s1}uv \right\}_0$
$\gamma_{y\mu}$	$\frac{V}{2h_0} [2k_y + t_{1,r}R_r + t_{1,s}R_s - t_{2,r}(k_r^* + \gamma_r b_M) - t_{2,s}(k_s^* + \gamma_s b_M)]$
$\gamma_{y\rho}$	$\frac{\bar{\mu}_0 v_0}{2h_0 \bar{\rho}_0} [-2k_y + t_{1,r}R_r + t_{1,s}R_s + t_{2,r}(k_r^* + \gamma_r b_M) + t_{2,s}(k_s^* + \gamma_s b_M)] - \frac{h_0}{\bar{\rho}_0} \frac{\partial \bar{p}_0}{\partial y}$
$\gamma_{xh}$	$\frac{\bar{\mu}_0}{h_0^2} \left\{ -2k_x u + k_r \Lambda + \frac{t_{1,r}R_r(u - \Lambda)}{2} + \frac{t_{1,s}R_s u}{2} + t_{2,r}(u - \Lambda) \left[ C_{rr} + \frac{k_r^*}{2} \right] + t_{2,s}u \left[ C_{rs} + \frac{k_s^*}{2} \right] \right\}_0$
$\gamma_{xx}$	$\bar{\mu}_0 \left\{ \frac{k_x}{h} + \frac{\left( Re_{\rho} \frac{\bar{\rho}}{\mu} \right)^2 h}{2} \left( \frac{t_{1,r}(u - \Lambda)^2}{R_r} + \frac{t_{1,s}u^2}{R_s} \right) + t_{2,r}f_{r1}(u - \Lambda)^2 + t_{2,s}f_{s1}u^2 \right\}_0$
$\gamma_{xy}$	$\bar{\mu}_0 \left\{ \frac{v \left( Re_{\rho} \frac{\bar{\rho}}{\mu} \right)^2 h}{2} \left( \frac{t_{1,r}(u - \Lambda)}{R_r} + \frac{t_{1,s}u}{R_s} \right) + t_{2,r}f_{r1}v(u - \Lambda) + t_{2,s}f_{s1}vu \right\}_0$
$\gamma_{x\mu}$	$\frac{1}{2h_0} [2k_x u - k_r^* \Lambda + t_{1,r}R_r(u - \Lambda) + t_{1,s}R_s u - t_{2,r}(u - \Lambda)(k_r^* + \gamma_r b_M) - t_{2,s}u(k_s^* + \gamma_s b_M)]_0$
$\gamma_{x\rho}$	$\frac{\bar{\mu}_0}{2h_0 \bar{\rho}_0} [-2k_x + k_r^* \Lambda + t_{1,r}R_r(u - \Lambda) + t_{1,s}R_s u + t_{2,r}(u - \Lambda)(k_r^* + \gamma_r b_M) + t_{2,s}u(k_s^* + \gamma_s b_M)]_0 - \frac{h_0}{\bar{\rho}_0} \frac{\partial \bar{p}_0}{\partial x}$
where	
$C_{rr} = 1/2 \left( \frac{R_r c_{M,r}}{c_s h_0} + b_M \right) \gamma_r$	$C_{rs} = 1/2 \left( \frac{R_s c_{M,s}}{c_s h_0} + b_M \right) \gamma_s$
$f_{r1} = \frac{\left( Re_{\rho} \frac{\bar{\rho}}{\mu} \right)^2 h_0}{2R_r} \left( f_r^* + \frac{\gamma_r b_M}{R_r} \right)$	$f_{s1} = \frac{\left( Re_{\rho} \frac{\bar{\rho}}{\mu} \right)^2 h_0}{2R_s} \left( f_s^* + \frac{\gamma_s b_M}{R_s} \right)$
$\gamma_r = \frac{-a_M \cdot e_M}{[f_r^*/a_M - 1]^{(1/e_M - 1)}}$	$\gamma_s = \frac{-a_M \cdot e_M}{[f_s^*/a_M - 1]^{(1/e_M - 1)}}$

and  $f_{r,s}^*$  is Moody's friction factor given by Eq. [11]. The friction factor curves shown in Figure 2 provide a gradual change in the transition flow regime. However, the variation in curvature at the transition zone proves to be of importance to the dynamic force characteristics of an annular seal. This will be shown later. Defining the following equations

$$t_{1,r,s} = \begin{cases} 0 & R_{r,s} \leq 1000 \\ \frac{6\xi_{r,s}(1 - \xi_{r,s})(k_{r,s}^* - 12)}{A_2} & 1000 < R_{r,s} < 3000 \\ 0 & R_{r,s} \geq 3000 \end{cases}$$

$$t_{2,r,s} = \begin{cases} 0 & R_{r,s} \leq 1000 \\ \xi_{r,s}^2(3 - 2\xi_{r,s}) & 1000 < R_{r,s} < 3000 \\ 1 & R_{r,s} \geq 3000 \end{cases}$$

and substituting the appropriate expressions into the general form of the perturbed shear coefficients gives the algebraic expressions listed in Table 1. These coefficients adjust the first-order equation for a more accurate prediction of the dynamic force coefficients in the transition flow regime. The simple formulation provided applies equally well to the laminar, transition, and fully developed turbulent flow regimes. Although the present work does not address the various phys-

ical aspects associated with transition regime flow, the model advanced is an effective tool to obtain engineering predictions for the seal rotordynamic coefficients in the transition regime to turbulence.

## PROCEDURE

The equations for the perturbed shear coefficients in the transition regime were incorporated into an existing computational program (11). Details of the numerical method used are given in the cited reference. Annular seal test cases for a process fluid (light oil) representative of a petrochemical application were analyzed. The following seal geometric parameters and operating conditions were used:  $P_i - P_a = 35$  bars, 17.2 bars;  $L = 0.0508$  m;  $D = 0.1524$  m;  $\Omega = 3000$  rpm ( $314.16 \text{ rad/s}$ );  $\rho = 900 \text{ kg/m}^3$ ;  $\mu = 13 \times 10^{-3} \text{ N}\cdot\text{s/m}^2$ ;  $\xi = 0.1$ ;  $\varepsilon_{X0} = \varepsilon_{Y0} = 0$ . In these calculations, the seal radial clearance was varied from  $190 \mu\text{m}$  to  $1100 \mu\text{m}$  with a nominal clearance of  $381 \mu\text{m}$ . Both the rotor and the stator are considered to be smooth. At the nominal clearance, the circumferential Reynolds number ( $Re_c = \rho \Omega R c_w / \mu_w$ ) is 631.4, and the axial flow Reynolds numbers ( $\rho V r_w / \mu_w = m / \pi l \mu_w$ ) are 1193.2 and 675.9 for 35 and 17.2 bar pressure drops, respectively. The use of this particular range of clearances represents one of two cases due to wear: a seal initially designed to perform in the laminar flow regime actually operates in the transition flow regime, or a seal designed to work in the transition flow regime actually operates in the turbulent flow regime.

## RESULTS

Generally, discontinuities that exist at the beginning of the transition flow regime for the conventional analysis are eliminated with the improved model. Figure 3 shows the seal flow rate to increase steadily with the seal clearance. In comparing the improved and traditional predictions for 35 bars (508 psi), the leakage in the transition regime is larger because the friction factor is lower than the friction factor corresponding to fully turbulent flow conditions. Predictions using

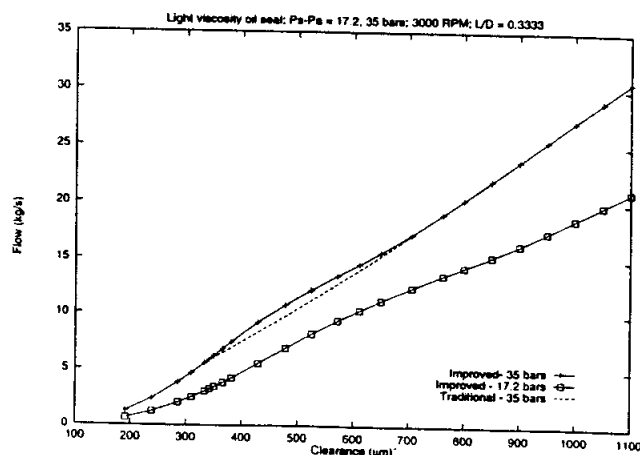


Fig. 3—Seal flow rate vs. operating clearance, improved vs. traditional bulk-flow model, centered seal.

the improved model for 17.2 bars (250 psi) are also included. Figure 4 shows the flow Reynolds number ( $Re_s$ ) and circumferential Reynolds number vs. seal clearance for a 35 bar (508 psi) pressure drop. The circumferential Reynolds number ( $Re_c$ ) increases linearly with seal clearance; however, the total stator Reynolds number ( $Re_s$ ) increases slightly for the improved model over the conventional model. The flow Reynolds number ( $Re_s$ ) and circumferential Reynolds number ( $Re_c$ ) are nearly the same at small clearances, indicating a dominance of shear flow. At large seal clearances, the flow within the seal is dominated by pressure-driven flow as shown by the large difference between the two Reynolds numbers.

Figure 5 shows a reduction in drag torque when operating from the laminar flow regime to the onset of the transition flow regime at both 17.2 bars (250 psi) and 35 bars (508 psi). Minimum torque is obtained at the onset of the transition regime and then rapidly increases into the turbulent flow regime. Note that the transition regime begins and ends at larger clearances for the predictions at 17.2 bars. The drag torque for the traditional model at 35 bars is grossly overpredicted and shows a sharp discontinuity. The actual torque may lie in a zone between the two models since the transition flow regime is known to be non-stationary in nature.

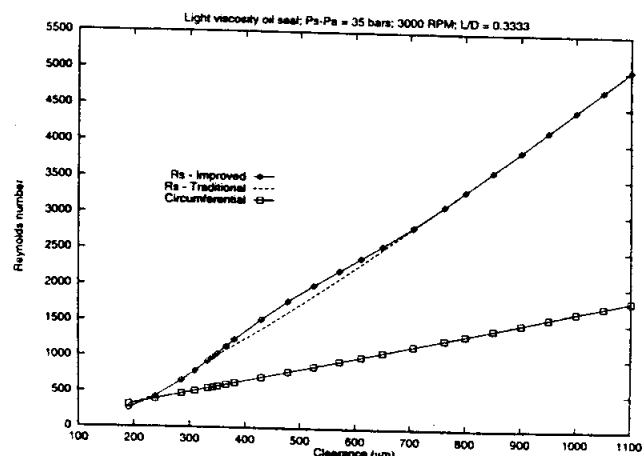


Fig. 4—Flow Reynolds number ( $Re_s$ ) and circumferential Reynolds number ( $Re_c$ ) vs. operating clearance, improved vs. traditional bulk-flow model, centered seal.

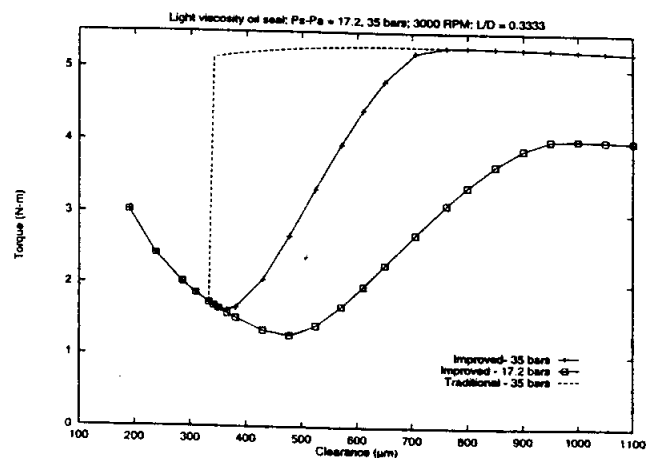


Fig. 5—Drag torque vs. operating clearance, improved vs. traditional bulk-flow model, centered seal.

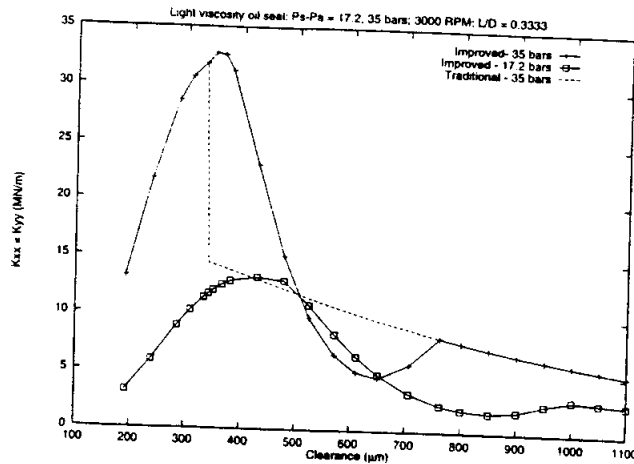


Fig. 6—Direct stiffness coefficients ( $K_{xx}$ ,  $K_{yy}$ ) vs. operating clearance, improved vs. traditional bulk-flow model, centered seal.

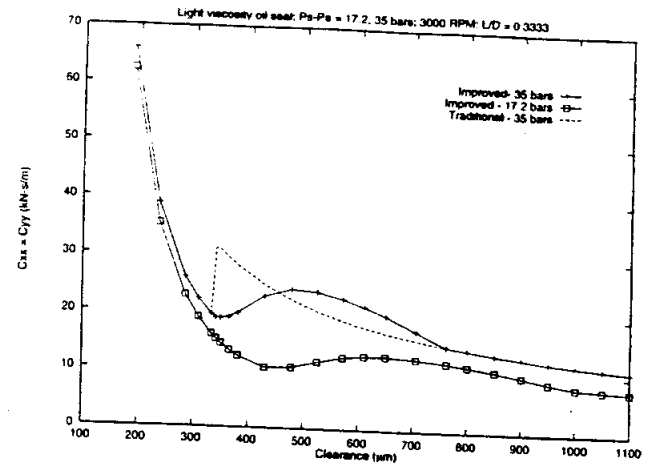


Fig. 8—Direct damping coefficients ( $C_{xx}$ ,  $C_{yy}$ ) vs. operating clearance, improved vs. traditional bulk-flow model, centered seal.

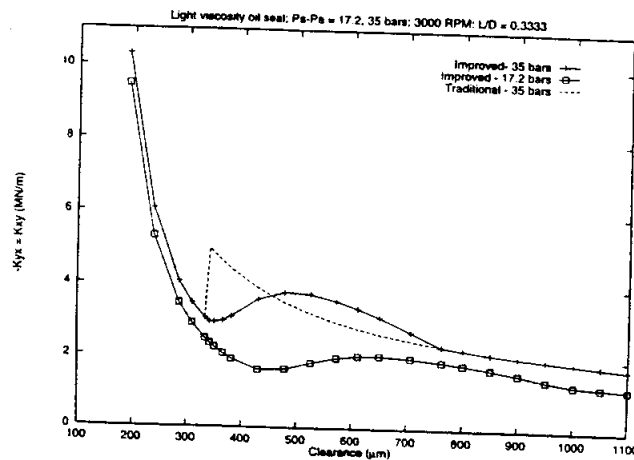


Fig. 7—Cross-coupled stiffness coefficients ( $K_{xy} = -K_{yx}$ ) vs. operating clearance, improved vs. traditional bulk-flow model, centered seal.

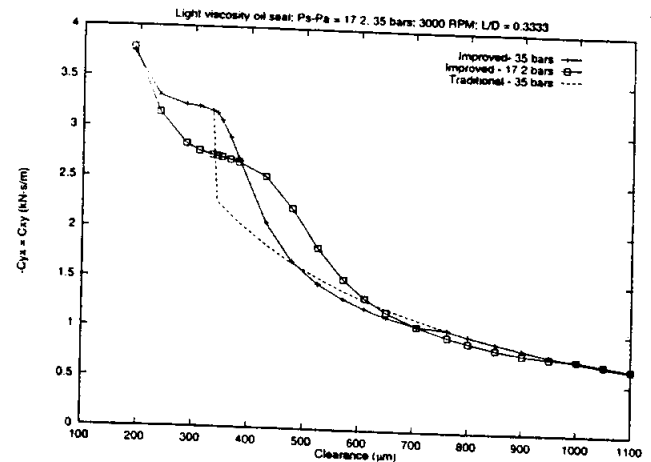


Fig. 9—Cross-coupled damping coefficients ( $C_{xy} = -C_{yx}$ ) vs. operating clearance, improved vs. traditional bulk-flow model, centered seal.

Figures 6–10 depict the synchronous dynamic force coefficients as they vary with seal clearance for the two pressure drops. For concentric operation, the direct coefficients are identical while the cross-coupled coefficients differ only in sign. The direct stiffness coefficients ( $K_{xx}$ ,  $K_{yy}$ ), shown in Fig. 6, continue to increase into the transition flow regime. After reaching a maximum in this zone, the direct stiffness coefficients generally decrease into the turbulent flow regime. Thus, an optimum (maximum) value for direct stiffness is obtained just after the onset of the transition flow regime. Close to the end of the transition zone, the direct stiffnesses show a dramatic drop and, under certain operating conditions, may eventually lead to negative values. This important characteristic, due to the change in curvature of the friction factor as shown in Fig. 2, has been observed in annular seal test rigs when raising the pressure drop across the seal to that required for fully turbulent flow conditions (2). Note that the conventional model (either laminar or turbulent flow) predictions show a sharp discontinuity in direct stiffnesses at the onset of the transition zone.

The cross-coupled stiffness coefficients ( $K_{xy} = -K_{yx}$ ) decrease rapidly from the laminar flow regime into the transition flow regime as shown in Fig. 7. After a slight rise in

the transition regime, the cross-coupled stiffness coefficients decrease to the onset of fully developed turbulence. The improved model results do not show the sharp discontinuity apparent in the calculations based on the traditional analysis.

Figure 8 shows the direct damping coefficients ( $C_{xx}$ ,  $C_{yy}$ ) to have an identical behavior to the cross-coupled stiffnesses. The cross-coupled damping coefficients ( $C_{xy} = -C_{yx}$ ), illustrated in Fig. 9 generally decrease with increasing seal clearance. The current analysis does not show the significant drops in the damping coefficients as predicted by the traditional model at the onset of the transition flow regime.

The direct inertia coefficients ( $M_{xx}$ ,  $M_{yy}$ ) are depicted in Fig. 10. From the laminar flow regime, the direct inertia coefficients decrease into the transition flow regime. After increasing slightly, the direct inertia continues decreasing into the turbulent flow regime. The cross-coupled inertia coefficients are one order of magnitude smaller than the direct coefficients and are not shown for brevity. It is important to note the seal whirl frequency ratio ( $K_{xy}/\Omega C_{xx}$ ) remains constant at approximately 0.5 for the two models. A seal whirl frequency ratio equal to 0.5 is a natural consequence of the inlet circumferential preswirl specified for the test cases.

The results of the analysis show that an annular seal de-

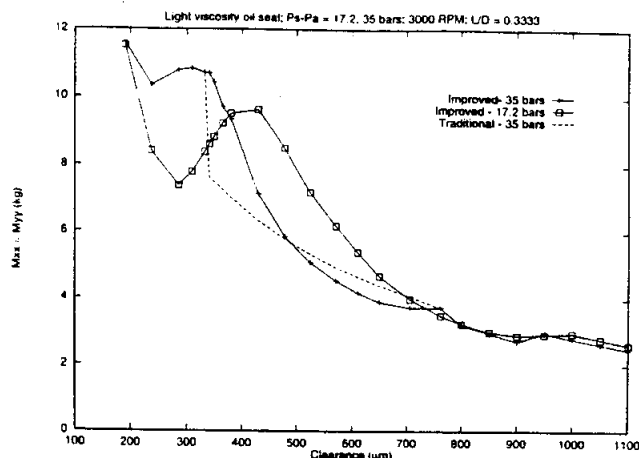


Fig. 10—Direct inertia coefficients ( $M_{xx}$ ,  $M_{yy}$ ) vs. operating clearance, improved vs. traditional bulk-flow model, centered seal.

signed for use in the laminar flow regime upon entering the transition flow regime after wearing will not only leak more, but may experience a significant rise in stiffness and a decrease in cross-coupled stiffness, direct damping, and direct inertia coefficients. On the other hand, a seal which initially operates in the transition zone after wearing may undergo a general reduction in all of its rotordynamic force coefficients. Further predictions for nominally turbulent flow seals operating eccentrically show the effect of local flow relaminarization on the rotordynamic force coefficients; however, these results are not shown here for brevity.

## CONCLUSIONS

Annular seals typically operate in the turbulent flow regime because of high axial pressure gradients and large clearance to radius ratios. However, high viscosity fluids and relatively slow rotor speeds along with worn clearances typical in petrochemical applications induce flows in the transition regime to turbulence. Traditional models for predicting force coefficients account for only laminar and/or turbulent flows and simplify the flow in the transition regime by extending turbulent friction factor lines to the onset of transition flow. To provide a better friction factor model for the determination of seal rotordynamic coefficients, the bulk-flow equations applicable to annular seals are modified to include the transition regime. A proposed cubic equation connecting the laminar friction factor line to turbulent friction factor lines on the Moody diagram renders a more accurate model for the friction factor within the transition flow regime. Computed predictions show the elimination of the discontinuities

that exist in traditional calculations for the dynamic force coefficients. The improved analysis also indicates an optimum value for direct stiffness just after the onset of the transition flow regime.

## ACKNOWLEDGMENTS

The graceful advice of Professor Dara Childs and the generous support of the TAMU Turbomachinery Research Consortium and the NASA Lewis Research Center are gratefully acknowledged.

## REFERENCES

- (1) Black, H. F., "Effects of Hydraulic Forces in Annular Pressure Seals on the Vibrations of Centrifugal Pump Rotors," *Jour. of Mech. Eng. Sci.*, **11**, pp 206-213, (1969).
- (2) Black, H. F. and Murray, J. L., "The Hydrostatic and Hybrid Bearing Properties of Annular Pressure Seals in Centrifugal Pumps," *The British Hydromechanics Res. Assoc., Paper No. 2.2*, (1969).
- (3) Black, H. F. and Jensen, D. N., "Effects of High Pressure Ring Seals on Pump Rotor Vibrations," *ASME Paper No. 71-WA/FF-38*, (1971).
- (4) Childs, D. W., "Dynamic Analysis of Turbulent Annular Seals Based on Hirs Lubrication Equation," *ASME Jour. of Lubr. Tech.*, **105**, pp 429-436, (1983).
- (5) Hirs, G. G., "A Bulk Flow Theory for Turbulence in Lubricating Films," *ASME Jour. of Lubr. Tech.*, **95**, 2, pp 137-146, (1973).
- (6) Von Pragenau, G. L., "Damping Seals for Turbomachinery," NASA, Washington, D.C., *NASA TP 1987*, (1982).
- (7) Childs, D. and Dressman, J., "Convergent-Tapered Annular Seals: Analysis and Testing for Rotordynamic Coefficients," *ASME Jour. of Trib.*, **107**, 3, pp 307-317, (1985).
- (8) Nelson, C. and Nguyen, B., "Comparison of Hirs' Equation with Moody's Equation for Determining Rotordynamic Coefficients of Annular Pressure Seals," *ASME Jour. of Trib.*, **109**, 1, pp 144-148, (1987).
- (9) Kirk, G. and Nicholas, J., "Analysis of High Pressure Seals for Optimum Rotor Turbo Compressor Dynamic Performance," in *Proc. of the 2nd Int'l. Conf. of Vibrations in Rotating Machinery*, IMech.E, Cambridge, UK, pp 125-134, (1980).
- (10) Singer, B. A. and Dinavahi, P. G., "Testing of Transition Regime Models," *ASME Jour. of Fluids Eng.*, **114**, 1, pp 73-79, (1992).
- (11) San Andres, L. A., "Analysis of Variable Fluid Properties, Turbulent Annular Seals," *ASME Jour. of Trib.*, **113**, pp 694-702, (1991).
- (12) Yang, Z., San Andres, L. and Childs, D., "Thermal Effects in Cryogenic Liquid Annular Seals Part I: Theory and Approximate Solution," *ASME Jour. of Trib.*, **115**, 2, pp 267-284, (1993).
- (13) Simon, F. and Frene, J., "Analysis for Incompressible Flow in Annular Seals," *ASME Jour. of Trib.*, **114**, 3, pp 431-438, (1992).
- (14) Venkatamaran, B. and Palazzolo, A., "Thermohydrodynamic Analysis of Turbulent Annular Seals Using Circumferential Spline Interpolation," *Trib. Trans.*, **39**, 4, (1996).
- (15) Ariles, A. F., "Users Manual for Computer Code ICYL Cylindrical Seals Lubricated by Incompressible Fluids," Mechanical Technology Incorporated, Latham, NY, Report No. **92TM13**, Contract No. **NAS3-25644**, (1992).
- (16) Lucas, V., Danaila, S., Bonneau, O. and Frene, J., "Roughness Influence on Turbulent Flow Through Annular Seals," *ASME Jour. of Trib.*, **116**, 2, pp 321-329, (1994).
- (17) Constantinescu, V. N. and Galetuse, S., "On the Possibilities of Improving the Accuracy of the Evaluation of Inertia Forces in Laminar and Turbulent Films," *ASME Jour. of Lubr. Tech.*, **96**, 1, pp 69-79, (1974).



4 "Thermal Effects in Liquid Oxygen Hybrid Bearings," 1996, San Andres, L., Yang, Z., and D. Childs, *STLE Tribology Transactions*, Vol. 39, 3, pp. 654-662, ( Preprint 95-TC-3A-1).



# Thermal Effects in Liquid Oxygen Hydrostatic Journal Bearings<sup>®</sup>

ZHOU YANG

Cummins Engine Company, Inc.  
Charleston, South Carolina 29405-8521  
and

LUIS SAN ANDRES and DARA W. CHILDS

Texas A&M University  
Department of Mechanical Engineering  
College Station, Texas 77843

*Numerical predictions for static performance and rotordynamic coefficients for a roughened stator LO<sub>2</sub> HJB operating at typical conditions in the SSME HPOTP are presented. The calculations are performed for an adiabatic THD model and an isothermal flow model. The two flow models predict almost identical static and dynamic performance characteristics, even though large temperature increases and fluid property variations in the bearing fluid film are*

*predicted by the THD model. However, a high temperature rise across the bearing affects not only the liquid properties but also the bearing geometry. A parametric study shows a strong impact of bearing clearance variations on the bearing performance and, hence, the importance of thermal effects becomes evident.*

## KEY WORDS

Journal Bearings, Hydrostatic Bearings

## INTRODUCTION

The current space shuttle main engine (SSME) high pressure oxygen turbopump (HPOTP) has a duplex pair of ball

Presented as a Society of Tribologists and Lubrication Engineers paper at the STLE/ASME Tribology Conference in Kissimmee, Florida, October 8-11, 1995  
Final manuscript approved July 27, 1995

## NOMENCLATURE

$b$  = recess circumferential length (m)  
 $c, c_c$  = radial clearance, characteristic clearance (m)  
 $C_d$  = empirical orifice discharge coefficient  
 $C_p$  = specific heat (J/kg·K)  
 $C_{XX}, \dots, C_{YY}$  = damping coefficients (N·s/m)  
 $D$  = journal diameter (m)  
 $d_o$  = orifice diameter (m)  
 $e_X, e_Y$  = displacements of the journal in X and Y direction (m)  
 $F$  = total fluid film force (= external load) (N)  
 $H, h_r$  =  $c + e_X \cos \theta + e_Y \sin \theta$  film thickness, recess depth (m)  
 $K_{XX}, \dots, K_{YY}$  = stiffness coefficients (N/m)  
 $L, l$  = bearing axial length, recess axial length (m)  
 $M$  = mass flow rate of a bearing (kg/s)  
 $M_{XX}, \dots, M_{YY}$  = inertia or added mass coefficients (kg)  
 $N_{rec}$  = number of bearing recesses  
 $P$  = fluid pressure (N/m<sup>2</sup>)  
 $P_s, P_a, P_r$  = supply, discharge and recess pressures (N/m<sup>2</sup>)  
 $P_r$  =  $(P_r - P_a) / (P_s - P_a)$ , pressure ratio  
 $Q_s$  = heat flux to the bounding surfaces (W/m<sup>2</sup>)  
 $R$  = journal radius (m)  
 $Re_a$  =  $\rho_s V c_s / \mu_s$ , reference axial flow Reynolds number  
 $Re_r$  =  $\rho_s R \Omega c_s / \mu_s$ , nominal circumferential flow Reynolds number  
 $Re_s$  =  $\rho_s R \omega c_s / \mu_s$ , nominal squeeze film Reynolds

number  
 $\tau_j, \tau_B$  = mean roughness depth at journal and bearing surfaces (m)  
 $T$  = two-dimensional bulk temperature in the fluid film (K)  
 $t$  = time (sec)  
 $T_s$  = inlet supply temperature at the orifice (°K)  
 $\Delta T$  = temperature-rise across bearing length (°K)  
 $U, V$  = mean flow circumferential and axial velocities (m/s)  
 $X, Y$  = inertial coordinates defining journal position in bearing  
 $x, y, z$  =  $(O, \pi D), (O, L), (O, H(x, y, t))$ , coordinates defining flow regions  
 $\beta_r$  = volumetric expansion coefficient (1/K)  
 $\alpha$  = circumferential velocity entrance swirl factor  
 $\Omega$  = rotational speed of journal (rad/sec)  
 $\omega$  = excitation or whirling frequency (rad/sec), ( $\omega = \Omega$ )  
 $\rho, \rho_s$  = fluid density, characteristic density (kg/m<sup>3</sup>)  
 $\mu, \mu_s$  = fluid viscosity, characteristic viscosity (Ns/m<sup>2</sup>)  
 $\xi_{x,y}$  = empirical entrance loss coefficients in X, Y directions  
 $\xi_{u,x,y}$  =  $\xi_x$  at up- and down-stream of recess/land entrance, respectively  
 $e_{x,y}$  =  $(e_X, e_Y) / c_s$  dimensionless journal eccentricities in X, y directions  
 $\tau_{xz}, \tau_{yz}$  = wall shear stresses in X and Y directions

bearings supporting both ends of the rotor (1). Although the HPOTP has operated successfully on every space shuttle flight, the ball bearings must be replaced after each flight due to the significant wear in the engine's liquid oxygen ( $\text{LO}_2$ ) environment. Therefore, hydrostatic journal bearings (HJBs) operating in liquid oxygen have been selected to increase the life of the turbopump and reduce both manufacturing and maintenance costs. Analytical methods and models for conventional HJBs with low speeds and viscous lubricants are no longer valid for cryogenic liquid HJBs where high speeds and loads are combined with large temperature variations (2). Cryogenic liquids present properties strongly dependent on their local state of pressure and temperature. Constant properties or even isothermo-barotropic fluid models can not describe the actual variations of the fluid properties, and predictions based on such assumptions are not appropriate (3).

### ANALYTICAL MODEL

The general type of bearing considered as a support element for cryogenic liquid turbopumps is a cylindrical hydrostatic journal bearing, orifice-compensated, with a variable number of feeding recesses or pockets machined in the surface of the bearing, as shown in Fig. 1 (4).

The unique flow characteristics of cryogenic liquid bearings determine fluid inertia, flow turbulence, fluid properties and thermal effects to be important for the accurate prediction of bearing performance. A bulk-flow thermohydrodynamic (THD) analysis has been developed to determine the static and dynamic performance characteristics of orifice-compensated product-lubricated HJBs in the turbulent flow regime (3), (5). Fluid inertia terms, both temporal and advective, are preserved in the analysis by using film-averaged momentum equations instead of the conventional Reynolds equation. Flow turbulence is accounted for in the momentum and energy equations through turbulence shear parameters based on friction factors derived from Moody's formulae. Pointwise evaluation of temperature and, hence, liquid properties is achieved through the solution of the energy equation in the fluid film with adiabatic boundaries. This apparent oversimplification has been validated for product-lubricated (such as  $\text{LO}_2$ ) annular seals with high axial pressure gradients (6). The two-dimensional bulk-flow governing equations for thin fluid film flows are (7):

#### Continuity Equation

$$\frac{\partial(\rho H)}{\partial t} + \frac{\partial(\rho H U)}{\partial x} + \frac{\partial(\rho H V)}{\partial y} = 0 \quad [1]$$

#### Circumferential-Momentum Equation

$$\begin{aligned} \frac{\partial(\rho H U)}{\partial t} + \frac{\partial(\rho H U^2)}{\partial x} + \frac{\partial(\rho H U V)}{\partial y} \\ = -H \frac{\partial P}{\partial x} + \tau_{xz}|_0^H \end{aligned} \quad [2]$$

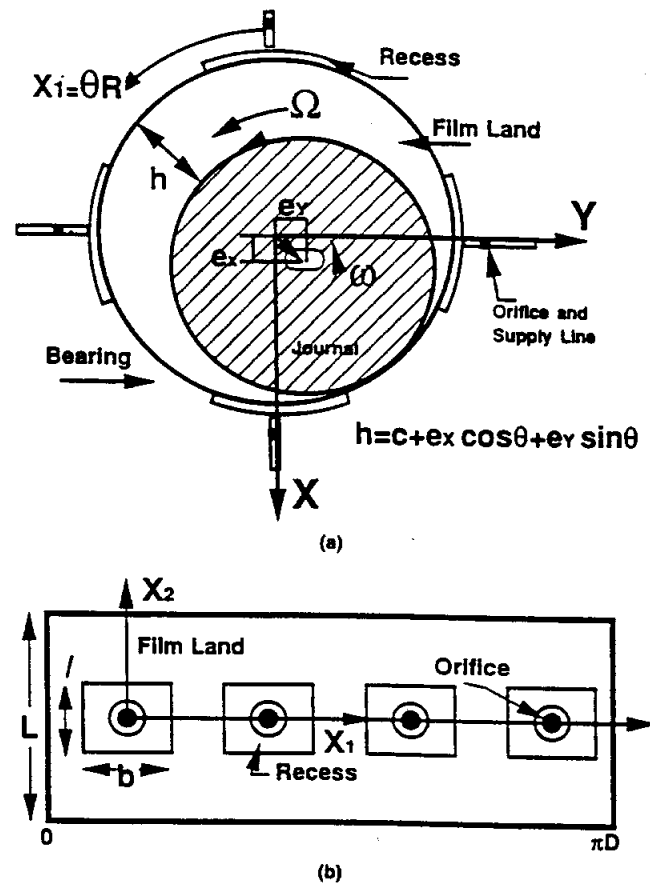


Fig. 1—Geometry of a hydrostatic journal bearing.  
(a) description of coordinate systems  
(b) unwrapped bearing surface for analysis

#### Axial-Momentum Equation

$$\begin{aligned} \frac{\partial(\rho H V)}{\partial t} + \frac{\partial(\rho H U V)}{\partial x} + \frac{\partial(\rho H V^2)}{\partial y} \\ = -H \frac{\partial P}{\partial y} + \tau_{yz}|_0^H \end{aligned} \quad [3]$$

#### Energy-Transport Equation

$$\begin{aligned} C_p \left( \frac{\partial(\rho H T)}{\partial t} + \frac{\partial(\rho H U T)}{\partial x} + \frac{\partial(\rho H V T)}{\partial y} \right) + Q_s \\ = T \beta_t H \left( \frac{\partial P}{\partial t} + U \frac{\partial P}{\partial x} + V \frac{\partial P}{\partial y} \right) \\ + R \Omega \tau_{xz}|^H - U \tau_{xz}|_0^H - V \tau_{yz}|_0^H \end{aligned} \quad [4]$$

where the bulk-flow primitive variables ( $U$ ,  $V$ ,  $P$ , and  $T$ ) are defined as average quantities across the film thickness, and  $Q_s$  represents the heat flux from the fluid film to the bounding solids (rotor and stator). For an adiabatic flow process,  $Q_s$  is zero.

Equations for global mass and energy conservations are derived at the bearing recess regions. The effects of fluid compressibility at the recess volumes and the orifice supply lines are also included. Fluid inertia at the recess edges are modeled by Bernoulli-type relationships, while a pressure rise in

the downstream portion of the recess due to journal rotation is considered and solved as a one-dimensional step bearing. The energy transport phenomenon in an HJB recess is controlled by the carryover of hot fluid from upstream to downstream of the recess, the mixing of cool fluid from the supply source into the recess volume, and the heat generation in the recess volume due to shear dissipation by journal rotation. Full details of the theoretical model can be found in recent publications (3), (5).

## NUMERICAL METHOD

The problem of calculating the flow and load performance characteristics of HJBs consists basically of determining the pressure, temperature, and flow field in the bearing film lands subject to the condition that the flow discharging from each recess through the bearing film lands must equal the flow entering that recess from supply pressure through a fixed orifice restrictor.

An efficient numerical scheme has been devised for solution of the velocity, temperature, and pressure fields in which zeroth-order fields represent the steady-state flow conditions at an equilibrium journal center position, while first-order fields determine the rotordynamic force coefficients of an HJB. The first-order linear equations are obtained from a perturbation of the flow equations for small-amplitude dynamic motions of the journal center about the static-equilibrium position.

The algorithm implemented is based on the well-known SIMPLEX procedure (8) in which the upwind scheme is used for the advection terms to make the numerical algorithm more stable. A Newton-Raphson scheme is implemented to update the recess pressure and to satisfy the mass continuity requirement at each recess. Convergence of the solution is achieved when the recess continuity constraints are satisfied. The numerical algorithm has been shown to be stable and efficient and not highly sensitive to variations of mesh sizes (9).

## RESULTS AND DISCUSSIONS

Numerical predictions from both the adiabatic THD and the isothermo-barotropic models are presented since no experimental measurements for LO<sub>2</sub> HJBs are available. The selection ranges of geometry and operating conditions for LO<sub>2</sub> HJBs are given by Ref. (4). Operating conditions and bearing geometry are assumed to be governed by the turbopump configuration. Available supply ( $P_s$ ) and discharge ( $P_a$ ) pressures, fluid supply temperature ( $T_s$ ) and the shaft speed ( $\Omega$ ) are set for the turbopump application. The journal diameter ( $D$ ) and bearing length ( $L$ ) must be compatible with space constraints, while the bearing radial clearance is determined by considerations cited by Butner and Murphy (4) such as:

1. Allowance for centrifugal growth of journal due to speed.
2. Margin for tolerances and distortion of the bearing.
3. Size of particles contained in the fluid.

4. Heat generation rates that increase with reduced clearances.
5. Allowance for unknown thermal effects.

Note that two of the five considerations (4) and (5) are related to thermal effects.

Table 1 presents the geometry and operating conditions for the LO<sub>2</sub> HJB test case. The orifice diameter ( $d_o$ ) is calculated by selecting the pressure ratio ( $p_r$ ) to be 0.5 for reasons explained later. The bearing stator surface is intentionally roughened ( $r_B/c_s = 4.4\%$ ) to reduce the cross-coupled hydrodynamic forces and, hence, to improve bearing stability. The empirical parameters for the numerical calculations are also given in Table 1. The orifice discharge coefficient ( $C_d$ ) is based on the experimental data for water HJBs as reported by Kurtin et al. (10), while the values of the recess edge entrance coefficients ( $\xi$ ) are taken directly from Scharrer et al. (1).

The LO<sub>2</sub> properties at the supply pressure  $P_s = 18.31$  MPa and temperature  $T_s = 90^\circ\text{K}$  are given as follows:

$$\rho_s = \rho_* = 1177 \text{ (kg/m}^3\text{)}, \quad \mu_s = 2.29 \times 10^{-4} \text{ (N-s/m}^2\text{)}$$

$$Cp_s = 1627 \text{ (J/kg}^\circ\text{K)}, \quad \beta_{ts} = 3.62 \times 10^{-3} \text{ (1/}^\circ\text{K)},$$

while the liquid properties at the discharge pressure  $P_a = 3.378$  MPa and supply temperature  $T_s = 90^\circ\text{K}$  are:

$$\rho_a = 1149 \text{ (kg/m}^3\text{)}, \quad \mu_a = 2.02 \times 10^{-4} \text{ (N-s/m}^2\text{)}$$

$$Cp_a = 1678 \text{ (J/kg}^\circ\text{K)}, \quad \beta_{ta} = 4.20 \times 10^{-3} \text{ (1/}^\circ\text{K)}.$$

These data show that the influence of pressure alone on LO<sub>2</sub> properties is small. The fluid compressibility at the recess pressure ( $p_r \approx 0.5$ ) is about  $1.65 \times 10^{-9} \text{ m}^2/\text{N}$ , showing that LO<sub>2</sub> is only slightly compressible.

The Reynolds numbers based on the supply properties are:

$$Re_c = 5.65 \times 10^4, \quad Re_a = 3.95 \times 10^6, \quad Re_s = 116$$

TABLE 1—GEOMETRY AND OPERATING CONDITIONS OF LIQUID OXYGEN HYDROSTATIC JOURNAL BEARINGS

Diameter ( $D$ )	74.168 mm
Length ( $L$ )	53.34 mm
Recess No. ( $N_{rec}$ )	8
Orifice Diameter ( $d_o$ )	1.4345 mm
Recess Area ( $l \times b$ )	$15.38 \times 15.38 \text{ mm}^2$
Recess Depth ( $H_r$ )	0.2286 mm
Radial Clearance ( $c$ )	0.0762 mm
Rotating Speed ( $\Omega$ )	37,360 cpm
Supply Pressure ( $P_s$ )	18.31 MPa
Discharge Pressure ( $P_a$ )	3.378 MPa
Supply Temp. ( $T_s$ )	$90^\circ\text{K}$
Stator Roughness ( $r_B/c_s$ )	4.4%
Orifice Flow Coeff. ( $C_d$ )	0.8852
Pre-swirling Factor ( $\alpha$ )	0.5
Recess Edge ( $\xi_a$ ) <sub>x</sub>	-0.5
Entrance Loss ( $\xi_d$ ) <sub>x</sub>	0.25
Coefficients ( $\xi_v$ )	-0.5

The high Reynolds numbers from both the shear flow ( $Re_r$ ) and pressure flow ( $Re_a$ ) show the importance of both hydrodynamic effects and flow turbulence. The squeeze-film-flow Reynolds number ( $Re_f$ ) is very large showing that fluid inertia (advection) is significant in  $LO_2$  HJBs.

### Orifice Diameter

The orifice diameter ( $d_o$ ) is a unique function of the recess pressure ratio ( $p_r$ ) for given bearing geometry parameters and operating conditions. For the concentric operating condition, the effects of the pressure ratio ( $p_r$ ) on the stiffness, damping, flow rate, and friction torque are determined by numerical calculations based on the THD model. Figures 2 and 3 show the orifice diameter ( $d_o$ ) as well as the static and dynamic performance characteristics of the bearing as a function of the pressure ratio. Both the orifice diameter and the mass flow rate increase rapidly with the pressure ratio. A higher pressure ratio ( $p_r$ ) results in a higher recess pressure ( $P_r$ ) and, hence, a larger mass flow rate for a bearing with fixed flow resistance of the bearing film due to the specified diameter ( $D$ ), length ( $L$ ) and radial clearance ( $c$ ). A larger flow rate, in turn, demands a smaller resistance of the orifice and, hence, a larger orifice diameter. Therefore, as the pressure ratio increases, the ratio of the film resistance to the orifice resistance increases and the friction torque also increases, as Fig. 2 shows.

The variation of centering stiffness and damping coefficients with pressure ratio is the focus of this parametric study. Figure 3 shows that maximum direct stiffness is attained at a pressure ratio equal to 0.6 while the maximum damping occurs at  $p_r$  equal to 0.4. The whirl frequency ratio (WFR) is not sensitive to the variation of the pressure ratio, as Fig. 2 shows. A recess pressure ratio equal to 0.5 is then adequate to compromise the optimum stiffness and damping. Bearings with either an exceedingly high or low pressure ratio will lose stiffness and have difficulty maintaining a steady film thickness. A recess pressure ratio of 0.5 is chosen and the corresponding orifice diameter is equal to 1.435 mm for the current  $LO_2$  HJB example.

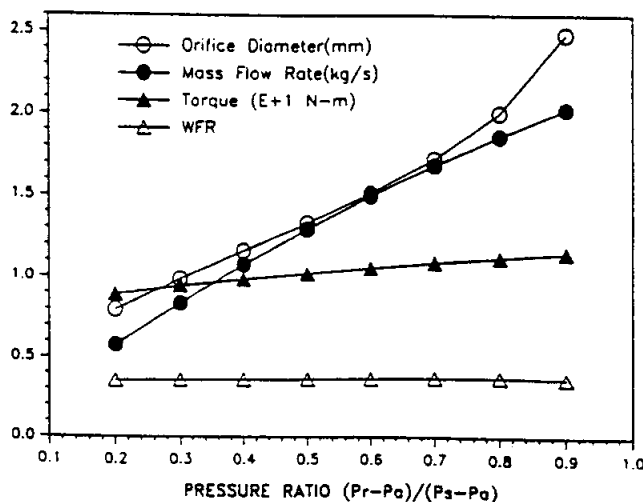


Fig. 2—Orifice diameter, leakage, torque, and WFR vs. pressure ratio ( $p_r$ ) ( $LO_2$  HJB:  $P_s = 18.31$  MPa,  $P_a = 3.378$  MPa,  $T_s = 90^\circ K$ ,  $\Omega = 37360$  rpm,  $r_g/c_s = 4.4\%$ ).

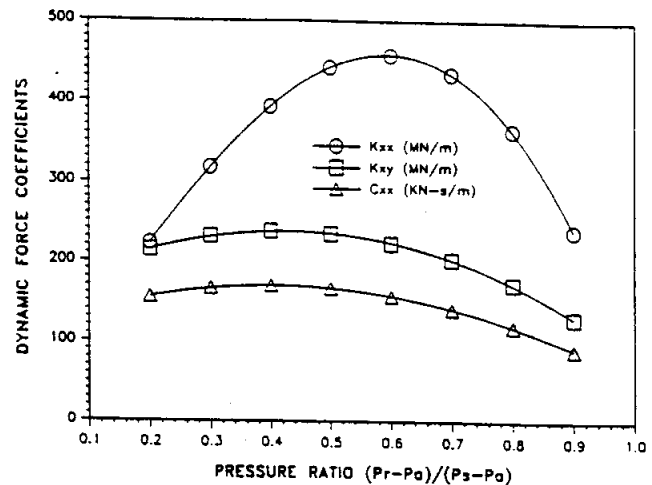


Fig. 3—Stiffness and direct damping coefficients vs. pressure ratio ( $p_r$ ) ( $LO_2$  HJB:  $P_s = 18.31$  MPa,  $P_a = 3.378$  MPa,  $T_s = 90^\circ K$ ,  $\Omega = 37360$  rpm,  $r_g/c_s = 4.4\%$ ).

### Static and Dynamic Performance Characteristics

Numerical results of the static and dynamic performance characteristics of the  $LO_2$  HJB example are given in Tables 2 and 3, respectively, where predictions by the THD model are presented in the first row for each journal eccentricity ratio, while results from the isothermo-barotropic model are given in the second row.

As the journal eccentricity ratio increases, the mass flow rate ( $M$ ) decreases. The two models predict approximately the same mass flow rate for all journal eccentricity ratios considered. The bearing reaction force ( $F$ ) increases almost linearly with increasing eccentricity ratio. The friction torque remains relatively constant for the THD prediction, and then shows a sudden reduction at a journal eccentricity ratio ( $\epsilon$ ) equal to 0.6 due to a large and sudden decrease in fluid viscosity (two-phase vaporization). The isothermal model predicts a larger friction torque which increases with eccentricity ratio. The maximum error in friction torque between the two models is 17.8% and occurs at the highest eccentricity ratio (0.7).

Figure 4 presents the dimensionless pressure maps for  $\epsilon = 0.7$ (a) and  $\epsilon = 0$  (b), respectively. The pressure field is symmetric both axially and circumferentially for  $\epsilon = 0$ , see Fig. 4(b). The sharp pressure drops at the recess/film entrances show the importance of fluid inertia at the recess edges. For  $\epsilon = 0.7$ , see Fig. 4(a), the pressure on the film lands increases in the converging film-thickness region, and then decreases in the diverging film region due to hydrodynamic effects. The maximum pressure occurs at the center of the film land between two recesses near the minimum film thickness. Unlike cavitation ( $P \leq P_a$ ), the local two-phase flow condition predicted due to liquid boiling has little influence on the pressure distribution.

The maximum temperature-rise in the fluid film predicted by the adiabatic THD model is  $19.2^\circ K$  at the concentric position and  $62.6^\circ K$  at a journal eccentricity ratio equal to 0.7. The large temperature rise is a direct consequence of the high rotational Reynolds number  $Re_r$  (turbulence) and the large value of stator roughness. Figure 5 shows the dimensionless temperature and film-thickness maps for the highest

TABLE 2—STATIC PERFORMANCE CHARACTERISTICS OF LO<sub>2</sub> HYDROSTATIC BEARING  
 $(\Omega = 37360 \text{ rpm}, P_s = 18.31 \text{ MPa}, P_a = 3.378 \text{ MPa},$   
 $r_B/c_s = 4.4\%, T_s = 90^\circ\text{K})$

$\epsilon_X$ ( $\epsilon_Y = 0$ )	$M$ (kg/s)	$F$ (N)	$T_{or}$ (N-m)	$T_{max}$ (°K)	$\rho_{min}$ (kg/m <sup>3</sup> )	$\mu_{min}$ (10 <sup>-4</sup> Ns/m <sup>2</sup> )
0.0*	1.293	0.0	10.21	109.2	1050	1.300
	1.300	0.0	11.04	90.0	1149	2.020
0.1*	1.291	3682	10.22	111.3	1039	1.240
	1.291	3643	11.06	90.0	1149	2.020
0.2*	1.278	7511	10.23	114.0	1023	1.170
	1.278	7493	11.10	90.0	1149	2.020
0.3*	1.257	11319	10.24	117.7	1001	1.080
	1.257	11237	11.16	90.0	1149	2.020
0.4*	1.228	15026	10.26	122.9	967	0.962
	1.227	14930	11.25	90.0	1149	2.020
0.5*	1.193	18522	10.25	130.6	911	0.805
	1.190	18326	11.38	90.0	1149	2.020
0.6*	1.154	21726	10.21	141.6	804	0.595
	1.150	21335	11.54	90.0	1149	2.020
0.7*	1.113	25045	10.01	152.6	121**	0.131**
	1.111	23981	11.78	90.0	1149	2.020

\* 1st row—THD model; 2nd row—Isothermo-barotropic model

\*\* Two-phase condition occurs locally in the bearing

eccentricity ratio ( $\epsilon = 0.7$ ) studied. These maps are symmetric about the circumferential center plane ( $y/R = 0$ ) due to geometric symmetry and no journal misalignment. The fluid temperatures increase axially and reach their maximum values at the discharge ends ( $y/R = L/D$ ). In the circumferential direction, the temperatures on the film lands increase in the converging film region, reaching their maximum values downstream of the minimum film thickness, maintaining the maximum values for a short distance, and then decreasing in the remaining diverging region. The maximum temperatures occur at the discharge ends near the location of the minimum film thickness.

Figure 6 shows the dimensionless density and viscosity maps for  $\epsilon = 0.7$  obtained from the THD model. Both density and viscosity near the bearing exit plane and minimum film region are reduced dramatically due to the large temperature rise. This temperature rise causes a two-phase flow condition to be predicted since the maximum fluid temperature is higher than the fluid saturation temperature. At the discharge pressure ( $P_a = 3.378 \text{ MPa}$ ), the saturation temperature is  $144.51^\circ\text{K}$  ( $\Delta T = 54.51^\circ\text{K}$ ). The saturation region between liquid and vapor is represented by the vaporization line and a larger pressure is accompanied by a higher saturation temperature (11). Note that most of the bearing is predicted to operate in a one-phase liquid regime since the phase change starts at a small local area around the maxi-

mum temperature and the minimum pressure location (in the bearing discharge plane). Note also that a two-phase flow condition due to liquid boiling in the bearing fluid film cannot be predicted by the isothermal model due to its uniform temperature assumption.

The stiffness, damping, and direct added mass rotor-dynamic force coefficients, and whirl frequency ratio are presented in Table 3. The cross-coupled added mass ( $M_{XY}$  or  $-M_{YX}$ ) is very small with negligible influence on the bearing dynamic performance. All the dynamic force coefficients remain relatively constant for journal eccentricity ratios equal to 0 to 0.4, and then the direct stiffness ( $K_{XX}$  or  $K_{YY}$ ) shows a sharp reduction while the cross-coupled stiffness ( $K_{XY}$  or  $-K_{YX}$ ) and direct damping ( $C_{XX}$  or  $C_{YY}$ ) increase for higher eccentricity ratios (0.5 to 0.7). The cross-coupled damping ( $C_{XY}$  or  $-C_{YX}$ ) coefficients are relatively small and their combined effect with the direct added mass ( $M_{XX}$  or  $M_{YY}$ ) coefficients on the bearing dynamic performance is negligible. Most rotordynamic codes only allow for fluid bearing models without added mass coefficients while retaining the cross-coupled damping. According to the analysis and results presented above, this kind of model will lead to substantial errors (9). The whirl frequency ratio (WFR) is relatively constant as the eccentricity ratio increases. The small magnitude ( $\leq 0.361$ ) of the WFR is a direct consequence of the roughened bearing stator surface. The maximum error

TABLE 3—DYNAMIC PERFORMANCE CHARACTERISTICS OF LO <sub>2</sub> HYDROSTATIC BEARING ( $\Omega = 37360$ rpm, $P_s = 18.31$ MPa, $P_a = 3.378$ MPa, $r_B/c_s = 4.4\%$ , $T_s = 90^\circ\text{K}$ )						
$\epsilon_X$ ( $\epsilon_Y = 0$ )	$K_{XX}/K_{YY}$ (MN/m)	$-K_{YX}/K_{XY}$ (MN/m)	$C_{XX}/C_{YY}$ (KN-s/m)	$-C_{YX}/C_{XY}$ (KN-s/m)	$M_{XX}/M_{YY}$ (kg)	WFR
0.0*	442/442	234/234	166/166	17.7/17.7	5.86/5.86	0.361
	442/442	235/235	169/169	21.3/21.3	7.19/7.19	0.358
0.1*	441/441	235/234	166/166	17.5/17.6	5.82/5.86	0.361
	442/442	235/235	169/169	21.2/21.3	7.16/7.19	0.357
0.2*	439/441	235/234	167/165	17.1/17.4	5.61/5.85	0.361
	440/442	235/235	171/169	20.8/21.2	7.02/7.20	0.356
0.3*	430/439	236/234	169/165	16.2/17.4	5.29/5.80	0.359
	429/440	236/235	173/169	20.0/21.5	6.83/7.20	0.354
0.4*	405/434	237/234	172/164	14.9/17.5	4.88/5.76	0.357
	400/434	236/234	176/169	19.0/22.0	6.63/7.22	0.351
0.5*	360/424	240/234	176/163	12.8/17.8	4.41/5.74	0.353
	347/422	239/234	180/168	17.1/23.2	6.53/7.27	0.345
0.6*	307/406	251/236	186/161	10.1/18.1	3.74/5.64	0.350
	276/401	253/235	193/168	14.7/25.3	6.57/7.38	0.337
0.7*	280/380	290/248	215/159	5.72/16.7	1.72/5.31	0.359
	203/371	300/241	229/170	11.5/28.4	6.76/7.53	0.335

\* 1st row—THD model; 2nd row—Isothermo-barotropic model

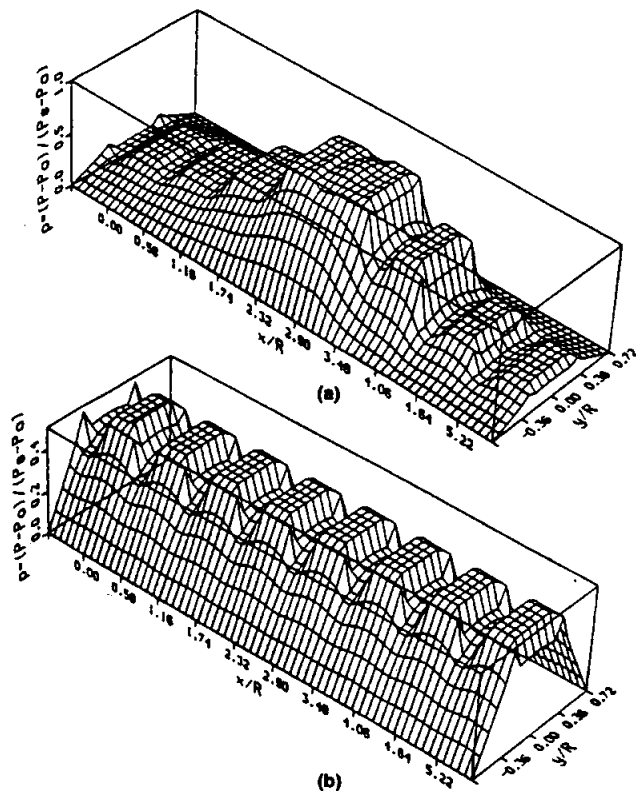


Fig. 4—Dimensionless pressure maps (LO<sub>2</sub> HJB, THD model)  
( $P_s = 18.31$  MPa,  $P_a = 3.378$  MPa,  $T_s = 90^\circ\text{C}$ ,  $\Omega = 37360$  rpm).  
(a)  $\epsilon = 0.7$   
(b)  $\epsilon = 0.0$

between the two models is 27.5% for direct stiffness, 3.5% for cross-coupled stiffness, 6.9% for direct damping and 6.7% for the WFR at the highest eccentricity ratio ( $\epsilon = 0.7$ ).

The fact that the two flow models predict almost identical static (except the friction torque) and dynamic performance characteristics for most of the eccentricity ratios considered is surprising, even though large temperature increases and property variations in the bearing fluid film are determined by the THD model. Butner and Murphy (4) performed a parametric study by varying inputs individually to determine the effects of bearing geometry and operating conditions on direct damping coefficients and showed that for LO<sub>2</sub> HJBs, the effects due to fluid density and viscosity alone are small. For a given bearing geometry (including orifice diameter,  $d_o$ ) and operating conditions, the flow resistance of the orifice is constant, while the reduction of fluid viscosity due to a temperature rise could reduce the flow resistance of the bearing film and, hence, lower the recess pressure ratios ( $p_r$ ) for the THD model. However, the variation of the recess pressure ratios is so small that the effects on the global bearing performance characteristics, like the mass flow rate, fluid film force, the dynamic force coefficients and the WFR, are negligible. The friction torque is an exception since it is directly proportional to the fluid effective viscosity.

However, the above comparison between the THD model and the isothermo-barotropic model does not exclude the importance of thermal effects in LO<sub>2</sub> HJBs. The high temperature rise predicted across the bearing affects not only the

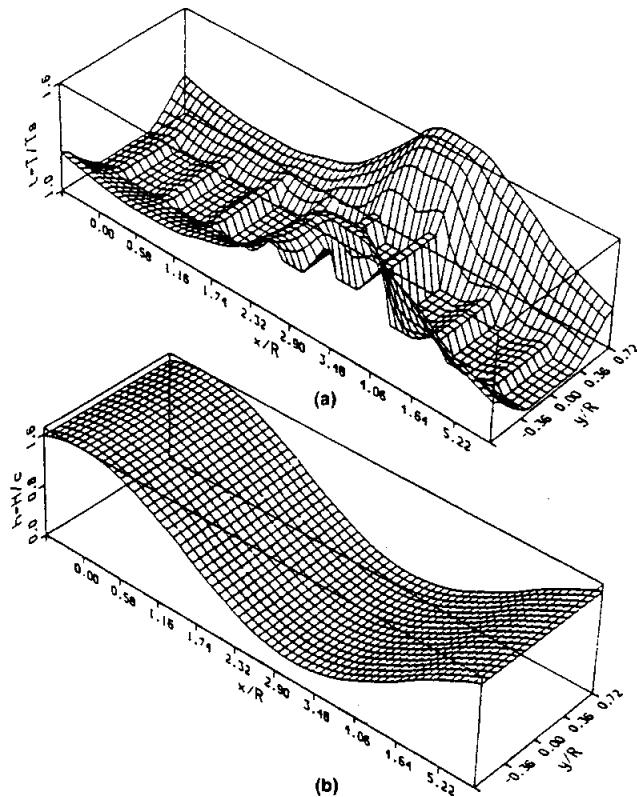


Fig. 5—Dimensionless temperature and film-thickness maps (LO<sub>2</sub> HJB) ( $\epsilon = 0.7$ ,  $P_s = 18.31$  MPa,  $P_r = 3.378$  MPa,  $T_s = 90^\circ\text{C}$ ,  $\Omega = 37360$  rpm).  
(a) temperature field  
(b) film-thickness

liquid properties, but also the operating clearance; this will have an impact on the bearing static and dynamic performance. In a recent publication, Morton (12) "maintains that the lack of agreement between theory and experiment on fixed arc journal bearings, as well as the differences between predictions and observed bearing-influenced characteristics on much rotating machinery, is simply due to neglecting thermal distortion of the bearing bush."

To account for elastic and thermal deformations in the journal and bearing, a more complicated model, namely a thermo-elastohydrodynamic (TEHD) model (13), is needed, where the continuity, momentum and energy equations in the fluid film and the heat conduction and elasticity equations in the solids must be solved simultaneously with additional boundary conditions. Here, the impact of thermal effects on bearing performance characteristics are demonstrated by simply varying the radial clearance.

#### Effects of Clearance Variation on Bearing Performance

As mentioned above, the bearing radial clearance is determined by several considerations among which thermal effects are important. The deformations of the bearing hardware due to thermal stresses sometimes can overshadow the deflections due to mechanical forces. Here, numerical predictions are performed using the THD model to determine the effects of varying radial clearance on bearing performance. All the other inputs of the bearing geometry, operating conditions and empirical parameters are as given in Table 1.

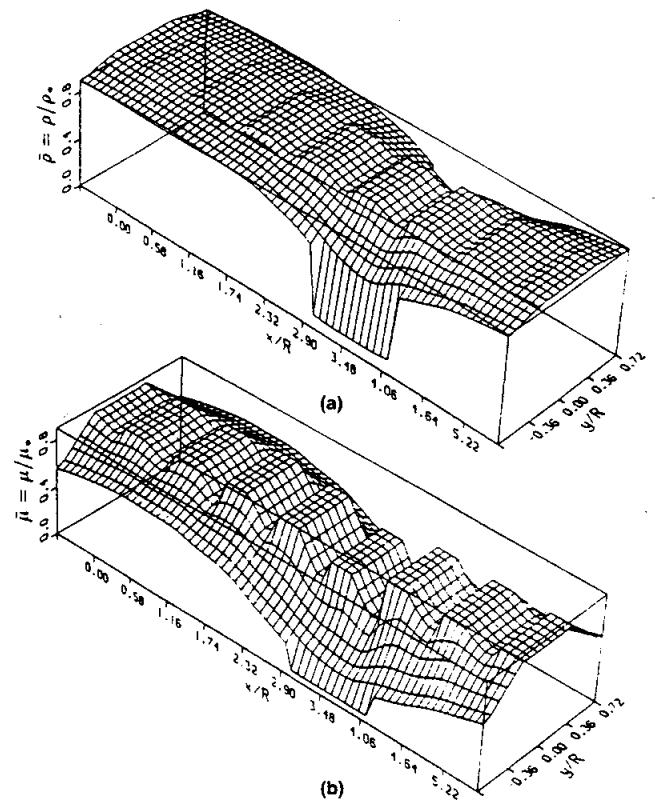


Fig. 6—Dimensionless density and viscosity maps (LO<sub>2</sub> HJB, THD model) ( $\epsilon = 0.7$ ,  $P_s = 18.31$  MPa,  $P_r = 3.378$  MPa,  $T_s = 90^\circ\text{C}$ ,  $\Omega = 37360$  rpm).  
(a) density field  
(b) viscosity field

Figures 7 and 8 show the bearing static and dynamic performance characteristics as a function of the radial clearance for the concentric operating conditions with the original orifice diameter of 1.435 mm. For convenience, the bearing with the original clearance of 0.0762 mm is taken as the baseline bearing.

As the radial clearance increases, the mass flow rate increases and the maximum fluid temperature decreases rapidly. The friction torque decreases slightly with increasing radial clearance except at the smallest clearance where the largest temperature rise ( $\Delta T = 40^\circ\text{K}$ ) induces a very low fluid viscosity and, hence, a low friction torque. The optimum recess pressure ratio of 0.5 for the baseline bearing is altered by the variation of the radial clearance. As the radial clearance increases from 0.0381 mm to 0.1143 mm, the recess pressure ratio decreases from 0.90 to 0.26.

The direct ( $K_{XX}$ ) and cross-coupled ( $K_{XY}$ ) stiffness and the direct damping ( $C_{XX}$ ) are presented in Fig. 8 as a function of the radial clearance. All these coefficients decrease greatly as the radial clearance increases except for the smallest clearance where a relatively low direct stiffness is predicted due to the extremely high recess pressure ratio ( $p_r = 0.9$ ). The whirl frequency ratio (WFR) decreases slightly with radial clearance (maximum difference: 15.6%) since a larger clearance provides a reduced film friction resistance and, hence, a smaller hydrodynamic effect.

For **eccentric** journal center operating conditions, the temperature rise in the fluid film is higher than that for the



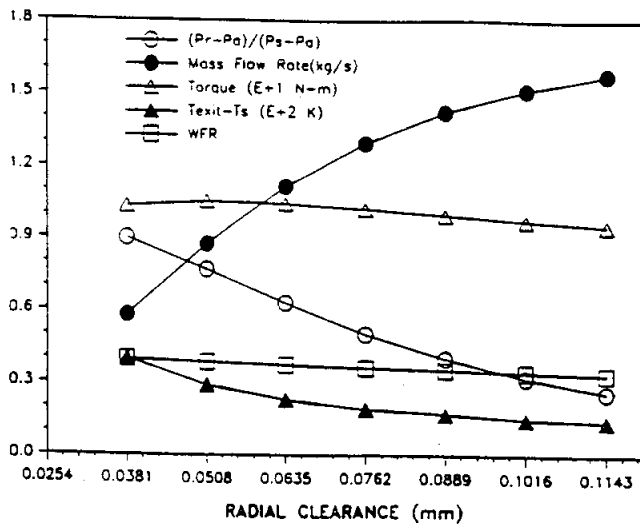


Fig. 7—Pressure ratio, leakage, torque, temperature and WFR vs. clearance ( $\text{LO}_2$  HJB:  $P_s = 18.31$  MPa,  $P_a = 3.378$  MPa,  $T_s = 90^\circ\text{K}$ ,  $\Omega = 37360$  rpm,  $r_B/c = 4.4\%$ ,  $d_o = 1.435$  mm).

concentric cases, and the nonuniform temperature distribution in the circumferential direction will induce a change in both the radial clearance and the eccentricity ratio. This will certainly aggravate the already serious thermal effects on the bearing performance.

## CONCLUSIONS AND RECOMMENDATIONS

Numerical predictions from both the THD model and the isothermo-barotropic model are presented for a roughened stator  $\text{LO}_2$  HJB operating at typical conditions in the SSME HPOTP. The maximum temperature rise in the fluid film predicted by the THD model is  $19.2^\circ\text{K}$  at the concentric position and  $62.6^\circ\text{K}$  at a journal eccentricity ratio equal to 0.7. The large temperature rise is a direct consequence of the high rotational Reynolds number  $Re_r$  (turbulence) and the large value of stator roughness. As journal eccentricity increases, both density and viscosity at the bearing exit are reduced dramatically due to the large temperature rise. The change is so large that at an eccentricity  $\epsilon_X = 0.7$ , a two-phase flow condition is predicted to occur by the THD model.

The two flow models predict almost identical static (except the friction torque) and rotordynamic coefficients for most journal eccentricity ratios considered, even though large temperature and fluid property variations in the bearing fluid film are predicted by the THD model. This result is explained because most of the HJB performance characteristics, like the flow rate, static force, and direct stiffness coefficients, are largely determined by the orifice flow (the pressure drop from supply to recess conditions). Therefore, for a given bearing geometry (including orifice diameter) and operating conditions, the effects of the fluid properties alone are small for  $\text{LO}_2$  HJBs. However, the extremely high temperature rise across the bearing affects not only the liquid properties but also the operating clearance. A parametric study shows the strong impact of clearance variations on the bearing static and dynamic performance and, hence, the importance of thermal effects in  $\text{LO}_2$  HJBs becomes apparent.

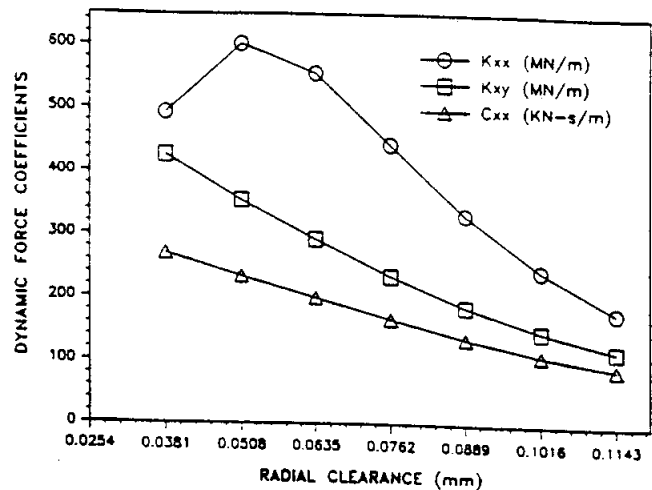


Fig. 8—Stiffness and direct damping coefficients vs. clearance ( $\text{LO}_2$  HJB:  $P_s = 18.31$  MPa,  $P_a = 3.378$  MPa,  $T_s = 90^\circ\text{K}$ ,  $\Omega = 37360$  rpm,  $r_B/c = 4.4\%$ ,  $d_o = 1.435$  mm).

The large temperature rise in the  $\text{LO}_2$  HJB predicted by the THD model cannot be overlooked. Excessive temperatures can lead to two-phase flow and the degradation of the working fluid or the bearing material. Steep temperature gradients may cause cracking of bearing material, and unequal thermal growth of components can induce distortion and seizure (14).

To reduce the variation of the bearing radial clearance due to the thermal effects, bearing materials with small thermal expansion coefficients are preferred. Moreover, the thermal expansion or contraction of the bearing materials should be compatible with their mating parts to avoid high thermal stresses and consequent cracking in the bearing materials. To account for simultaneous elastic and thermal deformations in the journal and bearing, a more complicated model, namely the TEHD model, is recommended.

## ACKNOWLEDGMENTS

The support of Pratt & Whitney Co. and NASA Lewis Research Center (NASA Grant NAG3-1434) is gratefully acknowledged.

## REFERENCES

- (1) Scharrer, J. K., Tellier, J. G. and Hibbs, R. L., "Start Transient Testing of Annular Hydrostatic Bearing in Liquid Oxygen," AIAA Paper No. 92-3404, (1992).
- (2) San Andres, L. A., "Analysis of Turbulent Hydrostatic Bearings with a Barotropic Cryogenic Fluid," *ASME J. of Trib.*, 114, pp 755-765, (1992).
- (3) Yang, Z., San Andres, L. and Childs, D., "Thermohydrodynamic Analysis of Process Liquid Hydrostatic Journal Bearings in Turbulent Regime, Part I: The Model and Perturbation Analysis; Part II: Numerical Solution and Results," *ASME J. of Appl. Mech.*, 117, (1995).
- (4) Butner, M. and Murphy, B., "SSME Long Life Bearings," NASA Report No. CR179455, (1986).
- (5) Yang, Z., San Andres, L. and Childs, D., "Process-Liquid Turbulent-Flow Hydrostatic Bearings: Analysis and Tests for Rotordynamic Coefficients," in *Proc. of the Fourth Int'l. Conf. on Rotor Dynamics*, Chicago, pp 233-241, (1994).

- (6) Yang, Z., San Andres, L. and Childs, D., "Importance of Heat Transfer from Fluid Film to Stator in Turbulent Flow Annular Seals," *Wear*, **160**, pp 269-277, (1993).
- (7) Yang, Z., San Andres, L. and Childs, D., "Thermal Effects in Cryogenic Liquid Annular Seals, Part I: Theory and Approximate Solution; Part II: Numerical Solution and Results," *ASME Jour. of Trib.*, **115**, pp 269-277, (1993).
- (8) Patankar, S., V., *Numerical Heat Transfer and Fluid Flow*, Hemisphere Publishing Corporation, McGraw-Hill Book Company, New York, (1980).
- (9) Yang, Z., "Thermohydrodynamic Analysis of Product-Lubricated Hydrostatic Bearings in Turbulent Regime," Ph.D. Dissertation, Texas A&M Univ., College Station, TX, (1992).
- (10) Kurtin, K. A., Childs, D., San Andres, L. and Hale, K., "Experimental vs. Theoretical Characteristics of a High-Speed Hybrid (Combination Hydrostatic and Hydrodynamic) Bearing," *ASME Jour. of Trib.*, **115**, pp 160-169, (1993).
- (11) Holman, J. P., *Thermodynamics*, McGraw-Hill Book Company, New York, (1969).
- (12) Morton, P. G., "Recent Advances in the Study of Oil Lubricated Journal Bearings," in *Proc. of the Fourth Int'l. Conf. on Rotor Dynamics*, pp 299-305, Chicago, (1994).
- (13) Khonsari, M. M. and Wang, S. H., "On the Fluid-Solid Interaction in Reference to Thermoelastohydrodynamic Analysis of Journal Bearings," *ASME Jour. of Trib.*, **113**, pp 398-404, (1991).
- (14) Pinkus, O., *Thermal Aspects of Fluid Film Tribology*, ASME Press, New York, (1990).

5 "Turbulent Flow, Flexure-Pivot Hybrid Bearings for Cryogenic Applications," 1996 San Andres, L., ASME *Journal of Tribology*, Vol. 118, 1, pp. 190-200, (ASME Paper 95-TRIB-14).

# Turbulent Flow, Flexure-Pivot Hybrid Bearings for Cryogenic Applications

Luis San Andres

Associate Professor,  
Department of Mechanical Engineering,  
Texas A&M University,  
College Station, TX 77843-2123

*The thermal analysis of flexure-pivot tilting-pad hybrid (combination hydrostatic-hydrodynamic) bearings for cryogenic turbopumps is presented. The advantages of this type of bearing for high speed operation are discussed. Turbulent bulk-flow, variable properties, momentum and energy transport equations of motion govern the flow in the bearing pads. Zeroth-order equations for the flow field at a journal equilibrium position render the bearing flow rate, load capacity, drag torque, and temperature rise. First-order equations for perturbed flow fields due to small amplitude journal motions provide rotordynamic force coefficients. A method to determine the tilting-pad moment coefficients from the force displacement coefficients is outlined. Numerical predictions correlate well with experimental measurements for tilting-pad hydrodynamic bearings. The design of a liquid oxygen, flexure-pad hybrid bearing shows a reduced whirl frequency ratio and without loss in load capacity or reduction in direct stiffness and damping coefficients.*

## Introduction

Advanced cryogenic turbomachinery designs demand a low part count number along with an *all-fluid-film-bearing* technology to increase life, improve efficiency, and reduce wear of system components. Advanced computational analyses (San Andres, 1990-93) have been validated with experimental data from a state of the art Hydrostatic Bearing Test Facility (Kurtin et al., 1993; Childs and Hale, 1994; Franchek et al., 1995). Despite the advantages provided by hybrid (combination hydrostatic and hydrodynamic) journal bearings (HJBs), fluid film bearing stability considerations and thermal phenomena accompanied by phase change are issues of primary concern for high speed cryogenic operation with large pressure differentials (San Andres, 1993). Bearing dynamic stability is related to hydrodynamic and liquid compressibility effects limiting severely the system operating speed to a value close to the first critical speed divided by the whirl frequency ratio (WFR). For fixed geometry-rotationally symmetric hybrid bearings handling incompressible liquids the WFR is just equal to 0.50 (San Andres, 1990) and verified by test measurements. Innovative fixed geometry hybrid bearings with improved stability have been designed and tested (Franchek et al., 1995). Some of these bearing configurations include rough-surface bearings, tangential liquid injection HJBs, and bearings with structural stiffness asymmetry.

The flexure-pad hybrid bearing (FPHB), see Fig. 1, is a promising alternative for use in high speed applications and without stability restrictions. Advanced automated machining processes are used to manufacture bearings of any specified tolerance for shape and film clearance as well as structural properties (Zeidan, 1992). The major advantage of this bearing over conventional tilting-pad bearings derives from its structured design and single-piece EDM manufacturing. The thin webs provide enough radial stiffness to support applied loads while allowing for rotational pad motions. Tilting-pad bearings

are mechanically complex due to their many parts, and on assembly, tolerances stack-up requiring a high degree of manufacturing accuracy to yield acceptable clearances. Furthermore, these bearings are supported on ball and socket type joints which are prone to rapid wear if the fluid media has no lubricity. This is the case with liquid cryogenics as well as with most process liquid applications. The flexure-pad structural arrangement offers a unique advantage to ensure combined hydrostatic and hydrodynamic actions with supply ports directly machined on the thin webs for delivery of a pressurized lubricant. This paper then presents the relevant analysis and computational predictions which demonstrate the feasibility of flexure-pad hybrid bearings for aerospace applications.

## Literature Review

Tilting-pad hydrodynamic journal bearings are used frequently as support elements in high speed rotating machinery requiring maximum stability. The ability of the bearing pads to rotate (about an individual pad pivot) determines a reduction or complete elimination of the undesirable cross-coupled stiffnesses which produce bearing instability in fixed geometry fluid film bearings. Flack and Allaire (1984), and Fillon et al. (1987, 1991) offer lucid reviews of the extensive theoretical literature relevant to tilting-pad bearings. Nicholas and Kirk (1979) and Nicholas (1994) discuss practical design issues in tilting-pad bearings and refer extensively to the many benefits these bearings have brought to rotating machinery.

The theoretical models describing the performance of tilting-pad journal bearings have steadily increased in complexity as well as in the number of parameters required to fully represent the flow. Three-dimensional thermohydrodynamic (THD) and structural effects as well as the lubricant feed and mixing mechanism are thought to be necessary for accurate prediction of peak pressure, minimum film thickness and temperature rise (Pinkus, 1990). Theoretical models currently account for variable fluid properties, heat transfer through the bearing pads, pad thermoelastic deformations, and pivot wear and flexibility. The analyses of Ettles (1980, 1992), Knight and Barrett (1988), and Taniguchi et al. (1990) are representative of these advanced developments.

Tilting-pad bearings have many more degrees of freedom than fixed geometry bearings, and consequently, their analysis is complicated and subject to a number of assumptions regard-

This work was funded by grant NAG3-1434 from NASA Lewis Research Center. Project Thermohydrodynamic Analysis of Cryogenic Liquid Turbulent Flow Fluid Film Bearings, Phase II.

Contributed by the Tribology Division of THE AMERICAN SOCIETY OF MECHANICAL ENGINEERS and presented at the STLE/ASME Tribology Conference, Orlando, FL, October 8-11, 1995. Manuscript received by the Tribology Division January 24, 1995; revised manuscript received June 15, 1993. Paper No. 95-Trib-14. Associate Technical Editor: R. F. Salant.

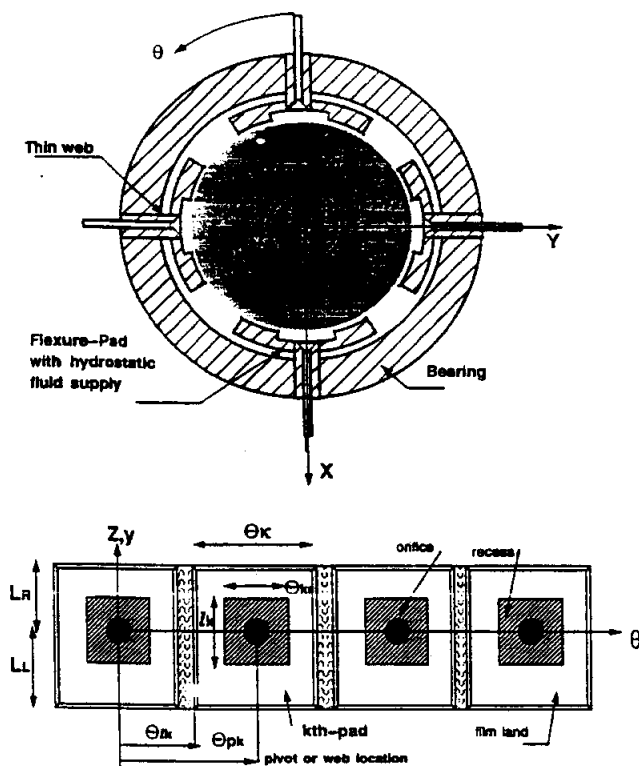


Fig. 1 Geometry of flexure-pad hybrid bearing

## Nomenclature

$A_0 = C_d \pi d_o^2 / 4$ , equivalent orifice area [m<sup>2</sup>]  
 $A_r = l \cdot R_* \cdot \Theta_r$ , recess area [m<sup>2</sup>]  
 $C_d$  = empirical orifice discharge coefficient  
 $C_p, C_m$  = pad clearance [m], assembled bearing clearance [m]  
 $C_{\alpha\beta}^k$  = pad damping coefficients,  $\alpha, \beta = X, Y, \delta$   
 $C_{Ra\beta}$  = reduced bearing damping coefficients;  $\alpha, \beta = X, Y$  [N·s/m]  
 $Cr_k$  = pad rotational damping coefficient [N·m·s/rad]  
 $c_p$  = fluid specific heat [J/kg·°K]  
 $D = 2 \cdot R$ , bearing diameter [m]  
 $d_o$  = orifice diameter [m]  
 $e_x, e_y$  = journal displacements in  $X$  and  $Y$  directions [m]  
 $f_{j,b} = a_M [1 + (b_M R_{j,b})^{e_M}]$ ;  
 $a_M = 0.001375$   
 $b_M = 500,000$   
 $e_M = 1/3.00$   
 turbulent flow friction factors at journal and bearing (smooth) surfaces  
 $F_x^k, F_y^k$  = pad fluid film forces along  $\{X, Y\}$  axes [N]  
 $i = \sqrt{-1}$  = imaginary unit  
 $I_k$  = pad mass moment of inertia [kg·m<sup>2</sup>]

$H$  = film thickness [m]  
 $H_r$  = recess depth [m]  
 $h_x, h_y, h_\delta^k = \cos \Theta, \sin \Theta, \sin(\Theta_\delta^k)$  perturbed film thickness components  
 $h_b, h_j$  = convection heat transfer coefficients [W/m<sup>2</sup>·°K]  
 $K_{\alpha\beta}^k$  = pad stiffness coefficients  $\alpha, \beta = X, Y, \delta$   
 $K_{Ra\beta}$  = reduced bearing stiffness coefficients;  $\alpha, \beta = X, Y$  [N/m]  
 $Kr_k$  = pad rotational structural stiffness coefficient [N·m/rad]  
 $L, l$  = bearing axial length, recess axial length [m]  
 $Ma = U_\Theta \cdot \sqrt{\beta_p \cdot \rho_r}$  orifice circumferential velocity Mach number  
 $M^k = R \{ \sin \Theta_\delta^k F_x^k - \cos \Theta_\delta^k F_y^k \}$  pad moment due to fluid film forces [N·m]  
 $N_{pad}$  = number of pads on bearing  
 $N_{recess}$  = number of recesses on pad  
 $P, Pr, P_r$  = fluid pressure, recess, and supply pressures [N/m<sup>2</sup>]  
 $P_r^-, P_r^+$  = pressures just before and after recess edge [N/m<sup>2</sup>]  
 $P_L, P_R$  = discharge pressures on left and right sides of bearing [N/m<sup>2</sup>]  
 $Q_j$  = heat flow to bearing and journal surfaces [W/m<sup>2</sup>]  
 $R$  = bearing radius [m]

$Re = (\rho \cdot \Omega \cdot C \cdot R / \mu)$ , nominal circumferential flow Reynolds number  
 $R_j, R_b = (\rho / \mu) H \times \sqrt{[(U_\Theta - \Omega \cdot R)^2 + U_z^2]} / \{(\rho / \mu) H \sqrt{U_\Theta^2 + U_z^2}\}$ ;  
 $r_p = C_p - C_m$ , pad preload [m]  
 $T$  = fluid bulk-flow temperature [°K]  
 $T_b, T_j$  = temperature at bearing and journal surfaces [°K]  
 $U_z, U_\Theta$  = bulk-flow velocities in axial and circumferential ( $\Theta$ ) dirs [m/s]  
 $V_r, V_s = (H_r + H) A_r + V_s$ , recess volume, Volume of orifice supply line [m<sup>3</sup>]  
 $W_x, W_y$  = components of external load on bearing [N]  
 $\{X, Y, Z\}$  = inertial coordinate system  
 $Z_{\alpha\beta}^k = K_{\alpha\beta}^k + i \omega C_{\alpha\beta}^k$ ,  $k$ th-pad impedance coefficients,  $\alpha, \beta = X, Y, \delta$   
 $\beta_p = (1/\rho)(\partial \rho / \partial P)$ , liquid compressibility coefficient [m<sup>2</sup>/N]  
 $\beta_T = -(1/\rho)(\partial \rho / \partial T)$ , liquid volumetric expansion factor [1/°K]  
 $\delta^k$  = pad rotation angle [rad]  
 $\eta = H / (H_r + H)$ , ratio of land film thickness to recess depth  
 $\Theta = x/R$ , circumferential or angular coordinate

ing the dynamic motion of journal and pads. Lund (1964) introduces rotordynamic force coefficients for tilting-pad bearings using an assembly method from a single generic fixed pad. Barrett et al. (1988) and White and Chan (1992) discuss the effect of excitation frequency on the bearing reduced force coefficients. Rouch (1983) includes pivot flexibility, and Lund and Bo-Pedersen (1986) and Kim and Palazzolo (1993) account for pad flexibility on the THD evaluation of rotordynamic coefficients. These investigations show that thermoelastic deformations reduce significantly the bearing damping force coefficients. Nicholas and Barrett (1986) also demonstrate, both theoretically and experimentally, that support flexibility has a significant effect on decreasing critical speeds of rotors supported on tilting-pad bearings.

Orcutt (1967) and Pinkus (1984/85) present analyses for prediction of tilting-pad bearing performance for turbulent flow and isothermal conditions. Taniguchi et al. (1990) provide tilting-pad bearing pressure and temperature experimental data and detailed correlations to numerical predictions from a complex three-dimensional, turbulent flow, thermohydrodynamic analysis including heat conduction through the bearing pads. Bouard et al. (1994) compare different turbulent flow models to the test data of Taniguchi et al. with no major differences among the models used. Recently, Ha et al. (1994) include a pad leading edge-ram pressure effect to improve the prediction of pressure and film thickness on large scale, turbulent flow tilting-pad bearings.

Relevant experimental investigations in tilting-pad bearings are given by Someya (1988), Brockwell and Kleibub (1989), and Fillon et al. (1991) for laminar flow conditions, and by Orcutt (1967), Taniguchi et al. (1990), and Ha et al. (1994)

for both laminar and turbulent flows. The detailed experimental works have concentrated on the static performance of tilting-pad bearings under various conditions of load and shaft speed with attention to the film and pads surface temperature and pressure evolution. In general, theoretical predictions agree well with measurements if all bearing parameters are known accurately. Actual operating clearance and preload, and the inlet pad temperature are perhaps the most important factors affecting tilting-pad bearing performance. Isothermal models suffice to predict well bearing performance for small loads (or large Sommerfeld numbers), while apparently a complete elasto-thermo-hydrodynamic model becomes mandatory for large loads (small Sommerfeld numbers) accompanied by small minimum film thickness and large temperature rises.

Measurements of tilting-pad journal bearing force coefficients have been relatively scarce in the technical literature until recently, see for example the relevant works of Someya (1988), Brockwell et al. (1990), Parkins and Horner (1992), and Arumugam et al. (1994). Test stiffness coefficients agree reasonably well with theoretical predictions. Measured damping coefficients are typically lower than calculated values. Pad thermoelastic deformations, pad pivot and shaft flexibilities appear to affect greatly the measured results. Flack and Zuck (1988) report experimental rotordynamic responses of two flexible rotors supported on tilting-pad bearings. These fundamental tests demonstrate unstable rotor-bearing behavior as a whip condition with whirl frequency equal to the first critical speed. The instabilities are thought to be bearing induced but the physical mechanism or bearing parameter(s) producing this highly unusual behavior (in tilting-pad bearings) are yet to be identified.

Zeidan (1992), and Zeidan and Paquette (1994) introduce flexure-pivot, tilting-pad bearings and discuss their advantages over conventional tilting-pad bearings. Armentrout and Paquette (1993) and Chen (1994) present analyses for evaluation of rotordynamic force coefficients in isothermal laminar flow, flexure-pad bearings. Zeidan (1992) and Chen (1994) describe applications in which flexure-pad bearings provided stability to otherwise unstable rotating machinery and with a performance superior to that of conventional tilting-pad bearings. De Choudhury et al. (1992) demonstrate experimentally that a flexure-pad bearing brings a lower temperature rise and frictional power loss when compared to a similar size five shoe tilting-pad journal bearing. This fact allowed the flexure-pad bearing to operate at a lower oil flow rate while providing acceptable oil throwoff temperatures.

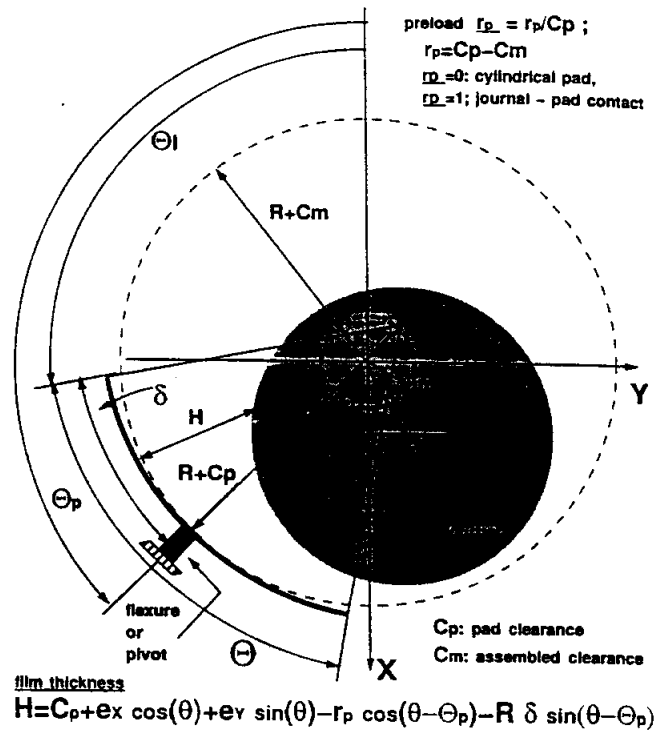


Fig. 2 Geometry and nomenclature for flexure- and tilting-pad

## Analysis

Consider the flow of a variable properties liquid in the thin film annular region between an inner rotating journal and a hydrostatic/hydrodynamic tilting pad bearing. Each bearing pad provides rotational stiffness ( $K_r$ ) and viscous damping ( $C_r$ ) with large radial rigidity. One or more recesses and orifice restrictors for radial liquid supply to the bearing are machined on the bearing pads. A characteristic tilting pad of angular extent  $\Theta_k$  is shown in Fig. 2. The leading edge of the  $k$ th pad is defined by the coordinate  $\Theta_{lk}$ , and  $\Theta_{pk}$  denotes the position of the pad pivot or rotational flexural node. At operating conditions, the journal position relative to the bearing housing is described with reference to the inertial axes ( $X, Y, Z$ ) by the journal center

## Nomenclature (cont.)

$\Theta_k$  =  $k$ th pad angular length [rad]  
 $\Theta_{lk}$  =  $k$ th pad angular position of pad leading edge [rad]  
 $\Theta_{pk}$  =  $k$ th-pad angular position of pivot [rad]  
 $\Theta_r^k$  =  $r$ th-recess angular length in  $k$ th-pad [rad]  
 $\kappa_z = \kappa_\theta = \frac{1}{2}(\kappa_J + \kappa_B)$ , turbulence shear factors in ( $z, \theta$ ) flow directions  
 $\kappa_J, \kappa_B = f_J \cdot R_J, f_B \cdot R_B$ , turbulent shear parameters at journal and bearing surfaces  
 $\kappa_r = (Re_r^{0.681}/7.753)$ , turbulent shear flow parameter at recess  
 $\kappa_p$  = pad leading edge pressure recovery factor

$\rho_l$  = fluid density [ $\text{Kg/m}^3$ ], characteristic density [ $\text{kg/m}^3$ ]  
 $\mu_l$  = fluid viscosity [ $\text{Ns/m}^2$ ], characteristic viscosity [ $\text{Ns/m}^2$ ]  
 $\xi_{\theta u}, \xi_{\theta d}$  = empirical recess-edge entrance loss coefficients in circumferential (upstream, downstream) direction  
 $\xi_{zu}, \xi_{zd}$  = empirical recess-edge entrance loss coefficients in axial direction (left and right of recess)  
 $\lambda_T$  = thermal mixing coefficient for pad heat carry over  
 $\Omega, \omega$  = rotational speed of journal, excitation or whirl frequency [ $1/\text{s}$ ]  
 $\tau = \omega t$ , dimensionless time coordinate

$\Gamma_r$  = recess boundary with outward normal  $\mathbf{n}$

## Subscripts

$J, B$  = journal and bearing surfaces  
 $0$  = zeroth-order flow solution  
 $\alpha, \beta$  = first-order solution for perturbations in ( $X, Y$ ) displacements and pad rotation ( $\delta$ )  
 $r, e$  = bearing recesses and edges (entrance)  
 $u, d$  = upstream and downstream edges of recess in  $\theta$  dir

## Superscripts

$k$  =  $k$ th-pad on bearing,  $k = 1, \dots$   
 $N_{\text{pad}}$

displacements ( $e_x, e_y$ ). The film thickness in the flow region of the  $k$ th bearing pad is

$$H^k(Z, \Theta, t) = C_p(Z) + e_x \cos(\Theta) + e_y \sin(\Theta) - r_p^k \cos(\Theta - \Theta_p^k) - R \cdot \delta^k \sin(\Theta - \Theta_p^k) \quad (1)$$

where  $\delta^k$  is the pad rotational angle;  $C_p$  is the pad machined radial clearance; and  $r_p = C_p - C_m$ , is the bearing preload with  $C_m$  as the bearing assembled clearance.

The fluid flow on a bearing pad is considered as fully developed with a turbulent character due to the large axial pressure drop, high rotor surface speed and the low viscosity typical of cryogenic liquids. The equations of continuity, momentum and energy transport for the variable properties, turbulent bulk-flow on the thin film lands of the  $k$ th pad are given by (San Andres, 1992, 1993; Yang, 1992) as:

$$\frac{\partial}{\partial t}(\rho H)^k + \frac{\partial}{\partial z}(\rho H U_z)^k + \frac{\partial}{\partial x}(\rho H U_x)^k = 0 \quad (2)$$

$$-H^k \frac{\partial P^k}{\partial z} = \frac{\mu}{H^k} \{ \kappa_z U_z \}^k + \frac{\partial(\rho H U_z)^k}{\partial t} + \left\{ \frac{\partial(\rho H U_z U_z)}{\partial z} + \frac{\partial(\rho H U_\Theta U_z)}{\partial x} \right\}^k \quad (3)$$

$$-H^k \frac{\partial P^k}{\partial x} = \frac{\mu}{H^k} \left\{ \kappa_\Theta U_\Theta - \kappa_z \frac{\Omega R}{2} \right\}^k + \frac{\partial(\rho H U_\Theta)^k}{\partial t} + \left\{ \frac{\partial(\rho H U_z U_\Theta)}{\partial z} + \frac{\partial(\rho H U_\Theta U_\Theta)}{\partial x} \right\}^k \quad (4)$$

$$c_p \left\{ \frac{\partial}{\partial t}(\rho H T) + \frac{\partial}{\partial x_i}(\rho H U_i T) \right\}^k + Q_i = \beta_T H T \left\{ \frac{\partial P}{\partial t} + U_i \frac{\partial P}{\partial x_i} \right\}^k + \Omega \cdot R \frac{H}{2} \frac{\partial P}{\partial x} + \frac{\mu}{H} \left\{ U_\Theta^2 + U_z^2 + \frac{1}{2} \Omega \cdot R \cdot U_\Theta \right\} + \kappa_i \Omega R \left( \frac{1}{4} \Omega R - U_\Theta \right) \quad i = x, z \quad k = 1, \dots, N_{\text{pad}} \quad (5)$$

on the flow region  $\{-L_L \leq Z \leq L_R; \Theta_{ik} \leq \Theta \leq \Theta_{ik} + \Theta_k\}$ ; and where,  $\kappa_i = \kappa_\Theta = (k_i + k_\Theta)/2$  are the wall shear stress difference coefficients taken as local functions of the turbulent friction factors and the flow Reynolds numbers relative to the rotating ( $R_j$ ) and stationary ( $R_s$ ) surfaces, i.e.  $\kappa_j = f_j R_j$ ,  $\kappa_s = f_s R_s$  (Hirs, 1973). The cryogenic liquid properties are calculated from the Benedict-Web-Rubin equation of state as given in the standard data base of McCarty (1986). In the energy equation (5),

$$Q_i = h_b(T - T_b) + h_j(T - T_j) \quad (6)$$

denotes the heat flow from the fluid film to the bearing and journal surfaces at temperatures ( $T_b$ ) and ( $T_j$ ), respectively, and with ( $h_b, h_j$ ) as the bulk-flow convection heat transfer coefficients. A full description of these parameters in turbulent bulk-flows is given by Yang (1992).

A mass conservation equation at each bearing recess of area  $(l \cdot R \cdot \Theta)^k$  and depth  $H$ , is defined by the global balance between the mass flow through the orifice restrictor, the mass flow into the film lands and the accumulation rate of fluid mass within the recess volume  $V_r$ , i.e.,

$$Q_{ro}^k = A_o \sqrt{2\rho_r(P_r - P_r^*)} = \int_{\Gamma_r} \left[ \rho H U \cdot \mathbf{n} \right]^k d\Gamma_r + \rho_r^k \frac{\partial V_r^k}{\partial t} + \rho_r^k V_r^k \left\{ \beta_p \frac{\partial P_r}{\partial t} - \beta_T \frac{\partial P_r}{\partial t} \right\}^k$$

for  $r = 1, 2, \dots, N_{\text{recess}}$  on the  $k$ th pad (7)

where  $A_o$  is the effective orifice area, and  $\beta_p, \beta_T$  represent the fluid compressibility and volumetric expansion coefficients, respectively. The orifice flow equation is valid only for small changes of the liquid density (Hall et al., 1986). In Eq. (7), the orifice discharge coefficient  $C_d$  is of utmost importance since experimental measurements have shown that numerical predictions require accurate  $C_d$  values for accurate results (Kurtin et al., 1993; Franchek et al., 1995).

The fluid edge pressure at the entrance to the film lands is given by the superposition of viscous shear effects on the recess extent and an entrance drop due to fluid inertia. Figure 3 shows the assumed pressure distribution within the recess volume and details the relevant nomenclature. On the circumferential direction, the pressure rise ( $P_r^-$ ) downstream of the recess orifice is given by (Constantinescu and DiMofte, 1987; San Andres, 1992):

$$\left[ P_r^- = P_r - \mu_r \kappa_r \frac{R \cdot \Theta_r}{2H_r^2} \left( U_\Theta(\rho_r^- / \rho_r) \eta - \frac{\Omega \cdot R}{2} \right) \frac{1}{(1 - M_a^2)} \right]^k \quad r = 1, 2, \dots, N_{\text{recess}} \text{ on } k\text{th pad} \quad (8.a)$$

where,  $Ma$  is the circumferential flow local Mach number at the orifice discharge. The entrance pressures ( $P_r^+$ ) to the film lands in the circumferential and axial directions are given by:

$$\left[ P_r^+ = P_r^- - \frac{\rho_r^+}{2} (1 + \xi_\Theta) \left\{ 1 - (\rho_r^+ / \rho_r^-)^2 \eta^2 \right\} U_\Theta^2 \right]^k \quad (8.b)$$

$$\left[ P_r^+ = P_r - \frac{\rho_r^+}{2} (1 + \xi_z) \left\{ 1 - (\rho_r^+ / \rho_r^-)^2 \eta^2 \right\} U_z^2 \right]^k$$

for  $r = 1, 2, \dots, N_{\text{recess}}$  on  $k$ th pad (8.c)

The analysis generalizes Eq. (8) for uneven empirical entrance loss factors  $\xi$  in the axial direction ( $Z$ ) and also circumferen-

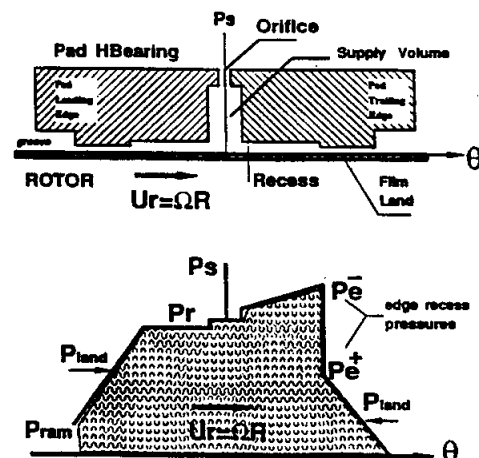


Fig. 3 Pressure rise and drop at recess edge of hydrostatic pad bearing and pressure ram at leading edge of pad

tially upstream ( $u$ ) and downstream ( $d$ ) of each recess. The Bernoulli like pressure drop occurs only if fluid flows from the recess toward the film lands. On the contrary, if fluid enters from the film lands into the bearing recess, then the edge pressure is regarded as equal to the recess pressure.

A simplified form of the energy transport equation at a bearing recess is easily derived from equation (5). A detailed exposition of the energy transport process in a bearing recess is given by San Andres (1993).

At low rotational speeds, the pressure at the side (right and left) boundaries of the  $k$ th pad equals a specified value of ambient or sump pressure, i.e.,

$$P^k(L_R, \Theta) = P_R^k; \quad P^k(-L_L, \Theta) = P_L^k \quad (9.a)$$

and at the pad leading and trailing edges,

$$P^k(Z, \Theta_{ik}) = P^k(Z, \Theta_{ik} + \Theta_i) \\ = f_s(P_R, P_L) \quad \text{on} \quad -L_L \leq Z \leq L_R \quad (9.b)$$

where ( $f_s$ ) denotes a linear pressure variation along the axial side of the bearing pad leading and trailing edges. At high journal surface speeds ( $\Omega \cdot R$ ) significant momentum changes occur at the pad leading edge ( $\Theta_{ik}$ ). Immediately upstream of the pad, the fluid entering the film lands can develop a dynamic head equal to some fraction of a reference dynamic pressure based on the bearing surface speed (Burton and Carper, 1967; Mori et al., 1991; Ettles and Cameron, 1968), i.e.,

$$\Delta P^k(Z, \Theta_{ik}) = \frac{1}{2} \kappa_p \cdot \rho^k \cdot \left( \frac{\Omega \cdot R}{2} \right)^2 \quad (9.c)$$

The coefficient ( $\kappa_p$ ) is an empirical ram pressure factor. Burton and Carper (1967) suggest a value of  $\kappa_p = 0.64$  for high speed flows with large turbulence levels. Note that the inlet pad pressure model given here is very simple. A more accurate knowledge of the entrance condition requires the analysis of the complex flow field on the axial groove and feeding port separating the bearing pads (Ha et al., 1994).

A further assumption about the external flow is necessary to fully specify the flow variables. The flow at the inlet (pad leading edge) to the film land in the pad bearing is regarded as parallel to the direction of surface motion, i.e.

$$-L_L \leq Z \leq L_R, \quad U_z^k(Z, \Theta_{ik}) = 0; \quad k = 1, \dots, N_{\text{pad}} \quad (10)$$

In the thermal analysis, the inlet bulk-flow temperature to a bearing pad is obtained using mass flow and energy balances of the upstream pad flow and temperature and incoming fresh fluid at a supply temperature ( $T_s$ ). The pad inlet bulk-flow temperature depends on the specification of a thermal mixing parameter ( $0 \leq \lambda_T \leq 1$ ) as given by Mitsui et al. (1983).

**Bearing Equilibrium Equation and Pad Equation of Rotational Motion.** In a multiple pad bearing, the sum of the individual pad forces must balance the externally applied load  $W$  with components ( $W_x, W_y$ ), respectively. Thus, the equilibrium force equation (in the absence of rotor-inertial effects) is given as:

$$W_x + \sum_{k=1}^{N_{\text{pad}}} F_x^k = 0; \quad W_y + \sum_{k=1}^{N_{\text{pad}}} F_y^k = 0 \quad (11)$$

where the fluid film forces are obtained from integration of the pressure field.

$$\begin{bmatrix} F_x^k \\ F_y^k \end{bmatrix} = \int_{-L_L}^{L_R} \int_{\Theta_{ik}}^{\Theta_{ik} + \Theta_i} P^k \cdot \begin{bmatrix} \cos \Theta \\ \sin \Theta \end{bmatrix} dZ \cdot R d\Theta^k \\ k = 1, 2 \dots N_{\text{pad}} \quad (12)$$

The equation of rotational motion for each bearing pad is given as:

$$I_k \ddot{\delta}^k + C r_k \dot{\delta}^k + K r_k \delta^k = M^k = R \{ \sin(\Theta_p^k) F_x^k - \cos(\Theta_p^k) F_y^k \} \\ k = 1, \dots, N_{\text{pad}} \quad (13)$$

where  $I_k, K r_k, C r_k$  correspond to the pad inertia, and flexural web rotational stiffness and viscous damping coefficients, respectively.

At an equilibrium position, an external static load ( $W_{x0}, W_{y0}$ ) is balanced by the sum of all the pad fluid film forces at the steady state journal eccentricity ( $e_{x0}, e_{y0}$ ) and with a set of stationary pad rotations  $\{\delta_0^k\}, k = 1, \dots, N_{\text{pad}}$ . To evaluate dynamic force coefficients, consider the motion of the journal as the superposition of small amplitude periodic motions about the equilibrium static position. That is let

$$e_x(t) = e_{x0} + \Delta e_x e^{i\omega t}, \quad e_y(t) = e_{y0} + \Delta e_y e^{i\omega t} \\ \delta^k(t) = \delta_0^k + \Delta \delta^k e^{i\omega t}, \quad i = \sqrt{-1} \quad k = 1, \dots, N_{\text{pad}} \\ |\{\Delta e_x, \Delta e_y, R \cdot \Delta \delta^k\}| / C_* \ll 1 \quad (14)$$

where  $\omega$  denotes the frequency of the whirl motion. Then, the part film thickness can be thought as the superposition of steady-state ( $H_0$ ) and dynamic ( $H_1$ ) components given by the real part of the following expression:

$$H^k = H_0^k + H_1^k e^{i\omega t} \quad (15)$$

where

$$H_1^k = \left\{ \Delta e_x + R \Delta \delta^k \sin(\Theta_p^k) \right\} \cos(\Theta) \\ + \left\{ \Delta e_y - R \Delta \delta^k \cos(\Theta_p^k) \right\} \sin(\Theta) \quad (16.a)$$

$$= \Delta e_x h_x + \Delta e_y h_y + R \Delta \delta^k h_\delta^k \quad (16.b)$$

with

$$h_x = \cos \Theta; \quad h_y = \sin \Theta;$$

$$h_\delta^k = \sin(\Theta_p^k) \cdot h_x - \cos(\Theta_p^k) \cdot h_y = \sin(\Theta_p^k - \Theta) \quad (16.c)$$

For each bearing pad the flow field variables ( $U_z, U_\theta, P, T$ ), as well as the fluid properties ( $\rho, \mu$ ) and the shear parameters ( $\kappa_\theta, \kappa_z$ ) are also formulated as the superposition of zeroth-order and first-order complex number flow fields describing an equilibrium for steady-state flow, and a perturbed condition for small amplitude dynamic journal motions, respectively. In general, these fields are expressed as:

$$\Psi^k = \Psi_0^k + e^{i\omega t} \{ \Delta e_x \Psi_x + \Delta e_y \Psi_y + R \Delta \delta \psi_\delta \}^k \\ = \Psi_0^k + e^{i\omega t} \Delta_\alpha \Psi_\alpha^k \\ \alpha = X, Y, \delta^k, \quad k = 1, 2 \dots N_{\text{pad}} \quad (17)$$

Substitution of (15) and (17) into the equations of motion (2-7) determines zeroth- and first-order equations describing the steady state and perturbed (dynamic) flow fields, respectively. Details of the perturbation analysis are omitted here for space considerations but a complete description can be found in the reference of San Andres (1994). The first-order equations can be written in the general form:

$$L(U_{\theta x}, U_{z x}, P_x, \rho_x, \mu_x)^k = h_x \quad (18.a)$$

$$L(U_{\theta y}, U_{z y}, P_y, \rho_y, \mu_y)^k = h_y \quad (18.b)$$

$$L(U_{\theta \delta}, U_{z \delta}, P_\delta, \rho_\delta, \mu_\delta)^k = h_\delta^k \\ = h_x \sin(\Theta_p^k) - h_y \cos(\Theta_p^k) \quad (18.c)$$

where  $L$  are linear differential operators with coefficients depending only on the zeroth-order flow field variables ( $U_{\theta 0}, U_{z 0}, P_0, T_0, H_0$ )<sup>k</sup>. From (18) it immediately follows that



$$\Psi_{\delta}^k = \sin(\Theta_p^k) \Psi_X^k - \cos(\Theta_p^k) \Psi_Y^k,$$

$$\text{where } \Psi_{\delta} = U_{\theta\delta}, U_{c\delta}, T_{\delta}, P_{\delta}, \rho_{\delta}, \mu_{\delta} \quad (19)$$

which shows that the first-order flow field due to a pad rotation is given by superposition of the perturbed flow fields due to journal displacements in the  $\{X, Y\}$  directions. This identity, Eq. (19), simplifies considerably the computational time required for the evaluation of force coefficients in tilting (or flexure-) pad bearings. From the perturbation analysis it also follows that the pad forces and pad moment equation can be written as:

$$\begin{aligned} F_X^k(t) &= F_{X0}^k - \{Z_{XX}^k \Delta e_X + Z_{XY}^k \Delta e_Y + Z_{X\delta}^k \Delta \delta^k\} e^{i\omega t} \\ F_Y^k(t) &= F_{Y0}^k - \{Z_{YX}^k \Delta e_X + Z_{YY}^k \Delta e_Y + Z_{Y\delta}^k \Delta \delta^k\} e^{i\omega t} \quad (20) \\ 0 &= Kr_k \delta_0^k - M_0^k = \{[Kr_k - \omega^2 I_k + i\omega C_{rk}] \Delta \delta^k \\ &\quad + Z_{\delta X}^k \Delta e_X + Z_{\delta Y}^k \Delta e_Y + Z_{\delta\delta}^k \Delta \delta^k\} e^{i\omega t} \quad (21) \end{aligned}$$

where  $Z_{\alpha\beta}^k = K_{\alpha\beta}^k + i\omega C_{\alpha\beta}^k$  are the pad impedance coefficients at frequency  $\omega$ . A major simplification in the evaluation of the pad impedance coefficients is possible using equation (19) to render:

$$\begin{aligned} Z_{\delta X}^k &= R\{\sin(\Theta_p^k) Z_{XX}^k - \cos(\Theta_p^k) Z_{YX}^k\} \\ Z_{\delta Y}^k &= R\{\sin(\Theta_p^k) Z_{XY}^k - \cos(\Theta_p^k) Z_{YY}^k\} \\ Z_{X\delta}^k &= R\{\sin(\Theta_p^k) Z_{XX}^k - \cos(\Theta_p^k) Z_{YX}^k\} \\ Z_{Y\delta}^k &= R\{\sin(\Theta_p^k) Z_{XY}^k - \cos(\Theta_p^k) Z_{YY}^k\} \\ Z_{\delta\delta}^k &= R\{\sin(\Theta_p^k) Z_{X\delta}^k - \cos(\Theta_p^k) Z_{Y\delta}^k\} \\ &= R^2[\sin^2(\Theta_p^k) Z_{XX}^k - \sin(\Theta_p^k) \cos(\Theta_p^k) (Z_{XY}^k + Z_{YX}^k) \\ &\quad + \cos^2(\Theta_p^k) Z_{YY}^k] \quad (22) \end{aligned}$$

where

$$Z_{\alpha\beta}^k = \int_{-L_k}^{L_k} \int_{\Theta_{ik}}^{\Theta_{ik} + \Theta_k} P_{\beta} h_{\alpha} dZ \cdot R d\Theta \quad \alpha, \beta = X, Y; \quad k = 1, 2 \dots N_{\text{pad}} \quad (23)$$

Equations (22) show five impedances calculated as linear combinations of  $\{Z_{\alpha\beta}^k\}_{\alpha, \beta = X, Y}$ , and indicate that only the dynamic pressure fields for journal center perturbations in the  $\{X, Y\}$  directions are (strictly) required.

In the practical analysis of tilting- and flexure-pad bearings, reduced bearing stiffness and damping coefficients,  $(K_{R\alpha\beta}, C_{R\alpha\beta})_{\alpha, \beta = X, Y}$ , are determined from the equilibrium position and for a particular frequency of excitation, typically synchronous ( $\omega = \Omega$ ). The relevant analysis is readily available in the literature (Barrett et al., 1988; White and Chan, 1992). For completeness here we merely list the appropriate formula:

$$K_{R\alpha\beta} = \sum_{k=1}^{N_{\text{pad}}} K_{R\alpha\beta}^k; \quad C_{R\alpha\beta} = \sum_{k=1}^{N_{\text{pad}}} C_{R\alpha\beta}^k \quad \alpha, \beta = X, Y \quad (24)$$

where

$$Z_{R\alpha\beta}^k = \left[ Z_{\alpha\beta}^k - \frac{Z_{\alpha\delta}^k \cdot Z_{\delta\beta}^k}{ZZ_{\delta\delta}^k} \right]^k = K_{R\alpha\beta}^k + i\omega C_{R\alpha\beta}^k \quad (25)$$

with

$$ZZ_{\delta\delta}^k = (K_{\delta\delta}^k + Kr_k - \omega^2 I_k) + i\omega(C_{\delta\delta}^k + Cr_k) \quad (26)$$

**Numerical Method of Solution.** The control-volume method of Launder and Leschziner (1978) is used to solve the differential equations of motion. Staggered grids containing control volumes for the primitive flow variables (circumferential and axial velocity, and pressure and temperature) cover the flow domain. Algebraic difference equations are derived on

each control volume for the conservation of mass, circumferential and axial momentum, and transport of energy. A pressure correction equation is derived from the conservation of mass equation at each control volume. The SIMPLEC procedure of Van Doormal and Raithby (1984) is adopted for solution of the non-linear difference equations along with a Newton-Raphson scheme for satisfaction of the recess mass flow constraint. Full descriptions on the method as applied to hybrid (hydrostatic and hydrodynamic) bearings are given in past publications from the author (San Andres, 1990–1993). An iterative method is used to determine the equilibrium journal position and pad rotation angles satisfying the applied load and pad moment constraints. It is important to note that most algorithms for tilting-pad bearing analysis have difficulty in determining the journal equilibrium position when one or more pads become unloaded. This is most frequent for bearings with null or even negative preload. The most used approach artificially increases the pad rotational angle until this becomes "just" loaded (Knight and Barrett, 1988). Another difficult problem arises when a pad goes from unloaded to loaded in the current iterative step. Here, unless the predicted (new) pad rotation angle is sufficiently large, the iterative scheme will bring the pad to a state of unloading when the actual solution indicates the opposite. The difficulty described is overcome easily by recognizing that a valid equilibrium (stable) pad rotational angle requires a positive pad moment stiffness, i.e.,  $(Kr_k + K_{\delta\delta}^k) > 0$ , evaluated at zero whirl frequency.

Nonreduced force coefficients for each bearing pad are found from perturbed analytical difference equations for journal displacements in two orthogonal directions. The pad moment coefficients and force coefficients due to pad angular motions are given as linear combinations of the force coefficients due to journal radial displacements. The method then avoids numerical

**Table 1 Flexure-pad liquid oxygen hybrid bearing**

**Geometry and operating conditions**

Diameter  $D = 92.71$  mm (3.65 in)  
Length  $L = 37.08$  mm (1.46 in)  
Clearance  $C_p = 76.2$   $\mu$ m (0.003 in), zero preload  
Recess depth  $H_r = 228$   $\mu$ m (0.009 in)

6 pads of length  $50^\circ$  and 1 recess per pad  
pad offset = 0.50  
pad pivots at  $0^\circ, 60^\circ, 120^\circ, 180^\circ, 240^\circ, 300^\circ$   
leading edge ram pressure coefficient  $\kappa_p = 0.32$

recess arc length  $23.5^\circ$  and axial length  $l = 19$  mm (0.75 in)

orifice diameter  $d_o = 2.58$  mm,  $C_d = 1.0$

edge loss coefficient  $\zeta_o, \zeta_c = 0.0$

Pad rotational stiffness ( $K_r$ ) varies

damping ( $C_r$ ) =  $0$  N·m·s/rad

Inertia :  $1.017\text{E-}4$  kg·m<sup>2</sup>,  
mass :  $0.283$  kg for thickness  $0.02$  m

Operating speed: 25 krpm

Pressure supply  $P_s = 26.71$  MPa (3874 psi)  
discharge  $P_a = 8.81$  MPa (1278 psi),  $\Delta P = 2600$  psi

Liquid oxygen at inlet temperature  $T_i = 90^\circ\text{K}$  ( $162^\circ\text{R}$ )

at  $(P_i, T_i)$ : density  $\rho_i = 1.192$  kg/m<sup>3</sup>,  
viscosity  $\mu_i = 0.2459\text{E-}03$  Pa·s,

Reynolds numbers at concentric position.

Circumferential flow  $Re_c = (\rho/\mu), \Omega \cdot R \cdot C = 44,832$   
Axial flow  $Re_a = (\rho/\mu), U_i \cdot C = 30,487 - 30,801$   
Squeeze film  $Re_s = (\rho/\mu), \omega \cdot C = 73.52$  ( $\omega = \Omega$ )

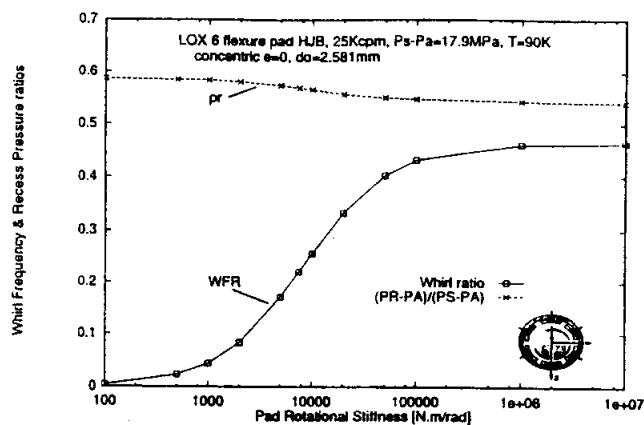


Fig. 4 Whirl frequency ratio and recess pressure ratio versus pad rotational stiffness. LOx flexure-pad hybrid bearing

evaluation of moment force coefficients due to pad rotations. Details on the numerical procedure to balance the bearing pads are given by San Andres (1994).

## Results and Discussion

The validity of the analysis and computational program was assessed by extensive comparisons to relevant experimental data and to predictions from analyses given in the literature. It is noted here that the present theoretical development has as its major objective the evaluation of the static and dynamic force performance characteristics of cryogenic liquid film bearings. This particular application is known to require high surface speeds or external pressurization to provide the required load capacity since cryogenic liquids are essentially inviscid. At this time there are no experimental results for tilting-pad or flexure-pad hybrid bearings handling cryogens, although measurements are planned for the summer of 1995. Test results for forces and force coefficients for fixed-arc (i.e., rigid surface) hybrid bearings with cryogens and surrogate fluids have appeared recently (Childs and Hale, 1994). Past publications (San Andres, 1990–93) present extensive comparisons to measurements from the hydrostatic test facility of Childs, as well as to other relevant investigations.

Kurtin et al. (1993), and Franchek et al. (1995) also produce sensitivity studies while describing comparisons between numerical predictions based on the present model and experimental measurements performed on water lubricated hydrostatic bearings (Childs and Hale, 1994). The sensitivity analysis involved changing an input parameter by  $\pm 10$  percent from its

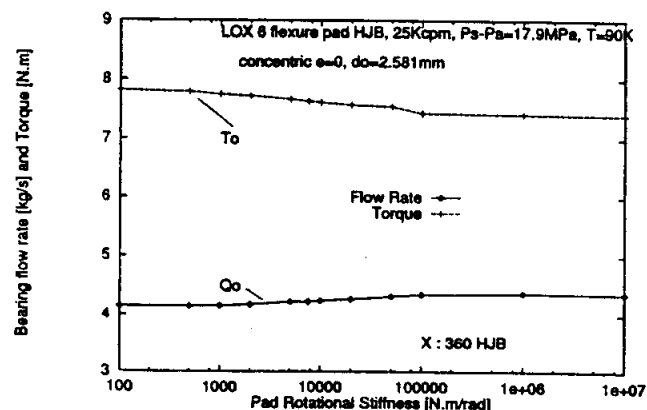


Fig. 5 Mass flow rate and torque versus pad rotational stiffness. LOx flexure-pad hybrid bearing-concentric operation

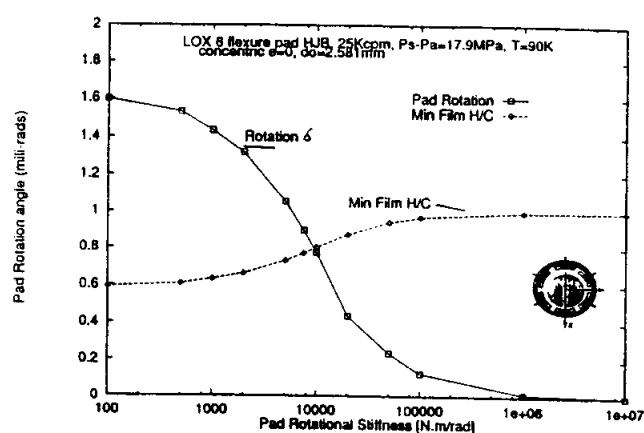


Fig. 6 Pad rotation and minimum film thickness versus rotational stiffness. LOx flexure-pad hybrid bearing

estimated experimental value for each operating condition while the other input parameters were kept invariant. The maximum difference between the numerical prediction and experimental value for each case was then compared with the maximum difference from the original results. Then, a relative sensitivity was determined by dividing the percentage change in maximum difference of the calculated parameter by the percentage change in the input parameter. The studies determined that flow rate and direct stiffness coefficients are particularly sensitive to changes in the orifice discharge coefficient ( $C_d$ ) for HJBs and less sensitive to variations in the entrance loss coefficients. Other force coefficients and the whirl frequency ratio for HJBs are particularly insensitive to variations in the empirical parameters.

San Andres (1994) compares predictions from the present analysis with theoretical values and experimental measurements presented by Taniguchi et al. (1990) for a tilting-pad bearing operating in the laminar and turbulent flow regimes. The comparisons correlate very well with measurements of the static journal eccentricity and provide an accurate representation of the film thickness variation with a representative distribution of the film bulk-flow temperature. Further comparisons were performed with analytical and experimental force coefficients for a laminar flow, five shoe tilting-pad bearing reported by Someya (1988). Isothermal predictions were identical to those of Someya while adiabatic thermal calculations were found to correlate better with the test data. The interested reader is encouraged to seek the author's aforementioned reference for details on the correlations to test data.

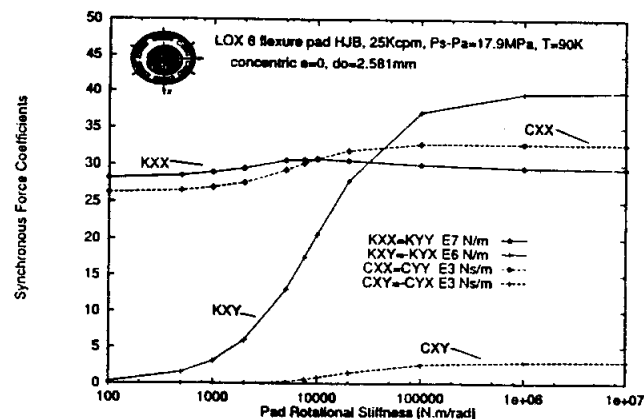


Fig. 7 Synchronous force coeffs versus pad rotational stiffness. LOx flexure-pad hybrid bearing-concentric

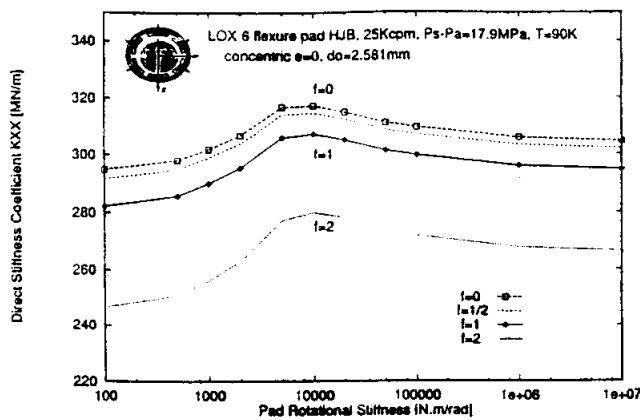


Fig. 8 Effect of frequency on direct stiffness  $K_{xx} = K_{yy}$ . LOx flexure-pad hybrid bearing-concentric operation

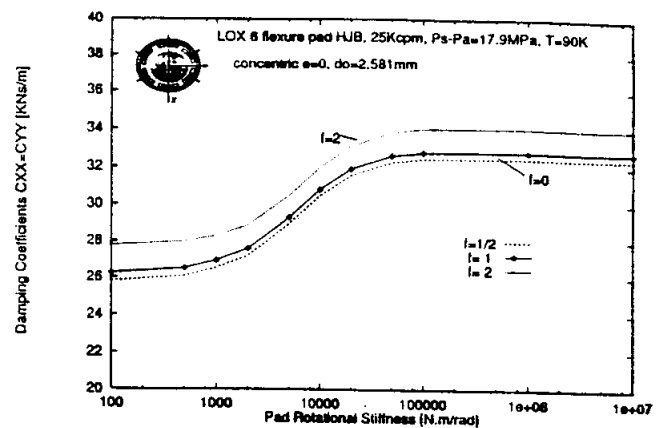


Fig. 10 Effect of frequency on direct damping  $C_{xx} = C_{yy}$ . LOx flexure-pad hybrid bearing-concentric operation

Further calculations are identical to those presented by Armentrout and Paquette (1993) and Chen (1994) for flexure-pivot tilting-pad bearings operating at high speeds and light viscous fluids under laminar flow conditions. Typical results show that, at the design load condition and as the pad rotational stiffness increases, the force coefficients vary from a tilting-pad regime passing through a transition zone and leading to a fixed-geometry performance regime. Designers typically select the pad rotational stiffness ( $K_r$ ) which renders the least value in the difference of cross-coupled stiffness coefficients ( $K_{xy} - K_{yx}$ ) just before the transition regime starts. Zeidan and Paquette (1994) report the use of a finite element program to design the geometry of the flexural web to render the required pad rotational stiffness while minimizing dynamic stresses.

The following discussion pertains to the numerical results obtained for a flexure-pad hybrid bearing for application in a liquid oxygen (LOx) turbopump. The geometry and operating conditions for the six-pad bearing are given in Table 1. Each pad has a rectangular recess and an orifice fluid supply line machined across the web supporting the flexure pad. The recess to pad ratio of areas is equal to 0.236 as recommended for a LOx application (Butner and Murphy, 1986). The values of supply and discharge pressure and rotational speed correspond to that on an Advanced Launching System (ALS) turbopump configuration. The large values of axial flow, circumferential, and squeeze film flow Reynolds numbers show a turbulent flow application with large fluid inertial effects. Calculations for both isothermal conditions and adiabatic heat flow with full pad leading edge thermal mixing were performed simultaneously. The results between both models differ little except for an increment

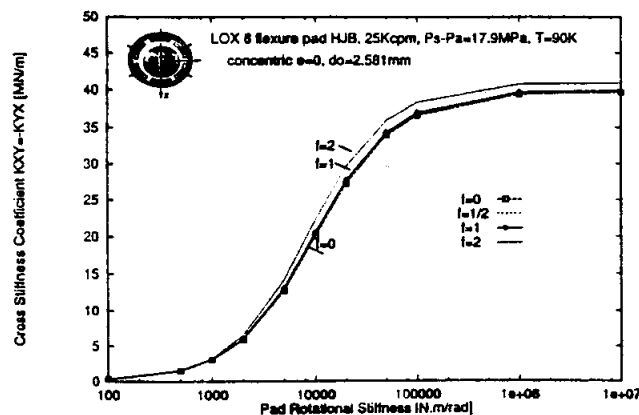


Fig. 9 Effect of frequency on cross stiffness  $K_{xy} = -K_{yx}$ . LOx flexure-pad hybrid bearing-concentric operation

in fluid temperature at the pad sides of 12°K and not sufficiently large to affect the bearing performance.

At the journal concentric position ( $e = 0$ ), Fig. 4 shows the predicted whirl frequency ratio (WFR) and recess pressure ratio for increasing values of the pad rotational stiffness. The lowest value of  $K_r$  represents an ideal tilting pad geometry with null restraining moments, while the largest rotational stiffness effectively represents a rigid (fixed) pad bearing configuration. The effect of the rotational stiffness on the stability indicator (WFR) is clear and shows the advantage of a movable pad geometry for this high speed application. As the pad rotational stiffness increases, the recess pressure ratio decreases while the flow rate increases (torque decreases) as shown in Fig. 5. The (X) marked on this figure represents the flow rate for a conventional cylindrical HJB with film lands of 360 deg extent. Figure 6 shows the pad rotation angle and the pad minimum film thickness (occurring at the pad trailing edge) versus the pad rotational stiffness. As this stiffness increases the pad is more constrained to move, and hence the minimum film thickness is that of the fixed pad. The largest rotations are expected in the tilting pad regime with a reduction in film thickness of 40 percent. The drag torque shown in Fig. 5 decreases with the pad rotational stiffness since the effective film thickness is essentially larger. This result then shows that a flexure-pad bearing has lower drag power than the conventional tilting pad bearing.

Figure 7 shows the synchronous force coefficients, i.e., evaluated at  $\omega = \Omega$ . At the concentric position, the direct coefficients are equal ( $K_{xx} = K_{yy}$ ) while the cross-coupled coefficients differ in sign ( $K_{xy} = -K_{yx}$ ). Note that the direct stiffness is about an order of magnitude larger than the cross-coupled stiffness coefficients for the fixed pad condition. The calculations show the great effect of the pad rotational stiffness coefficient on the rise of the cross-coupled coefficients. Figures 8 to 11 show the effect of frequency excitation on the stiffness ( $K_{xx}$ ,  $K_{xy}$ ), and damping ( $C_{xx}$ ,  $C_{xy}$ ) coefficients, respectively. The results denote calculations at frequency ratios  $f = \omega/\Omega$  equal to 0, 0.5, 1 and 2 times the rotational speed. The direct stiffness  $K_{xx}$  decreases with the frequency ratio  $f$  mainly due to fluid inertia effects, with a maximum direct stiffness at a pad rotational stiffness equal to 10,000 N·m/rad. The excitation frequency appears not to affect the cross-coupled coefficients showing then low values of cross-coupled inertia forces.

Next, a pad rotational stiffness ( $K_r$ ) of 10 kNm/rad<sup>2</sup> was selected to perform calculations for the load capacity of the

<sup>2</sup> Based on a finite element calculation, the flexural web has dimensions of 10 mm height and 5.4 mm wide for a material with an elastic modulus of 207GPa (steel). The web thickness is large enough to allow for the orifice supply line of 2.581 mm diameter. The web radial stiffness is equal to 4.135 MN/m which is an order of magnitude larger than the fluid film direct stiffness  $K_{xx}$ . Maximum elastic radial deformations of less than 3  $\mu$ m are expected for the largest load applied of 12 kN.

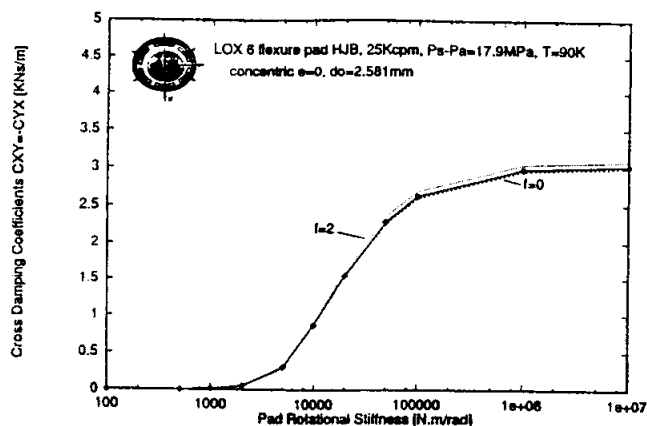


Fig. 11 Effect of frequency on cross damping  $C_{xy} = -C_{yx}$ . LOX flexure-pad hybrid bearing-concentric operation

bearing at the rated operating condition. The load ( $W$ ) applied to the bearing increased to a maximum of 12 kN (2,700 lbs) denoting a specific load ( $W/LD$ ) equal to 3.5 MPa (507 psi). Two cases were considered, (A) load applied towards the center of a bearing pad-LOP, (B) load applied at 30 deg from the vertical line, i.e., between pads-LBP. Figure 12 shows a linear relationship between the journal eccentricity (and minimum film thickness) at the bottom pad with the applied load. Note that the smallest film thickness is just 40 percent of the nominal bearing clearance for the largest load applied. The selected rotational stiffness results in a whirl frequency ratio equal to 0.25. This structural stiffness value, although not low enough to eliminate hydrodynamic instability, constitutes a major advancement over the rigid bearing pad configuration.

Figures 13 and 14 show the synchronous stiffness and damping coefficients versus the applied load, respectively. Note that the stiffness coefficients are virtually constant for loads to 8 kN (1800 lb). The cross-coupled stiffnesses for the case of load between pads (B) show the largest deviations at the largest load applied, while the direct damping coefficients decrease slightly with the applied load. Figure 15 shows the calculated centerline pressure ( $P - P_a$ )/( $P_s - P_a$ ) and film thickness for a load of 12 kN. The largest film pressures along with minimum film occur at pad 4 where the journal load is applied. The results show a small "ram" pressure at the pads inlet and hydrodynamic pressure rises in the downstream region of the bearing recesses. Note also the large inertial pressure drops at the recess edges.

The calculations performed show that a flexure-pad hybrid bearing keeps virtually all the benefits of a hydrostatic pad

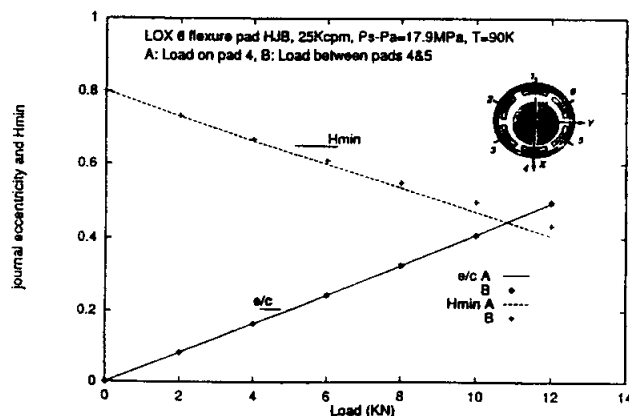


Fig. 12 Equilibrium eccentricity versus load for  $K_r = 10$  k Nm/rad (A\_ on pad, B\_ between pads)

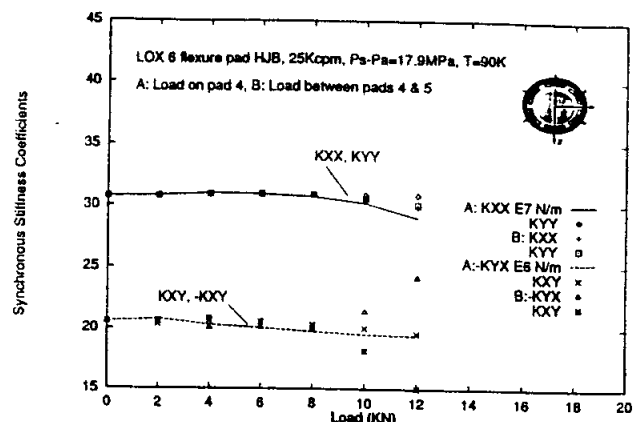


Fig. 13 Stiffness Coefficients versus load for  $K_r = 10$  k Nm/rad (A\_ on pad, B\_ between pads)

application (large direct stiffness and damping coefficients) while offering an accurate control on the cross-coupled stiffness coefficients and reduction in the whirl frequency ratio.

## Conclusions

An analysis for calculation of the dynamic force performance of tilting-pad and flexure-pad hybrid (combination hydrostatic and hydrodynamic) bearings operating in the turbulent flow regime is detailed. Flexure-pad bearings offer an alternative to improve (and eliminate) the limited stability characteristics of conventional fixed geometry hybrid bearings. Flexure-pad bearing technology provides accuracy of manufacturing without difficulty for bearing assembly and calibration, adequate control of bearing preload and flexural stiffnesses (radial and rotational), and absence of wear between shoe and pivot support. Flexure-pad bearings lend themselves to a hydrostatic application since the ports for the pressurized fluid can be easily machined on the supporting web without added mechanical complexities and at a reduced cost.

Bulk-flow equations of mass conservation, momentum and energy transport describe the motion of a variable properties fluid within the thin film lands of a bearing. A mass conservation equation at the recess volumes with a simple formulation for the recess pressure and temperature fields are also considered. Fluid inertia effects, temporal and advective, are fully accounted for flows with large pressure differentials or large journal speeds. Zeroth- and first-order flow equations are numerically solved to determine the flow field and the bearing fluid film forces and force coefficients.

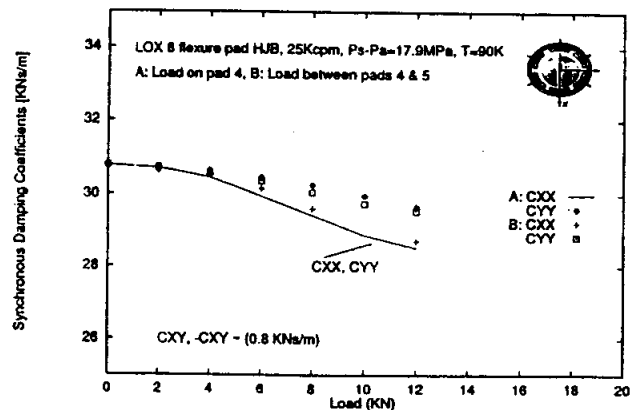


Fig. 14 Damping Coefficients versus load for  $K_r = 10$  k Nm/rad (A\_ on pad, B\_ between pads)

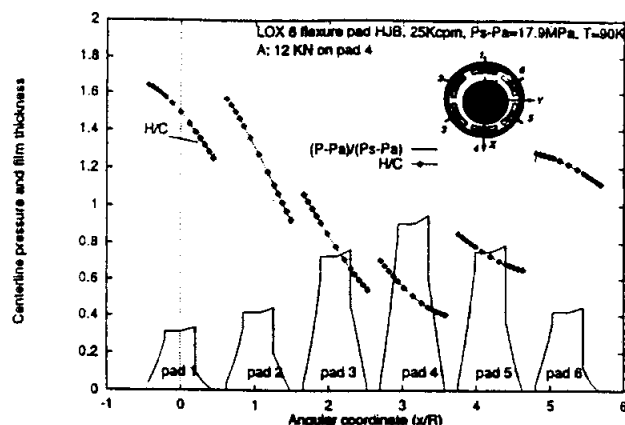


Fig. 15 Centerline pressure and film thickness for  $K_r = 10 \text{ k Nm/rad}$  and 10 kN load on pad #4

Predictions for a flexure-pad hybrid bearing handling liquid oxygen at operating conditions typical of a turbopump application demonstrate the ability of this type of bearing to reduce the stability whirl ratio, without degradation on the static load performance or reduction in direct stiffness and damping coefficients. The test example shows that hybrid bearings satisfy in excess the load requirements typical of present and future cryogenic turbopumps.

Future developments of the analysis could account for pad radial flexibility. Industrial applications with large loads may also demand a thermoelastic model for accurate determination of pad surface temperature and minimum film thickness. These considerations may not be of great importance in a cryogenic turbopump application.

## Acknowledgments

The interest of Mr. James Walker and the financial support of NASA Lewis Research Center under NASA Grant NAG3-1434 is gratefully acknowledged. Thanks also to Dr. Fouad Zeidan from KMC, Inc., for the valuable discussions related to flexure-pivot bearing technology.

## References

- Armentrout, R., and Paquette, D., 1993, "Rotordynamic Characteristics of Flexure-Pivot Tilting Pad Journal Bearings," *STLE Tribology Transactions*, Vol. 36, No. 3, pp. 443-451.
- Arumugam, P., Swarnamani, S., and Prabhu, B. S., 1994, "Experimental Identification of Linearized Oil Film Coefficients of Cylindrical and Tilting Pad Bearings," ASME Paper 94-GT-81.
- Barrett, L. E., Allaire, P. E., and Wilson, B. W., 1988, "The Eigenvalue Dependence of Reduced Tilting Pad Bearing Stiffness and Damping Coefficients," *STLE Tribology Transactions*, Vol. 31, No. 4, pp. 411-419.
- Bouard, L., Fillon, M., and Frene, J., 1994, "Comparison Between Three Turbulent Models-Application to Thermohydrodynamic Performances of Tilting-Pad Bearings," International Tribology Conference, AUSTRIAN '94, Perth, Australia, Dec., pp. 119-126.
- Brockwell, K., and Kleibub, D., 1989, "Measurement of the Steady State Operating Characteristics of the Five Shoe Tilting Pad Journal Bearing," *STLE Tribology Transactions*, Vol. 32, No. 2, pp. 267-275.
- Brockwell, K., Kleibub, D., and Dmochowski, W., 1990, "Measurement and Calculation of the Dynamic Operating Characteristics of the Five Shoe Tilting Pad Journal Bearing," *STLE Tribology Transactions*, Vol. 33, No. 4, pp. 481-492.
- Burton, R. A., and Carper, H. J., 1967, "An Experimental Study of Annular Flows with Applications in Turbulent Film Lubrication," *ASME JOURNAL OF LUBRICATION TECHNOLOGY*, pp. 381-391.
- Butner, M., and Murphy, B., 1986, "SSME Long Life Bearings," NASA CR Report 179455.
- Chen, W. J., 1994, "Bearing Dynamic Coefficients of Flexible Pad Bearings," *STLE Transactions*, Preprint No. 94-TC-4D-1.
- Childs, D., and Hale, K., 1994, "A Test Apparatus and Facility to Identify the Rotordynamic Coefficients of High Speed Hydrostatic Bearings," *ASME JOURNAL OF TRIBOLOGY*, Vol. 116, No. 1, pp. 337-344.
- Constantinescu, V. N., and DiMofte, F., 1987, "On the Influence of the Mach Number on Pressure Distribution in Gas Lubricated Step Bearings," *Rev. Roum. Sci. Tech.-Mec. Appl.*, Tome 32, No. 1, pp. 51-56.
- De Choudhury, P., Hill, M., and Paquette, D., "A Flexible Pad Bearing System for a High Speed Centrifugal Compressor," *Proceedings of the 21st Turbomachinery Symposium*, Dallas, TX, Sept. 1992, pp. 57-65.
- Etles, C., and Cameron, A., 1968, "Considerations of Flow Across a Bearing Groove," *ASME JOURNAL OF LUBRICATION TECHNOLOGY*, pp. 312-319.
- Etles, C. M., 1980, "The Analysis and Performance of Pivoted Pad Journal Bearings Considering Thermal and Elastic Effects," *ASME JOURNAL OF LUBRICATION TECHNOLOGY*, Vol. 102, pp. 182-192.
- Etles, C. M., 1992, "The Analysis of Pivoted Pad Journal Bearing Assemblies Considering Thermoelastic Deformation and Heat Transfer Effects," *STLE Tribology Transactions*, Vol. 35, No. 1, pp. 156-162.
- Fillon, M., Bligoud, J.-C., and Frene, J., 1991, "Experimental Study of Tilting-Pad Journal Bearings-Comparison with Theoretical Thermoelastohydrodynamic Results," *ASME JOURNAL OF TRIBOLOGY*, Paper 91-Trib-17.
- Fillon, M., Frene, J., and Boncompain, R., 1987, "Historical Aspects and Present Development on Thermal Effects in Hydrodynamic Bearings," *Proceedings of the 13th Leeds-Lyon Symposium*, pp. 27-47.
- Flack, R. D., and Allaire, P. E., 1984, "Literature Review of Tilting Pad and Turbulent Hydrostatic Journal Bearings for Nuclear Main Coolant Pumps," *The Shock and Vibration Digest*, Vol. 16, No. 7, pp. 3-12.
- Flack, R. D., and Zuck, C. J., 1988, "Experiments on the Stability of Two Flexible Rotors in Tilting Pad Bearings," *STLE Tribology Transactions*, Vol. 31, No. 2, pp. 251-257.
- Franchek, N., Childs, D., and San Andres, L., 1995, "Theoretical and Experimental Comparisons for Rotordynamic Coefficients at a High-Speed, High-Orifice-Compensated Hybrid Bearings," *ASME JOURNAL OF TRIBOLOGY*, Vol. 117, No. 2, pp. 285-290.
- Ha, H. C., Kim, H. J., and Kim, K. W., 1994, "Inlet Pressure Effects on the Thermohydrodynamic Performance of a Large Tilting Pad Journal Bearing," *ASME Paper 94-Trib-26*.
- Hall, K. R., Eubank, P., Holste, J., and Marsh, K., 1986, "Performance Equations for Compressible Flow Through Orifices and Other  $\Delta P$  Devices: A Thermodynamics Approach," *AIChE Journal*, Vol. 32, No. 3, pp. 517-519.
- Hirs, G. G., 1973, "A Bulk-Flow Theory For Turbulence in Lubricating Films," *ASME JOURNAL OF LUBRICATION TECHNOLOGY*, pp. 135-146.
- Kim, J., and Palazzolo, A., 1993, "Dynamic Characteristics of TEHD Tilt Pad Journal Bearing Simulation Including Multiple Mode Pad Flexibility Model," *ASME 1993 Vibrations Conference, Vibrations of Rotating Systems, DE-Vol. 60*, pp. 363-379.
- Knight, J. D., and Barrett, L. E., 1988, "Analysis of Tilting Pad Journal Bearings with Heat Transfer Effects," *ASME JOURNAL OF TRIBOLOGY*, Vol. 110, pp. 128-133.
- Kurtin, K., Childs, D., San Andres, L. A., and Hale, K., 1993, "Experimental versus Theoretical Characteristics of a High Speed Hybrid (combination Hydrostatic and Hydrodynamic) Bearing," *ASME JOURNAL OF TRIBOLOGY*, Vol. 115, No. 2, pp. 160-169.
- Lauder, B., and Leschziner, M., 1978, "Flow in Finite Width Thrust Bearings Including Inertial Effects," *ASME JOURNAL OF LUBRICATION TECHNOLOGY*, Vol. 100, pp. 330-345.
- Lund, J., 1964, "Spring and Damping Coefficients for the Tilting Pad Journal Bearing," *ASLE Transactions*, Vol. 7, pp. 342-352.
- Lund, J., and Bo Pedersen, L., 1986, "The Influence of Pad Flexibility on the Dynamic Coefficients of a Tilting Pad Journal Bearing," *ASME Paper 86-Trib-49*.
- McCarty, R. D., 1986, NBS Standard Reference Data Base 12, Thermophysical Properties of Fluids, MIPROPS 86, Thermophysics Division, Center for Chemical Engineering, National Bureau of Standards, CO.
- Mitsui, J., Hori, Y., and Tanaka, M., 1983, "Thermohydrodynamic Analysis of Cooling Effect of Supply Oil in Circular Journal Bearing," *ASME JOURNAL OF LUBRICATION TECHNOLOGY*, Vol. 105, pp. 414-421.
- Nicholas, J. C., and Kirk, R. G., 1979, "Selection and Design of Tilting Pad and Fixed Lobe Journal Bearings for Optimum Rotordynamics," *Proc. of the 8th Turbomachinery Symposium*, Turbomachinery Laboratory, Texas A&M University, Dallas, pp. 43-58.
- Nicholas, J. C., and Barrett, L. E., 1986, "The Effect of Bearing Support Flexibility on Critical Speed Prediction," *ASLE Transactions*, Vol. 29, No. 3, pp. 329-338.
- Nicholas, J. C., 1994, "Tilting Pad Design," *Proc. of the 23th Turbomachinery Symposium*, Turbomachinery Laboratory, Texas A&M University, Dallas, pp. 179-194.
- Orcutt, F. K., 1967, "The Steady-State Characteristics of the Tilting-Pad Journal Bearing in Laminar and Turbulent Flow Regimes," *ASME JOURNAL OF LUBRICATION TECHNOLOGY*, pp. 392-404.
- Parkins, D. W., and Horner, D., 1992, "Tilting Pad Journal Bearings-Measured and Predicted Stiffness Coefficients," *STLE Transactions*, Pre-print No. 92-TC-3D-2.
- Pinkus, O., 1984/85, "Optimization of Tilting Pad Journal Bearings Including Turbulence and Thermal Effects," *Israel Journal of Technology*, Vol. 22, pp. 142-154.
- Pinkus, O., 1990, *Thermal Aspects of Fluid Film Tribology*, ASME Press, NY.
- Rouch, K. E., 1983, "Dynamics of Pivoted-Pad Journal Bearings, Including Pad Translation and Rotation Effects," *ASLE Transaction*, Vol. 26, No. 1, pp. 102-109.

San Andres, L. A., 1990, "Turbulent Hybrid Bearings with Fluid Inertia Effects," ASME JOURNAL OF TRIBOLOGY, Vol. 112, pp. 699-707.

San Andres, L. A., 1992, "Analysis of Turbulent Hydrostatic Bearings with a Barotropic Fluid," ASME JOURNAL OF TRIBOLOGY, Vol. 114, No. 4, pp. 755-765.

San Andres, L., 1993, "Thermohydrodynamic Analysis of Cryogenic Liquid, Turbulent Flow Fluid Film Bearings, Phase I," Annual Progress Report to NASA Lewis Research Center, NASA Grant NAG3-1434, December.

San Andres, L., 1994, "Thermohydrodynamic Analysis of Cryogenic Liquid, Turbulent Flow Fluid Film Bearings, Phase II," Annual Progress Report to NASA Lewis Research Center, NASA Grant NAG3-1434, December.

San Andres, L., Yang, Z., and Childs, D., 1993, "Thermal Effects in Cryogenic Liquid Annular Seals, I: Theory and Approximate Solutions; II: Numerical Solution and Results," ASME JOURNAL OF LUBRICATION TECHNOLOGY, Vol. 115, No. 2, pp. 267-284.

Someya, T., (ed.), *Journal-Bearing Databook*, Springer-Verlag, pp. 227-229, 1988.

Taniguchi, S., Makino, T., Takeshita, K., and Ichimura, T., 1990, "A Thermohydrodynamic Analysis of Large Tilting-Pad Journal Bearing in Laminar and Turbulent Flow Regimes with Mixing," ASME JOURNAL OF TRIBOLOGY, Vol. 112, pp. 542-549.

Van Doormal, J. P., and Raithby, D., 1984, "Enhancements of the SIMPLE Method for Predicting Incompressible Fluid Flows," *Numerical Heat Transfer*, Vol. 7, pp. 147-163.

White, M. F., and Chan, S. H., 1992, "The Subsynchronous Behavior of Tilting-Pad Journal Bearings," ASME JOURNAL OF TRIBOLOGY, Vol. 114, pp. 167-173.

Yang, Z., 1992, "Thermohydrodynamic Analysis of Product Lubricated Hydrostatic Bearings in the Turbulent Flow Regime," Ph.D. dissertation, Mechanical Engineering Department, Texas A&M University, December.

Zeidan, F., 1992, "Developments in Fluid Film Bearing Technology," *Turbomachinery International Magazine*, Sept/Oct.

Zeidan, F., and Paquette, D. J., 1994, "Application of High Speed and High Performance Fluid Film Bearings in Rotating Machinery," *Proc. of the 23th Turbomachinery Symposium*, Turbomachinery Laboratory, Texas A&M University, Dallas, pp. 209-234.



The American Society of  
Mechanical Engineers

# infocentral@asme.org

**YOU CAN NOW REACH ASME INFORMATION CENTRAL REPRESENTATIVES BY E-MAIL. SIMPLY USE THE ABOVE NUMBER AND GET TOP PRIORITY ON ALL ASME SERVICES OR PRODUCT INQUIRIES. FOR YOUR CONVENIENCE YOU CAN ALSO USE THE PHONE OR FAX NUMBERS, OR MAIL ADDRESS LISTED BELOW. REACHING ASME INFORMATION CENTRAL IS EASIER THAN EVER!**

.....

TELEPHONE	FAX	MAIL
<b>TOLL FREE IN US &amp; CANADA</b>	<b>201-882-1717</b>	<b>ASME</b>
<b>800-THE-ASME</b>	<b>OR 201-882-5155</b>	<b>22 LAW DRIVE</b>
<b>(800-843-2763)</b>		<b>P.O. BOX 2900</b>
<b>TOLL FREE IN MEXICO</b>		<b>FAIRFIELD, NEW JERSEY</b>
<b>95-800-843-2763</b>		<b>07007-2900</b>
<b>OUTSIDE NORTH AMERICA</b>		
<b>201-882-1167</b>		

6 "Turbulent Flow Hydrostatic Bearings: Analysis and Experimental Results," 1995, Yang, Z., San Andres, L., and D. Childs, *International Journal of Mechanical Sciences*, Vol. 37, 8, pp. 815-829.



0020-7403(94)00104-9

## TURBULENT-FLOW HYDROSTATIC BEARINGS: ANALYSIS AND EXPERIMENTAL RESULTS

LUIS SAN ANDRES<sup>†</sup>, DARA CHILDS<sup>†</sup> and ZHOU YANG

<sup>†</sup>Mechanical Engineering Department, Texas A&M University, College Station, Texas 77843, U.S.A. and  
Cummins Engine Company, Inc., Charleston, South Carolina 29405, U.S.A.

(Received 29 June 1994; and in revised form 8 November 1994)

**Abstract**—A bulk-flow thermohydrodynamic (THD) analysis for prediction of the static and dynamic performance characteristics of turbulent-flow, process-liquid hydrostatic journal bearings (HJBs) is presented. The film-averaged momentum transport and energy equations replace the lubrication Reynolds equation, and fluid inertia on film lands and at recess edges are preserved in the analysis. Flow turbulence is accounted through turbulence shear parameters based on friction factors derived from Moody's formulae. Numerical predictions are compared successfully to experimental results from a five-recess, turbulent-flow, water-lubricated hydrostatic bearing operating at a high rotational speed. HJBs operating in a hydrob mode (i.e. with journal rotation) provide no better stability characteristics than hydrodynamic journal bearings and are likely to show half-speed whirl.

### NOTATION

- $A$   $\pi DL$ , journal or bearing surface area [ $\text{m}^2$ ]  
 $A_0$   $C_d \pi d_0^2/4$ , equivalent orifice area [ $\text{m}^2$ ]  
 $A_r$   $bl$ , recess area [ $\text{m}^2$ ]  
 $b$  recess circumferential length [ $\text{m}$ ]  
 $c, c_m$  radial clearance, characteristic clearance ( $= \{c(y)\}_{\min}$ ) [ $\text{m}$ ]  
 $C_{ij}$  damping force coefficients [ $\text{Ns m}^{-2}$ ]  
 $C_d$  empirical orifice discharge coefficient  
 $C_p$  specific heat [ $\text{J kg}^{-1} \text{K}^{-1}$ ]  
 $D$  journal diameter [ $\text{m}$ ]  
 $d_0$  orifice diameter [ $\text{m}$ ]  
 $e_x, e_y$  displacements of the journal [ $\text{m}$ ]  
 $f_j, f_B$   $a_m[1 + (c_m r_{j,B}/H + b_m/R_{j,B})^{e_m}]$ , turbulent friction factors based on Moody's equation,  
 $a_m = 0.001375$ ;  $b_m = 5 \times 10^3$ ;  $c_m = 10^6$ ;  $e_m = 1/83$   
 $F_x, F_y$  fluid film forces [ $\text{N}$ ]  
 $H, h_r$  film thickness, recess depth [ $\text{m}$ ]  
 $K_{ij}$  stiffness force coefficients [ $\text{Nm}^{-1}$ ]  
 $k_x, k_y$   $(k_j + k_B)/2$   
 $k_j, k_B$   $f_j, R_j, f_B, R_B$ , turbulent shear parameters  
 $L, l$  bearing and recess axial lengths [ $\text{m}$ ]  
 $M_{ij}$  inertia force coefficients [ $\text{kg}$ ]  
 $\dot{m}$  flow rate over differential segments [ $\text{kg s}^{-1}$ ]  
 $\dot{M}$  bearing mass flow rate [ $\text{kg s}^{-1}$ ]  
 $n$  normal vector to recess boundary  
 $N_{\text{rec}}$  number of bearing recesses  
 $P$  fluid pressure [ $\text{Nm}^{-2}$ ]  
 $P_s, P_a, P_r$  external supply, ambient and recess pressures [ $\text{Nm}^{-2}$ ]  
 $P_x, P_y$  Perturbed (dynamic pressures) [ $\text{Nm}^{-2}$ ]  
 $R$  journal radius [ $\text{m}$ ]  
 $\text{Re}_c$   $\rho_s R \Omega c_m / \mu_s$ , nominal circumferential flow Reynolds number  
 $R_j$   $\rho H \sqrt{(U - \Omega R)^2 + V^2} / \mu$ , Reynolds number relative to journal surface  
 $R_B$   $\rho H \sqrt{U^2 + V^2} / \mu$ , Reynolds number relative to bearing surface  
 $r_j, r_B$  mean roughness depth at journal and bearing surfaces [ $\text{m}$ ]  
 $T$  bulk fluid-film temperature [ $\text{K}$ ]  
 $\Delta T$   $T_{\text{exit}} - T_i$  [ $\text{K}$ ]  
 $t$  time [ $\text{s}$ ]  
 $T_{\text{ox}}$   $\tau_{xz}^H A_r R$ , torque over a recess [ $\text{Nm}$ ]  
 $U, V$  mean velocities [ $\text{m s}^{-1}$ ]  
 $U$   $U_i + V_j$



$V_r$	$(H_r + H)A_r + V_{r,}$ recess volume [ $\text{m}^3$ ]
$V_s$	volume of orifice supply line [ $\text{m}^3$ ]
$X, Y$	inertial coordinates
$x, y, z$	$(0, \pi D), (0, L), (0, H(x, y, t))$
$\alpha$	$(U _{r=0})/(\Omega R)$ , circumferential velocity entrance swirl factor
$\Omega$	rotational speed of journal [ $\text{rad s}^{-1}$ ]
$\omega$	excitation or whirling frequency [ $\text{rad s}^{-1}$ ]
$\rho$	fluid density [ $\text{kg m}^{-3}$ ]
$\mu$	fluid viscosity [ $\text{N s m}^{-2}$ ]
$\xi_{x,y}$	empirical entrance loss coefficients
$\xi_{x,u,d}$	$\xi_x$ at up-, down-stream recess edges
$e$	$e/c_*$ , dimensionless journal eccentricity
$\tau$	$\omega t$ dimensionless time coordinate
$\tau_{xx}, \tau_{yy}$	wall shear stresses

## Scripts:

a	refers to ambient or discharge conditions
r	refers to recess conditions
s	refers to supply conditions
J	refers to journal
B	refers to bushing
$i, j$	refers to first-order perturbations ( $i, j \rightarrow X, Y$ directions)
*	refers to characteristic (supply) values

## 1. INTRODUCTION

One of the most significant indicators of historical change in tribology has been the use of process fluids as lubricants in fluid-film bearing systems [1]. Process-liquid or product-lubricated hydrostatic journal bearings (HJBs) are now used in liquefied natural gas (LNG) pumps, and consequently overhaul intervals are extended to several times those of LNG pumps supported on conventional ball bearings [2]. HJBs have also been selected as support elements in future cryogenic high-speed turbomachinery such as the High Pressure Fuel Turbopump (HPFTP) and the High Pressure Oxygen Turbopump (HPOTP) of the Space Shuttle Main Engine (SSME) [3].

A systematic research program on HJBs for potential cryogenic turbopump applications has been carried out at the authors' University since 1989. A test facility was designed and built to measure both static and dynamic performance characteristics of hybrid (hydrostatic/hydrodynamic) bearings for the application described above. Purified, heated ( $55^\circ\text{C}$ ) water is used as the lubricant in the facility to achieve comparatively high Reynolds numbers in the test bearing without using cryogenic liquids. A description of the test facility and program as well as some of the test results is given in [4].

Along with the experimental investigation, San Andres [5, 6] introduced a turbulent-inertial bulk flow analysis for prediction of the isothermal performance characteristics of orifice-compensated HJBs with incompressible liquids. Film-averaged momentum equations replace the lubrication Reynolds equation to keep fluid inertial terms typically neglected in conventional models. Fluid inertia at the film lands reduces flow rates and enhances hydrodynamic effects. For laminar flow HJBs, recess-volume fluid compressibility is shown to deteriorate the bearing dynamic stability characteristics [7].

To avoid the complexity of a full THD analysis but still partially accounting for the fluid properties variation, San Andres [8] extended the incompressible liquid model to a barotropic fluid model for analysis of cryogenic liquid HJBs. The fluid properties are considered to depend solely on the local pressure and a mean operating (uniform) temperature. Numerical results show the effects of variable properties to be significant for a  $\text{LH}_2$  (liquid hydrogen, highly compressible) hydrostatic bearing, but show no significant difference between the two models for a  $\text{LO}_2$  (liquid oxygen, less compressible than  $\text{LH}_2$ ) bearing.

Here, a bulk-flow thermohydrodynamic (THD) analysis is introduced to determine the static and dynamic performance characteristics for turbulent flow HJBs. Numerical predictions of flow and rotordynamic force coefficients are compared with experimental results from a water-lubricated hydrostatic bearing. In the analysis, pointwise evaluation of

temperature and hence liquid properties is achieved through the solution of the energy transport equation in the fluid film with an adiabatic boundary assumption justified for HJBs with large mass flow rates. The static characteristics of a HJB include the film pressure, fluid velocity and temperature fields, mass flow rate, fluid-film forces or bearing load capacity, friction torque, and power dissipation. The dynamic force characteristics refer to the stiffness ( $K_{ij}$ ), damping ( $C_{ij}$ ), and added mass ( $M_{ij}$ ) coefficients required for rotordynamic analysis. These coefficients are defined by the following relationship:

$$\begin{bmatrix} F_X \\ F_Y \end{bmatrix} = \begin{bmatrix} F_{X0} \\ F_{Y0} \end{bmatrix} - \begin{bmatrix} K_{XX} & K_{XY} \\ K_{YX} & K_{YY} \end{bmatrix} \begin{bmatrix} \Delta X \\ \Delta Y \end{bmatrix} - \begin{bmatrix} C_{XX} & C_{XY} \\ C_{YX} & C_{YY} \end{bmatrix} \begin{bmatrix} \Delta \dot{X} \\ \Delta \dot{Y} \end{bmatrix} - \begin{bmatrix} M_{XX} & M_{XY} \\ M_{YX} & M_{YY} \end{bmatrix} \begin{bmatrix} \Delta \ddot{X} \\ \Delta \ddot{Y} \end{bmatrix} \quad (1)$$

where  $\Delta X(t)$  and  $\Delta Y(t)$  are components of the journal-center dynamic displacement about an equilibrium position. The dynamic-force coefficients defined by Eqn (1) are important measures of dynamic bearing performance since they influence the system critical speeds, the resonant amplitude response, and stability of the rotor-bearing system.

## 2. MATHEMATICAL MODEL

The general type of bearing considered as a support element for cryogenic liquid turbopumps is a 360-degree hydrostatic journal bearing, orifice-compensated, with a variable number of feeding recesses or pockets machined in the surface of the bearing [3]. The flow is confined to the thin annular region between an inner rotating journal and a stationary bearing bushing (Fig. 1).

### 2.1. Governing equations for turbulent fluid-film flows

Large pressure gradients typical in cryogenic HJBs cause high axial turbulent flow Reynolds numbers, and the effect of turbulent mixing far outweighs molecular diffusivity. In consequence, the temperature rise produced by viscous dissipation tends to be distributed uniformly across the film thickness and thus temperature gradients in the cross-film

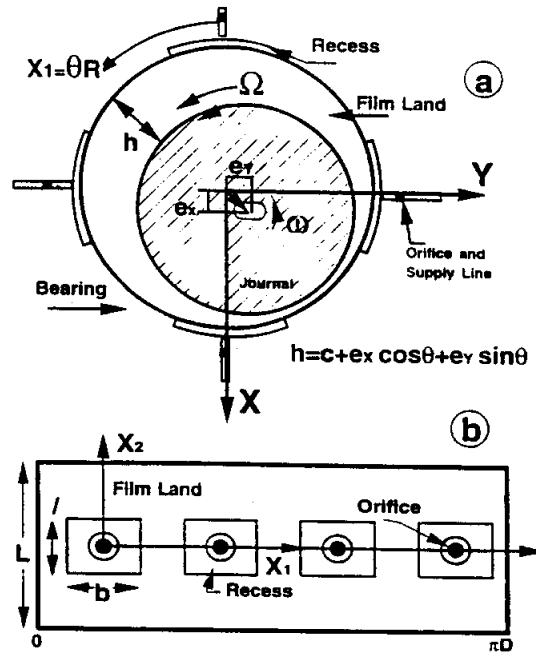


Fig. 1. Geometry of a hydrostatic journal bearing: (a) Axial view and coordinate system. (b) Unwrapped bearing surface.

coordinate ( $z$ ) are confined to turbulent flow boundary layers adjacent to the bounding (bearing and journal) surfaces [9, 10]. Furthermore, in the absence of regions of reversed flow or recirculation, the fluid velocity field presents the same characteristics as discussed above.

The considerations presented allow the three-dimensional continuity, momentum and energy equations to be integrated across the film thickness to determine the two-dimensional bulk-flow governing equations for thin fluid-film flows [11, 12]:

*Continuity equation*

$$\frac{\partial(\rho H)}{\partial t} + \frac{\partial(\rho H U)}{\partial x} + \frac{\partial(\rho H V)}{\partial y} = 0 \quad (2)$$

*Circumferential-momentum equation*

$$\frac{\partial(\rho H U)}{\partial t} + \frac{\partial(\rho H U^2)}{\partial x} + \frac{\partial(\rho H U V)}{\partial y} = -H \frac{\partial P}{\partial x} + \tau_{xz}|_0^H \quad (3)$$

*Axial-momentum equation*

$$\frac{\partial(\rho H V)}{\partial t} + \frac{\partial(\rho H U V)}{\partial x} + \frac{\partial(\rho H V^2)}{\partial y} = -H \frac{\partial P}{\partial y} + \tau_{yz}|_0^H \quad (4)$$

*Energy-transport equation*

$$C_p \left( \frac{\partial(\rho H T)}{\partial t} + \frac{\partial(\rho H U T)}{\partial x} + \frac{\partial(\rho H V T)}{\partial y} \right) + Q_s = T \beta_r H \left( \frac{\partial P}{\partial t} + U \frac{\partial P}{\partial x} + V \frac{\partial P}{\partial y} \right) + R \Omega \tau_{xz}|_0^H - U \tau_{xz}|_0^H - V \tau_{yz}|_0^H \quad (5)$$

where the bulk-flow primitive variables ( $U$ ,  $V$ ,  $P$ , and  $T$ ) are defined as average quantities across the film thickness, and  $Q_s$  represents the heat flux from the fluid film to the bounding solids. Note that the momentum fluxes in Eqns (3–5) are assumed to be aligned with the mass mean velocities. This simplification is fully justified for large Reynolds number flows [13, 14].

The wall shear stresses are calculated according to the bulk-flow theory for turbulence in thin film flows [12, 13]:

$$\begin{aligned} \tau_{xz}|_0^H &= -\frac{\mu}{H} \left( k_x U - k_j \frac{R\Omega}{2} \right) \\ \tau_{yz}|_0^H &= -\frac{\mu}{H} (k_y V) \\ \tau_{xx}|^H &= \frac{H}{2} \frac{\partial P}{\partial x} + \frac{\mu}{4H} [U k_B - (U - R\Omega) k_j] \end{aligned} \quad (6)$$

where the turbulent shear parameters ( $k_x$ ,  $k_y$ ) and ( $k_j$ ,  $k_B$ ) are local functions of the Reynolds numbers and friction factors based on Moody's formulae [15]. The model chosen to represent the wall shear stresses as functions of the rotational speed and bulk-flow velocities is based on its simplicity of implementation, its ability to characterize directly rough surface conditions, and most importantly, on its accuracy when compared to other classical turbulent lubrication models [16, 17].

## 2.2. Mass conservation at a recess

The continuity equation at the recess is defined by the global balance between the flow through the orifice restrictor, the recess outflow into the film lands ( $Q_r$ ) and the temporal change of fluid mass within the recess volume ( $V_r$ ). The recess flow continuity equation is expressed as:

$$A_0 \sqrt{2\rho_r(P_s - P_r)} = Q_r + \rho_r \frac{\partial V_r}{\partial t} + \rho_r V_r \left( \beta \frac{\partial P}{\partial t} - \beta_t \frac{\partial T}{\partial t} \right) \quad (7)$$

where

$$\beta = \frac{1}{\rho} \left( \frac{\partial \rho}{\partial P} \right)_T, \quad \beta_t = -\frac{1}{\rho} \left( \frac{\partial \rho}{\partial P} \right)_P \quad (8)$$

are the liquid compressibility factor and volumetric expansion coefficient, respectively; and

$$Q_r = \int_{\Gamma_r} \rho H (\mathbf{U} \cdot \mathbf{n}) d\Gamma \quad (9)$$

is the mass flow rate across the recess edges ( $\Gamma_r$ ) and entering the film lands.

### 2.3. Global energy balance equation at a recess

A global energy balance equation at a bearing recess is derived, reflecting the heat carry-over (advection) and mixing effects, and the friction heat generation (dissipation) in the recess (Fig. 2):

$$C_p \frac{\partial(\rho T)}{\partial t} V_r + C_p \left( \sum \dot{m}_d T_d + 2 \sum \dot{m}_{\text{side}} T_{\text{side}} \right) = C_p \left( \sum \dot{m}_u T_u + Q_r T_s \right) + T_{\text{or}} \Omega \quad (10)$$

where

$$T_{\text{or}} = \tau_{xz}^H A_r R \quad (11)$$

is the torque over the recess area,  $Q_r$  is the total mass flow rate through the supply orifice,  $V_r$  is the recess volume, and the subscripts "u", "d" and "side" refer to the upstream, downstream, and side edges of a rectangular recess, respectively.

The temperatures at the downstream and side edges of the recess are approximately equal to the recess temperature:

$$T_d = T_{\text{side}} = T_r = \text{constant} \quad (12)$$

while the temperature at the upstream of the recess is given by:

$$T_u = \begin{cases} T_r & \text{if } (\mathbf{U} \cdot \mathbf{n}) > 0; \\ \text{upstream values} & \text{otherwise.} \end{cases} \quad (13)$$

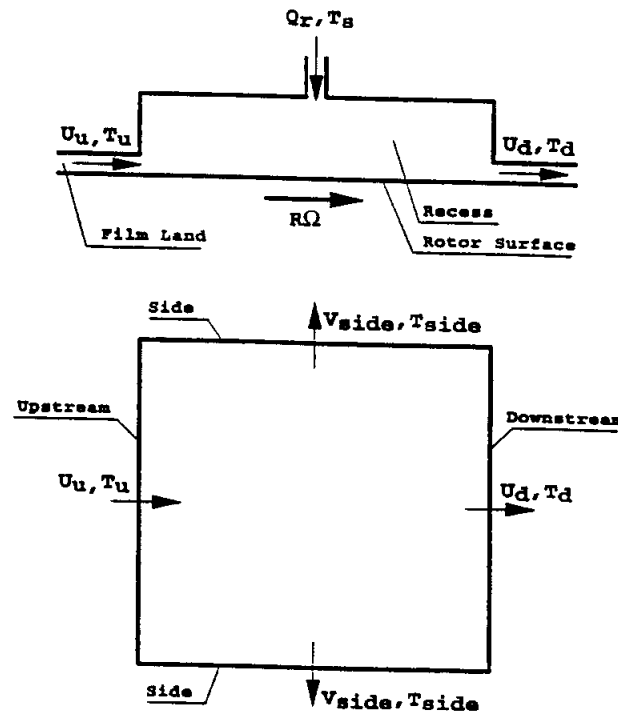


Fig. 2. Conceptual description of global energy balance at a recess.

### 3. BOUNDARY CONDITIONS

The boundary conditions for the flow variables are expressed as:

- (a) On the 360° extended film land, the pressure, velocity and temperature fields are continuous and single-valued in the circumferential ( $x$ ) direction.
- (b) Due to geometric symmetry and no journal misalignment, the axial velocity ( $V$ ) and the axial gradients ( $d/dy$ ) of all the flow variables are zero at the circumferential center line ( $y = 0$ ) of the bearing.
- (c) At the bearing exit plane ( $y = L$ ), the fluid pressure takes a constant value equal to the discharge or ambient pressure ( $P_a$ ) for subsonic flow conditions.
- (d) The recess-edge temperatures are obtained as described above. Fluid inertia at the recess edges is treated through a Bernoulli-type relationship [8], while the velocity vector is considered to be normal to the recess edges.
- (e) At the fluid/journal and the fluid/bearing interfaces, the heat flux to the bounding surfaces  $Q$ , is assumed to be zero. This apparent oversimplification is fully justified in lieu of the extensive numerical work performed by Yang *et al.* [18].

### 4. PERTURBATION AND NUMERICAL ANALYSES

For small amplitude motions of the journal about an equilibrium position, all flow variables are expressed as the superposition of zeroth- and first-order fields representing the steady state and dynamic motion conditions, respectively. Expansion of the governing equations in the perturbation variables yields the zeroth- and first-order flow equations. References [8] and [11] provide complete descriptions of the analysis and the numerical method used. Fluid-film forces and rotordynamic coefficients are found by integration of the calculated pressure fields on the journal surface, i.e.,

$$\begin{bmatrix} F_x \\ F_y \end{bmatrix} = R \int_0^L \int_0^{2\pi} P_0 \begin{bmatrix} \cos \theta \\ \sin \theta \end{bmatrix} d\theta dy \quad (14)$$

where  $P_0$  corresponds to the zeroth-order pressure field, and

$$K_{ij} - \omega^2 M_{ij} + i\omega C_{ij} = -R \int_0^L \int_0^{2\pi} P_j h_i d\theta dy \quad (15)$$

$$\text{with } i, j = X, Y \quad h_X = \cos \theta \quad h_Y = \sin \theta$$

and  $P_X, P_Y$  are the dynamic pressure fields for journal motions in the  $X$  and  $Y$  directions, respectively [8].

A cell finite-difference scheme is implemented to solve the nonlinear differential equations on the film lands [13], and a Newton-Raphson scheme is used to update the recess pressures and to satisfy the mass continuity constraint at each bearing recess [8]. The numerical procedure uses the SIMPLEC algorithm introduced by Van Doormaal and Raithby [19]. This algorithm is well known in the literature, and details on its superior convergence rate, grid refinement sensitivity, and accuracy are well documented [20, 21].

Past simpler models from the same author [5, 8] have evolved to the current THD model and provide a more accurate yet efficient computational tool. The computational analyses have been validated with extensive correlations to experimental measurements in turbulent flow, water-lubricated hydrostatic bearings [4, 22]. Further validations to experimental force coefficient data for LH<sub>2</sub> HJBs are given by Yang *et al.* [23]. Kurtin *et al.* [4] and Franchek *et al.* [22] also report sensitivity analyses of the numerical predictions relative to experimental values for a  $\pm 10\%$  variation in the input empirical parameters (orifice discharge coefficient  $C_d$ , inlet losses  $\xi_{x,y}$ , and relative surface roughness).

In general, calculations show that a relatively small number of grid points for discretization of the bearing surface is typically required to get grid independent results. Less than 3% difference in bearing static and dynamic performance characteristics are obtained when comparing the results from a 49 by 8 grid (number of circumferential  $\times$  axial points) with those from a 79 by 16 grid for the test bearing reported in this paper.

## 5. RESULTS AND DISCUSSION

The numerical example refers to a HJB article tested by Mosher *et al.* [24]. The test bearing is a five-recess, orifice-compensated, smooth-surface hydrostatic bearing with characteristics outlined in Table 1. A complete description of the test facility, experimental procedure and parameter identification technique is given by Childs and Hale [25]. The operating condition for the bearing includes:

- (a) 3 rotational speeds: 10 000, 17 500, and 25 000 rpm
- (b) 2 supply pressures: 4.0, 5.5, and 7.0 MPa (600, 800, 1000 psi)
- (c) 6 journal eccentricity ratios: 0.0, 0.1, 0.2, 0.3, 0.4, and 0.5
- (d) 1 supply temperature: 55 °C (130 °F).

Empirical parameters like the orifice discharge coefficients ( $C_d$ ), the pre-swirl factor ( $\alpha$ ), and the entrance coefficients at the recess edges ( $\xi_{xu}$ ,  $\xi_{xd}$ , and  $\xi_y$ ) are needed for numerical calculations. Table 2 presents the values of these parameters which are determined by matching measured flow rates with the calculated ones for the concentric cases. The resulting parameters are then used for the numerical calculations of all non-zero-eccentricity ratio cases.

The viscosity and density of water are estimated from the following formulae given by Sherman [26]:

$$\mu = 1.005 \times 10^{-3} \left( \frac{T}{293} \right)^{8.9} e^{(4700(1/T - 1/293))} \quad (16)$$

$$\rho = 1000 e^{-4.85 \times 10^{-4}[(T - 293) - (P - 0.1)]} \quad (17)$$

where the temperature ( $T$ ) is in K and the pressure ( $P$ ) is in MPa. All the other properties of water are taken as constant.

The rotational Reynolds number ( $Re_c = \rho_* \Omega R c_* / \mu_*$ ) based on the supply properties and the nominal clearance is equal to  $2.5 \times 10^4$  for 25 000 rpm, thus showing an application where hydrodynamic effects and flow turbulence are significant.

The measured and predicted bearing dynamic characteristics, such as stiffness, damping, and added mass coefficients, the whirl frequency ratio as well as static load, flow rate and temperature are presented as follows.

Table 1. Characteristics of water HJB [24, 25]

Diameter ( $D$ )	76.441 mm (3.0095 in)
Length ( $L$ )	76.2 mm (3 in)
No. of recesses ( $N_{rec}$ )	5
Recess volume ( $V_r$ )	$0.185 \times 10^{-6} \text{ m}^3$ (0.0112891 in <sup>3</sup> )
Recess area ratio ( $A_r/A$ )	0.2
Orifice diameter ( $d_o$ )	2.49 mm (0.098 in)
Orifice supply line volume ( $V_s$ )	$0.129 \times 10^{-6} \text{ m}^3$ (0.00787173 in <sup>3</sup> )
Land roughness (peak-peak) ( $r_l$ and $r_B$ )	0.33 $\mu\text{m}$ (13 $\mu\text{in}$ )
Square recess ( $A_r \times B_r$ )	$27 \times 27 \text{ mm}^2$ (1.064 $\times$ 1.064 in <sup>2</sup> )
Nominal clearance (at zero speed) ( $c_*$ )	0.127 mm (0.005 in)
Supply fluid temperature ( $T_s$ )	328 K (130 °F)

Table 2. Empirical parameters for water HJBs

$\Omega$ (rpm)	$P_s$ (MPa)	$C_d$	$\alpha$	$\xi_{xu}$	$\xi_{xd}$	$\xi_y$
17400	4.0	0.9035	0.5	0.25	0.5	0.5
	7.0	0.8578	0.5	0.25	0.5	0.5
24600	4.0	0.8812	0.5	0.25	0.5	0.5
	7.0	0.8984	0.5	0.25	0.5	0.5

### 5.1. Static performance characteristics

**Static load capacity.** Fig. 3 shows the experimental and theoretical eccentricity ratios as a function of the static load for the highest speed tested (24 600 rpm). Note that solid symbols in the figures represent experimental results, while hollow symbols represent numerical predictions. The journal displacement in the bearing increases almost linearly with the static load, which is a common feature for incompressible fluid hydrostatic bearings and annular seals. The bearing load capacity also increases with supply pressure and rotational speed, since a higher supply pressure provides a larger hydrostatic force and increasing rotational speed generates a greater hydrodynamic force. The numerical predictions correlate very well with experimental measurements (maximum difference: 7.4%). Note that the experiments do not start at zero static load, that is, the test bearing is slightly eccentric for zero applied load.

**Mass flow rate.** Fig. 4 shows the experimental and theoretical mass flow rate as a function of the eccentricity ratio for supply pressures equal to 4 MPa and 7 MPa. Note that the symbols do not coincide with each other on the horizontal axis since the eccentricity ratios are actually functions of the given external static loads. The mass flow rate of the bearing decreases slowly with the eccentricity ratio. As expected, a higher supply pressure (i.e. higher pressure drop across the orifice) produces a larger mass flow rate. The mass flow rate decreases with rotational speeds due to the fluid viscous forces generated by journal rotation and the reduction of the radial clearance from the centrifugal growth of the shaft.

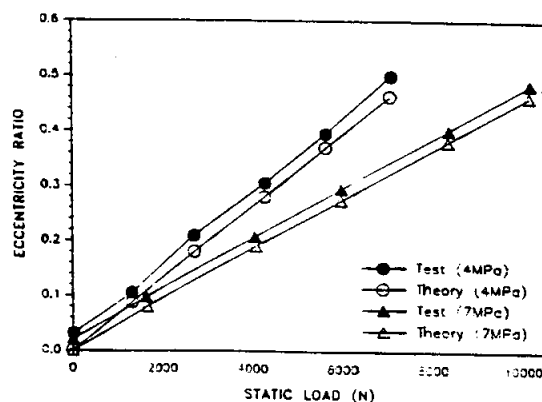


Fig. 3. Eccentricity ratio vs static load (Water HJB) ( $P_s = 4$  and  $7$  MPa,  $P_a = 0.1$  MPa,  $T_s = 55^\circ\text{C}$ ,  $\Omega = 24\,700$  rpm).

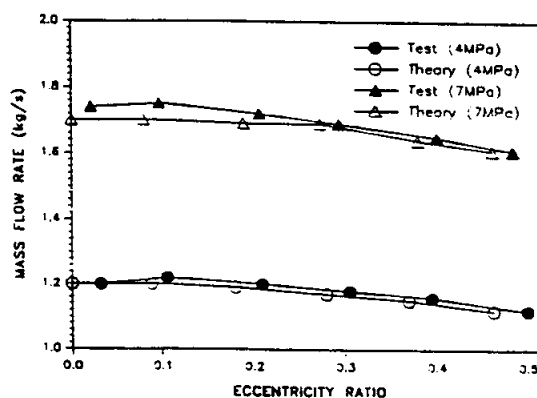


Fig. 4. Mass flow rate vs eccentricity ratio (Water HJB) ( $P_s = 4$  and  $7$  MPa,  $P_a = 0.1$  MPa,  $T_s = 55^\circ\text{C}$ ,  $\Omega = 24\,700$  rpm).

The lowest flow rate occurs at the low supply pressure (4 MPa), high eccentricity (0.5) and high speed (24 600 rpm) condition. The numerical predictions match the experimental data very well (maximum difference < 3%).

**Fluid exit temperature.** Fig. 5 shows the experimental and theoretical temperatures near the exit region of the bearing versus the eccentricity ratio. The supply temperature is also presented in the figures (dashed line). The exit temperature increases with the eccentricity ratio. The maximum temperature rise across the bearing length ( $\Delta T$ ) is about 4 °C at the highest speed (24 600 rpm) and eccentricity ratio (0.5), but the lowest supply pressure (4.0 MPa) condition. This is expected since the temperature rise across the bearing length is proportional to the rotational drag power (increasing with journal eccentricity), but inversely proportional to the mass flow rate which increases with the supply pressure. Note that the contribution of the radial-clearance reduction due to journal rotation to the film temperature rise could be important since a smaller clearance produces a larger friction torque along with a smaller bearing flow rate. Most of the predicted exit temperatures are higher than the measured values presumably due to the adiabatic surfaces condition imposed on the analysis. The maximum difference between the predicted and measured exit temperatures is less than 2% and occurs at the largest eccentricity ratio (0.5), rotational speed (24 600 rpm), and supply pressure (7 MPa) condition. If only the temperature rise ( $\Delta T$ ) is considered, the maximum difference of prediction is about 27%. However, as to a point-wise match, the numerical predictions are good, and the adiabatic flow assumption is fully justified for the bearing studied.

Experimental data for water HJBs with smaller clearances ( $c_* = 0.0762$  mm and 0.1016 mm) are also available but not presented here. Yang *et al.* [18] show that the adiabatic flow assumption is adequate for fluid-film flows with large mass flow rates ( $\dot{M}$ ). This is a typical flow conditions for annular pressure seals and HJBs where axial heat advection dominates the thermal process. As the bearing clearance decreases, the mass flow rate decreases but the viscous dissipation increases. Table 3 presents the theoretical and experimental exit temperatures of water HJBs with three different clearances and for the largest speed (24 600 rpm) and supply pressure (7 MPa) tested. Predictions of fluid temperatures for the small clearance ( $c_* = 0.0762$  mm) water HJB are not as good as those for the large ( $c_* = 0.127$  mm) or the medium ( $c_* = 0.1016$ ) clearance water HJBs. Predictions of all the other bearing performance characteristics like mass flow rate, load capacity, and rotordynamic force coefficients, are not affected by the small temperature variations ( $\Delta T < 10^\circ\text{C}$ ) in the three water HJBs.

### 5.2. Dynamic performance characteristics

The numerical results for the dynamic force coefficients defined in Eqn (1) are evaluated for synchronous operation ( $\omega = \Omega$ ) and compared with the experimental data.

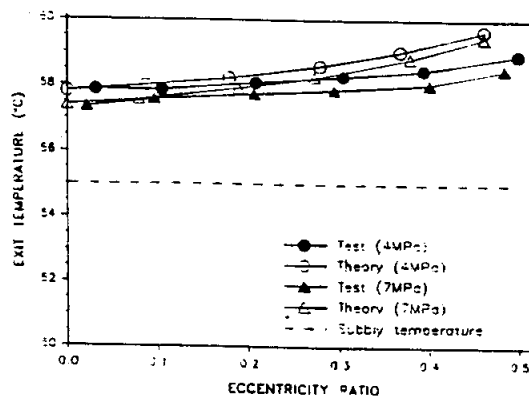


Fig. 5. Exit temperature vs eccentricity ratio (Water HJB) ( $P_s = 4$  and 7 MPa,  $P_a = 0.1$  MPa,  $T_s = 55^\circ\text{C}$ ,  $\Omega = 24\,700$  rpm).



Table 3. Theoretical and experimental exit temperatures ( $T_{\text{exit}}$ ) of water HJBs with different radial clearances ( $\Omega = 24\,600$  rpm,  $P_s = 7$  MPa,  $P_a = 0.1$  MPa,  $T_i = 55^\circ\text{C}$ )

$T_{\text{exit}}$ ( $^\circ\text{C}$ )*	$\epsilon = 0.0$	$\epsilon = 0.1$	$\epsilon = 0.2$	$\epsilon = 0.3$	$\epsilon = 0.4$	$\epsilon = 0.5$	$\dot{M}$
$c_s = 0.0762$ mm	61.67	61.76	62.07	62.52	63.25	64.48	$\approx 0.5$ kg s $^{-1}$
	60.03	60.14	60.33	60.36	59.93	61.50	
$c_s = 0.1016$ mm	58.06	58.37	58.73	59.17	59.82	60.95	$\approx 1.4$ kg s $^{-1}$
	58.01	58.09	58.21	58.61	59.20	59.62	
$c_s = 0.1270$ mm	57.41	57.59	57.92	58.27	58.85	59.48	$\approx 1.7$ kg s $^{-1}$
	57.34	57.58	57.74	57.87	58.03	58.50	

\*1st row—theoretical results; \*\*2nd row—experimental results

**Direct stiffness.** Fig. 6 shows the direct stiffness coefficients ( $K_{xx}$ ) as a function of the static journal eccentricity ratio. These coefficients are almost constant as the eccentricity ratio increases from 0 to 0.5. The direct stiffness increases with increasing supply pressure since a higher supply pressure provides a larger load capacity (Fig. 3). There is a small increase of direct stiffness with rotational speed (not illustrated here) due to a hydrodynamic effect. The maximum difference between the numerical predictions and the experimental measurements is 22.55%.

**Cross-coupled stiffness.** Cross-coupled stiffness coefficients ( $K_{xy}$ ) are presented in Fig. 7 as a function of the eccentricity ratio. Generally, these coefficients decrease slightly with eccentricity ratio. The magnitude of the cross-coupled stiffness is comparable to that of the direct stiffnesses, which demonstrates the importance of hydrodynamic effects. For the present test bearing, a higher supply pressure yields larger cross-coupled stiffness coefficients due to a higher turbulent viscosity induced by the large pressure drop across the bearing. There is a great increase of the cross-coupled stiffness with rotational speed (not illustrated here) showing the significance of the hydrodynamic influence on the bearing dynamic performance. The maximum difference between the theoretical predictions and the experimental data is 22.41% and occurs at the high speed (24 600 rpm), low supply pressure (4 MPa) condition.

**Direct damping.** Fig. 8 shows direct damping coefficients ( $C_{xx}$ ) versus the eccentricity ratio. Like the direct stiffnesses, the direct damping coefficients are relatively insensitive to the variation of the eccentricity ratio. A higher supply pressure generates larger direct damping coefficients, but the influence of rotational speed on direct damping is relatively small. The theoretical predictions match very well with the experimental data and the maximum difference is about 8%.

**Cross-coupled damping.** Fig. 9 shows cross-coupled damping coefficients ( $C_{xy}$ ) as a function of the eccentricity ratio. The prediction shows that these coefficients increases with

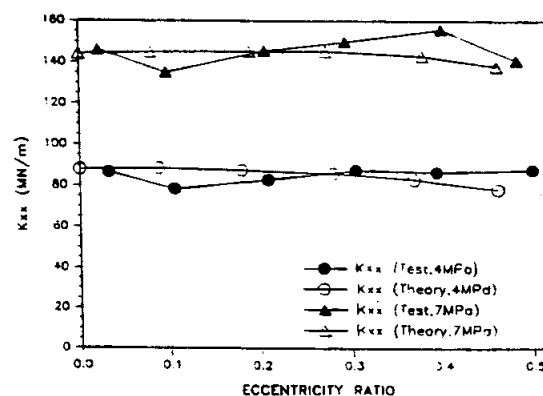


Fig. 6. Direct stiffness ( $K_{xx}$ ) vs eccentricity ratio (Water HJB) ( $P_s = 4$  and 7 MPa,  $P_a = 0.1$  MPa,  $T_i = 55^\circ\text{C}$ ,  $\Omega = 24\,700$  rpm).

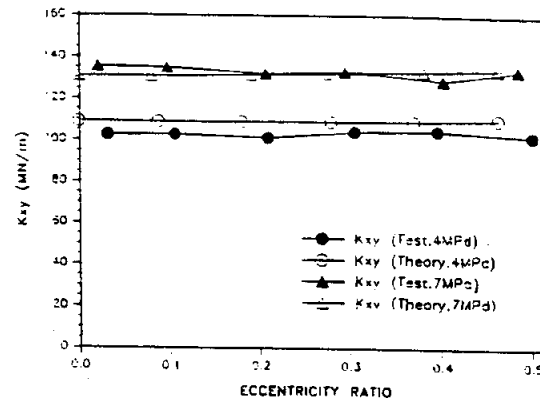


Fig. 7. Cross-coupled stiffness ( $K_{xy}$ ) vs eccentricity ratio ( $P_s = 4$  and  $7$  MPa,  $P_a = 0.1$  MPa,  $T_s = 55^\circ\text{C}$ ,  $\Omega = 24\,700$  rpm).

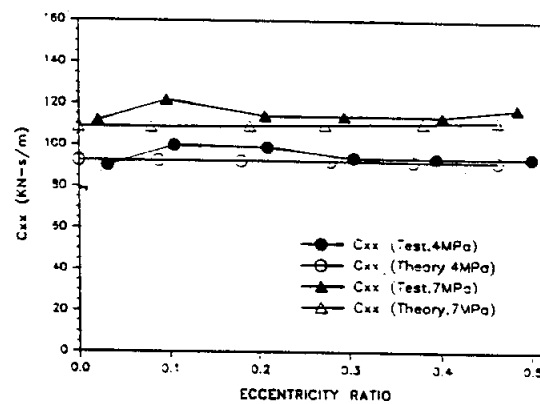


Fig. 8. Direct damping ( $C_{xx}$ ) vs eccentricity ratio (Water HJB) ( $P_s = 4$  and  $7$  MPa,  $P_a = 0.1$  MPa,  $T_s = 55^\circ\text{C}$ ,  $\Omega = 24\,700$  rpm).

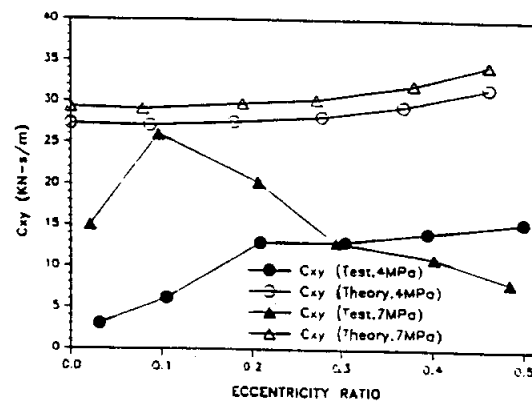


Fig. 9. Cross-coupled damping ( $C_{xy}$ ) vs eccentricity ratio ( $P_s = 4$  and  $7$  MPa,  $P_a = 0.1$  MPa,  $T_s = 55^\circ\text{C}$ ,  $\Omega = 24\,700$  rpm).

increasing eccentricity ratio, while the experimental data behave irregularly. The magnitudes of the cross-coupled damping coefficients are much smaller than the direct ones. However, according to Eqn (1), these coefficients have a pronounced gyroscopic-like effect on the radial-bearing force component at a high whirl frequency ( $\omega$ ). The numerical

predictions are generally poor. The combined effect of the cross-coupled damping with the direct added mass coefficients will be presented later.

**Added mass.** The added mass coefficients are usually neglected in conventional rotor-bearing dynamic analysis. Very few experimental data are available in the open literature for these coefficients. Fig. 10 shows the direct added mass coefficients ( $M_{xx}$ ) as a function of eccentricity ratio, while the cross-coupled added mass coefficients ( $M_{xy}$ ) are presented in Fig. 11. The experimental added masses behave irregularly as the journal eccentricity increases. Note that the direct added mass coefficients could be as large as the mass of the test bearing (11.34 kg), which shows that fluid inertial effects are very important for turbulent flow HJBs and cannot be neglected. Like the cross-coupled damping, the added mass coefficients are poorly predicted. However, as will be shown below, the combined effect of the cross-coupled damping with the direct added mass on the effective stiffness is most important.

**Effective stiffness and damping coefficients.** For a small circular orbit and synchronous ( $\omega = \Omega$ ) whirling around the static equilibrium position, the effective stiffness and damping can be simply derived from Eqn (1) as

$$K_{xxe} = K_{xx} + \Omega C_{xy} - \Omega^2 M_{xx} \quad (18)$$

$$K_{yye} = K_{yy} - \Omega C_{yx} - \Omega^2 M_{yy} \quad (19)$$

$$C_{xxe} = C_{xx} - K_{xy}/\Omega + \Omega M_{xy} \quad (20)$$

$$C_{yye} = C_{yy} + K_{yx}/\Omega - \Omega M_{yx} \quad (21)$$

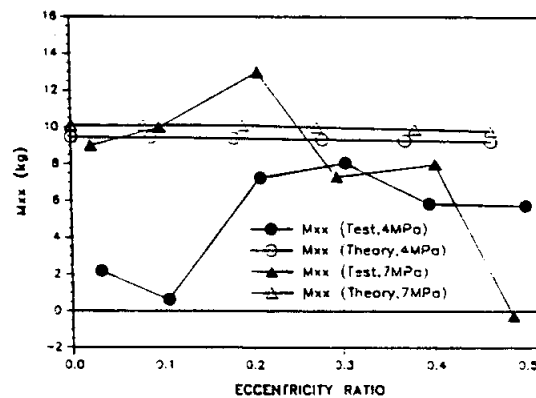


Fig. 10. Direct added mass ( $M_{xx}$ ) vs eccentricity ratio ( $P_s = 4$  and 7 MPa,  $P_a = 0.1$  MPa,  $T_s = 55^\circ\text{C}$ ,  $\Omega = 24\,700$  rpm).

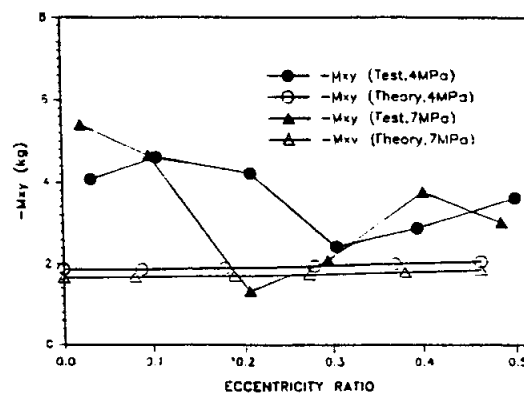


Fig. 11. Cross-coupled added mass ( $-M_{xy}$ ) vs eccentricity ratio ( $P_s = 4$  and 7 MPa,  $P_a = 0.1$  MPa,  $T_s = 55^\circ\text{C}$ ,  $\Omega = 24\,700$  rpm).

From Eqns (18–21), it can be seen that positive cross-coupled damping ( $C_{xy}$ ) and negative direct added mass ( $M_{xx}$ ) increase the effective stiffness, while positive cross-coupled stiffness ( $K_{xy}$ ) and negative cross-coupled added mass ( $M_{yy}$ ) lower the effective damping. Table 4 shows the contributions of the cross-coupled damping and direct added mass to the direct stiffness, while the effects of the cross-coupled stiffness and added mass on the direct damping are presented in Table 5 for the high speed (24 600 rpm), high pressure (7.0 MPa) and zero eccentricity condition.

The combined contribution of the cross-coupled damping and the direct added mass ( $\Omega C_{xy} - \Omega^2 M_{xx}$ ) to the direct stiffness is relatively small (about 10%) even though the individual contribution of  $C_{xy}$  or  $M_{xx}$  is large (about 50%). The cross-coupled stiffness greatly reduces the direct damping (about 50%), while the effect of the cross-coupled added mass is small. These results explain why the cross-coupled damping and the added mass coefficients sometimes can both be neglected and still obtain meaningful predictions for the rotordynamic performance of HJBs.

Table 6 presents the maximum difference, average difference, and standard deviation for all the effective stiffness and damping coefficients. These results show that the dynamic performance characteristics of the bearing are well predicted.

*Whirl frequency ratio.* Like the effective stiffness and damping coefficients, the whirl frequency ratio (WFR) is a dynamic parameter which acts as an indicator of bearing stability. A low WFR indicates enhanced ability of a bearing/journal system to safely operate at higher running speeds relative to the first critical speed of the system.

Fig. 12 illustrates the WFR as a function of the eccentricity ratio. The WFR is approximately 0.5 for all conditions. Thus, hydrostatic (hybrid) bearings offer no better stability

Table 4. Contribution of cross-coupled damping and direct added mass to effective stiffness, ( $\Omega = 24\,600$  rpm,  $P_s = 7$  MPa,  $\varepsilon = 0$ )

$\Omega C_{xy}$ (MN m <sup>-1</sup> )	$\Omega^2 M_{xx}$ (MN m <sup>-1</sup> )	$\Omega C_{xy} - \Omega^2 M_{xx}$ (MN m <sup>-1</sup> )	$K_{xx}$ (MN m <sup>-1</sup> )	$(\Omega C_{xy} - \Omega^2 M_{xx})/K_{xx}$ (%)
75.5*	67.0	8.45	144	5.9
38.6**	59.7	- 21.10	146	- 14.0

\*1st row—theoretical results; \*\*2nd row—experimental results

Table 5. Contribution of cross-coupled stiffness and added mass to effective damping, ( $\Omega = 24\,600$  rpm,  $P_s = 7$  MPa,  $\varepsilon = 0$ )

$K_{xy}/\Omega$ (K N s m <sup>-1</sup> )	$\Omega M_{yy}$ (K N s m <sup>-1</sup> )	$-K_{xy}/\Omega + \Omega M_{yy}$ (K N s m <sup>-1</sup> )	$C_{xx}$ (K N s m <sup>-1</sup> )	$(-K_{xy}/\Omega + \Omega M_{yy})/C_{xx}$ (%)
50.8*	- 4.25	- 55.1	109	- 50.1
52.6**	- 13.90	- 66.5	112	- 59.4

\*1st row—theoretical results; \*\*2nd row—experimental results

Table 6. Prediction difference and standard deviation for effective stiffness and damping coefficients

Item	Maximum difference	Average difference	Standard deviation
$K_{xx}$	42.3%	16.6%	11.6%
$K_{yy}$	16.5%	8.6%	4.6%
$C_{xx}$	24.9%	11.1%	7.9%
$C_{yy}$	21.3%	8.8%	5.5%

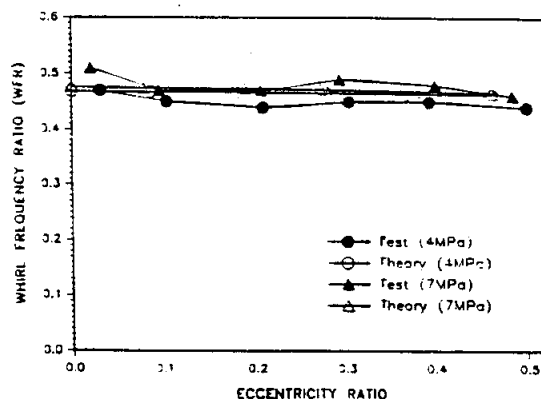


Fig. 12. Whirl frequency ratio vs eccentricity ratio (Water HJB) ( $P_s = 4$  and  $7$  MPa,  $P_a = 0.1$  MPa,  $T_s = 55^\circ\text{C}$ ,  $\Omega = 24\,700$  rpm).

characteristics than hydrodynamic bearings and show the likelihood of half-speed whirl. The maximum difference between the theoretical and experimental results is 8.35% which, added to the good simulation of the effective stiffness and damping, shows that the bearing dynamic performance characteristics can be well predicted by the theoretical model and computer code developed.

## 6. CONCLUSIONS

A bulk-flow thermohydrodynamic (THD) analysis is developed for accurate predictions of the static and dynamic performance characteristics of process-liquid turbulent-flow hydrostatic journal bearings (HJBs). A finite difference scheme is implemented to solve the nonlinear differential equations on the film lands, while an iterative scheme is used to update the recess pressures and to satisfy the mass continuity requirement at each bearing recess. Extensive comparisons between numerical results and experimental data of turbulent flow water HJBs show very good correlations and demonstrate the correctness and accuracy of the adiabatic flow THD analysis and the numerical scheme implemented.

The bearing load capacity increases linearly with journal eccentricity and a higher supply pressure or rotational speed provides a larger load capacity. The mass flow rate of the bearing decreases with eccentricity ratio and rotational speed but increases with supply pressure. The exit fluid temperature increases with eccentricity ratio and rotational speed but decreases with supply pressure.

All the dynamic force coefficients remain relatively constant for the eccentricity ratios tested (0 to 0.5). The whirl frequency ratio appears to be 0.5 for all conditions, showing that HJBs with journal rotation present stability characteristics similar to those of plain journal bearings. The combined effects of the cross-coupled damping ( $C_{xy}$  or  $-C_{yx}$ ) and the direct added mass ( $M_{xx}$  or  $M_{yy}$ ) coefficients on the effective stiffness ( $K_{xx}$ ) are negligible. Note that most rotordynamic codes only allow for a bearing model without the added mass coefficients while retaining the cross-coupled damping. According to the analysis and results presented, this modeling procedure will lead to errors. If the mass terms cannot be incorporated into the analysis, the cross-coupled damping terms should also not be included.

**Acknowledgements**—The support of Pratt&Whitney Co. and NASA Lewis Research Center are gratefully acknowledged. Thanks to Mr. James Walker of NASA Lewis RC for his continued interest in this work.

## REFERENCES

1. D. D. Fuller, Hydrodynamic and hydrostatic fluid-film bearings. *Achievements in Tribology* (edited by L. B. Sibley and F. E. Kennedy) Trib-Vol. 1, ASME, Warrendale, PA (1990).
2. T. Katayama and A. Okada, Liquefied natural gas pump with hydrostatic journal bearings. *Proc. 9th Int. Pump Users Symposium*, Houston, Texas, pp. 39–50 (1992).

3. M. Butner and B. Murphy, "SSME Long Life Bearings," NASA Report, CR179455 (1986).
4. K. A. Kurtin, D. Childs, L. San Andres and K. Hale, Experimental versus theoretical characteristics of a high-speed hybrid (combination hydrostatic and hydrodynamic) bearing. *ASME J. Tribol.* **115**, 160-9 (1993).
5. L. San Andres, Turbulent hybrid bearings with fluid inertia effects. *ASME J. Tribol.* **112**, 699-707 (1990).
6. L. San Andres, Approximate analysis of turbulent hybrid bearings: static and dynamic performance for centered operation. *ASME J. Tribol.* **112**, 692-8 (1990).
7. L. A. San Andres, Effect of fluid compressibility on the dynamic response of hydrostatic journal bearings. *Wear* **146**, 269-83 (1991).
8. L. A. San Andres, Analysis of turbulent hydrostatic bearings with a barotropic cryogenic fluid. *ASME J. Tribol.* **114**, 755-65.
9. T. Suganami and A. Z. Szeri, A thermohydrodynamic analysis of journal bearings. *ASME J. Lubr. Technol.* **101**, 21-7 (1979).
10. F. Di Pasquantonio and P. Sala, Influence of thermal field on the resistance law in turbulent bearing-lubrication theory. *ASME J. Tribol.* **106**, 368-76 (1984).
11. Z. Yang, L. San Andres and D. Childs, Thermal effects in cryogenic liquid annular seals, part I: theory and approximate solution; part II: numerical solution and results. *ASME J. Tribol.* **115**, 267-84 (1993).
12. G. G. Hirs, A bulk-flow theory for turbulence in lubricant films. *ASME J. Lubr. Technol.* **95**, 137-46 (1973).
13. B. E. Launder and M. Leschziner, Flow in finite width thrust bearings including inertial effects, I-laminar flow, II-turbulent flow. *ASME J. Lubr. Technol.* **100**, 330-45 (1978).
14. F. Simon and J. Frene, Analysis for incompressible flow in annular seals. *ASME J. Tribol.* **114**, 431-8 (1992).
15. B. S. Massey, *Mechanics of Fluids*. Van Nostrand Reinhold, Workingham, U.K. (1992).
16. C. C. Nelson and D. T. Nguyen, Comparison of Hirs equation with Moodys equation for determining rotordynamic coefficients of annular pressure seals. *ASME J. Lubr. Technol.* **109**, 144-8 (1987).
17. L. San Andres, Improved analysis of high speed, turbulent hybrid bearings. *4th NASA Conf. on Advanced Earth-to-Orbit Propulsion Technology*, NASA CP 3092, Vol ii, pp. 414-31 (1990).
18. Z. Yang, L. San Andres and D. Childs, Importance of heat transfer from fluid film to stator in turbulent annular seals. *Wear* **160**, 269-77 (1993).
19. J. P. Van Doormaal and G. D. Raithby, Enhancements of the SIMPLE method for predicting incompressible fluid flows. *Numer. Heat Transfer* **7**, 147-63 (1984).
20. J. P. Van Doormaal and G. D. Raithby, An evaluation of the segregated approach for predicting incompressible fluid flow. *ASME Paper 85-HT-9* (1985).
21. D. S. Jang, R. Jetli and S. Acharya, Comparison of the PISO, SIMPLER, and SIMPLEC algorithms for the treatment of the pressure-velocity coupling in steady flow problems. *Numer. Heat Transfer* **10**, 209-28 (1986).
22. N. Franchek, D. Childs and L. San Andres, Theoretical and experimental comparisons for rotordynamic coefficients on a high-speed, high-pressure, orifice compensated hybrid bearing. *ASME Paper 94-Trib-3* (1994).
23. Z. Yang, L. San Andres and D. Childs Thermohydrodynamic analysis of process liquid hydrostatic bearings in turbulent regime, I: theory, II: numerical solution and results. *ASME J. Appl. Mech.* (1995).
24. P. Mosher, N. Franchek, C. Rouvas, H. Hale and D. Childs, Experimental rotordynamic coefficient results for a square-recess smooth-land straight-orifice large-clearance hybrid bearing. Research Report, TAMU-0508, Texas A&M University, College Station, TX 77843 (1991).
25. D. Childs and K. Hale, A test apparatus and facility to identify the rotordynamic coefficients of high-speed hydrostatic bearings. *ASME J. Tribol.* **116**, 337-44 (1994).
26. F. S. Sherman, *Viscous Flow*. McGraw-Hill, New York (1990).

**7a** "Thermohydrodynamic Analysis of Process Liquid Hydrostatic Bearings in Turbulent Regime, Part I: The Model and Perturbation Analysis," 1995, Yang, Z., L. San Andres and D. Childs, *ASME Journal of Applied Mechanics*, Vol. 62, 3, pp. 674-684.

# Thermohydrodynamic Analysis of Process-Liquid Hydrostatic Journal Bearings in Turbulent Regime, Part I: The Model and Perturbation Analysis

Zhou Yang

Cummings Engine Company, Inc.  
Columbus, IN 47201  
Assoc. Mem. ASME

L. San Andres

Assoc. Mem. ASME

D. W. Childs

Fellow ASME

Mechanical Engineering Department,  
Texas A&M University,  
College Station, TX 77843

*A bulk-flow thermohydrodynamic (THD) analysis is developed for prediction of the static and dynamic performance characteristics of turbulent-flow, process-liquid, hydrostatic journal bearings (HJBs). Pointwise evaluation of temperature and hence liquid properties is achieved through the solution of the energy equation in the fluid film with insulated boundaries, and justified for fluid film bearings with external pressurization. Fluid inertia within the film lands and at recess edges is preserved in the analysis. Flow turbulence is accounted through turbulence shear parameters based on friction factors derived from Moody's formulae. The effects of fluid compressibility and temperature variation in the bearing recesses are included. Numerical solution and results are presented in the second part of this work and compared with some limited experimental data for a liquid hydrogen ( $LH_2$ ) bearing.*

## 1 Introduction

There is an increasing interest in the use of process liquid, fluid film bearings in high-performance turbomachinery. Hydrostatic journal bearings (HJBs) are now being used in liquefied natural gas (LNG) pumps, where the working fluid on the bearings is the LNG delivered from the pump, and consequently, overhaul intervals are extended to several times those of LNG pumps supported on conventional ball bearings (Katayama and Okada, 1992). HJBs have also been selected as support elements in future cryogenic high-speed turbomachinery such as the High Pressure Fuel Turbopump (HPFTP) and the High Pressure Oxygen Turbopump (HPOTP) of the Space Shuttle Main Engine (SSME). HJBs, unlike rolling-element bearings, have no apparent DN limit (bore diameter in mm multiplied by journal speed in rpm); therefore, shaft speeds can be allowed to increase to a level more suitable for high operating efficiency with a reduced machinery size and weight. This bearing type has other advantages over conventional rolling-element bearings, such as high radial stiffness, accuracy of positioning, good vibration-damping characteristics, low starting torque, and extremely long life.

Despite their attractive features, HJBs operating at high speeds and with cryogenic liquids are yet not fully understood. The thermophysical properties of cryogenic liquids are strongly dependent on their local state of pressure and temperature. Although process liquids (like  $LH_2$ ) offer very small viscosities, the trends toward higher rotational speeds and larger pressure differentials, as well as the implementation of intentionally roughened surfaces to improve bearing dynamic stability (Von Pragenau, 1990), provide unique flow characteristics and operating conditions where high levels of turbulence (energy dissipation) may yield

significant thermal effects. Viscous dissipation due to shear motion and pressure extrusion, and heat transfer from or to bearing surfaces can generate significant temperature and viscosity variations within the fluid film and affect pronouncedly the bearing static and dynamic force characteristics. Prediction of bearing performance is then no longer meaningful when based on an isothermal or isoviscous assumption.

Prediction of HJB performance has been commonly based on analysis of the isothermal form of the Reynolds equation (or the Bulk-Flow equations) due to the following considerations. First, conventional HJBs operate at low journal speeds and in the laminar flow regime with low heat generation and hence small temperature variations in the fluid film. Second, the flow of fresh fluid into the film region causes thermal effects in HJBs to be less severe than in hydrodynamic bearings where hot lubricants recirculate in the fluid film region. Third, including thermal effects in HJB analysis greatly increases the analytical complexity. Pointwise evaluation of temperature and viscosity in the fluid film (the thermohydrodynamic or THD theory) requires the solution of the energy equation. The boundary temperatures in the fluid film region are related to the thermal transport in the journal and bearing solids. The coupling of the heat conduction equations in the solids with the governing equations in the fluid film leads to a trial-and-error solution of the liquid/solid interface boundary temperatures. Such a nonlinear iterative problem is costly and may be very sensitive and prone to numerical instabilities.

Reddecliff and Vohr (1969) initially studied HJBs for use in high-pressure cryogenic rocket engine turbopumps. In their analysis, the turbulent model provided by Elrod and Ng (1967) was introduced into the Reynolds equation. The inertia effects at the edges of the recesses were found to change the pressure distribution, which reduced the flow rate but did not affect the total bearing load capacity. The nonlinear fluid advective inertial terms could not be accounted for due to numerical difficulties. Variable fluid properties were treated as linear between those at the supply and discharge pressures, and steady-state predictions were reported to agree well with experimental results. The scatter in the measured recess pressures was attributed to measure-

Contributed by the Applied Mechanics Division of THE AMERICAN SOCIETY OF MECHANICAL ENGINEERS for publication in the ASME JOURNAL OF APPLIED MECHANICS.

Discussion on this paper should be addressed to the Technical Editor, Prof. Lewis T. Wheeler, Department of Mechanical Engineering, University of Houston, Houston, TX 77204-4792, and will be accepted until four months after final publication of the paper itself in the ASME JOURNAL OF APPLIED MECHANICS.

Manuscript received by the ASME Applied Mechanics Division, Feb. 11, 1993; final revision, Apr. 4, 1994. Associate Technical Editor: S. A. Berger.



ment inaccuracies and to variations in bearing clearance caused by temperature differences between the bearing and shaft.

Artiles et al. (1982) presented a numerical solution to the static and dynamic performance characteristics of hydrostatic journal bearings. A turbulent Reynolds equation with constant fluid properties was solved by the column-matrix method, while a Newton-Raphson scheme was implemented for efficient calculation of the recess pressures. Turbulent-to-laminar flow power-loss ratios were reported to be in the range of 25 to 30 for the Reynolds numbers considered. Even though there were neither energy considerations nor thermal effects in the analysis, large temperature rises (up to 24.5°C) in the fluid film were reported for LO<sub>2</sub> bearings, while temperature rises in LH<sub>2</sub> bearings were negligibly small.

Braun et al. (1987) introduced a comprehensive THD analysis for a two-row recess LH<sub>2</sub> hydrostatic journal bearings. On the fluid film region, a variable-properties Reynolds equation was coupled to a two-dimensional energy transport equation. The heat transfer to the bounding solids (shaft and bush) was analyzed in its three-dimensional complexity. Bulk-flow heat-transfer coefficients were used to represent the boundary conditions at the fluid/solid interfaces, and fluid inertia effects were considered only at the pocket's edges with no recess volume-liquid compressibility effects. Braun et al.'s analysis regarded the fluid flow as laminar, although large pressure differentials and rotational speeds were considered in the applications studied. A small temperature increment was found in the fluid film, and thermal effects were shown to be minimal relative to a constant properties liquid model. No conclusions were made as to the effects of heat transfer from the fluid film to the bounding solids. The numerical predictions presented show circumferential flow Reynolds numbers as large as 100,000 with a laminar flow model.

San Andres (1990a, b) introduced a turbulent bulk-flow analysis for prediction of the performance characteristics of orifice-compensated HJBs. Here bulk-flow equations with fluid inertia replace the conventional Reynolds equation, and include recess volume-fluid compressibility effects known to deteriorate the bearing stability characteristics due to pneumatic hammer (San Andres, 1991a). For example, the whirl frequency ratio, an indicator of bearing stability, is predicted to be larger than 0.5 for nonzero recess-fluid compressibility. San Andres (1992a) extended his incompressible liquid model to a barotropic fluid model for analysis of cryogenic liquid HJBs. The variable fluid properties are considered to depend on the local pressure and a mean operating (uniform) temperature. The barotropic label applies to the fluid and not to the complex flow process in the fluid film bearing. Numerical results show the effects of variable properties to be significant for a LH<sub>2</sub> (highly compressible) hydrostatic bearing, but show no significant difference between the two models for a LO<sub>2</sub> bearing.

Yang et al. (1993a) developed a thermohydrodynamic model for analysis of turbulent flow annular seals with process liquids and gases. Fluid inertia, flow turbulence, and actual fluid properties for cryogenics are all considered. Numerical results show that large temperature rises occur in LO<sub>2</sub> seals with significant effects on the fluid properties and the onset of two-phase flow conditions at relatively small values of rotor eccentricity. Seal leakage and torque are lower than those from an isothermal solution (San Andres, 1991b). A difference up to 20 percent was found for the predicted direct stiffness coefficients. The analysis has been shown to correlate well with experimental data and successfully used in the industrial design of annular damping seals (Scharrer et al., 1992a, b).

Heat transfer from fluid film to the bounding surfaces of a cryogenic turbulent-flow annular seal has been studied both analytically and numerically (Yang et al., 1993b). In the full numerical THD analysis, the fluid flow equations in the film are treated by the finite difference method (FDM) while the three-dimensional heat conduction equation in the seal stator is

solved by the boundary element method (BEM). The numerical example of a LO<sub>2</sub> seal shows that there is substantially no difference in the predictions from the full THD analysis and the adiabatic flow approximation. The heat generated in the fluid is carried away mainly by fluid advection due to the large flow rate produced by the imposed high axial pressure gradient in the seal. Heat transfer from the fluid film to the stator (or shaft) is found to be negligible and adiabatic bounding surfaces are shown to be a good assumption for externally pressurized turbulent flows in cryogenic liquid seals.

The unique flow characteristics of cryogenic liquid HJBs determine that fluid inertia, flow turbulence, actual fluid properties, and thermal effects are important for the accurate prediction of the static and dynamic performance characteristics of the bearings. The static characteristics include the film pressure, fluid velocity and temperature fields, mass flow rate, fluid-film forces or bearing load capacity, friction torque, and power dissipation. The dynamic force characteristics refer to the stiffness ( $K$ ), damping ( $C$ ), and added mass ( $M$ ) coefficients required for rotordynamic analysis. These coefficients are defined by the following expression for the bearing forces:

$$\begin{bmatrix} F_x \\ F_y \end{bmatrix} = \begin{bmatrix} F_{x0} \\ F_{y0} \end{bmatrix} - \begin{bmatrix} K_{xx} & K_{xy} \\ K_{yx} & K_{yy} \end{bmatrix} \begin{bmatrix} \Delta X \\ \Delta Y \end{bmatrix} - \begin{bmatrix} C_{xx} & C_{xy} \\ C_{yx} & C_{yy} \end{bmatrix} \begin{bmatrix} \Delta \dot{X} \\ \Delta \dot{Y} \end{bmatrix} - \begin{bmatrix} M_{xx} & M_{xy} \\ M_{yx} & M_{yy} \end{bmatrix} \begin{bmatrix} \Delta \ddot{X} \\ \Delta \ddot{Y} \end{bmatrix}, \quad (1)$$

where ( $F_{x0}$ ,  $F_{y0}$ ) are the static fluid film forces at the journal equilibrium position ( $e_{x0}$ ,  $e_{y0}$ ); and  $\Delta X = \Delta e_x e^{i\tau}$  and  $\Delta Y = \Delta e_y e^{i\tau}$  are the components of the journal-center dynamic displacement. The dynamic-force coefficients defined by Eq. (1) are important measures of dynamic bearing force performance since they influence the critical speeds, resonant amplitude response, and rotordynamic stability of a rotor-bearing system.

A bulk-flow thermohydrodynamic (THD) analysis is introduced to determine the static and dynamic performance characteristics for turbulent flow process liquid HJBs. Pointwise evaluation of temperature and hence liquid properties is achieved through the solution of the energy equation in the fluid film with adiabatic journal and bearing surfaces. Flow turbulence is accounted through turbulence shear parameters based on friction factors derived from Moody's formulae. Fluid inertia on film lands and at recess edges are preserved. The effects of fluid compressibility and temperature variation in the recess are included. Cryogenic fluid properties are calculated from standard 32-term state equations (McCarty, 1986).

## 2 Mathematical Model

The general type of bearing selected as a support element for cryogenic liquid turbopumps is a 360-deg hydrostatic journal bearing, orifice-compensated, with a variable number of feeding recesses or pockets machined in the surface of the bearing (Butner and Murphy, 1986). The flow is confined to the thin annular region between an inner journal of radius ( $R$ ) rotating at an angular speed ( $\Omega$ ) and a stationary bushing (Fig. 1). The fluid flow is characterized by high levels of turbulence due to the externally imposed large axial pressure drop across the bearing and/or the high journal surface speed.

The problem of calculating the flow and load performance characteristics of HJBs consists basically of determining the pressure, temperature, and flow distribution in the bearing film lands subject to the condition that the flow discharging from each recess through the bearing film lands must equal the flow entering that recess from the supply source through a fixed orifice restrictor.

**2.1 Governing Equations for Turbulent Fluid Film Flows.** Large pressure gradients typical in low viscosity fluid HJBs cause high axial turbulent flow Reynolds numbers, and the

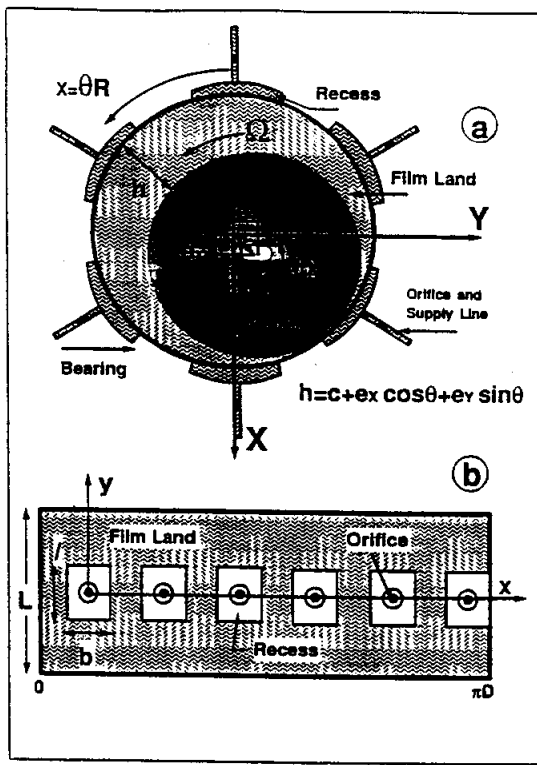


Fig. 1 Geometry of a hydrostatic journal bearing; (a) axial view and coordinate systems, (b) unwrapped bearing surface

effect of turbulent mixing far outweighs molecular diffusivity. In consequence, the temperature rise produced by viscous dissipation tends to be distributed uniformly across the film thickness; hence, temperature gradients in the cross-film coordinate ( $z$ ) are confined to turbulent flow boundary layers adjacent to the bounding (bearing and journal) surfaces (Suganami and Szeri, 1979; Di Pasquantonio and Sala, 1984). Furthermore, in the absence of regions of reversed flow or recirculation, the fluid velocity field presents the same characteristics as discussed above.

These considerations allow the three-dimensional continuity, momentum, and energy equations to be integrated across the film thickness to determine the two-dimensional bulk-flow governing equations for thin fluid film flows (Yang et al., 1993a):

*Continuity Equation.*

$$\frac{\partial(\rho H)}{\partial t} + \frac{\partial(\rho H U)}{\partial x} + \frac{\partial(\rho H V)}{\partial y} = 0 \quad (2)$$

*Circumferential-Momentum Equation.*

$$\frac{\partial(\rho H U)}{\partial t} + \frac{\partial(\rho H U^2)}{\partial x} + \frac{\partial(\rho H U V)}{\partial y} = -H \frac{\partial P}{\partial x} + \tau_{xz}|_0^H \quad (3)$$

*Axial-Momentum Equation.*

$$\frac{\partial(\rho H V)}{\partial t} + \frac{\partial(\rho H U V)}{\partial x} + \frac{\partial(\rho H V^2)}{\partial y} = -H \frac{\partial P}{\partial y} + \tau_{yz}|_0^H \quad (4)$$

*Energy-Transport Equation.*

$$\begin{aligned} & C_p \left[ \frac{\partial(\rho H T)}{\partial t} + \frac{\partial(\rho H U T)}{\partial x} + \frac{\partial(\rho H V T)}{\partial y} \right] + Q_r \\ &= T \beta_r H \left( \frac{\partial P}{\partial t} + U \frac{\partial P}{\partial x} + V \frac{\partial P}{\partial y} \right) \\ &+ R \Omega \tau_{xz}|_0^H - U \tau_{xz}|_0^H - V \tau_{yz}|_0^H \quad (5) \end{aligned}$$

where the circumferential and axial coordinates are denoted by ( $x$ ) and ( $y$ ). The bulk-flow primitive variables, velocities ( $U$ ,  $V$ ), pressure ( $P$ ), and temperature ( $T$ ), are defined as average quantities across the film thickness ( $H$ ). The density ( $\rho$ ), viscosity ( $\mu$ ), specific heat ( $C_p$ ), and volumetric expansion coefficient ( $\beta_r$ ) represent the material fluid properties.  $Q_r$  denotes the heat flux from the fluid film to the bounding solids.

The wall shear stress differences ( $\tau$ ) in the circumferential and axial directions are based on the bulk-flow turbulence theory in thin film flows (Hirs, 1973; Launder and Leschziner, 1978):

$$\tau_{xz}|_0^H = -\frac{\mu}{H} \left( k_r U - k_f \frac{R \Omega}{2} \right);$$

$$\tau_{yz}|_0^H = -\frac{\mu}{H} (k_y V);$$

$$\tau_{xz}|^H = \frac{H}{2} \frac{\partial P}{\partial x} + \frac{\mu}{4H} [U k_B - (U - R \Omega) k_f] \quad (6)$$

where the turbulent shear parameters ( $k_r$ ,  $k_f$ ) and ( $k_f$ ,  $k_B$ ) are local functions of the Reynolds numbers and friction factors based on Moody's formulae (Massey, 1983; Nelson et al., 1987). The present turbulence model is selected due to its simplicity and ability to represent surface roughness conditions.

The variation of temperature in the axial direction and the energy generated by compression work are retained in the analysis due to the strong influence of the large pressure drop across the bearing. These conditions differentiate the present problem from conventional THD analyses of viscous, incompressible fluids in hydrodynamic journal bearings.

## 2.2 Governing Equations for Bearing Recess Flows.

The analysis of turbulent flow in a HJB recess is complicated and not yet fully understood. To date, only two-dimensional laminar flow numerical solutions are available for rectangular recesses (see, for example, San Andres and Velthuis, 1992b; Braun et al., 1993). While the actual prediction of flow fields in the recess may give a better description of the recess-edge boundary conditions, the global mass and energy conservation principles at the recess are known to be both efficient and sufficiently accurate in hydrostatic bearings with radial ports (San Andres, 1992a).

*Mass Conservation at a Recess.* The continuity equation at the recess is defined by the global balance between the flow through the orifice restrictor of effective area ( $A_0$ ), the recess outflow into the film lands ( $\dot{M}_r$ ), and the temporal change of fluid mass within the recess volume ( $\nabla_r$ ). The fluid external supply pressure is  $P_s$  and drops to a value  $P_r$  at the recesses. The flow continuity equation at each bearing recess is expressed as

$$\begin{aligned} & A_0 \sqrt{2 \rho_r (P_s - P_r)} \\ &= \dot{M}_r + \rho_r \frac{\partial \nabla_r}{\partial t} + \rho_r \nabla_r \left( \beta_r \frac{\partial P}{\partial t} - \beta_r \frac{\partial T}{\partial t} \right), \quad (7) \end{aligned}$$

where

$$\beta_r = \frac{1}{\rho} \left( \frac{\partial \rho}{\partial P} \right)_T, \quad \beta_t = -\frac{1}{\rho} \left( \frac{\partial \rho}{\partial T} \right)_P \quad (8)$$

are the liquid compressibility factor and volumetric expansion coefficient, respectively, and

$$\dot{M}_r = \int_{\Gamma_r} \rho H (\vec{U} \cdot \vec{n}) d\Gamma \quad (9)$$

is the mass flow rate across the recess boundary ( $\Gamma_r$ ) into the film lands.

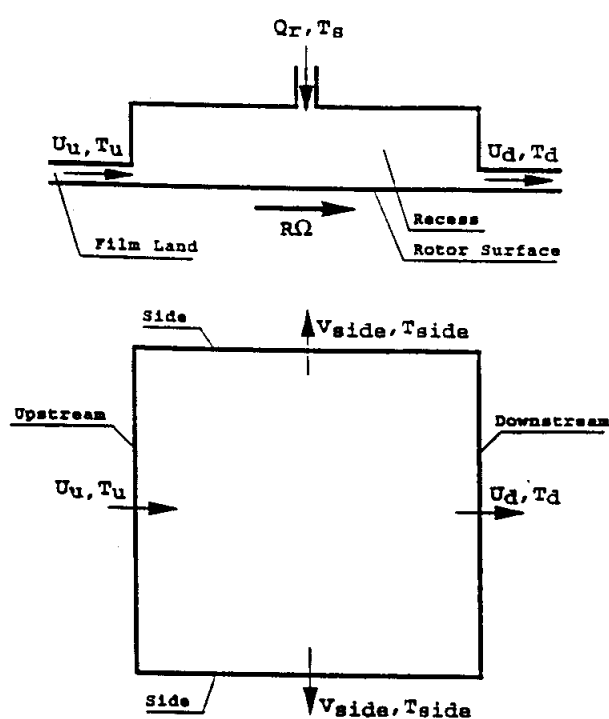


Fig. 2 Conceptual description of global energy balance at a recess

**Global Energy Balance Equation at a Recess.** The energy-transport phenomenon in a HJB recess is controlled by the following three mechanisms: the carryover of hot fluid from upstream to downstream of the recess, the mixing of cool fluid from the supply source into the recess volume, and the heat generation in the recess volume due to shear dissipation by journal rotation. Energy transport produced by pressure gradients, kinetic energy changes, and heat conduction are negligible due to the uniform recess pressure and the large mass flow rate through the recess. Based on these considerations, a global energy balance equation at the recess is derived, reflecting the heat carryover and mixing effects, and the friction heat generation (dissipation) in the recess (Fig. 2):

$$C_p \frac{\partial(\rho_r T_r)}{\partial t} \nabla_r + C_p (\sum \dot{m}_d T_d + 2 \sum \dot{m}_{side} T_{side}) = C_p (\sum \dot{m}_u T_u + \dot{M} T_s) + T_{or} \Omega \quad (10)$$

where

$$T_{or} = \tau_{\kappa}^H A_r R \quad (11)$$

is the drag torque on the recess area,  $\dot{M}$  is the total mass flow rate through the supply orifice,  $\nabla_r$  is the recess volume, and the subscripts "u," "d" and "side" refer to the upstream, downstream, and side edges of a rectangular recess, respectively. The temperatures at the downstream and side edges of the recess are approximately equal to the recess temperature since liquid flows from the orifice to the sides at a large velocity:

$$T_d = T_{side} = T_r = \text{Constant}, \quad (12)$$

while the temperature at the upstream of the recess is given by

$$T_u = \begin{cases} T_r, & \text{if } (\vec{U} \cdot \vec{n}) > 0; \\ \text{Upstream values,} & \text{otherwise.} \end{cases} \quad (13)$$

**Recess/Film Entrance Pressure Rise/Drop.** For purely hydrostatic operation, a uniform pressure in the recess volume is achieved by deepening the recesses. However, a minimum re-

cess volume is required to avoid a typical pneumatic hammer instability associated to compressible fluids. Design criteria for uniformity of recess pressure and pneumatic hammer instability are given by Redcliffe and Vohr (1969) and San Andres (1991a).

For hybrid operation, a pressure rise is produced in the downstream portion of the recess due to the journal rotation (Chaoimleffel and Nicholas, 1986). San Andres (1992a) considers this region as a one-dimensional step bearing and adopted Constantinescu et al.'s (1975) model to evaluate the pressure rise just in front of the downstream recess edge. The local acceleration of fluid from the deep recess to the thin film lands causes a sudden pressure drop at the recess edge. The pressure drop at the entrance to the film lands is then modeled by a simple Bernoulli-type relation. Details of the recess-edge pressure equations can be found in the analyses of Artiles et al. (1982) and San Andres (1992a) for incompressible and compressible fluids, respectively.

### 3 Boundary Conditions

The boundary conditions for the flow variables are expressed as

(a) On the 360-degree extended film land, the pressure, velocity, and temperature fields are continuous and single-valued in the circumferential ( $x$ ) direction.

(b) At the bearing exit plane ( $y = L$ ), the fluid pressure takes a constant value equal to the discharge or ambient pressure ( $P_a$ ) for unchoked conditions. The present analysis is limited to subsonic flow conditions over the lands of the HJB.

(c) The axial velocity ( $V$ ) and the axial gradients ( $d/dy$ ) of all the flow variables are null at the circumferential center line ( $y = 0$ ) of the bearing if this is axially symmetric and has no journal misalignment. This allows solution of the flow field on only half the bearing. The nonsymmetric bearing case with journal misalignment requires solution over the whole bearing plane.

(d) The recess-edge temperatures and pressures are obtained as described in the previous sections. The velocity vector at the interface with the recess boundary is regarded as normal to the recess edges (Artiles et al., 1982).

(e) At the fluid/journal and the fluid/bearing interfaces, the heat flux to the bounding surfaces  $Q_r$  is assumed to be zero. This oversimplification is fully justified by the analysis of Yang et al. (1993b), where the heat transfer from fluid film to the bounding surfaces of a cryogenic turbulent flow annular seal is studied. The numerical example of a LO<sub>2</sub> seal (high temperature rise in the fluid film) shows that there is substantially no difference in the predictions from the full THD analysis and the adiabatic flow approximation. The heat generated in the fluid is carried away mainly by the axial fluid velocity (large flow rate) produced by the imposed high pressure gradient. This assertion also applies to the fluid flow in HJBs due to the similarity in geometry and operating environment.

### 4 Perturbation Analysis

The inertial coordinate system  $\{X, Y\}$  shown in Fig. 1 helps to define the position of the rotating journal. For steady-state operating conditions, the journal center is at the equilibrium position  $(e_{x0}, e_{y0})$ , and, superimposed on this, the journal describes motions of small amplitude  $\Delta e_x$  and  $\Delta e_y$  and whirl frequency  $\omega$ . The film thickness is represented by the real part of the following equation:

$$H = H_0 + e^{i\tau} (\Delta e_x h_x + \Delta e_y h_y) \quad (14)$$

where

$$H_0 = H_0^* + e_{x0} h_x + e_{y0} h_y, \quad \tau = \omega t, \quad i = \sqrt{-1}, \quad (15)$$

$$h_x = \cos \theta, \quad h_y = \sin \theta, \quad (16)$$

and  $H_0^* = c + e_r \cos \theta + e_\theta \sin \theta$  for uniform radial clearance or,  $H_0^* = c(\theta, y)$  is a general function of the axial coordinate for nonuniform clearance bearings (San Andres, 1991b).

For small amplitude motions of the journal, all the bulk-flow variables ( $P, U, V, T$ ) as well as the fluid properties ( $\rho, \mu, \beta, C_p$ ) are expressed as the superposition of zeroth and first-order fields representing the steady-state and dynamic motion conditions, respectively. In general,

$$\phi = \phi_0 + e^{i\tau}(\Delta e_x \phi_x + \Delta e_y \phi_y),$$

$$\phi = U, V, P, T, \rho, \mu, \beta, k_x, k_y, \dots, \text{etc.} \quad (17)$$

Substitution of the perturbation variables into the dimensionless governing equations yields the zeroth and first-order flow equations which are omitted here for brevity. A complete description of the analysis is given by San Andres (1993). The bearing static and dynamic force characteristics are evaluated once a solution to the flow equations is obtained. Fluid film forces are calculated by integration of the pressure field over the journal surface. The components of the static equilibrium force are given by

$$F_{i0} = \int_0^L \int_0^{2\pi} P_0 h_i R d\theta dy \quad i = X, Y. \quad (18)$$

The Taylor series expansion of the dynamic forces (Eq. (1)) allows the dynamic force coefficients to be calculated from integration of the first-order complex pressure field ( $P_j$ ) over the journal surface,

$$K_{ij} - \omega^2 M_{ij} + i\omega C_{ij} = - \int_0^L \int_0^{2\pi} P_j h_i R d\theta dy;$$

$$i, j = X, Y. \quad (19)$$

From the above equation, the first-order equations need to be solved for at least two different frequencies to obtain the added mass coefficients.

The friction torque is given by integration of the wall shear stress at the journal surface as

$$T_{or} = \int_0^L \int_0^{2\pi} \tau_{xz}^H dx dy \quad (20)$$

where the wall shear stress at the journal surface  $\tau_{xz}^H$  is determined from the bulk-flow velocities as given by the third expression on Eq. (6).

## 5 Summary of the Analysis

The unique flow characteristics of cryogenic liquid bearings determine fluid inertia, flow turbulence, actual fluid properties and thermal effects to be important for the accurate prediction of bearing performance. A bulk-flow thermohydrodynamic (THD) analysis for determination of the static and dynamic performance characteristics of orifice-compensated liquid hydrogen (LH<sub>2</sub>) HJBs in the turbulent flow regime is introduced. Turbulence shear parameters in the momentum and energy transport equations are determined in terms of the bulk-flow velocities and friction factors derived from Moody's formula. Pointwise evaluation of temperature and hence liquid properties is achieved through the solution of the energy equation in the fluid film with insulated bounding surfaces. This simplification is justified for cryogenic liquid bearings with large pressure gradients.

Equations for global mass conservation and energy transport are presented at the bearing recesses. Effects of fluid compressibility at the recess volume and the orifice supply line are also included. Fluid inertia at the recess edges is modeled by Bernoulli-type relationships, while a pressure rise due to journal rotation in the downstream portion of the recess is considered as a one-dimensional step-bearing. The energy transport phe-

nomenon in a HJB recess is controlled by the carry over of hot fluid from upstream to downstream of the recess, the mixing of fresh fluid from the supply orifice into the recess volume, and the heat generation in the recess volume due to shear dissipation by journal rotation.

Predictions from the numerical solution are presented on the second part of this paper. Numerical results are compared with limited experimental data available for a liquid hydrogen (LH<sub>2</sub>) bearing.

## References

- Antiles, A., Walowit, J., and Shapiro, W., 1982, "Analysis of Hybrid Fluid Film Journal Bearings with Turbulence and Inertia Effects," *Advances in Computer Aided Bearing Design*, ASME Press, ASME, New York.
- Braun, M. J., Wheeler, R. L., III, and Hendricks, R. C., 1987, "A Fully Coupled Variable Properties Thermohydraulic Model for a Cryogenic Hydrostatic Journal Bearing," *ASME Journal of Tribology*, Vol. 109, pp. 405-416.
- Braun, M. J., Don, Q., and Choy, F. K., 1993, "The Effects of a Hydrostatic Pocket Aspect Ratio, and its Supply Orifice Position and Attack Angle on Steady-State Flow Patterns, Pressure and Shear Characteristics," *ASME Journal of Tribology*, Vol. 115, pp. 678-685.
- Butner, M., and Murphy, B., 1986, "SSME Long Life Bearings," NASA Report, CR179455.
- Chaoieffell, J. P., and Nicholas, D., 1986, "Experimental Investigation of Hybrid Journal Bearings," *Tribology International*, Vol. 19, pp. 253-259.
- Constantinescu, V. N., and Galetuse, S., 1975, "Pressure Drop due to Inertia Force in Step Bearings," *ASME Paper*, 75-LUB-34.
- Di Pasquantonio, F., and Sala, P., 1984, "Influence of Thermal Field on the Resistance Law in Turbulent Bearing-Lubrication Theory," *ASME Journal of Tribology*, Vol. 106, pp. 368-376.
- Elrod, Jr., H. G., and Ng, C. W., 1967, "A Theory for Turbulent Fluid Films and Its Application to Bearings," *ASME Journal of Lubrication Technology*, Vol. 89, pp. 346-362.
- Hirs, G. G., 1973, "A Bulk-Flow Theory for Turbulence in Lubricant Films," *ASME Journal of Lubrication Technology*, Vol. 95, pp. 137-146.
- Katayama, T., and Okada, A., 1992, "Liquefied Natural Gas Pump with Hydrostatic Journal Bearings," *Proceedings of the 9th International Pump Users Symposium*, Houston, Texas, pp. 39-50.
- Lauder, B. E., and Leschziner, M., 1978, "Flow in Finite Width Thrust Bearings Including Inertial Effects, I—Laminar Flow, II—Turbulent Flow," *ASME Journal of Lubrication Technology*, Vol. 100, pp. 330-345.
- Massey, B. S., 1983, *Mechanics of Fluids*, Van Nostrand Reinhold (UK) Co. Ltd., Workingham, Berkshire, U.K.
- McCarty, R. D., NBS Standard Reference Data Base 12, 1986, "Thermophysical Properties of Fluids, MIPROPS-86," Thermophysics Div., Center for Chemical Engineering, National Bureau of Standards, Colorado.
- Nelson, C. C., and Nguyen, D. T., 1987, "Comparison of Hirs Equation with Moody's Equation for Determining Rotordynamic Coefficients of Annular Pressure Seals," *ASME Journal of Lubrication Technology*, Vol. 109, pp. 144-148.
- Reddecliff, J. M., and Vohr, J. H., 1969, "Hydrostatic Bearings for Cryogenic Rocket Engine Turbopumps," *ASME Journal of Lubrication Technology*, Vol. 91, pp. 557-575.
- San Andres, L., 1990a, "Turbulent Hybrid Bearings with Fluid Inertia Effects," *ASME Journal of Tribology*, Vol. 112, pp. 699-707.
- San Andres, L., 1990b, "Approximate Analysis of Turbulent Hybrid Bearings: Static and Dynamic Performance for Centered Operation," *ASME Journal of Tribology*, Vol. 112, pp. 692-698.
- San Andres, Luis A., 1991a, "Effect of Fluid Compressibility on the Dynamic Response of Hydrostatic Journal Bearings," *Wear*, Vol. 146, pp. 269-283.
- San Andres, Luis A., 1991b, "Analysis of Variable Fluid Properties, Turbulent Annular Seals," *ASME Journal of Tribology*, Vol. 113, pp. 694-702.
- San Andres, Luis A., 1992a, "Analysis of Turbulent Hydrostatic Bearings with a Barotropic Cryogenic Fluid," *ASME Journal of Tribology*, Vol. 114, pp. 755-765.
- San Andres, L., and Velthuis, J. F. M., 1992b, "Laminar Flow in a Recess of a Hydrostatic Bearing," *STLE Tribology Transactions*, Vol. 35, pp. 738-744.
- San Andres, Luis A., 1993, "Thermohydrodynamic Analysis of Cryogenic Liquid Turbulent Flow Fluid Film Bearings," Annual Research Progress Report to NASA Lewis Research Center, Project NAG3-1434, Dec.
- Scharer, J. K., Hibbs, R. I., and Nolan, S. A., 1992a, "Extending the Life of the SSME HPOTP Through the Use of Annular Hydrostatic Bearings," AIAA 92-3401.
- Scharer, J. K., Tellier, J. G., and Hibbs, R. I., 1992b, "Start Transient Testing of an Annular Hydrostatic Bearings in Liquid Oxygen," AIAA 92-3404.
- Suganami, T., and Szeri, A. Z., 1979, "A Thermohydrodynamic Analysis of Journal Bearings," *ASME Journal of Lubrication Technology*, Vol. 101, pp. 21-27.
- Von Pragenau, G. L., 1990, "Damping Bearings for Turbomachines," NASA Conference Publication 3092, Vol. II, Advanced Earth-to-Orbit Propulsion Technology, pp. 155-162.
- Yang, Z., San Andres, L., and Childs, D., 1993a, "Thermal Effects in Cryogenic Liquid Annular Seals," *ASME Journal of Tribology*, Vol. 115, pp. 267-284.
- Yang, Z., San Andres, L., and Childs, D., 1993b, "Importance of Heat Transfer from Fluid Film to Stator in Turbulent Annular Seals," *Wear*, Vol. 160, pp. 269-277.

**7b** "Thermohydrodynamic Analysis of Process Liquid Hydrostatic Bearings in Turbulent Regime, Part II: Numerical Solution and Results," 1995, Yang, Z., L. San Andres and D. Childs, *ASME Journal of Applied Mechanics*, Vol. 62, 3, pp. 674-684.

# Thermohydrodynamic Analysis of Process-Liquid Hydrostatic Journal Bearings in Turbulent Regime, Part II: Numerical Solution and Results

Zhou Yang

Cummins Engine Company, Inc.  
Columbus, IN 47201  
Assoc. Mem. ASME

L. San Andres

Assoc. Mem. ASME

D. W. Childs

Fellow ASME

Mechanical Engineering Department,  
Texas A&M University,  
College Station, TX 77843

*A finite difference scheme is implemented to solve the nonlinear differential equations describing the turbulent bulk-flow on the film lands of a hydrostatic journal bearing (HJB). A Newton-Raphson scheme is used to update the recess pressures and to satisfy the mass continuity requirement at each bearing recess. Comparisons of numerical predictions from the thermohydrodynamic (THD) model with experimental measurements of mass flow rate, fluid temperature, and static stiffness coefficient from a LH<sub>2</sub> test HJB article show very good agreement. In particular, the exit temperature of the bearing is lower than the supply temperature; i.e., the liquid temperature decreases along the bearing length. Similar values of direct stiffness and damping coefficients are predicted by the adiabatic THD model and other considering isothermal flow characteristics. However, the THD model predicts lower cross-coupled stiffness and whirl frequency ratio ( $WFR < 0.5$ ). The results show that for the application presented, the LH<sub>2</sub> hydrostatic bearing is more stable than previously thought.*

## 1 Introduction

High rotor speeds, large pressure drops, and intentionally roughened bearing-stator surfaces provide unique flow characteristics on cryogenic liquid hydrostatic journal bearings (HJBs), and determine fluid inertia, flow turbulence, actual fluid properties and thermal effects to be important for the accurate prediction of bearing performance. Within the range of practical cryogenic applications, the material properties of liquid hydrogen (LH<sub>2</sub>) depend strongly on both pressure and temperature.

Yang et al. (1995, Part I) introduced a bulk-flow thermohydrodynamic (THD) model for the determination of performance characteristics in process liquid HJBs. Fluid inertia, flow turbulence, and actual fluid properties for cryogenics are considered in the analysis. Boundary conditions at the recess/film entrances (recess edges) are obtained through global mass conservation and energy balance at each bearing recess. Fluid compressibility and temperature variation in the recess volume are also included. A perturbation method is used for calculation of the zeroth and first-order flow equations defining the fluid film bearing steady-state response and dynamic force coefficients, respectively.

Part II complements the analysis of Yang et al. (1995) and discusses the numerical solution to the non linear governing equations. The solution scheme is based on efficient and accurate CFD algorithms and calculates the performance characteristics of single-phase process liquid HJBs at centered and off-centered journal positions. Numerical predictions for mass flow

rate, static stiffness, and operating eccentricity are compared with experimental results from a LH<sub>2</sub> HJB article tested by Butner and Murphy (1986). In addition, the dynamic force coefficients for the same bearing are compared for two different bulk-flow models, namely the adiabatic THD and the isothermal-variable properties models. A discussion on the thermal effects and their significance on the performance of the reference HJB are detailed.

## 2 Numerical Solution Procedure

The mathematical model of a bulk-flow THD analysis of process liquid HJBs is given in Part I (Yang et al., 1995). The coupling of the nonlinear bulk-flow equations at the film lands with the mass and energy conservation equations for each recess is a complicated problem which can not be solved analytically. A finite difference scheme is implemented to solve the governing equations on the film lands. The procedure is based on the forward marching scheme presented by Launder and Leschziner (1978) and uses the SIMPLEX algorithm of Van Doormaal and Raithby (1984). The SIMPLEX algorithm is well known in the literature, and details on its superior convergence rate, grid refinement sensitivity, and accuracy can be found elsewhere (Van Doormaal and Raithby, 1984, 1985; Jang et al., 1986). The procedure has been adapted by San Andres (1992) to solve isothermal fluid film bearing problems, and extended here for the thermohydrodynamic analysis. The flow domain is discretized into a series of staggered rectangular control volumes for the primitive variables (Patankar, 1980). The velocities are located at points which lie at interfaces midway between the nodes where the pressure is determined. The discrete temperature field shares the same control volumes as the pressure field. The governing equations are integrated on the finite size control volumes to give sets of nonlinear algebraic difference equations with local mass flow conservation for each primitive variable.

The pressure, temperature, and velocity fields on the bearing film lands are determined so that the flow discharging from

Contributed by the Applied Mechanics Division of THE AMERICAN SOCIETY OF MECHANICAL ENGINEERS for publication in the ASME JOURNAL OF APPLIED MECHANICS.

Discussion on this paper should be addressed to the Technical Editor, Prof. Lewis T. Wheeler, Department of Mechanical Engineering, University of Houston, Houston, TX 77204-4792, and will be accepted until four months after final publication of the paper itself in the ASME JOURNAL OF APPLIED MECHANICS.

Manuscript received by the ASME Applied Mechanics Division, Feb. 11, 1993; final revision, Apr. 4, 1994. Associate Technical Editor: S. A. Berger.

each recess through the film lands must equal the flow entering that recess from supply pressure through the orifice restrictor. The Newton-Raphson scheme is used to update the recess pressure and to satisfy the mass continuity requirement at the bearing recesses. For bearing operation at the concentric position, the numerical scheme is at its peak efficiency. Under this condition, the flow fields for only one recess need to be calculated due to symmetry and continuity. Flow fields for the other recesses are then obtained by proper rotations (San Andres, 1990).

Extensive numerical calculations for HJBs with different working fluids show that the numerical algorithm is stable and efficient. Another feature of the algorithm is the small number of grid points required to get grid independent results. In fact, less than two percent difference in the bearing static and dynamic performance characteristics is detected when comparing the results from a 67 by 16 grid (number of circumferential points  $\times$  axial points) with those from a 85 by 26 grid for the six-recess  $LH_2$  HJB studied in this paper. Details of the numerical solution procedure are provided by Yang (1992).

### 3 Results and Discussion

Experimental results for the static and dynamic performance parameters of turbulent flow HJBs are given by Kurtin et al. (1993) and Franchek et al. (1993). Water heated to 55°C is used as the lubricant to achieve comparatively high Reynolds numbers in the test bearings without using cryogenic liquids. The measurements are performed for HJBs of different geometries and at journal speeds ranging from 10,200 to 24,600 rpm and supply pressures from 4 to 7 MPa. Extensive comparisons show a good correlation between the experimental results and the numerical predictions based on the variable properties, bulk-flow model of San Andres (1990, 1992), and also with the present thermohydrodynamic model (Yang, 1992).

Comparisons of numerical predictions with other flow models existing in the literature are given elsewhere. San Andres (1991) presents results for static and dynamic force characteristics on a water HJB and compares calculations with those obtained from the analysis of Artiles et al. (1982). The correlation shows the model of Artiles et al. to be in error with force coefficients offering a nonlinear jump-like response as the journal rotational speed increases. Numerical comparisons with the advanced thermal analysis of Braun et al. (1987) are totally impractical. The numerical predictions presented by Braun et al. refer to a HJB with a circumferential flow Reynolds number as large as 100,000, with the flow being considered as laminar and inertialess.

Numerical predictions from the present THD model are here compared with limited experimental data available from a  $LH_2$  HJB article tested by Butner and Murphy (1986). Dynamic force coefficients are calculated for an adiabatic THD condition and compared with predictions from the isothermal model of San Andres (1992). The experimental measurements include mass flow rate ( $\dot{M}$ ), exit temperature ( $T_e$ ), and a stiffness coefficient ( $K_{xx}$ ) extracted from a statically applied load and mea-

**Table 1 Characteristics of  $LH_2$  bearing (Butner and Murphy, 1986)**

Bearing characteristics	Dimension
Diameter ( $D$ )	75.04 mm (2.954 in.)
Length ( $L$ )	35.0 mm (1.38 in.)
No. of recesses ( $N_{rec}$ )	6
Orifice diameter ( $d_o$ )	1.27 mm (0.05 in.)
Rectangular recess ( $A_r = b \times l$ )	$8.89 \times 11.41 \text{ mm}^2$ ( $0.35 \times 0.449 \text{ in.}^2$ )
Recess area ratio ( $N_{rec}A_r/(\pi DL)$ )	0.1
Recess depth ( $H_r$ )	0.2286 mm (0.009 in.)
Nominal clearance (at zero speed) ( $c_*$ )	0.05334 mm (0.0021 in.)

**Table 2 Operating conditions of  $LH_2$  bearing (fixed radial load) (Butner and Murphy, 1986)**

Speed (cpm)	$P_s$ (MPa)	$P_o$ (MPa)	$T_s$ (K)	Load (N)	Clearance $c$ (mm)
0	16.27	2.358	46.7	1801	0.05334
12800	16.14	2.393	45.0	2006	0.05080
25000	16.14	2.468	45.6	2064	0.04570
36400	16.14	2.393	46.1	2046	0.03810

sured journal eccentricity. The objectives of the experimental program of Butner and Murphy were to test hybrid bearings designed to replace ball bearings in the SSME high pressure fuel turbopump (HPFTP), and to provide reliable empirical data to anchor computational models used in hydrostatic bearing design. The hydrostatic bearings were designed with emphasis on maximizing stiffness and damping and minimizing friction torque and flow rate. Table 1 presents the geometry for the six-recess test hydrostatic bearing. The bearing and journal surfaces are regarded as perfectly smooth since no information is available on this aspect. The fixed radial load and concentric operation test conditions are given in Tables 2 and 3, respectively. The bearing was tested at different speeds to 36,400 cpm, a pressure supply ( $P_s$ ) of 16.3 MPa, two pressure drops ( $\Delta P = P_s - P_o$ ) equal to 6.9 and 13.8 MPa, and a supply temperature around  $T_s = 46$  K typical of a cryogenic turbopump environment.

In the experimental procedure and for bearing eccentric operation (Table 2), a fixed radial load ( $W \approx 2000$  N) was applied after a steady-state speed and supply pressure conditions were achieved. The measured eccentricity ratio ( $\epsilon = e/c$ ) ranges from 0.1271 to 0.1675 for the design pressure drop of 13.8 MPa. The static stiffness was obtained by dividing the fixed radial load by the corresponding static displacement of the journal. The static displacement of the journal under the fixed load was too large ( $\epsilon = 0.433$ ) for the half design pressure drop ( $\Delta P = 6.9$  MPa). At such large journal displacement or eccentricity ratio, the numerical predictions show that some of the flows through the bearing orifices are choked (sonic speed is reached). The present model can not handle choked flows, and therefore, the half design pressure drop case ( $\Delta P = 6.9$  MPa) is not presented here. A close examination of the experimental results confirms that the orifice flow in the bearing recess opposite to the load direction is choked. This situation is not desirable in a  $LH_2$  HJB since it will certainly cause a pneumatic hammer instability under dynamic operation. The measurements at 12,000 cpm and  $\epsilon = 0.433$  show a recess pressure of 3.692 MPa with an orifice speed of 635 m/s while the fluid sonic speed is equal to 611 m/s.

It is of importance to observe the effect of pressure on the material properties of  $LH_2$ . At a supply pressure  $P_s = 16.27$  MPa and temperature  $T_s = 46.7$  K these are

$$\rho_* = 65.25 \text{ (kg/m}^3\text{)}, \quad \mu_* = 9.55 \times 10^{-6} \text{ (N-s/m}^2\text{)}$$

$$C_{p,*} = 12720 \text{ (J/kg K)}, \quad \beta_* = 1.18 \times 10^{-2} \text{ (1/K)},$$

**Table 3 Operating conditions of  $LH_2$  bearing (concentric case) (Butner and Murphy, 1986)**

Speed (cpm)	$P_s$ (MPa)	$P_o$ (MPa)	$T_s$ (K)	$c$ (mm)
10950	16.18	2.406	46.1	0.05091
14040	16.18	2.413	46.1	0.05070
22450	16.19	2.406	46.7	0.04758
26080	16.18	2.413	46.7	0.04565
32520	16.20	2.399	47.2	0.04169
36270	16.18	2.406	47.8	0.03821

**Table 4 Empirical parameters for  $LH_2$  bearing**

$C_d$	$\alpha$	$\xi_{su}$	$\xi_{sd}$	$\xi_v$
0.90	0.50	0.50	0.50	0.50

while at a discharge pressure  $P_a = 2.358$  MPa and supply temperature  $T_* = 46.7$  K, the fluid properties are

$$\rho_a = 16.09 \text{ (kg/m}^3\text{)}, \quad \mu_a = 2.96 \times 10^{-6} \text{ (N-s/m}^2\text{)}$$

$$C_{pa} = 17760 \text{ (J/kg K)}, \quad \beta_{ia} = 4.60 \times 10^{-2} \text{ (1/K)}.$$

The ratio of properties between discharge to supply conditions is equal to 0.25 for density and 0.31 for viscosity. Note that the fluid operating conditions are well above the critical temperature and pressure for  $LH_2$  given as 32.94 K and 1.284 MPa, respectively. The compressibility factor ( $\beta_p$ ) at the recess pressure ( $P_r \approx 0.5P_s$ ) is about  $5 \times 10^{-8} \text{ m}^2/\text{N}$  (1/2,900 psi) demonstrating the large compressibility of the liquid in the recess.

The circumferential flow ( $Re_c$ ) and axial flow ( $Re_a$ ) Reynolds numbers based on the top journal speed (36,000 cpm) and the largest mass flow rate are equal to

$$Re_c = \rho_* R \Omega c_* / \mu_* = 3.71 \times 10^4$$

$$Re_a = \rho_* V c_* / \mu_* = \dot{M} / (2\pi D \mu_*) \approx 6.11 \times 10^4$$

$$Re_r = \rho_* \omega c_*^2 / \mu_* = 37.65.$$

Note that the axial flow Reynolds number is higher than  $Re_c$  even though the rotational speed is rather large. For  $LH_2$  HJBs, a high pressure drop across the bearing along with the low viscosity of the working fluid causes an axially dominant flow which is turbulent even at zero rotational speed. The squeeze-film-flow Reynolds number ( $Re_s$ ) with synchronous whirl frequency ( $\omega = \Omega$ ) is much larger than unity and demonstrates that fluid inertia effects are not negligible in this bearing application.

The empirical parameters for the numerical calculations are given in Table 4. The orifice discharge coefficient ( $C_d$ ) in Table 4 is determined as the average of the experimentally calculated  $C_d$ 's for a hydrostatic water bearing (Franchek et al., 1993; Yang, 1992), and very close to the value reported by Butner and Murphy (1986) from their measurements. The  $\xi$  parameters refer to the entrance loss (nonisentropic) coefficients in the axial ( $y$ ) and circumferential ( $x$ ) directions, ( $u$ ) upstream and downstream ( $d$ ), of the recess edges, respectively. These empirical parameters and the fluid entrance swirl ratio ( $\alpha$ ) are determined by matching the measured flow rate with a calculated one for the case of 36,400 cpm. The resulting parameters are then used for all other cases.

### 3.1 Static Performance Characteristics.

**Static Stiffness.** Figure 1 shows the theoretical and experimental static stiffness as a function of rotational speed. This stiffness as identified from the load versus journal displacement curve increases with increasing rotational speed mainly due to the reduction of the bearing radial clearance from centrifugal growth of the rotating journal. The exception corresponds to the measured data at zero rotational speed. Numerical predictions from both the adiabatic THD and the isothermal models correlate well with the experimental data. The maximum error between the theoretical and experimental results is 10.3 percent. Note that the discrepancy at zero speed (purely hydrostatic operation) is much higher (22.2 percent), but the measured stiffness may be in error since it is larger than the experimental value at 12,800 cpm which has a smaller operating clearance.

**Static Load Capacity.** Figure 2 shows the journal eccentricity ratio under a fixed radial load ( $\approx 2000N$ ) as a function of increasing rotational speed. The data at zero speed are excluded

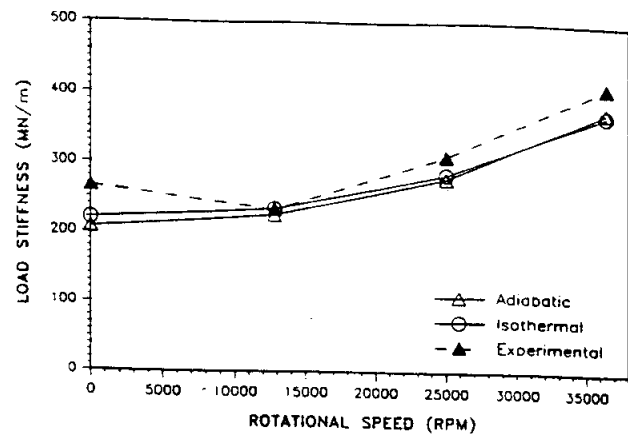


Fig. 1 Static stiffness ( $K_{xx}$ ) versus rotational speed (fixed load); ( $LH_2$  HJB tested by Butner and Murphy, 1986)

since the experimental radial load for purely hydrostatic operation is different ( $\approx 1800N$ ). The eccentricity ratio decreases with rotational speed, demonstrating that a higher speed provides slightly larger load capacity which is consistent with the behavior of the static stiffness in Fig. 1. The predictions from the adiabatic THD model are better than the isothermal model. The maximum error between the test and prediction is 2.6 percent for the THD model, and eight percent for the constant temperature model.

The measurement of dynamic force coefficients for  $LH_2$  HJBs was not successful due to signal interference by casing resonances as reported by Butner and Murphy (1986). However, the test program did provide valuable static performance characteristics like flow rates and discharge temperatures for concentric operations (Table 3).

**Mass Flow Rate.** Figure 3 shows the mass flow rate to decrease with journal speed due to a reduction of the operating bearing radial clearance. The contribution of the hydrodynamic effect to the reduction of the mass flow rate with speed is negligible since the viscosity of  $LH_2$  is very small. The numerical predictions from both the adiabatic THD and the isothermal models correlate very well with the experimental measurements.

**Exit Temperature.** Figure 4 shows a comparison between the measured exit temperature and numerical predictions as the journal speed increases. The supply fluid temperatures obtained from the test data are also presented in the figure to demonstrate the temperature difference across the bearing length. Note particularly that the exit temperatures are lower than the supply

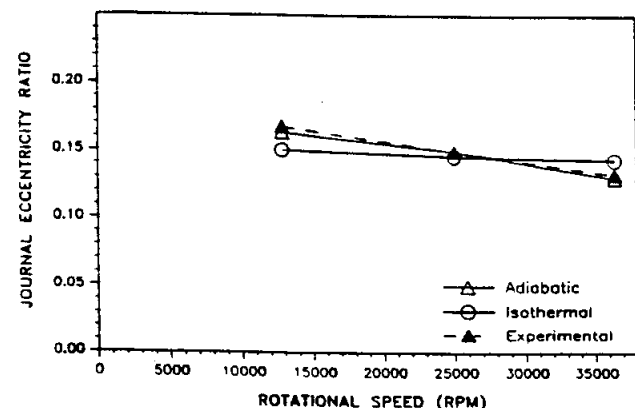


Fig. 2 Eccentricity ratio ( $e$ ) versus rotational speed (fixed load); ( $LH_2$  HJB tested by Butner and Murphy, 1986)



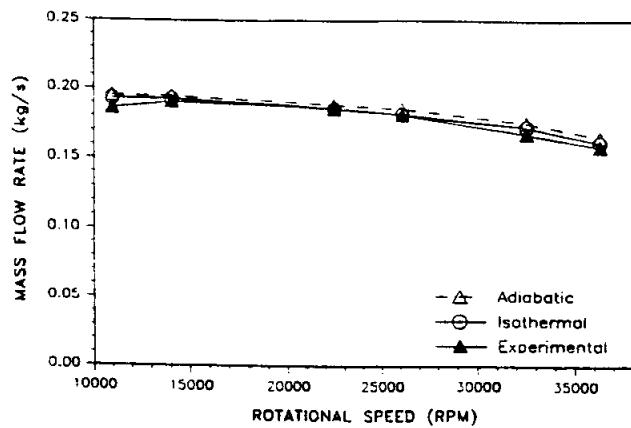


Fig. 3 Mass flow rate ( $M$ ) versus rotational speed ( $\epsilon = 0$ ); (LH<sub>2</sub> HJB tested by Butner and Murphy, 1986)

temperatures ( $\Delta T = T_{\text{exit}} - T_i \leq -5$  K), which show that the liquid temperature *decreases* instead of increasing along the bearing length. This phenomenon unusual in a liquid bearing is accurately predicted by the THD model and can be explained as follows.

Half of a symmetric HJB (from the circumferential center plane ( $y = 0$ ) to the discharge plane ( $y = L/2$ )) behaves approximately like an annular pressure seal. Therefore, the examination of temperature variations in an annular seal will, at least conceptually, be helpful in understanding those of a HJB. For an adiabatic flow in a centered pressure annular seal (or a HJB), the temperature difference across the seal length (or half of the bearing length) can be approximated as (Yang, 1993):

$$\Delta T = T_{\text{exit}} - T_i = \frac{T_{\text{or}} \Omega}{C_{pA} \dot{M}} + (1 - \beta_{\text{th}} T_i) \frac{\Delta P}{\rho_A C_{pA}} - \frac{\rho_A (U^2 + V^2)|_0^L}{2 \rho_A C_{pA}} \quad (1)$$

where

$$\Delta P = \begin{cases} P_s - P_a, & \text{for annular pressure seals;} \\ P_r - P_a, & \text{for hydrostatic bearings} \end{cases} \quad (2)$$

and the subscript "A" represents the average value across the seal/bearing length.

The first term on the right-hand side of Eq. (1) is generated from viscous dissipation by shear friction and is always positive. The second term shows the pressure extrusion which is zero

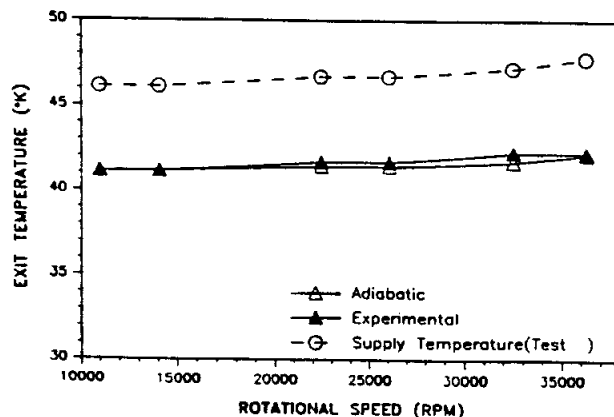


Fig. 4 Exit temperature ( $T_{\text{exit}}$ ) versus rotational speed ( $\epsilon = 0$ ); (LH<sub>2</sub> HJB tested by Butner and Murphy, 1986)

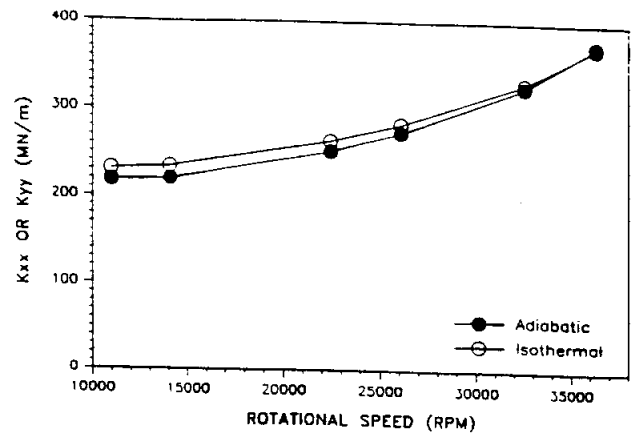


Fig. 5 Direct stiffness ( $K_{xx}$ ) versus rotational speed ( $\epsilon = 0$ ); (bearing parameters presented in Tables 1 to 3)

for ideal gases ( $\beta_{\text{th}} T_i = 1$ ). The last term is the kinetic energy variation which is generally negative for compressible fluid flows in annular pressure seals or HJBs, since by mass conservation the discharge velocity is larger than the inlet one.

For viscous liquids of low compressibility, such as oils, water, and other conventional lubricants, the viscous dissipation is large, the thermal expansion coefficient is small ( $\beta_{\text{th}} T_i < 1$ ), and the kinetic energy variation is negligible, which always results in a temperature rise across the seal/bearing length by Eq. (1).

For an ideal gas, Eq. (1) usually gives a temperature decrease along the seal/bearing length due to the large kinetic energy variation, small viscous dissipation, and null pressure extrusion work. However, for seals/bearings with roughened surfaces (including labyrinth seals), the gas temperature could increase in the seals/bearings due to the high viscous dissipation and reduced mass flow rate.

Even though liquid hydrogen is highly compressible, its behavior is different from an ideal gas. The properties of an ideal gas, like density and viscosity, are less sensitive to absolute temperature variation than those of liquid hydrogen. Depending on the operating condition (supply temperature and pressure, sump pressure, and rotational speed), the rate of temperature growth across the seal/bearing length could be positive or negative. Usually, the fluid supply temperature is the control parameter. A higher supply temperature offers a lower fluid viscosity and a higher thermal expansion coefficient ( $\beta_{\text{th}} T_i > 1$ ) leading to a temperature decrease across the seal/bearing length, which corresponds to the present bearing test article.

**3.1 Dynamic Performance Characteristics.** The relevant experimental data from Butner and Murphy (1986) did not provide rotordynamic force coefficients for the bearing configuration tested. The importance of the proper identification of force coefficients can be hardly overlooked. This is an area where detailed testing is needed with cryogenics or appropriate surrogate fluids. Undaunted by the lack of experimental results, the following figures present numerical predictions for the dynamic force coefficients using the adiabatic THD model (solid symbols) and the isothermal model (hollow symbols). Note that at the centered position ( $\epsilon = 0$ ), the dynamic coefficient matrices (Eq. (1), Yang et al., 1995) are

$$\phi_{xx} = \phi_{yy}, \quad \phi_{xy} = -\phi_{yx}, \quad \text{where } \phi = K, C, \text{ or } M. \quad (3)$$

**Direct Stiffness Coefficient.** Figure 5 shows the direct stiffness coefficients ( $K_{xx}$  or  $K_{yy}$ ) as a function of rotational speed. The increase of the direct stiffness coefficients with rotational speed is caused by the reduction of the radial clearance and it is also illustrated in Fig. 1 where the bearing is operating eccentrically. The isothermal model predicts a higher direct

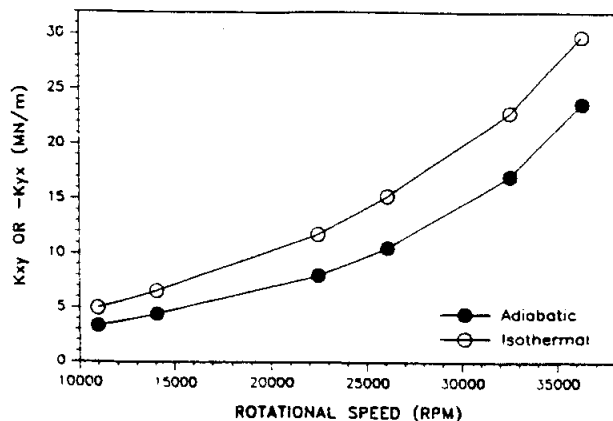


Fig. 6 Cross-coupled stiffness ( $K_{xy}$  or  $-K_{yx}$ ) versus rotational speed ( $\epsilon = 0$ ); (bearing parameters presented in Tables 1 to 3)

stiffness except at the highest speed (36,270 cpm) where the adiabatic thermal model shows a more pronounced hydrodynamic effect due to the temperature decrease in the bearing and hence the larger fluid viscosity. The maximum difference between the two models is 6.4 percent.

**Cross-Coupled Stiffness.** Figure 6 illustrates the cross-coupled stiffness coefficients ( $K_{xy}$  or  $-K_{yx}$ ) versus rotational speed. The cross-coupled stiffness coefficients increase rapidly with increasing rotational speed. The magnitude of the cross-coupled stiffness coefficients is much smaller than the direct ones showing that the hydrodynamic force component in  $LH_2$  HJBs is small. However, as has been shown before, the bearing stability is a combined effect of the dynamic coefficients, especially the cross-coupled stiffness and the direct damping. The THD model predicts lower cross-coupled stiffness coefficients and hence smaller destabilizing forces in the bearing with a maximum discrepancy of 49.3 percent between the two models. This is surprising since the lower fluid temperature and hence larger viscosity predicted by the THD model should provide a higher cross-coupled stiffness (San Andres, 1992). This result might be explained by the fact that, unlike laminar flows where a rise in viscosity leads directly to a gain of shear force, in a turbulent flow this gain is overshadowed by the simultaneous decrease in the Reynolds number and the turbulent shear gradients at the bearing surfaces.

**Direct Damping.** Figure 7 shows the direct damping coefficients ( $C_{xx}$  or  $C_{yy}$ ) as a function of rotational speed. The direct damping coefficients increase with rotational speed. The small

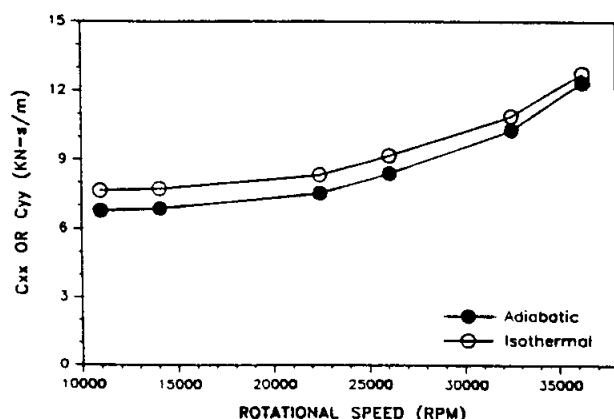


Fig. 7 Direct damping ( $C_{xx}$ ) versus rotational speed ( $\epsilon = 0$ ); (bearing parameters presented in Tables 1 to 3)

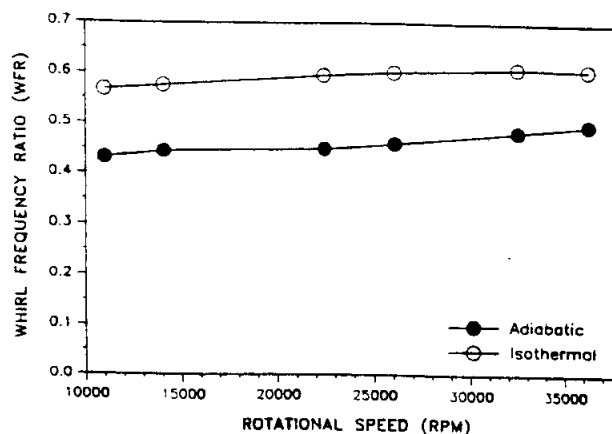


Fig. 8 Whirl frequency ratio versus rotational speed ( $\epsilon = 0$ ); (bearing parameters presented in Tables 1 to 3)

viscosity of  $LH_2$  not only generates small cross-coupled stiffness, but also provides low direct damping when compared to a more viscous liquid such as liquid oxygen ( $LO_2$ ). Again, the THD model predicts smaller direct damping coefficients. However, the difference for direct damping between the two models (maximum difference: 13 percent) are smaller than that for the cross-coupled stiffness.

Other dynamic force coefficients, such as the cross-coupled damping and the added mass, are very small for this  $LH_2$  bearing geometry and will not influence the bearing dynamic performance. This condition is well known to be valid for light-density liquid and gas bearings and seals.

**Whirl Frequency Ratio.** The whirl frequency ratio (WFR) is an indicator of bearing stability as it relates in a single expression the effect of destabilizing cross-coupled forces and stabilizing viscous damping forces. A low WFR indicates enhanced ability of a fluid film bearing to safely operate at higher running speeds relative to the first critical speed of the rotor-bearing system. For concentric operation, Fig. 8 shows the whirl frequency ratio (WFR) to increase with the journal rotational speed. The adiabatic THD model predicts lower WFR's than the isothermal model, and asymptotically appears to approach the maximum value of 0.50 at the highest speed (36,270 cpm). The largest difference between the two models is 31.6 percent.

For an incompressible liquid cylindrical bearing with smooth surfaces, the WFR should approach 0.50 at the concentric position (Rowe, 1980). This has been verified by the experimental measurements on hydrostatic water bearings (Franchek et al., 1993). However, the isothermal model of San Andres (1992) also shows that the stability indicator in a HJB is larger than 0.50 for compressible liquids. In general, a higher compressibility ratio ( $\beta_{pr}$ ) determines a higher WFR. This conclusion can not be drawn from the results predicted by the THD model, and unfortunately, no experimental data on the stability of  $LH_2$  HJBs is available to date.

#### 4 Conclusions and Recommendations

A bulk-flow thermohydrodynamic (THD) analysis is developed for calculation of the static and dynamic performance characteristics of turbulent flow, process liquid hydrostatic journal bearings (HJBs). A finite difference scheme is implemented to solve the governing equations on the film lands, while the Newton-Raphson scheme is used to update the recess pressures and satisfy the mass continuity requirement at each recess.

Comparisons of numerical predictions from the THD model with experimental measurements of mass flow rate, fluid temperature, and load stiffness coefficient from a  $LH_2$  HJB tested by Butner and Murphy (1986) show very good agreement. In

particular, the exit temperature of the  $\text{LH}_2$  HJBs is lower than the supply temperature; i.e., the liquid temperature decreases along the bearing length. This phenomenon unusual in a conventional liquid bearing is predicted correctly by the THD model. Both the THD model and an isothermal model predict well the mass flow rate and the stiffness coefficient of the  $\text{LH}_2$  HJBs, while the static load capacity is predicted better by the THD model. The orifice-discharge coefficient ( $C_d$ ) is the major uncertain parameter in the calculation of performance characteristics in orifice-compensated HJBs. For the  $\text{LH}_2$  bearing configuration studied, choked flows through the orifice restrictors are not unlikely to occur at journal eccentric operation.

For concentric journal operating conditions, numerical predictions of dynamic force coefficients for the test  $\text{LH}_2$  HJB are presented. No experimental data is yet available for the dynamic force coefficients. The adiabatic THD and isothermal flow models predict approximately the same direct stiffness (maximum difference: 6.4 percent) and damping coefficients (maximum difference: 13 percent), while the THD model predicts much lower cross-coupled stiffness (maximum difference: 49.3 percent) and whirl frequency ratio (WFR) (maximum difference: 31.6 percent), and thus, it shows a bearing with better dynamic stability characteristics.

The analysis shows that the variation of temperature (increase or decrease) in a  $\text{LH}_2$  HJB is largely dependent on the operating conditions such as supply temperature and pressure, sump pressure, and journal rotational speed. The fluid inlet temperature to the bearing is one of the control parameters. A low supply temperature (lower than the critical temperature:  $T_c < 32.9 \text{ K}$ ) will make  $\text{LH}_2$  behave more like a liquid rather than a gas. Larger supply temperatures may produce choked flows or significant temperature gradients within the bearing. Also, a low supply temperature will keep the state of  $\text{LH}_2$  away from the saturation region and hence avoid two-phase flow conditions.

## Acknowledgments

The support from Pratt & Whitney and the NASA Center for the Commercial Development of Space is gratefully acknowledged. Also thanks to NASA Lewis Research Center Grant NAG3-1434 for their interest and continued support for this research program. Thanks to Mr. Robert Hendricks from NASA LeRC for his invaluable comments to this work.

## References

- Antiles, A., Walowit, J., and Shapiro, W., 1982, "Analysis of Hybrid Fluid Film Journal Bearings with Turbulence and Inertia Effects," *Advances in Computer Aided Bearing Design*, ASME Press, New York.
- Braun, M. J., Wheeler, R. L. III, and Hendricks, R. C., 1987, "A Fully Coupled Variable Properties Thermohydraulic Model for a Cryogenic Hydrostatic Journal Bearing," *ASME Journal of Tribology*, Vol. 109, pp. 405-416.
- Butner, M., and Murphy, B., 1986, "SSME Long Life Bearings," NASA Report CR 179455.
- Franchek, N., and Childs, D., 1993, "Experimental Test Results for Four High-Speed, High-Pressure, Orifice-Compensated Hybrid Bearings," *ASME Paper 93-Trib-24*.
- Jang, D. S., Jetli, R., and Acharya, S., 1986, "Comparison of the PISO, SIMPLER, and SIMPLEC algorithms for the Treatment of the Pressure-Velocity Coupling in Steady Flow Problems," *Numerical Heat Transfer*, Vol. 10, pp. 209-228.
- Kurtin, K. A., Childs, D., San Andres, L., and Hale, K., 1993, "Experimental Versus Theoretical Characteristics of a High-Speed Hybrid (Combination Hydrostatic and Hydrodynamic) Bearing," *ASME Journal of Tribology*, Vol. 115, pp. 160-169.
- Lauder, B. E., and Leschziner, M., 1978, "Flow in Finite Width Thrust Bearings Including Inertial Effects. I—Laminar Flow, II—Turbulent Flow," *ASME Journal of Lubrication Technology*, Vol. 100, pp. 330-345.
- Patankar, S. V., 1980, *Numerical Heat Transfer and Fluid Flow*, Hemisphere, New York.
- Rowe, W. B., 1980, "Dynamic and Static Properties of Recessed Hydrostatic Journal Bearing by Small Displacement Analysis," *ASME Journal of Lubrication Technology*, Vol. 102, pp. 71-79.
- San Andres, L., 1990, "Turbulent Hybrid Bearings with Fluid Inertia Effects," *ASME Journal of Tribology*, Vol. 112, pp. 699-707.
- San Andres, L., 1991, "Improved Analysis of High Speed, Turbulent Hybrid Bearings," 4th NASA Conference on Advanced Earth-to-Orbit Propulsion Technology, NASA CP 3092, Vol. 2, May, pp. 414-431.
- San Andres, Luis A., 1992, "Analysis of Turbulent Hydrostatic Bearings with a Barotropic Cryogenic Fluid," *ASME Journal of Tribology*, Vol. 114, pp. 755-765.
- Van Doormaal, J. P., and Raithby, G. D., 1984, "Enhancements of the SIMPLE Method for Predicting Incompressible Fluid Flows," *Numerical Heat Transfer*, Vol. 7, pp. 147-163.
- Van Doormaal, J. P., and Raithby, G. D., 1985, "An Evaluation of the Segregated Approach for Predicting Incompressible Fluid Flow," *ASME Paper 85-HT-9*.
- Yang, Z., 1992, "Thermohydrodynamic Analysis of Product-Lubricated Hydrostatic Bearings in Turbulent Regime," Ph.D. Dissertation, Texas A&M University, College Station, TX, December.
- Yang, Z., San Andres, L., and Childs, D., 1993, "Thermal Effects in Cryogenic Liquid Annular Seals. Part I: Theory and Approximate Solution; Part II: Numerical Solution and Results," *ASME Journal of Tribology*, Vol. 115, pp. 267-284.
- Yang, Z., San Andres, L., and Childs, D., 1995, "Thermohydrodynamic Analysis of Liquid Hydrostatic Journal Bearings in Turbulent Regime, Part I: The Model and Perturbation Analysis," *ASME JOURNAL OF APPLIED MECHANICS*, Vol. 62, pp. 674-678.

8 "Thermohydrodynamic Analysis of Fluid Film Bearings for Cryogenic Applications," 1995, San Andres, L., *AIAA Journal of Propulsion and Power*, Vol. 11, 5, pp. 964-972.

# Thermohydrodynamic Analysis of Fluid Film Bearings for Cryogenic Applications

Luis San Andres\*

Texas A&M University, College Station, Texas 77843

A thermohydrodynamic analysis and computer program for prediction of the static and dynamic force response of hydrostatic journal bearings, annular seals, or damping bearings, and fixed arc-pad bearings are presented. The study includes the most important flow characteristics found in cryogenic fluid film bearings such as flow turbulence, fluid inertia, liquid compressibility, and thermal effects. Numerical results detail a comparison of the static performance and dynamic force coefficients for a six-recess hydrostatic bearing and a damping bearing-seal for the Space Shuttle Main Engine high-pressure oxidizer turbopump. The calculations indicate that turbulent-flow, externally pressurized bearings support the expected loads with moderate journal center eccentricities and with force coefficients of relevant magnitude for this critical application.

## Nomenclature

$A_o$  =  $C_d \pi d^2/4$ , equivalent orifice area,  $m^2$   
 $A_r$  =  $bl$ , recess area,  $m^2$   
 $b$  = recess circumferential length,  $m$   
 $C_d$  = empirical orifice discharge coefficient  
 $C_{ij}$  = damping force coefficients,  $Ns/m$   
 $C_p$  = specific heat,  $J/kg \cdot K$   
 $c, c_*$  = radial clearance, characteristic clearance  
 $(= \{c(y)\}_{min})$ ,  $m$   
 $D$  = journal diameter,  $m$   
 $d_o$  = orifice diameter,  $m$   
 $e_x, e_y$  = journal center displacements,  $m$   
 $F_x, F_y$  = fluid film forces along  $\{X, Y\}$  axes,  $N$   
 $f_j, f_R$  =  $a_m[1 + (c_m r_{j,n}/H + b_m/R_{j,n})^{c_m}]$ , turbulent friction factors based on Moody's equation,  
 $a_m = 0.001375$ ;  $b_m = 5 \times 10^5$ ;  $c_m = 10^4$ ;  
 $e_m = 1/3.0$   
 $H, H_r$  = film thickness, recess depth,  $m$   
 $K_{ij}$  = stiffness force coefficients,  $N/m$   
 $k_j, k_R$  =  $f_j R_j, f_R R_R$ , turbulent shear parameters  
 $k_r$  =  $Re_r^{0.681}/7.753$ , turbulent shear flow recess parameter  
 $k_r, k_r$  =  $(k_j + k_R)/2$   
 $L$  = bearing or seal axial length,  $m$   
 $l$  = recess axial lengths,  $m$   
 $M_{ij}$  = inertia force coefficients,  $kg$   
 $M_r$  =  $\alpha R \Omega \sqrt{\beta_p \rho_r}$ , recess flow Mach number due to journal rotation  
 $\dot{m}$  = flow rate over differential segments,  $kg/s$   
 $N_{rec}$  = number of bearing recesses  
 $n$  = normal vector to recess boundary  
 $P$  = fluid pressure,  $N/m^2$   
 $P_s, P_a, P_r$  = external supply, ambient, and recess pressures,  $N/m^2$   
 $P_x, P_y$  = perturbed (dynamic pressures),  $N/m^2$   
 $\dot{Q}_r$  = mass flow rate from recess to land,  $kg/s$   
 $\dot{Q}$  = heat flux to bearing and journal surfaces,  $W/m^2$   
 $R$  = journal radius,  $m$   
 $R_R$  =  $\rho H \sqrt{U^2 + V^2}/\mu$ , Reynolds number relative to bearing surface

$Re_c$  =  $\rho_* R \Omega c_*/\mu_*$ , nominal circumferential flow Reynolds number  
 $Re_{ii}$  =  $\rho_* R \Omega H_i/\mu_*$ , Reynolds number at recess edges  
 $Re_r$  =  $\rho_* R \Omega (H_r + H)/\mu_*$ , Reynolds number at recess volume due to rotation  
 $R_j$  =  $\rho H \sqrt{(U - \Omega R)^2 + V^2}/\mu$ , Reynolds number relative to journal surface  
 $r_j, r_R$  = mean roughness depth at journal and bearing surfaces,  $m$   
 $T$  = bulk-flow fluid temperature,  $K$   
 $T_{rr}$  =  $\tau_{rz}'' A_r R$ , torque over a recess,  $N \cdot m$   
 $T_s$  = inlet supply temperature,  $K$   
 $t$  = time,  $s$   
 $U, V$  = bulk-flow velocities in circumferential and axial directions,  $m/s$   
 $U$  =  $U_i + V_j$   
 $X, Y$  = inertial coordinate system  
 $x, y, z$  =  $(0, \pi D), (0, L), [0, H(x, y, t)]$ , coordinates defining thin film flow region  
 $\alpha$  =  $(U|_{r=0})/(\Omega R)$ , circumferential velocity entrance swirl factor  
 $\beta_p$  =  $(1/\rho)(\partial \rho / \partial P)_T$ , liquid compressibility factor,  $m^2/N$   
 $\beta_T$  =  $-(1/\rho)(\partial \rho / \partial T)_p$ , volumetric expansion coefficient,  $1/K$   
 $\xi_{x,y}$  =  $1.95/Re_{ii}^{0.43}$ , 0, recess edge loss coefficients  
 $\eta$  =  $H/(H_r + H)$ , ratio of land film thickness to recess depth  
 $\mu$  = fluid viscosity,  $Ns/m^2$   
 $\xi_{u,d}$  = entrance loss coefficients at up-, downstream recess edges  
 $\xi_{x,y}$  = empirical entrance loss coefficients in  $x, y$  directions  
 $\rho$  = fluid density,  $kg/m^3$   
 $\tau_{xz}, \tau_{yz}$  = wall shear stresses  
 $\Omega$  = rotational speed of journal,  $rad/s$   
 $\omega$  = excitation or whirling frequency,  $rad/s$   
 $V_r$  =  $(H_r + H)A_r + V_s$ , recess volume of hydrostatic bearing,  $m^3$   
 $V_s$  = volume of orifice supply line,  $m^3$

## Subscripts

$a$  = ambient or discharge conditions  
 $B$  = bearing  
 $e$  = entrance or recess edge conditions  
 $i, j$  = first-order perturbations  
 $(i, j \rightarrow X, Y \text{ directions})$   
 $J$  = journal

Received July 5, 1994; revision received Sept. 15, 1994; accepted for publication Sept. 30, 1994. Copyright © 1995 by the American Institute of Aeronautics and Astronautics, Inc. All rights reserved.

\*Associate Professor, Mechanical Engineering Department.

- $r$  = recess conditions  
 $s$  = supply conditions  
 $*$  = characteristic values

## 1. Introduction

**H**YDROSTATIC Journal Bearings (HJBs) are the ideal candidates to replace rolling element bearings as support elements in cryogenic turbomachinery. These bearings along with hydrostatic annular seals will be used for primary space-power applications due to their long lifetime, low friction and wear, significant load capacity, and large direct stiffness and damping force coefficients. Fluid film bearings, unlike rolling element bearings, have no diameter  $\times$  rotational speed (DN) limit. Rotating machinery, free of this constraint, can operate at higher speeds with better efficiency and reduced overall weight and size. Durability in fluid film bearings is assured by the absence of contact between stationary and moving parts during steady-state operation, while long life reduces the frequency of required overhauls. Despite these attractive features, dynamic stability considerations and thermal phenomena along with two-phase flow operation are primary concerns for high-speed operation in bearings with large pressure differentials. Fluid film bearing stability is essentially related to hydrodynamic and liquid compressibility effects, whereas thermal effects are of importance due to flow turbulence with substantial energy dissipation.

San Andres<sup>1-3</sup> provides a comprehensive literature review on the subject of hydrostatic bearings and annular seals relevant to cryogenic liquid applications. Kurtin et al.<sup>4</sup> and Childs and Hale<sup>5</sup> describe a test facility for the measurement of loads and frequency domain identification of dynamic force coefficients in turbulent-flow, water-lubricated hydrostatic bearings, and annular pressure seals. Tests are routinely performed for bearings of different geometries and at journal speeds ranging from 10,000 to 25,000 rpm and pressure supplies from 4 to 7 MPa. Lindsey<sup>6</sup> has recently reported measured force coefficients for short-length annular seals with uniform, convergent, and divergent axial clearances. Kurtin et al.,<sup>4</sup> Mosher,<sup>7</sup> and Franchek et al.<sup>8,9</sup> report experimental data for the static load and dynamic force coefficients of water-lubricated hydrostatic bearings at the operating conditions noted. The test results refer to bearing clearances from 76 to 125  $\mu\text{m}$ , different recess pressure ratios and shapes, smooth and rough bearing surfaces, and radial vs angled liquid orifice injection.

Along with the experimental investigations, San Andres<sup>2</sup> developed a turbulent-inertial bulk flow analysis for prediction of the performance characteristics of orifice-compensated HJBs with variable-property fluids, and demonstrated the advantages of the model when compared to traditional approaches based on laminar-flow, classical lubrication theory. Yang et al.<sup>10,11</sup> then introduced a thermohydrodynamic (THD) analysis for the prediction of the static and dynamic performance characteristics of cryogenic liquid annular seals and hydrostatic journal bearings. Shear parameters based on friction factors derived from Moody's formulas account for flow turbulence. The effects of fluid compressibility and temperature variation in the bearing recesses are included. Comparisons of experimental results vs numerical predictions for water-lubricated hydrostatic bearings with radial fluid injection are reported.<sup>4,7,9</sup> The correlations validate the numerical models,<sup>2-11</sup> although accurate theoretical results depend greatly on the knowledge of the bearing operating clearance, bearing surface conditions, and most importantly, on the orifice discharge coefficients. Numerical results show the effects of fluid compressibility to be significant for liquid hydrogen ( $\text{LH}_2$ ) hydrostatic bearings with the potential of a stability indicator worse than that found in plain journal bearings due to pneumatic hammer at the bearing recesses.<sup>2</sup> Predictions from the THD model<sup>11</sup> correlate well with measured temperatures for the preburner impeller rear wear-ring seal

of the Space Shuttle Main Engine (SSME) high-pressure oxidizer turbopump (HPOTP). Calculations performed for a high-speed, rough-surface liquid oxygen ( $\text{LO}_2$ ) seal also predict a large temperature rise and the onset of two-phase flow conditions (liquid boiling) at moderate shaft eccentricities despite the large pressure differential across the seal. It is imperative to note that large temperature rises in cryogenic liquid seals and bearings can lead to thermal solid distortions affecting the operating clearance and may cause a significant reduction on the direct (hydrostatic) stiffnesses.

This article presents the thermohydrodynamic analysis of variable-property, fluid film bearings for cryogenic applications. The bearings studied include hydrostatic pad bearings with rectangular recesses, annular pressure seals or damping bearings, and cylindrical rigid-pad hydrodynamic bearings. The theoretical model refers to bearings of asymmetric geometry, nonuniform pressure discharges, and arbitrary clearance distribution. The motion of a liquid on the thin-film annular region of a fluid film bearing is described by a set of mass, momentum conservation, and energy transport equations for the primitive turbulent bulk-flow variables, and accompanied by realistic thermophysical state equations for evaluation of the fluid material properties. Zeroth-order equations describe the fluid flowfield for a journal static equilibrium position, while first-order linear equations govern the fluid flow for small-amplitude journal center translational motions and journal axis conical motions.

The solution to the zeroth-order flowfield equations provides the bearing flow rate, load capacity, torque, and restoring moments due to journal misalignment. The solution to the first-order equations determines the rotordynamic force and moment coefficients due to journal lateral and angular motions. For lateral shaft (journal) excursions, the dynamic force characteristics refer to the stiffness  $K_{ij}$ , damping  $C_{ij}$ , and added mass  $M_{ij}$  coefficients, and related to the dynamic forces by

$$\begin{aligned}
 \begin{bmatrix} F_x \\ F_y \end{bmatrix} &= \begin{bmatrix} F_{x0} \\ F_{y0} \end{bmatrix} - \begin{bmatrix} K_{xx} & K_{xy} \\ K_{yx} & K_{yy} \end{bmatrix} \begin{bmatrix} \Delta X \\ \Delta Y \end{bmatrix} \\
 &- \begin{bmatrix} C_{xx} & C_{xy} \\ C_{yx} & C_{yy} \end{bmatrix} \begin{bmatrix} \dot{\Delta X} \\ \dot{\Delta Y} \end{bmatrix} - \begin{bmatrix} M_{xx} & M_{xy} \\ M_{yx} & M_{yy} \end{bmatrix} \begin{bmatrix} \ddot{\Delta X} \\ \ddot{\Delta Y} \end{bmatrix} \quad (1)
 \end{aligned}$$

where  $\Delta X(t)$  and  $\Delta Y(t)$  are the components of the journal-center dynamic displacement about an equilibrium position. The dynamic-force coefficients defined by Eq. (1) are important measures of bearing dynamic performance since they influence the system critical speeds, the resonant amplitude response, and the stability of the rotor-bearing system.

## II. Mathematical Model

### A. Governing Equations for Turbulent Fluid Film Flows

Figures 1 and 2 show the schematic drawings of a hydrostatic bearing and a damping bearing (annular seal) considered for the analysis. Large pressure gradients typical of cryogenic bearings cause high-axial turbulent-flow Reynolds numbers, and the effect of turbulent mixing far outweighs molecular diffusivity. The temperature rise produced by viscous dissipation tends to be distributed uniformly across the film thickness, and thus, temperature gradients in the cross-film coordinate are confined to turbulent-flow boundary layers adjacent to the bounding (bearing and journal) surfaces.<sup>12</sup> Furthermore, in the absence of regions of reversed flow or recirculation, the fluid velocity field presents the same characteristics as discussed above. The flow studied is confined to the thin annular region between an inner rotating journal and a stationary bearing. The considerations detailed allow the

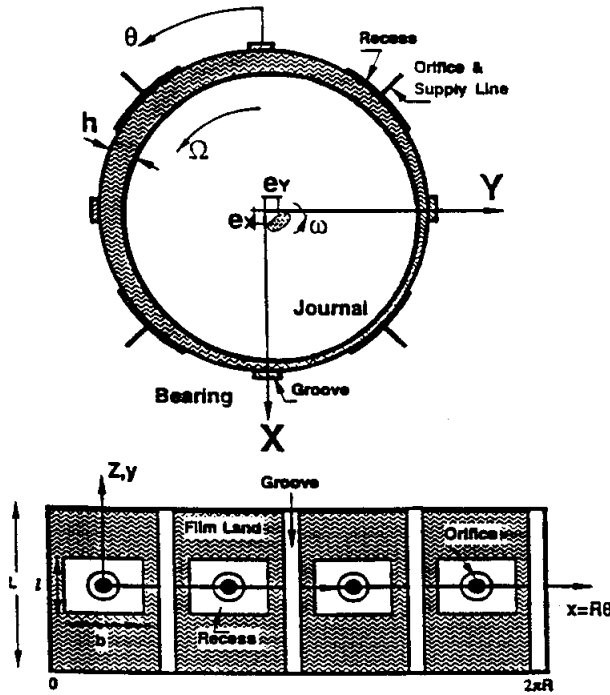


Fig. 1 Geometry of hydrostatic pad bearing.

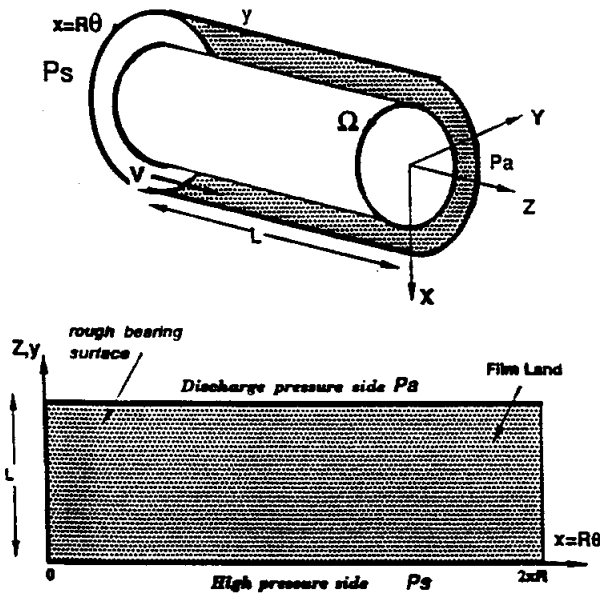


Fig. 2 Geometry of annular (damper) seal.

fluid motion to be described by a set of bulk-flow governing equations<sup>10,11</sup>:

*Continuity equation*

$$\frac{\partial(\rho H)}{\partial t} + \frac{\partial(\rho H U)}{\partial x} + \frac{\partial(\rho H V)}{\partial y} = 0 \quad (2)$$

*Circumferential-momentum equation*

$$\frac{\partial(\rho H U)}{\partial t} + \frac{\partial(\rho H U^2)}{\partial x} + \frac{\partial(\rho H U V)}{\partial y} = -H \frac{\partial P}{\partial x} + \tau_{xz}|_0'' \quad (3)$$

*Axial-momentum equation*

$$\frac{\partial(\rho H V)}{\partial t} + \frac{\partial(\rho H U V)}{\partial x} + \frac{\partial(\rho H V^2)}{\partial y} = -H \frac{\partial P}{\partial y} + \tau_{yz}|_0'' \quad (4)$$

*Energy-transport equation*

$$\begin{aligned} C_p \left[ \frac{\partial(\rho H T)}{\partial t} + \frac{\partial(\rho H U T)}{\partial x} + \frac{\partial(\rho H V T)}{\partial y} \right] + Q_r \\ = T \beta_r H \left( \frac{\partial P}{\partial t} + U \frac{\partial P}{\partial x} + V \frac{\partial P}{\partial y} \right) + R \Omega \tau_{xz}|_0'' \\ - U \tau_{xz}|_0'' - V \tau_{yz}|_0'' \end{aligned} \quad (5)$$

where the bulk-flow primitive variables ( $U$ ,  $V$ ,  $P$ , and  $T$ ) are defined as average quantities across the film thickness, and  $Q_r$  represents the heat flux from the fluid film towards the journal and bearing surfaces.

The wall shear stresses are calculated according to the bulk-flow theory for turbulence in thin film flows<sup>13,14</sup>:

$$\begin{aligned} \tau_{xz}|_0'' &= -\frac{\mu}{H} \left( k_x U - k_f \frac{R \Omega}{2} \right) \\ \tau_{yz}|_0'' &= -\frac{\mu}{H} (k_y V) \\ \tau_{xz}|_0'' &= \frac{H}{2} \frac{\partial P}{\partial x} + \frac{\mu}{4H} [U k_n - (U - R \Omega) k_f] \end{aligned} \quad (6)$$

where the turbulent shear parameters ( $k_x$ ,  $k_y$ ) and ( $k_f$ ,  $k_n$ ) are local functions of the Reynolds numbers and friction factors based on Moody's formulas.<sup>15</sup>

#### B. Mass Conservation at a Bearing Recess

The analysis of turbulent flow in a HJB recess is complicated and not yet fully studied on its three-dimensional complexity.<sup>16-18</sup> Fundamental measurements have shown non-uniform pressures within a bearing recess of shallow depth, and with a hydrodynamic pressure rise generated on its downstream section.<sup>19,20</sup> Nonetheless, approximate formulations capturing the physics of the flow in its global sense are still of value to predict the overall flow rate and force performance of bearings with pressurized recesses.<sup>20</sup> The continuity equation at a recess of a hydrostatic bearing relates the global balance among the flow through the orifice restrictor, the recess outflow into the film lands  $Q_r$ , and the temporal change of fluid mass within the recess volume  $V_r$ , and expressed as

$$A_o \sqrt{2\rho_r(P_r - P_r)} = Q_r + \rho_r \frac{\partial V_r}{\partial t} + \rho_r V_r \left( \beta_p \frac{\partial P}{\partial t} - \beta_T \frac{\partial T}{\partial t} \right), \quad (7)$$

where

$$Q_r = \int_{\Gamma_r} \rho H (U \cdot n) d\Gamma \quad (8)$$

is the mass flow rate across the recess edges  $\Gamma_r$  and entering the film lands; and ( $\beta_p$ ,  $\beta_T$ ) are the fluid compressibility and volumetric expansion coefficients, respectively. In general,

$$\beta_p, \beta_T \begin{cases} = 0 & \text{for incompressible liquids} \\ = 1/P, 1/T & \text{for ideal gases} \\ > 0 & \text{for cryogenic liquids} \end{cases} \quad (9)$$

For purely hydrostatic operation, a uniform recess pressure is desirable to increase the bearing load capacity. This condition can be achieved by deepening the bearing recesses, although a minimum recess volume is required to avoid the characteristic pneumatic hammer instability associated with fluid compressibility.<sup>21</sup> For hybrid operation (combined hydrostatic-hydrodynamic), a pressure rise occurs due to the journal rotation,<sup>20</sup> as shown in Fig. 3. A simple one-dimen-

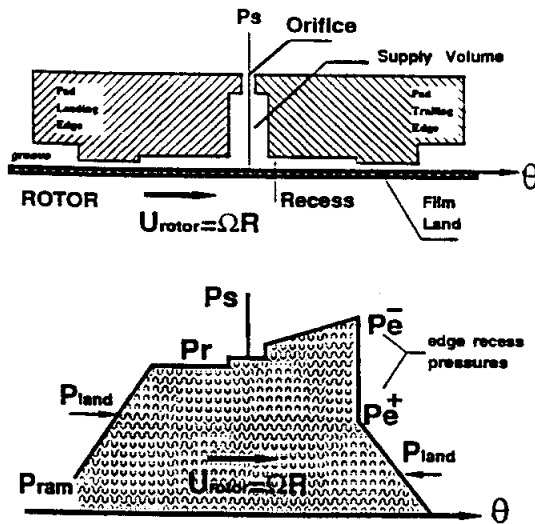


Fig. 3 Conceptual description of pressure rise and drop at recess edge of a hydrostatic bearing, and pressure ram effect at leading edge of bearing pad.

sional step-bearing model predicts the pressure rise just in front of the downstream recess edge  $P_e$  as<sup>22</sup>

$$P_e = \left\{ P_r - \frac{b\eta^2\mu k_r}{2H^2(1 - M_r^2)} \left[ U\eta \left( \frac{\rho_c}{\rho_r} \right) - \frac{V_r}{2} \right] \cdot n \right. \\ \left. \text{for } (U \cdot n) > 0, \quad \begin{array}{l} \text{in } x \text{ direction} \\ \text{in } y \text{ direction} \end{array} \right. \quad (10)$$

where  $n$  is the normal to the recess boundary  $\Gamma_r$ , and

$$U = U_i + V_j, \quad V_r = R\Omega i + 0j \quad (11)$$

Refer to the Nomenclature for a description of all variables. The local acceleration of fluid from the deep recess to the film lands causes a sudden pressure drop at the recess edges (see Fig. 3). The pressure at the entrance to the film lands is modeled by simple Bernoulli-type relations based on the turbulent flow theory developed by Constantinescu and Galetuse<sup>22</sup> and Artiles et al.<sup>23</sup>:

$$P_e = P_r - (\rho_r/2)(1 + \zeta_r)(1 + \xi_r)[1 - \eta^2(\rho_c/\rho_r)](U \cdot n)^2 \\ (U \cdot n) > 0 \quad (12)$$

where  $\zeta_r = \{\zeta_x, \zeta_y\}$ ,  $\xi_r = \{\xi_x, \xi_y\}$  are empirical entrance loss coefficients. The pressure at the entrance of an annular pressure seal can be obtained similarly by using a Bernoulli-type relation. The corresponding expression is given later in the boundary conditions section.

### C. Global Energy Balance Equation at a Recess

A global energy balance equation at a hydrostatic bearing recess shows the heat carry-over (advection) and mixing effects, and the friction heat generation (dissipation) in the recess (see Fig. 4):

$$C_p \frac{\partial(\rho T)}{\partial t} V_r + C_p \left( \sum \dot{m}_u T_u + 2 \sum \dot{m}_{side} T_{side} \right) \\ = C_p \left( \sum \dot{m}_d T_d + Q_r T_r \right) + T_{r,\Omega} \Omega \quad (13)$$

where  $T_{r,\Omega}$  is the shear-induced torque over the recess area,  $Q_r$  is the total mass flow rate through the supply orifice,  $V_r$  is the recess volume, and the subscripts  $u$ ,  $d$ , and  $side$  refer to the upstream, downstream, and side edges of a rectangular

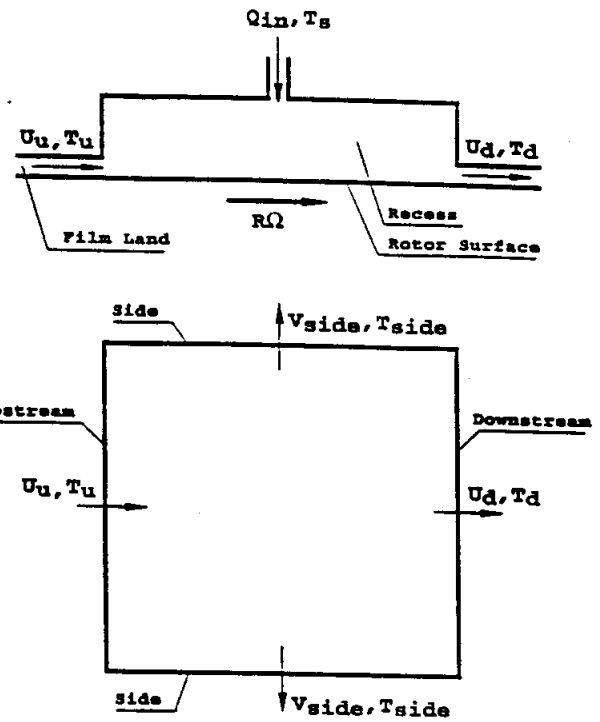


Fig. 4 Conceptual description of global energy balance at a recess.

recess, respectively. The temperatures at the downstream and side edges of the recess are approximately equal to the recess temperature:

$$T_d = T_{side} = T_r = \text{const} \quad (14)$$

while the temperature at the upstream of the recess is given by

$$T_u = \begin{cases} T_r & \text{if } (U \cdot n) > 0 \\ \text{upstream values,} & \text{otherwise} \end{cases} \quad (15)$$

### III. Boundary Conditions

The boundary conditions for the flow variables are expressed as follows:

- 1) The pressure, velocity, and temperature fields are continuous and single-valued in the circumferential direction for annular seals and hydrostatic bearings without axial grooves.
- 2) At the bearing exit plane, the fluid pressure takes a value equal to the discharge or ambient pressure  $P_a$  for subsonic operating conditions. The exit pressure may vary circumferentially to represent existing conditions in some turbopump applications.
- 3) For annular pressure seals, an entrance pressure drop occurs at the seal inlet plane ( $y = 0$ ) and is modeled with a simple Bernoulli equation<sup>10</sup>:

$$P(x, 0) = P_a - \frac{1}{2}(1 + \xi_y)\rho V_{(x,0)}^2 \quad \text{if } V_{(x,0)} > 0 \quad (16)$$

with the inlet circumferential velocity prescribed by a swirl ratio  $\alpha$  as

$$U(x, 0) = \alpha R\Omega \quad (17)$$

- 4) At the fluid/journal and the fluid/bearing interfaces, the heat flux to the bounding surfaces  $Q$ , is assumed to be zero. That is, the current thermal model considers the bearing and journal surfaces to be insulated. This condition is representative of turbulent flow, externally pressurized bearings.<sup>10,11</sup>



San Andres<sup>3</sup> provides further details and a thorough discussion on boundary conditions for pad journal bearings and grooved hydrostatic bearings, including the generation of a "ram" pressure at the leading edge of a hydrodynamic pad.

#### IV. Perturbation and Numerical Analyses

For small-amplitude journal motions about an equilibrium position, all the dependent flow variables as well as the fluid properties are expressed as the superposition of zeroth- and first-order fields representing the steady-state and dynamic motion conditions, respectively. Expansion of the governing equations in the perturbation variables yields zeroth- and first-order flow equations as presented in detail by San Andres.<sup>3</sup> Fluid film forces and rotordynamic coefficients are found by integration of the pressure fields on the journal surface, i.e.,

$$\begin{bmatrix} F_X \\ F_Y \end{bmatrix} = R \sum_{k=1}^{N_{pad}} \int_0^L \int_0^{r_{pad}} P_0^k \begin{bmatrix} \cos \theta \\ \sin \theta \end{bmatrix} d\theta dy \quad (18)$$

where  $P_0^k$  corresponds to the zeroth-order pressure field for the  $k$ th bearing pad. The force coefficients due to journal center displacements are determined from

$$K_{ij} - \omega^2 M_{ij} + i\omega C_{ij} = -R \sum_{k=1}^{N_{pad}} \int_0^L \int_0^{r_{pad}} P_1^k h_i d\theta dy$$

with  $i, j = X, Y$   $h_X = \cos \theta$   $h_Y = \sin \theta$  (19)

and  $P_1^X, P_1^Y$  are the dynamic pressure fields for journal motions in the  $X$  and  $Y$  directions, respectively.<sup>3</sup>

A cell finite difference scheme is implemented to solve the nonlinear differential equations on the film lands,<sup>14</sup> whereas the Newton-Raphson scheme is used to update the recess pressure and to satisfy the mass continuity constraint at each bearing recess.<sup>3</sup> The numerical procedure is based on the forward-marching scheme of Launder and Leschziner<sup>14</sup> and uses the SIMPLEC algorithm introduced by Van Doormaal and Raithby.<sup>24</sup> The SIMPLEC scheme is well known in literature, and details on its superior convergence rate, grid refinement sensitivity, and accuracy have been well documented.<sup>24-26</sup>

Past simpler models from the same author<sup>1,2</sup> have evolved to the present advanced THD model<sup>3,10,11</sup> and responded to the need for more accurate yet efficient computational programs. These codes have been validated with extensive correlations to experimental measurements.<sup>1,2,4,6,7,9</sup> Further validations to experimental force coefficient data for LH<sub>2</sub> HJBs,<sup>27</sup> and water HJBs<sup>6</sup> are reported by Yang et al.<sup>11,28</sup> San Andres<sup>3</sup> also presents detailed comparisons to test force coefficients for an oil-lubricated HJB from Adams et al.,<sup>29</sup> journal bearing load measurements from Tonnesen and Hansen,<sup>30</sup> and numerical predictions by Braun et al.<sup>31</sup> for the performance of LO<sub>2</sub> journal bearings.

In general, calculations show that a relatively small number of grid points for discretization of the bearing surface is typically required to get grid independent results. Less than 2% difference in bearing static and dynamic performance characteristics are obtained when comparing the results from a 67 × 16 grid (number of circumferential points × axial points) with those from a 85 × 26 grid for the bearing cases reported in this article. Note also that the applicability of the analysis and computer program developed<sup>3</sup> include fluid film bearings for industrial applications in the laminar-flow regime with conventional lubricants.

Several empirical parameters are used in the analysis of hydrostatic bearings and annular pressure seals. Entrance loss coefficients  $\xi_v, \xi_s$  and rotor (journal) and stator (bearing) surface roughnesses  $r_s, r_n$  are needed for seals and HJBs, while orifice discharge coefficients  $C_d$  are also required for hydrostatic bearings. Lindsey<sup>6</sup> presents a sensitivity analysis for

annular seals, and Kurtin et al.,<sup>4</sup> Mosher,<sup>7</sup> and Franchek et al.<sup>12</sup> present similar studies for hydrostatic bearings. These references describe detailed comparisons between numerical predictions based on the present model and experimental measurements performed on water-lubricated seals and hydrostatic bearings at an existing test facility.<sup>5</sup> The sensitivity analysis involved changing an input parameter by  $\pm 10\%$  from its estimated experimental value for each operating condition while the other input parameters were kept invariant. The maximum difference between the numerical prediction and experimental value for each case was then compared with the maximum difference from the original results. Then, a relative sensitivity was determined by dividing the percentage change in maximum difference of the calculated parameter by the percentage change in the input parameter (10%).<sup>12</sup> The studies found that flow rate and direct stiffness coefficients are particularly sensitive to changes in  $C_d$  for HJBs and less sensitive to variations in the entrance loss coefficients. On the other hand, flow rate and direct stiffness coefficients for annular pressure seals are highly sensitive to the changes in inlet loss coefficient  $\xi_v$  and surface roughness conditions. Other force coefficients and the whirl frequency ratio for HJBs are particularly insensitive to variations in the empirical parameters ( $C_d$  and  $\xi_{s,v}$ ). For further details on the sensitivity analyses and major results, the interested reader is encouraged to seek the references cited.

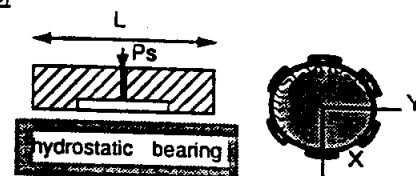
#### V. Results and Discussion

A one-to-one comparison for bearing performance in terms of flow, load capacity, and rotordynamic force coefficients for a hydrostatic bearing and a damping bearing (parallel-land damper seal) operating in LO<sub>2</sub> is presented here. The HJB and the damping bearing are designed to replace the pump-end duplex ball bearings in the LO<sub>2</sub> HPOTP. The fluid operating conditions (pressure and temperature) as well as the actual bearing clearance, and most importantly, the load supported by the bearings, are a function of the rotating speed of the pump. Information relevant to the load characteristics in the HPOTP were obtained from Shoup<sup>32</sup> and the fluid operating conditions directly extracted from Heshmat.<sup>33</sup> The hydrostatic bearing has six recesses of rectangular shape and orifice restrictors, while the damping bearing consists of two parallel annular seals of convergent tapered clearance separated by a deep feeding central groove.<sup>34</sup> The seals have a rough stator surface of knurled type while the hydrostatic bearing and journal surfaces are perfectly smooth. The damping bearing is also sometimes referred to as an annular hydrostatic bearing.<sup>35</sup> Figure 5 shows a description of the bearing geometries along with the values of actual clearances, supply, and discharge pressures and supply temperature for LO<sub>2</sub>, and the nominal load acting on the bearings as the operating speed increases from 14,035 to 30,367 rpm. Note that the load and pressures are proportional to the second power of the rotational speed. At the nominal operating conditions, here taken as 26,000 rpm, the operating clearance in the HJB is equal to 0.175 mm, while the inlet and exit clearances in the damping bearing are equal to 0.221 and 0.129 mm (ratio = 1.715), with an average clearance identical to that of the hydrostatic journal bearing.

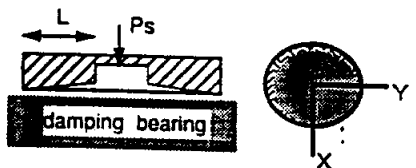
The hydrostatic bearing is designed for operation at the nominal speed with a concentric pressure ratio equal to 0.60 to provide maximum direct stiffness coefficients. On the other hand, the ratio of inlet to discharge clearance in the damping bearing has been optimized to also obtain the largest direct stiffness coefficients. The maximum specific load (load divided by bearing projected area) is equal to 6.55 MPa (950 psi) and 7.22 MPa (1048 psi) for the hydrostatic bearing and damper seal, respectively. These specific loads are large considering the nature of the bearing application with a fluid of very low viscosity such as LO<sub>2</sub>. The calculations for the static and dynamic performance characteristics of the HJB and

**Hydrostatic Bearing:** Number of recesses  $N_{rec} = 6$ 

Diameter (D)	Length (L)	Clearance (C*)	Recess Depth	Recess Axial Length(l)	Recess Circ. length(b)
85.1 mm	48.85 mm	175.2 $\mu$ m	508 $\mu$ m	24.42 mm	22.3 mm
(3.35 in)	(1.92 in)	(6.9 mils)	(20 mils)	(0.96 in)	(0.88 in)

journal and bearing surface conditions: **smooth**. $L/D=0.57$ ;  $Hr/C=2.9$ ;  $l/L=0.5$ ; Recess area ratio=0.25;  $C/R=0.0041$ Orifice  $C_d=0.90$ ; diameter  $d_o = 4.44$  mmRecess edge coefficients  $\xi_{xu}=0.0$ ;  $\xi_{xd}=0.50$ ;  $\xi_y=0.0$ **Damping Bearing:** Two parallel seal lands ( $2 \times L$ ) (groove width unspecified)

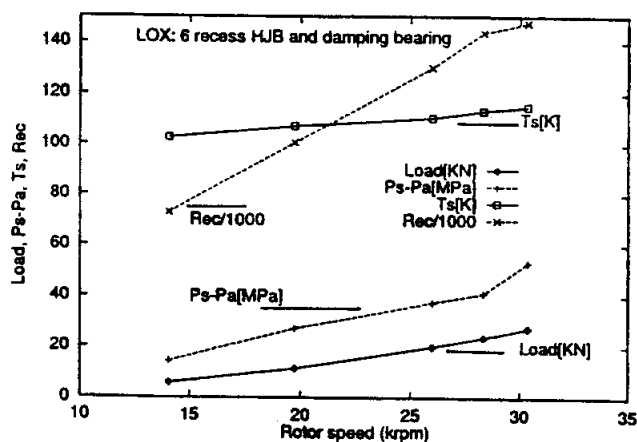
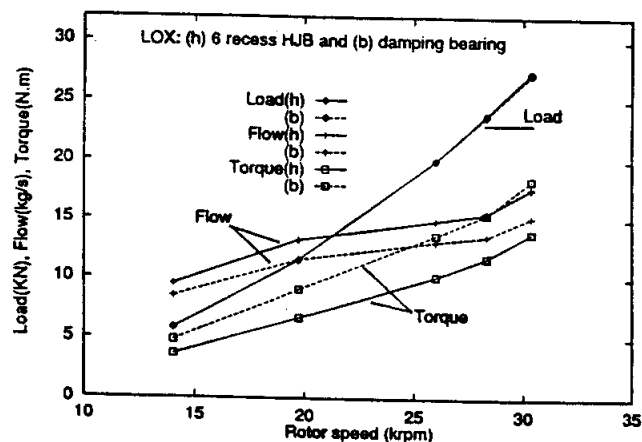
Diameter (D)	Length (L)	Inlet Clearance	Exit Clearance	Ratio	Average Clearance
85.1 mm	22.2 mm	221.3 $\mu$ m	129.1 $\mu$ m	1.71	175.2 $\mu$ m
(3.35 in)	(0.874 in)	(8.7 mils)	(5.08 mils)		(6.9 mils)

journal surface smooth, bearing surface rough,  $rb/C = 0.044$  (Knurled)Seal entrance coefficient  $\xi_y=0.25$ Inlet swirl ratio  $\alpha = 0.50$ **Operating Conditions for both bearings:**

Speed cpm	Psupply MPa	Pa	Tsupply K	Tsat K	Load N	Reynolds# Rec	Average Clearance* ( $\mu$ m)
14,035	16.00	1.654	102.77	128.9	5,828	72,816	180
19,732	29.59	1.792	107.22	130.5	11,519	100,700	177.7
26,000	39.60	2.089	110.55	133.7	20,000	130,130	175.2
28,340	43.60	2.434	111.33	137.0	23,762	143,720	174.3
30,367	55.69	2.551	115.00	138.0	27,282	147,600	173.2

**Fluid Properties:** LO<sub>2</sub> (liquid oxygen) at 110.6 K (200R)

P (MPa)	$\rho$ (kg/m <sup>3</sup> )	$\mu$ (E-3 Pa.s)	$C_p$ (J/kg-K)
39.60	1134.4	0.177	1,606.4
2.09	1038.1	0.124	1,827.2

Fig. 5 Geometry and operating conditions of a hydrostatic bearing and a damping bearing for load support in the LO<sub>x</sub> SSME-HPOTP.Fig. 6 Supply temperature, pressure drop, circumferential Reynolds number and load vs rotational speed for LO<sub>x</sub> six-recess hydrostatic bearing and damping bearing.Fig. 7 Flow rate, applied load, and drag torque vs rotational speed for LO<sub>x</sub> (h) six-recess HJB and (b) damping bearing.

damping bearing are performed using an adiabatic journal (rotor) and bearing (stator) thermal model.

Numerical calculations for the damping bearing are performed only for the thin land (seal) portion and then multiplied by two. The central groove and its effect on load capacity and dynamic force coefficients are altogether neglected. This oversimplification seems appropriate as a first attempt to correlate the performance of the HJB and the damping bearing. However, it is now known that central feeding grooves do have a pronounced effect on the dynamic force response of

fluid film bearings, in particular with regard to inertia and cross-coupled damping force coefficients.<sup>6,36</sup>

Figure 6 depicts the fluid supply temperature, pressure drop, and expected load to be carried by the HJB or the damping bearing as the rotational speed of the pump increases. The largest load of 27,282 N (6137 lb) corresponds to the highest operating speed. The figure also shows the values of the nominal circumferential flow Reynolds number  $Re_c = \rho_s R \Omega c_s / \mu_s$  to range from approximately 70,000 to 150,000 as the rotor speed rises. Figure 7 shows the HJB and damping bearing flow rates and drag torques as the journal speed increases.

The hydrostatic bearing (h) shows approximately 14% more flow rate than the damping bearing (b), while the HJB produces approximately 27% less drag torque than the seals at the largest operating speed. These results are a direct consequence of the rough stator surface in the damping bearing.

Figure 8 presents the journal operating eccentricity and attitude angle as well as the maximum temperature rise in the HJB and damping bearing as the operating speed increases. Note that as the speed rises so does the applied load at a rate proportional to the journal speed squared. The load for the HJB is directed towards the bottom of a bearing recess ( $X$  direction). The dimensionless journal eccentricity is given here as the ratio between the journal off-center displacement divided by the nominal clearance at 26,000 rpm, i.e., 0.175 mm. Note that the attitude angle is less than 10 deg for both bearings, and the journal eccentric displacement is rather moderate considering the magnitude of the loads applied. The low value in the attitude angle indicates dominance of hydrostatic effects over hydrodynamic effects. The maximum temperature in the film lands of the hydrostatic and damping bearings increases rapidly with journal speed. The HJB shows a larger thermal differential between the bearing supply condition and discharge planes. The results also indicate that both bearings operate well below the critical temperature of  $T_c = 154.6$  K (278°R) for  $LO_2$ .

Figures 9–11 present the synchronous stiffness, damping, and inertia force coefficients vs the rotational speed for the HJB and damping bearings, respectively. The similar values

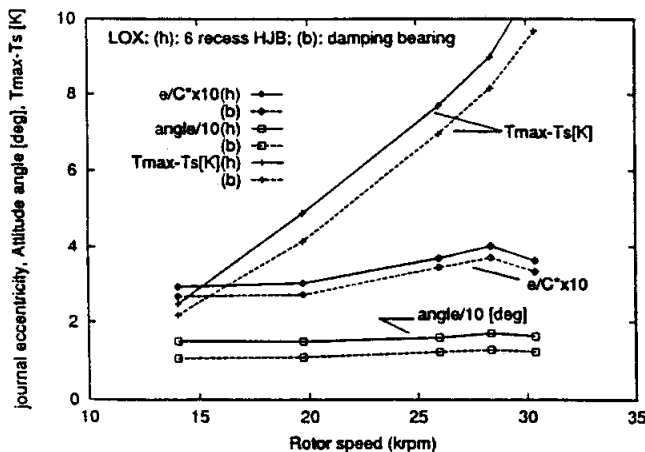


Fig. 8 Journal eccentricity, attitude angle, and maximum temperature rise vs rotational speed for  $LO_2$  (h) six-recess HJB and (b) damping bearing.

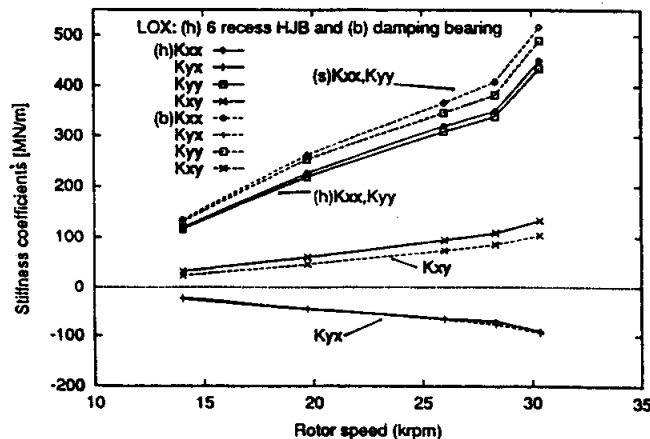


Fig. 9 Synchronous stiffness coefficients  $K_{ij}$  vs rotational speed for  $LO_2$  (h) six-recess HJB and (b) damping bearing.

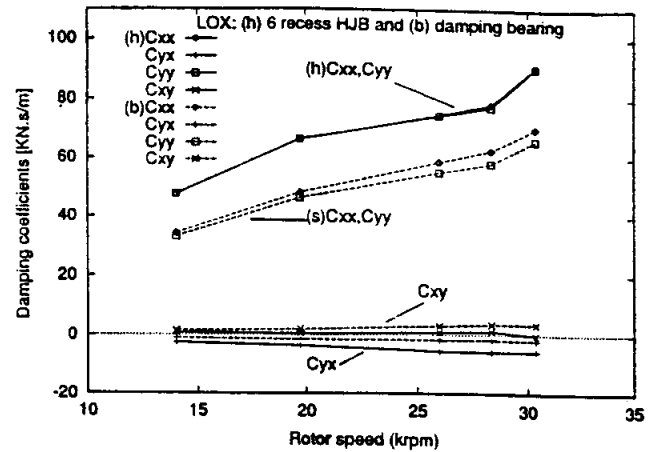


Fig. 10 Synchronous damping coefficients  $C_{ij}$  vs rotational speed for  $LO_2$  (h) six-recess HJB and (b) damping bearing.

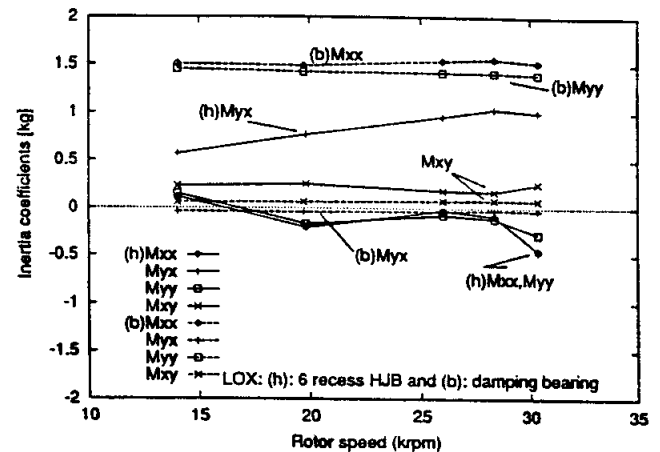


Fig. 11 Inertia force coefficients  $M_{ij}$  vs rotational speed for  $LO_2$  (h) six-recess HJB and (b) damping bearing.

between the direct coefficients (e.g.,  $K_{xx}$  and  $K_{yy}$ ) and cross-coupled coefficients (e.g.,  $K_{xy}$  and  $-K_{yx}$ ) denote that the HJB and damper bearing seal have very uniform force coefficients as the operating eccentricity (and load) increases with the operating speed. Figure 9 shows an HJB with slightly smaller direct stiffness coefficients ( $K_{xx}$  and  $K_{yy}$ ) than the damping bearing, while its cross-coupled stiffness ( $K_{xy}$ ) is larger. Note the dominance of hydrostatic (direct) coefficients over the cross-coupled coefficients induced solely by journal rotation.

Figure 10 shows the hydrostatic bearing to have larger direct damping coefficients ( $C_{xx}$  and  $C_{yy}$ ) than the damping bearing (approximately 47% higher). These results produce at the largest journal speed a whirl frequency ratio (WFR) equal to 0.39 and 0.45 for the HJB and damping bearing, respectively. Thus, in this example when the inlet swirl ratio is equal to 0.50, the HJB offers slightly better dynamic stability characteristics than the damping bearing. The values of WFR quoted remain approximately constant for all speeds studied. Note that low-frequency pneumatic-hammer effects are of little importance here since  $LO_2$  is nearly incompressible at the operating conditions and the bearing recesses are quite shallow ( $H/C = 2.9$ ).

Figure 11 shows the damping-bearing direct inertia force coefficients ( $M_{xx}$  and  $M_{yy}$ ) to be on the order of 1.5 kg and larger than the HJB direct inertia coefficients. The reason for this lies on the tapered geometry of the damper bearing seal with a small clearance at the exit plane. The cross-coupled inertia coefficients ( $M_{xy}$  and  $M_{yx}$ ) are small in nature. Here,

it is noted that in practice the direct inertia coefficients for the damping bearing will be much larger than the ones predicted. The central feeding groove acts as a parallel inertia and compliance to the seal lands, increases the magnitude of the inertia coefficients, and may reduce substantially the direct dynamic stiffness of the damping bearing.<sup>35</sup> Experimental results showing this behavior have been reported recently by Lindsey.<sup>6</sup>

It is worth noting that the original study included a three-pad journal bearing with a clearance similar to that of the HJB, but with a bearing preload of 0.076 mm. The results are not reproduced here because the hydrodynamic bearing produced a rather large temperature rise, and offered a low load capacity in comparison to those obtained from the six-recess hydrostatic and damping journal bearings.<sup>3</sup>

## VI. Conclusions

Accurate prediction of the performance and static and dynamic force characteristics of process-liquid, turbulent-flow fluid film bearings requires a thermohydrodynamic analysis. A set of bulk-flow equations for mass conservation, momentum, and energy transport describes the fluid motion in turbulent flow bearings with cryogenic liquids. The nonlinear flow equations are solved with a finite difference scheme combined with the Newton-Raphson method to satisfy the mass continuity requirement at each hydrostatic bearing recess. Published comparisons between numerical results and experimental data of turbulent flow water HJBs and seals are favorable and demonstrate the validity of the THD analysis and the computer program developed.

Numerical predictions show that properly designed hydrostatic bearings and damping journal bearings can support effectively the loads expected in the LO<sub>2</sub> HPOTP. The results indicate that an HJB or a damping bearing will operate at low journal eccentricities with uniform force coefficients. The case studied shows an important application of the fluid hydrostatic principle where sound engineering practice utilizes the available pressure differential in a cryogenic turbopump to provide a reliable fluid film bearing support.

## Acknowledgments

This research was funded under NASA Grant NAG3-1434. Acknowledgments are due to NASA Lewis Research Center for its support, and in particular to James Walker for his interest on this work.

## References

- <sup>1</sup>San Andres, L., "Analysis of Variable Fluid Properties, Turbulent Annular Seals," *Journal of Tribology*, Vol. 113, No. 4, 1991, pp. 694-702.
- <sup>2</sup>San Andres, L., "Analysis of Turbulent Hydrostatic Bearings with a Barotropic Cryogenic Fluid," *Journal of Tribology*, Vol. 114, No. 4, 1992, pp. 755-765.
- <sup>3</sup>San Andres, L., "Thermohydrodynamic Analysis of Cryogenic Liquid Turbulent Flow Fluid Film Bearings," Texas A&M Univ., Research Progress Rept., NASA Grant NAG3-1434, College Station, TX, Dec. 1993.
- <sup>4</sup>Kurtin, K. A., Childs, D., San Andres, L., and Hale, K., "Experimental Versus Theoretical Characteristics of a High Speed Hybrid (Combination Hydrostatic and Hydrodynamic) Bearing," *Journal of Tribology*, Vol. 115, No. 1, 1993, pp. 160-168.
- <sup>5</sup>Childs, D., and Hale, K., "A Test Apparatus and Facility to Identify the Rotordynamic Coefficients of High-Speed Hydrostatic Bearings," *Journal of Tribology*, Vol. 116, 1994, pp. 337-344.
- <sup>6</sup>Lindsey, T., "Experimental vs. Theoretical Comparison of the Effects of Taper on the Rotordynamic Coefficients in Short Smooth Annular Seals Used in High-Speed Turbomachinery," M.S. Thesis, Texas A&M Univ., College Station, TX, May 1993.
- <sup>7</sup>Mosher, P., "Effect of Design Parameter Variations on Hybrid (Combination Hydrostatic and Hydrodynamic) Bearings for Use in High Speed Turbomachinery," M.S. Thesis, Texas A&M Univ., College Station, TX, May 1993.
- <sup>8</sup>Franchek, N., and Childs, D., "Experimental Test Results for Four High-Speed, High-Pressure Orifice Compensated Hybrid Bearings," *Journal of Tribology*, Vol. 116, No. 1, 1994, pp. 147-153.
- <sup>9</sup>Franchek, N., Childs, D., and San Andres, L., "Theoretical and Experimental Comparisons for Rotordynamic Coefficients on a High-Speed, High-Pressure, Orifice Compensated Hybrid Bearing," American Society of Mechanical Engineers Paper 94-Trib-3, 1994.
- <sup>10</sup>Yang, Z., San Andres, L., and Childs, D., "Thermal Effects in Cryogenic Liquid Annular Seals, Part I: Theory and Approximate Solution; Part II: Numerical Solution and Results," *Journal of Tribology*, Vol. 115, No. 2, 1993, pp. 285-290.
- <sup>11</sup>Yang, Z., San Andres, L., and Childs, D., "Thermohydrodynamic Analysis of Process Liquid Hydrostatic Bearings in Turbulent Regime, I: Theory, II: Numerical Solution and Results," *Journal of Applied Mechanics* (to be published).
- <sup>12</sup>Di Pasquantonio, F., and Sala, P., "Influence of Thermal Field on the Resistance Law in Turbulent Bearing-Lubrication Theory," *Journal of Tribology*, Vol. 106, No. 3, 1984, pp. 368-376.
- <sup>13</sup>Hirs, G. G., "A Bulk-Flow Theory for Turbulence in Lubricant Films," *Journal of Lubrication Technology*, Vol. 95, No. 1, 1973, pp. 137-146.
- <sup>14</sup>Lauder, B. E., and Leschziner, M., "Flow in Finite Width Thrust Bearings Including Inertial Effects, I—Laminar Flow, II—Turbulent Flow," *Journal of Lubrication Technology*, Vol. 100, 1978, pp. 330-345.
- <sup>15</sup>Childs, D., *Turbomachinery Rotordynamics*, Wiley, New York, 1993, pp. 233-235.
- <sup>16</sup>San Andres, L., and Velthuis, J. F. M., "Laminar Flow in a Recess of a Hydrostatic Bearing," *Tribology Transactions*, Vol. 35, No. 4, 1992, pp. 736-744.
- <sup>17</sup>Braun, M. J., Don, Q., and Choy, F. K., "The Effects of a Hydrostatic Pocket Aspect Ratio, and Its Supply Orifice Position and Attack Angle on Steady-State Flow Patterns, Pressure and Shear Characteristics," *Journal of Tribology*, Vol. 115, No. 4, 1993, pp. 678-685.
- <sup>18</sup>Braun, M. J., Zhou, Y., and Choy, F. K., "Transient Flow Patterns and Pressure Characteristics in a Hydrostatic Pocket," *Journal of Tribology*, Vol. 116, No. 1, 1994, pp. 139-146.
- <sup>19</sup>Ho, Y. S., and Chen, N. N., "Pressure Distribution in a Six-Pocket Hydrostatic Journal Bearing," *Wear*, 1984, Vol. 98, pp. 89-100.
- <sup>20</sup>Chaoimleffel, J. P., and Nicholas, D., "Experimental Investigation of Hybrid Journal Bearings," *Tribology International*, Vol. 19, No. 5, 1986, pp. 253-259.
- <sup>21</sup>Reddecliff, J. M., and Vohr, J. H., "Hydrostatic Bearings for Cryogenic Rocket Engine Turbopumps," *Journal of Lubrication Technology*, Vol. 91, 1969, pp. 557-575.
- <sup>22</sup>Constantinescu, V. N., and Galetuse, S., "Pressure Drop due to Inertia Force in Step Bearings," American Society of Mechanical Engineers Paper 75-Lub-34, 1975.
- <sup>23</sup>Artiles, A., Walowit, J., and Shapiro, W., "Analysis of Hybrid Fluid Film Journal Bearings with Turbulence and Inertia Effects," *Advances in Computer Aided Bearing Design*, American Society of Mechanical Engineers Publication G0020, 1982, pp. 25-52.
- <sup>24</sup>Van Doormaal, J. P., and Raithby, G. D., "Enhancements of the SIMPLE Method for Predicting Incompressible Fluid Flows," *Numerical Heat Transfer*, Vol. 7, 1984, pp. 147-163.
- <sup>25</sup>Van Doormaal, J. P., and Raithby, G. D., "An Evaluation of the Segregated Approach for Predicting Incompressible Fluid Flow," American Society of Mechanical Engineers Paper 85-HT-9, 1985.
- <sup>26</sup>Jang, D. S., Jetli, R., and Acharya, S., "Comparison of the PISO, SIMPLER, and SIMPLER Algorithms for the Treatment of the Pressure-Velocity Coupling in Steady Flow Problems," *Numerical Heat Transfer*, Vol. 10, No. 2, 1986, pp. 209-228.
- <sup>27</sup>Butner, M., and Murphy, B., "SSME Long Life Bearings," NASA CR-179455, 1986.
- <sup>28</sup>Yang, Z., San Andres, L., and Childs, D., "Process Liquid Turbulent Flow Hydrostatic Bearings: Analysis and Tests for Rotordynamic Coefficients," *Proceedings of the IFTOMM Rotordynamics Conference* (Chicago), 1994, pp. 233-241.
- <sup>29</sup>Adams, M., Sawicki, J. T., and Capaldi, R., "Experimental Determination of Hydrostatic Journal Bearing Coefficients," International Conf. in Vibrations in Rotating Machinery, Vibration Inst., Paper C432/145, IMechE 1992-6, Willowbrook, IL, Sept. 1992.
- <sup>30</sup>Tonnesen, J., and Hansen, P. K., "Some Experiments on the Steady State Characteristics of a Cylindrical Fluid-Film Bearing Considering Thermal Effects," *Journal of Lubrication Technology*, Vol. 103, 1981, pp. 107-114.
- <sup>31</sup>Braun, M. J., Wheeler, R. L., III, and Hendricks, R. C., "Ther-

mal Shaft Effects on Load-Carrying Capacity of a Fully Coupled, Variable Properties Cryogenic Journal Bearing." *STLE Tribology Transactions*, Vol. 30, No. 2, 1987, pp. 282-292.

"Shoup, T., private communication, Sverdrup-NASA Marshall Space Center, Huntsville, AL, Oct. 1993.

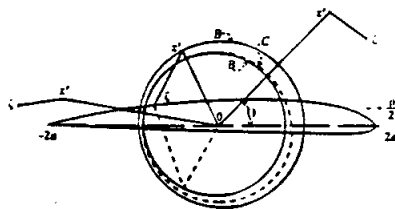
"Heshmat, H., "Investigation of Foil Bearings for Use in High-Thrust Liquid Rocket Engines." NASA CR-197099, April 1991.

"Von Pragenau, G. L., "Damping Bearings for Turbomachinery."

NASA TP 3092, Vol. II, 1990, pp. 155-162.

"Scharrer, J. K., Hibbs, R. I., and Nolan, S., "Extending the Life of the SSME HPOTP Through the Use of Annular Hydrostatic Bearings." AIAA Paper 92-3401, July 1992.

"Arauz, G., and San Andres, L., "Effect of a Circumferential Feeding Groove on the Force Response of a Short Squeeze Film Damper." *Journal of Tribology*, Vol. 116, No. 2, 1994, pp. 369-377.



## A Modern View of Theodore Theodorsen, Physicist and Engineer

Earl H. Dowell, editor

A giant in the youthful days of aeronautics, Theodore Theodorsen still stands tall among those who have followed him. This text focuses on Theodorsen's research contributions through a reprinting of selected papers and appreciations authored by notable scholars in several of the fields in which he was active.

Contents: Foreword; Introduction; Critical Essays; Biography; Selected Reprints of Theodorsen's Chief Works; Bibliography by Subject

1992, 372 pp, illus. Hardback, ISBN 0-930403-85-1  
AIAA Members \$20.00, Nonmembers \$30.00  
Order #: 85-1 (830)

Place your order today! Call 1-800/682-AIAA



American Institute of Aeronautics and Astronautics

Publications Customer Service, 9 Jay Gould Ct., P.O. Box 753, Waldorf, MD 20604  
FAX 301/843-0159 Phone 1-800/682-2422 8 a.m. - 5 p.m. Eastern

Sales Tax: CA residents, 8.25%; DC, 6%. For shipping and handling add \$4.75 for 1-4 books (call for rates for higher quantities). Orders under \$100.00 must be prepaid. Foreign orders must be prepaid and include a \$20.00 postal surcharge. Please allow 4 weeks for delivery. Prices are subject to change without notice. Returns will be accepted within 30 days. Non-U.S. residents are responsible for payment of any taxes required by their government.

9 "Inertia Effects in a Hybrid Bearing with a 45 degree Entrance Region," 1995, Hill., D., E. Baskharone, and L. San Andres, *ASME Journal of Tribology*, Vol. 117, 3, pp. 498-505.

# Inertia Effects in a Hybrid Bearing With a 45 Degree Entrance Region

D. L. Hill\*

E. A. Baskharone

Associate Professor,  
Mem. ASME.

Luis San Andres

Associate Professor,  
Mem. ASME.

Department of Mechanical Engineering,  
Texas A & M University,  
College Station, TX 77843-3123

*An investigation is presented that illustrates the effects of inertia on the flow and pressure field throughout a hybrid bearing with a 45 degree entrance region. This type of bearing has been previously shown to offer better performance over the hybrid bearing with a normal entry region. A two-dimensional planar approach is adopted and the resulting flow governing equations are solved using the Galerkin Weighted Residual finite element method. This algorithm incorporates an advanced streamline upwinding method to evaluate the nonlinear effects of the convection terms. The results demonstrate the complex nature of the velocity field and its subsequent impact on the pressure field. This comprehensive parametric study also shows why traditional lubrication approaches that typically exclude convection effects will become unreliable at high operating speeds of turbomachinery. A set of loss coefficients modeling the pressure 'ram' effects are provided to illustrate the inertia effects in the entrance region of the film lands. In a hybrid bearing, these effects have to be characterized according to the operating parameters of the bearing and the journal direction of rotation.*

## 1 Introduction

The development of fluid film bearing technology is currently being driven by the need for better support elements in cryogenic high speed turbomachinery. Fluid film hybrid bearings utilize both hydrodynamic and hydrostatic principles to achieve their design load capacity and rotordynamic requirements. Reduced wear and lower friction are expected to extend the life of the hybrid bearing past the conventional ball-type bearing found in the Space Shuttle Main Engine (SSME). Although hybrid bearing technology is not currently being used on any cryogenic turbomachinery, no evidence has been offered to date that disputes the attractive performance features of the hybrid bearing concept.

The performance of a typical hybrid bearing is significantly affected by inertia and turbulence effects that are generated within the lubricant. These complex mechanisms stem from the convective nature of the flow fluid, and are driven by a combination of high operating speeds, low viscosity of the lubricant, large external pressures, and the complexity of the bearing geometry. For the bearing recess region, convection effects will lead to a non-linear pressure distribution. Other flow resistance mechanisms have been attributed to the pressure "ram" effects which occur as the fluid enters the film lands. This particular group of losses can no longer be characterized as a simple function of the journal speed through the film/surface Reynolds number. Instead, for a

hybrid bearing, the pressure ram effects have to be parameterized on the basis of the inlet feed conditions, journal speed, and bearing geometry. In general, one would expect a unique set of characteristic loss curves for each case where the journal moves toward or away from the entrance region of the film land. As the fluid flows through the film lands, higher pressure drops due to increased shear effects will result in higher power losses.

One of the early analyses of a hybrid bearing was reported by Artiles et al. (1982). In their work, the classical lubrication approach, which neglects convection effects in the principle flow directions, was used to analyze a four recess bearing configuration with a radial entry feed system. The effects of inertia and turbulence were simulated at the bearing recess boundaries through a pressure loss coefficient that represented only the effect of the moving journal. The resulting loss coefficients were then used in a mass balancing scheme to resolve the pressure drop across each of the orifice and recess boundaries. In this study, the pressure was fictitiously assumed constant in the recess region. Turbulence coefficients, given by Ng and Pan (1965) and Elrod et al. (1967), are used as multiplication factors in the film lands to model the increased shear effects. A finite difference Newton Raphson approach, using the column matrix method, was used to solve the resulting Reynolds equations.

Bou-Said and Chaomleffel (1989) used a Hermitian formulation of the Galerkin finite element method to solve the turbulent flow Reynolds equations in the film lands. Their mass balancing scheme for the recess regions incorporated the theory of Constantinescu (1959) to account for circumferential inertia effects across the recess boundaries. This the-

\*Ph.D. candidate, Formerly Senior Engineer with Pratt & Whitney Aircraft, West Palm Beach, FL.

Contributed by the Tribology Division for publication in the JOURNAL OF TRIBOLOGY. Manuscript received by the Tribology Division October 25, 1993; revised manuscript received August 10, 1994. Associate Technical Editor: M. J. Braun.

ory does not consider the case where the journal moves toward the contracting area and excludes any hydrostatic effects. Turbulence effects in the film lands are modeled using the friction factor approach developed by Elrod et al. (1967) and Constantinescu (1959). The results are compared with the experimental data for a three recess hybrid water bearing with a normal entry feed system. The experimental work was previously reported by Chaomleffel (1983) and included pressure, flow rate, and load capacity data.

San Andres (1990) presented an improved bulk-flow algorithm that incorporates the convection terms in the principle flow directions. A model for the pressure ram effects at the recess boundaries is developed from the one-dimensional step theory of Constantinescu and Galetuse (1976). This theory, however, accounts for neither the direction of journal rotation nor hydrostatic effects. The pressure is assumed constant throughout the recess region and compressibility effects are included in the bearing recess volume. The governing bulk-flow equations for the film region of the bearing implemented turbulent shear factors based on the fundamental work of Hirs (1973) and Nelson et al. (1987). San Andres' numerical algorithm is based on a finite volume method which uses the pressure-based approach of Van Doormaal and Raithby (1984). More recently, Kurtin et al. (1993) compared theoretical calculations to experimental data obtained from a five recess water hybrid bearing rig with a radial lubricant feed.

There have been many notable investigations focusing on the pressure losses at the entrance of thin film lands. This body of work, however, has examined only the loss mechanisms due to hydrodynamic effects. Pan (1974) developed a perturbation analysis to investigate a bearing operating at high speeds. This work based on the linearized turbulent lubrication theory treats the inertial effects as small corrections to the non-inertial solution. A forward facing step geometry was used as the baseline model and the direction of the journal rotation was into the contracting step area. Another analytical approach was reported by Tipei (1982) where a model for the flow at the inlet of a narrow passage was developed. This model was based on complex potential flow theory that utilized a source-sinks approach to model the small gap. The pressure losses presented in this work only contained the component due to convection.

A numerical analysis including both viscous and inertia effects for a thrust bearing was reported by Heckelman and Ettles (1988). The SIMPLE approach by Patankar (1980) was

used to develop the numerical algorithm and the model domain reproduced the test bearing of Ettles (1965). The recess depth to film thickness ratio for this set of calculations varied from approximately 685:1 to 160:1. Typical depth ratios for cryogenic applications, however, range from 5:1 to 1:1 to avoid the so-called "water hammer" effects. A similar investigation has recently been reported by Mori et al. (1992). Their model uses the penalty finite element method formulation developed by Hughes et al. (1978) to solve the two-dimensional governing set of flow equations. The authors reported that initial numerical stability problems were solved by increasing the entrance height to the film lands, thus deviating from the correct bearing geometry.

The recent work of San Andres and Velthuis (1992) simulates the loss characteristics of a hybrid bearing with a normal feed line operating at moderate speeds in the laminar flow regime. A numerical algorithm was developed to solve the two-dimensional flow governing equations using the finite volume pressure based formulation of Van Doormaal and Raithby (1984). Dependence of the flow structure in the recess region on the bearing operating parameters, namely the inlet and surface Reynolds numbers was investigated. The pressure entrance losses in this study were estimated by considering only the section of the bearing that makes up the forward facing step. Braun et al. (1993) also reported a thorough parametric study that focused on the two-dimensional flow structure in a recess cavity and adjacent film lands of a hybrid bearing. In this particular study, the pocket aspect ratio, jet position, and inclination, as well as Reynolds number were varied. The derived flow governing equations were solved using the finite volume algorithm of Patankar (1980).

Recent experimental work by Franchek and Childs (1993) has shown that a hybrid bearing system with angled entry feed lines offers better static and dynamic responses than the conventional hybrid bearing with a radial supply line. This finding motivated the current study, in which a hybrid bearing with a 45 degree entry region is numerically investigated. A two-dimensional planar model is used to represent the entry region, recess region and the film lands. The analysis is based on a mixed interpolation Galerkin Weighted Residual finite element approach. Convection effects are modeled using an accurate streamline upwinding technique. The flow structure as well as the pressure variation inside the recess region are both resolved simultaneously with the pressure "ram" losses in the entry region of the film lands. The

## Nomenclature

$dl$  = differential length  
 $dA^e$  = differential element area  
 $k$  = pressure "ram" loss coefficient,  
 $\Delta p^*$  at film entrance region  
 $L$  = dimensional length scale,  $L_a$   
 (mm)  
 $L_a$  = inlet width of bearing (mm)  
 $L_c$  = recess region height (mm)  
 $M_i$  = bilinear interpolation function  
 $n$  = unit normal vector  
 $N_i$  = quadratic interpolation function  
 $p$  = static pressure (N/m<sup>2</sup>)  
 $P$  = ambient pressure (N/m<sup>2</sup>)  
 $p^*$  = nondimensional pressure,  
 $(p - P)/\rho U^2$   
 $R$  = bearing radius (m)  
 $Re$  = inlet Reynolds number,  
 $UL_a \rho/\mu$

$Re_r$  = surface Reynolds number,  
 $U_r L_c \rho/\mu$   
 $U$  = dimensional velocity scale, aver-  
 age inlet velocity (m/s)  
 $U_r = \Omega R$ , velocity of journal surface  
 (m/s)  
 $u$  = velocity component in  $x$ -direc-  
 tion (m/s)  
 $u_s$  = velocity along a streamline (m/s)  
 $u^*$  = nondimensional velocity in  $x$ -di-  
 rection,  $u/U$   
 $v$  = velocity in  $y$ -direction (m/s)  
 $v^*$  = nondimensional velocity in  $y$ -di-  
 rection,  $v/U$   
 $W_i$  = weighting function  
 $x$  = coordinate axis in sliding direc-  
 tion (m)

$x^*$  = nondimensional coordinate axis  
 in sliding direction,  $x/L$   
 $y$  = coordinate axis perpendicular to  
 $x$ -axis (m)  
 $y^*$  = nondimensional coordinate axis  
 perpendicular to  $x$ -axis,  $y/L$   
 $\Omega$  = rotational speed (rad/s)  
 $\rho$  = fluid density (kg/m<sup>3</sup>)  
 $\mu$  = fluid viscosity (Pa s)  
 $\nabla$  = gradient operator

### Subscript

$s$  = reference to the streamline di-  
 rection

### Superscript

$*$  = nondimensional quantities



computed results can be used to enhance currency bulk-flow algorithms so that they can effectively be used to design hybrid bearings for cryogenic applications.

## 2 Analysis

The steady motion of a fluid that is incompressible, two-dimensional, and laminar is governed by the following set of equations (White, 1974).

continuity:

$$\frac{\partial u}{\partial x} + \frac{\partial v}{\partial y} = 0 \quad (1)$$

x-momentum:

$$\rho u \frac{\partial u}{\partial x} + \rho v \frac{\partial u}{\partial y} = -\frac{\partial p}{\partial x} + \frac{\partial}{\partial x} \left( \mu \frac{\partial u}{\partial x} \right) + \frac{\partial}{\partial y} \left( \mu \frac{\partial u}{\partial y} \right) \quad (2)$$

y-momentum:

$$\rho u \frac{\partial v}{\partial x} + \rho v \frac{\partial v}{\partial y} = -\frac{\partial p}{\partial y} + \frac{\partial}{\partial x} \left( \mu \frac{\partial v}{\partial x} \right) + \frac{\partial}{\partial y} \left( \mu \frac{\partial v}{\partial y} \right) \quad (3)$$

Next, define the following group of nondimensional variables.

$$u^* = \frac{u}{U}, \quad v^* = \frac{v}{U}, \quad p^* = \frac{p - P}{\rho U^2} \quad (4)$$

$$x^* = \frac{x}{L}, \quad y^* = \frac{y}{L}$$

where,  $U$  is the averaged inlet velocity,  $L$  is the inlet channel width, and  $P$  is taken to be the ambient pressure. Inserting these relations into Eqs. (1)–(3) renders the equivalent nondimensional form of the governing equations, namely:

continuity:

$$\frac{\partial u^*}{\partial x^*} + \frac{\partial v^*}{\partial y^*} = 0 \quad (5)$$

x-momentum:

$$u^* \frac{\partial u^*}{\partial x^*} + v^* \frac{\partial u^*}{\partial y^*} = -\frac{\partial p^*}{\partial x^*} + \frac{1}{\text{Re}} \left( \frac{\partial^2 u^*}{\partial x^{*2}} + \frac{\partial^2 u^*}{\partial y^{*2}} \right) \quad (6)$$

y-momentum:

$$u^* \frac{\partial v^*}{\partial x^*} + v^* \frac{\partial v^*}{\partial y^*} = -\frac{\partial p^*}{\partial y^*} + \frac{1}{\text{Re}} \left( \frac{\partial^2 v^*}{\partial x^{*2}} + \frac{\partial^2 v^*}{\partial y^{*2}} \right) \quad (7)$$

The resulting Reynolds number is based on the inlet parameters of the bearing. Using Eqs. (5)–(7), the general form of the finite element weighted residual equations can now be directly written.

continuity:

$$\int W_i \left( \frac{\partial u^*}{\partial x^*} + \frac{\partial v^*}{\partial y^*} \right) dA^e = 0 \quad (8)$$

x-momentum:

$$\int W_i \left( u^* \frac{\partial u^*}{\partial x^*} + v^* \frac{\partial u^*}{\partial y^*} \right) dA^e = - \int W_i \frac{\partial p^*}{\partial x^*} dA^e + \frac{1}{\text{Re}} \int W_i \left( \frac{\partial^2 u^*}{\partial x^{*2}} + \frac{\partial^2 u^*}{\partial y^{*2}} \right) dA^e \quad (9)$$

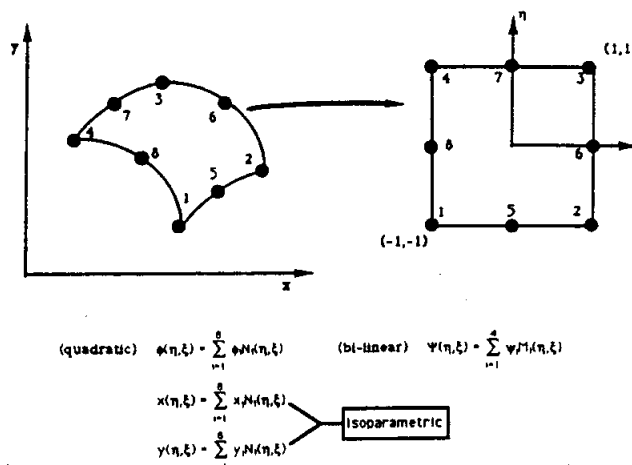


Fig. 1 The 8-noded element from the Serendipity family

y-momentum:

$$\int W_i \left( u^* \frac{\partial v^*}{\partial x^*} + v^* \frac{\partial v^*}{\partial y^*} \right) dA^e = - \int W_i \frac{\partial p^*}{\partial y^*} dA^e + \frac{1}{\text{Re}} \int W_i \left( \frac{\partial^2 v^*}{\partial x^{*2}} + \frac{\partial^2 v^*}{\partial y^{*2}} \right) dA^e \quad (10)$$

Integration by parts is now performed on the diffusion terms in both of the momentum equations (Huebner and Thornton, 1982).

x-momentum:

$$\int W_i \left( u^* \frac{\partial u^*}{\partial x^*} + v^* \frac{\partial u^*}{\partial y^*} \right) dA^e + \frac{1}{\text{Re}} \int \left( \frac{\partial W_i}{\partial x^*} \frac{\partial u^*}{\partial x^*} + \frac{\partial W_i}{\partial y^*} \frac{\partial u^*}{\partial y^*} \right) dA^e = - \int W_i \frac{\partial p^*}{\partial x^*} dA^e + \frac{1}{\text{Re}} \int W_i (\nabla u^* \cdot \mathbf{n}) dl \quad (11)$$

y-momentum:

$$\int W_i \left( u^* \frac{\partial v^*}{\partial x^*} + v^* \frac{\partial v^*}{\partial y^*} \right) dA^e + \frac{1}{\text{Re}} \int \left( \frac{\partial W_i}{\partial x^*} \frac{\partial v^*}{\partial x^*} + \frac{\partial W_i}{\partial y^*} \frac{\partial v^*}{\partial y^*} \right) dA^e = - \int W_i \frac{\partial p^*}{\partial y^*} dA^e + \frac{1}{\text{Re}} \int W_i (\nabla v^* \cdot \mathbf{n}) dl \quad (12)$$

The resulting line integrals are considered natural boundary conditions that can be evaluated on boundary regions if Dirichlet type conditions are not given. Note that when fully developed flow occurs at a boundary region, the natural boundary conditions given in Eqs. (11) and (12) are exactly zero so that no explicit effort has to be made to impose this condition on the momentum equations.

The finite element interpolation expressions of the field variables for the 8-noded element of the Serendipity family (Fig. 1) can be written in the general form:

$$u^* = \sum_{j=1}^8 N_j u_j^*, \quad v^* = \sum_{j=1}^8 N_j v_j^*, \quad p^* = \sum_{j=1}^4 M_j p_j^* \quad (13)$$

$$x^* = \sum_{j=1}^8 N_j x_j^*, \quad y^* = \sum_{j=1}^8 N_j y_j^*$$

Equations (8), (11), (12), and (13) are now used to develop

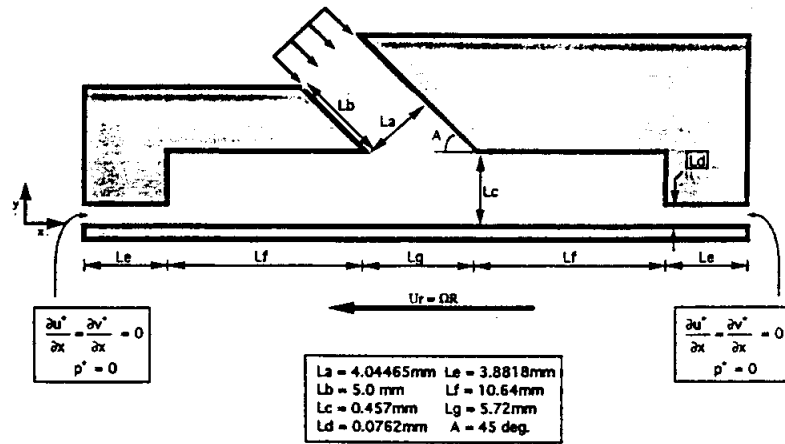


Fig. 2 Hybrid bearing geometry and boundary conditions

the final weighted residual finite element form of the governing set of equations.

continuity:

$$\int W_i \left( \frac{\partial N_j}{\partial x^*} u_j^* + \frac{\partial N_j}{\partial y^*} v_j^* \right) dA^e = 0 \quad (14)$$

x-momentum:

$$\begin{aligned} \int W_i \left( N_k u_k^* \frac{\partial N_j}{\partial x^*} + N_k v_k^* \frac{\partial N_j}{\partial y^*} \right) u_k^* dA^e \\ + \frac{1}{\text{Re}} \int \left( \frac{\partial W_i}{\partial x^*} \frac{\partial N_j}{\partial x^*} + \frac{\partial W_i}{\partial y^*} \frac{\partial N_j}{\partial y^*} \right) u_k^* dA^e \\ = - \int W_i \frac{\partial M_j}{\partial x^*} p_j^* dA^e + \frac{1}{\text{Re}} \int W_i (\nabla u^* \cdot n) dl \end{aligned} \quad (15)$$

y-momentum:

$$\begin{aligned} \int W_i \left( N_k u_k^* \frac{\partial N_j}{\partial x^*} + N_k v_k^* \frac{\partial N_j}{\partial y^*} \right) v_k^* dA^e \\ + \frac{1}{\text{Re}} \int \left( \frac{\partial W_i}{\partial x^*} \frac{\partial N_j}{\partial x^*} + \frac{\partial W_i}{\partial y^*} \frac{\partial N_j}{\partial y^*} \right) v_k^* dA^e \\ = - \int W_i \frac{\partial M_j}{\partial y^*} p_j^* dA^e + \frac{1}{\text{Re}} \int W_i (\nabla v^* \cdot n) dl \end{aligned} \quad (16)$$

The current form of the advection terms in Eqs. (15) and (16) is the traditional form resulting from the weighted residual approach. These expressions, however, are not desirable because they express the effects of convection in a unrealistic symmetric manner. Such a representation will cause the algorithm to be driven unstable as the Reynolds number is increased. This behavior is equivalent to the instability problems that result when central differencing is applied to the convection terms for a computational cell that has a cell Reynolds number greater than 2. Consequently, these terms are replaced with an upwinding scheme which is based on a direct streamline approach. The accuracy of the method and details of applying it to quadratic elements is given by Hill and Baskharone (1993). The following notation is used to represent the upwinding technique.

$$u_s \int W_i \frac{\partial u^*}{\partial s} dA^e = \int W_i \left( N_k u_k^* \frac{\partial N_j}{\partial x^*} + N_k v_k^* \frac{\partial N_j}{\partial y^*} \right) u_j^* dA^e \quad (17)$$

$$u_s \int W_i \frac{\partial v^*}{\partial s} dA^e = \int W_i \left( N_k u_k^* \frac{\partial N_j}{\partial x^*} + N_k v_k^* \frac{\partial N_j}{\partial y^*} \right) v_j^* dA^e \quad (18)$$

where, the (s) subscript refers to values along a streamline. Using these relations and choosing the weighting functions to

satisfy the Babruska-Brezzi compatibility conditions described by Zienkiewicz and Taylor (1988), the complete set of finite element equations is obtained.

continuity:

$$\int M_i \left( \frac{\partial N_j}{\partial x^*} u_j^* + \frac{\partial N_j}{\partial y^*} v_j^* \right) dA^e = 0 \quad (19)$$

x-momentum:

$$\begin{aligned} u_s \int N_i \frac{\partial u^*}{\partial s} dA^e + \frac{1}{\text{Re}} \int \left( \frac{\partial N_i}{\partial x^*} \frac{\partial N_j}{\partial x^*} + \frac{\partial N_i}{\partial y^*} \frac{\partial N_j}{\partial y^*} \right) u_j^* dA^e \\ = - \int N_i \frac{\partial M_j}{\partial x^*} p_j^* dA^e + \frac{1}{\text{Re}} \int N_i (\nabla u^* \cdot n) dl \end{aligned} \quad (20)$$

y-momentum:

$$\begin{aligned} u_s \int N_i \frac{\partial v^*}{\partial s} dA^e + \frac{1}{\text{Re}} \int \left( \frac{\partial N_i}{\partial x^*} \frac{\partial N_j}{\partial x^*} + \frac{\partial N_i}{\partial y^*} \frac{\partial N_j}{\partial y^*} \right) v_j^* dA^e \\ = - \int N_i \frac{\partial M_j}{\partial y^*} p_j^* dA^e + \frac{1}{\text{Re}} \int N_i (\nabla v^* \cdot n) dl \end{aligned} \quad (21)$$

Equations (19)–(21) are the discretized form of the governing flow equations. The system of equations is solved in a nonsegregated manner using the frontal method of Hood (1976) to invert the global matrix. Double precision is used for all computations and the solution is declared converged when the relative error residual of the flow field variables ( $u$ ,  $v$ , and  $p$ ) has been reduced at least three orders of magnitude.

$$\sum_1^{\text{pts}} \left| \frac{\phi^n - \phi^{n-1}}{\phi^n} \right| \leq 1.e - 0.3, \quad \phi = u^*, v^*, \text{ and } p^*$$

where  $n$  and  $n - 1$  stand for the current and past iterative values. Further iteration below this residual level did not cause any measurable variations in pressure distribution along the journal surface. Details of the accuracy and superior convergence rate of this type of primitive variable approach are given by Fletcher (1991), Baskharone et al. (1989), and Baskharone et al. (1981).

### 3 Results

The geometry of the hybrid bearing used in this study is nearly identical in size and shape to the hybrid bearing used by San Andres (1990) and is assumed to have smooth surfaces. The primary difference between the two bearing geometries is that the current investigation uses a 45 degree entrance region instead of a 90 degree configuration. The computational domain of the hybrid bearing configuration

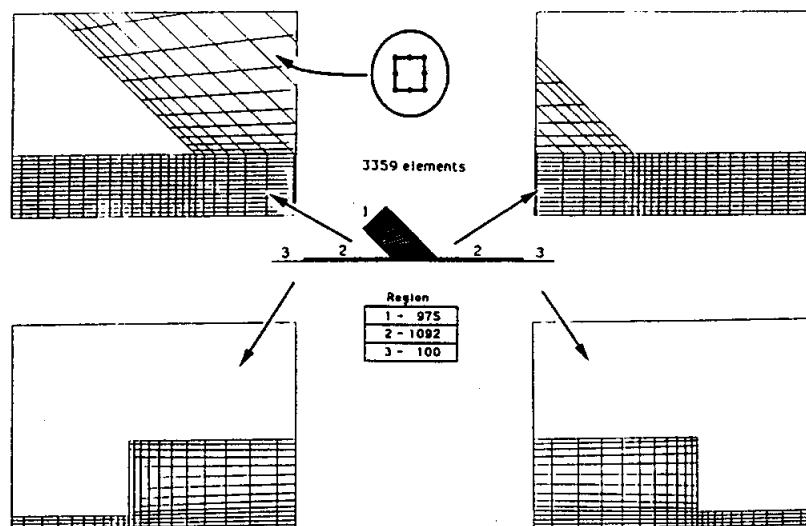


Fig. 3 The finite element model

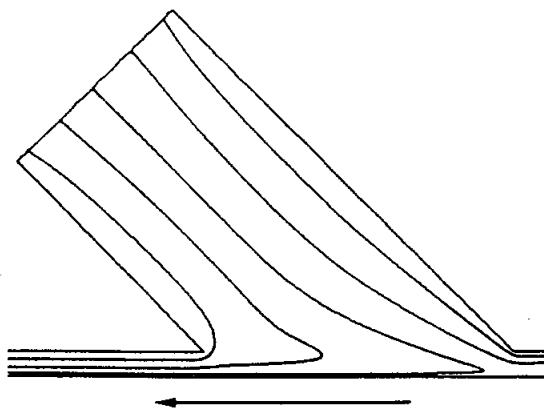


Fig. 4 Streamline trace for the entrance region at a inlet/surface Reynolds number = 300/100

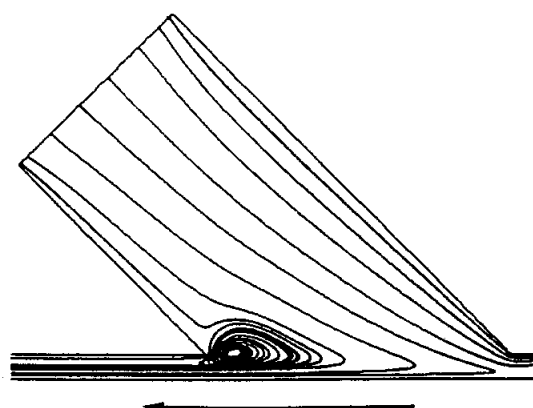


Fig. 5 Streamline trace for the entrance region at a inlet/surface Reynolds number = 300/300

studied is shown in Fig. 2 along with the necessary boundary conditions. The velocity field is specified at the entrance (supply) as a bulk (flat) profile based on typical entry regions from plenums to constricted areas (Schlichting, 1979). The no-slip boundary condition is imposed at all stationary wall regions, while on the moving surface the fluid takes the wall velocity. A constant ambient pressure along with zero velocity gradients in the streamwise direction are specified as boundary conditions at the exit regions.

The finite element model used for all computations is shown in Fig. 3. The center illustration in this figure shows the bearing model to scale. Critical regions where steep gradients of the flow field are expected are enlarged so that the intensity of the element distribution can be viewed. These regions include both corners where the fluid makes the turn into the bearing recess and at each location where the fluid enters the film land. A total of 3359 quadratic elements are used to discretize the bearing flow path. The number of elements chosen for this problem is consistent in size with those used in the authors' previous laminar flow work and with the current numerical work cited in the present literature review. Further numerical experiments with refined grids are planned with future turbulent flow work using the hybrid bearing geometry.

The parametric study was conducted by systematically varying the inlet nondimensional velocity and journal nondimensional velocity to account for the influence of inertia forces. In addition, the density ( $\rho$ ) and viscosity ( $\mu$ ) were

kept constant for all computations. The chosen values of the inlet  $Re$  are 300, 600, and 1200. These operating inlet conditions are representative of the flow regime under consideration, namely laminar. By specifying the ratio of the inlet Reynolds number to the surface Reynolds number ( $Re/Re_s$ ), the value of  $Re_s$  was determined, then used to calculate the velocity boundary condition for nodes lying on the moving journal surface. The ratio of the Reynolds numbers was kept between 1:1 and 3:1 which is typical for cryogenic turbomachinery. The number of selected intervals or calculation frequency between these bounding ratios were not the same for each  $Re$  investigated. As the  $Re$  increased, the number of intervals had to increase so that the changes in the flow field variables could be accurately determined.

The results from the parametric study are presented to show the effects of varying the inlet/surface velocities, as related by their respective Reynolds numbers, on each flow region within the bearing. Figures 4 and 5 show the flow streamlines for inlet/surface Reynolds number combinations of 300/100 and 300/300, respectively. The first figure shows that the flow entering the hybrid bearing flow domain has a large enough inertia to keep a recirculation zone from forming just upstream of the recess cavity. The recirculation zone shown in Fig. 5 is driven by the recess region through the high shear rates generated by the moving journal. This particular case was the only one in which the inlet inertia was low enough to allow the shear driven flow to dominate the entire flow path. The rest of the cases investigated resulted in

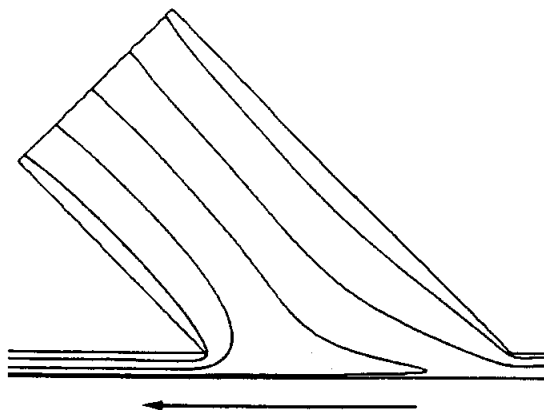


Fig. 6 Streamline trace for the entrance region at a inlet/surface Reynolds number = 1200/400

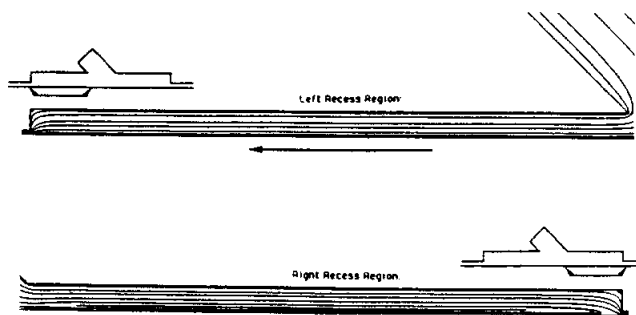


Fig. 7 Streamline trace for the recess region at a inlet/surface Reynolds number = 300/100

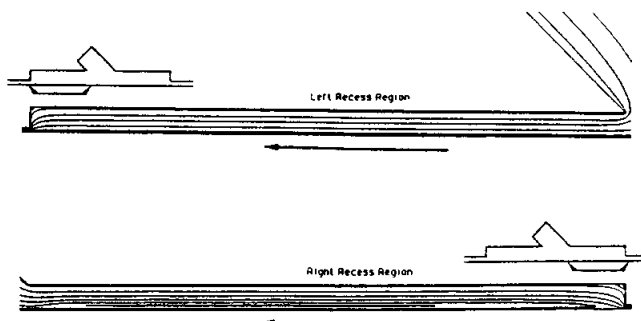


Fig. 8 Streamline trace for the recess region at a inlet/surface Reynolds number = 600/200

streamlines which are characteristically similar to those depicted in Fig. 4. This feature is further illustrated in Fig. 6 which corresponds to an inlet/surface Reynolds number combination of 1200/400.

The streamlines for the recess region are shown in Figs. 7-9 for the limiting Reynolds number ratio of 3:1. The flow structure in the left side of the recess region is virtually similar for all  $Re$  values investigated. Each solution has a small recirculation zone located in the step region that is approximately the same size. However, the right side of the recess region has a recirculation zone in its step region that grows as the  $Re$  is increased. Also, established in these calculations is the fact that the right side of the recess region has another recirculation zone that is driven by the moving journal and is shifted to the left as the step recirculation zone grows.

The results of the limiting Reynolds number ratio of 1:1 are shown in Figs. 10-12. As seen in these figures, the left side of the recess region for all three cases is generally

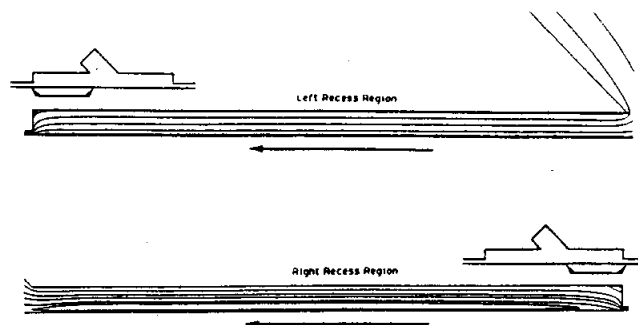


Fig. 9 Streamline trace for the recess region at a inlet/surface Reynolds number = 1200/400

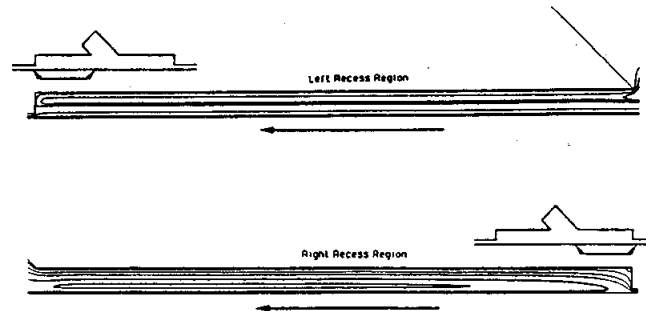


Fig. 10 Streamline trace for the recess region at a inlet/surface Reynolds number = 300/300

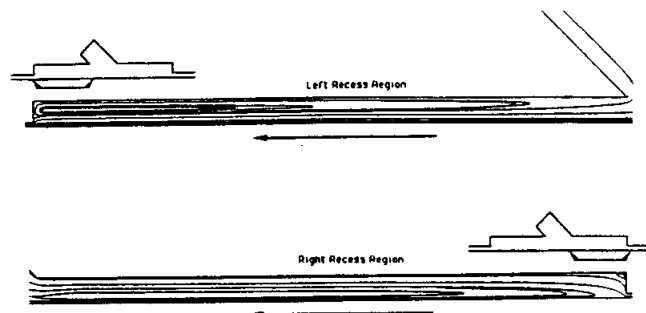


Fig. 11 Streamline trace for the recess region at a inlet/surface Reynolds number = 600/600

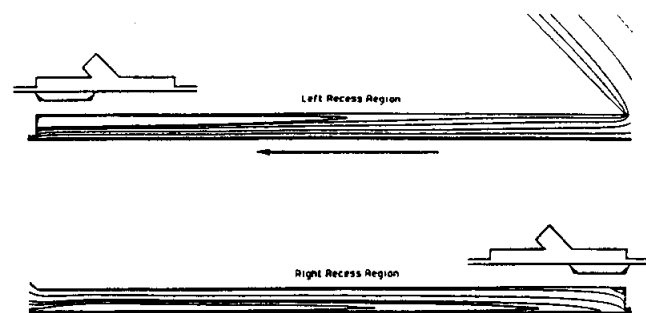


Fig. 12 Streamline trace for the recess region at a inlet/surface Reynolds number = 1200/1200

dominated by the step region recirculation zone. As the inlet  $Re$  is increased, the size of the recirculation zone is reduced and pushed toward the entrance of the film land. These figures also show that the recirculation zone found in the right side of the bearing recess next to the step grows with increasing  $Re$ . The other recirculation zone found in this region does not change much in size but does fill approximately half of the flow passage.

The pressure distribution along the bottom surface ( $y = 0$ ) is shown in Fig. 13 for  $Re = 300$  and  $Re$ , ranging from 100 to 300. This figure was produced using every third value from

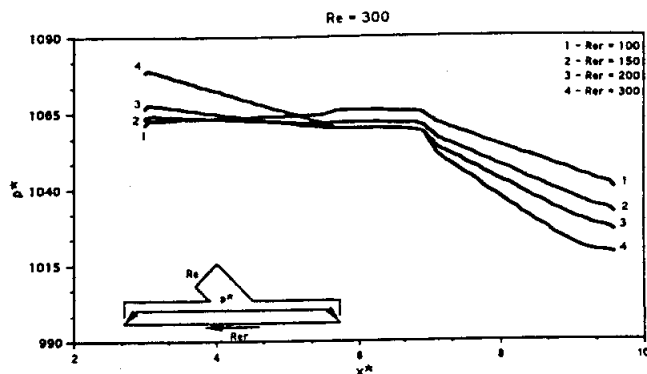


Fig. 13 Pressure profile along the journal surface for an inlet  $Re = 300$  and surface  $Re$ , varying from 100 to 300

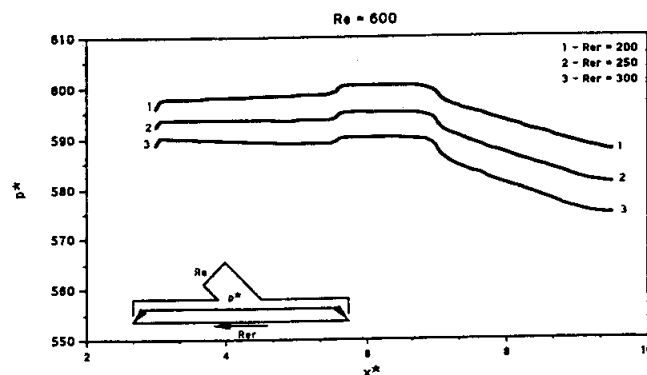


Fig. 14(a) Pressure profile along the journal surface for an inlet  $Re = 600$  and surface  $Re$ , varying from 200 to 300

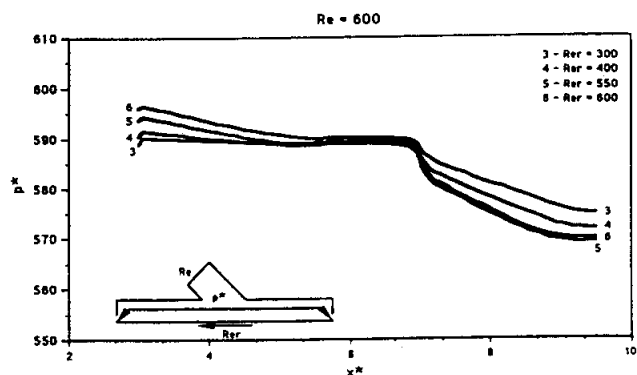


Fig. 14(b) Pressure profile along the journal surface for an inlet  $Re = 600$  and surface  $Re$ , varying from 300 to 600

the solution and the entire pressure drop across the film land is not included. As  $Re_s$  increases, both the pressure rise in the left part of the recess and the pressure drop in the right part of the recess region is shown to increase. At this relatively low  $Re$ , the shape of the pressure profile is largely controlled by the shear effects stemming from the moving journal surface. In addition, the reader is reminded that the average inlet velocity,  $U$  is different for each case presented.

For  $Re = 600$ , the pressure profiles along the journal surface are shown in Figs. 14(a) and 14(b). Two figures are used to help demonstrate the peculiar behavior of the pressure as  $Re_s$  increases. Figure 14(a) shows the entire pressure distribution to shift downward as the Reynolds number ratio goes from the 3:1 to 2:1. As  $Re_s$  is further increased, Fig. 14(b) shows that the shear effects from the journal begin to strongly influence the flow field which eventually causes similar trends in the pressure at the downstream portion of the recess as previously indicated for  $Re = 300$ .

The effects of inertia on the journal surface pressure

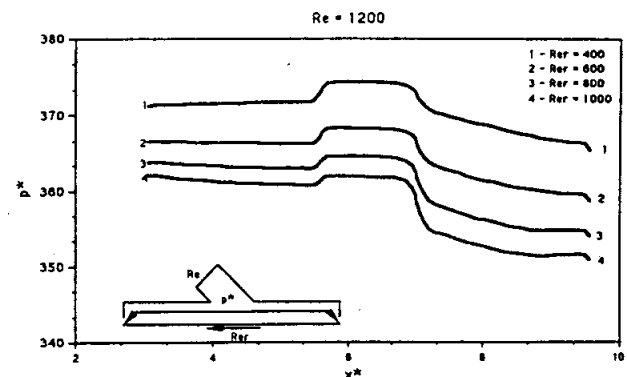


Fig. 15(a) Pressure profile along the journal surface for an inlet  $Re = 1200$  and surface  $Re$ , varying from 400 to 1000

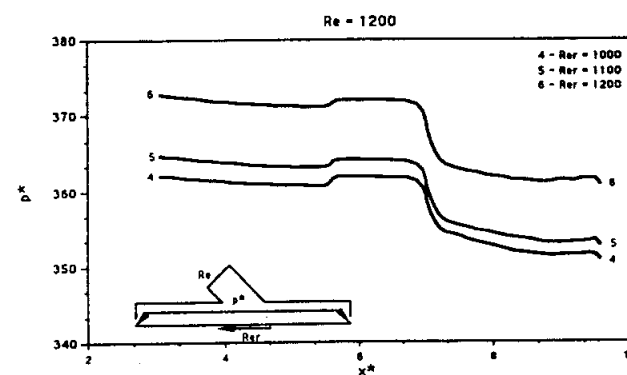


Fig. 15(b) Pressure profiles along the journal surface for an inlet  $Re = 1200$  and surface  $Re$ , varying from 1000 to 1200

distribution are shown in Figs. 15(a) and 15(b) for  $Re = 1200$  and varying  $Re_s$ . For this case, Fig. 15(a) shows the pressure initially being shifted downward as the  $Re_s$  is increased. When the Reynolds number ratio reaches approximately 1.2:1, the pressure begins to shift upward with increasing  $Re_s$ . From the shape of the pressure profiles shown in Fig. 15(b), the shear dominated regime for this  $Re$  is never reached.

The pressure ram effects are investigated at each film land where the journal is moving away from and towards the contracting step area. The loss coefficients ( $k$ ) representing both the inertia and shear effects are shown in Figs. 16(a) and 16(b). These values were calculated by subtracting the area averaged pressure values obtained just upstream and downstream of each step. The loss coefficients for each film land entrance are characteristically similar but vary distinctly in magnitude. The increase in the Reynolds number ratio has the effect of shifting the loss coefficient curves downward for the case of the journal moving into the area contraction, and upward for the case where the journal move away from the area contraction. It should be noted that as the  $Re$  increases further, there will be a limiting loss coefficient which will be primarily due to inertia. The curve fits of these loss coefficients are given below as a function of the inlet Reynolds number and Reynolds number ratio for each side of the bearing. Note that the use of three points to represent the loss coefficient distribution over the laminar flow region was deemed acceptable only after reviewing the detailed analytical/experimental work of Chaomleffel (1983) in which the loss coefficient curves were shown to be continuous and well-behaved throughout both the laminar and turbulent flow regimes.

*journal moving into the film lands:*

$$Re/Re_s \text{ Ratio} = 3:1 \quad k = (8258.98/Re) + 66.9598 \quad (22a)$$

$$Re/Re_s \text{ Ratio} = 1:1 \quad k = (9968.46/Re) + 79.9885 \quad (22b)$$

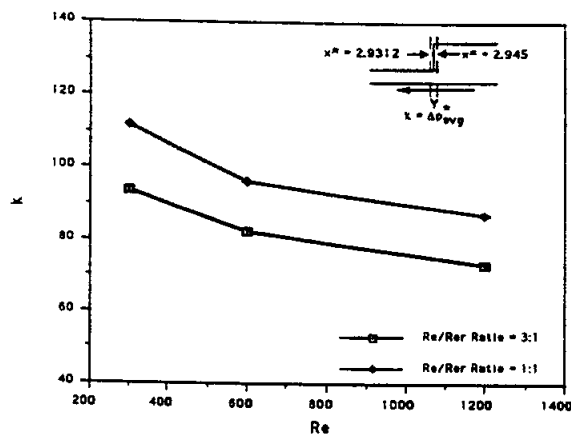


Fig. 16(a) Loss coefficient profile for the case where the journal travels into the film land (contraction)

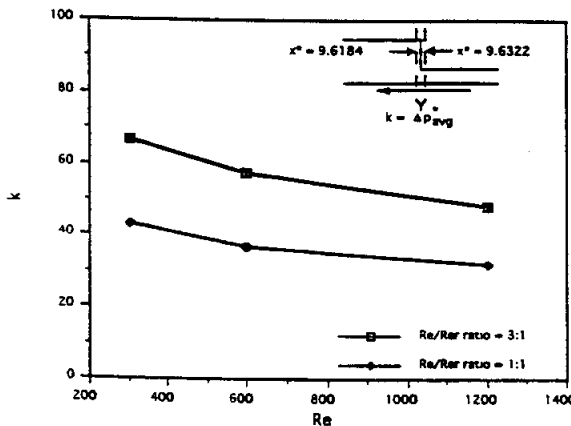


Fig. 16(b) Loss coefficient profile for the case where the journal travels away from the film land (expansion)

journal moving away from the film lands:

$$\text{Re}/\text{Re}_r \text{ Ratio} = 3:1 \quad k = (7179.85/\text{Re}) + 43.5485 \quad (23a)$$

$$\text{Re}/\text{Re}_r \text{ Ratio} = 1:1 \quad k = (4448.57/\text{Re}) + 28.71 \quad (23b)$$

#### 4 Conclusions

A detailed numerical study of the inertia effects inside a hybrid bearing is presented. A mixed interpolation finite element algorithm that incorporates an accurate streamline upwind method is used to solve the governing flow equations. Streamline traces representing the velocity field are presented at various inlet/surface Reynolds number combinations to illustrate the non-unidirectional flow behavior inside the bearing recess region. The resulting behavior of the pressure field is depicted along the journal surface for this region. At the higher inlet Reynolds numbers investigated, this pressure distribution is shown to exhibit a "saddle-like" behavior as the surface Reynolds number increases. Pressure ram losses are calculated and shown to be dependent on the operating parameters and the journal direction of travel. Curvefits for these losses are given for each film land entrance region as a function of inlet Reynolds number and the inlet/surface Reynolds number ratio.

#### 4 Acknowledgments

This study was funded by the Turbomachinery Research Consortium under contract 32519-15190 and NASA Lewis Research Center under contract NAG-1434.

#### References

- Artiles, A., Walowit, J., and Shapiro, W., 1982, "Analysis of Hybrid Film Journal Bearings with Turbulence and Inertial Effects," *Advances in Computer Aided Bearing Design*, ASME Publication G00220, pp. 25-52.
- Baskharone, E. A., and Hensel, S. J., 1989, "A New Model for Leakage Prediction in Shrouded-Impeller Turbopumps," *ASME Journal of Fluids Engineering*, Vol. 111, pp. 118-123.
- Baskharone, E., and Hamed, A., 1981, "A New Approach in Cascade Flow Analysis Using the Finite Element," *AIAA Journal*, Vol. 19, No. 1, pp. 65-71.
- Bou-Said, B., and Chaomleffell, J. P., 1988, "Hybrid Journal Bearings, Theoretical and Experimental Results," ASME Paper 88-Trib-55.
- Braun, M. J., Choy, F. K., and Dong, Q., 1993, "The Effects of a Hydrostatic Pocket Aspect Ratio, Supply Orifice Position, and Attack Angle on Steady-State Flow Patterns, Pressure and Shear Characteristics," *ASME JOURNAL OF TRIBOLOGY*, Vol. 115, Oct., pp. 678-684.
- Chaomleffell, J. P., 1983, "Influence des forces d'inerties en lubrification hybride," These de Docteur Ingenieur, I.N.S.A. Lyon.
- Constantinescu, V. N., and Galetuse, S., 1975, "Pressure Drop Due to Inertia Forces in Step Bearings," ASME Paper 75-Lub-34.
- Constantinescu, V. N., 1959, "On Turbulent Lubrication," *Proceedings of the Inst. of Mechanical Engineers*, Vol. 173, No. 38, pp. 891-900.
- Elrod, H. G., and Ng, C. W., 1967, "A Theory for Turbulent Films and Its Application to Bearings," *ASME JOURNAL OF LUBRICATION TECHNOLOGY*, p. 346.
- Ettles, C. M. M., 1965, "Hydrodynamic Thrust Bearing Study," Ph.D. thesis, Mech. Eng. Dept., Imperial College, London, SW7 2BX.
- Fletcher, C. A. J., 1991, *Computational Techniques for Fluid Dynamics*, Volume 1, Springer-Verlag, Germany, Ch. 5.
- Franchek, N. M., and Childs, D., 1993, "Experimental Test Results for Four High-Speed, High-Pressure Orifice-Compensated Hybrid Bearings," STLE/ASME Tribology Conference, 92-Trib-24.
- Heckelman Jr., D. D., and Ettles, C. M., 1988, "Viscous and Inertial Pressure Effects at the Inlet to a Bearing Film," *Trib. Trans.*, Vol. 31, No. 1, pp. 1-5.
- Hill, D. L., and Baskharone, E. A., 1993, "A Monotone Streamline Upwind Method for Quadratic Finite Elements," *Int. J. Numer. Methods Fluids*, Vol. 17, No. 6, pp. 463-475.
- Hirs, G. G., 1973, "A Bulk Flow Theory for Turbulence in Lubricant Films," *ASME JOURNAL OF LUBRICATION TECHNOLOGY*, pp. 146-173.
- Hood, P., 1976, "Frontal Solution Program for Unsymmetric Matrices," *Int. J. Num. Meth. Engr.*, Vol. 10, No. 2, pp. 379-399.
- Huebner, K. H., and Thornton, E. A., 1982, *The Finite Element Method for Engineers*, Wiley, New York.
- Hughes, T. J. R., Taylor, J. A., and Levy, J. F., 1978, "High Reynolds Number Steady Incompressible Flows by a Finite Element Method," *Finite Elements in Fluids*, Vol. III, Wiley, pp. 55-72.
- Kurtin, K. A., Childs, D., San Andres, L., and Hale, K., 1993, "Experimental Versus Theoretical Characteristics of a High-Speed Hybrid (Combination Hydrostatic and Hydrodynamic) Bearing," *ASME JOURNAL OF TRIBOLOGY*, Vol. 115, pp. 160-169.
- Mori, A., Makino, T., and Mori, H., 1992, "Entry Flow and Pressure Jump in Submerged Multi-Pad Bearings and Grooved Bearings," *ASME JOURNAL OF TRIBOLOGY*, Vol. 114, pp. 370-377.
- Nelson, C. C., and Nguyen, D. T., 1987, "Comparison of Hirs' Equation With Moody's Equation for Determining Rotordynamic Coefficients of Annular Pressure Seals," *ASME JOURNAL OF LUBRICATION TECHNOLOGY*, Vol. 109, pp. 144-148.
- Ng, C. W., and Pan, C. H. T., 1965, "A Linearized Turbulent Theory," *ASME Journal of Basic Engineering*, Vol. 87, p. 675.
- Pan, C. H. T., 1974, "Calculation of Pressure, Shear, and Flow in Lubrication Films for High Speed Bearings," *ASME JOURNAL OF LUBRICATION TECHNOLOGY*, Vol. 96, No. 1, pp. 80-94.
- Patankar, S. V., 1980, *Numerical Heat Transfer and Fluid Flow*, McGraw-Hill, New York.
- San Andres, L., and Velthuis, J. F. M., 1992, "Laminar Flow in a Recess of a Hydrostatic Bearing," *Trib. Trans.*, Vol. 35, No. 4, pp. 738-744.
- San Andres, L., 1990, "Turbulent Hybrid Bearings with Fluid Inertia Effects," *ASME JOURNAL OF TRIBOLOGY*, Vol. 112, pp. 699-707.
- Schlichting, H., 1976, *Boundary-Layer Theory*, McGraw-Hill, New York, p. 92.
- Tipei, N., 1982, "Flow and Pressure Head at the Inlet of Narrow Passages Without Upstream Free Surface," *ASME JOURNAL OF LUBRICATION TECHNOLOGY*, Vol. 104, pp. 80-94.
- Van Doormaal, J. P., and Raithby, G. D., 1984, "Enhancements of the SIMPLE Method for Predicting Incompressible Fluid Flows," *Numerical Heat Transfer*, Vol. 7, pp. 147-163.
- White, F. M., 1974, *Viscous Fluid Flow*, McGraw-Hill, New York.
- Zienkiewicz, O. C., and Taylor, R. L., 1988, *The Finite Element Method, Vol. 1: Basic Formulation and Linear Problems*, McGraw-Hill, 4th edition, New York.

**10** "Turbulent Flow Foil Bearings for Cryogenic Applications", 1995, San Andres, L., ASME *Journal of Tribology*, Vol. 117, 1, pp. 185-195, (ASME Paper 94-TRIB-33).

# Turbulent Flow Foil Bearings for Cryogenic Applications<sup>1</sup>

**Luis San Andres**

Associate Professor,  
Mechanical Engineering Department,  
Texas A&M University,  
College Station, TX 77843

*Fluid film foil bearings are an innovative bearing technology proposed for rotor support in cryogenic turbomachinery. These bearings offer system life and rotor speeds currently unachievable with rolling element bearings alone. An isothermal analysis for the turbulent bulk-flow of a variable properties liquid in a foil bearing with a simple elastic matrix is introduced. Numerical predictions compare the static and dynamic force performance of a three pad foil bearing with a rigid surface bearing for a high speed application in liquid oxygen. The major advantages of the foil bearing are immediately apparent, namely linearity in the load versus eccentricity curve, uniform rotordynamic coefficients, and overall unsurpassed stability conditions. The effects of excitation frequency and the foil structural damping on the dynamic force coefficients are discussed.*

## Introduction

Process liquid lubricated bearings used as support elements in high performance turbomachinery can provide life and speeds currently unachievable with rolling element bearings alone. Fluid film bearings if properly designed offer radial stiffness, accuracy of positioning and good damping characteristics. Furthermore, process fluid bearings reduce the size and weight of machine components, consume less energy, and provide a safe alternative to comply with current and future environmental constraints. The current goal for aerospace applications is a reliable *fluid film bearing* technology for advanced turbopump designs.

*Fluid film foil bearings* are one of the innovative bearing technologies proposed to support cryogenic turbopumps (O'Connor, 1993). Bending-type gas foil bearings have been applied successfully in light weight, high speed rotating machinery for the past 20 years (Licht, 1973, Heshmat et al., 1982), and recent test have demonstrated the applicability of leaf-type foil bearings for cryogenic environments (Saville et al., 1991, Genge et al., 1993). The advantages of foil bearings include:

- (a) capability of operation at extreme temperatures, both cryogenic and large enough for conventional lubricants to survive.
- (b) ability to tolerate misalignment, manufacturing inaccuracies, thermal gradients and differential expansion of bearing components.
- (c) tolerance of contaminants and abrasive particles (Heshmat et al., 1983).

<sup>1</sup>This work was funded by grant NAG3-1434 from NASA Lewis Research Center, Project Thermohydrodynamic Analysis of Cryogenic Liquid Turbulent Flow Fluid Film Bearings.

Contributed by the Tribology Division of THE AMERICAN SOCIETY OF MECHANICAL ENGINEERS and presented at the ASME/STLE Tribology Conference, Maui, Hawaii, October 16-19, 1994. Manuscript received by the Tribology Division January 14, 1994; revised manuscript received June 27, 1994. Paper No. 94-Trib-33. Associate Technical Editor: K. Tønder.

Foil bearings operate on the hydrodynamic principle with load capacity dependent on the journal speed and effective film thickness. Their major advantage however comes from the foil resilience and inherent structural damping; and the underlying foil elastic matrix can be manipulated to provide a wide range of predetermined dynamic structural properties (Heshmat et al., 1983, Oh and Rhode, 1976). The effective stiffness of the foil fluid film bearing is typically low, and when in conjunction with a relatively rigid rotor, it results in rotordynamic operation at speeds well above two low rigid mode-critical speeds (Gu, 1988). In this manner, the auto-balancing principle of rotating structures spinning above their natural frequencies can be used to advantage. Certain types of gas foil bearings have very large damping coefficients (3,000 lb·s/in) at low frequencies with a demonstrated specific load capacity in excess of 0.69 MPa (100 psi), and virtually free of wear after prolonged periods of operation (Ku et al., 1993a, Heshmat, 1993). The innovations in foil bearing design and advances in surface coating materials have already brought a technological breakthrough since bearing applications which handle low viscosity fluids, such as air, hydrocarbon process gases and cryogens, do not offer near optimum viscous damping characteristics for satisfactory dynamic performance at all speeds. Foil bearings approach closely to the concept of a *SMART BEARING*, i.e., a self-adapting, low friction mechanical support element able to modify the entire rotor-bearing system frequency response by controlling its stiffness and suppressing critical speeds.

Wallowit and Anno (1973) and Ho and Rhode (1976) introduced the basic operating principles of bump-foil and leaf-foil bearings, respectively; and, determined approximate relationships for evaluation of the bearing compliance coefficient. Heshmat et al. (1983) first presented an analysis detailing the static performance of bump-foil bearings by solving the lubrication Reynolds equation with a film thickness coupled to the hydrodynamic pressure by a local elastic deformation



of the compliant foil structure. Extensive tests performed by Heshmat et al. (1982) have shown the superior load performance of air foil bearings for high speed applications. The advances on recent years have been most significant since the specific load from these bearings has almost doubled in the last 10 years (Heshmat, 1993).

Analytical tools for engineering design of foil bearings have lagged the rapid developments of the emerging foil bearing technology. Only recently, Ku et al. (1992a, b, 1993a, b) provided a lucid theoretical model for the mechanism of deformation of bump-foil strips and calculation of foil structural stiffness and equivalent viscous damping. The analysis includes the friction forces between top foil and bumps, housing and bumps, and the coupling forces to adjacent bumps. Measurements show that the foil structural stiffness increases with the applied static load and decreases with the amplitude of dynamic deformation. Tests at low frequencies also show equivalent values of viscous damping coefficients which are exceedingly large. A damping coefficient equal to 526 kN·s/m (3,000 lb·s/in) at 1 Hz is inferred from the experimental results for one test specimen (Ku, 1993a, b). The test data also reveals that the energy dissipation mechanism in a bump-foil strip is of structural type and amenable to be modeled with a simple complex stiffness  $[K(1+i\eta)]$  in terms of a loss coefficient ( $\eta$ ) (Craig, 1981). This loss factor depends on the type of surface coatings of the materials in relative motion. Typical values of  $\eta = 0.2$  to  $0.6$  appear to be appropriate for the foil strips tested. Note that the correct theoretical interpretation of the mechanism of energy dissipation in a foil bearing is most important to provide compatibility with its observed performance.

Carpino et al. (1991, 1993a, b) and Peng et al. (1993a, b) have introduced the fundamental analysis for elastically supported gas foil bearings operating in the laminar flow regime. The model considers a thin foil supported by an elastic foundation. Frictional effects due to the relative motion in the sub-foil structure are included with an equivalent viscous damping element or a dry-friction (Coulomb like) dissipation mechanism. The effects of foil membrane and bending stresses, and

journal misalignment have been analyzed in detail. For small amplitude journal motions about an equilibrium position, a perturbation analysis of the Reynolds equation coupled to the structural elastic model of the foil assembly determines zeroth and first-order equations to calculate the static and dynamic force performance of the foil bearing. Peng and Carpino first presented dynamic stiffness and damping coefficients for foil bearings, and chose to study those at frequencies synchronous with the journal rotational speed. The rotordynamic force coefficients in a compressible fluid film bearing further coupled to a flexible damped structure are known to be strong functions of the excitation frequency. This issue has not been explored in detail in the current literature. The elegant work of Carpino et al. brings fundamental understanding to a complicated problem. "In the absence of detailed measurements, analysis is essential to provide insight and quantitative support for the selection and design of these bearings in critical applications" (Carpino et al., 1993a).

Long-life cryogenic turbopumps require innovative fluid film bearing designs with predictable rotordynamic characteristics. The fluid flow in these bearings is inevitably turbulent since cryogenics have very small kinematic viscosity and the rotor operates at very high speeds with large pressurization. Typical circumferential flow Reynolds numbers ( $Re_c$ ) range from  $10^4$  to  $2 \cdot 10^5$ . Hydrostatic journal bearings (HJB) and damper bearings appear to be suitable candidates for load support due to their extreme accuracy in positioning, large direct stiffness and damping coefficients (San Andres, 1992, 1993). Scharrer and Henderson (1992a) detail the specifications and design of hydrostatic bearings for the STME fuel turbopump. HJBs are selected to provide maximum life and design flexibility at the minimum turbopump cost. Scharrer et al. (1992b) provide a similar study for the design of a damper bearing for the SSME HPOTP which acts both as a load support element and a wear ring seal, and replaces the duplex ball bearing which had been the primary life limiting component in the turbopump. Full scale testing of the new fluid film bearing shows improved pump vibration characteristics as compared to prior tests with

## Nomenclature

$a_c = \Delta P_*/K_f C$ , compliance coefficient	$K_{\delta\alpha\beta}, C_{\delta\alpha\beta}$ = moment stiffness and damping coefficients due to displacements [N, N s]
$c(z), C, \bar{c}$ = bearing clearance function [m], nominal clearance, $c(z)/C$	$K_{\delta\alpha\beta}, C_{\delta\alpha\beta}$ = force stiffness and damping coefficients due to rotations [N m, N m s]
$D$ = bearing diameter [m]	$K_{\alpha\delta\beta}, C_{\alpha\delta\beta}$ = force stiffness and damping coefficients due to rotations [N/rad, N s/rad]
$f_{J,B} = a_m \left[ 1 + \left( \frac{b_M}{R_{J,B}} \right)^{e_M} \right]; a_M = 0.0001375, b_M = 500,000, e_M = 1/3.00$	$L$ = bearing axial length [m]
turbulent friction factors at journal and bearing (smooth) surfaces	$M_X, M_Y$ = film moments (couples) around {X, Y} axes [N·m]
$F_X, F_Y$ = film forces along {X, Y} axes [N]	$N_{\text{foil}}$ = number of foils on bearing
$f_X, f_Y, -f_{\delta X}, -f_{\delta Y}$ = 1, 1, z, z, axial perturbation functions	$P, Pa$ = fluid pressure, ambient pressure [N/m <sup>2</sup> ]
$i = \sqrt{-1}$ , imaginary unit	$\Delta P_* = \mu_a \Omega (R/C)^2$ , characteristic pressure for hydrodynamic bearing
$h_0 = H_0/C$ , dimensionless zeroth-order film thickness	$p = (P - P_a)/\Delta P_*$ , dimensionless fluid film pressure
$h_1 = \Delta\alpha \{f_\alpha h_\alpha + \bar{w}_\alpha\}$ , perturbed film thickness	$p_X, p_Y, p_{\delta X}, p_{\delta Y}$ = dimensionless dynamic (first-order) pressures
$h_X, h_Y, h_{\delta X}, h_{\delta Y} = \cos \Theta, \sin \Theta, -\sin \Theta, -\cos \Theta$ , circumferential film thickness components	$R$ = journal radius [m]
$K_f$ = foil structural stiffness per unit area [Pa/m]	$Re_c = \rho_a \Omega \cdot C \cdot R / \mu_a$ , nominal circumferential flow Reynolds number
$K_{\alpha\beta}, C_{\alpha\beta}$ = force stiffness and damping coefficients due to displacements [N/m, Ns/m]	$Re_c^* = Re_c \cdot (C/R)$ , modified Reynolds number

ball bearings (Nolan et al., 1993). Fundamental transient operation tests for lift-off and touch-down operation in a liquid nitrogen HJB are given by Scharrer et al. (1991). The experimental results show early (and predictable) lift-off, unmeasurable wear of the bearing articles, and capability of the HJBs to survive (repeated) start transients with similar loads as those found in actual turbopumps. The start-up transient performance of an annular hydrostatic bearing in liquid oxygen is given by Scharrer et al. (1992c). The experimental results showed that the fluid bearing supported effectively the radial loads imposed and that lift-off speeds could be predicted accurately with state-of-the-art analytical tools. Measurements for the static and dynamic force characteristics of turbulent flow, water HJBs reproducing cryogenic operating conditions are given by Kurtin et al. (1993) and Franchek (1993). Test bearing articles with a roughened bearing surface and with angled injection show an impressive rotordynamic response with near absence of hydrodynamic whirl instability.

Leaf-type foil bearings have been tested successfully in cryogenic liquids under carefully controlled conditions (Gu, 1988; Saville et al., 1991; Genge et al., 1993; Gilbrech et al., 1993). The bearings demonstrated a load capacity over 1.38 MPa (200 psi) with system damping coefficients in excess of 7 KN·s/m (40 lb·s/in) and continued start-stop operation without signs of sustained wear. Rotordynamic force coefficients are yet to be measured in leaf-foil bearings. Furthermore, the lack of analysis capable of predicting the measured performance of these bearings constitutes a serious shortcoming for the selection, design and application of this technology to actual turbopump hardware.

Heshmat et al. (1991, 1992) provide a feasibility study for the application of bump-foil bearings to the HPOTP turbopump. The authors discuss the required bearing load capacity as a function of the operational speed (power level). Several foil journal geometries are then analyzed with performance predictions extrapolated from a numerical program strictly valid for rigid surface bearings. The flow conditions in the bearings are highly turbulent with large levels of energy dis-

sipation and thermal effects. Results from the work show that to satisfy the required load capacity (around 3,000 lbs), the journal needs to operate at exceedingly large eccentricities (99.9 percent of nominal clearance) in a bearing with a foil substructure of large stiffness per unit area ( $K_f = 89.7$  MPa/mm). Bump-foil bearings of a hydrostatic nature are then proposed as an alternative to cope with the large specific loads (above 350 psi) required in a LOX turbopump. Bump-foil bearings are yet to be tested under cryogenic conditions but their use for high speed gas applications shows a remarkable record (Heshmat, 1993).

The discussion above shows that significant progress in fluid film bearing technology has been made over the past few years in order to replace roller bearing elements as the sole means of support in current and future cryogenic turbopump configurations. However, detailed analysis related to the operating conditions and fluids of interest are still needed, along with experimental results to address the validity of the models devised. For cryogenic applications, the analysis need to account for flow turbulence, fluid inertia, heat flow transport and power dissipation, and most importantly, an adequate but simple representation of the bearing compliant elements (Walker, 1992).

The present paper introduces an analysis for the turbulent bulk-flow of a cryogenic liquid on a foil bearing. The bearing compliance is modeled as a simple elastic foundation where an axially averaged pressure is used to couple the flow field to the structural deformation (Carpino, et al., 1993b). The model advances the experimentally validated computational bulk-flow analysis developed earlier for prediction of the static and dynamic performance of turbulent flow annular seals and hydrostatic bearings (San Andres, 1992, 1993). The structural foil element model is too simple in recognition of the elegant work of Carpino and co-workers. The analysis does not intend to be formally complete, and its sole purpose is to aid in the understanding of the dynamic force response of turbulent flow foil bearings. An example for a three pad, liquid oxygen foil bearing is taken directly from the literature (Heshmat, 1991).

## Nomenclature (cont.)

$Re_s$	$= \rho_a \omega \cdot C^2 / \mu_a$ , nominal squeeze film Reynolds number
$R_J, R_B$	$= (\rho/\mu)H[U_\theta - \Omega \cdot R]^2 + U_z^2)^{1/2}$ , $(\rho/\mu)H[U_\theta^2 + U_z^2]^{1/2}$ , flow Reynolds numbers relative to journal and bearing surfaces
$T_*$	$=$ fluid mean operating temperature [°K]
$u_z, u_\theta$	$= (U_z, U_\theta)/\Omega R$ , dimensionless bulk-flow velocities in axial ( $z$ ) and circumferential ( $\theta$ ) directions
$w, \bar{w}$	$=$ foil elastic foundation deflection [m], $w/C$
$\{X, Y, Z\}$	$=$ inertial coordinate system
$z$	$= Z/R$ , dimensionless axial coordinate
$\beta$	$= (1/\rho)(\partial\rho/\partial P)$ , liquid compressibility coefficient [m <sup>2</sup> /N]
$\epsilon_X, \epsilon_Y$	$= (e_X, e_Y)/C$ , journal eccentricity ratios in $X$ and $Y$ directions
$\delta_X, \delta_Y$	$=$ journal axis angular rotations around $X, Y$ axes
$\Delta_{\epsilon X}, \Delta_{\epsilon Y}, \Delta_{\delta X}, \Delta_{\delta Y}$	$=$ dimensionless dynamic (perturbed) eccentricities and rotations
$\eta$	$=$ foil structural (hysteretic) loss factor
$\theta$	$=$ circumferential coordinate

$\Theta_{pi}, \Theta_i$	$=$ pad angular length, angular position of pad leading edge [rad]
$\kappa_z = \kappa_\theta$	$= 1/2(\kappa_J + \kappa_B)$ , turbulence shear factors in ( $z, \theta$ ) flow directions
$\kappa_J, \kappa_B$	$= f_J \cdot R_J, f_B \cdot R_B$ , turbulence shear parameters at journal and bearing surfaces
$\rho, \rho_a, \bar{\rho}$	$=$ fluid density [kg/m <sup>3</sup> ], characteristic density [kg/m <sup>3</sup> ], $\rho/\rho_a$ dimensionless density
$\mu, \mu_a, \bar{\mu}$	$=$ fluid viscosity [Ns/m <sup>2</sup> ], characteristic viscosity [Ns/m <sup>2</sup> ], $\mu/\mu_a$ dimensionless viscosity
$\Omega, \omega$	$=$ rotational speed of journal, excitation or whirl frequency [1/s]
$\sigma$	$= \omega/\Omega$ , ratio of excitation frequency to journal speed
$\tau$	$= \omega t$ , dimensionless time coordinate

## Subscripts

$z, \theta$	$=$ in direction of local axial and circumferential coordinates in plane of bearing [ $z, \theta$ ]
0	$=$ zeroth-order solution
$\alpha, \beta$	$=$ first-order solution for perturbations in ( $X, Y$ ) displacements and ( $\delta_X, \delta_Y$ ) rotations

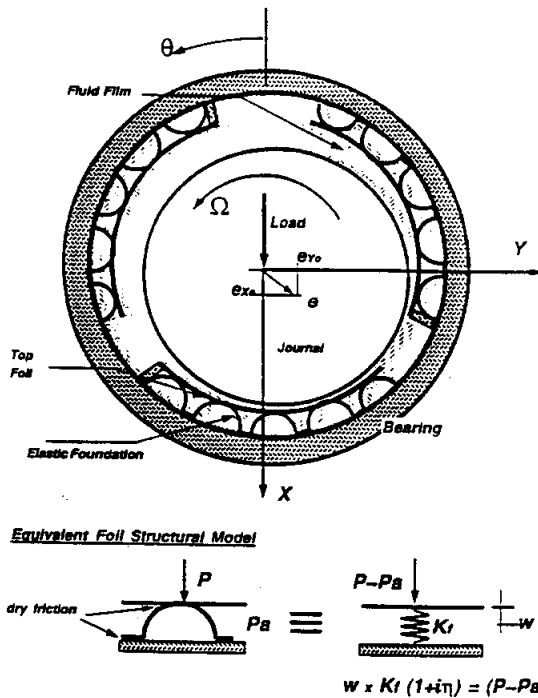


Fig. 1 Geometry of three-pad foil bearing

To the author it seems more appropriate to compare the dynamic performance of foil bearings to their rigid counterpart for the same applied external load, rather than to provide numerous data for identical journal eccentricities. Foil bearings by virtue of their inherent compliance have a substantially smaller load capacity than a rigid bearing of the same geometry operating at the same eccentricity. However, a foil bearing also provides a resilient structural support which adapts to the externally applied load in such a way that it reduces the undesirable cross-coupled stiffness coefficients and eliminates any potential half whirl instability. The predictions reveal the most important advantages of a foil bearing in terms of uniform force coefficients and increased damping values at low frequency excitations. The material presented helped the author to clarify his perspective on foil bearings, and allowed him to comprehend some of the relevant issues associated with foil bearing technology.

## Analysis

Consider the turbulent and isothermal bulk-flow of a variable properties fluid in the region between a rotating journal and a bearing surface of compliant characteristics. Figure 1 shows the geometry of a 3-pad foil-journal bearing, the coordinate systems and variables of interest. The fluid material properties are solely defined by the local pressure and a mean flow uniform temperature. The flow model ignores thermal effects on the flow field, although turbulent energy dissipation mechanisms may bring large temperature rises in the fluid and solids bounding the flow. This oversimplification is solely justified in terms of simplicity. Thermohydrodynamic models for cryogenic liquid annular seals and hydrostatic bearings are given by Yang et al. (1993a, b).

The bearing is constructed of a continuous thin foil supported on an elastic foundation whose local deflection depends only on the pressure at the point of application. Bending and membrane stresses on the foil are neglected for simplicity. A formally correct though more complex model for the foil and elastic foundation has been advanced by Carpino et al. (1993a).

The radial foil structural deflection ( $w$ ) is related to the local pressure by the equation:

$$w \cdot K_f = P - P_a \quad (1)$$

where  $K_f$  is the structural stiffness per unit area and  $P_a$  is the ambient pressure beneath the foil. Values of the structural stiffness range from 14.7 MPa/mm (54 Kpsi/in) for gas bearing applications to values around 133 MPa/mm (490 Kpsi/in) for high load applications like in a cryogenic turbopump (Heshmat, 1991).

Consider the motion of the journal as the superposition of small amplitude harmonic motions around an equilibrium static position. That is, the journal center displacements and journal axis rotations are expressed as

$$\begin{aligned} e_x(t) &= e_{x0} + \Delta e_x e^{i\omega t}, \quad e_y(t) = e_{y0} + \Delta e_y e^{i\omega t}; \\ \delta_x(t) &= \delta_{x0} + \Delta \delta_x e^{i\omega t}, \quad \delta_y(t) = \delta_{y0} + \Delta \delta_y e^{i\omega t} \end{aligned} \quad (2)$$

$$i = \sqrt{-1}$$

where  $\omega$  denotes the frequency of the whirl motion. The magnitudes of the dynamic perturbations in journal displacements and rotations,  $|\{\Delta e_x, \Delta e_y\}/C, \Delta \delta_x, \Delta \delta_y|$ , are very small (i.e.,  $\ll 1$ ). The film thickness ( $H$ ), flow field variables ( $U_z, U_\theta, P$ ), as well as the fluid properties ( $\rho, \mu$ ) and turbulent shear parameters are also formulated as the superposition of zeroth-order and first-order complex fields describing the static condition and the perturbed dynamic motion, respectively. In general, these fields are expressed as:

$$\begin{aligned} \psi &= \psi_0 + e^{i\tau} \{\Delta e_x \psi_x + \Delta e_y \psi_y + \Delta \delta_x (R/C) \psi_{\delta x} \\ &\quad + \Delta \delta_y (R/C) \psi_{\delta y}\} = \psi_0 + e^{i\tau} \Delta_\alpha \psi_\alpha \\ \alpha &= X, Y, \delta_x, \delta_y \end{aligned} \quad (3)$$

The film thickness is written in dimensionless form as:

$$h = H/C = h_0 + h_1 e^{i\omega t} \quad (4)$$

where

$$\begin{aligned} h_0 &= \bar{c}(z) + \{\epsilon_{x0} f_x + \delta_{y0} f_{\delta y} (R/C)_* \} \cos \theta \\ &\quad + \{\epsilon_{y0} f_y + \delta_{x0} f_{\delta x} (R/C)_* \} \sin \theta + \bar{w}_0 \end{aligned} \quad (5a)$$

and

$$\bar{w}_0 = a_c p_0, \quad \text{with } a_c = \Delta P_* / \{C \cdot K_f\} \quad (5b)$$

defined as the bearing compliance coefficient. And,

$$\begin{aligned} h_1 &= \Delta_\alpha \{f_\alpha h_\alpha + \bar{w}_\alpha\} = \Delta e_x [f_x \cos \theta + \bar{w}_x] + \Delta e_y [f_y \sin \theta + \bar{w}_y] \\ &\quad + \Delta \delta_x (R/C) [f_{\delta x} \sin \theta + \bar{w}_{\delta x}] + \Delta \delta_y (R/C) [f_{\delta y} \cos \theta + \bar{w}_{\delta y}] \end{aligned} \quad (6a)$$

with

$$\bar{w}_\alpha = \frac{a_c}{1 + i\eta} \cdot p_\alpha \quad (6b)$$

For harmonic motions, the foil structure has been modeled as a complex structural stiffness with  $\eta$  as a loss-factor denoting hysteretical damping (Craig, 1981). The rationale for the formulation presented is based on the experimental results presented by Ku (1993a, b) which show bump-foil bearings to provide a damping like action in terms of a pure dry-friction mechanism.

The perturbed film thickness functions in the axial and circumferential directions are given by:

$$\begin{aligned} f_x &= f_y = 1; \quad -f_{\delta x} = f_{\delta y} = z \\ h_x &= h_{\delta y} = \cos \theta; \quad h_y = h_{\delta x} = \sin \theta \end{aligned} \quad (7)$$

The functions defined in Eqs. (3-7) greatly facilitate the comprehension of the perturbed flow field equations and the re-

sulting rotordynamic force and moment coefficients given latter.

Turbulent bulk-flow continuity and momentum equations for thin film bearing geometries have been given elsewhere (San Andres, 1992). For the present foil bearing model, the zeroth- and first-order equations governing the flow for the steady-state or equilibrium journal position, and the perturbed flow for the small amplitude dynamic journal motions are:

#### Zeroth-Order Dimensionless Equations.

$$\frac{\partial}{\partial z} (\bar{\rho}_o h_o u_{zo}) + \frac{\partial}{\partial \theta} (\bar{\rho}_o h_o u_{\theta o}) = 0 \quad (8)$$

$$-h_o \frac{\partial p_o}{\partial z} = \frac{\bar{\mu}_o}{h_o} \left\{ k_{zo} u_{zo} \right\} + \text{Re}_c^* \left\{ \frac{\partial}{\partial z} (\bar{\rho}_o h_o u_{zo} u_{zo}) + \frac{\partial}{\partial \theta} (\bar{\rho}_o h_o u_{zo} u_{\theta o}) \right\} \quad (9)$$

$$-h_o \frac{\partial p_o}{\partial \theta} = \frac{\bar{\mu}_o}{h_o} \left\{ k_{\theta o} u_{\theta o} - \frac{1}{2} k_f \right\} + \text{Re}_c^* \left\{ \frac{\partial}{\partial z} (\bar{\rho}_o h_o u_{\theta o} u_{zo}) + \frac{\partial}{\partial \theta} (\bar{\rho}_o h_o u_{\theta o} u_{\theta o}) \right\} \quad (10)$$

where  $\text{Re}_c^* = \rho \Omega C^2 / \mu$  is the modified circumferential flow Reynolds number. Please refer to the Nomenclature for definition of all dimensionless variables in Eqs. (8-10). The fluid properties are functions of its local thermophysical state, i.e.,  $\rho_o = \rho_o(p_o, T_*)$ ,  $\mu_o = \mu_o(p_o, T_*)$ .

**First-Order Dimensionless Equations.** The first-order motion equations for perturbations in the film thickness due to journal displacements ( $\Delta e_x, \Delta e_y$ ) and rotations ( $\Delta \delta_x, \Delta \delta_y$ ) can be expressed in the single form:

$$i \cdot \sigma \bar{\rho}_o \left\{ [\bar{\beta}_\alpha h_o + a_c / (1 + i\eta)] p_\alpha + f_\alpha h_\alpha \right\} + \frac{\partial}{\partial z} \bar{\rho}_o \left\{ [\bar{\beta}_\alpha h_o + a_c / (1 + i\eta)] u_{zo} \cdot p_\alpha + f_\alpha h_\alpha u_{zo} + h_o u_{z\alpha} \right\} + \frac{\partial}{\partial \theta} \bar{\rho}_o \left\{ [\bar{\beta}_\alpha h_o + a_c / (1 + i\eta)] u_{\theta o} \cdot p_\alpha + f_\alpha h_\alpha u_{\theta o} + h_o u_{\theta\alpha} \right\} = 0 \quad (11)$$

$$-h_o \frac{\partial p_\alpha}{\partial z} = \{ \gamma_{zx} + i \cdot \text{Re}_s \bar{\rho}_o h_o \} u_{z\alpha} + \gamma_{z\theta} u_{\theta\alpha} + \gamma_{zh} f_\alpha \cdot h_\alpha + \gamma_{z\theta} p_\alpha + \text{Re}_c^* \left\{ \frac{\partial}{\partial z} (\bar{\rho}_o h_o u_{zo} u_{z\alpha}) + \frac{\partial}{\partial \theta} (\bar{\rho}_o h_o u_{\theta o} u_{z\alpha}) + \bar{\rho}_o h_o \left[ u_{z\alpha} \frac{\partial u_{zo}}{\partial z} + u_{\theta\alpha} \frac{\partial u_{zo}}{\partial \theta} \right] \right\} \quad (12)$$

$$-h_o \frac{\partial p_\alpha}{\partial \theta} = \{ \gamma_{\theta\theta} + i \cdot \text{Re}_s \bar{\rho}_o h_o \} u_{\theta\alpha} + \gamma_{\theta z} u_{z\alpha} + \gamma_{\theta h} f_\alpha \cdot h_\alpha + \gamma_{\theta\theta} p_\alpha + \text{Re}_c^* \left\{ \frac{\partial}{\partial z} (\bar{\rho}_o h_o u_{zo} u_{\theta\alpha}) + \frac{\partial}{\partial \theta} (\bar{\rho}_o h_o u_{\theta o} u_{\theta\alpha}) + \bar{\rho}_o h_o \left[ u_{z\alpha} \frac{\partial u_{\theta o}}{\partial z} + u_{\theta\alpha} \frac{\partial u_{\theta o}}{\partial \theta} \right] \right\} \quad (13)$$

where

$$\gamma_{z\theta} = \gamma_{zh} \cdot a_c / (1 + i\eta) + \gamma_{z\theta} \partial \bar{\rho} / \partial p|_o + \gamma_{z\mu} \partial \bar{\mu} / \partial p|_o$$

$$\gamma_{\theta\theta} = \gamma_{\theta h} \cdot a_c / (1 + i\eta) + \gamma_{\theta\theta} \partial \bar{\rho} / \partial p|_o + \gamma_{\theta\mu} \partial \bar{\mu} / \partial p|_o \quad (14)$$

and

$$\bar{\beta}_\alpha = (1/\bar{\rho}_o) (\partial \bar{\rho} / \partial p)|_o \quad (15)$$

is a dimensionless fluid compressibility factor at the film lands. In the equations above ( $h_\alpha \cdot f_\alpha$ ) correspond to the perturbation fields in film thickness as defined by Eqs. (6). The coefficients  $\gamma_{ij}$ 's arise from perturbation of the shear stress factors  $k_z, k_\theta$ ,

and  $k_f$ , and their explicit formulae are detailed by San Andres (1992). Equations (8) to (13) reduce to those provided to Peng et al. (1993b) if the flow is regarded as laminar and inertialess.

**Boundary Conditions.** At the foil discharge planes, and leading and trailing edge lines, the zeroth-order dimensionless exit pressure takes the value of the ambient pressure:

$$p_o(\theta, L/2) = p_o(\theta, -L/2) = p_o(\theta_i, z) = p_o(\theta_i + \theta_{pi}, z) = p_a = 0 \quad (16)$$

A value of dynamic pressure ( $p_\alpha$ ) equal to zero is imposed at all locations where time invariant pressures are specified. Across the foil leading edge,  $-L/2 \leq z \leq L/2$ , the flow is regarded as parallel to the foil pad, i.e.,

$$u_{zo}, u_{z\alpha}(z, \theta_i) = 0 \quad (17)$$

Although subambient pressures do not normally occur since the foil lifts off the foundation, no mechanism is provided on this simple model.

**Fluid Film Forces, Moments, and Dynamic Coefficients.** Fluid film forces and moments on each foil are calculated by integration of the zeroth-order pressure field on the journal surface. Total forces and moments are then obtained by direct addition of the individual foil components:

$$F_{\alpha o} = \sum_{i=1}^{N_{\text{foil}}} \Delta P_\alpha \cdot R^2 \cdot \int_{-L/D}^{L/D} \int_{\theta_i}^{\theta_i + \theta_{pi}} P_o \cdot h_\alpha dz \cdot d\theta; \quad \alpha = X, Y \quad (18)$$

$$M_{\alpha o} = \sum_{i=1}^{N_{\text{foil}}} \Delta P_\alpha \cdot R^3 \cdot \int_{-L/D}^{L/D} \int_{\theta_i}^{\theta_i + \theta_{pi}} P_o \cdot f_\alpha \cdot h_\alpha dz \cdot d\theta; \quad \alpha = \delta X, \delta Y \quad (19)^2$$

The perturbation analysis allows the dynamic force and moment coefficients due to journal center displacements and journal axis rotations to be obtained from the general expressions:

force/displacement coefficients:

$$K_{\alpha\beta} + i\omega \cdot C_{\alpha\beta} = -\frac{\Delta P_\alpha \cdot R^2}{C} \sum_{i=1}^{N_{\text{foil}}} \int_{-L/D}^{L/D} \int_{\theta_i}^{\theta_i + \theta_{pi}} P_\beta f_\alpha \cdot h_\alpha dz \cdot d\theta \quad \alpha, \beta = X, Y \quad (20)$$

force/rotation coefficients:

$$K_{\alpha\delta\beta} + i\omega \cdot C_{\alpha\delta\beta} = -\frac{\Delta P_\alpha \cdot R^3}{C} \sum_{i=1}^{N_{\text{foil}}} \int_{-L/D}^{L/D} \int_{\theta_i}^{\theta_i + \theta_{pi}} P_{\delta\beta} f_\alpha \cdot h_\alpha dz \cdot d\theta \quad \alpha = X, Y; \quad \delta_\beta = \delta X, \delta Y \quad (21)$$

moment/displacement coefficients:

$$K_{\delta\alpha\beta} + i\omega \cdot C_{\delta\alpha\beta} = -\frac{\Delta P_\alpha \cdot R^3}{C} \sum_{i=1}^{N_{\text{foil}}} \int_{-L/D}^{L/D} \int_{\theta_i}^{\theta_i + \theta_{pi}} P_\beta f_{\delta\alpha} h_{\delta\alpha} dz \cdot d\theta \quad \beta = X, Y; \quad \delta_\alpha = \delta X, \delta Y \quad (22)$$

moment/rotation coefficients:

$$K_{\delta\alpha\delta\beta} + i\omega \cdot C_{\delta\alpha\delta\beta} = -\frac{\Delta P_\alpha \cdot R^4}{C} \sum_{i=1}^{N_{\text{foil}}} \int_{-L/D}^{L/D} \int_{\theta_i}^{\theta_i + \theta_{pi}} P_{\delta\beta} f_{\delta\alpha} h_{\delta\alpha} dz \cdot d\theta \quad \delta_\beta, \delta_\alpha = \delta X, \delta Y \quad (23)$$

<sup>2</sup>For a general axial clearance function and journal axis rotations, the pressure field is not symmetric about the bearing midplane; and consequently fluid restoring moments arise.

The dynamic stiffness and damping coefficients are frequency dependent due to fluid inertia, fluid compressibility and the flexibility of the structural bearing element.

**The Numerical Solution Procedure.** San Andres (1992) discusses the SIMPLEC procedure for the numerical solution of the nonlinear flow equations. The differential equations of motion are integrated on staggered control volumes for each primitive variable, and a procedure to solve the algebraic flow equations along constant value axial lines is implemented from the literature (Lauder and Leschziner, 1978). The material


properties for cryogenic liquids are determined from 32-term state equations as given by McCarty (1986). The computer program is relatively fast although the algorithm can not handle foil bearings with a large compliance coefficient. In general, a compliance coefficient  $a_c$  of the same order of magnitude as the dimensionless pressure (typically of order one) causes the program to diverge and provide erroneous results. These cases are fortunately of no practical value for cryogenic liquid usages. These applications typically demand a specific load greater than 1.34 MPa (200 psi) which is not attainable with soft compliant elements.

Calculations for a gas foil bearing from Peng et al. (1993a) were performed to check the validity of the program developed. For increasing values of the compliance coefficient ( $a_c$ ) and at various eccentricity conditions, the predictions for load capacity and synchronous force coefficients from the present analysis are virtually identical to those given by Peng et al. However, the predicted stiffness coefficients at zero whirl frequency are similar to those reported by Heshmat et al. (1983). The test case then indicated the importance of frequency on the evaluation of the dynamic force coefficients in foil bearings.

## Results and Discussion

The analysis intends to provide insight into the static and dynamic force performance of foil bearings in a cryogenic application. Table 1 presents the geometry and operating characteristic of a three pad foil bearing for use in liquid oxygen.

**Table 1 Three pad foil journal bearing for a cryogenic application**

	Journal Diameter $D$ : 88.90 mm (3.5 in)
	Bearing Length $L$ : 57.15 mm (2.25 in), $L/D=0.643$
	Nominal clearance $C$ : 38.1 $\mu\text{m}$ (0.0015 in), $R/C=1,166$
	Pad extent: $\phi = 115$ deg, $l=1.2, 3$
	Rotational speed, $\Omega$ : 3,123.8 rad/s (29,830 RPM)
	Ambient Pressure, $P_a$ : 5.51 MPa (800 psi) at $T^* = 95$ K (171 R)
	Fluid: Liquid Oxygen at ( $P_a, T^*$ ):
	Density $\rho = 1,129$ kg/m <sup>3</sup> , viscosity $\mu = 183.23 \text{ E-}06$ Pa-s
	Characteristic Pressure $\Delta P^* = \mu \Omega (R/C)^2 = 0.778$ MPa (113 psi)
	Foil structural stiffness $K_f = 89.7$ GPa/m (330,332 psi/in)
	Compliance coefficient $a_c = \Delta P^* / (K_f C) = 0.2280$
	Shear flow Reynolds Number $Re_c = (\rho \mu) \Omega R C = 32,616$
	Squeeze Reynolds Number $Re_s = Re_c / C = 28$ at $\omega = \Omega$
	Foil bearing geometry and operating conditions based on Heshmat (1991).

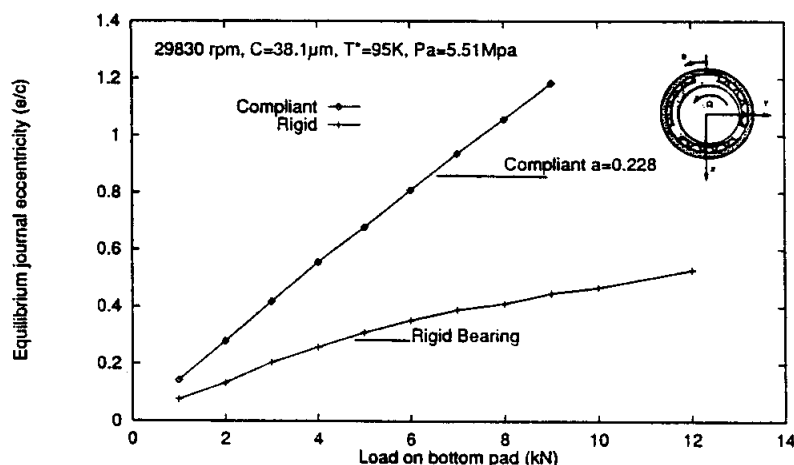


**Fig. 2(a) Equilibrium eccentricity versus applied load for LO<sub>2</sub> three pad compliant and rigid bearings**

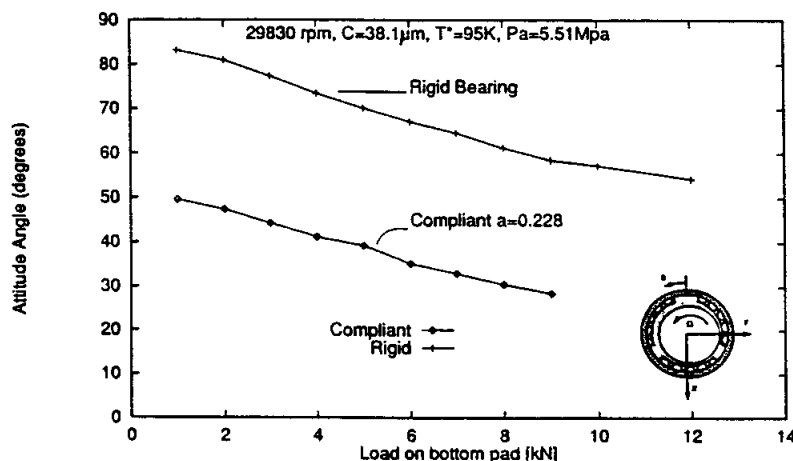


**Fig. 2(b) Attitude angle vs. applied load for LO<sub>2</sub> three pad compliant and rigid bearings**

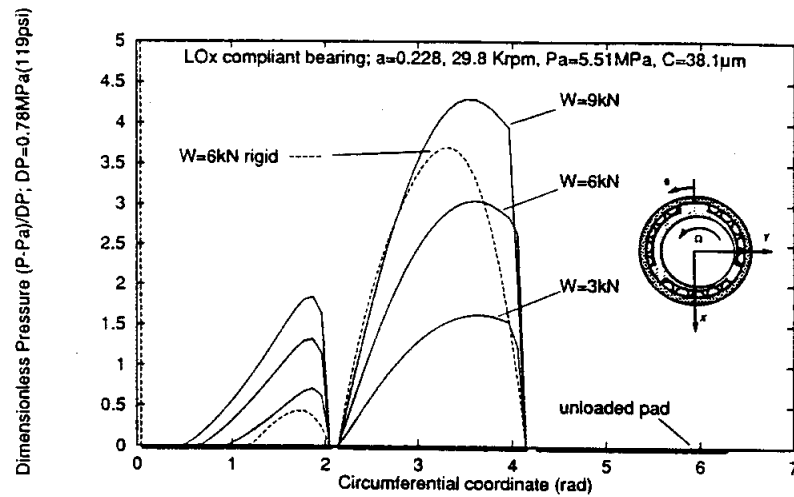


Fig. 3 Dimensionless centerline pressure for compliant bearing and increasing values of applied load

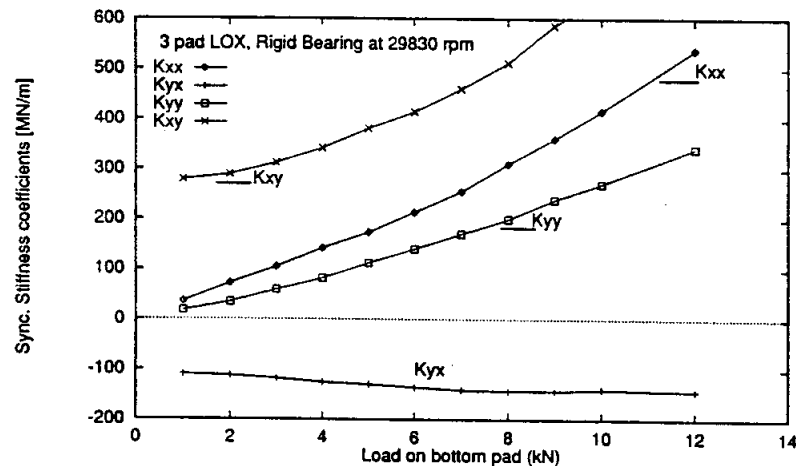


Fig. 4(a) Stiffness coefficients for rigid bearing versus applied load

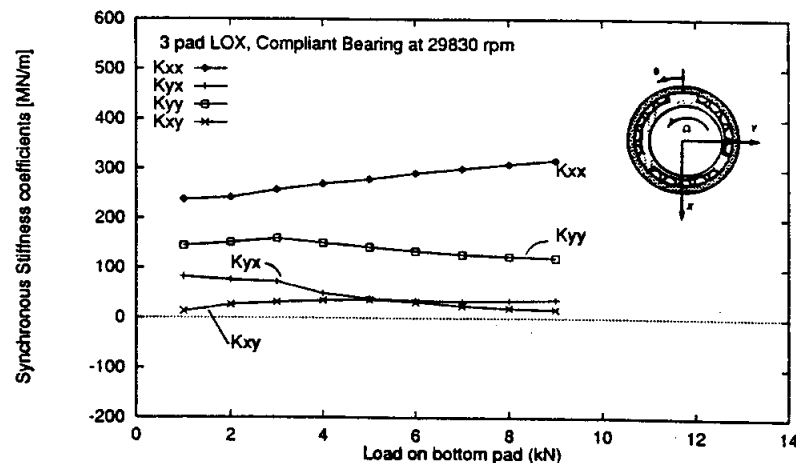


Fig. 4(b) Stiffness coefficients for compliant bearing versus applied load. Synchronous excitation. Compliance  $a_c=0.228$ , loss factor  $\eta=0.0$ .

The bearing data has been taken directly from Heshmat et al. (1991). Note that the foil structural stiffness ( $K_f$ ) is rather large (compliance coefficient  $a_c$  small) in order to provide enough load capacity for the application. Also, the circumferential flow Reynolds number  $Re_c$  is equal to 32,616 at nominal conditions and shows a flow field bearing dominated by turbulence effects. The static and dynamic force performance of the foil

bearing is compared to an identical three pad bearing of fixed geometry with rigid surface, ( $a_c=0$ ).

Figure 2 shows the equilibrium journal eccentricity ( $e/c$ ) and load attitude angle vs. an applied static load along the  $X$  axis (directed towards the bottom pad). The figure shows that the foil-bearing has smaller load capacity than the rigid bearing. However, two distinct features of the compliant bearing are

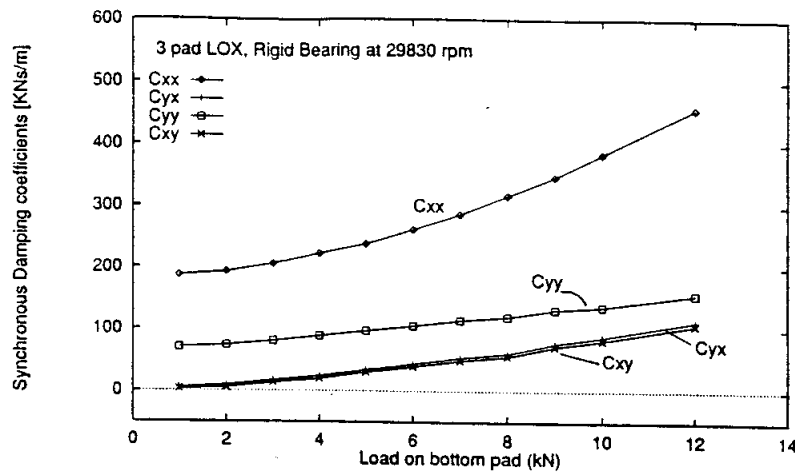


Fig. 5(a) Damping coefficients for rigid bearing versus applied load

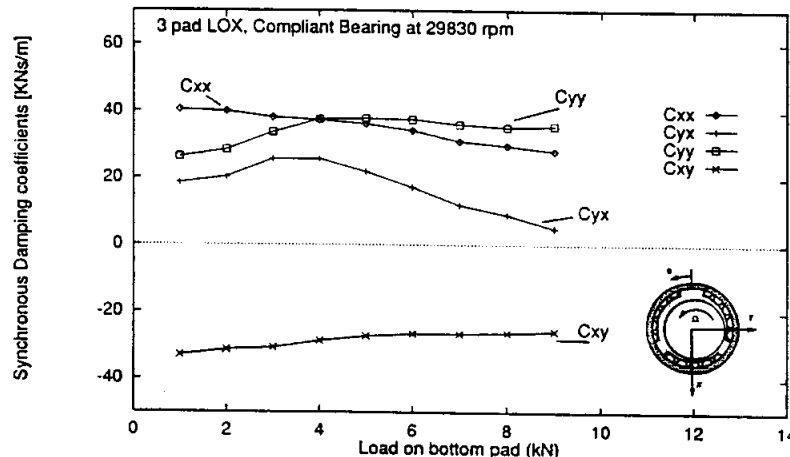


Fig. 5(b) Damping coefficients for compliant bearing versus applied load. Synchronous excitation. Compliance  $a_c = 0.228$ , loss factor  $\eta = 0.0$

evident. First, the foil-bearing shows a linear load—journal displacement behavior with a uniform load stiffness of about  $190 \text{ MN/m}$  ( $1.08 \times 10^6 \text{ lb/in}$ ), and second, the attitude angle is about half that of the rigid bearing. These two features alone explain why foil bearings are so attractive as light load supports in high speed turbomachinery. The largest load capacity of the foil bearing is slightly over  $9000 \text{ N}$  with the journal operating well above the nominal clearance. The maximum specific load ( $W/LD$ ) calculated is then equal to  $1.77 \text{ MPa}$  ( $257 \text{ psi}$ ). The linearity of the load vs. journal displacement curve has also been reported by Oh and Rhode (1976, 1977) for gas foil bearings. Figure 3 shows the centerline dimensionless pressure field for different applied loads. Note that the third foil is unloaded for all bearing loads. Figure 3 also shows the pressure for the rigid bearing at a load of  $6 \text{ kN}$  to have a larger peak value than the foil bearing.

Figures 4 and 5 show the dynamic stiffness and damping coefficients for the rigid (a) and foil (b) bearing versus the applied load. The force coefficients are calculated at an excitation frequency ( $\omega$ ) equal to the angular speed ( $\Omega = 3,123 \text{ rad/s}$ ). The coefficients for the foil bearing have been evaluated for  $\eta = 0$ , i.e., with null structural damping at the elastic foundation. The cross-coupled stiffness coefficients ( $K_{xy}$ ,  $K_{yx}$ ) for the rigid bearing are of large magnitude and opposite in sign, while for the foil bearing the cross-stiffnesses are small without skew symmetry. The damping coefficients for the foil bearing are about an order of magnitude smaller than the coefficients for the rigid bearing, in particular the direct coef-

ficients. However, the magnitude of the force coefficients is meaningless unless these are related to the dynamics of a rotor-bearing system. In the literature, along with the bearing force coefficients it is customary to quote also the whirl frequency ratio (WFR), or stability indicator, and the critical mass needed to initiate dynamic instability at the speed of operation with a whirl frequency equal to a fraction of the rotor speed. The whirl frequency usually corresponds to the rotor-bearing system first critical speed. The fundamentals for the simple stability analysis of a rigid rotor supported on fluid film bearings are given by Lund (1965). For the rigid bearing, the calculated whirl frequency ratio is close to  $0.50$  for all loads. On the other hand, the foil bearing shows a zero WFR value and is able to provide stable dynamic behavior at all loads. The critical mass of the rigid bearing rises from a low value of  $7.55 \text{ kg}$  at  $1 \text{ kN}$  load to a value equal to  $126 \text{ kg}$  at a load of  $12 \text{ kN}$ . It is well known that for very small loads, a rigid bearing of fixed geometry provides essentially no stability since its equivalent stiffness is almost null in spite of the large values of its rotordynamic coefficients. The foil bearings on the other hand provide adequate rotordynamic stability although the force coefficients appear to be low. This unique stabilizing feature of the foil bearing derives from the ability of its compliant surface to adapt to the applied load. The mechanism of stability is then very similar to that of a tilting-pad bearing.

The effects of excitation frequency on the force coefficients are discussed next. Figures 6 to 9 show for the load condition of  $6 \text{ kN}$ , the stiffness and damping coefficients as the excitation

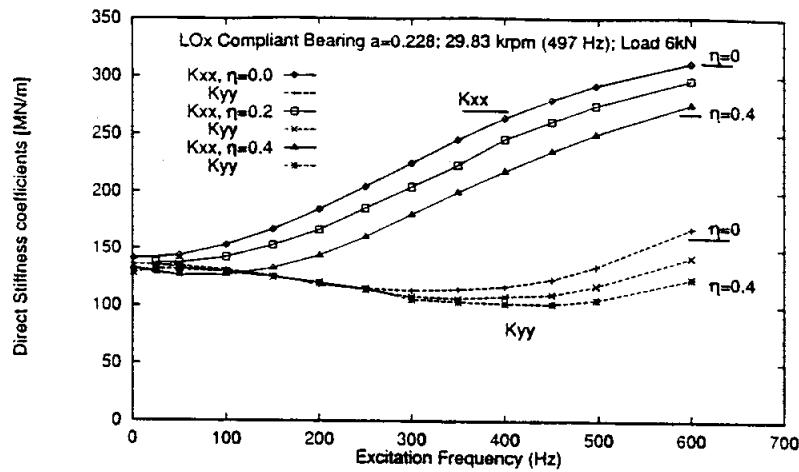


Fig. 6 Direct stiffness coefficients versus excitation frequency. Loss coefficient ( $\eta$ ) varies from 0.0 to 0.40.

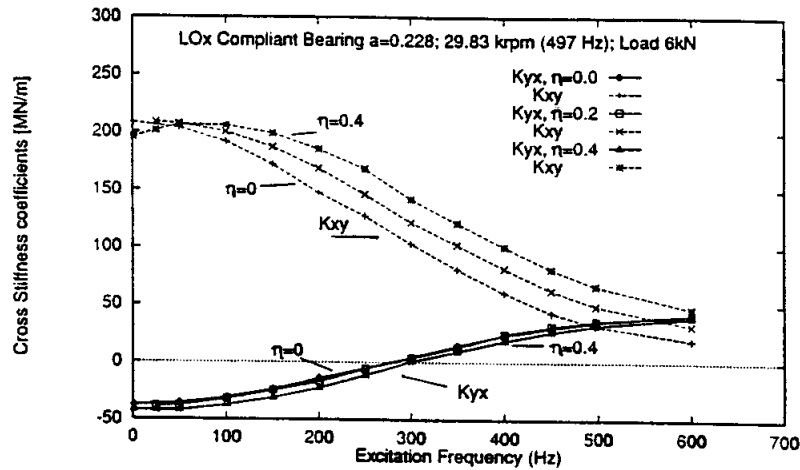


Fig. 7 Cross coupled stiffness coefficients versus excitation frequency. Loss coefficient ( $\eta$ ) varies from 0.0 to 0.40.

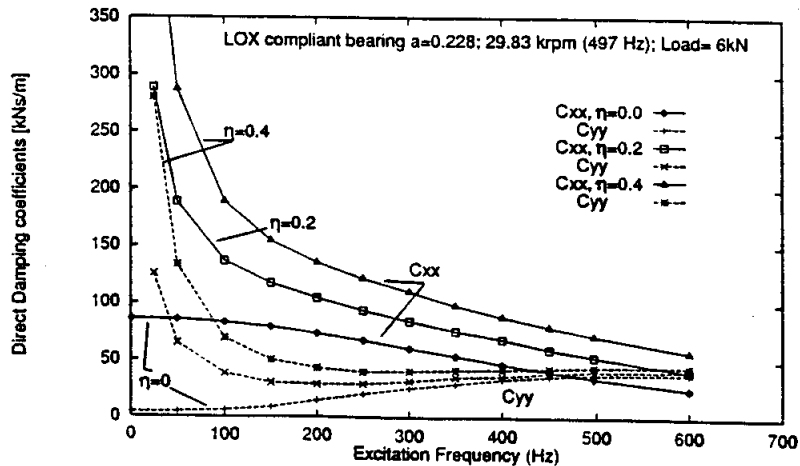


Fig. 8 Direct damping coefficients versus excitation frequency. Loss coefficient ( $\eta$ ) varies from 0.0 to 0.40.

frequency increases from 0 to 600 Hz and for three values of the structural damping factor ( $\eta = 0, 0.2, 0.4$ ). Ku (1992a-b) reports experimental values of the loss coefficient as large as 0.6. Synchronous excitation ( $\omega = \Omega$ ) corresponds in the figures to a value of frequency very close to 500 Hz. The force coefficients show a strong dependency on frequency since they represent the combined (series like) action of the fluid film

and elastic foundation. The structural loss factor ( $\eta$ ) is shown to reduce the direct stiffness coefficients ( $K_{xx}, K_{yy}$ ) while increasing the cross-stiffness  $K_{xy}$ . Note that at low frequencies the dynamic behavior is dominated by the cross coupled stiffnesses, while at large frequencies the direct stiffness play a major role. Most important is the shift in sign of the cross-stiffness coefficient  $K_{yx}$  at about 60 percent of the synchron-



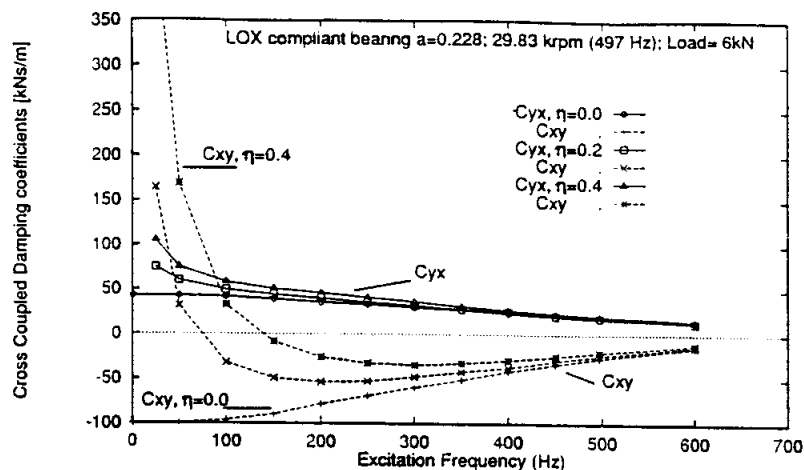


Fig. 9 Cross coupled damping coefficients versus excitation frequency. Loss coefficient ( $\eta$ ) varies from 0.0 to 0.40

Table 2 Performance of three pad foil bearing for speed dependent loads. Load along X axis (toward middle of bottom pad).

Speed (krpm)	Load kN	e/c	attitude angle(°)	Torque N-m	Power kWatts	Re <sub>c</sub>
12.0	0.85	0.286	55.25	1.17	2.72	13,120
19.0	2.60	0.505	42.50	4.82	9.59	20,773
24.3	3.50	0.542	41.00	7.38	18.77	26,604
29.8	9.00	1.183	28.42	11.03	34.42	32,614

Synchronous force coefficients without structural damping ( $\eta=0$ )									
Speed (krpm)	$K_{XX}$ MN/m	$K_{YY}$ MN/m	$K_{TT}$	$K_{XY}$	$C_{XX}$	$C_{YY}$ kNs/m	$C_{TT}$	$C_{XY}$	WFR
12.0	82.44	-10.24	39.73	64.08	92.28	25.46	44.84	-16.67	0.29
19.0	220.90	20.91	82.95	49.79	55.17	19.62	40.26	-36.14	0.00
24.3	243.70	20.58	118.10	48.00	45.62	23.04	41.93	-31.11	0.00
29.8	318.80	36.34	121.00	16.88	28.13	4.99	35.65	-25.74	0.00

ous frequency. The rigid bearing shows on the other hand direct stiffness coefficients steadily decreasing with frequency due to inertia effects, while the cross-coupled coefficients remain almost invariant and have opposite signs.

Figures 8 and 9 show the direct ( $C_{XX}$ ,  $C_{YY}$ ) and cross-coupled ( $C_{XY}$ ,  $C_{YX}$ ) damping coefficients versus frequency for increasing values of the structural loss factor ( $\eta$ ). The profound effect of the structural damping on the bearing damping coefficients at low frequencies is immediately evident. Theoretically these should be infinite at zero frequency. The results explain the very large damping coefficients determined from dynamic loading at low frequencies as given by Ku (1993a-b) for a test bump-foil strip. The effects of the structural foil damping is minimal at high frequencies except for the direct damping coefficient  $C_{XX}$ . The fact that the damping coefficients are small at large frequencies and not influenced by the hysteretic damping is not necessarily a shortcoming of the foil bearing. It would actually be an advantage if the rotor bearing system is designed to operate well above its first rigid body critical speed. This happens by necessity since foil bearing have a smaller equivalent stiffness than a rigid bearing. In practice, rotors supported in foil bearings operate at speeds which exceed two or more times the system critical speed (Gu, 1988), and the force coefficients at the resonant frequency are of utmost importance. For dynamic excitation at frequencies close to system resonance but well below the synchronous frequency ( $\omega = \Omega$ ), the results show that the foil bearing provides very large damping coefficients. Thus, the foil bearing ability to dissipate undesirable vibration energy is enhanced by the mechanism of structural damping at low frequencies, and thus it provides controllable rotordynamic characteristics for good dynamic operation.

The study also included the determination of the foil bearing force response for rotor speed dependent loads as found in a typical cryogenic turbopump. Table 2 presents a summary of

the results for the synchronous force coefficients without the effect of the structural loss factor ( $\eta=0$ ). It is noted that at the lowest rotational speed, 12,000 rpm, the foil bearing has a definite whirl frequency ratio, WFR = 0.294, but still lower than that of a rigid bearing. Results for the fixed geometry bearing are omitted for brevity. It is imperative to note that both the foil and rigid bearings provide essentially the same torque and power induced by fluid shear. The results show the drag power to be exceedingly large at the highest speed. This drag power needs to be conveyed to and carried away by the fluid with a consequent temperature rise. The present analysis for foil bearings is not able yet to include thermal effects or the transport of energy within the fluid film bearing.

San Andres et al. (1994) have also developed a thermohydrodynamic (THD) analysis for cryogenic fluid film bearings of fixed geometry. For the rigid bearing with adiabatic flow conditions, the THD model predicts a temperature rise of the fluid equal to 55°K (99°K) with a mean fluid temperature of approximately 130°K. The calculations show a modest decrease in load capacity (about 2 percent) when compared to the isothermal model of this paper. The dynamic force coefficients show a greater percent wise variation (about 20 percent). Further discussion on this issue is out of the scope of the present work. However, the thermal model results shows that the analysis of foil bearings with large turbulence effects and energy dissipation needs to be thermohydrodynamic in character. Thus the present results for the isothermal model are conservative and describe in a qualitative form the static and dynamic force performance of a compliant surface bearing.

## Conclusions

Foil fluid film bearings are regarded as a reliable alternative for rotor support in cryogenic turbomachinery. These bearings offer system life and rotor speeds currently unachievable with rolling element bearings alone. Significant advances have demonstrated the applicability of foil bearings for secondary power space turbopumps. However, detailed bearing analysis related to the operating conditions and liquids used in space propulsion have lagged the technological developments.

An isothermal analysis for the turbulent bulk-flow of a variable properties liquid in a foil bearing geometry with a simple elastic matrix is introduced. In the foil structure, hysteretic damping effects are included in the form of a complex dynamic stiffness. Numerical predictions compare the static and dynamic force performance of a three pad foil bearing with a rigid surface bearing for a high speed application in liquid oxygen. The foil bearing by virtue of its inherent compliance has a smaller load capacity than the rigid bearing. However, the foil bearing due to its structural resilience adapts to the

externally applied load in such a way that it reduces the undesirable cross-coupled stiffness coefficients, eliminates any potential half whirl instability, and offers enough damping to handle safely the dynamics of a rigid rotor bearing system. The computed predictions show the foil bearing to have a linear load vs. eccentricity relationship, with a profound effect of excitation frequency and structural damping factor on the stiffness and damping coefficients.

The foil bearing is shown to dissipate the same level of shear induced power as the rigid surface bearing. For a high speed fully turbulent operating condition the mechanical energy needs to be carried away by the fluid and it will cause a large temperature rise in the fluid film, journal and bearing. Thus, accurate design of hydrodynamic foil bearings will by necessity require a comprehensive thermohydrodynamic treatment. Such undertaking is now in progress.

## Acknowledgments

The present work has been funded by NASA grant NAG3-1434. Thanks are in order to Mr. James Walker of NASA Lewis Research Center for his support, interest on the subject, and strong desire to promote engineering design excellence by solving real problems.

## References

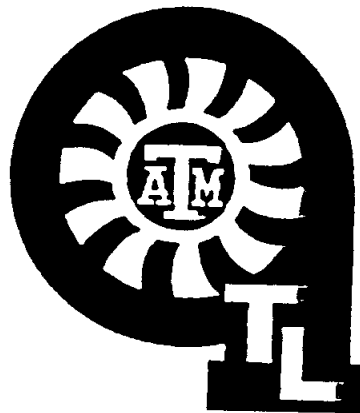
- Carpino, M., and Peng, J. P., 1991, "Theoretical Performance of Foil Journal Bearings," 27th AIAA/SAE/ASME Joint Conference, Sacramento, CA, Paper 91-2105.
- Carpino, M., Peng, J., and Medvetz, L., 1993a, "Misalignment in a Complete Shell Gas Foil Journal Bearings," accepted for publication at STLE Tribology Transactions.
- Carpino, M., Medvetz, L., and Peng, J., 1993b, "Effects of Membrane Stresses in the Prediction of Foil Bearing Performance," 48th STLE Annual Meeting, Calgary, CA, STLE Preprint 93-AM-2E-1.
- Craig, R., 1981, *Structural Dynamics*, John Wiley, pp. 101.
- Franchek, N., and Childs, D., 1993, "Experimental Test Results for Four High-Speed, High-Pressure Orifice-Compensated Hybrid Bearings," ASME Paper No. 93-Trib-34, STLE/ASME Tribology Conference, New Orleans, LA, Oct.
- Genge, G. G., Saville, M., and Gu, A., 1993, "Foil Bearing Performance in Liquid Nitrogen and Liquid Oxygen," AIAA/SAE/ASME/ASEE 29th Joint Propulsion Conference and Exhibit, Monterrey, CA, June, Paper AIAA-93-2536.
- Gilbrech, R., Gu, A., Rigney, T., Saville, M., Rossoni, M., 1993, "Liquid-Hydrogen Foil-Bearing Turbopump," AIAA/SAE/ASME/ASEE 29th Joint Propulsion Conference and Exhibit, Monterrey, CA, June, Paper AIAA-93-2537.
- Gu, A., 1988, "Process Fluid Foil Bearing Liquid Hydrogen Turbopump," AIAA/ASME/SAE/ASEE 24th Joint Propulsion Conference, Boston, Mass., Paper AA-88-3130.
- Heshmat, H., Shapiro, W., and Gray, S., 1982, "Development of Foil Journal Bearings for High Load Capacity and High Speed Whirl Stability," ASME JOURNAL OF LUBRICATION TECHNOLOGY, Vol. 104, pp. 149-156.
- Heshmat, H., Walowit, J. A., and Pinkus, O., 1983, "Analysis of Gas Lubricated Foil Journal Bearings," ASME JOURNAL OF LUBRICATION TECHNOLOGY, Vol. 105, pp. 647-655.
- Heshmat, H., 1991, "Investigation of Foil Bearings for Use in High-Thrust Liquid Rocket Engines," NASA CR-187099, April.
- Heshmat, H., Shapiro, W., and Artiles, A., 1992, "Application of Compliant Fluid-Film Bearings to the High-Pressure Oxygen Turbopump of the SSME," NASA Earth-To-Orbit Propulsion Conference, Huntsville, Alabama, May.
- Heshmat, H., 1993, "The Advancement in Performance of Aerodynamic Foil Journal Bearings: High Speed and Load Capability," presented at the STLE/ASME Tribology Conference, New Orleans, LA, Oct., ASME Paper 93-Trib-32.
- Ku, C-P. R., 1993a, "An Experimental and Theoretical Study of the Dynamic Structural Stiffness in Compliant Foil Journal Bearings," 14th Biennial Conference on Mechanical Vibration and Noise, Albuquerque, NM, Sept., DE-Vol. 63, *Vibration of Mechanical Systems and the History of Mechanical Design*, ASME 1993, pp. 83-88.
- Ku, C-P. R., 1993b, "Dynamic Structural Properties in Compliant Foil Thrust Bearings—Comparisons between Experimental and Theoretical Results," ASME Paper 93-Trib-10, ASME/STLE Joint Conference, Oct., New Orleans, LA.
- Ku, C-P. R., and Heshmat, H., 1992a, "Compliant Foil Bearing Structural Stiffness Analysis, Part I: Theoretical Model Including Strip and Variable Bump Foil Geometry," ASME JOURNAL OF TRIBOLOGY, Vol. 114, pp. 394-400.
- Ku, C-P. R., and Heshmat, H., 1992b, "Compliant Foil Bearing Structural Stiffness Analysis, Part II: Experimental Investigation," *Trans.*, ASME Paper 92-Trib-6.
- Ku, C-P. R., and Heshmat, H., 1993a, "Structural Stiffness and Coulomb Damping in Compliant Foil Journal Bearings: Theoretical Considerations," presented at the 48th STLE Annual Meeting, Calgary, CA, May.
- Ku, C-P. R., and Heshmat, H., 1993b, "Structural Stiffness and Coulomb Damping in Compliant Foil Journal Bearings: Parametric Studies," presented at the 48th STLE Annual Meeting, Calgary, CA, May.
- Kurtin, K., Childs, D., Hale, K., and San Andres, L., 1993, "Experimental vs. Theoretical Characteristics of a High Speed Hybrid Bearing," ASME JOURNAL OF TRIBOLOGY, Vol. 115, pp. 160-169.
- Lauder, B. E., and Leschziner, M., 1978, "Flow in Finite Width, Thrust Bearings Including Inertial Effects," ASME JOURNAL OF LUBRICATION TECHNOLOGY, Vol. 100, pp. 330-345.
- Licht, L., Branger, M., and Anderson, W. J., 1973, "Gas-Lubricated Bearings for High Speed Turboalternator—Construction and Performance," ASME Paper 73-Lub-5.
- Lund, J., 1965, "The Stability of an Elastic Rotor in Journal Bearings with Flexible Damped Supports," ASME JOURNAL OF APPLIED MECHANICS, pp. 911-925.
- McCarty, R. D., 1986, Thermophysical Properties of Fluids, MIPROPS 86, NBS Standard Reference Data Base 12, Thermophysics Division, Center for Chemical Engineering, National Bureau of Standards, Colorado.
- Nolan, S., Hibbs, R., and Genge, G., 1993, "Hotfire Testing of a SSME HPOTP with an Annular Hydrostatic Bearing," *Proceedings of the 7th Workshop on Rotordynamic Instability Problems in High Performance Turbomachinery*, Texas A&M University, May.
- O'Connor, Leo, 1993, "Fluid Film Foil Bearings Control Engine Heat," *Mechanical Engineering*, May, pp. 72-75.
- Oh, K. P., and Rhode, S. M., 1976, "A Theoretical Investigation of the Multileaf Journal Bearing," ASME JOURNAL OF APPLIED MECHANICS, pp. 237-242.
- Oh, K. P., and Rhode, S. M., 1977, "A Theoretical Analysis of a Compliant Shell Air Bearing," ASME JOURNAL OF LUBRICATION TECHNOLOGY, pp. 75-81.
- Peng, J., and Carpino, M., 1993a, "Calculation of Stiffness and Damping Coefficients for Elastically Supported Gas Foil Bearings," ASME JOURNAL OF TRIBOLOGY, Vol. 115, pp. 2-27.
- Peng, J., and Carpino, M., 1993b, "Coulomb Friction Damping Effects in Elastically Supported Gas Foil Bearings," 48th STLE Annual Meeting, Calgary, CA, May, STLE Preprint 93-AM-2E2.
- San Andres, L., 1992, "Analysis of Turbulent Hydrostatic Bearings with a Barotropic Fluid," ASME JOURNAL OF TRIBOLOGY, Vol. 115, No. 4, pp. 755-765.
- San Andres, L., 1993, "The Effect of Journal Misalignment on the Operation of a Turbulent Fluid Hydrostatic Bearing," ASME JOURNAL OF TRIBOLOGY, Vol. 115, pp. 355-363.
- San Andres, L., and Yang, Z., 1994, "Thermohydrodynamic Analysis of Fluid Film Bearings for Cryogenic Applications," 6th NASA Conference on Advanced Earth-To-Orbit Technology, Huntsville, AL, May.
- Saville, M., Gu, A., and Capaldi, R., 1991, "Liquid Hydrogen Turbopump Foil Bearings," 27th AIAA/SAE/ASME Joint Conference, Sacramento, CA, Paper 91-2108.
- Scharrer, J. K., Tellier, J., and Hibbs, R., 1991, "A Study of the Transient Performance of Hydrostatic Journal Bearings: Part I—Test Apparatus and Facility, Part II—Experimental Results," STLE Tribology Transactions Preprints 91-TC-3B-1 & 2.
- Scharrer, J. K., Henderson, T. W., 1992a, "Hydrostatic Bearing Selection for the STME Hydrogen Turbopump," AIAA Paper 92-3283, 28th AIAA/SAE/ASME/ASEE Joint Propulsion Conference, July 6-8, TN.
- Scharrer, J. K., Hibbs, R., and Nolan, S., 1992b, "Extending the Life of the SSME HPOTP through the Use of Annular Hydrostatic Bearings," AIAA Paper 92-3401, 28th AIAA/SAE/ASME/ASEE Joint Propulsion Conference, July 6-8, TN.
- Scharrer, J. K., Tellier, J., and Hibbs, R., 1992c, "Start Transient of an Annular Hydrostatic Bearing in Liquid Oxygen," AIAA Paper 92-3404, 28th AIAA/SAE/ASME/ASEE Joint Propulsion Conference, July 6-8, TN.
- Walowit, J. A., and Anno, J., 1975, *Modern Developments in Lubrication Mechanics*, Chapter 7: Foil Bearing, Applied Science Publisher Ltd., London, pp. 180-233.
- Walker, J., 1992, Personal Communication, Closure to Workshop on Fluid Film Bearing Technology, held at NASA Lewis RC, December, 1991.
- Yang, Z., San Andres, L., and Childs, D., 1993a, "Thermal Effects in Cryogenic Liquid Annular Seals, I: Theory and Approximate Solutions, II: Numerical Solution and Results," ASME JOURNAL OF TRIBOLOGY, Vol. 115, No. 2, pp. 267-284.
- Yang, Z., San Andres, L., and Childs, D., 1993b, "Thermohydrodynamic Analysis of Process Liquid Hydrostatic Bearings in Turbulent Regime, Part I: Theory, Part II: Numerical Solution and Results," accepted for publication at ASME JOURNAL OF APPLIED MECHANICS, Dec.

**11** "Angled Injection, Turbulent Flow Hybrid Bearings, Comparison to Test Results," 1996, San Andres, L., and D. Childs, Proceedings of the 8<sup>th</sup> *Workshop on Instability Problems in Rotating Machinery*, Texas A&M University, May.

THE EIGHTH  
WORKSHOP ON ROTORDYNAMIC  
INSTABILITY PROBLEMS IN  
HIGH-PERFORMANCE TURBOMACHINERY

MAY 6-8, 1996

RUDDER TOWER  
TEXAS A&M UNIVERSITY  
COLLEGE STATION, TEXAS



SPONSORED BY THE:

TURBOMACHINERY LABORATORY  
TEXAS A&M UNIVERSITY

# ANGLED INJECTION - TURBULENT FLOW HYBRID BEARINGS COMPARISON TO TEST RESULTS

Luis San Andres  
Associate Professor  
Dara Childs  
Leland T. Jordan Professor

Mechanical Engineering Department  
Texas A&M University  
College Station, TX 77843

## ABSTRACT

Hydrostatic/hydrodynamic (hybrid) journal bearings handling process liquids have limited dynamic stability characteristics and their application as support elements to high speed flexible rotating systems is severely restricted. Measurements on water hybrid bearings with angled orifice injection have demonstrated improved rotordynamic performance with virtual elimination of cross-coupled stiffness coefficients and null or negative whirl frequency ratios. A bulk-flow model for prediction of the static performance and force coefficients of hybrid bearings with angled orifice injection is advanced. The analysis reveals that the fluid momentum exchange at the orifice discharge produces a pressure rise in the hydrostatic recess which retards the shear flow induced by journal rotation, and thus, reduces cross-coupling forces. The predictions from the model are compared with experimental measurements for a 45° angled orifice injection, 5 recess water hybrid bearing operating at 10.2, 17.4 and 24.6 krpm and with supply pressures of 4, 5.5 and 7 MPa. The correlations include recess pressures, flow rates, and rotordynamic force coefficients at the journal centered position.

## NOMENCLATURE

$A_o$	$C_d \pi d_o^2 / 4$ . Effective orifice area [m <sup>2</sup> ].
$b$	recess circumferential length [m].
$C$	Radial clearance function [m].
$C_p$	Fluid specific heat [J/kg · °K].
$C_{xx}, C_{xy}, C_{yx}, C_{yy}$	Damping force coefficients [Ns/m].
$C_d$	Orifice discharge coefficient
$D$	$2 \cdot R$ . Bearing diameter [m].
$d_o$	Orifice diameter [m]
$f_{J,B}$	$\left[ 1 + \left( c_M \frac{r_{J,B}}{H} + \frac{b_M}{R_{J,B}} \right) \epsilon_M \right];$

$$\begin{aligned} a_M &= 0.001375 \\ b_M &= 500,000; c_M = 10.0 \\ \epsilon_M &= 1/3.00 \end{aligned}$$

Turbulent flow friction factors at journal and bearing surfaces.

$e_x, e_y$	Journal center eccentricity components [m]
$F_x, F_y$	Bearing fluid film forces along {X,Y} axes [N].
$h_x, h_y$	$\cos(\Theta), \sin(\Theta)$
$H$	$C + e_x(t) \cos(\Theta) + e_y(t) \sin(\Theta)$ . Film thickness [m].
$H_r$	Recess depth [m].
$H_e$	Effective film depth for rough surface bearing [m].
$K_{xx}, K_{xy}, K_{yx}, K_{yy}$	Bearing force stiffness coefficients [N/m]
$L, l$	Bearing axial length, recess axial length [m].
$M_{xx}, M_{xy}, M_{yx}, M_{yy}$	Bearing inertia force coefficients [kg].
$P, P_r, P_s$	Fluid pressure, recess pressure, supply pressure [N/m <sup>2</sup> ]
$Q_o$	$(\rho V_o A_o)$ . Flow rate across orifice [kg/s].
$Re$	$(\rho \Omega CR / \mu)_*$ . Nominal circumferential flow Reynolds number.
$R_j, R_B$	$(\rho/\mu)H \sqrt{[(U_x - \Omega R)^2 + U_y^2]}; (\rho/\mu)H \sqrt{U_x^2 + U_y^2}$
	Flow Reynolds numbers relative to journal and bearing surfaces.
$r_j, r_B$	Roughness depths at journal and bearing surfaces [m].
$t$	Time [s].
$T, T_s$	Temperature, supply temperature [°K].
$U_x, U_y$	Bulk-flow velocities in circ.(x) and axial (y) directions [m/s].
$V_o$	fluid velocity through recess orifice [m/s]
$V_r$	Recess volume including supply line [m <sup>3</sup> ].
$W_x, W_y$	External loads applied on journal [N].
$x, y$	Coordinate system on plane of bearing [m].
$X, Y$	Inertial coordinate system [m].
$\alpha$	Fluid swirl ratio at recess edges.
$\beta_p$	$(1/\rho)(\partial \rho / \partial P)$ . Liquid compressibility coefficient [m <sup>2</sup> /N].
$\beta_T$	$-(1/\rho)(\partial \rho / \partial T)$ . Liquid volumetric expansion coefficient [1/°K].
$\delta$	angle of injection on orifice of recess [rad].
$\Delta P_{rv}$	Hydrodynamic pressure rise within recess [N/m <sup>2</sup> ]
$\Delta p_{rm}$	Recess pressure drop due to momentum exchange [N/m <sup>2</sup> ].
$\Theta$	$x/R$ . Circumferential or angular coordinate.
$\kappa_y = \kappa_x$	$\frac{1}{2}(\kappa_j + \kappa_B)$ . Turbulence shear factors in (y,x) flow directions.
$\kappa_j, \kappa_B$	$f_j \cdot R_j, f_B \cdot R_B$ . Turbulent shear parameters at journal and bearing surfaces.
$\rho, \mu$	Fluid density [Kg/m <sup>3</sup> ], viscosity [Ns/m <sup>2</sup> ].
$\xi_{xu}, \xi_{xd}$	Empirical recess-edge entrance loss coefficients in circumferential (upstream, downstream) direction.
$\xi_y$	Empirical recess-edge entrance loss coefficients in axial direction.
$\Omega, \omega$	Rotational speed of journal, excitation or whirl frequency [1/s]
Subscripts refer to:	
$x, y$	In direction of local circumferential and axial coordinates inplane of bearing.
$o$	Orifice
$r, e$	Bearing recesses and edges (entrance).
$u, d$	Upstream and downstream of recess.
$B, J$	Refer to bearing and journal surfaces.

## INTRODUCTION

The importance of hybrid (combination hydrostatic and hydrodynamic) journal bearings as support elements in cryogenic turbomachinery has steadily grown over the past few years. Hybrid journal bearings (HJBs) enable smaller and lighter turbopumps through no bearing DN life limitation and no sub-critical rotor operation. HJBs have durability, low friction and wear, accuracy of positioning, and large direct stiffness and damping force coefficients. The growth of an "all-fluid-film-bearing" technology for advanced and less expensive (per launching cost) turbopumps demands the development of analytical models and design tools, the testing of components, and the implementation of the technology (Pelfrey, 1995).

Primary power cryogenic turbomachinery operates at high speeds and produces large fluid pressure rises (max. 30 MPa). These typical operating conditions determine the flow in the supporting fluid film bearings to be fully turbulent with dominance of fluid inertia and thermal transport effects. San Andres (1990-5) provides bulk-flow analyses and computational programs for the calculation of cryogenic bearing performance and rotordynamic force coefficients. Measurements of bearing rotordynamic force coefficients and load performance are routinely performed at a high-speed Hydrostatic Bearing Test Facility (HBTF) (Childs and Hale, 1994). Tests have been conducted with water on over 30 hybrid journal bearings and damper seals with rotational speeds ranging from 10 to 25 krpm and pressure differentials from 4 to 7 MPa (Childs and Hale, 1994). Kurtin et al. (1993), Franchek et al. (1994-5), Mosher and Childs (1995), and Yang et al. (1995) report extensive experimental data for the static performance characteristics of a 5 recess HJB for the operating conditions noted and three different bearing clearances (76 to 127  $\mu\text{m}$ ). These studies show bulk-flow model calculations to correlate favorably with the experimental results. Accurate predictions depend greatly on the knowledge of the bearing operating clearances, and most importantly, on the orifice discharge coefficients. The references cited along with San Andres (1995a) also discuss the sensitivity of the computed predictions to variations in the input empirical parameters.

Despite the many advantages offered by HJBs, hydrodynamic and "pneumatic hammer" stability limits and two-phase flow operation are issues of primary concern for high speed operation with large pressure differentials. Fluid vaporization is possible since the cryogenic liquid enters the bearing (or seal) at conditions close to its saturation temperature. "Pneumatic hammer" effects are avoided by appropriate selection of the flow restrictor, by designing bearing recesses with small volumes, and by restricting bearing operation to flow conditions where the pressure differential is a small fraction of the liquid bulk modules (Redecliff and Vohr, 1969).

The stability of a simple rotor-bearing system is defined by its threshold speed and the whirl frequency ratio (WFR). This instability is due to the effect of journal rotational speed on the bearing flow field. The threshold speed corresponds to the rotor speed at which a bearing is deprived from its effective damping and any small perturbation from an equilibrium position will determine unbounded rotor motions. The WFR denotes the ratio between the onset whirl frequency (typically the system first critical speed) and the threshold speed of instability. Plain journal bearings show a WFR equal to 0.50 for small to moderate operating eccentricities (light loads), and thus instability at a rotational speed equal to twice the system first critical speed is likely to occur. Measurements in hybrid bearings verify closely the theoretical WFR prediction. In some circumstances the WFR even increases above 0.50, in particular for low rotational speeds and large supply pressures (Franchek, 1992, Franchek et al. 1995).

The WFR=0.50 condition limits severely the application of HJBs to high speed, light weight turbomachinery, and thus, the research has concentrated on conceiving hybrid bearings with improved

stability and without loss in centering stiffness and damping ability. Some of the technological advances have been the natural outcome of analysis and engineering design, while others follow empirical evidence and past experience when a mathematical model is yet to be crafted. Other recommended fixes to improve the hydrodynamic stability of hybrid bearings by reducing or eliminating the WFR are the following:

- Use of machine roughened bearing surfaces to decrease the cross-coupled stiffness coefficients. Test results show a rough knurled-pattern HJB to have WFR as low as 0.30 but with a reduced load capacity and direct stiffness when compared to a smooth surface HJB (Franchek, 1992).
- Use of circumferentially asymmetric pad bearings and recesses to produce enough an isotropy on the rotordynamic force coefficients. Measurements and analysis for an engineered two pad HJB validated the concept (San Andres, 1995b). However, this bearing configuration is highly sensitive to the direction of applied static loads.
- Use of flexure-pivot, tilting pad HJBs or compliant surface (foil) journal bearings due to their inherent stability. San Andres (1995c, 1994) discusses at length these concepts and evaluates their potential for cryogenic uses. Flexure-pivot HJBs constitute a novel alternative and full-scale testing is planned for the first semester of 1996. Foil bearings have also demonstrated their performance in cryogenic turbomachinery (Genge et al., 1993). The current foil bearing technology allows only for specific loads applicable to secondary power cryogenic turbopumps. The interested reader should recall the cited references for further details.
- Use of hybrid bearings with angled liquid injection opposing journal rotation to reduce the development of the circumferential flow velocity and with virtual elimination of cross-coupled stiffness coefficients. This concept has lacked firm theoretical modeling though it has proved successful in some applications (Tondl, 1967, Brown and Hart, 1986). Experimental measurements for a 5 recess water HJB demonstrate that angled injection aids in reducing the whirl frequency ratio without decreasing the bearing centering stiffness and load capacity (Franchek, 1992, Franchek and Childs, 1995).

The thermohydrodynamic analysis of real properties, hybrid bearings with angled orifice injection is advanced. The objective is to develop a model able to predict reliably the performance of angled injection HJBs in lieu of their favorable (measured) rotordynamic performance. The motion of a fluid through the thin film lands is governed by mass, momentum and energy transport equations for the bulk-flow velocities, pressure and temperature, along with thermophysical state equations for evaluation of the cryogen material properties. The turbulent bulk-flow is modeled with simple friction coefficients and include effective film depths to accommodate for macroscopic surface roughness. A simple analysis for the angled injection - orifice flow reveals that the fluid momentum exchange produces a pressure rise in the recess which retards the shear flow induced by journal rotation. The numerical predictions from the model are correlated extensively with the experimental data of Franchek (1992).

## ANALYSIS

Figure 1 shows the geometry of a hybrid (combination hydrostatic/hydrodynamic) journal bearing and the relevant nomenclature. A liquid at high pressure ( $P_i$ ) and inlet temperature ( $T_i$ ) is supplied (radially or angled) through orifice restrictors and impinges into the bearing recesses with a mean



pressure ( $P_r$ ). The pressure field within the recesses is determined from flow continuity with the film lands, momentum exchange at the orifice plane and a viscous rise due to journal rotation. At the recess edges, an inertial pressure drop also occurs due to the sudden transition from the recess of depth ( $H_r$ ) into the film lands of thickness ( $H$ ). Past the recesses, the liquid then flows through the film lands and the pressure drops to the discharge value ( $P_s$ ).

### **Equations of flow on the bearing film lands**

On the thin film lands flow turbulence, fluid inertia and compressibility effects are important. The model then assumes a fully developed turbulent bulk-flow of a fluid whose material properties depend on its local thermophysical state of pressure and temperature. The equations of mass, axial and circumferential momentum, and adiabatic-flow energy transport for the bulk-flow velocities, pressure and temperature in the bearing film lands are given as (Yang et al., 1995, Kleyhans and Childs, 1995):

$$\frac{\partial}{\partial t}(\rho H_e) + \frac{\partial}{\partial y}(\rho H U_y) + \frac{\partial}{\partial x}(\rho H U_x) = 0 \quad (1)$$

$$-H \frac{\partial P}{\partial y} = \frac{\mu}{H} \{ \kappa_y U_y \} + \frac{\partial(\rho H_e U_y)}{\partial t} + \left\{ \frac{\partial(\rho H U_y U_y)}{\partial y} + \frac{\partial(\rho H U_y U_x)}{\partial x} \right\} \quad (2)$$

$$-H \frac{\partial P}{\partial x} = \frac{\mu}{H} \left\{ \kappa_x U_x - \kappa_j \frac{\Omega R}{2} \right\} + \frac{\partial(\rho H_e U_x)}{\partial t} + \left\{ \frac{\partial(\rho H U_y U_y)}{\partial y} + \frac{\partial(\rho H U_x U_x)}{\partial x} \right\} \quad (3)$$

$$C_p \left\{ \frac{\partial}{\partial t}(\rho H_e T) + \frac{\partial}{\partial x_\alpha}(\rho H U_\alpha T) \right\} = \beta_T H T \left\{ \frac{\partial P}{\partial t} + U_\alpha \frac{\partial P}{\partial x_\alpha} \right\} + \Omega \cdot R \frac{H}{2} \frac{\partial P}{\partial x} \\ + \frac{\mu}{H} \left\{ \kappa_x \left( U_x^2 + U_y^2 + \frac{1}{2} \Omega R U_x \right) + \kappa_j \Omega R \left( \frac{1}{4} \Omega R - U_x \right) \right\} \quad \alpha = x, y \quad (4)$$

Please refer to the Nomenclature for a description of all variables.  $\kappa_y = \kappa_x = (k_j + k_B)/2$  are the wall shear stress parameters determined as local functions of turbulent friction factors which depend on the bearing and journal surface conditions and the flow Reynolds numbers relative to the rotating ( $R_j$ ) and stationary ( $R_B$ ) surfaces, i.e  $\kappa_j = f_j \cdot R_j$ ,  $\kappa_B = f_B \cdot R_B$  (Hirs, 1973). The cryogenic liquid properties are extracted from the Benedict-Web-Rubin equation of state as given in the standard data base of McCarty (1986).

The fluid pressure at the sides of the bearing ( $y = \pm L/2$ ) equals the discharge or ambient value ( $P_s$ ). At the interface with the bearing recesses, continuity of flow and pressure must be attained as detailed below.

### Angled Injection - Recess Flow and Pressure Equations

Figure 2a depicts a hydrostatic bearing recess (or pocket) with axial length ( $l$ ) and circumferential extent ( $b$ ). The figure shows the direction of the journal surface speed ( $\Omega \cdot R$ ), and relative to this velocity the recess is divided into upstream ( $u$ ) and downstream ( $d$ ) regions. The fluid supply orifice port with injection angle ( $\delta$ ) is located at a distance  $b_o$  from the upstream recess edge. The orifice has an effective area  $A_o$  normal to the feed speed  $V_o$ . Radial fluid supply is indicated by  $\delta=0$  while a tangential feed opposite to journal rotation is given by  $\delta = \pi/2$  ( $90^\circ$ ).

Conventional analysis of hydrostatic bearings do not calculate the flow field within the recess since these are typically deep and enclose large nearly stagnant fluid volumes. Analysis then accounts only for flow continuity with the film lands and determines a (uniform) recess pressure using a simple orifice equation based on Bernoulli's principle. The complexity of the flow field in hydrostatic pockets has been discussed by Hill et al. (1995) and Braun et al. (1993, 1995) with the aid of two-dimensional computational fluid mechanics analyses. Numerical results reveal the generation of hydrodynamic pressures within the pocket and followed by sharp inertial pressure drops at the recess edges. This field of study is of utmost importance for the development of a mature technology on hybrid bearings for cryogenic applications.

The analysis of angled injection - hydrostatic pockets follows here a simplified approach which intends to be of practical use without resorting to computationally intensive three dimensional flow calculations. The flow model is evidently crude yet it grasps the fundamental mechanisms of pressure generation within the bearing pockets. The favorable correlation with hybrid bearing experimental performance characteristics given later justifies the method used.

A mass conservation equation at each bearing recess of area ( $l \cdot b$ ) and depth  $H_r$  is defined by the global balance between the mass flow through the orifice restrictor ( $Q_{r,o}$ ), the mass flow into the film lands and the time rate of change of liquid mass within the recess and supply line volume ( $V_r$ ), i.e.

$$Q_{r,o} = \rho_r A_o V_o = \int_{\Gamma_r} [\rho H \vec{U} \cdot \vec{n}] d\Gamma_r + \frac{\partial}{\partial t} (\rho_r V_r) \quad (5)$$

for  $r = 1, 2, \dots, N_{recess}$

where  $A_o = C_d \pi d_o^2/4$  is the effective orifice area with  $C_d$  as an empirical discharge coefficient.  $\Gamma_r$  denotes the closure of the recess with the film lands and has a normal  $\vec{n}$  along the boundary line. At the orifice discharge plane, the mean recess pressure is denoted by  $P_r$  (see Figure 2b) and given from Bernoulli's equation as:

$$(P_s - P_r) = (1/2) \rho_r V_o^2 \quad (6)$$

Computational fluid mechanics analysis reveals that the axial pressure within the recess is (to a first approximation) practically uniform. Hence, modeling of the flow in the pocket as a one-dimensional bulk-flow bearing determines that the pressure difference (downstream - upstream) on a recesses is given by two contributions:

a) a viscous pressure rise ( $\Delta P_{r,v}$ ) due to shear flow induced by journal rotation (San Andres, 1992):

$$\Delta P_{rr} = [P_d - P_u] = \mu_r \kappa_{rr} \frac{b}{H_r^2} \left( \frac{\Omega \cdot R}{2} - U_{rx} \right) \quad (7)$$

b) a pressure drop ( $\Delta P_{rm}$ ) at the orifice injection plane and due to the exchange of fluid momentum, and simply stated as:

$$\Delta P_{rm} = [P_d - P_u]_m = - \frac{Q_o V_o \sin(\delta)}{H_r \cdot 1} = - \frac{2A_o}{H_r \cdot 1} \cdot (P_s - P_r) \sin(\delta) \quad (8)$$

where the orifice equation (6) has been used on the right hand side of eqn (8). Note that for radial injection ( $\delta = 0$ ) there is no momentum pressure drop at the supply port, while the largest pressure drop occurs for large pressure differentials ( $P_s - P_r$ ) and tangential injection ( $\delta = 90^\circ$ ). For simplicity the pressure field within the hydrostatic pocket is then taken as linear and combines the two pressure differences as shown pictorially in Figure 2b. Note that this simplification avoids the calculation of the complex flow field on the entire bearing recess.

Finally, the entrance pressures ( $P_e$ ) to the film lands in the circumferential (upstream and downstream) and axial directions are given by (San Andres, 1992):

$$P_e]_{u,d} = \left[ P_r - \frac{\rho}{2} (1 + \xi_x) \{1 - U_x^2\} \right]_{u,d} \quad (9.a)$$

$$P_e = P_r - \frac{\rho}{2} (1 + \xi_y) \{1 - U_y^2\} \quad (9.b)$$

These equations are used only when fluid flows from the recess towards the film lands. Details of energy transport at the recesses are given by Yang et al. (1995).

### **Perturbation Analysis**

Consider the motion of the journal as the superposition of small amplitude periodic motions of frequency ( $\omega$ ) around a static equilibrium position. That is, the journal center displacements are given as

$$e_X(t) = e_{Xo} + \Delta e_X e^{i\omega t}, \quad e_Y(t) = e_{Yo} + \Delta e_Y e^{i\omega t}; \quad i = \sqrt{-1} \quad (10)$$

The magnitudes of the dynamic perturbations in journal displacements are small, i.e.,  $|\{\Delta e_X, \Delta e_Y\}| \ll C$ . The film thickness ( $H$ ) can then be regarded as the superposition of a steady-state ( $H_o$ ) and dynamic components given by the real part of the following expression:

$$H = H_o + \{\Delta e_X h_X + \Delta e_Y h_Y\} e^{i\omega t} \quad (11)$$

where  $H_o = C(y) + e_{x0} h_x + e_{y0} h_y$ ; and  $h_x = \cos(\theta)$ ,  $h_y = \sin(\theta)$

The flow field variables ( $U_x$ ,  $U_y$ ,  $P$ ,  $T$ ), as well as the fluid properties ( $\rho$ ,  $\mu$ ) and the shear parameters ( $\kappa_x$ ,  $\kappa_y$ ) are also formulated as the superposition of zeroth-order and first-order complex fields describing an equilibrium for steady-state flow, and the perturbed condition for small amplitude dynamic journal motions, respectively. In general, these fields are expressed as:

$$\Psi = \Psi_o + \{\Delta e_x \Psi_x + \Delta e_y \Psi_y\} e^{i\omega t} \quad (12)$$

Substitution of equations (11) and (12) into the flow equations (1-9) renders zeroth- and first-order equations for determination of the steady-state and perturbed flow-fields. These equations are not reproduced here for brevity but can be found in their full extent in the reference of San Andres (1993). The bearing static and dynamic force characteristics are evaluated once a solution to the flow equations is obtained. Fluid film forces ( $F_x$ ,  $F_y$ ) and force coefficients (stiffness  $K_{\alpha\beta}$ , damping  $C_{\alpha\beta}$  and inertia  $M_{\alpha\beta}$ ) are calculated by integration of the pressure fields over the journal surface. The appropriate formulae are:

$$F_\alpha = \int_0^L \int_0^{2\pi} P_o h_\alpha R \cdot d\Theta \cdot dy; \quad \alpha = X, Y \quad (13)$$

$$K_{\alpha\beta} - \omega^2 M_{\alpha\beta} + i\omega C_{\alpha\beta} = \int_0^L \int_0^{2\pi} P_\beta h_\alpha R \cdot d\Theta \cdot dy; \quad \alpha, \beta = X, Y \quad (14)$$

### Numerical Method of Solution

The control-volume method of Launder and Leschziner (1978) is used to solve the differential equations of motion. Staggered grids containing control volumes for the primitive flow variables (circumferential and axial velocity, pressure and temperature) cover the flow domain. Algebraic difference equations are derived on each control volume for the conservation of mass, axial and circumferential momentum, and balance of energy. A pressure correction equation is derived using the SIMPLEC procedure of Van Doormaal and Raithby (1984). A Newton-Raphson scheme is also used for satisfaction of the recess mass flow constraint. Full descriptions on the accuracy and parameter sensitivity of the method as applied to hybrid bearings and annular pressure seals are given in past publications (San Andres, 1990-1995). The interested reader should consult the cited references for a detailed exposition of the numerical method used.

### **COMPARISONS TO TEST RESULTS FROM A WATER 5-RECESS HYBRID BEARING**

Franchek (1992) presents an experimental study of five hybrid bearings with distinctive geometrical configurations. These are namely, smooth bearings with radial injection and rectangular (baseline), triangular and circular recesses, a knurled rough-surface bearing with rectangular recesses, and a smooth surface bearing with rectangular recesses and a 45° angled orifice injection. The tests consisted of the measurement of load vs. journal eccentricity, torque and flow rate, and the

identification of rotordynamic force coefficients. Childs and Hale (1994) provide a full description of the test apparatus and the experimental procedure. The nominal test conditions include:

- (a) 3 rotational speeds: 10.0, 17.4 and 24.6 krpm
- (b) 3 supply pressures: 4.0, 4.5 and 7.0 MPa (600, 800 and 1000 psig)
- (c) 6 journal eccentricity ratios ( $e/c$ ): 0.0 to 0.5 at a fluid supply temperature of 55°C (130°F).

Franchek and Childs (1994) and Franchek et al. (1995) briefly report the measurements with comparisons to predictions for the radial injection bearing (conventional design). Table 1 describes the geometry of the test bearing with angled (45°) injection. At the journal centered position the measured data for flow rate, supply and average recess pressures and operating clearance is also given. From these values, empirical orifice loss coefficients ( $C_d$ ) are estimated for each test condition and used in all computations including journal off-centered operations. The values of circumferential ( $Re_c$ ) and axial flow Reynolds ( $Re_a$ ) numbers demonstrate the character of the flow within the test bearing. San Andres (1995e) reports detailed comparisons of predictions and test results for both radial and angled (45°) injection hybrid bearings. Selected experimental measurements (broken lines) along with predictions from the model (continuous lines) follow.

#### Static Performance Characteristics of Angled Injection Bearing

Figure 3 depicts the journal eccentricity versus applied load ( $W_x$ ) at a nominal supply pressure of 7.0 MPa and three rotational speeds. The journal eccentricity increases linearly with the applied load as is typical in externally pressurized bearings. The predictions correlate very well with the measurements and also demonstrate that the stiffness coefficients for the bearing will not vary (greatly) with the journal center position. Figure 4 shows the predicted journal center loci as the load increases. Note the negative attitude angle at the lowest speed (10.2 krpm), an almost null angle at the medium speed (17.4 krpm), and a positive angle at the highest speed (24.6 krpm). Test results are not shown since these were not included by Franchek (1992). The predictions reveal the fundamental effect of angled injection on the bearing static load performance. Engineering design could then lead to a hybrid bearing free of cross-coupling effects with the appropriate combination of injection angle, supply pressure and operating speed.

Figure 5 depicts the recess pressure ratios  $\{(P_r - P_a)/(P_s - P_a)\}$  at the journal concentric position for the three nominal supply pressures and speeds. Recess pressure ratios rise with the journal speed and decrease with supply pressures since land flow resistance and turbulence are greater. The correlations with the model predictions are good except at the largest speed and lowest supply pressure. Note that the comparisons have been made with averaged test recess pressures. Actual measured recess pressures vary as much as 13% from the calculated (experimental) average. Figure 6 shows the predicted flow rates to agree with the measurements at the low (10.2 krpm) and medium speeds (17.4 krpm). The discrepancies at the highest test speed are attributed to the larger predicted recess pressures.

#### Dynamic Performance Characteristics at Journal Centered Position

The test results and numerical predictions demonstrate that the rotordynamic force coefficients are practically insensitive to the applied load for journal eccentricities to 50% of the bearing clearance. Hence, in the following, only force coefficients at the concentric position are presented.

The whirl frequency ratio (WFR), a stability indicator of paramount importance for the application of hybrid bearings to high speed applications, is depicted in Figure 7. Although not shown

here, the radial bearing presents a (measured) WFR ranging from 0.60 to 0.48 for most operating conditions (Franchek, 1992). On the other hand, the angled ( $45^\circ$ ) injection bearing shows a (large) negative WFR at the lowest speed and raising to the 0.5 limit as the rotational speed increases. The numerical predictions agree well with the measurements at the middle and high speeds, i.e. 17.4 and 24.6 krpm. Note that the advantages of angled injection are then lost as the journal speed increases and determines dominance of hydrodynamic effects over hydrostatic effects.

Figure 8 depicts the cross-coupled stiffness coefficients ( $K_{xy} = -K_{yx}$ ) as the journal speed increases for the three nominal supply pressures. In the radial injection bearing, the cross-coupled stiffness are always positive and increase with the journal speed (Franchek et al., 1995). On the other hand, the angled injection bearing presents negative cross-coupled coefficient at the lowest speed. From a rotordynamics point of view this is a desirable occurrence since then these coefficients render forces opposing the development of forward whirl motions. The numerical predictions show the same trends as the measurements but do not agree well with the measurements.

Figure 9 presents the direct stiffness coefficients ( $K_{xx} = K_{yy}$ ) versus the journal speed and nominal supply pressures. The experimental results show significant discrepancies between  $K_{xx}$  and  $K_{yy}$  and attributed to minute differences in the diameters of the feeding orifices. The numerical predictions agree well with the measurements except at the lowest speed and highest pressure where the tests show an unexpected behavior.

The direct damping coefficients ( $C_{xx} = C_{yy}$ ) are depicted in Figure 10. The predictions and measurements show direct damping to increase with journal speed and supply pressure. Correlation test and model is best at the lowest (10.2 krpm) speed. However, direct damping is underpredicted by as much as 25% at 24.6 krpm.

Figure 11 shows the predicted cross-coupled damping coefficients ( $C_{xy} = -C_{yx}$ ) to increase with journal speed and with little influence of the external supply pressure. On the other hand, the test results show a different behavior with cross-damping coefficients being the largest at the middle test speed (17.4 krpm). No conclusive remark can be made in regard to the correlation of prediction and identified test coefficients.

Comparisons to inertia force coefficients are given by San Andres (1995e) and not reported here for brevity. The predictions show added mass coefficients independent of external supply pressure and with a slow variation as the journal speed increases. The experimentally identified inertia coefficients are of the same order of magnitude as the predictions but present an erratic behavior. Franchek and Childs (1994) indicate the test inertia coefficients have average uncertainties of 53%.

## CONCLUSIONS

The growth of an "all-fluid-film-bearing" technology for support of advanced cryogenic turbopumps demands the development of models and design tools, the testing of components, and the implementation of the technology on actual hardware. Conventional hybrid fluid film bearings have demonstrated adequate load support, direct stiffness and damping, but suffer from limited hydrodynamic stability which deters their use to high speed applications and flexible rotating structural systems. On the other hand, experiments on hybrid bearings with angled orifice injection have shown virtual elimination of cross-coupled stiffness coefficients and null or negative whirl frequency ratios. No firm analysis was available at the time of the measurements, and hence, further technological developments since then were prevented.

A bulk-flow analysis for prediction of the static load and force coefficients of hybrid bearings with angled orifice injection is advanced. A simple model reveals that the fluid momentum exchange

at the orifice discharge produces a pressure rise in the recess which retards the shear flow induced by journal rotation, and consequently, reduces cross - coupling forces. The predictions from the model are compared with measurements for a hybrid bearing with a 45° angled injection. The test bearing nominal clearance is 125  $\mu\text{m}$  and operates with water from 10.2 krpm to 24.6 krpm and with supply pressures from 4 to 7 MPa. Comparison of experiments and model calculations for load, flow rate and recess pressures are good and verify the soundness of the bulk-flow model. Correlations of model and test direct stiffness and damping coefficients are also favorable. The predictions show the same trends as the test values for the whirl frequency ratio and cross-coupled stiffness coefficients but large differences are apparent. Inertia force coefficients do not agree with the experimental values perhaps due to the large uncertainty in the test coefficients. The predictions as well as the measurements demonstrate that the advantages of angled injection in hybrid bearings are lost as the journal speed increases and brings dominance of hydrodynamic over hydrostatic effects.

## ACKNOWLEDGMENTS

The support of NASA Lewis Research Center under NASA Grant NAG-1434 is gratefully acknowledged. Thanks to Mr. James Walker of NASA LeRC for his interest on this work. Thanks to my daughter, Maria Jose (12), who helped on the graphical art.

## REFERENCES:

- Braun, M.J., Choy, F.K., and Y.M. Zhou, 1993, "The Effects of a Hydrostatic Pocket Aspect Ratio, Supply Orifice Position and Attack Angle on Steady-State Flow Patterns, Pressure and Shear Characteristics," ASME Journal of Tribology, Vol. 115, pp. 678-685.
- Braun, M.J., M. Dzodzo, 1995, "Effects of the Feedline and the Hydrostatic Pocket Depth on the Flow Patterns and Pressure Distribution," ASME Journal of Tribology, Vol. 117, pp. 224-233.
- Brown, R.D., J. A. Hart, 1986, "A Novel Form of Damper for Turbomachinery," Proceedings of the Workshop on Rotordynamic Instability Problems in High Performance Turbomachinery, Texas A&M University, pp. 325, 348, NASA CP 2443.
- Childs, D., and K. Hale, 1994, "A Test Apparatus and Facility to Identify the Rotordynamic Coefficients of High Speed Hydrostatic Bearings", ASME Journal of Tribology, Vol. 116, pp. 337-344.
- Franchek, N., 1992, "Theory Versus Experimental Results and Comparisons for Five Recessed, Orifice Compensated, Hybrid Bearing Configurations," Texas A&M University, M.S. Thesis, TAMU Turbomachinery Laboratories, August 1992.
- Franchek, N., and D. Childs, 1994, "Experimental Test Results for Four High-Speed, High-Pressure, Orifice-Compensated Hybrid Bearings," ASME Journal of Tribology, Vol. 116, 2, pp. 285-290.
- Franchek, N., D. Childs, and L. San Andres, 1995, "Theoretical and Experimental Comparisons for Rotordynamic Coefficients of a High-Speed, High-Pressure, Orifice-Compensated Hybrid Bearings," ASME Journal of Tribology, Vol. 117, 2, pp. 285-290.
- Genge, G.G., Saville, M., and A. Gu, 1993, "Foil Bearing Performance in Liquid Nitrogen and Liquid Oxygen," AIAA/SAE/ASME/ASEE 29th Joint propulsion Conference and Exhibit, Monterrey, CA, June, Paper AIAA-93-2537.
- Hill, D., E. Baskharone, and L. San Andres, 1995, "Inertia Effects in a Hybrid Bearing with a 45 degree Entrance Region," ASME Journal of Tribology, Vol. 117, 3, pp. 498-505.
- Hirs, G. G., 1973, "A Bulk-Flow Theory for Turbulence in Lubricating Films," ASME Journal of Lubrication Technology, Vol. 95, pp. 135-146.
- Kleynhans, G., and D. Childs, 1995, "The Acoustic Influence of Cell Depth on the Rotordynamic Characteristics of Smooth-Rotor/Honeycomb-Stator Annular Gas Seals," Seals Code Development Workshop, NASA Lewis Research Center, Cleveland, OH, June 15, 1995.
- Kurtin, K., Childs, D., San Andres, L. and Hale, K., 1993, "Experimental versus Theoretical Characteristics of a High Speed Hybrid (combination Hydrostatic and Hydrodynamic) Bearing,"

ASME Journal of Tribology, Vol. 115, 1, pp. 160-169.

Lauder, B., and M. Leschziner, 1978, "Flow in Finite Width Thrust Bearings Including Inertial Effects," ASME Journal of Lubrication Technology, Vol. 100, pp. 330-345.

McCarty, R.D., 1986, NBS Standard Reference Data Base 12, Thermophysical Properties of Fluids, MIPROPS 86, Thermophysics Division, Center for Chemical Engineering, National Bureau of Standards, Colorado.

Mosher, P., and D. Childs, 1995, "Theory Versus Experiment for the Effect of Pressure Ratio on the Performance of an Orifice-Compensated Hybrid Bearing," 1995 ASME Design Engineering Technical Conference, "DE-Vol 84-2, Vol.3-Part B., pp. 1119-1129.

Pelfrey, P., 1995, "Pratt & Whitney Fluid-Film Bearing and Seal Technology Development and Implementation," Seals Code Development Workshop, NASA Lewis Research Center, Cleveland, OH, June 15, 1995.

Redecliff, J.M. and J.H. Vohr, 1969, "Hydrostatic Bearings for Cryogenic Rocket Engine Pumps," ASME Journal of Lubrication Technology, pp. 557-575.

San Andres, L.A., 1990, "Turbulent Hybrid Bearings with Fluid Inertia Effects", ASME Journal of Tribology, Vol. 112, pp. 699-707.

San Andres, L., 1992, "Analysis of Turbulent Hydrostatic Bearings with a Barotropic Fluid," ASME Journal of Tribology, Vol. 114, 4, pp. 755-765, 1992.

San Andres, L., 1993, "Thermohydrodynamic Analysis of Cryogenic Liquid Turbulent Flow Film Bearings for Cryogenic Applications," Research Progress Report to NASA Lewis Research Center, NASA Grant NAG3-1434, December.

San Andres, L., 1995a, "Thermohydrodynamic Analysis of Fluid Film Bearings for Cryogenic Applications," AIAA Journal of Propulsion and Power, Vol. 11, 5, pp. 964-972.

San Andres, L., 1995b, "Two Pad Axially Grooved Hydrostatic Bearing," U.S. Patent 5,433,528, July, 18.

San Andres, L., 1995c, "Turbulent Flow, Flexure-Pivot Hybrid Bearings for Cryogenic Applications," 1995, STLE/ASME Tribology Conference, Orlando, ASME Journal of Tribology, ASME Paper 95-TRIB-14.

San Andres, L., 1995d, "Turbulent Flow Foil Bearings for Cryogenic Applications," ASME Journal of Tribology, Vol. 117, 1, pp. 185-195.

San Andres, L., 1995e, "Angled Injection - Hybrid Fluid Film Bearings for Cryogenic Applications," Annual Research Progress Report to NASA Lewis Research Center, NASA Grant NAG3-1434, December.

Tondl, A., 1967, "Bearings with a Tangential Gas Supply," Gas Bearing Symposium, University of Southampton, Dept. of Mechanical Engineering.

Van Doormaal, J.P., and D. Raithby, 1984, "Enhancements of the SIMPLE Method for Predicting Incompressible Fluid Flows," Numerical Heat Transfer, Vol. 7, pp. 147-163.

Yang, Z., L. San Andres and D. Childs, 1995, "Thermohydrodynamic Analysis of Process Liquid Hydrostatic Bearings in Turbulent Regime, Part I: The Model and Perturbation Analysis, Part II: Numerical Solution and Results," ASME Journal of Applied Mechanics, Vol. 62, 3, pp. 674-684.



Table 1. Description of water lubricated orifice compensated hybrid bearing tested by Franchek and Childs (1994).

No of recesses (N <sub>rec</sub> )	5
Clearance nominal (C)	125.4 $\mu$ m (0.005 in)
Diameter (D)	76.2 mm (3 in)
Length (L)	76.2 mm (3 in)
Land roughness (peak-peak)	0.33 $\mu$ m (13 $\mu$ in)

Recess dimensions: square (l) 27 mm x (b) 27 mm x 254  $\mu$ m (depth) Supply volume  $V_s = 0.1289$  dm<sup>3</sup>  
 Orifices at midplane of recess diameter  $d = 2.49$  mm, angled injection ( $d = p/4$  [45°])  
 Lubricant: water at  $T_s = 328.3^\circ$  K  
 Viscosity ( $\mu$ ) 0.4929E-3 Pa.s Density ( $\rho$ ) 986.26 kg/m<sup>3</sup>  
 Discharge pressure  $P_a$ : 0.0 MPa (0 psig)  
 Empirical parameters: Entrance loss factors  $\xi_a, \xi_r = 0.0$ , Inlet swirl  $\alpha = 0.5$

Test Conditions and Estimated Parameters at Centered Operation

Speed Kcpm	P MPa	C $\mu$ m	Q l/min	P <sub>r</sub> MPa	C <sub>d</sub>	Re ( $\rho Q R c / \mu$ )	Re <sub>s</sub> ( $Q a / \pi D u$ )
10.2	4.133	122.8	79.94	1.128	0.700	9,988.0	11,136.0
	5.519	124.4	92.21	1.252	0.680	10,129.1	12,845.6
	6.877	124.9	102.29	1.434	0.660	10,169.8	14,249.9
17.4	4.154	120.5	79.60	1.866	0.800	16,737.3	11,088.3
	5.521	121.5	91.67	2.148	0.763	16,876.2	11,088.9
	6.846	122.7	101.75	2.316	0.726	17,042.0	14,174.0
24.6	4.135	119.4	78.07	2.424	0.907	23,447.2	10,875.8
	5.532	120.8	92.21	2.870	0.859	23,722.0	12,942.4
	6.844	117.1	101.38	3.206	0.808	23,000.0	14,123.0

(\*) C<sub>d</sub> values estimated from measured flow rate and average recess pressures

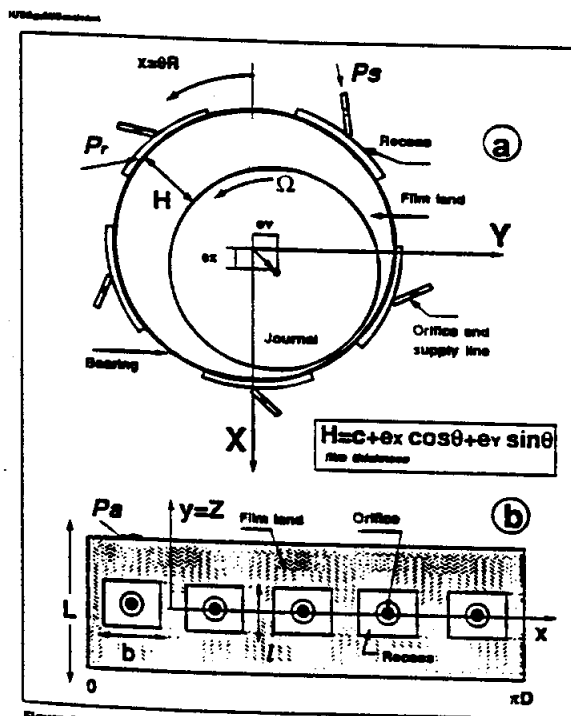


Figure 1. Geometry of an orifice compensated - angled injection hybrid bearing.  
 a) Axial View and Coordinate System, b) Unwrapped Bearing Surface

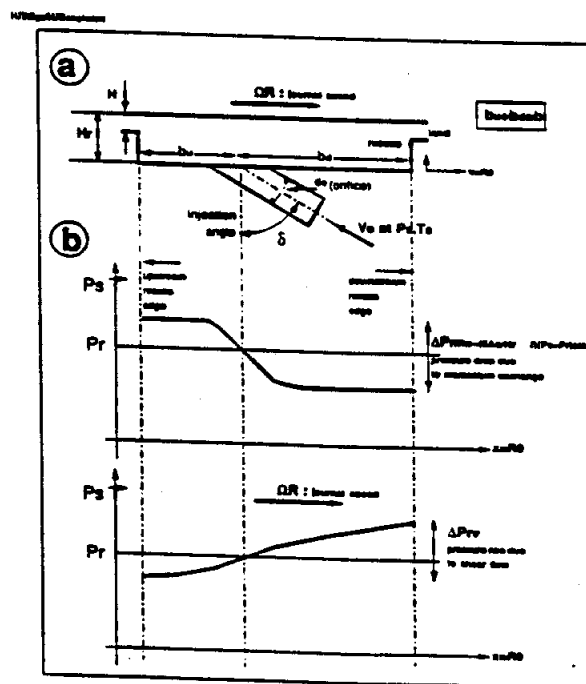


Figure 2. (a) Description of hydrostatic recess with angled injection  
 (b) Assumed pressure field within hydrostatic recess

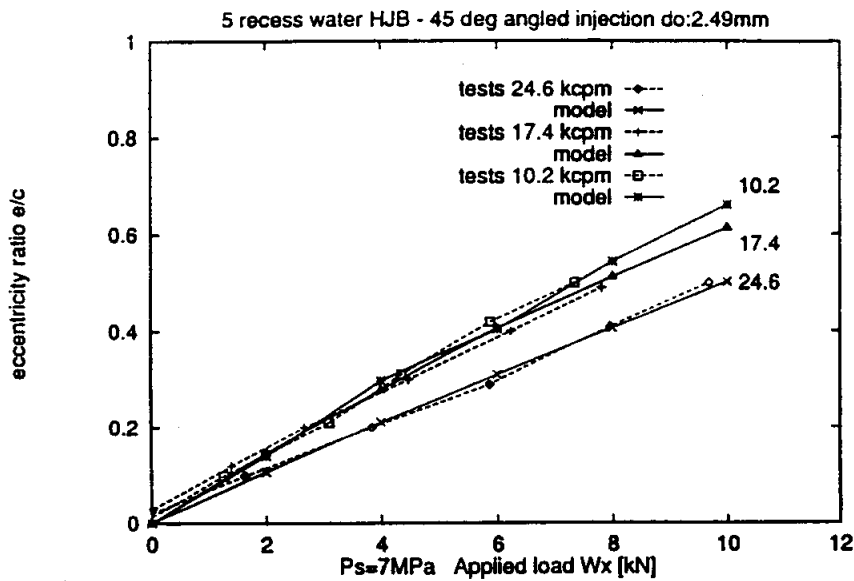


Figure 3. Journal eccentricity vs. applied load  $W_x$  for water - 5 recess hybrid bearing. Comparison to experimental results.

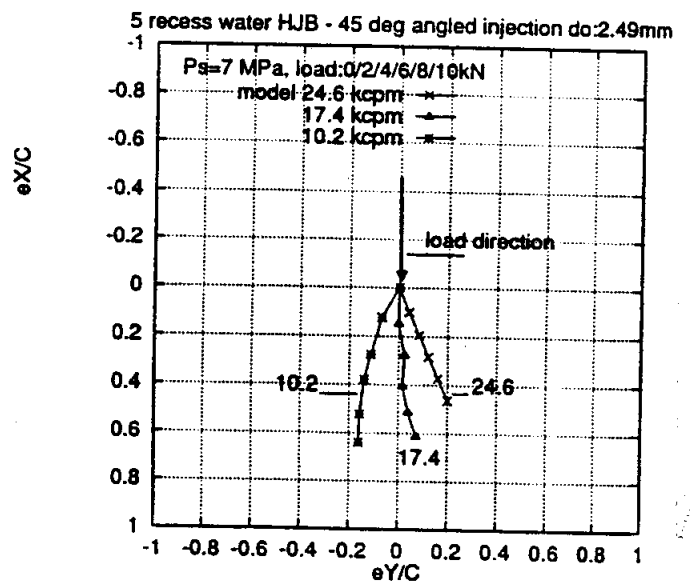


Figure 4. Journal center locus for water - 5 recess hybrid bearing. Numerical predictions for increasing loads.

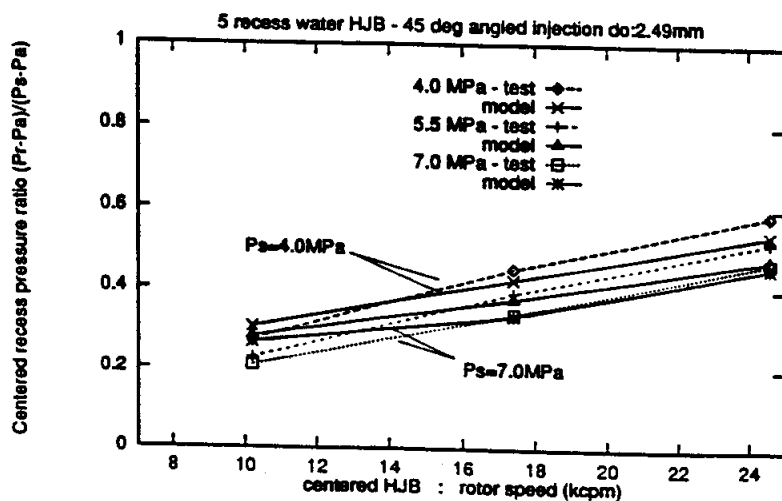


Figure 5. Centered recess pressure ratio  $(P_r - P_s)/(P_s - P_a)$  for water - 5 recess hybrid bearing. Comparison to experimental results.

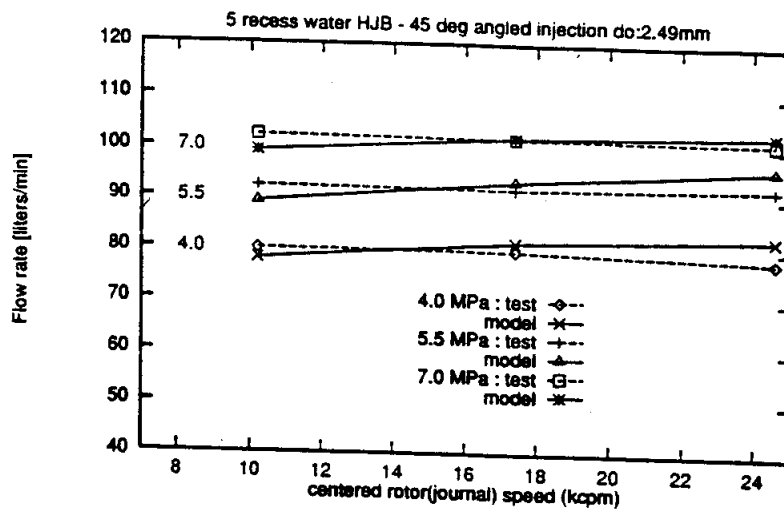


Figure 6. Bearing flow rate vs. journal speed for water - 5 recess hybrid bearing. Comparison to experimental results.

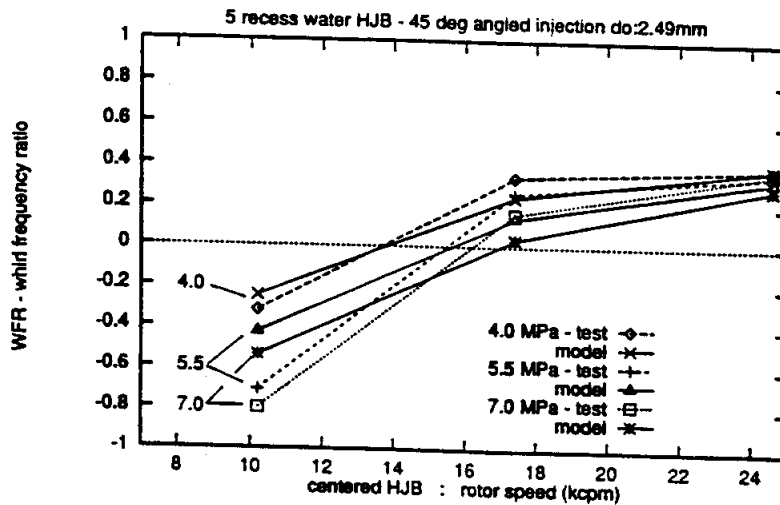


Figure 7. Whirl frequency ratio vs. journal speed for water - 5 recess hybrid bearing. Comparison to experimental results.

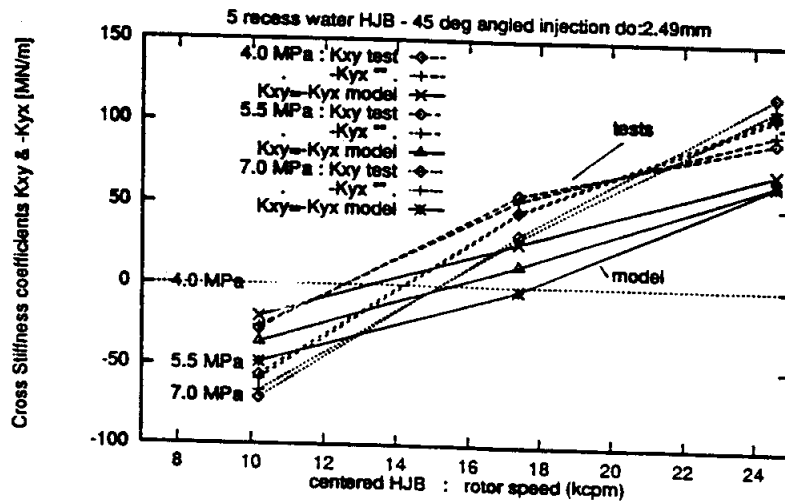


Figure 8. Cross-stiffness coefficients (Kxy, -Kyx) vs. journal speed for water - 5 recess hybrid bearing. Comparison to experimental results.

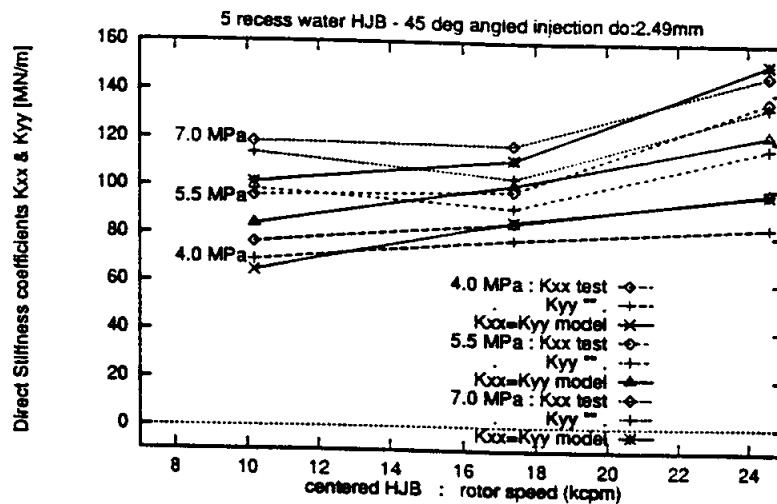


Figure 9. Direct stiffness coefficients ( $K_{xx}$ ,  $K_{yy}$ ) vs. journal speed for water - 5 recess hybrid bearing. Comparison to experimental results.

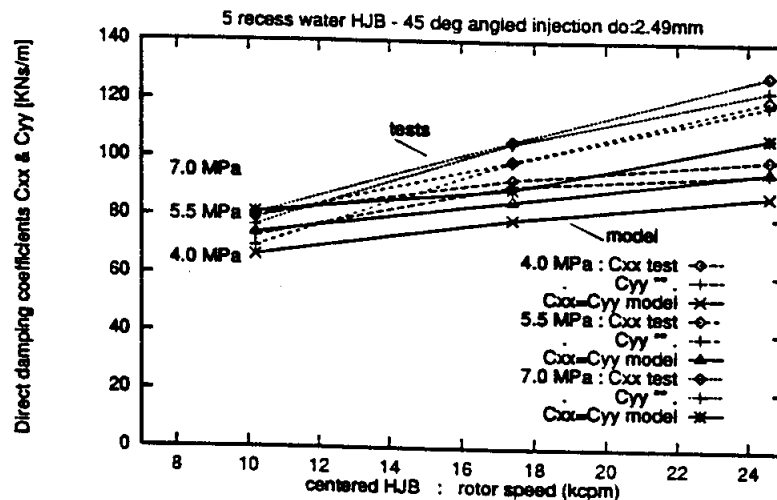


Figure 10. Direct damping coefficients ( $C_{xx}$ ,  $C_{yy}$ ) vs. journal speed for water - 5 recess hybrid bearing. Comparison to experimental results.

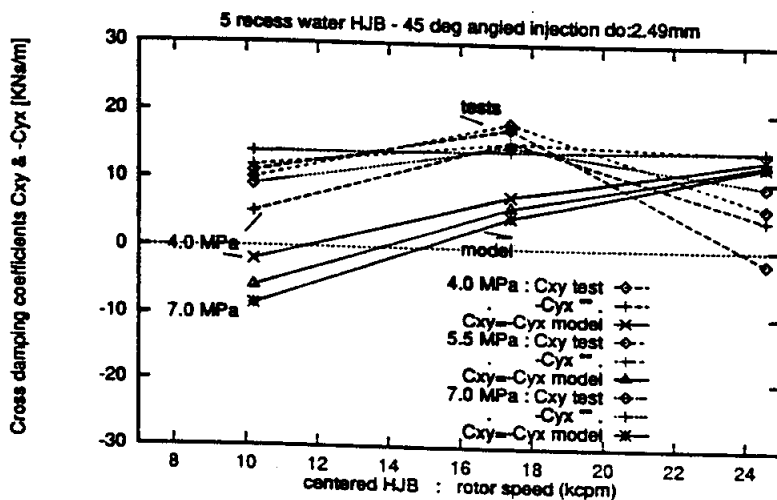


Figure 11. Cross-damping coefficients ( $C_{xy}$ ,  $-C_{yx}$ ) vs. journal speed for water - 5 recess hybrid bearing. Comparison to experimental results.

**12** "Process Liquid Turbulent Flow Hydrostatic Bearings: Analysis and Tests for Rotordynamic Coefficients," 1994, Yang, Z., L. San Andres, and D. Childs, Proceedings of the 4th International IFToMM Rotordynamics Conference, pp. 233-242, Chicago, September.

# PROCESS-LIQUID TURBULENT-FLOW HYDROSTATIC BEARINGS: ANALYSIS AND TESTS FOR ROTORDYNAMIC COEFFICIENTS

*Zhou Yang, Luis San Andres, and Dara W. Childs*

Mechanical Engineering Department  
Texas A&M University  
College Station, Texas 77843

## ABSTRACT

A bulk-flow thermohydrodynamic (THD) analysis is developed for accurate predictions of the static and dynamic performance characteristics of turbulent-flow, process-liquid hydrostatic journal bearings (HJBs). The film-averaged Navier-Stokes equations and energy equation are used to replace the conventional Reynolds equation. Fluid inertia on film lands and at recess edges are preserved in the analysis. Flow turbulence is accounted through turbulence shear parameters based on friction factors derived from Moody's formulae. The effects of fluid compressibility and temperature variation in the recess are included. Extensive comparisons between numerical results and experimental data from a five-recess turbulent-flow water HJB show good agreement. HJBs with journal rotation provide no better stability characteristics than self-acting journal bearings and possess the possibility of half-speed whirl.

## 1. INTRODUCTION

Over the years, one of the most significant indicators of historical change in tribology has been the use of process fluids as lubricants in bearing systems [1]. Process-liquid or product-lubricated hydrostatic journal bearings (HJBs) are now used in liquefied natural gas (LNG) pumps, and consequently, overhaul intervals are extended to several times those of LNG pumps supported on conventional ball bearings [2]. HJBs have also been selected as support elements in future cryogenic high speed turbomachinery such as the High Pressure Fuel Turbopump (HPFTP) and the High Pressure Oxygen Turbopump (HPOTP) of the Space Shuttle Main Engine (SSME) [3].

A systematic research program on HJBs for potential cryogenic turbopump applications has been carried out at the authors' University since 1989. A test facility was designed and built to measure both static and dynamic performance characteristics of hybrid (hydrostatic/hydrodynamic) bearings for the application described above. Purified, heated (55°C) water is used as the lubricant in the facility to achieve comparatively high Reynolds numbers in the test bearing without using cryogenic



Zhao Yang, technical specialist for Cummings Diesel Engines, obtained his B.S. at the Jingzheden Ceramic Institute (1982), M.S. at the Southwest Petroleum Institute (1984) in China, and his Ph.D. in Mechanical Engineering at Texas A&M University (1992). Dr. Yang's expertise is in the areas of computational mechanics and fluid film lubrication.



Luis A. San Andres, Associate Professor of Mechanical Engineering, received his M.S. for the University of Pittsburgh in 1983, and is Ph.D. from the Texas A&M University in 1985. He was awarded the 1989 Applied Science and Technology Award from the Organization of American States.

His research interests are in the areas of fluid film lubrication at high speeds, the mechanics of squeeze film flows, and rotordynamics. Dr. San Andres has performed experimental work on squeeze film damper apparatus typical of jet engine applications. Dr. San Andres current research interests include the development of sound and efficient computational fluid flow models for prediction of static and dynamic force performance of hydrostatic journal and pad bearings, and annular pressure seals for cryogenic liquid applications.



Dara W. Childs, Tenneco Professor of Mechanical Engineering at Texas A&M University. He received his B.S. (1961) and M.S. (1962) degrees in Civil Engineering from Oklahoma State University, and his Ph.D. in Engineering Mechanics from the University of Texas (1968). He has worked for Rocketdyne Division of Rockwell International (1962-65), Colorado State University (1968-71), and the University of Louisville (1971-80), before joining Texas

A&M in 1980.

Dr. Childs' expertise is in the general area of dynamics, vibrations, and controls, with an emphasis over the past several years in the area of rotordynamics. His recent research has concentrated on the influence of seal forces in rotordynamics. He has conducted research and engineering projects for NASA, DOS, and various private firms related to rotordynamics, dynamics, and controls.

He is the author of numerous reviewed publications related to rotordynamics and vibrations, is currently carrying out tests on annular gas seals and hydrostatic bearings. He was named a ASME Fellow Member in 1990.

Proceedings of the 4th International *IFTOMM Rotordynamics Conference*,  
The Vibration Institute, Chicago, IL., September, 1994, pp. 233-242.

liquids. A description of the test facility and program as well as some of the test results is given in [4].

Along with the experimental investigation, San Andres [5,6] introduced a turbulent-inertial bulk flow analysis for prediction of the performance characteristics of orifice-compensated HJBs with incompressible liquids. The film-averaged Navier-Stokes equations were used to replace the conventional Reynolds equation, so that the fluid inertial terms neglected in the classical model could be retained in the analysis. Fluid inertia at the film lands reduces flow rates and enhances hydrodynamic effects. This advanced model also includes the effects of recess volume-fluid compressibility. For laminar flow HJBs recess-volume fluid compressibility is shown to deteriorate the bearing dynamic stability characteristics [7].

To avoid the complexity of a full THD analysis but still partially accounting for the fluid properties variation, San Andres [8] extended the incompressible liquid model to a barotropic fluid model for analysis of cryogenic liquid HJBs. The fluid properties are considered to depend solely on the local pressure and a mean operating (uniform) temperature. Numerical results show the effects of variable properties to be significant for a  $LH_2$  (liquid hydrogen, highly compressible) hydrostatic bearing, but show no significant difference between the two models for a  $LO_2$  (liquid oxygen, less compressible than  $LH_2$ ) bearing.

Here, a bulk-flow thermohydrodynamic (THD) analysis is introduced to determine the static and dynamic performance characteristics for turbulent flow HJBs. Pointwise evaluation of temperature and hence liquid properties is achieved through the solution of the energy transport equation in the fluid film with an adiabatic boundary assumption justified for HJBs with large mass flow rates. The film-averaged Navier-Stokes equations are used to replace the conventional Reynolds equation. Flow turbulence is accounted through turbulence shear parameters based on friction factors derived from Moody's formulae. Numerical predictions of the static and dynamic performance characteristics are compared with experimental data.

The static characteristics of a HJB include the film pressure, fluid velocity and temperature fields, mass flow rate, fluid-film forces or bearing load capacity, friction torque, and power dissipation. The dynamic force characteristics refer to the stiffness ( $K_{ij}$ ), damping ( $C_{ij}$ ), and added mass ( $M_{ij}$ ) coefficients required for rotordynamic analysis. These

coefficients are defined by the following relationship:

$$\begin{bmatrix} F_X \\ F_Y \end{bmatrix} = \begin{bmatrix} F_{X0} \\ F_{Y0} \end{bmatrix} - \begin{bmatrix} K_{XX} & K_{XY} \\ K_{YX} & K_{YY} \end{bmatrix} \begin{bmatrix} \Delta X \\ \Delta Y \end{bmatrix} - \begin{bmatrix} C_{XX} & C_{XY} \\ C_{YX} & C_{YY} \end{bmatrix} \begin{bmatrix} \dot{\Delta X} \\ \dot{\Delta Y} \end{bmatrix} - \begin{bmatrix} M_{XX} & M_{XY} \\ M_{YX} & M_{YY} \end{bmatrix} \begin{bmatrix} \ddot{\Delta X} \\ \ddot{\Delta Y} \end{bmatrix} \quad (1)$$

where  $\Delta X(t)$  and  $\Delta Y(t)$  are the components of the journal-center dynamic displacement about an equilibrium position. The dynamic-force coefficients defined by Eq.(1) are important measures of dynamic bearing performance since they influence the system critical speeds, the resonant amplitude response, and stability of the rotor-bearing system.

## 2. MATHEMATICAL MODEL

The general type of bearing considered as a support element for cryogenic liquid turbopumps is a 360-degree hydrostatic journal bearing, orifice-compensated, with a variable number of feeding recesses or pockets machined in the surface of the bearing [3]. The flow is confined to the thin annular region between an inner rotating journal and a stationary bushing (Fig. 1).

### 2.1 Governing Equations for Turbulent Fluid Film Flows

Large pressure gradients typical in cryogenic HJBs cause high axial turbulent flow Reynolds numbers, and the effect of turbulent mixing far outweighs molecular diffusivity. In consequence, the temperature rise produced by viscous dissipation tends to be distributed uniformly across the film thickness and thus, temperature gradients in the cross-film coordinate ( $z$ ) are confined to turbulent flow boundary layers adjacent to the bounding (bearing and journal) surfaces [9,10]. Furthermore, in the absence of regions of reversed flow or recirculation, the fluid velocity field presents the same characteristics as discussed above.

The considerations presented allow the three dimensional continuity, momentum and energy equations to be integrated across the film thickness to determine the two-dimensional bulk-flow governing equations for thin fluid film flows [11]:

*Continuity Equation*

$$\frac{\partial(\rho H)}{\partial t} + \frac{\partial(\rho H U)}{\partial x} + \frac{\partial(\rho H V)}{\partial y} = 0 \quad (2)$$

*Circumferential-Momentum Equation*

$$\frac{\partial(\rho H U)}{\partial t} + \frac{\partial(\rho H U^2)}{\partial x} + \frac{\partial(\rho H U V)}{\partial y} = -H \frac{\partial P}{\partial x} + \tau_{xz}|_0^H \quad (3)$$

### Axial-Momentum Equation

$$\frac{\partial(\rho HV)}{\partial t} - \frac{\partial(\rho HUV)}{\partial x} - \frac{\partial(\rho HV^2)}{\partial y} = -H \frac{\partial P}{\partial y} - \tau_{yz}|_0^H \quad (4)$$

### Energy-Transport Equation

$$\begin{aligned} C_p \left[ \frac{\partial(\rho HT)}{\partial t} + \frac{\partial(\rho HUT)}{\partial x} + \frac{\partial(\rho HVT)}{\partial y} \right] - Q_r \\ = T\beta_t H \left( \frac{\partial P}{\partial t} - U \frac{\partial P}{\partial x} + V \frac{\partial P}{\partial y} \right) + R\Omega \tau_{xz}|_0^H \\ - U \tau_{xz}|_0^H - V \tau_{yz}|_0^H \end{aligned} \quad (5)$$

where the bulk-flow primitive variables ( $U, V, P$ , and  $T$ ) are defined as average quantities across the film thickness, and  $Q_r$  represents the heat flux from the fluid film to the bounding solids.

The wall shear stresses are calculated according to the bulk-flow theory for turbulence in thin film flows [12,13]:

$$\begin{aligned} \tau_{xz}|_0^H &= -\frac{\mu}{H} (k_x U - k_r \frac{R\Omega}{2}); \\ \tau_{yz}|_0^H &= -\frac{\mu}{H} (k_y V); \\ \tau_{xz}|_0^H &= \frac{H}{2} \frac{\partial P}{\partial x} + \frac{\mu}{4H} [U k_b - (U - R\Omega) k_r] \end{aligned} \quad (6)$$

where the turbulent shear parameters ( $k_x, k_y$ ) and ( $k_r, k_b$ ) are local functions of the Reynolds numbers and friction factors based on Moody's formulae [14].

### 2.2 Mass Conservation at a Recess

The continuity equation at the recess is defined by the global balance between the flow through the orifice restrictor, the recess outflow into the film lands ( $Q_r$ ) and the temporal change of fluid mass within the recess volume ( $\forall_r$ ). The recess flow continuity equation is expressed as:

$$\begin{aligned} A_0 \sqrt{2\rho_r(P_s - P_r)} = Q_r + \rho_r \frac{\partial \forall_r}{\partial t} \\ + \rho_r \forall_r \left( \beta \frac{\partial P}{\partial t} - \beta_t \frac{\partial T}{\partial t} \right)_r \end{aligned} \quad (7)$$

where

$$\beta = \frac{1}{\rho} \left( \frac{\partial \rho}{\partial P} \right)_r, \quad \beta_t = -\frac{1}{\rho} \left( \frac{\partial \rho}{\partial T} \right)_r \quad (8)$$

are the liquid compressibility factor and volumetric expansion coefficient, respectively; and

$$Q_r = \int_{\Gamma_r} \rho H (\vec{U} \cdot \vec{n}) d\Gamma \quad (9)$$

is the mass flow rate across the recess edges ( $\Gamma_r$ ) and entering the film lands.

### 2.3 Global Energy Balance Equation at a Recess

A global energy balance equation at a bearing recess is derived, reflecting the heat carry-over (advection) and mixing effects, and the friction heat generation (dissipation) in the recess (Fig. 2):

$$\begin{aligned} C_p \frac{\partial(\rho T)}{\partial t} \forall_r - C_p \left( \sum \dot{m}_d T_d + 2 \sum \dot{m}_{s,de} T_{s,de} \right) \\ = C_p \left( \sum \dot{m}_u T_u + Q_r T_s \right) + T_{or}^r \Omega \end{aligned} \quad (10)$$

where

$$T_{or}^r = \tau_{xz}^H A_r R \quad (11)$$

is the torque over the recess area.  $Q_r$  is the total mass flow rate through the supply orifice,  $\forall_r$  is the recess volume, and the subscripts "u", "d" and "side" refer to the upstream, downstream, and side edges of a rectangular recess, respectively.

The temperatures at the downstream and side edges of the recess are approximately equal to the recess temperature:

$$T_d = T_{s,de} = T_r = \text{Constant}, \quad (12)$$

while the temperature at the upstream of the recess is given by:

$$T_u = \begin{cases} T_r, & \text{if } (\vec{U} \cdot \vec{n}) > 0; \\ \text{Upstream values}, & \text{otherwise.} \end{cases} \quad (13)$$

### 3. BOUNDARY CONDITIONS

The boundary conditions for the flow variables are expressed as:

(a) On the 360-degree extended film land, the pressure, velocity, and temperature fields are continuous and single-valued in the circumferential ( $x$ ) direction.

(b) Due to geometric symmetry and no journal misalignment, the axial velocity ( $V$ ) and the axial gradients ( $\frac{d}{dy}$ ) of all the flow variables are zero at the circumferential center line ( $y = 0$ ) of the bearing.

(c) At the bearing exit plane ( $y = L$ ), the fluid pressure takes a constant value equal to the



discharge or ambient pressure ( $P_a$ ) for subsonic conditions.

(d) The recess-edge temperatures are obtained as described above. Fluid inertia at the recess edges is treated through a Bernoulli type relationship [8], while the velocity vector is considered to be normal to the recess edges.

(e) At the fluid/journal and the fluid/bearing interfaces, the heat flux to the bounding surfaces  $Q$ , is assumed to be zero.

#### 4. PERTURBATION AND NUMERICAL ANALYSIS

For small amplitude motions of the journal, all the dependent variables as well as the fluid properties are expressed as the superposition of zeroth- and first-order fields representing the steady state and dynamic motion conditions, respectively. Expansion of the governing equations in the perturbation variables yields the zeroth- and first-order flow equations which are derived in detail elsewhere [11].

The coupling of the nonlinear flow equations at the film lands with the mass and energy conservation equations for each recess is a complicated problem which can not be solved analytically. A finite difference scheme is implemented to solve the nonlinear differential equations on the film lands, while the Newton-Raphson scheme is used to update the recess pressure and to satisfy the mass continuity requirement at each bearing recess. Once the zeroth-order and first-order flow fields are obtained, the fluid film forces and the dynamic force coefficients are calculated by integration of the pressure field over the journal surface.

#### 5. RESULTS AND DISCUSSION

The numerical example refers to a HJB article tested by Mosher et al. [15]. The test bearing is a five-recess, orifice-compensated, smooth-surface hydrostatic bearing with characteristics outlined in Table 1. The operating condition for the bearing includes:

- a) 3 Rotational Speeds: 10000, 17500, and 25000 rpm
- b) 3 Supply Pressures: 4.0, 5.5, and 7.0 MPa (600, 800, 1000 psi)
- c) 6 Journal Eccentricity Ratios: 0.0, 0.1, 0.2, 0.3, 0.4, and 0.5
- d) 1 Supply Temperature: 55°C (130°F).

Empirical parameters like the orifice discharge coefficients ( $C_d$ ), the preswirl factor ( $\alpha$ ), and the entrance coefficients at the recess edges ( $\xi_{xu}$ ,  $\xi_{xd}$ , and  $\xi_y$ ) are needed for numerical calculations. Table 2 presents the values of these parameters which are determined by matching measured flow rates with

the calculated ones for the concentric cases. The resulting parameters are then used for the numerical calculations of all non-zero-eccentricity ratio cases.

The viscosity and density of water are calculated from the following formulae given by Sherman [16]:

$$\mu = 1.005 \times 10^{-3} \left( \frac{T}{293} \right)^{8.9} e^{[4700(\frac{1}{T} - \frac{1}{293})]} \quad (14)$$

$$\rho = 1000 e^{-4.85 \times 10^{-4}[(T-293)-(P-0.1)]} \quad (15)$$

where the temperature (T) is in °K and the pressure (P) is in MPa. All the other properties of water are taken as constant.

The rotational Reynolds number ( $Re_c = \rho \cdot \Omega R_c / \mu$ ) based on the supply properties and the nominal clearance is equal to  $2.5 \times 10^4$  for 25000 rpm, thus showing an application where hydrodynamic effects and flow turbulence are quite significant.

Both the measured and predicted bearing dynamic characteristics, such as stiffness, damping, added mass coefficients and whirl frequency ratio as well as static load, flow rate and temperature are presented as follows.

##### 5.1 Static Performance Characteristics

- Static Load Capacity. Fig. 3 shows the experimental and theoretical eccentricity ratios as a function of the static load for the highest speed tested (24600rpm). Note that solid symbols in the figures represent experimental results, while hollow symbols represent numerical predictions. The journal displacement in the bearing increases almost linearly with the static load, which is a common feature for incompressible fluid hydrostatic bearings and annular seals. The bearing load capacity also increases with supply pressure and rotational speed, since a higher supply pressure provides a larger hydrostatic force, and increasing rotational speed generates a greater hydrodynamic force. The numerical predictions correlate very well with experimental measurements (maximum error: 7.4%). Note that the experiments do not start at zero static load, that is, the test bearing is slightly eccentric for zero applied load.

- Mass flow rate. Fig. 4 shows the experimental and theoretical mass flow rate as a function of the eccentricity ratio for supply pressures equal to 4MPa and 7MPa. Note that the symbols do not coincide with each other on the horizontal axis since the eccentricity ratios are actually functions of the given external static loads. The mass flow rate of the bearing decreases slowly with the eccentricity ratio. As expected, a higher supply pressure (i.e.,

higher pressure drop across the orifice) produces a larger mass flow rate. The mass flow rate decreases with rotational speeds due to the fluid viscous forces generated by journal rotation and the reduction of the radial clearance from the centrifugal growth of the shaft. The lowest flow rate occurs at the low supply pressure (4MPa), high eccentricity (0.5) and high speed (24600rpm) condition. The numerical predictions match the experimental data very well (maximum difference <3%).

- **Fluid Temperature.** Fig. 5 shows the experimental and theoretical temperatures near the exit region of the bearing versus the eccentricity ratio. The supply temperature is also presented in the figures (dashed line). The exit temperature increases with the eccentricity ratio. The maximum temperature-rise across the bearing length ( $\Delta T$ ) is about  $4^{\circ}\text{C}$  at the highest speed (24600rpm) and eccentricity ratio (0.5), but the lowest supply pressure (4.0MPa) condition. This is expected since the temperature-rise across the bearing length is proportional to the rotational speed and the torque which increases with eccentricity, but inversely proportional to the mass flow rate which increases with the supply pressure. Note that the contribution of the radial-clearance reduction due to journal rotation to the film temperature rise could be important since a smaller clearance produces a larger friction torque but a smaller bearing leakage. Most of the predicted exit temperatures are higher than the measured values presumably due to the adiabatic flow assumption. The maximum difference between the predicted and measured exit temperatures is less than 2% and occurs at the highest eccentricity ratio (0.5), rotational speed (24600rpm), and supply pressure (7MPa) condition. If only the temperature-rise ( $\Delta T$ ) is considered, the maximum error of prediction is about 27%. However, as to a point-wise match, the numerical predictions are good, and the adiabatic flow assumption is fully justified for the bearing studied.

Experimental data for water HJBs with smaller clearances ( $c=0.0762\text{mm}$  and  $0.1016\text{mm}$ ) are also available but are not presented here. Yang et al. [17] showed that the adiabatic boundary assumption is adequate for fluid film flows with large mass flow rates ( $\dot{M}$ ) (axial heat advection dominates), typical flow conditions for cryogenic liquid annular seals and HJBs. As the bearing clearance decreases, the mass flow rate decreases but the viscous dissipation increases. Table 3 presents the theoretical and experimental exit temperatures of

water HJBs with three different clearances and for the largest speed (24600rpm) and supply pressure (7MPa) tested. Predictions of fluid temperatures for the small clearance ( $c=0.0762\text{mm}$ ) water HJB are not as good as those for the large ( $c=0.127\text{mm}$ ) or the medium ( $c=0.1016$ ) clearance water HJBs. Predictions of all the other bearing performance characteristics like mass flow rate, load capacity, and rotordynamic force coefficients, are not affected by the small temperature variations ( $\Delta T < 10^{\circ}\text{C}$ ) in the three water HJBs.

## 5.2 Dynamic Performance Characteristics

The numerical results for the dynamic force coefficients defined in Eq.(1) are evaluated for synchronous operation ( $\omega=\Omega$ ) and compared with the experimental data as follows.

- **Direct Stiffness.** Fig. 6 shows the direct stiffness coefficients ( $K_{xx}$ ) as a function of the eccentricity ratio. These coefficients are almost constant as the eccentricity ratio increases from 0 to 0.5. The direct stiffness increases with increasing supply pressure since a higher supply pressure provides a larger load capacity (Fig. 3). There is a small increase of direct stiffness with rotational speed (not illustrated here) due to a hydrodynamic effect. The maximum error between the numerical predictions and the experimental measurements is 22.55%.

- **Cross-Coupled Stiffness.** Cross-coupled stiffness coefficients ( $K_{xy}$ ) are presented in Fig. 7 as a function of the eccentricity ratio. Generally, these coefficients decrease slightly with eccentricity ratio. The magnitude of the cross-coupled stiffness is comparable to that of the direct stiffness, which demonstrates the importance of hydrodynamic effects. For the present test bearing, a higher supply pressure yields larger cross-coupled stiffness coefficients due to a higher turbulent viscosity induced by the large pressure drop across the bearing. There is a great increase of the cross-coupled stiffness with rotational speed (not illustrated here) showing the significance of the hydrodynamic influence on the bearing dynamic performance. The maximum error between the theoretical predictions and the experimental data is 22.41% and occurs at the high speed (24600rpm), low supply pressure (4MPa) condition.

- **Direct Damping.** Fig. 8 shows direct damping coefficients ( $C_{xx}$ ) versus the eccentricity ratio. Like the direct stiffness, the direct damping coefficients are relatively insensitive to the variation of the eccentricity ratio. A higher supply pressure generates larger direct damping coefficients, but the influence of rotational speed on direct damping is relatively

small. The theoretical predictions match very well with the experimental data and the maximum error is about 8%.

- **Cross-Coupled Damping.** Fig. 9 shows cross-coupled damping coefficients ( $C_{xy}$ ) as a function of the eccentricity ratio. The prediction shows that these coefficients increase with increasing eccentricity ratio, while the experimental data behave irregularly. The magnitude of the cross-coupled damping coefficients are much smaller than the direct ones. However, according to Eq.(1), these coefficients have a pronounced gyroscopic-like effect on the radial bearing force component at a high whirl frequency ( $\omega$ ). The numerical predictions are generally poor. The combined effect of the cross-coupled damping with the direct added mass coefficients will be presented later.

- **Added Mass.** The added mass coefficients are usually neglected in conventional rotor-bearing dynamic analysis. Very little experimental data are available in the open literature for these coefficients. Fig. 10 shows the direct added mass coefficients ( $M_{xx}$ ) as a function of eccentricity ratio, while the cross-coupled added mass coefficients ( $M_{xy}$ ) are presented in Fig. 11. The experimental added masses behave irregularly as the journal eccentricity increases. Note that the direct added mass coefficients could be as large as the mass of the test bearing (11.34kg), which shows that fluid inertial effects are very important for turbulent flow HJBs and can not be neglected. Like the cross-coupled damping, the added mass coefficients are poorly predicted. However, as will be shown below, the combined effect of the cross-coupled damping with the direct added mass on the effective stiffness is most important.

- **Effective Stiffness and Damping.** For a small circular orbit and synchronous ( $\omega = \Omega$ ) whirling around the static equilibrium position, the effective stiffness and damping can be simply derived from Eq.(1) as

$$K_{xxe} = K_{xx} + \Omega C_{xy} - \Omega^2 M_{xx} \quad (16)$$

$$K_{yye} = K_{yy} - \Omega C_{yx} - \Omega^2 M_{yy} \quad (17)$$

$$C_{xxe} = C_{xx} - K_{xy}/\Omega + \Omega M_{xy} \quad (18)$$

$$C_{yye} = C_{yy} + K_{yx}/\Omega - \Omega M_{yx} \quad (19)$$

From these equations, it can be seen that positive cross-coupled damping ( $C_{xy}$ ) and negative direct added mass ( $M_{xx}$ ) increase the effective stiffness, while positive cross-coupled stiffness ( $K_{xy}$ ) and negative cross-coupled added mass ( $M_{yx}$ ) lower

the effective damping. Table 4 shows the contributions of the cross-coupled damping and direct added mass to the direct stiffness, while the effects of the cross-coupled stiffness and added mass on the direct damping are presented in Table 5 for the high speed (24600rpm), high pressure (7.0MPa) and zero eccentricity condition.

The combined contribution of the cross-coupled damping and the direct added mass ( $\Omega C_{xy} - \Omega^2 M_{xx}$ ) to the direct stiffness is relatively small (about 10%) even though the individual contribution of  $C_{xy}$  or  $M_{xx}$  is large (about 50%). The cross-coupled stiffness greatly reduces the direct damping (about 50%), while the effect of the cross-coupled added mass is small. These results explain why the cross-coupled damping and the added mass coefficients sometimes can both be neglected and still obtain meaningful predictions for the rotordynamic performance of HJBs.

Table 6 presents the maximum error, average error, and standard deviation for all the effective stiffness and damping coefficients. These results show that the dynamic performance characteristics of the bearing are well predicted.

- **Whirl Frequency Ratio.** Like the effective stiffness and damping coefficients, the whirl frequency ratio (WFR) is a dynamic parameter which acts as an indicator of bearing stability. A low WFR indicates enhanced ability of a bearing/journal system to safely operate at higher running speeds relative to the first critical speed of the system.

Fig. 12 illustrates the whirl frequency ratio as a function of the eccentricity ratio. The WFR is approximately 0.5 for all conditions. Thus, hydrostatic (hybrid) bearings offer no better stability characteristics than hydrodynamic bearings and show the likelihood of half-speed whirl. The maximum difference between the theoretical and experimental results is 8.35% which, added to the good simulation of the effective stiffness and damping, shows that the bearing dynamic performance characteristics can be well predicted by the theoretical model and computer code developed.

## 6. CONCLUSIONS

A bulk-flow thermohydrodynamic (THD) analysis is developed for accurate predictions of the static and dynamic performance characteristics of process-liquid turbulent-flow hydrostatic journal bearings (HJBs). A finite difference scheme is implemented to solve the nonlinear differential equations on the film lands, while the Newton-Raphson scheme is used to update the recess pressures and

to satisfy the mass continuity requirement at each bearing recess. Extensive comparisons between numerical results and experimental data of turbulent flow water HJBs show very good correlations and demonstrate the correctness and accuracy of the THD analysis and the numerical scheme implemented.

The bearing load capacity increases almost linearly with journal eccentricity and a higher supply pressure or rotational speed provides a larger load capacity. The mass flow rate of the bearing decreases with eccentricity ratio and rotational speed but increases with supply pressure. The exit fluid temperature increases with eccentricity ratio and rotational speed but decreases with supply pressure.

All the dynamic force coefficients remain relatively constant for the eccentricity ratios tested (0 to 0.5). The whirl frequency ratio appears to be 0.5 for all conditions, showing that HJBs with journal rotation present stability characteristics similar to those of plain journal bearings. The combined effects of the cross-coupled damping ( $C_{xy}$  or  $-C_{yx}$ ) and the direct added mass ( $M_{xx}$  or  $M_{yy}$ ) coefficients on the effective stiffness ( $K_{xxe}$ ) are negligible. Note that most rotordynamic codes only allow for a bearing model without the added mass coefficients while retaining the cross-coupled damping. According to the analysis and results presented this modeling procedure will lead to errors. If the mass terms can not be incorporated into the analysis, the cross-coupled damping terms should also be dropped.

#### ACKNOWLEDGMENTS

The support of Pratt&Whitney Co. and NASA Lewis Research Center are gratefully acknowledged. Thanks to Mr. James Walker of NASA Lewis for his encouragement on developing this work.

#### REFERENCES

- [1] Fuller, D.D., 1990, "Hydrodynamic and Hydrostatic Fluid-Film Bearings," *Achievements in Tribology*, Edited by L.B. Sibley and F.E. Kennedy, Trib-Vol.1, Published by ASME.
- [2] Katayama, T., and Okada, A., 1992, "Liquefied Natural Gas Pump with Hydrostatic Journal Bearings," Proceedings of the 9th International Pump Users Symposium, Houston, Texas, pp.39-50.
- [3] Butner, M., and Murphy, B., 1986, "SSME Long Life Bearings," NASA Report, CR179455.
- [4] Kurtin, K.A., Childs, D., San Andres, L., and Hale, K., 1991, "Experimental Versus Theoretical Characteristics of a High-Speed Hybrid (Combination Hydrostatic and Hydrodynamic) Bearing," ASME Papers, 91-Trib-35.
- [5] San Andres, L., 1990a, "Turbulent Hybrid Bearings with Fluid Inertia Effects," ASME JOURNAL OF TRIBOLOGY, Vol. 112, pp.699-707.
- [6] San Andres, L., 1990b, "Approximate Analysis of Turbulent Hybrid Bearings: Static and Dynamic Performance for Centered Operation," ASME JOURNAL OF TRIBOLOGY, Vol. 112, pp.692-698.
- [7] San Andres, Luis A., 1991a, "Effect of Fluid Compressibility on the Dynamic Response of Hydrostatic Journal Bearings," *Wear*, Vol. 146, pp.269-283.
- [8] San Andres, Luis A., 1991b, "Analysis of Turbulent Hydrostatic Bearings with a Barotropic Cryogenic Fluid," ASME Papers, 91-TRIB-47.
- [9] Suganami, T., and Szeri, A.Z., 1979, "A Thermohydrodynamic Analysis of Journal Bearings," ASME JOURNAL OF LUBRICATION TECHNOLOGY, Vol. 101, pp.21-27.
- [10] Di Pasquantonio, F., and Sala, P., 1984, "Influence of Thermal Field on the Resistance Law in Turbulent Bearing-Lubrication Theory," ASME JOURNAL OF TRIBOLOGY, Vol. 106, pp.368-376.
- [11] Yang, Z., San Andres, L., and Childs, D., 1992a, "Thermal Effects in Cryogenic Liquid Annular Seals, Part I: Theory and Approximate Solution; Part II: Numerical Solution and Results," ASME Papers, 92-TRIB-4&5, also to be published in ASME JOURNAL OF TRIBOLOGY.
- [12] Hirs, G.G., 1973, "A Bulk-Flow Theory for Turbulence in Lubricant Films," ASME JOURNAL OF LUBRICATION TECHNOLOGY, Vol. 95, pp.137-146.
- [13] Launder, B.E., and Leschziner, M., 1978, "Flow in Finite Width Thrust Bearings Including Inertial Effects, I- Laminar Flow, II- Turbulent Flow," ASME JOURNAL OF LUBRICATION TECHNOLOGY, Vol. 100, pp.330-345.
- [14] Massey, B.S., 1983, *Mechanics of Fluids*, Van Nostrand Reinhold (UK) Co. Ltd., Workingham, Berkshire, England.
- [15] Mosher, P., Franchek, N., Rouvas, C., Hale, H., and Childs, D., 1991, "Experimental Rotordynamic Coefficient Results for a Square-Recess Smooth-Land Straight-Orifice Large-Clearance Hybrid Bearing," Research Report, TAMU-0508, Texas A&M University, College Station, TX 77843.
- [16] Sherman, F.S., 1990, *Viscous Flow*, McGraw-Hill, New York.
- [17] Yang, Z., San Andres, L., and Childs, D., 1992b, "Importance of Heat Transfer from Fluid Film to Stator in Turbulent Annular Seals," accepted for publication in *Wear*.

# NOMENCLATURE

$A$	$\pi DL$ , journal or bearing surface area [ $m^2$ ]	$r_r, r_B$	mean roughness depth at journal and bearing surfaces [ $m$ ]
$A_o$	$C_d \pi d_o^2 / 4$ , equivalent orifice area [ $m^2$ ]	$T$	bulk fluid-film temperature [ $K$ ]
$A_r$	bl. recess area [ $m^2$ ]	$\Delta T$	$T_{exit} - T$ , [ $K$ ]
$b$	recess circumferential length [ $m$ ]	$t$	time [sec]
$c, c_r$	radial clearance, characteristic clearance ( $=\{c(y)\}_{min}$ ) [ $m$ ]	$T_{or}^r$	$\tau_{xz}^H \cdot A_r R$ , torque over a recess [ $N \cdot m$ ]
$C_d$	empirical orifice discharge coefficient	$U, V$	mean velocities [ $m/s$ ]
$C_p$	specific heat [ $J/kg \cdot K$ ]	$\bar{U}$	$U\bar{i} + V\bar{j}$
$D$	journal diameter [ $m$ ]	$\nabla_r$	$(H_r + H)A_r + \nabla_r$ , recess volume [ $m^3$ ]
$d_o$	orifice diameter [ $m$ ]	$\nabla_s$	volume of orifice supply line [ $m^3$ ]
$e_x, e_r$	displacements of the journal [ $m$ ]	$X, Y$	inertial coordinates
$f_j, f_B$	$a_m [1 + (c_m r_{j,B} / H + b_m / R_{j,B})^{e_m}]$ , turbulent friction factors based on Moody's equation, $a_m = 0.001375$ ; $b_m = 5 \times 10^5$ ; $c_m = 10^4$ ; $e_m = \frac{1}{2.65}$	$x, y, z$	$(0, \pi D), (0, L), (0, H(x, y, t))$
$F_x, F_y$	fluid film forces [ $N$ ]	$\alpha$	$(U _{y=0}) / (\Omega R)$ , circumferential velocity entrance swirl factor
$H, H_r$	film thickness, recess depth [ $m$ ]	$\Omega$	rotational speed of journal [rad/sec]
$k_x, k_y$	$(k_j + k_o) / 2$	$\omega$	excitation or whirling frequency [rad/sec]
$k_j, k_o$	$f_j R_j, f_B R_B$ , turbulent shear parameters	$\rho$	fluid density [ $kg/m^3$ ]
$L, l$	bearing & recess axial lengths [ $m$ ]	$\mu$	fluid viscosity [ $Ns/m^2$ ]
$\dot{m}$	flow rate over differential segments [ $kg/s$ ]	$\xi_{x,y}$	empirical entrance loss coefficients
$\dot{M}$	bearing mass flow rate [ $kg/s$ ]	$\xi_{xu,d}$	$\xi_x$ at up-, down-stream recess edges
$\bar{n}$	normal vector to recess boundary	$\varepsilon$	$e/c_r$ , dimensionless journal eccentricity
$N_{rec}$	number of bearing recesses	$\tau$	$\omega t$ dimensionless time coordinate
$P$	fluid pressure [ $N/m^2$ ]	$\tau_{xz}, \tau_{yz}$	wall shear stresses
$R$	journal radius [ $m$ ]	<b>Scripts:</b>	
$Re_c$	$\rho \cdot R \Omega c_r / \mu_r$ , nominal circumferential flow Reynolds number	$a$	refers to ambient or discharge conditions
$R_j$	$\rho H \sqrt{(U - \Omega R)^2 + V^2} / \mu$ , Reynolds number relative to journal surface	$r$	refers to recess conditions
$R_B$	$\rho H \sqrt{U^2 + V^2} / \mu$ , Reynolds number relative to bearing surface	$s$	refers to supply conditions
		$j$	refers to journal
		$B$	refers to bushing
		$*$	refers to characteristic (supply) values

Table 1 Characteristics of Water HJB [15].

Diameter (D)	76.441 mm (3.0095 in)
Length (L)	76.2 mm (3 in)
No. of Recesses ( $N_{rec}$ )	5
Recess Volume ( $\nabla_r$ )	$0.185 \times 10^{-6} m^3$ (0.0112891 in <sup>3</sup> )
Recess Area Ratio ( $A_r/A$ )	0.2
Orifice Diameter ( $d_o$ )	2.49 mm (0.098 in)
Orifice Supply Line Volume ( $\nabla_s$ )	$0.129 \times 10^{-6} m^3$ (0.00787173 in <sup>3</sup> )
Land Roughness (peak-peak) ( $r_j$ & $r_B$ )	0.33 $\mu m$ (13 $\mu in$ )
Square Recess ( $A_r \times B_r$ )	$27 \times 27 mm^2$ (1.064 $\times$ 1.064 in <sup>2</sup> )
Nominal Clearance (at zero speed) ( $c_r$ )	0.127 mm (0.005 in)
Supply Fluid Temperature ( $T_s$ )	328°K (130°F)

Table 2 Empirical Parameters for Water HJB.

$\Omega$ (rpm)	$P_s$ (MPa)	$C_d$	$\alpha$	$\xi_{xu}$	$\xi_{xd}$	$\xi_y$
17400	4.0	0.9035	0.5	0.25	0.5	0.5
	7.0	0.8578	0.5	0.25	0.5	0.5
24600	4.0	0.8812	0.5	0.25	0.5	0.5
	7.0	0.8984	0.5	0.25	0.5	0.5

Table 3 Theoretical and Experimental Exit Temperatures ( $T_{exit}$ ) of Water HJBs with Different Radial Clearances. ( $\Omega=24600$ rpm,  $P_s=7$ MPa,  $P_a=0.1$ MPa,  $T_s=55^\circ\text{C}$ )

$T_{exit}(^\circ\text{C})^*$	$\varepsilon=0.0$	$\varepsilon=0.1$	$\varepsilon=0.2$	$\varepsilon=0.3$	$\varepsilon=0.4$	$\varepsilon=0.5$	$M$
$c_r=0.0762\text{mm}$	61.67	61.76	62.07	62.52	63.25	64.48	$\approx 0.5$
	60.03	60.14	60.33	60.36	59.93	61.50	kg/s
$c_r=0.1016\text{mm}$	58.06	58.37	58.73	59.17	59.82	60.95	$\approx 1.4$
	58.01	58.09	58.21	58.61	59.20	59.62	kg/s
$c_r=0.1270\text{mm}$	57.41	57.59	57.92	58.27	58.85	59.48	$\approx 1.7$
	57.34	57.58	57.74	57.87	58.03	58.50	kg/s

Table 4 Contribution of Cross-Coupled Damping and Direct Added Mass to Effective Stiffness. ( $\Omega=24600$ rpm,  $P_s=7$ MPa,  $\varepsilon=0$ )

$\Omega C_{xy}$ (MN/m)	$\Omega^2 M_{xx}$ (MN/m)	$\Omega C_{xy} - \Omega^2 M_{xx}$ (MN/m)	$K_{xx}$ (MN/m)	$(\Omega C_{xy} - \Omega^2 M_{xx})/K_{xx}$ (%)
75.5*	67.0	8.45	144	5.9
38.6**	59.7	-21.1	146	-14

\* 1st row—Theoretical results; \*\* 2nd row—Experimental results

Table 5 Contribution of Cross-Coupled Stiffness and Added Mass to Effective Damping. ( $\Omega=24600$ rpm,  $P_s=7$ MPa,  $\varepsilon=0$ )

$K_{xy}/\Omega$ (KNs/m)	$\Omega M_{xy}$ (KNs/m)	$-K_{xy}/\Omega + \Omega M_{xy}$ (KNs/m)	$C_{xx}$ (KNs/m)	$(-K_{xy}/\Omega + \Omega M_{xy})/C_{xx}$ (%)
50.8*	-4.25	-55.1	109	-50.1
52.6**	-13.9	-66.5	112	-59.4

\* 1st row—Theoretical results; \*\* 2nd row—Experimental results

Table 6 Prediction Error and Standard Deviation for Effective Stiffness and Damping Coefficients.

Item	Maximum Error	Average Error	Standard Deviation
$K_{xxe}$	42.3%	16.6%	11.6%
$K_{yye}$	16.5%	8.6%	4.6%
$C_{xxe}$	24.9%	11.1%	7.9%
$C_{yye}$	21.3%	8.8%	5.5%

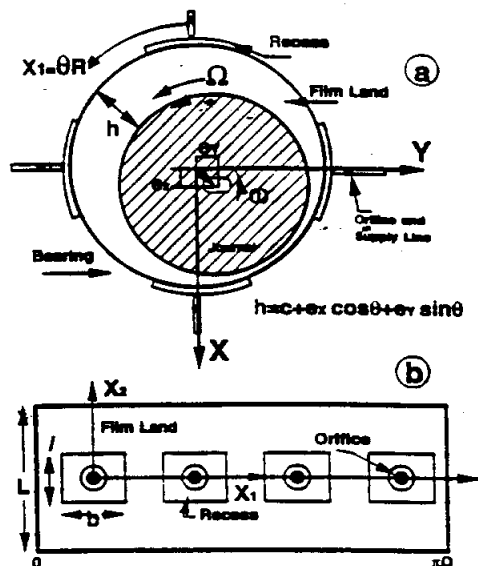


Fig. 1 Geometry of a hydrostatic journal bearing:  
a) Axial View and Coordinate System.  
b) Unwrapped Bearing Surface

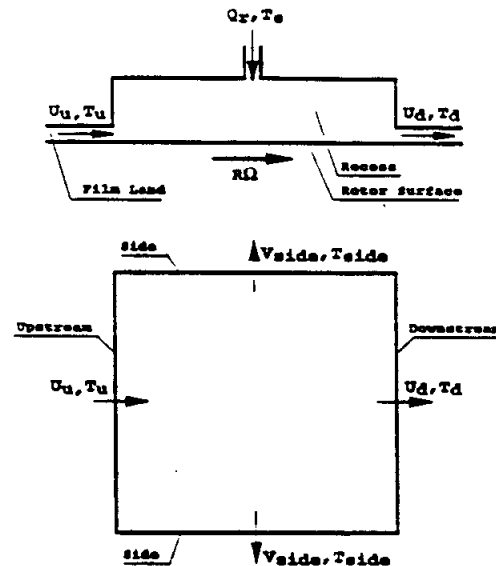


Fig. 2 Conceptual description of global energy balance at a recess

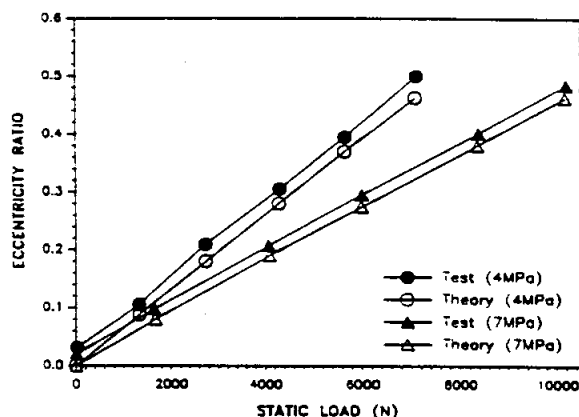


Fig. 3 Eccentricity ratio versus static load (Water HJB)  
( $P_s=4$  &  $7\text{MPa}$ ,  $P_a=0.1\text{MPa}$ ,  $T_s=55^\circ\text{C}$ ,  $\Omega=24,700\text{rpm}$ )

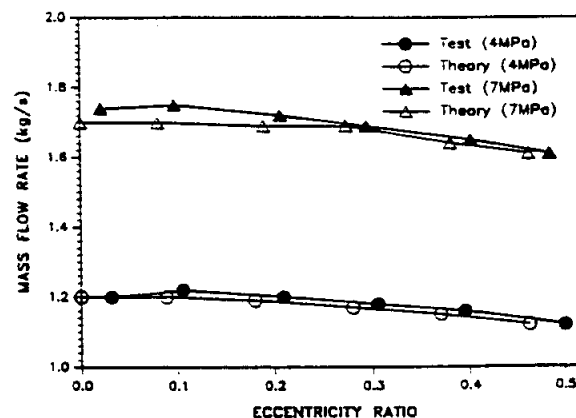


Fig. 4 Mass flow rate vs eccentricity ratio (Water HJB)  
( $P_s=4$  &  $7\text{MPa}$ ,  $P_a=0.1\text{MPa}$ ,  $T_s=55^\circ\text{C}$ ,  $\Omega=24,700\text{rpm}$ )

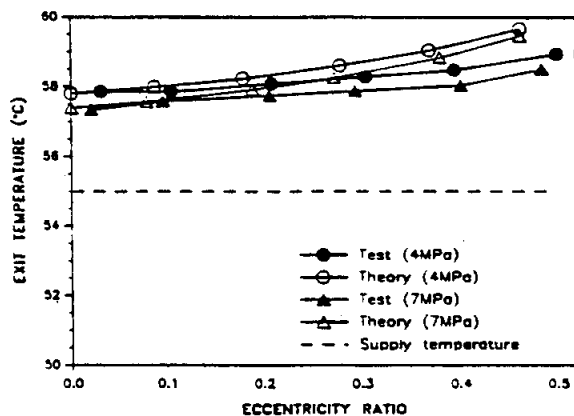


Fig. 5 Exit temperature vs eccentricity ratio (Water HJB)  
( $P_s=4$  &  $7\text{MPa}$ ,  $P_a=0.1\text{MPa}$ ,  $T_s=55^\circ\text{C}$ ,  $\Omega=24,700\text{rpm}$ )

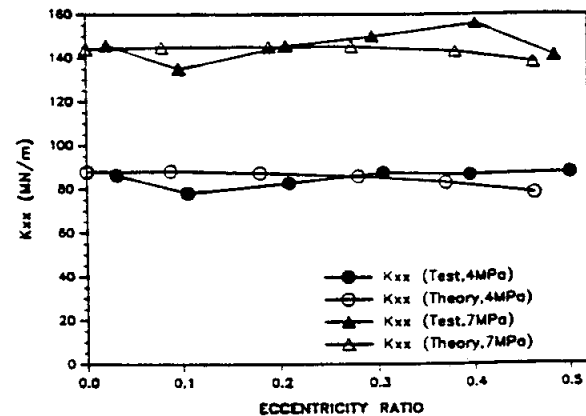


Fig. 6 Direct stiffness ( $K_{xx}$ ) vs eccentricity ratio (Water HJB)  
( $P_s=4$  &  $7\text{MPa}$ ,  $P_a=0.1\text{MPa}$ ,  $T_s=55^\circ\text{C}$ ,  $\Omega=24,700\text{rpm}$ )

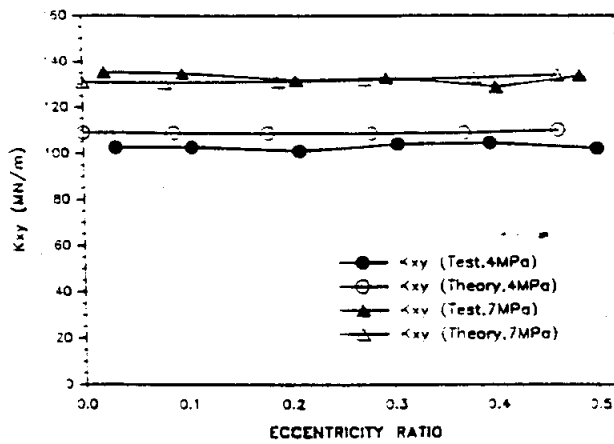


Fig. 7 Cross-coupled stiffness ( $K_{xy}$ ) vs eccentricity ratio ( $P_s=4$  &  $7\text{MPa}$ ,  $P_a=0.1\text{MPa}$ ,  $T_s=65^\circ\text{C}$ ,  $\Omega=24,700\text{rpm}$ )

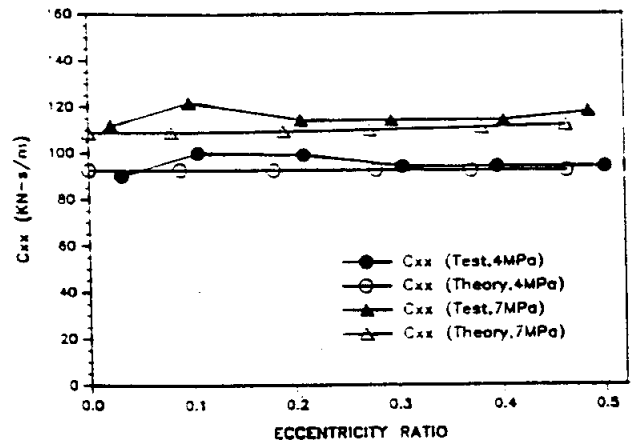


Fig. 8 Direct damping ( $C_{xx}$ ) vs eccentricity ratio (Water HJB) ( $P_s=4$  &  $7\text{MPa}$ ,  $P_a=0.1\text{MPa}$ ,  $T_s=65^\circ\text{C}$ ,  $\Omega=24,700\text{rpm}$ )

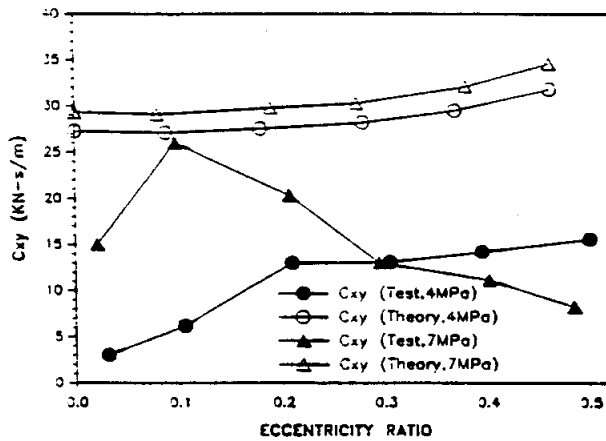


Fig. 9 Cross-coupled damping ( $C_{xy}$ ) vs eccentricity ratio ( $P_s=4$  &  $7\text{MPa}$ ,  $P_a=0.1\text{MPa}$ ,  $T_s=65^\circ\text{C}$ ,  $\Omega=24,700\text{rpm}$ )

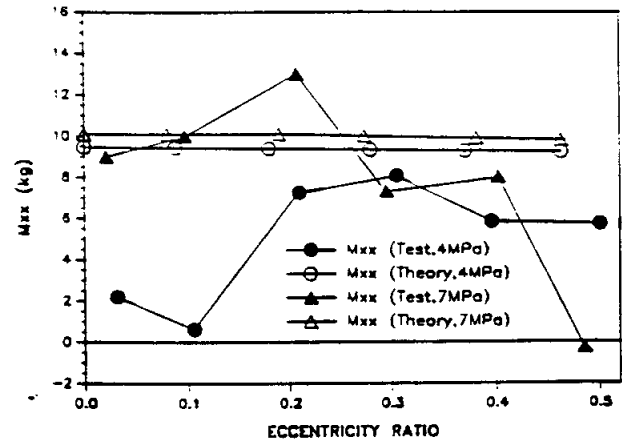


Fig. 10 Direct added mass ( $M_{xx}$ ) vs eccentricity ratio ( $P_s=4$  &  $7\text{MPa}$ ,  $P_a=0.1\text{MPa}$ ,  $T_s=65^\circ\text{C}$ ,  $\Omega=24,700\text{rpm}$ )

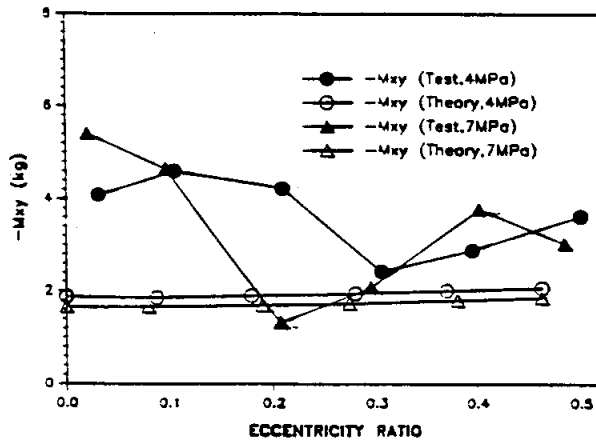


Fig. 11 Cross-coupled added mass ( $-M_{xy}$ ) vs eccentricity ratio ( $P_s=4$  &  $7\text{MPa}$ ,  $P_a=0.1\text{MPa}$ ,  $T_s=65^\circ\text{C}$ ,  $\Omega=24,700\text{rpm}$ )

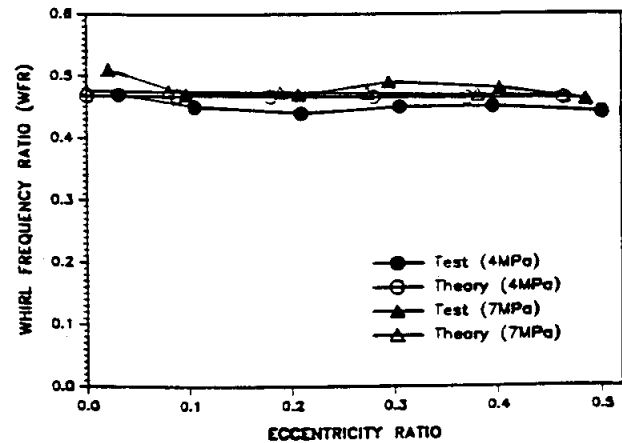


Fig. 12 Whirl frequency ratio vs eccentricity ratio (Water HJB) ( $P_s=4$  &  $7\text{MPa}$ ,  $P_a=0.1\text{MPa}$ ,  $T_s=65^\circ\text{C}$ ,  $\Omega=24,700\text{rpm}$ )



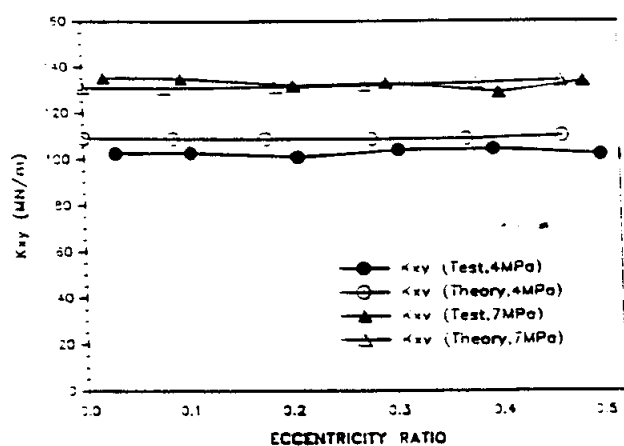


Fig. 7 Cross-coupled stiffness ( $K_{xy}$ ) vs eccentricity ratio ( $P_s=4$  &  $7\text{MPa}$ ,  $P_a=0.1\text{MPa}$ ,  $T_s=65^\circ\text{C}$ ,  $\Omega=24,700\text{rpm}$ )

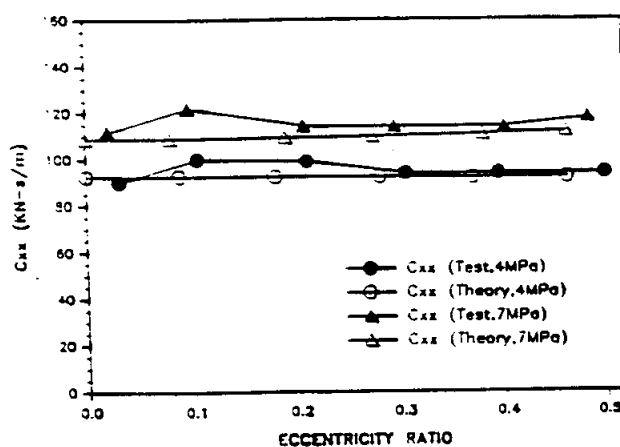


Fig. 8 Direct damping ( $C_{xx}$ ) vs eccentricity ratio (Water HJB) ( $P_s=4$  &  $7\text{MPa}$ ,  $P_a=0.1\text{MPa}$ ,  $T_s=65^\circ\text{C}$ ,  $\Omega=24,700\text{rpm}$ )

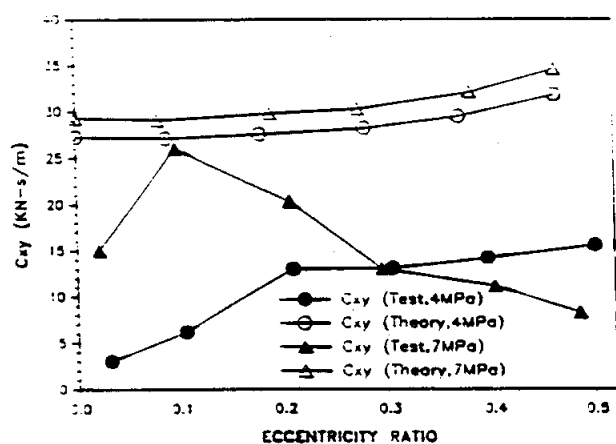


Fig. 9 Cross-coupled damping ( $C_{xy}$ ) vs eccentricity ratio ( $P_s=4$  &  $7\text{MPa}$ ,  $P_a=0.1\text{MPa}$ ,  $T_s=65^\circ\text{C}$ ,  $\Omega=24,700\text{rpm}$ )

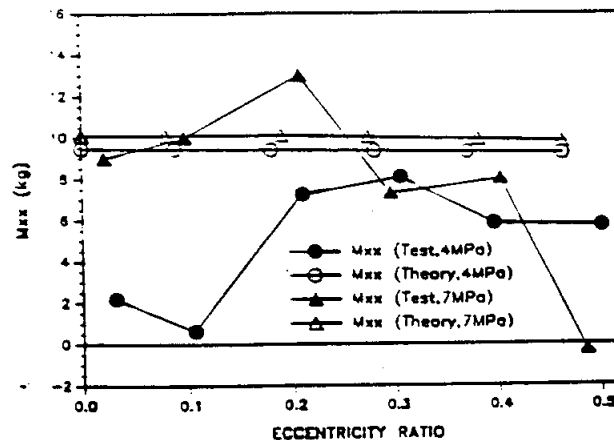


Fig. 10 Direct added mass ( $M_{xx}$ ) vs eccentricity ratio ( $P_s=4$  &  $7\text{MPa}$ ,  $P_a=0.1\text{MPa}$ ,  $T_s=65^\circ\text{C}$ ,  $\Omega=24,700\text{rpm}$ )

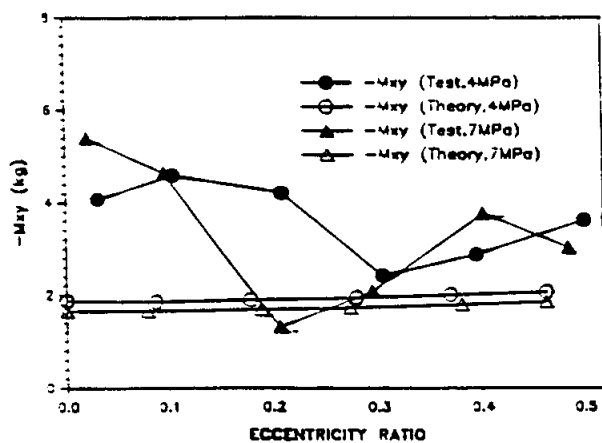


Fig. 11 Cross-coupled added mass ( $-M_{xy}$ ) vs eccentricity ratio ( $P_s=4$  &  $7\text{MPa}$ ,  $P_a=0.1\text{MPa}$ ,  $T_s=65^\circ\text{C}$ ,  $\Omega=24,700\text{rpm}$ )

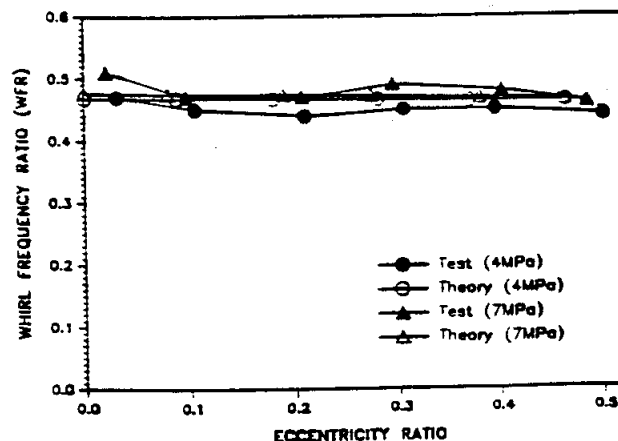


Fig. 12 Whirl frequency ratio vs eccentricity ratio (Water HJB) ( $P_s=4$  &  $7\text{MPa}$ ,  $P_a=0.1\text{MPa}$ ,  $T_s=65^\circ\text{C}$ ,  $\Omega=24,700\text{rpm}$ )

**13** "Thermohydrodynamic Analysis of Fluid Film Bearings for Cryogenic Applications," 1994, San Andres, L., and Yang, Z., Proceedings of the 6th NASA Conference on Advanced Earth-to-Orbit Propulsion Technology, Huntsville, Alabama, May, NASA CP 3282, Vol. II, pp. 421-430.



# Advanced Earth-to-Orbit Propulsion Technology – 1994

---

*Edited by*  
*R.J. Richmond and S.T. Wu*

## NOTICE

This document contains information which falls under the purview of the U.S. Munitions List, as defined in the International Traffic in Arms Regulations. It shall not be transferred to foreign nationals, in the U.S., or abroad, without specific approval. Penalty for violations is described in ITAR, section 127.

Proceedings of a conference held  
at NASA George C. Marshall Space Flight Center  
Marshall Space Flight Center, Alabama  
May 17-19, 1994

---

September 1994

# THERMOHYDRODYNAMIC ANALYSIS OF FLUID FILM BEARINGS FOR CRYOGENIC APPLICATIONS

Luis San Andres, Associate Professor  
Zhou Yang, Research Associate

Mechanical Engineering Department  
Texas A & M University  
College Station, Texas 77843

## ABSTRACT

A thermohydrodynamic analysis and a computer code are developed for prediction of the static and dynamic force response of hydrostatic journal bearings (HJBs), annular seals or damping bearings, and fixed arc pad bearings. The study includes the most important flow characteristics found in cryogenic fluid film bearings such as flow turbulence, fluid inertia, liquid compressibility and thermal effects. Predictions from the numerical model correlate well with experimental results for both laminar flow and turbulent flow bearing configurations. Numerical results detail a comparison of the static performance and dynamic force coefficients for a hydrostatic bearing and a damping bearing-seal for the HPOTP. The calculations indicate that turbulent flow, externally pressurized bearings support the expected loads with moderate journal center eccentricities, and with force coefficients of relevant magnitude for this critical application.

## 1. INTRODUCTION

Hydrostatic Journal Bearings (HJBs) are the ideal candidates to replace roller bearings as support elements in cryogenic turbomachinery. These bearings along with hydrostatic annular seals will be used for primary space-power applications due to their long lifetime, low friction and wear, significant load capacity, and large direct stiffness and damping force coefficients. Fluid film bearings, unlike rolling element bearings, have no DN limit. Rotating machinery free of this constraint can operate at larger speeds with better efficiency and reduced overall weight and size. Durability in fluid film bearings is assured by the absence of contact between stationary and moving parts during steady-state operation, while long life reduces the frequency of required overhauls. Despite these attractive features, dynamic stability considerations and thermal phenomena along with two-phase flow operation are primary concerns for high speed operation in bearings with large pressure differentials. Fluid film bearing stability is essentially related to hydrodynamic and liquid compressibility effects, while thermal effects are of importance due to flow turbulence with substantial energy dissipation.

A comprehensive literature review on the subject of hydrostatic bearings and annular seals relevant to cryogenic liquid applications has been presented elsewhere (San Andres, 1990-93). A systematic experimental and computational research program on HJBs and seals for cryogenic turbopump applications has been carried out at Texas A & M University since 1989. The test facility has provided relevant experimental data for the static and dynamic force characteristics of turbulent flow, water lubricated hydrostatic bearings and annular seals. Experimental measurements are routinely performed for bearings of different geometries and at journal speeds ranging from 10,000 to 25,000 rpm and pressure supplies from 4 to 7 MPa (Childs and Hale, 1993). Lindsey (1993) has recently reported measured force coefficients for short length-annular seals with uniform, convergent and divergent axial clearances. Kurtin et al. (1993), Franchek (1992) and Mosher (1993) have reported experimental data for the static load and dynamic force coefficients of 5 recess, water HJBs at the operating conditions noted. The test results refer to bearing clearances from 76 to 125 microns, different recess pressure ratios and shapes, smooth and rough bearing surfaces, and radial vs. angled liquid orifice injection. The experimental results correlate favorably with predictions from the numerical models developed by San Andres (1990,92). Accurate theoretical results depend greatly on the knowledge of the bearing operating clearance, bearing surface conditions, and most importantly, on the orifice discharge coefficients.

Along with the experimental investigation, San Andres (1990,1992) developed a turbulent-inertial bulk flow analysis for prediction of the performance characteristics of orifice-compensated HJBs with variable properties fluids, and demonstrated the advantages of the model when compared to traditional approaches based on laminar flow, classical lubrication theory. Yang, San Andres and Childs (1993, 1994) have introduced a thermohydrodynamic (THD) analysis for the prediction of the static and dynamic performance characteristics of

cryogenic liquid annular seals and hydrostatic journal bearings. Shear parameters based on friction factors derived from Moody's formulae account for flow turbulence. The effects of fluid compressibility and temperature variation in the bearing recesses are included. Numerical results show the effects of fluid compressibility to be significant for  $LH_2$  hydrostatic bearings with the potential of a stability indicator worse than that found in plain journal bearings due to pneumatic hammer at the bearing recesses. Predictions from the THD model correlate well with measured temperatures for the Pre-burner Impeller Rear Wear-Ring Seal of the SSME high pressure oxidizer turbopump. Calculations performed for a high speed, rough surface  $LO_2$  seal predict a large temperature rise and the onset of two-phase flow conditions (liquid boiling) at moderate shaft eccentricities despite the large pressure differentials imposed across the seal. It is imperative to note that large temperature rises in a cryogenic seals and bearings can lead to thermal solid distortions affecting the operating clearance and possibly causing a significant reduction on the direct stiffness of the hydrostatic seal.

This paper presents the thermohydrodynamic analysis of real properties, fluid film bearings for cryogenic applications. The bearings studied include hydrostatic pad bearings with rectangular recesses, annular pressure seals or damping bearings, and cylindrical rigid-pad hydrodynamic bearings. The theoretical model refers to bearings of asymmetric geometry, non-uniform pressure discharges, and arbitrary clearance distribution. The motion of a liquid on the thin film annular region of a fluid film bearing is described by a set of mass, momentum conservation, and energy transport equations for the primitive turbulent bulk-flow variables, and accompanied by realistic thermophysical state equations for evaluation of the fluid material properties. Zeroth-order equations describe the fluid flow field for a journal static equilibrium position, while first-order linear equations govern the fluid flow for small amplitude journal center translational motions and journal axis conical motions.

Solution to the zeroth-order flow field equations provides the bearing flow rate, load capacity, torque, and restoring moments due to journal misalignment. Solution to the first-order equations determines the rotordynamic force and moment coefficients due to journal lateral and angular motions. For lateral shaft (journal) excursions, the dynamic force characteristics refer to the stiffness ( $K_{ij}$ ), damping ( $C_{ij}$ ), and added mass ( $M_{ij}$ ) coefficients,

and related to the dynamic forces by:

$$\begin{bmatrix} F_x \\ F_y \end{bmatrix} = \begin{bmatrix} F_{x0} \\ F_{y0} \end{bmatrix} - \begin{bmatrix} K_{xx} & K_{xy} \\ K_{yx} & K_{yy} \end{bmatrix} \begin{bmatrix} \Delta X \\ \Delta Y \end{bmatrix} - \begin{bmatrix} C_{xx} & C_{xy} \\ C_{yx} & C_{yy} \end{bmatrix} \begin{bmatrix} \Delta \dot{X} \\ \Delta \dot{Y} \end{bmatrix} - \begin{bmatrix} M_{xx} & M_{xy} \\ M_{yx} & M_{yy} \end{bmatrix} \begin{bmatrix} \Delta \ddot{X} \\ \Delta \ddot{Y} \end{bmatrix} \quad (1)$$

where  $\Delta X(t)$  and  $\Delta Y(t)$  are the components of the journal-center dynamic displacement about an equilibrium position. The dynamic-force coefficients defined by Eq.(1) are important measures of bearing dynamic performance since they influence the system critical speeds, the resonant amplitude response, and stability of the rotor-bearing system.

## 2. MATHEMATICAL MODEL

### 2.1 Governing Equations for Turbulent Fluid Film Flows

Figures 1 and 2 show the schematic drawings of a hydrostatic bearing and a damping bearing (annular seal) considered for the analysis. Large pressure gradients typical of cryogenic bearings cause high axial turbulent flow Reynolds numbers, and the effect of turbulent mixing far outweighs molecular diffusivity. The temperature rise produced by viscous dissipation tends to be distributed uniformly across the film thickness and thus, temperature gradients in the cross-film coordinate are confined to turbulent flow boundary layers adjacent to the bounding (bearing and journal) surfaces (Di Pasquaton and Sala, 1984). Furthermore, in the absence of regions of reversed flow or recirculation, the fluid velocity field presents the same characteristics as discussed above. The flow studied is confined to the thin annular region between an inner rotating journal and a stationary bearing. The considerations detailed allow the fluid motion to be described by a set of bulk-flow governing equations (Yang et al., 1993, 1994):

*Continuity Equation*

$$\frac{\partial(\rho H)}{\partial t} + \frac{\partial(\rho H U)}{\partial x} + \frac{\partial(\rho H V)}{\partial y} = 0 \quad (2)$$

*Circumferential-Momentum Equation*

$$\frac{\partial(\rho H U)}{\partial t} + \frac{\partial(\rho H U^2)}{\partial x} + \frac{\partial(\rho H U V)}{\partial y} = -H \frac{\partial P}{\partial x} + \tau_{xz} \Big|_0^H \quad (3)$$

*Axial-Momentum Equation*

$$\frac{\partial(\rho H V)}{\partial t} + \frac{\partial(\rho H U V)}{\partial x} + \frac{\partial(\rho H V^2)}{\partial y} = -H \frac{\partial P}{\partial y} + \tau_{yz} \Big|_0^H \quad (4)$$

$$C_p \left[ \frac{\partial(\rho HT)}{\partial t} + \frac{\partial(\rho HUT)}{\partial x} + \frac{\partial(\rho HVT)}{\partial y} \right] + Q_r \\ = T\beta_t H \left( \frac{\partial P}{\partial t} + U \frac{\partial P}{\partial x} + V \frac{\partial P}{\partial y} \right) + R\Omega \tau_{xz}|^H \\ - U \tau_{xz}|_0^H - V \tau_{yz}|_0^H \quad (5)$$

where the bulk-flow primitive variables ( $U, V, P$ , and  $T$ ) are defined as average quantities across the film thickness, and  $Q_r$  represents the heat flux from the fluid film towards the journal and bearing surfaces.

The wall shear stresses are calculated according to the bulk-flow theory for turbulence in thin film flows (Hirs, 1973, Launder and Leschziner, 1978):

$$\tau_{xz}|_0^H = -\frac{\mu}{H} \left( k_x U - k_j \frac{R\Omega}{2} \right); \\ \tau_{yz}|_0^H = -\frac{\mu}{H} (k_y V); \\ \tau_{zz}|^H = \frac{H}{2} \frac{\partial P}{\partial x} + \frac{\mu}{4H} [U k_b - (U - R\Omega) k_j] \quad (6)$$

where the turbulent shear parameters ( $k_x, k_y$ ) and ( $k_j, k_b$ ) are local functions of the Reynolds numbers and friction factors based on Moody's formulae (Massey, 1983).

## 2.2 Mass Conservation at a Recess

A uniform pressure in the recess volume is required for hydrostatic action to take place effectively. However, a minimum recess volume is needed to avoid a typical pneumatic hammer instability associated to compressible fluids (Redecliff and Vohr, 1969). The continuity equation at a recess of a hydrostatic bearing relates the global balance between the flow through the orifice restrictor, the recess outflow into the film lands ( $Q_r$ ) and the temporal change of fluid mass within the recess volume ( $V_r$ ), and expressed as:

$$A_0 \sqrt{2\rho_r(P_s - P_r)} = Q_r + \rho_r \frac{\partial V_r}{\partial t} \\ + \rho_r V_r \left( \beta \frac{\partial P}{\partial t} - \beta_t \frac{\partial T}{\partial t} \right), \quad (7)$$

where

$$\beta = \frac{1}{\rho} \left( \frac{\partial \rho}{\partial P} \right)_T, \quad \beta_t = -\frac{1}{\rho} \left( \frac{\partial \rho}{\partial T} \right)_P \quad (8)$$

are the liquid compressibility factor and volumetric expansion coefficient, respectively; and

$$Q_r = \int_{\Gamma_r} \rho H (\vec{U} \cdot \vec{n}) d\Gamma \quad (9)$$

is the mass flow rate across the recess edges ( $\Gamma_r$ ) and entering the film lands.

## 2.3 Global Energy Balance Equation at a Recess

A global energy balance equation at a hydrostatic bearing recess shows the heat carry-over (advection) and mixing effects, and the friction heat generation (dissipation) in the recess (Fig. 3):

$$C_p \frac{\partial(\rho T)}{\partial t} V_r + C_p \left( \sum \dot{m}_d T_d + 2 \sum \dot{m}_{side} T_{side} \right) \\ = C_p \left( \sum \dot{m}_u T_u + Q_r T_r \right) + T_{or}^r \Omega \quad (10)$$

where

$$T_{or}^r = \tau_{zz}^H A_r R \quad (11)$$

is the shear induced torque over the recess area,  $Q_r$  is the total mass flow rate through the supply orifice,  $V_r$  is the recess volume, and the subscripts "u", "d" and "side" refer to the upstream, downstream, and side edges of a rectangular recess, respectively.

The temperatures at the downstream and side edges of the recess are approximately equal to the recess temperature:

$$T_d = T_{side} = T_r = \text{Constant}, \quad (12)$$

while the temperature at the upstream of the recess is given by:

$$T_u = \begin{cases} T_r, & \text{if } (\vec{U} \cdot \vec{n}) > 0; \\ \text{Upstream values,} & \text{otherwise.} \end{cases} \quad (13)$$

## 2.4 Recess-Film Entrance Pressures Rise and Drop

For hybrid operation (combined hydrostatic-hydrodynamic), a pressure rise occurs at the downstream zone of the recess due to the journal rotation (Chaomleffel and Nicholas, 1986). San Andres (1992) considered this region as a one-dimensional step bearing and adopted Constantinescu et al.'s (1975) model to evaluate the pressure rise just in front of the downstream recess edge. The local acceleration of fluid from the deep recess to the thin film lands causes a sudden pressure drop at the recess edge. The pressure drop at the entrance to the

film lands is then modeled by a simple Bernoulli type relation. Details of the recess-edge pressure equations can be found in the analyses of Artiles et al. (1982) and San Andres (1992) for incompressible and compressible fluids, respectively.

### 3. BOUNDARY CONDITIONS

The boundary conditions for the flow variables are expressed as:

(a) The pressure, velocity, and temperature fields are continuous and single-valued in the circumferential direction for annular seals and hydrostatic bearings without axial grooves.

(b) At the bearing exit plane, the fluid pressure takes a value equal to the discharge or ambient pressure ( $P_a$ ) for subsonic operating conditions. The exit pressure may vary circumferentially to represent existing conditions in some turbopump applications.

(c) For annular pressure seals, an entrance pressure drop occurs at the seal inlet. This condition is also modeled with a simple Bernoulli-like relationship as given by Yang et al. (1993).

(d) At the fluid/journal and the fluid/bearing interfaces, the heat flux to the bounding surfaces  $Q$ , is assumed to be zero. That is, the present model considers the bearing and journal surfaces to be insulated. This condition is representative of turbulent flow, externally pressurized bearings (Yang et al., 1993).

### 4. PERTURBATION AND NUMERICAL ANALYSES

For small amplitude journal motions all the dependent flow variables as well as the fluid properties are expressed as the superposition of zeroth- and first-order fields representing the steady state and dynamic motion conditions, respectively. Expansion of the governing equations in the perturbation variables yields zeroth- and first-order flow equations as presented in detail by (San Andres, 1993).

A cell finite difference scheme is implemented to solve the nonlinear differential equations on the film lands, while the Newton-Raphson scheme is used to update the recess pressure and to satisfy the mass continuity constraint at each bearing recess. Details of the computational fluid mechanics algorithm can be found in the relevant work of Launder and Leschziner (1978). Once the zeroth-order and first-order flow fields are obtained, the fluid film forces and the dynamic force coefficients are calculated by integration of the pressure field over the journal surface. These forces are given by:

$$\begin{bmatrix} F_{X0} \\ F_{Y0} \end{bmatrix} = R \sum_{k=1}^{N_{pad}} \int_{-L_L}^{L_R} \int_0^{\theta_{rad}} P_0^k \begin{bmatrix} \cos \theta \\ \sin \theta \end{bmatrix} d\theta dy \quad (14)$$

where  $P_0^k$  corresponds to the zeroth-order pressure field for the  $k$ -th bearing pad. The force coefficients due to journal center displacements are determined from:

$$K_{ij} - \omega^2 M_{ij} + i\omega C_{ij} = -\frac{R}{c} \sum_{k=1}^{N_{pad}} \int_{-L_L}^{L_R} \int_0^{\theta_{rad}} P_j^k h_i d\theta dy; \quad (15)$$

$$\text{with } i, j = X, Y \quad h_x = \cos \theta, \quad h_y = \sin \theta$$

and  $P_X^k, P_Y^k$  are the dynamic pressure fields for journal motions in the X and Y directions, respectively.

### 5. RESULTS AND DISCUSSION

Numerical predictions from the analysis and computer program developed correlate favorably with experimental results available in the literature (San Andres, 1993). The results demonstrate the generality of the analysis, validate the computational model, and extend the range of applicability of the analysis to conventional bearings handling viscous lubricants.

A one-to-one comparison for bearing performance in terms of flow, load capacity and rotor-dynamic force coefficients for a hydrostatic bearing and a damper bearing seal operating in liquid oxygen is presented here. The HJB and damper seal are designed to replace the duplex ball bearings next to the left inducer in the liquid oxygen high pressure turbopump ( $LO_2$  HPOTP). The fluid operating conditions (pressure and temperature) as well as the actual bearing clearance, and most importantly, the load supported by the bearings are a function of the rotating speed of the pump. Information relevant to the load characteristics in the HOPTP were obtained from Shoup (1993) and the fluid operating conditions directly extracted from the technical report of Heshmat (1991). The hydrostatic bearing has 6 recesses of rectangular shape and orifice restrictors, while the damper seal consists of two parallel annular seals of convergent tapered clearance and separated by a deep feeding central groove (Von Pragenau, 1990). The damper seal has a rough stator surface of knurled type while the hydrostatic bearing and journal surfaces are perfectly smooth. This type of damper seal geometry is also known as an annular hydrostatic bearing (Scharrer et al., 1992). Table 1 shows a description of the bearing geometries with the values of actual clearances, supply and discharge pressures and supply temperature for liquid oxygen, and the nominal load acting on the bearings as the operating speed increases

from 14,035 cpm to 30,367 cpm. Note that the load and pressures are proportional to the second power of the rotational speed. At the nominal operating conditions, here taken as 26,000 cpm, the nominal clearance in the HJB is equal to 0.175 mm, while the inlet and exit clearances in the damper seal are equal to 0.221 mm and 0.129 mm (ratio = 1.715) with an average clearance identical to that of the hydrostatic journal bearing.

The hydrostatic bearing is designed for operation at the nominal speed with a concentric pressure ratio equal to 0.60 to provide maximum direct stiffness coefficients. On the other hand, the ratio of inlet to discharge clearance in the damper seal has been optimized to also obtain the largest direct stiffness coefficients. The maximum specific load (load divided by bearing projected area) is equal to 6.55 MPa (950 psi) and 7.22 MPa (1048 psi) for the hydrostatic bearing and damper seal, respectively. These specific loads are very large considering the nature of the bearing application with a fluid of very low viscosity such as liquid oxygen. The calculations for the static and dynamic performance characteristics of the HJB and seal are performed using the adiabatic journal (rotor) and bearing (stator) thermal model. Numerical calculations for the damper seal are performed only for the thin land portion and then multiplied by two. The central groove and its effect on load capacity and dynamic force coefficients are altogether neglected. This oversimplification seems appropriate as a first attempt to correlate the performance of the HJB and damping bearing seal. However, it is now known that central feeding grooves do have a pronounced effect on the dynamic force response of fluid film bearings, in particular with regard to inertia and cross-coupled damping force coefficients (Arauz et al., 1993, Lindsey, 1993).

Figure 4 depicts the fluid supply temperature, bearing load and pressure drop across the HJB and damping bearing seals as the rotational speed of the pump increases. The largest load of 27,282 N (6,137 lbs) corresponds to the highest operating speed. The Figure also shows the values of the nominal circumferential flow Reynolds number  $Re_c = \rho \cdot R \Omega c / \mu$  to range from approximately 70,000 to 150,000 as the rotor speed rises. Figure 5 presents the HJB and damper seal flow rate and drag torque as the journal speed increases. The hydrostatic bearing (h) shows approximately 14 percent more flow rate than the damper seal (s), while it produces approximately 27 percent less drag torque than the seal at the largest operating speed. These

results are a direct consequence of the rough stator surface in the damping bearing seal.

Figure 6 presents the journal operating eccentricity and attitude angle as well as the maximum temperature rise in the HJB and damper seal as the operating speed increases. Note that as the speed rises so does the applied load at a rate proportional to the journal speed squared. The load for the HJB is directed towards the bottom of a bearing recess (X direction). The dimensionless journal eccentricity is given here as the ratio between the journal off-center displacement divided by the nominal clearance at 26,000 cpm, i.e. 0.175 mm. Note that the attitude angle is less than  $10^\circ$  for both bearings and the journal eccentric displacement is rather moderate considering the magnitude of the loads applied. The low value in the attitude angle indicates dominance of hydrostatic effects over hydrodynamic effects. The maximum temperature in the film lands of the hydrostatic bearing and seals increases rapidly with journal speed. The HJB shows a larger thermal differential between the bearing supply condition and discharge planes. The results also indicate that both HJB and damper seal operate well below the critical temperature of  $T_c = 154.6^\circ\text{K}$  ( $278^\circ\text{R}$ ) for liquid oxygen.

Figures 7 to 9 present the synchronous stiffness, damping and inertia force coefficients versus the rotational speed for the HJB and damping bearings, respectively. Note the similar values between all direct coefficients (say  $K_{xx}$  and  $K_{yy}$ ) and cross coupled coefficients (say  $K_{xy}$  and  $-K_{yx}$ ) which denote that the HJB and damper bearing seal have very uniform force coefficients as the operating eccentricity (and load) increases with the operating speed. Figure 7 shows a HJB with slightly smaller direct stiffness coefficients ( $K_{xx}$  and  $K_{yy}$ ) than the damper seal, while its cross-coupled stiffness ( $K_{xy}$ ) is larger. Note the dominance of hydrostatic (direct) coefficients over the cross-coupled coefficients induced solely by journal rotation.

Figure 8 shows the HJB to have larger direct damping coefficients ( $C_{xx}$  and  $C_{yy}$ ) than the damper seals (approximately 47 percent higher). These results produce at the largest journal speed a whirl frequency ratio (WFR) equal to 0.39 and 0.45 for the HJB and damping bearing, respectively. Thus, in this example when the inlet swirl ratio is equal to 0.50, the HJB offers slightly better dynamic stability characteristics than the parallel lands damper seal.

Figure 9 shows the damping-bearing direct



inertia force coefficients ( $M_{xx}$  and  $M_{yy}$ ) to be the on the order of 1.5 kg and larger than the HJB direct inertia coefficients. The reason for this lies on the tapered geometry of the damper bearing seal with a small clearance at the exit plane. The cross-coupled inertia coefficients ( $M_{xy}$  and  $M_{yx}$ ) are small in nature. Here it is noted that in practice the direct inertia coefficients for the damping bearing will be much larger than the ones predicted. The central feeding groove acts as a parallel inertia and compliance to the seal lands, increases the magnitude of the inertia coefficients, and reduces substantially the direct dynamic stiffness of the damper seal. Experimental results showing this behavior have been reported recently by Lindsey (1993).

It is worth noting that the original test case included a three pad journal bearing with a clearance similar to that of the HJB but with a bearing preload of 0.076 mm. The results are not reproduced here because the hydrodynamic bearing produced a rather large temperature rise, and offered a very low load capacity in comparison with the HJB and damper seal. Details of these calculations can be found elsewhere (San Andres, 1993).

## 6. CONCLUSIONS

Accurate prediction of the performance and static and dynamic force characteristics of process-liquid turbulent-flow fluid film bearings requires of an advanced thermohydrodynamic analysis. A set of bulk-flow equations for mass conservation, momentum and energy transport describe the fluid motion in turbulent flow bearings with cryogenic liquids. The nonlinear flow equations are solved with a CFD finite difference scheme combined with the Newton-Raphson method to satisfy the mass continuity requirement at each hydrostatic bearing recess. Extensive comparisons between numerical results and experimental data of turbulent flow water HJBs and seals are favorable demonstrating the validity of the THD analysis and the computer program developed.

Numerical predictions show that properly designed HJBs or a parallel damper bearings can support effectively the loads expected in the  $LO_x$  HP turbopump. The results indicate that the HJB and damping bearing will operate at low eccentricity ratios with uniform force coefficients. The case studied shows an important application of the hydrostatic principle where sound engineering practice utilizes the available pressure differential in a cryogenic turbopump to provide a reliable fluid film bearing support.

## ACKNOWLEDGEMENTS

This research was funded under NASA Grant NAG3-1434. Acknowledgements are due to NASA-LeRC for its support, and in particular to Mr. James Walker for his interest on this work.

## REFERENCES

- Arauz, G., and L. San Andres, 1993, "Effect of a Circumferential Feeding Groove on the Force Response of a Short Squeeze Film Damper," ASME Paper 93-Trib-15.
- Artiles, A., Walowit, J., and Shapiro, W., 1982, "Analysis of Hybrid Fluid Film Journal Bearings with Turbulence and Inertia Effects," *Advances in Computer Aided Bearing Design*, ASME Press.
- Chaomleffel, J.P., and Nicholas, D., 1986, "Experimental Investigation of Hybrid Journal Bearings," *Tribology International*, Vol. 19, No. 5, pp. 253-259.
- Childs, D., and K. Hale, 1993, "A Test Apparatus and Facility to Identify the Rotordynamic Coefficients of High-Speed Hydrostatic Bearings," ASME Paper 93-Trib-48.
- Constantinescu, V.N., and S. Galetuse, 1975, "Pressure Drop due to Inertia Force in Step Bearings," ASME Papers, 75-Lub-34.
- Di Pasquantonio, F., and Sala, P., 1984, "Influence of Thermal Field on the Resistance Law in Turbulent Bearing-Lubrication Theory," *ASME JOURNAL OF TRIBOLOGY*, Vol. 106, pp.368-376.
- Franchek, N., 1992, "Theory Versus Experimental Results and Comparisons for Five Orifice Compensated Hybrid Bearing Configurations" Master Thesis, December, Texas A&M University, College Station, TX 77843.
- Heshmat, H., 1991, "Investigation of Foil Bearings for Use in High-Thrust Liquid Rocket Engines," NASA Contractor Report CR-197099, MTI 90-TR58, April.
- Hirs, G.G., 1973, "A Bulk-Flow Theory for Turbulence in Lubricant Films," *ASME JOURNAL OF LUBRICATION TECHNOLOGY*, Vol. 95, pp.137-146.
- Kurtin, K.A., Childs, D., San Andres, L., and Hale, K., 1993, "Experimental Versus Theoretical Characteristics of a High Speed Hybrid (Combination Hydrostatic and Hydrodynamic) Bearing," *ASME JOURNAL OF TRIBOLOGY*, Vol. 115, pp.160-168.
- Lauder, B.E., and Leschziner, M., 1978, "Flow in Finite Width Thrust Bearings Including Inertial Effects, I- Laminar Flow, II- Turbulent Flow," *ASME JOURNAL OF LUBRICATION TECHNOLOGY*, Vol. 100, pp.330-345.
- Lindsey, T., 1993, "Experimental vs. Theoretical Comparison of the Effects of Taper on the Rotordynamic Coefficients in Short Smooth Annular Seals

Used in High-Speed Turbomachinery," Master Thesis, May, Texas A&M University, College Station, TX 77843.

Massey, B.S., 1983, *Mechanics of Fluids*, Van Nostrand Reinhold (UK) Co. Ltd., Workingham, Berkshire, England.

Mosher, P., 1993, "Effect of Design Parameter Variations on Hybrid (Combination Hydrostatic and Hydrodynamic) Bearings for Use in High Speed Turbomachinery," Master Thesis, May, Texas A&M University, College Station, TX 77843.

Reddecliff, J.M., and Vohr, J.H., 1969, "Hydrostatic Bearings for Cryogenic Rocket Engine Turbopumps," *JOURNAL OF LUBRICATION TECHNOLOGY*, Vol. 91, pp.557-575.

San Andres, L., 1990, "Turbulent Hybrid Bearings with Fluid Inertia Effects," *ASME JOURNAL OF TRIBOLOGY*, Vol. 112, pp.699-707.

San Andres, Luis A., 1991, "Analysis of Variable Fluid Properties, Turbulent Annular Seals," *ASME JOURNAL OF TRIBOLOGY*, Vol. 113, pp.694-702.

San Andres, Luis A., 1992, "Analysis of Turbulent Hydrostatic Bearings with a Barotropic Cryogenic Fluid," *ASME JOURNAL OF TRIBOLOGY*, Vol. 114, pp.755-765.

San Andres, L., 1993, "Thermohydrodynamic Analysis of Cryogenic Liquid Turbulent Flow Fluid Film Bearings," Research Progress Report, NASA Grant NAG3-1434, December, Texas A&M University, College Station, TX 77843.

Scharrer, J.K., Hibbs, R.I., and Nolan, S., 1992, "Extending the Life of the SSME HPOTP through the Use of Annular Hydrostatic Bearings," AIAA Paper 92-3401, 28th AIAA/SAE/ASME/ASEE Joint Propulsion Conference, July 6-8, Tennessee.

Shoup, T., Private Communication, 1993, Sverdrup NASA Marshall Space Center, October 15.

Von Pragenau, G.L., 1990, "Damping Bearings for Turbomachinery," NASA TP 3092, Vol. II, pp. 155-162.

Yang, Z., San Andres, L., and Childs, D., 1993, "Thermal Effects in Cryogenic Liquid Annular Seals, Part I: Theory and Approximate Solution; Part II: Numerical Solution and Results" *ASME JOURNAL OF TRIBOLOGY*, Vol. 115, pp.267-284.

Yang, Z., San Andres, L., and Childs, D., 1994, "Thermohydrodynamic Analysis of Process Liquid Hydrostatic Bearings in Turbulent Regime, I: Theory, II: Numerical solution and Results", accepted for publication at *ASME Journal of Applied Mechanics*.

## NOMENCLATURE

$A_o$   $C_d \pi d_o^2/4$ , equivalent orifice area [ $m^2$ ]

$A_r$	$bl$ , recess area [ $m^2$ ]
$b$	recess circumferential length [ $m$ ]
$c, c_c$	radial clearance, characteristic clearance ( $=\{c(y)\}_{min}$ ) [ $m$ ]
$C_{ij}$	damping force coefficients [ $Ns/m$ ]
$C_d$	empirical orifice discharge coefficient
$C_p$	specific heat [ $J/kg \cdot K$ ]
$D$	journal diameter [ $m$ ]
$d_o$	orifice diameter [ $m$ ]
$e_x, e_y$	journal center displacements [ $m$ ]
$F_x, F_y$	fluid film forces along $\{X, Y\}$ axes [ $N$ ]
$f_j, f_b$	$a_m[1 + (c_m r_{j,b}/H + b_m/R_{j,b})e_m]$ , turbulent friction factors based on Moody's equation, $a_m=0.001375$ ; $b_m=5 \times 10^5$ ; $c_m=10^4$ ; $e_m=\frac{1}{3.0}$
$H, H_r$	film thickness, recess depth [ $m$ ]
$K_{ij}$	stiffness force coefficients [ $N/m$ ]
$k_x, k_y$	$(k_j + k_b)/2$
$k_j, k_b$	$f_j R_j, f_b R_b$ , turbulent shear parameters
$L, l$	bearing & recess axial lengths [ $m$ ]
$M_{ij}$	inertia force coefficients [ $kg$ ]
$\dot{m}$	flow rate over differential segments [ $kg/s$ ]
$\vec{n}$	normal vector to recess boundary
$N_{pad}$	number of pads on bearing
$N_{rec}$	number of bearing recesses
$P$	fluid pressure [ $N/m^2$ ]
$Q_r$	mass flow rate from recess to land [ $kg/s$ ]
$R$	journal radius [ $m$ ]
$Re_c$	$\rho R \Omega c_c / \mu$ , nominal circumferential flow Reynolds number
$R_j$	$\rho H \sqrt{(U - \Omega R)^2 + V^2} / \mu$ , Reynolds number relative to journal surface
$R_b$	$\rho H \sqrt{U^2 + V^2} / \mu$ , Reynolds number relative to bearing surface
$r_j, r_b$	mean roughness depth at journal and bearing surfaces [ $m$ ]
$T$	bulk-flow fluid temperature [ $K$ ]
$t$	time [ $sec$ ]
$T_{or}^H$	$\tau_{xz}^H A_r R$ , torque over a recess [ $N \cdot m$ ]
$U, V$	mean velocities [ $m/s$ ]
$\vec{U}$	$U\vec{i} + V\vec{j}$
$\forall_r$	$(H_r + H)A_r + \forall_r$ , recess volume [ $m^3$ ]
$\forall_r$	volume of orifice supply line [ $m^3$ ]
$X, Y$	inertial coordinates
$x, y, z$	$(0, \pi D), (0, L), (0, H(x, y, t))$
$\Omega$	rotational speed of journal [ $rad/sec$ ]
$\omega$	excitation or whirling frequency [ $rad/sec$ ]
$\rho$	fluid density [ $kg/m^3$ ]
$\mu$	fluid viscosity [ $Ns/m^2$ ]
$\tau$	$\omega t$ dimensionless time coordinate

Subscripts:

a refers to ambient or discharge conditions  
 r refers to recess conditions  
 s refers to supply conditions

j refers to journal  
 b refers to bearing  
 c refers to characteristic (supply) values

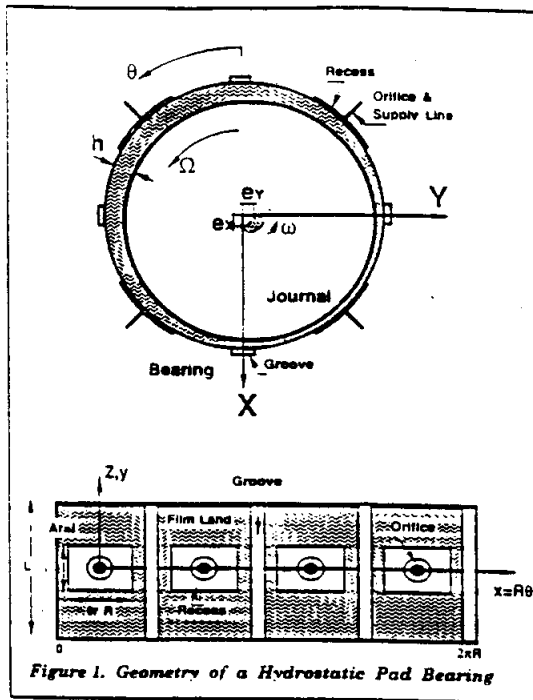


Figure 1. Geometry of a Hydrostatic Pad Bearing

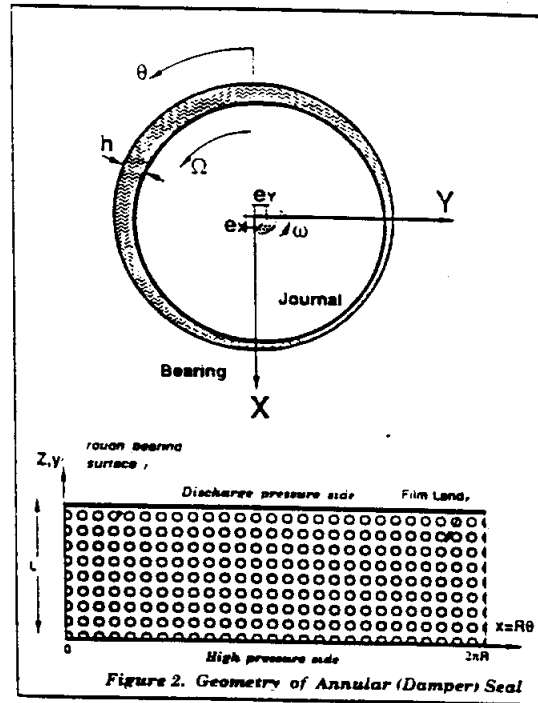


Figure 2. Geometry of Annular (Damper) Seal

Table 1. Geometry and operating characteristics of hydrostatic bearing and damper seals for load support in LOx HPOTP.

Hydrostatic Bearing: Number of recesses  $N_{rec} = 6$

Diameter (D)	Length (L)	Clearance (C)	Recess Depth	Recess Arc
85.1 mm (3.35 in)	48.85 mm (1.92 in)	175.2 $\mu$ m (6.9 mils)	50 $\mu$ m (20 mils)	24.42 mm (0.96 in)

Journal and bearing surface conditions: smooth  
 $L/D=0.57$ ;  $H/C=2.8$ ;  $R/C=0.5$ ; Recess area ratio=0.25;  $C/R=0.0041$   
 Orifice  $C=0.90$ ; Diameter  $d_o = 4.44$  mm  
 Recess area ratio=0.25;  $\xi_x=0.0$ ;  $\xi_y=0.50$ ;  $\xi_z=0.0$

Damper Seal: Two parallel seal land (2 x L) (groove width undeformed)

Diameter (D)	Length (L)	Clearance	Clearance Ratio	Average Clearance*
85.1 mm (3.35 in)	22.2 mm (0.874 in)	221.3 $\mu$ m (8.7 mils)	129.1 $\mu$ m (5.08 mils)	175.2 $\mu$ m (6.9 mils)

Journal smooth, bearing rough,  $rh = 0.044$  (Rounded)  
 Entrance conditions  $\xi_y=0.25$

Operating Conditions:

Speed rpm	Supply Pa	Supply K	Ts K	Load N	Reynolds Rac	Average Clearance* $\mu$ m
14,035	16.00	1.654	102.77	128.9	5.828	72.816
19,732	29.59	1.792	107.22	130.5	11.519	100.700
26,000	39.60	2.089	110.55	133.7	20.000	130.130
28,340	43.60	2.434	111.33	137.0	23.762	143.720
30,367	55.59	2.551	115.00	138.0	27.282	147.600

Inner seal ratio  $Q=0.50$

Fluid: LO2 (liquid oxygen) at 110.6 K (200R)

P (MPa)	$\rho$ (kg/m <sup>3</sup> )	$\mu$ (E-3 Pa-s)	$C_p$ (J/kg-K)
39.60	1134.4	0.177	1,606.4
2.09	1038.1	0.124	1,827.2

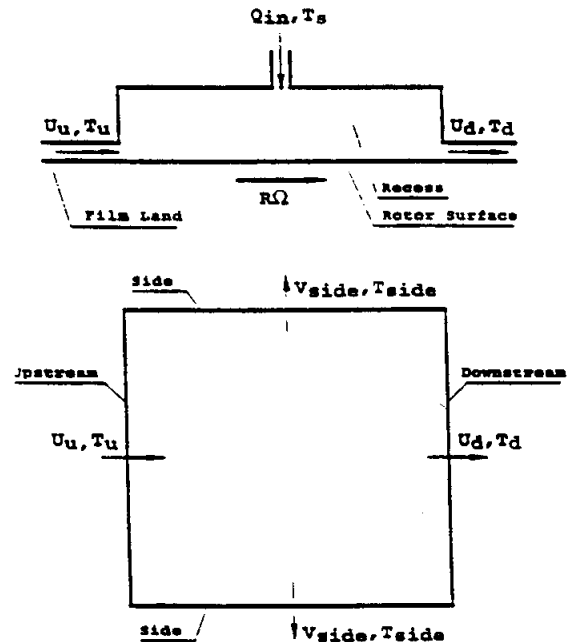


Fig. 3. Conceptual description of global energy balance at a recess

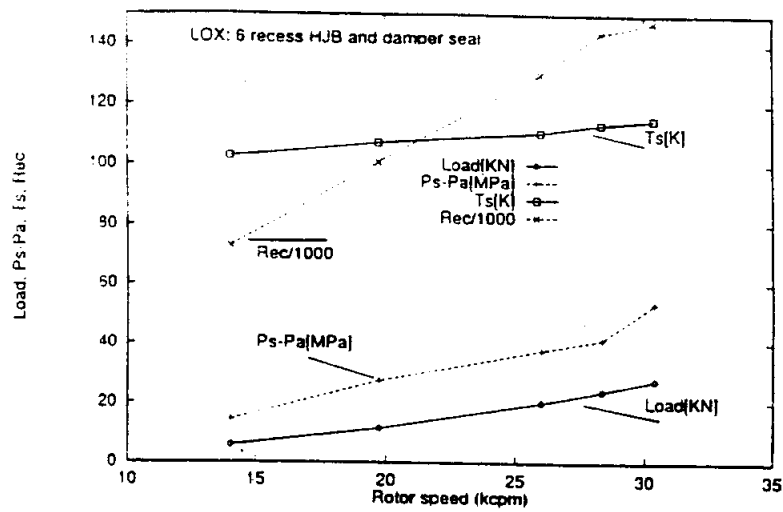


Fig. 4. Supply temperature, pressure drop, Reynolds number and load vs. rotational speed for LOx 6 recess HJB and damper seal.

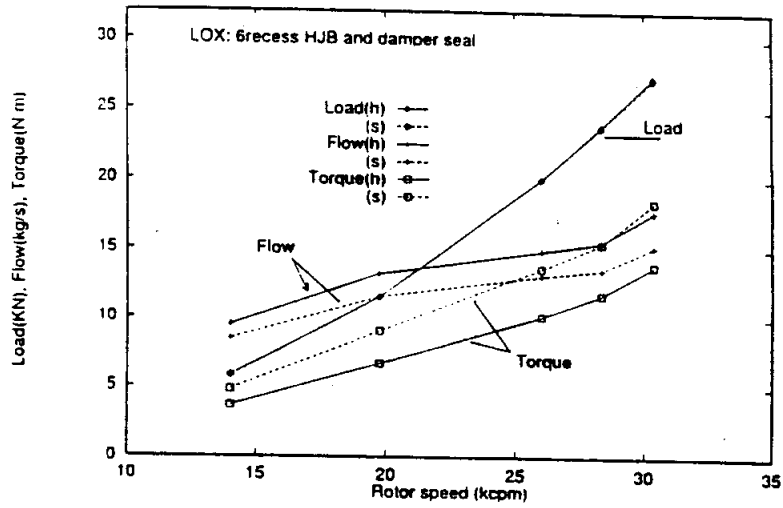


Fig. 5. Flow rate and drag torque vs. rotational speed for LOx (h) 6 recess HJB and (s) parallel damper seal.

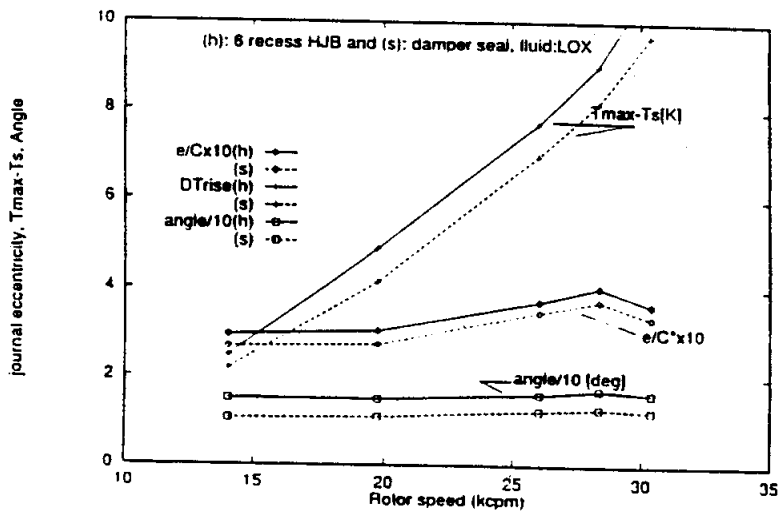


Fig. 6. Journal eccentricity and attitude angle and maximum temperature rise vs. rotational speed for LOx (h) 6 recess HJB and (s) parallel damper seal.

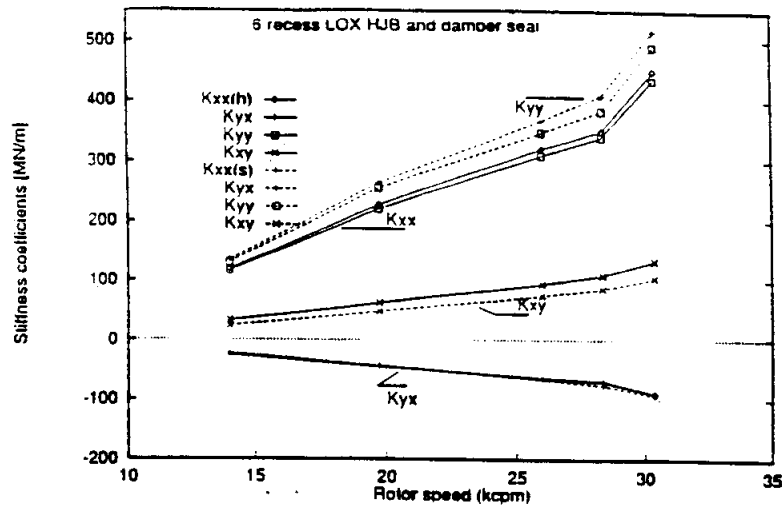


Fig. 7. Stiffness Coefficients vs. rotational speed for LOx (h) 6 recess HJB and (s) parallel damper seal.

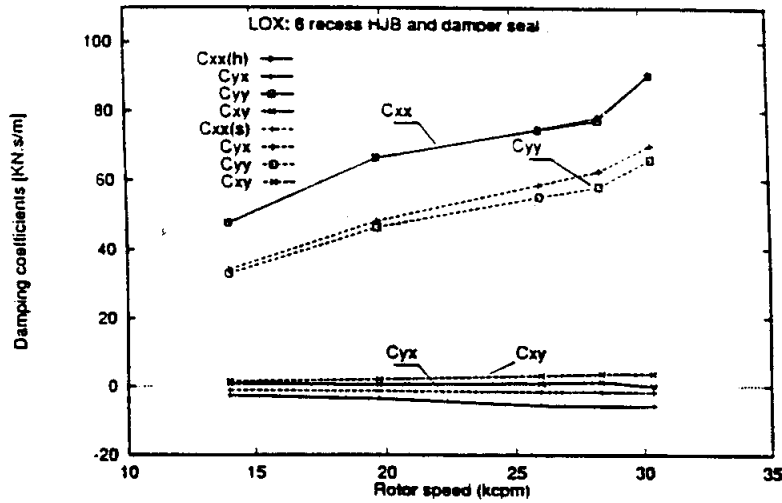


Fig. 8. Damping Coefficients vs. rotational speed for LOx (h) 6 recess HJB and (s) parallel damper seal.

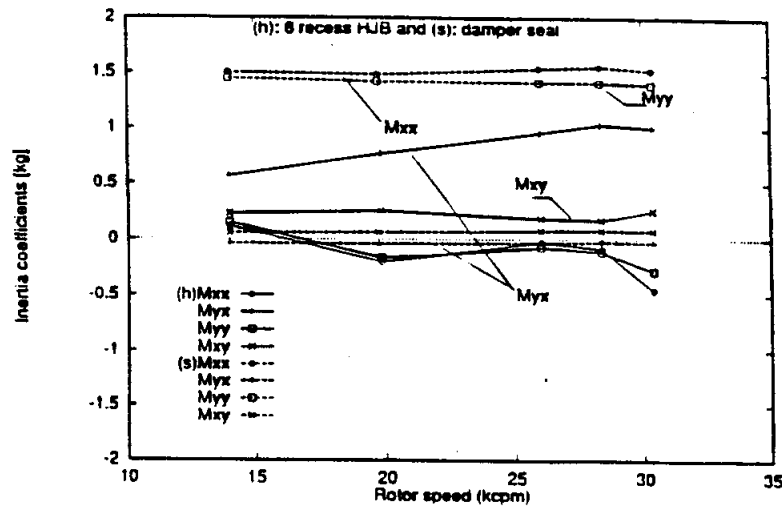


Fig. 9. Inertia Coefficients vs. rotational speed for LOx (h) 6 recess HJB and (s) parallel damper seal.

**14** "Analysis of Arbitrary Recess Geometry Hydrostatic Bearings," 1994, San Andres, L.,  
Proceedings. of the 6th NASA Conference on Advanced Earth-to-Orbit Propulsion Technology,  
Huntsville, Alabama, May, NASA CP 3282, Vol. II, pp. 431-441.



# Advanced Earth-to-Orbit Propulsion Technology – 1994

---

*Edited by  
R.J. Richmond and S.T. Wu*

## NOTICE

This document contains information which falls under the purview of the U.S. Munitions List, as defined in the International Traffic in Arms Regulations. It shall not be transferred to foreign nationals, in the U.S., or abroad, without specific approval. Penalty for violations is described in ITAR, section 127.

Proceedings of a conference held  
at NASA George C. Marshall Space Flight Center  
Marshall Space Flight Center, Alabama  
May 17–19, 1994

---

September 1994

# Analysis of Arbitrary Recess Geometry Hydrostatic Bearings

Luis San Andres  
Mechanical Engineering Department  
Texas A&M University  
College Station, TX 77843-3123

## ABSTRACT

A finite-element model to calculate the static and dynamic force performance characteristics of laminar flow hybrid (combination hydrostatic - hydrodynamic) journal bearings with arbitrary recess geometry is presented. The analysis details a perturbation method to determine the equilibrium bearing forces and rotordynamic force coefficients from zeroth- and first-order Reynolds equations for the static and dynamic pressure fields. Numerical predictions correlate well with experimental values of force coefficients for a laminar flow, rectangular recess, multipad hydrostatic journal bearing operating at low rotational speeds. Examples for hydrostatic bearings with various recess shapes show that a triangular recess bearing with vertex downstream of the supply orifice (and in the direction of journal rotational speed) has smaller cross-coupled stiffness coefficients and a lower whirl frequency ratio than a conventional rectangular recess bearing. Thus, recess geometry could be optimized to improve the bearing dynamic force coefficients and insure better hydrodynamic stability characteristics.

## INTRODUCTION

Hydrostatic journal bearings (HJBs) are typically used as support elements in heavily loaded rotating machinery where high rigidity, accuracy of positioning and precision are required to warrant good machine performance. HJBs are also considered as reliable support elements in cryogenic turbopumps and low-viscosity product-lubricated turbomachinery because of their long lifetime, low friction and capability to support high loads independent of fluid viscosity (San Andres, 1992a).

The analysis of laminar flow hydrostatic bearings with rectangular recess shapes is well known in the literature. The text of Rowe (1983) offers an excellent reference for design of HJBs in

conventional laminar flow applications with viscous lubricants. Ghosh et al. (1978, 1979) have also presented elegant analyses for the calculation of the dynamic force coefficients in laminar flow HJBs with capillar and orifice restrictors. Ghosh et al. found that the recess pressure ratio for maximum stiffnesses decreases as journal eccentricity increases, while optimum damping coefficients are attained at small recess pressure ratios. Rohde and Ezzat (1976) included the effect of fluid compressibility at the orifice supply line and bearing recess volumes and identified a "break" whirl frequency above which direct damping coefficients decrease rapidly while direct stiffnesses increase dramatically. San Andres (1991) reported similar results for compressible liquid, turbulent flow HJBs. At low excitation frequencies, the likeliness of a pneumatic hammer instability in deep recess volumes becomes important. The whirl frequency ratio for hybrid (hydrostatic - hydrodynamic) compressible liquid HJBs is larger than 0.5 and demonstrates the limited stability of hydrostatic bearings with flexible rotating structures.

Hydrostatic journal bearings with large levels of external pressurization and handling low viscosity fluids determine flow conditions of turbulent character with dominance of fluid inertia effects. Redeclyff and Vohr (1969), Heller (1974) and Artiles et al. (1982) provide detailed analyses for the force performance of turbulent hydrostatic bearings with incompressible fluids. Braun et al. (1984, 1987) present a variable properties fluid model for application to HJBs in cryogenic environments and show that a fluid inertia induced pressure drop at the recess-land interface produces a significant reduction in fluid film forces, direct stiffnesses and flow rates. San Andres (1990, 1992a) introduced a detailed bulk-flow analysis for calculation of the static and dynamic force performance characteristics of high speed, turbulent flow hybrid bearings for cryogenic fluid and process-liquid applications. The analysis departs from classical lubrication theory, and includes real liquid



properties, fluid inertia effects at the bearing lands, and recess-volume liquid compressibility. Flow turbulence is modeled using the bulk-flow theory (Hirs, 1973) and Moody's friction factors to account for bearing surface macroscopic roughness. The numerical predictions from this analysis have been validated with experimental data from Chaomleffel and Nicholas (1986), Butner et al. (1986), and Kurtin et al. (1993).

Hybrid bearings (combination hydrostatic-hydrodynamic) have limited stability characteristics because of cross-coupled forces generated by the journal rotation and loss of damping due to pneumatic hammer effects at the bearing recess volumes. Some alternatives have been proposed to improve the dynamic response of this type of externally pressurized bearings. These are namely: use of a rough bearing surface, angled lubricant injection at the bearing recesses, inclusion of wear ring seals, and variations of the recess geometry to disturb the development of the circumferential flow velocity (Franchek and Childs, 1994). This paper presents a study on the dynamic force performance and whirl frequency ratio of HJBs with various recess geometries. A finite element model of the laminar flow field in hybrid bearings is discussed. The flow domain is discretized into finite cells where the mesh is generated using a body-fitted coordinate algorithm (Thompson, 1974). Flow rate, bearing load (or journal position) and drag torque are calculated for a steady-state journal eccentric position (or applied external load), while bearing dynamic force coefficients are obtained from a flow perturbation for small amplitude journal motions about the equilibrium position. The results of the analysis help to elucidate the effect of recess shape on the static and dynamic performance of hydrostatic bearings.

## ANALYSIS

Figure 1 depicts a typical four-recess hydrostatic journal bearing. Pressurized lubricant is fed into the bearing via the supply orifices, and then flows through the bearing thin film lands to the side discharge planes. The inertial coordinate system ( $X, Y$ ) is used to define the journal eccentricity position ( $e_x, e_y$ ), fluid film forces ( $F_x, F_y$ ) and dynamic force coefficients  $K_{a0}, C_{a0}$ , while the coordinate system ( $x, y$ ), on the plane of the bearing surface is used to describe the lubricant fluid flow on the thin film lands. Figure 2 depicts the unwrapped flow domain for triangular, rectangular- and circular-shaped recesses. The lubricant flow at the bearing

lands is governed by the continuity and momentum equations. For inertialess laminar flows these equations are combined and represented by the classical Reynolds equation for incompressible isoviscous fluids. This classical equation is given as (Pinkus et al., 1961):

$$\frac{\partial}{\partial x} \left( \frac{H^3}{12\mu} \frac{\partial P}{\partial x} \right) + \frac{\partial}{\partial y} \left( \frac{H^3}{12\mu} \frac{\partial P}{\partial y} \right) = \frac{\Omega R}{2} \frac{\partial H}{\partial x} + \frac{\partial H}{\partial t} \quad (1)$$

where the right hand side shows the effects of journal rotation and squeeze film action on the generation of a pressure field. The mass conservation equation at each bearing recess is given by the global balance between the flow through the restrictor orifice, the leakage to the bearing lands and the flow accumulated in the recess volume:

$$A_o C_d \sqrt{\frac{2(P_s - P_r)}{\rho}} - \oint_r Q_n \cdot d\Gamma_r = A_r \frac{dH}{dt} + V_r \beta \frac{dP_r}{dt} \quad (2)$$

$r = 1, 2, \dots, N_{rec}$

where  $C_d$  is the orifice discharge coefficient,  $A_r$  and  $V_r$  are the area and recess volumes respectively, and  $\beta$  is the fluid compressibility factor. The recess pressure is regarded as uniform over the entire recess for simplicity (Ghosh et al., 1979).

At the bearing sides, the pressure takes the value of the exit pressure  $P_e$ . The Reynolds model is used to account for liquid cavitation if present, i.e. the pressure gradient is equal to zero at the cavitation inception point ( $\partial P / \partial x = 0$ ), and the pressure within the cavitation region is equal to  $P_{cav}$ .

Fluid film bearings are mechanical elements supporting static and dynamic loads. The static load (typically a fraction of the rotor weight) displaces the rotor center to an eccentric position where it is balanced by the fluid film bearing reaction force. Dynamic loads generated in the rotating system by rotor imbalance, flow disturbances in the turbomachine components, etc., produce motions of the journal in the plane ( $X, Y$ ), and these in turn cause fluid film bearing dynamic forces which exert their action on the rotor-bearing system. The static (zeroth-order) and dynamic (first-order) fluid film bearing forces are obtained by means of a perturbation analysis which considers a steady journal eccentricity ( $e_x, e_y$ ) and a precessional journal motion

of frequency  $\omega$  with small amplitudes ( $\Delta e_x$ ,  $\Delta e_y$ ) around the static equilibrium position. The film thickness is then defined as:

$$H = H_o + e^{i\omega t}(\Delta e_x H_x + \Delta e_y H_y) \quad (3)$$

where,

$$H_o = C + e_x \cos(\Theta) + e_y \sin(\Theta), \quad H_x = \cos(\Theta), \quad H_y = \sin(\Theta) \quad (4)$$

For small amplitude journal motions, the pressure field is also expressed as zeroth- and first-order fields describing the equilibrium and dynamic conditions, i.e.

$$P = P_o + e^{i\omega t}(\Delta e_x P_x + \Delta e_y P_y) \quad (5)$$

where  $P_x$  and  $P_y$  are dynamic pressure fields due to journal dynamic displacements in the X and Y directions, respectively. Substitution of (4) and (5) into (1) to (2) leads to a set of zeroth- and first-order Reynolds equations. The bearing static (equilibrium) performance is governed by the zeroth-order equation, while the linear rotordynamic bearing force response is ruled by first-order equations. On the bearing lands, the zeroth-order Reynolds equation takes the form:

$$\frac{\partial}{\partial x} \left( \frac{H_o^3}{12\mu} \frac{\partial P_o}{\partial x} \right) + \frac{\partial}{\partial y} \left( \frac{H_o^3}{12\mu} \frac{\partial P_o}{\partial y} \right) = \frac{\Omega R}{2} \frac{\partial H_o}{\partial x} \quad (6)$$

where the zeroth-order flow rates per unit side length in the circumferential and axial directions are given by:

$$Q_{xo} = \frac{\Omega R}{2} H_o - \frac{H_o^3}{12\mu} \frac{\partial P_o}{\partial x}; \quad Q_{yo} = -\frac{H_o^3}{12\mu} \frac{\partial P_o}{\partial y} \quad (7)$$

And, at the bearing recesses, the zeroth-order continuity equation is:

$$Q_{ro} = A_o C_d \sqrt{\frac{2(P_s - P_{ro})}{\rho_r}} = \oint Q_{\eta o} d\Gamma_r, \quad r = 1, 2, \dots, N_{rec} \quad (8)$$

where  $Q_{ro}$  is the total normal flow rate crossing the recess boundary with normal  $\tilde{\eta}$ :

$$Q_{\eta o} = -\frac{H_o^3}{12\mu} \frac{\partial P_o}{\partial \eta} + \frac{\Omega R}{2} H_o \eta_x \quad (9)$$

The first-order equations for the dynamic pressure fields are:

$$\begin{aligned} & \frac{\partial}{\partial x} \left( \frac{H_o^3}{12\mu} \frac{\partial P_\alpha}{\partial x} + \frac{3H_o^2 H_\alpha}{12\mu} \frac{\partial P_o}{\partial x} \right) + \\ & \frac{\partial}{\partial y} \left( \frac{H_o^3}{12\mu} \frac{\partial P_\alpha}{\partial y} + \frac{3H_o^2 H_\alpha}{12\mu} \frac{\partial P_o}{\partial y} \right) = \frac{\Omega R}{2} \frac{\partial H_\alpha}{\partial x} + i\omega H_\alpha \\ & \alpha = X, Y \end{aligned} \quad (10)$$

where X and Y represent the direction of journal dynamic displacement. The first order flow rates are:

$$\begin{aligned} Q_{x\alpha} &= \frac{\Omega R}{2} H_\alpha - \frac{3H_o^2 H_\alpha}{12\mu} \frac{\partial P_o}{\partial x} - \frac{H_o^3}{12\mu} \frac{\partial P_\alpha}{\partial x} \\ Q_{y\alpha} &= -\frac{3H_o^2 H_\alpha}{12\mu} \frac{\partial P_o}{\partial y} - \frac{H_o^3}{12\mu} \frac{\partial P_\alpha}{\partial y} \\ & \alpha = X, Y \end{aligned} \quad (11)$$

At the bearing recesses, the first-order continuity equation takes the form:

$$\begin{aligned} & \frac{-Q_{ro}}{2(P_s - P_{ro})} P_{r\alpha} = \oint Q_{\eta\alpha} d\Gamma_r + i\omega (A_r H_\alpha + \beta V_{ro} P_{r\alpha}) \\ & \alpha = X, Y; \quad r = 1, 2, \dots, N_{rec} \end{aligned} \quad (12)$$

where  $Q_{ro}$  is the perturbed normal flow rate across the recess closure and expressed as,

$$\begin{aligned} Q_{\eta\alpha} &= -\frac{H_o^3}{12\mu} \frac{\partial P_\alpha}{\partial \eta} - \frac{3H_o^2 H_\alpha}{12\mu} \frac{\partial P_o}{\partial \eta} + \\ & \frac{\Omega R}{2} H_\alpha \cdot \eta_x; \quad \alpha = X, Y \end{aligned} \quad (13)$$

The bearing fluid film forces are obtained by integrating the static pressure field over the bearing surface. On the other hand, bearing dynamic force

coefficients come from the integration of the perturbed pressure fields. These are respectively,

$$F_{\alpha} = 2 \int_0^{L/2} \int_0^{2\pi R} P_{\alpha} H_{\alpha} dx dy \quad \alpha = X, Y \quad (14)$$

$$K_{\alpha\beta} + i\omega C_{\alpha\beta} = 2 \int_0^{L/2} \int_0^{2\pi R} P_{\beta} H_{\alpha} dx dy \quad \alpha, \beta = X, Y \quad (15)$$

Note that no fluid inertia effects are accounted in the present analysis.

The flow domain in the bearing lands can be complex depending on the geometry of the bearing recesses. Finite element methods are used here because they are more appropriate to handle calculations in geometrically complicated domains as those presented here. The Galerkin approach (Taylor et al., 1972) is employed to integrate the zeroth- and first-order differential equations on each finite element. The flow domain is discretized in quadrilateral finite elements by means of an body fitted - automatic mesh generation program as described by Thompson (74). Isoparametric, four-noded finite elements along with bilinear shape functions are used in the analysis. The interpolation formula for the pressure field within an element in the flow domain is given by,

$$P^e = \sum_{j=1}^4 P_j \psi_j(\xi, \eta) \quad (16)$$

where  $\{\psi_j\}_{j=1}^4$  is the set of bilinear shape functions. Equations (17) is replaced into the weak formulation equivalent to the set of differential equations (6) and (10) to transform them into systems of algebraic equations. The zeroth-order Reynolds equation on an element basis takes the form:

$$[K_{ij}]^e (P_{oj})^e = -(Q_i)^e + (G_i)^e \quad (17)$$

where,

$$[K_{ij}]^e = \int_{\Omega_e} \frac{H_o^3}{12\mu} (\psi_{i,x} \psi_{j,x} + \psi_{i,y} \psi_{j,y}) d\Omega_e ;$$

$$(Q_i)^e = \oint_{\Gamma_e} \psi_i^e Q_n^e d\Gamma_e \quad (18)$$

$$(G_i)^e = \frac{\Omega R}{2} \int_{\Omega_e} H_o^e \psi_{i,x}^e d\Omega_e \quad i, j = 1, 2, \dots, N$$

The finite element equations (18) are assembled over the entire flow domain. The set of algebraic equations are condensed by enforcing known pressures and finally the resultant symmetric system of equations is decomposed and solved to obtain the discrete pressure field. The finite element procedure on the first-order Reynolds equations follows basically the same procedure presented by Klit and Lund (1986). Once the nodal pressures are known, the flow rates can be obtained from the equation above by solving for  $Q_i^e$  along the element boundaries where the flow rates need to be evaluated. A Newton-Raphson scheme has been implemented to update the bearing recess pressures and to satisfy the constraint on equality of orifice flow rate and recess-to-land flow rate. Details on this procedure are omitted for brevity.

## RESULTS AND DISCUSSION

Table 1 presents the geometric and operating conditions of the four hybrid bearings studied. The first one is a conventional hydrostatic bearing with rectangular recesses (baseline bearing); the second bearing has circular recesses, while the third and fourth bearings have triangular recesses with their vertexes downstream (triangular I) and upstream (triangular II) of the recess orifice (in the sense of the journal speed), respectively (See Figure 2). The bearing recesses were chosen so that their areas were identical for a recess to land area ratio equal to 20%. The values of the orifice diameters given in Table 1 correspond to a concentric recess pressure ratio equal to 0.5. Details on the static performance characteristics (flow rate and load capacity) have been reported earlier (San Andres, 1992b). In brief, the flow rate decreases with the operating journal eccentricity, and the circular recess HJB has a lower flow rate (5% less) than the rectangular recess HJB, while the triangular shape recess HJBs show a 3% flow rate increment relative to the baseline bearing. All the HJBs studied have approximately the same hydrostatic force ( $F_h$ ), while the triangular recess II

bearing shows the smallest hydrodynamic (cross-coupled) force ( $-F_y$ ) as the operating eccentricity increases. Hydrodynamic forces (due to journal rotation) become dominant in the bearing static force performance for journal eccentricities above 0.60.

Figures 3 and 4 show the direct stiffness coefficients  $K_{xx}$  and  $K_{yy}$  for the four laminar flow hydrostatic bearings. At the concentric position,  $K_{xx}$  and  $K_{yy}$  are the same for the bearings with rectangular and circular recesses. On the other hand, the direct stiffness for the bearings with triangular recesses are 8% smaller respect to the previous ones. As journal eccentricity increases, the evolution of  $K_{xx}$  and  $K_{yy}$  for the bearings with rectangular and circular recesses is similar.  $K_{xx}$  decreases slightly before the cavitation onset ( $ex/C=0.5$ ); and then increases for eccentricity ratios larger than 0.5. The bearing identified as triangular-I has a uniform  $K_{xx}$  before the cavitation onset. Afterwards,  $K_{xx}$  steadily increases with eccentricity. The triangular-II bearing presents a much pronounced decay of  $K_{xx}$  for eccentricity ratios smaller than 0.5 (cavitation onset) followed by a sharper increase at larger eccentricity ratios. Figure 4 shows that  $K_{yy}$  in all cases slightly decreases before the cavitation onset. Once the bearing cavitates,  $K_{yy}$  increases steadily with the journal eccentricity ratio.

Figures 5 and 6 present the cross-coupled dynamic coefficients  $K_{xy}$  and  $-K_{yx}$  versus eccentricity ratio. At the concentric position, the bearing with circular recesses has a cross-coupled stiffness 4% larger than the bearing with rectangular recesses (baseline bearing). The triangular-I bearing has the same cross-coupled stiffness than the baseline bearing (rectangular recess), while the triangular-II bearing presents a cross-coupled stiffness 15% smaller than the baseline bearing, denoting a potential for improved stability characteristics. For the bearings with circular and rectangular recesses,  $K_{xy}$  is almost constant for small eccentricities, but decreases sharply, and turns negative at large eccentricity ratios due to hydrodynamic effects. On the other hand, the bearings with triangular recesses show a uniform cross-coupled stiffness coefficient  $K_{xy}$  for eccentricity ratios smaller than 0.8. Figure 5 shows a steady decrease in  $K_{yx}$  as journal eccentricity increases. The trends observed are slightly perturbed by the onset of cavitation at a journal eccentricity  $ex/C=0.5$ .

Figures 7 and 8 depict the direct damping coefficients as the journal eccentricity ratio increases. For concentric operation, the bearing with circular

recesses has 3% more damping respect to the baseline bearing. However, the bearing stability indicator at concentric position is not improved, as shown by the whirl frequency ratio (WFR) depicted in Figure 9. In this bearing the stabilizing effect of the increased damping is neutralized by the presence of large cross-coupled stiffness coefficients. The bearing with triangular recesses have 9% less direct damping than the baseline bearing for concentric operation. This characteristic, along with the large cross-coupled stiffness presented by the triangular-I bearing produces a less stable bearing, as shown in Figure 9. In fact, the whirl frequency ratio for the triangular-I bearing is 0.55. This means that the threshold speed of instability is reduced to 1.82 times the first critical speed on a rigid rotor supported on hydrostatic bearings. For the baseline bearing the WFR is 0.50. On the other hand, the triangular-II bearing presents a combination of dynamic coefficients such that the whirl frequency ratio for concentric operation is reduced to 0.46, as shown in Figure 9. This means that the threshold speed of instability is raised to 2.2 times the first critical speed in a simple rotor-bearing system. Therefore, the triangular-II bearing presents a more stable rotordynamic performance than all the other bearings studied. Figures 8 also shows a steady increase of direct damping  $C_{xx}$  with eccentricity ratio for all the bearings with a higher rate of change at large eccentricities. On the other hand, the direct damping  $C_{yy}$  is almost constant for all journal eccentricity ratios. Finally, figure 9 shows that for all bearings, the whirl frequency ratio decreases as eccentricity increases denoting a more stable condition at high eccentricities (larger applied external load). This result is well known in the dynamic analysis and practical experience of hydrodynamic journal bearings. For journal eccentricity ratios smaller than 0.5, the triangular-II bearing presents the smallest whirl frequency ratio, and therefore, the most stable rotordynamic performance, while the triangular-I bearing always has the least stable rotordynamic characteristics. The results for the triangular-I and rectangular recess HJBs agree qualitatively with measured force coefficients for a turbulent-flow, five recess, water HJB tested by Franchek and Childs (1994) with levels of external pressurization to 7.0 MPa and journal speeds from 10,200 cpm to 24,600 cpm.

The accuracy of the finite element, laminar flow model for analysis of HJBs is evaluated by comparing numerical predictions of force coefficients with experimental data published by Adams et al. (1992); and with calculated results from a computer

model (*hydrosealt*) developed by San Andres (1993). This last computational model calculates static and dynamic force characteristics of rectangular recess, pad hydrostatic bearings operating on the laminar and turbulent flow regimes. Table 2 presents the geometric and operating characteristics of Adams et al. hydrostatic bearing. The bearing has four pads separated by deep axial grooves and the lubricant corresponds to SAE 10 grade oil. Each pad has a large rectangular recess with a recess to land area ratio equal to 0.46. The hydrostatic bearing was tested at two supply pressures, 1.21 MPa and 2.59 MPa, with a concentric recess pressure ratio equal to 0.40, and at two journal speeds corresponding to 1,000 and 2,000 rpm. In the experiments, dynamic force coefficients at small static journal eccentricities were determined by two separate identification procedures, and with a difference in measured results of less than 2% between the two methods. The flow in the bearing is laminar as evidenced by the small values of the circumferential and axial flow Reynolds numbers. Furthermore, fluid inertia effects are not important on this test bearing due to the smallness of the excitation frequency (synchronous) which determines a very low value of the squeeze film Reynolds number.

Table 3 summarizes the experimental results obtained by Adams et al. (1992), and the numerical predictions from the present finite element model and the finite difference scheme of San Andres (1993). The results from the two numerical models are virtually identical and determined at the bearing concentric position. The test values presented refer to average quantities with minimum and maximum deviations from the mean value. Note that the experimental results show very large variations for the damping coefficients. The numerical predictions from the two models are virtually identical. The differences among them are most likely due to small recess-edge entrance effects not considered on the laminar flow model. In comparison with the average experimental values, the numerical models overpredict the direct stiffness coefficients (20 to 30% larger), while underpredict slightly the test-average cross-coupled stiffness coefficients for most test conditions. For laminar flow conditions, the numerical models predict damping force coefficients which are independent of rotational speed. In particular, the cross-coupled damping coefficients are calculated to be negligible. On the other hand, the test results show all damping force coefficients to be of the same magnitude with the cross-coefficients

showing large deviations from their mean values. The predicted direct damping coefficients ( $C_{xx}C_{yy}$ ) show a good correlation with the test values and lie within the band of experimental minimum and maximum test results. Adams et al. (1992) also presented test values for inertia force coefficients but these appear to be too large for this bearing geometry excited at too low frequencies for fluid inertia effects to be measurable with certainty.

## CONCLUSIONS

A finite-element model to calculate the static and dynamic force performance characteristics of laminar flow hydrostatic journal bearings with arbitrary recess geometry is presented. The flow domain is discretized into body fitted shaped finite elements using an automatic mesh generator. The analysis details a perturbation method to determine the static bearing forces and dynamic force coefficients for small amplitude journal motions about an equilibrium position. Numerical predictions from the model correlate well with experimental values of force coefficients for a laminar flow, multipad hydrostatic journal bearing operating at low rotational speeds.

Hybrid bearings (combination hydrostatic - hydrodynamic) with conventional rectangular recesses and others with circular and triangular recess shapes are studied to determine their dynamic force coefficients, evaluate the magnitude of the whirl frequency ratio, and identify the range of their dynamic stability characteristics. A bearing with a triangular recess shape and vertex downstream of the orifice supply (in the sense of the journal surface speed) shows about 15% less cross-coupled stiffness coefficients than the other bearings, while the direct damping coefficients are approximately 9% smaller than the conventional rectangular recess bearing. At the concentric journal position, this triangular shaped bearing presents a whirl frequency ratio equal to 0.46 as compared to a value of 0.50 for the conventional rectangular recess shape bearing. Thus, the limited stability characteristics in a hybrid (hydrostatic - hydrodynamic) bearing can be slightly improved by modifying (and optimizing) the recess shapes.

## ACKNOWLEDGEMENTS

The author wishes to thank graduate students Mr. Julio Semanate and Ms. Anu Ghali who helped in typing parts of the program and performed some of the calculations. The support of the TAMU

Turbomachinery Consortium and NASA LeRC through NASA Grant NAG3-1434 is also acknowledged. Thanks to Mr. James Walker from NASA LeRC for his interest on this work.

## REFERENCES

- Adams, M.L., Sawicki, J.T. Capaldi, R.J., 1992, "Experimental Determination of Hydrostatic Journal Bearing Rotordynamic Coefficients," *Proceedings of the Institution of Mechanical Engineers*, pp. 365-374.
- Artiles, A., Walowit, J., Shapiro, W., 1982, "Analysis of Fluid Film Journal Bearings with Turbulence and Inertia Effects," *Advances in Computer Aided Bearing Design*, ASME Publication.
- Braun, M.J., Adams M.L. and Mullen R.L., 1984, "Analysis of a Two Row Hydrostatic Journal Bearing with Variable Properties, Inertia Effects and Surface Roughness," *Israel Journal of Technology*, Vol. 22, pp. 155-164.
- Braun, M.J., Wheeler R.L. and Hendricks R.C., 1987, "A Fully Coupled Variable Properties Thermohydraulic Model for a Cryogenic Hydrostatic Journal Bearing," *ASME Journal of Tribology* Vol 109, pp. 405-414.
- Butner, M., and B. Murphy, 1986, "SSME Long Life Bearings," NASA Report CR 179455.
- Chaomleffel J.P. and Nicholas D., 1986, "Experimental Investigation of Hybrid Journal Bearings," *Tribology International*, Vol 19, No 5, pp.253-259.
- Franchek, N., and D.W. Childs, 1994, "Experimental Test Results for Four High-Speed, High Pressure, Orifice Compensated Hybrid Bearings," *ASME Journal of Tribology*, Vol. 116, pp. 147-153.
- Ghosh M.K. and Majumdar B.C., 1978 "Stiffness and Damping Characteristics of Hydrostatic Multirecess Oil Journal Bearings," *Int. J. Mach. Tool Des. Res.*, Vol 18, pp. 139-151.
- Ghosh M.K., Majumdar B.C. and Rao J.S., 1979, "Steady State and Dynamic Behavior of Multirecess Hybrid Oil Journal Bearings," *Journal of Mechanical Engineering Science*, Vol 21., No. 5, pp. 345-351.
- Heller, S., 1974, "Static and Dynamic Performance of Externally Pressurized Fluid Film Journal Bearings in the Turbulent Regime," *ASME Journal of Lubrication Technology*, Vol. 96, pp. 381-390.
- Hirs, C.G., 1973, "A Bulk-Flow Theory for Turbulence in Lubricant Films," *ASME Journal of Lubrication Technology*, Vol. 95, pp.173-176.
- Klit, P. and Lund, J.W., 1988, "Calculation of the Dynamic Coefficients of a Journal Bearing, Using a Variational Approach," *ASME Journal of Tribology*, Vol. 108, pp. 421-425.
- Kurtin, K., D. Childs, K. Hale, and L. San Andres, 1993, "Experimental Versus Theoretical Characteristics of a High Speed Hybrid (Combination Hydrostatic and Hydrodynamic Bearing)," *ASME Journal of Tribology*, Vol.115, pp. 160-168.
- Pinkus, O. and Sternlicht, B., 1961, "Theory of Hydrodynamic Lubrication," McGraw-Hill, pp.12.
- Redecliffe, J. and Vohr, J., 1969, "Hydrostatic Bearings for Cryogenic Rocket Engine Turbopumps," *ASME Journal of Lubrication Technology*, pp. 557-575.
- Rohde S.M., and Ezzat H.A., 1976, "On the Dynamic Behavior of Hybrid Journal Bearings," *ASME Journal of Lubrication Technology*, pp. 90-94.
- Rowe, W., 1983, *Hydrostatic and Hybrid Bearing Design*, Butterworths Pressm London, U.K.
- San Andres, Luis, 1990, "Turbulent Hybrid Bearings with Fluid Inertia Effects," *ASME Journal of Tribology*, Vol. 112, pp. 699-707.
- San Andres, Luis, 1991, "Fluid Compressibility Effects on the Dynamic Response of Hydrostatic Journal Bearings," *WEAR*, Vol. 146, pp. 269-283.
- San Andres, Luis, 1992a, "Analysis of Turbulent Hydrostatic Bearings with a Barotropic Cryogenic Fluid," *ASME Journal of Tribology*, Vol. 114, pp. 755-764.
- San Andres, Luis, 1992b, "Laminar Flow Hydrostatic Bearings with Optimum Recess Geometry," *TAMU Turbomachinery Research Consortium*, Report TRC-B&C-1-92, April, Texas A&M University.
- San Andres, Luis., 1993, "Thermohydrodynamic Analysis of Cryogenic Liquid Fluid Film Bearings," Final Technical Report to NASA LeRC, Grant NAG3-1434, December, Texas A&M University, Research Progress Report.
- Taylor, C. and O'Callaghan, J.F., 1972, "A Numerical Solution of the Elastohydrodynamic Lubrication Problem Using Finite Elements," *Journal of Mechanical Engineering Science*, Vol 14, No 4, pp. 229-237.
- Thompson, J., 1974, "Automatic Numerical Generation of Boddy-Fitted Curvilinear Coordinate System for Fields Containing Any Number of Arbitrary Two-Dimensional Bodies," *Journal of Computational Physics*, Vol. 15, pp. 299-319.

# NOMENCLATURE

$A_o C_d \pi d_o^2 / 4$	Equivalent orifice area (m <sup>2</sup> ).
$A_r$	Recess area (m <sup>2</sup> ).
$C$	Bearing radial clearance (m).
$C_{xx}, C_{xy}, C_{yx}, C_{yy}$	Damping coefficients (Ns/m).
$C_d$	Orifice discharge coefficient.
$D = 2.R$	Bearing diameter (m).
$d_o$	Orifice diameter (m).
$e_x, e_y$	Journal eccentricity in X and Y directions (m).
$F_x, F_y$	Fluid film forces in X and Y directions (N).
$H$	Fluid film thickness (m).
$H_x, H_y$	$\cos(\theta), \sin(\theta)$ . First order film thickness.
$H_r$	Recess depth (m).
$K_{xx}, K_{xy}, K_{yx}, K_{yy}$	Stiffness coefficients (N/m).
$L$	Bearing length (m).
$N_{rec}$	Number of recesses.
$P$	Fluid pressure (Pa).
$P_s, P_a, P_r$	Supply, external and recess pressures (Pa).
$P_x, P_y$	Dynamic perturbed pressures in X and Y directions (Pa/m).
$Q_r$	Recess-to-land flow rate (m <sup>3</sup> /s)
$Q_x, Q_y$	Flow rates in x and y directions (m <sup>3</sup> /s).
$t$	time (s).
$V_r$	Total recess volume (m <sup>3</sup> ).
$\{X, Y\}$	Inertial coordinate system (m).
$\{x, y\}$	Coordinate system on bearing plane (m).
$\rho$	Fluid density (kg/m <sup>3</sup> ).
$\mu$	Fluid viscosity (Pa.s).
$\beta$	$(1/\rho)(\partial\rho/\partial P)$ . Liquid compressibility factor (1/Pa).
$\Delta e_x, \Delta e_y$	Dynamic eccentricities in X and Y directions (m).
$\theta$	$x/R$ . Circumferential coordinate (rad).
$\omega$	Whirl frequency (rad/s).
$\Omega$	Journal rotational speed (rad/s).
$\{\Psi\}_{i=1}^N$	Bilinear shape functions.
$\xi, \eta$	Coordinates on the transformed isoparametric plane.

Subscripts refer to:

$o$	The zeroth-order solution
$\eta$	Direction normal to the recess boundary.
$r$	Bearing recess.

Superscripts refer to:

$e$	Finite element.
$\alpha$	First-order solution.

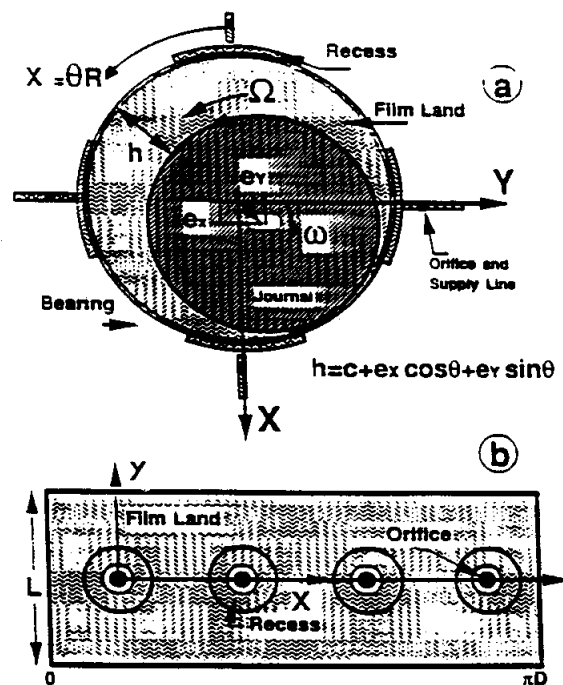


Figure 1. Geometry of an Orifice Compensated Hydrostatic Bearing  
a) Axial View and Coordinate System, b) Unrecessed Bearing Surface

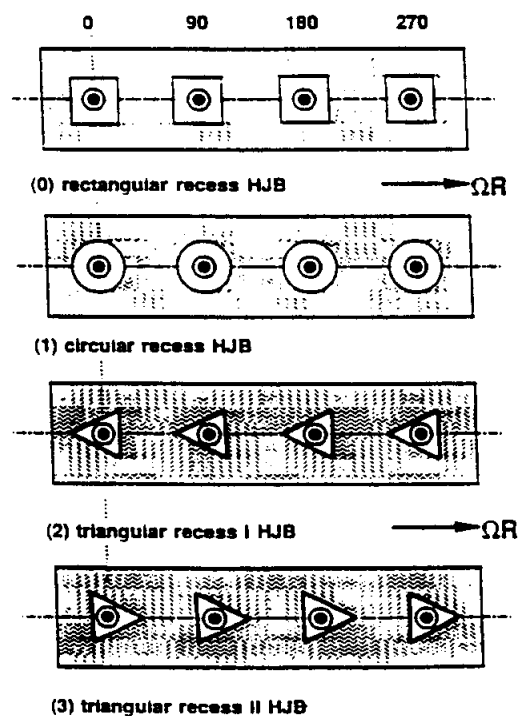


Figure 2. Hydrostatic Bearings with different recess geometry.  
Nrec=ArxLD1e0.20, Nrec=4

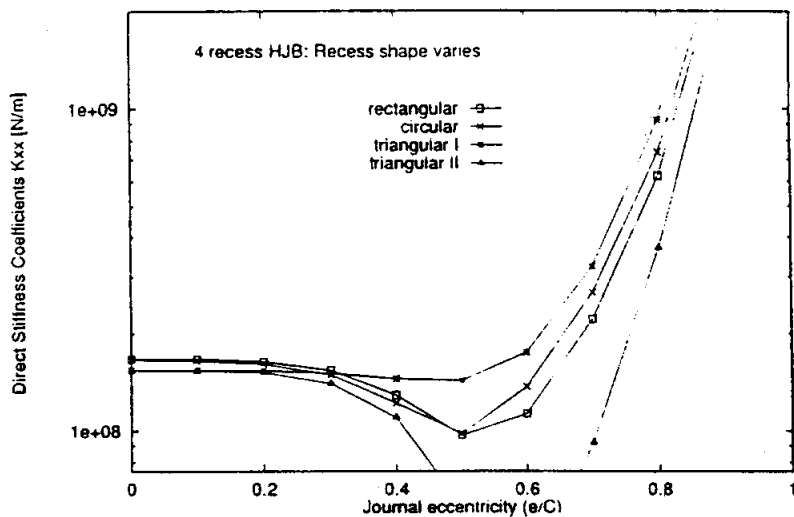


Fig. 3. Direct Stiffness Coefficient  $K_{xx}$  vs. journal eccentricity  $e_x$  for various HJB recess geometries. (10 Kcpm,  $P_s = P_a = 3.44$  MPa,  $P_r/P_s = 0.50$ )

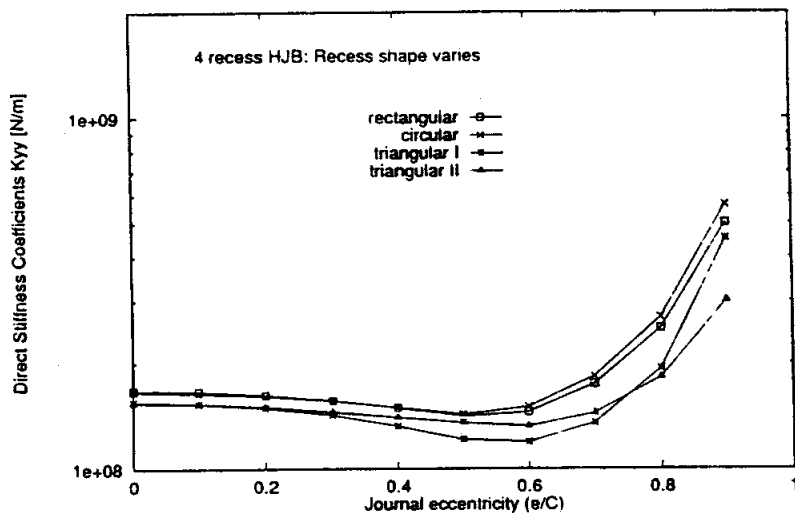


Fig. 4. Direct Stiffness Coefficient  $K_{yy}$  vs. journal eccentricity  $e_x$  for various HJB recess geometries. (10 Kcpm,  $P_s = P_a = 3.44$  MPa,  $P_r/P_s = 0.50$ )

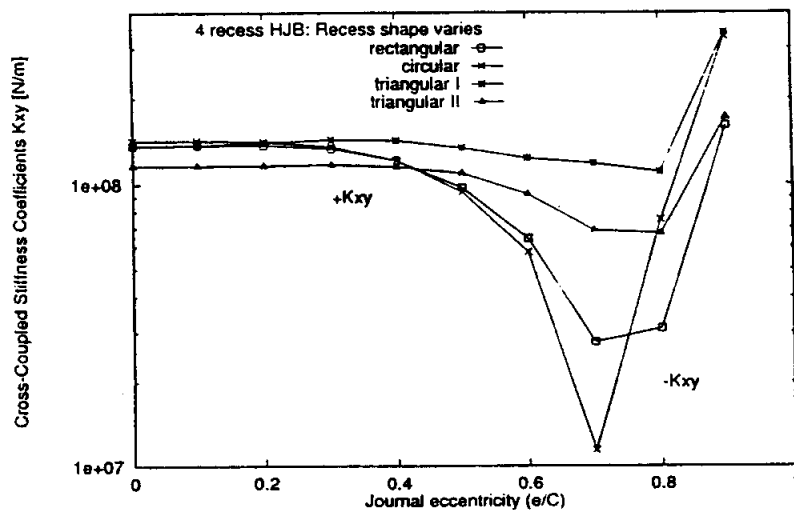


Fig. 5. Cross-Stiffness Coefficient  $K_{xy}$  vs. journal eccentricity  $e_x$  for various HJB recess geometries. (10 Kcpm,  $P_s = P_a = 3.44$  MPa,  $P_r/P_s = 0.50$ )

Table 1. Geometry and Operating Conditions of Hydrostatic Bearings

Number recesses $N_{rec} = 4$				
journal and bearing surface conditions: smooth				
Diameter $D$	Length $L$	clearance $C$	depth $H_r$	
76.2 mm	76.2 mm	76.2 $\mu$ m	0.254 mm	
(3 in.)	(3 in.)	(3 mils)	(10 mils)	
$L/D=1$ , Recess area Ratio=0.20, $C/R=0.002$ , $H_r/C=3.33$ , Discharge Coefficient $C_d=1.00$				
Incompressible Fluid: $\mu=0.005$ Pa-s, $\rho=900$ Kg/m <sup>3</sup>				
Recess Dimensions Orifice $d_o$				
Rectangular	(30 x 30) mm <sup>2</sup>		1.112 mm	
Circular	$\phi$ (16.95 mm) <sup>2</sup>		1.084 mm	
Triangular	(22.5 x 40) mm <sup>2</sup>		1.285 mm	
Operating Parameters:				
Rotations speed: 10,000 rpm, $\Omega=1,047$ rad/s				
Pressure supply: $P_s=3.44$ MPa (500 psig)				
at: $P_a=0.00$ MPa (0 psig)				
Recess Pressure: $P_r=1.72$ MPa (500 psig) at $e=0$				
TYP. Reynolds numbers:				
Rect=60, RC=547.14				
Recess=1112 $\mu$ D $\mu=90.85$ LAMINAR FLOW				



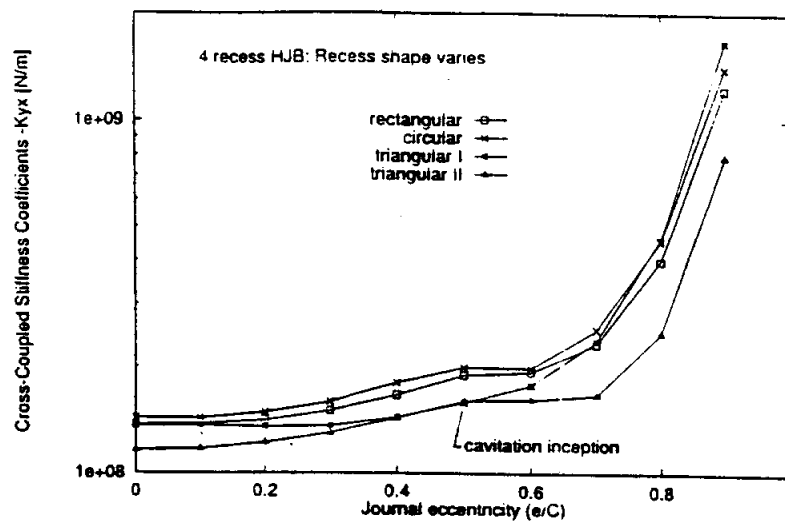


Fig. 6. Cross-Stiffness Coefficient  $-K_{yx}$  vs. Journal eccentricity  $e_x$  for various HJB recess geometries (10 Kcom,  $P_s - P_a = 3.44$  MPa,  $P_a/P_s = 0.50$ )

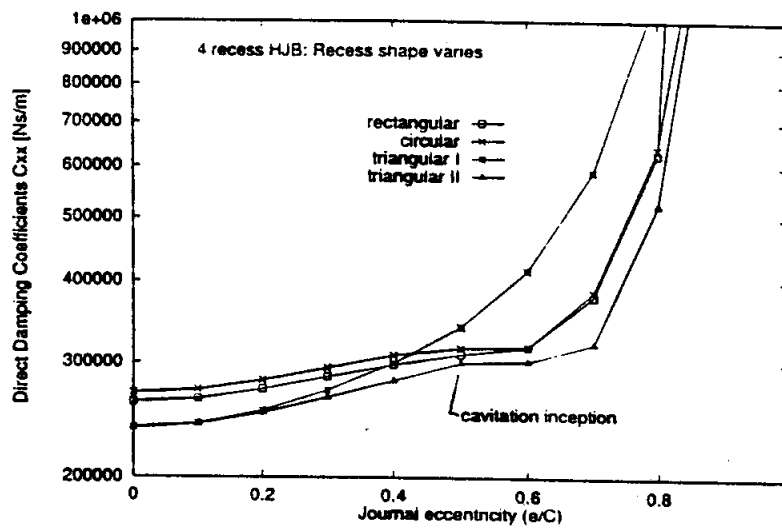


Fig. 7. Direct Damping Coefficient  $C_{xx}$  vs. Journal eccentricity  $e_x$  for various HJB recess geometries (10 Kcom,  $P_s - P_a = 3.44$  MPa,  $P_a/P_s = 0.50$ )

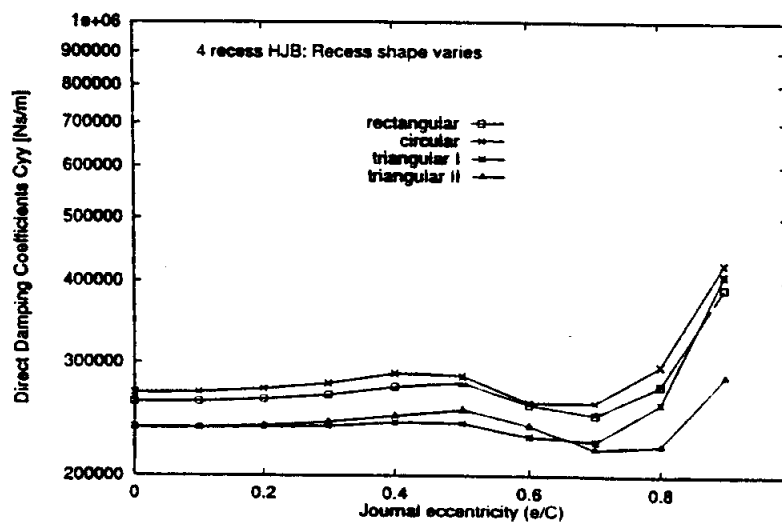


Fig. 8. Direct Damping Coefficient  $C_{yy}$  vs. Journal eccentricity  $e_x$  for various HJB recess geometries (10 Kcom,  $P_s - P_a = 3.44$  MPa,  $P_a/P_s = 0.50$ )

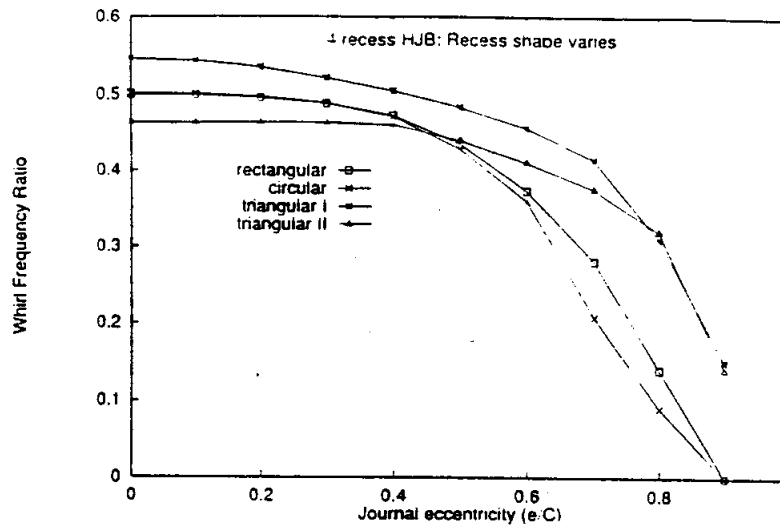


Fig. 9. Whirl Frequency Ratio vs. journal eccentricity for various HJB recess geometries. (10 Kcpm,  $P_s = P_a = 3.44$  MPa,  $P_r = 0.50$ , Area ratio = 0.20)

Table 2. Geometry and Operating Conditions of Pad Hydrostatic Bearing from Adams et al. (1992).

Number of Pads:  $N_{pad} = 4$  Number recesses/pad  $N_{rec} = 1$   
journal and bearing surfaces condition: smooth.

Diameter  $D$ , length  $L$ , clearance  $C$ , length  $L_r$ , diam.  $H_r$   
114.7 mm 53.98 mm 210.8 mm 35.56 mm 4.763 mm  
(4.51 in) (2.12 in) (8.3 in) (1.40 in) (0.187 in)

Pads: circumferential length  $\Theta_p = 80.50$  deg.

groove width = 9.50 deg.

Recess: circumferential length  $\Theta_r = 56$  deg.

$L/D = 0.47$ ,  $L_r/L = 0.659$ ,  $\Theta_r/\Theta_p = 0.696$ , Area Ratio = 0.459,  
 $C/R = 0.0037$ ,  $H_r/C = 22.6$

Orifice  $C_o = 1.00$ , diameter  $\phi_o = 1.265$  mm for concentric  
recess pressure ratio  $p_r/p_o = 0.40$ .

#### Operating Parameters:

Rotational speed: 1,000 and 2,000 rpm  
Pressure supply,  $P_s = 1.206$  MPa (175 psig), 2.586 MPa (375 psig)  
exd.,  $P_a = 0.00$  MPa (0 psig)  
Recess Pressure,  $P_r = 0.483$  MPa (70 psig), 1.034 MPa (150 psig)

Fluid: SAE 30 oil at 310K (100°F).

$\mu = 0.09787$  Pa-s,  $\rho = 890.00$  Kg/m<sup>3</sup>

#### TYP Reynolds numbers: LAMINAR FLOW

$Re_{pad} = \rho R C_o \omega / \mu = 11.5$  (1 Kcpm), 23.0 (at 2 Kcpm)  
 $Re_{recess} = \rho V (2\pi C) / \mu = 4.03$  ( $P_r = 70$  psig), 8.64 ( $P_r = 150$  psig)

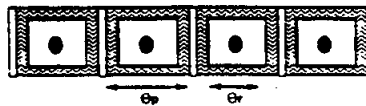


Table 3. Performance Characteristics of Four Pad Hydrostatic Bearing at eccentricity  $e/C = 0.0$ . Comparison to test results from Adams et al. (1992)

Speed	Pressure	Orifice	Flow	Torque	temperature	Reynolds #	Squeeze
Kcpm	MPa	mm	mm <sup>3</sup> /s	N-m	°C	Min/Max	Reynolds #s
1.0	0.48	1.59	0.285	1.556	1.05	2.66/9.59	0.042
1.03	1.03	1.93	0.616	1.543	4.28		
2.0	0.48		0.285	3.100	1.10	8.32/19.26	0.084
1.03			0.612	3.102	1.10	5.10/19.31	

Speed	Pressure	KXX	KYY	KXY	KYX	Model
Kcpm	Mpa		MM/mm			
1.0	0.48	26.28	26.28	4.06	-4.07	hydrostatic
		26.78	26.78	4.04	-4.04	finite elements
		21.17-2.46	22.32-3.28	5.25-1.15	-3.05-1.28	experimental
		-1.97	-1.66	-0.82	-0.88	
1.03		56.16	56.20	4.94	-4.78	hydrostatic
		57.37	57.37	4.04	-4.04	finite elements
		44.81-8.86	43.66-5.58	5.91-1.97	-4.27-3.28	experimental
		-5.42	-3.28	-2.95	-2.62	
2.0	0.48	26.00	26.00	8.19	-8.19	hydrostatic
		26.78	26.78	8.09	-8.09	finite elements
		19.17-1.84	22.78-2.45	7.88-1.57	-7.35-1.57	experimental
		-1.84	-2.80	-1.58	-2.10	
1.03		55.76	55.78	7.99	-7.98	hydrostatic
		57.38	57.38	8.09	-8.09	finite elements
		41.50-8.40	45.34-9.28	9.80-3.85	-9.80-4.55	experimental
		-5.25	-5.95	-3.50	-4.90	

Speed	Pressure	CXX	CYY	CXY	CYX	Model
Kcpm	Mpa		KN/mm			
1.0	0.48	78.08	79.07	0.30	-0.29	hydrostatic
		88.66-10.10	70.70-10.00	2.81-12.3	-4.33-4.32	experimental
		-5.06	-10.10	-9.54	-8.65	
1.03		77.78	78.00	-6.47	5.98	hydrostatic
		48.91-24.25	64.74-31.00	-67.7-37.4	-30.25-20.80	experimental
		-27.03	-15.50	-8.0	-82.30	
2.0	0.48	78.38	78.37	0.41	-0.40	hydrostatic
		78.30-6.83	75.62-25.85	13.78-10.54	-0.21-8.29	experimental
		-5.30	-15.92	-13.78	-3.43	
1.03		78.14	78.12	0.58	-0.58	hydrostatic
		87.34-1.68	87.54-53.90	-10.10-33.7	20.2-10.1	experimental
		-3.37	-30.30	-20.2	-3.36	
all		77.14	77.14	0.02	-0.02	finite elements

Experimental values obtained from graphical values shown by Adams et al. (1992).  
Values refer to average quantities over maximum and minimum deviations from average.

15. "Analysis of Two Phase Flow in Cryogenic Damper Seals. Part I: Theoretical Model," 1996, Arauz, G., and L. San Andres, submitted for peer review to *ASME Journal of Tribology*, November.

# ANALYSIS OF TWO-PHASE FLOW IN CRYOGENIC DAMPER SEALS. PART I: THEORETICAL MODEL<sup>1</sup>

Grigory L. Arauz  
Research Assistant  
Luis San Andres  
Associate Professor  
Texas A&M University  
College Station, TX 77843-3123  
11/96

## ABSTRACT

Cryogenic fluid damper seals operating close to the liquid-vapor region (near the critical point or slightly sub-cooled) are likely to develop a two-phase flow region and which affects the seal performance and reliability. An all-liquid, liquid-vapor, and all-vapor, i.e. a "continuous vaporization" bulk-flow model is presented for prediction of the seal dynamic forced response. Continuity, momentum and energy (enthalpy) transport equations govern the two-phase flow of a homogeneous saturated mixture in thermodynamic equilibrium. Static and dynamic force performance characteristics for the seal are obtained from a perturbation analysis of the governing equations. Theoretical predictions and comparisons to experimental measurements in a liquid and gaseous nitrogen seal are presented in Part II. The effects of two-phase flow regimes on the dynamic force coefficients and stability of an oxygen damper seal are also discussed.

## NOMENCLATURE

- c: radial clearance [m].
- $E_i$ :  $i_* / U_*^2$ , dimensionless parameter in energy equation.
- $F_X, F_Y$ : Fluid film forces in X and Y directions [N].
- $f_{r,s}$ :  $a_m[1 + (c_m r_{r,s}/H + b_m/Re_{r,s})^{em}]$ , turbulent friction factors at rotor and stator surfaces.  
 $a_m = 0.001375$ ;  $b_m = 5 \times 10^5$ ;  $c_m = 10^4$ ;  $e_m = 1/3$
- $H, h$ : film thickness [m],  $H/c$ .
- $i, i_*, \bar{i}$ : fluid enthalpy, characteristic enthalpy at supply [J/kg],  $i/i_*$ .
- $i_l, i_g$ : liquid, vapor saturated enthalpy [J/kg].
- $K_{\alpha\beta}, C_{\alpha\beta}$ : stiffness and damping rotordynamic force coefficients [N/m, N.s/m].  $\alpha\beta = X, Y$
- $k_r, k_s$ :  $f_s Re_s, f_r Re_r$ , turbulent shear parameters at stator and rotor surfaces.
- $k_x, k_y$ :  $(k_r + k_s)/2$ , dimensionless shear parameters in circumferential and axial directions.
- L: seal length [m].
- n:  $\mu_g/\mu_l$ , vapor-to-liquid viscosity ratio.
- P: fluid pressure [Pa].
- $P_s, P_a$ : supply and discharge pressure [Pa].
- p:  $(P - P_a)/(P_s - P_a)$ , dimensionless fluid pressure.
- R: rotor radius [m].
- $Re_r$ :  $\rho H[(U - \Omega R)^2 + V^2]^{0.5}/\mu$ , Reynolds number relative to rotor surface.
- $Re_s$ :  $\rho H[U^2 + V^2]^{0.5}/\mu$ , Reynolds number relative to stator surface.
- $Re_s$ :  $\rho \omega_* c^2/\mu_*$ , squeeze film Reynolds number.

<sup>1</sup> Research sponsored by NASA Lewis Research Center through grant NAG3-1434. Project "Thermohydrodynamic Analysis of Cryogenic Liquid Turbulent Flow Fluid Film Bearings".

$Re_p^*$ :  $\rho_* U_* c^2 / (\mu_* R)$ , modified reference pressure flow Reynolds number.  
 $r_r, r_s$ : mean roughness depth at rotor and stator surfaces [m].  
 $T, T_*$ : fluid temperature, characteristic temperature [°K].  
 $\bar{T}$ :  $T/T_*$ , dimensionless temperature.  
 $t$ : time [s].  
 $u, v$ :  $(U, V)/U_*$ , dimensionless circumferential and axial mean flow velocities.  
 $U_*$ :  $c^2(P_s - P_a)/(\mu R)$ , characteristic velocity [m/s].  
 $X, Y$ : inertial coordinates for rotor center position within seal stator [m].  
 $\dot{X}, \dot{Y}$ : rotor center velocity with respect to inertial coordinates [m/s].  
 $\ddot{X}, \ddot{Y}$ : rotor center acceleration with respect to inertial coordinates [m/s<sup>2</sup>].  
 $x, y$ : circumferential and axial coordinates [m].  
 $\bar{x}$ :  $x/R = \theta$ , dimensionless circumferential coordinate.  
 $\bar{y}$ :  $y/R$ , dimensionless axial coordinate.  
 $\alpha$ : circumferential velocity entrance swirl factor.  
 $\epsilon_{XY}$ : dimensionless rotor eccentricities in X and Y directions.  
 $\Gamma$ : first order coefficients (Appendix 1).  
 $\gamma$ : first order shear coefficients (Appendix 1).  
 $\Psi$ : void fraction (vapor-to-mixture volume ratio).  
 $\Lambda$ :  $\Omega R/U_*$ , dimensionless rotor velocity.  
 $\lambda$ : vapor-to-mixture mass ratio (quality).  
 $\mu, \mu_*, \bar{\mu}$ : fluid viscosity, characteristic viscosity [Pa.s],  $\mu/\mu_*$ .  
 $\Omega$ : rotational speed of journal [rad/s].  
 $\omega$ : excitation whirl frequency [rad/s].  
 $\rho, \rho_*, \bar{\rho}$ : fluid density, characteristic density [kg/m<sup>3</sup>],  $\rho/\rho_*$ .  
 $\sigma$ :  $\omega R/U_*$ , dimensionless frequency parameter.  
 $\tau_{ij}$ : wall shear stresses [Pa].  
 $\xi$ : empirical entrance loss coefficient.

#### Subscripts:

$o$ : refers to zeroth order solution.  
 $\alpha$ : X, Y, refers to first order solution.  
 $l$ : refers to liquid phase.  
 $g$ : refers to vapor gaseous phase.  
 $i$ : refers to seal inlet conditions.  
 $s$ : refers to seal supply conditions.  
 $sat$ : refers to fluid saturation conditions.  
 $+$ : refers to mixture properties when void fraction  $\Psi=0.3$ .

## INTRODUCTION

The importance of process fluid damper bearing seals and hybrid journal bearings in high performance turbomachinery has grown steadily in the past few years. Fluid film bearings allow for more compact and lighter rotors, supercritical speed operation and no bearing life limitations. These characteristics along with increased durability, reduced wear and friction, and more importantly, predictable rotordynamic force coefficients have fueled the advance of an "all-fluid-film-bearing" technology for advanced cryogenic turbomachinery (San Andres, 1995, 1996). Interstage (damper) seals in turbopumps not only control leakage but should also operate as load supports with additional damping to enhance the stability of the rotor-bearing system.

Operation close to the fluid critical point, likely to occur in cryogenic fluid damper seals due to the steep variations of pressure and temperature, may result in fluid vaporization and the consequent formation of a single component two-phase mixture (Hendricks et al., 1987, Yang et al., 1993). This transformation implies large variations in the overall mixture properties, modifying the pressure and temperature gradients within the seal, and affecting the overall seal performance.

This paper, parts I and II, advances a bulk-flow analysis for the prediction of the dynamic forced response of damper seals operating under two-phase flow conditions. Part I reviews the relevant literature related to two-phase flows in face and annular seals. Next, a general bulk-flow model for both single and two-phase flow regimes within annular seal is presented. Finally, a perturbation analysis of the governing equations for small amplitude rotor motions about the centered position is carried out to determine the dynamic stiffness and damping coefficients. Part II (Arauz and San Andres., 1997) outlines the numerical solution method, presents correlations of computed predictions with experimental flow rates and pressure drop measurements for a liquid nitrogen seal undergoing a phase change at the seal exit plane. A discussion of the effect of supply temperature on the computed force coefficients of an annular seal for an oxidizer turbopump follows. The closure emphasizes the large effect of fluid compressibility for low quality mixtures on the dynamic force coefficients and stability of the annular seal studied.

Fluid film forces generated in damper seals, and fluid film bearings in general, are typically described in terms of frequency independent rotordynamic force coefficients as given by (Childs, 1993):

$$\begin{bmatrix} F_x \\ F_y \end{bmatrix} = \begin{bmatrix} K_{xx} & K_{xy} \\ K_{yx} & K_{yy} \end{bmatrix} \begin{bmatrix} X \\ Y \end{bmatrix} + \begin{bmatrix} C_{xx} & C_{xy} \\ C_{yx} & C_{yy} \end{bmatrix} \begin{bmatrix} \dot{X} \\ \dot{Y} \end{bmatrix} + \begin{bmatrix} M_{xx} & M_{xy} \\ M_{yx} & M_{yy} \end{bmatrix} \begin{bmatrix} \ddot{X} \\ \ddot{Y} \end{bmatrix} \quad (1)$$

where the stiffness ( $K_{ij}$ ), damping ( $C_{ij}$ ) and fluid inertia ( $M_{ij}$ ) coefficients represent the force components proportional to the rotor displacements, velocities and accelerations, respectively. The direct coefficients in the main diagonal characterize a force that is in the same direction as the motion; whereas the off diagonal

(cross-coupled) coefficients represent forces that although proportional to the generalized displacement, velocity or acceleration, act in a direction perpendicular to it. The linear model in the above equation is valid only for rigid surface seals operating at sufficiently low frequencies and with incompressible fluids (San Andres, 1996).

## AN APPRAISAL OF THE LITERATURE

The analysis of multi-phase flows in seals is of relevance since these applications have similar operating conditions as annular pressure seals. Hughes et al. (1978), and Yasuna and Hughes (1992) study the vaporization of a lubricant in liquid face seals. The flow through the seal is divided into two separate regions at the same vaporization temperature, one liquid and one gaseous with separate equations of motion for pressure, temperature and mass flow rate in each fluid phase. The model predicts that the maximum flow rate is reached for the all-liquid condition. On the other hand, when two-phase flow occurs most of the pressure drop takes place in the vapor phase. Yasuna and Hughes (1990) present a "continuous boiling" model as opposed to the previous "discrete boiling" analysis. The flow along the seal is divided into three regions: all-liquid, liquid-gas, and all-gas. The two-phase region is considered as a homogeneous mixture of saturated liquid and vapor in thermodynamic equilibrium. Results show the extent of the two-phase region to be considerable in all cases, even when the flow is nearly isothermal (discrete model).

Beatty and Hughes (1987) present a turbulent flow, steady and adiabatic model for concentric annular pressure seals. Here the fluid flow is also divided into three regions: all liquid, liquid-vapor, and all vapor. Numerical results for a case example emulating an inter-stage seal of the Space Shuttle Main Engine (SSME) High-Pressure Oxidizer Turbo-Pump (HPOTP) show that the leakage rate is reduced by clearance reduction, increment of rotor speed, lengthening of the seal, and vapor production. It is concluded that subcooling of the liquid before the seal inlet reduces vapor production, therefore increasing the leakage rate.

Beatty and Hughes (1990) later introduce a different model based on the stratified flow of the boiling liquid and vapor phases due to centrifugal fluid inertia forces. The model regards the fluid streams as adiabatic and moving at different bulk-flow velocities, with the vapor layer closer to the rotating shaft. The stratified model predicts slightly larger leakage rates and it is less sensitive to rotational speed than the homogeneous-mixture model. These small deviations then show centrifugal effects to be not important in annular seals where curvature effects are negligible due to the smallness of the film thickness compared to the length and diameter of the seal. The results also indicate the two phases to move closely together, and therefore, a one component mixture should suffice to model the flow. In addition, the large levels of turbulence (typical of annular seals) enhance mixing and homogenize the liquid-vapor mixture.

Hendricks (1987) presents a unique experimental study on uniform clearance, non-rotating, cylindrical seals for the SSME-HPOTP. The work focuses on the measurement of leakage rates and pressure profiles for several fluids ( $\text{LN}_2$  and  $\text{LH}_2$ ), and for concentric and fully eccentric seal positions. The experiments demonstrate that low back pressures lead to a two-phase flow condition at the seal discharge. Later, Hendricks et al. (1987) describe a theoretical model for laminar flow of a variable properties fluid through cylindrical seals, and show that two-phase flow regions may appear even when the supply and discharge pressures are well above the critical point. For seals or bearings operating highly eccentric the minimum pressure associated with the maximum film thickness location may be low enough to fall below the critical pressure and reach saturation conditions. These "nested" two-phase regions affect the fluid pressure and temperature fields, and therefore seal static and dynamic force characteristics may differ significantly to those of a full single-phase seal.

Salhi et al. (1992) conducted tests to measure the pressure gradient in a two-phase flow (nitrogen on diluted oil) at low void fractions ( $\sim 5\%$ ) in a narrow annular space between concentric rotating cylinders. The measured flow rates and pressure drops combined in the form of a *conventional* friction factor coefficient ( $f=4\Delta P/[L\rho V^2/c]$ ) for the mixture demonstrate that the correlation  $f = a \text{Re}^n$ , where  $\text{Re}$  is a characteristic Reynolds number and as used for all-liquid and all-gas flows, is also valid for two-phase mixtures with low vapor (mass) concentration.

Iwatsubo et al. (1993) provide measurements of the dynamic force coefficients of an annular seal with a mixture of water and air and volume fractions up to 70 %. Test results show the significant effect of two-phase flow conditions on the seal dynamic force performance. Fluid film forces are found to decrease as mixture void fraction increases, but more importantly, a reduction of whirl frequency ratio (destabilizing-to-stabilizing forces ratio) is observed for mixtures with void fraction equal to 25%. However, due to the large difference in density between the two mixture components (air and water) the compositions tested represent very small concentrations of gas in terms of mixture quality (gas-to-mixture mass ratio).

San Andres et al. (1991, 1995, 1996), and Yang et al. (1993) have developed computational mechanic models for prediction of bearing and seal dynamic forced performance, and accounting for the important flow phenomena present in cryogenic applications, i.e. flow turbulence, fluid inertia at the seal inlet and discharge, thermal effects, and different geometries (grooves, recesses, etc.). Computed predictions have been correlated extensively (and successfully) to experimental data from a water hydrostatic bearing and seal test bed (Childs and Hale, 1994). These bulk-flow models are here extended to account for two-phase flow regimes, thus addressing the current needs for cryogenic fluid damper seals.



## ANALYSIS

Figure 1 shows a typical geometry of an annular (damper) seal. The seal is comprised by two concentric cylinders, the rotor spins at speed ( $\Omega$ ) and the outer cylinder (stator) is stationary. A thin fluid film of thickness  $H$ , exaggerated in the figure for clarity, separates the rotor from the stator. This thin gap acts as a resistance path to the fluid flow from the high pressure supply ( $P_s$ ) zone to the relatively low pressure discharge side ( $P_a$ ). The following assumptions are appropriate:

- Two-dimensional bulk-flow (in the circumferential and axial directions) due to the smallness of the film thickness as compared to the other seal dimensions.
- Fully developed turbulent and adiabatic flow due to the large pressure gradient along the seal which produces large axial velocities and Reynolds numbers around 50,000 and higher. At these velocities the heat flow carried by fluid advection is much larger than the heat conducted through the seal walls (Yang et al., 1993).
- Three flow regions are possible: all-liquid, liquid-vapor, and all-vapor, i.e. a "continuous" vaporization model (Beatty and Hughes, 1987).
- If a phase change occurs, then the liquid-vapor mixture is regarded as homogeneous, saturated, and in thermodynamic equilibrium.

### Bulk-flow Governing Equations

The turbulent bulk-flow of a variable properties fluid inside an annular pressure seal is described by the continuity, momentum and energy transport equations given by Yang (1992). These equations are valid for a variable properties fluid, and thus can be applied directly to the all-liquid or the all-vapor regions. The energy transport equation is here expressed in terms of fluid enthalpy to include both single and two-phase flow conditions. Note that the fluid temperature is not independent of pressure on the two-phase region. The bulk-flow transport equations are:

#### Continuity:

$$\frac{\partial(\rho H)}{\partial t} + \frac{\partial(\rho H U)}{\partial x} + \frac{\partial(\rho H V)}{\partial y} = 0 \quad (2)$$

#### Circumferential Momentum:

$$\frac{\partial(\rho H U)}{\partial t} + \frac{\partial(\rho H U^2)}{\partial x} + \frac{\partial(\rho H U V)}{\partial y} = -H \frac{\partial P}{\partial x} + \tau_{xz} \Big|_0^H \quad (3)$$

Axial Momentum:

$$\frac{\partial(\rho HV)}{\partial t} + \frac{\partial(\rho HUV)}{\partial x} + \frac{\partial(\rho HV^2)}{\partial y} = -H \frac{\partial P}{\partial y} + \tau_{yz} \Big|_0^H \quad (4)$$

Energy:

$$\begin{aligned} \frac{\partial(\rho Hi)}{\partial t} + \frac{\partial(\rho HUi)}{\partial x} + \frac{\partial(\rho HVi)}{\partial y} = H \left[ \frac{\partial P}{\partial t} + U \frac{\partial P}{\partial x} + V \frac{\partial P}{\partial y} \right] \\ + R\Omega \tau_{xz} \Big|_0^H - U \tau_{xz} \Big|_0^H - V \tau_{yz} \Big|_0^H \end{aligned} \quad (5)$$

where the density ( $\rho$ ) is that of the mixture in the two-phase region.

### **Shear stress model**

Yang et al. (1993) uses Hirs' bulk-flow theory for turbulence in thin films flows. This model works well for all-liquid and all-gaseous flows. The use of friction factors based on Moody's formulae facilitates the inclusion of macroscopically rough stator surfaces into the model. These considerations and the assumption of a homogeneous mixture for the two-phase region makes Hirs' shear stress model adequate for the proposed two-phase flow model. The validity of this model for low gas concentration two-phase mixtures is also demonstrated by the experiments of Salhi et al. (1992), as detailed in the literature review. Thus, the wall shear stresses in the bulk flow governing equations are defined as:

$$\begin{aligned} \tau_{xz} \Big|_0^H &= -\frac{\mu}{H} \left( k_x U - k_r \frac{R\Omega}{2} \right) \\ \tau_{yz} \Big|_0^H &= -\frac{\mu}{H} k_y V \\ \tau_{xx} \Big|_0^H &= \frac{H}{2} \frac{\partial P}{\partial x} + \frac{\mu}{4H} \left[ U k_s - (U - R\Omega) k_r \right] \end{aligned} \quad (6)$$

The turbulent shear parameters ( $k_x$ ,  $k_y$ ) and ( $k_r$ ,  $k_s$ ) are given in the Nomenclature.

### **Mixture Fluid Properties**

A two-phase flow condition within the seal is determined by comparison of the fluid enthalpy ( $i$ ) with the liquid ( $i_l$ ) and vapor ( $i_g$ ) saturated enthalpies corresponding to the local pressure.

$$\begin{aligned} \text{If } i &\leq i_{l(P)} && \Rightarrow \text{LIQUID} \\ \text{If } i &\geq i_{g(P)} && \Rightarrow \text{VAPOR} \\ \text{If } i_{l(P)} &< i < i_{g(P)} && \Rightarrow \text{TWO-PHASE} \end{aligned} \quad (7)$$

with the mixture quality ( $\lambda$ ), i.e. the vapor to mixture mass ratio, given by the ratio:

$$\lambda = \frac{i - i_l}{i_g - i_l} \quad (8)$$

The mixture properties such as entropy, internal energy, specific heat, specific volume, etc. are defined in terms of the quality ( $\lambda$ ) as (Look, 1986):

$$\Phi = \lambda \Phi_g + (1-\lambda) \Phi_l \quad (9)$$

where  $\Phi$  represent the mixture property, and ( $\Phi_g$ ,  $\Phi_l$ ) are the vapor and liquid saturated properties, respectively. The mixture density, by definition the inverse of the specific volume, is therefore given as:

$$\frac{1}{\rho} = \frac{\lambda}{\rho_g} + \frac{1-\lambda}{\rho_l} \quad (10)$$

The mixture viscosity is treated separately in light of empirical evidence of a peculiar behavior of the viscosity for mixtures with low concentrations of a gaseous phase. The mixture viscosity models most commonly used in two-phase flow studies are those proposed by McAdams et al. (1942), Cicchitti et al. (1960) and Dukler (1964), as discussed by Carey (1992). These models consider that the mixture viscosity decreases between the value of saturated liquid face viscosity to that of the saturated vapor viscosity as the mixture quality increases. However, some experimental data (Hayward, 1961, Zeidan et al., 1990) demonstrates that the mixture viscosity increases with respect to the viscosity of the liquid at low vapor concentrations (i.e. small qualities). Models for such variation are presented in Chamniprasart (1992) and there attributed to Einstein (1906), Jeffery (1922) and Taylor (1932). According to these theoretical models, when the suspension (gaseous phase) is so diluted that the distances between contiguous particles are large compared with their dimensions (low vapor concentration), the presence of the disperse particles induces an excess of the rate of dissipation of energy over that which occur if the particles were removed and their space is filled with the base fluid. These models then state that the rise in viscosity is a function of mixture volume concentration and of the ratio of vapor-to-liquid viscosity. A piece-wise continuous expression for mixture viscosity is here defined for concentrations up to 30% in volume (void fraction  $\Psi=0.3$ ). For higher mixture compositions the expression proposed by McAdams is adapted to account for the variation of viscosity between its maximum value at  $\Psi=0.3$  and the value for vapor ( $\Psi=1$ ). Thus,

$$\begin{aligned} \frac{\mu}{\mu_l} &= 1 + 2.5 \left( \frac{n+0.4}{n+1} \right) \Psi \quad ; \quad n = \frac{\mu_g}{\mu_l} \quad \text{for } \Psi \leq 0.3 \\ \frac{1}{\mu} &= \left[ \left( \frac{\lambda_+}{\mu_g} - \frac{1}{\mu_+} \right) + \left( \frac{1}{\mu_+} - \frac{1}{\mu_g} \right) \lambda \right] \frac{1}{\lambda_+ - 1} \quad \text{for } \Psi > 0.3 \end{aligned} \quad (11)$$

where  $\lambda_+$  and  $\mu_+$  are the quality and mixture viscosity at void fraction  $\Psi=0.3$ , given by:

$$\lambda_+ = \frac{0.3}{0.3 + 0.7 \frac{\rho_l}{\rho_g}} \quad ; \quad \mu_+ = \frac{1.3\mu_l^2 + 1.75\mu_l\mu_g}{\mu_l + \mu_g} \quad (12)$$

For a homogeneous mixture, quality and void fraction are related by:

$$\lambda = \frac{\Psi}{\Psi + (1 - \Psi) \frac{\rho_l}{\rho_g}} \quad ; \quad \Psi = \frac{\lambda}{\lambda + (1 - \lambda) \frac{\rho_g}{\rho_l}} \quad (13)$$

As a relevant example, the variation of mixture density and viscosity with mixture quality are presented in Figure 2 for oxygen at a pressure of 1.8 MPa ( $T_{\text{sat}}=130.58$  °K). Density and viscosity are presented in dimensionless form, i.e. normalized with respect to the supply conditions given for the annular seal studied by Hughes (1987), ( $P_s=2.79$  MPa,  $P_a=1.8$  MPa and  $T_s=130$  °K) with  $\rho^*=825.4$  kg/m<sup>3</sup>,  $\mu^*=62.94$  μPa-s. More details on this seal example are given in Part II of this paper.

## THE FLOW GOVERNING EQUATIONS FOR CENTERED SEAL OPERATION

The flow within damper seals is described by the bulk-flow equations (2) through (5). A dynamic perturbation on the film thickness for small amplitude rotor motions ( $e_x$ ) of frequency ( $\omega$ ) about the seal concentric position leads to zeroth and first order bulk-flow equations. Solution of the zeroth order equation provides the seal static characteristics such as leakage, drag torque, and velocity, pressure, temperature and mixture composition fields within the seal. The first order pressure fields render the dynamic force coefficients. The concentric seal operation assumption is justified since (annular pressure) damper seals show force coefficients with little dependency on rotor eccentricity (San Andres, 1991-5).

The small amplitude harmonic motions of the rotor allow the film thickness and the flow variables  $\Phi = (U, V, P, \text{ etc})$  to be expressed as a superposition of a zeroth and first order fields representing the steady state and the dynamic components, respectively, i.e., say along the X direction,

$$\begin{aligned}
h &= h_o + \epsilon_x \cos \theta e^{i\alpha} \quad ; \quad i = \sqrt{-1} \\
\Phi &= \Phi_o + \epsilon_x (\Phi_c \cos \theta + \Phi_s \sin \theta) e^{i\alpha}
\end{aligned} \tag{14}$$

Introducing these perturbed flow variables into the governing equations (2) through (5) renders:

### Dimensionless Zeroth Order Equations for Centered Operation

#### Continuity

$$\frac{d}{d\bar{y}} (\bar{\rho}_o h_o v_o) = 0 \tag{15}$$

#### Circumferential Momentum

$$\text{Re}_p^* \frac{d(\bar{\rho}_o h_o u_o v_o)}{d\bar{y}} = -\frac{\bar{\mu}_o}{h_o} \left( k_{xo} u_o - k_{ro} \frac{\Lambda}{2} \right) \tag{16}$$

#### Axial Momentum

$$\text{Re}_p^* \frac{d(\bar{\rho}_o h_o v_o^2)}{d\bar{y}} = -h_o \frac{dp_o}{d\bar{y}} - \frac{\bar{\mu}_o}{h_o} (k_{yo} v_o) \tag{17}$$

#### Energy (adiabatic)

$$\text{Re}_p^* E_1 \frac{d(\bar{\rho}_o h_o v_o \bar{i}_o)}{d\bar{y}} = h_o v_o \frac{dp_o}{d\bar{y}} + \frac{\bar{\mu}_o}{h_o} \left[ \left( u_o^2 + v_o^2 + \frac{u_o \Lambda}{2} \right) k_{xo} + \left( \frac{\Lambda^2}{4} - u_o \Lambda \right) k_{ro} \right] \tag{18}$$

### Dimensionless First Order Equations for Centered Seal

With the first order variables defined as:

$$\mathbf{u}_1 = \begin{bmatrix} u_c \\ u_s \end{bmatrix}; \quad \mathbf{v}_1 = \begin{bmatrix} v_c \\ v_s \end{bmatrix}; \quad \mathbf{p}_1 = \begin{bmatrix} p_c \\ p_s \end{bmatrix}; \quad \bar{\mathbf{i}}_1 = \begin{bmatrix} \bar{i}_c \\ \bar{i}_s \end{bmatrix}; \quad \bar{\mathbf{p}}_1 = \begin{bmatrix} \bar{\rho}_c \\ \bar{\rho}_s \end{bmatrix} \tag{19}$$

the first order governing equations are given as:

#### Continuity:

$$\begin{bmatrix} i\sigma \bar{\rho}_o + \frac{d(\bar{\rho}_o v_o)}{d\bar{y}} \\ -\bar{\rho}_o u_o \end{bmatrix} + \begin{bmatrix} i\sigma h_o & h_o u_o \\ -h_o u_o & i\sigma h_o \end{bmatrix} \bar{\mathbf{p}}_1 + \begin{bmatrix} 0 & \bar{\rho}_o h_o \\ -\bar{\rho}_o h_o & 0 \end{bmatrix} \mathbf{u}_1 + \frac{d}{d\bar{y}} (\bar{\rho}_o h_o \mathbf{v}_1 + h_o v_o \bar{\mathbf{p}}_1) = \mathbf{0} \tag{20}$$

### Circumferential Momentum:

$$\begin{aligned} \text{Re}_p^* \frac{d}{dy} (\bar{\rho}_o h_o v_o \mathbf{u}_1) = & \begin{bmatrix} \Gamma_{uu} - i\sigma \text{Re}_p^* \bar{\rho}_o h_o & -\text{Re}_p^* \bar{\rho}_o h_o u_o u_{\alpha\alpha} \\ \text{Re}_p^* \bar{\rho}_o h_o u_o u_{\alpha\alpha} & \Gamma_{uu} - i\sigma \text{Re}_p^* \bar{\rho}_o h_o \end{bmatrix} \mathbf{u}_1 + \Gamma_{uv} \mathbf{v}_1 + \begin{bmatrix} \Gamma_{uh} \\ 0 \end{bmatrix} \\ & + \Gamma_{u\mu} \bar{\mu}_1 + \Gamma_{u\rho} \bar{\rho}_1 + \begin{bmatrix} 0 & h_o \\ -h_o & 0 \end{bmatrix} \mathbf{p}_1 \end{aligned} \quad (21)$$

### Axial Momentum:

$$\begin{aligned} \text{Re}_p^* \frac{d}{dy} (\bar{\rho}_o h_o v_o \mathbf{v}_1) = & \begin{bmatrix} \Gamma_{vv} - i\sigma \text{Re}_p^* \bar{\rho}_o h_o & -\text{Re}_p^* \bar{\rho}_o h_o v_o v_{\alpha\alpha} \\ \text{Re}_p^* \bar{\rho}_o h_o v_o v_{\alpha\alpha} & \Gamma_{vv} - i\sigma \text{Re}_p^* \bar{\rho}_o h_o \end{bmatrix} \mathbf{v}_1 + \Gamma_{vu} \mathbf{u}_1 \\ & + \begin{bmatrix} \Gamma_{vh} \\ 0 \end{bmatrix} + \Gamma_{v\mu} \bar{\mu}_1 + \Gamma_{v\rho} \bar{\rho}_1 - h_o \frac{d\mathbf{p}_1}{dy} \end{aligned} \quad (22)$$

### Energy:

$$\begin{aligned} \text{Re}_p^* E_I \frac{d}{dy} (\bar{\rho}_o h_o v_o \bar{\mathbf{i}}_1) = & \begin{bmatrix} -i\sigma \text{Re}_p^* E_I \bar{\rho}_o h_o & -\text{Re}_p^* E_I \bar{\rho}_o h_o u_o \bar{i}_{\alpha\alpha} \\ \text{Re}_p^* E_I \bar{\rho}_o h_o u_o \bar{i}_{\alpha\alpha} & -i\sigma \text{Re}_p^* E_I \bar{\rho}_o h_o \end{bmatrix} \bar{\mathbf{i}}_1 + i\sigma \bar{\rho}_o h_o \mathbf{p}_1 + \Gamma_{iv} \mathbf{v}_1 + \Gamma_{iu} \mathbf{u}_1 \\ & + \begin{bmatrix} \Gamma_{ih} \\ 0 \end{bmatrix} + \Gamma_{i\mu} \bar{\mu}_1 + \Gamma_{i\rho} \bar{\rho}_1 + \begin{bmatrix} 0 & \left(u_o + \frac{\Lambda}{2}\right) h_o \\ -\left(u_o + \frac{\Lambda}{2}\right) h_o & 0 \end{bmatrix} \mathbf{p}_1 + v_o h_o \frac{d\mathbf{p}_1}{dy} \end{aligned} \quad (23)$$

The coefficients  $\Gamma_{ij}$ , defined as functions of the zeroth order flow fields and shear stresses, are given in Appendix 1. The perturbed fluid properties are determined from the first order pressure and enthalpy fields, i.e.

$$\begin{aligned} \bar{\rho}_{c,s} &= \left( \frac{\partial \bar{\rho}}{\partial p} \right)_{T_o} p_{c,s} + \left( \frac{\partial \bar{\rho}}{\partial \bar{i}} \right)_{p_o} \bar{i}_{c,s} \\ \bar{\mu}_{c,s} &= \left( \frac{\partial \bar{\mu}}{\partial p} \right)_{T_o} p_{c,s} + \left( \frac{\partial \bar{\mu}}{\partial \bar{i}} \right)_{p_o} \bar{i}_{c,s} \end{aligned} \quad (24)$$

### Boundary Conditions

The supply pressure and temperature and discharge pressure in a seal are determined by the operating conditions at each of the stages in the turbomachine. Thus, the boundary conditions for the flow field variables are:

- a) A sudden drop in pressure occurs at the seal inlet due to the local acceleration of the fluid from stagnant conditions ( $P_s, T_s$ ) to an inlet velocity at the seal entrance. The inlet pressure  $(p_i)_{y=0}$  in terms of zeroth and first order components is given by (Yang, 1992):

$$p_{io} = 1 - \frac{(1+\xi)}{2} \text{Re}_p^* \bar{\rho}_{io} v_{io}^2 ; \quad p_{1i} = -\frac{(1+\xi)}{2} \text{Re}_p^* [2\bar{\rho}_o v_o v_{1i} + v_o^2 \bar{\rho}_{1i}] \quad (25)$$

where the subscripts  $s$  and  $i$  denote supply and seal inlet conditions respectively.  $(\xi)$  is an empirical entrance loss coefficient to account for the non-isentropic effects of the process.

- b) The inlet enthalpy is also affected by the acceleration of the fluid through the seal entrance, and its zeroth and first order components are given by:

$$\bar{h}_{io} = 1 - \frac{(1+\xi)}{2} \frac{v_{io}^2}{E_I} ; \quad \bar{h}_{1i} = -\frac{(1+\xi)}{2} \frac{2v_o v_{1i}}{E_I} \quad (26)$$

- c) Depending on upstream conditions (due to seal straightening vanes) the circumferential velocity at the seal entrance is given as a fraction of the rotor surface speed,

$$u_{io} = \alpha \Lambda ; \quad u_{1i} = 0 \quad (27)$$

where  $\alpha$  is a preswirl factor .

- d) For subsonic flow conditions the fluid pressure at the seal exit equals the discharge pressure ( $P_a$ ). Thus,

$$p_{o(\bar{y}=L/R)} = 0 ; \quad p_{1(\bar{y}=L/R)} = 0 \quad (28)$$

No fluid inertia effects producing a pressure recovery are considered at the seal exit. If the flow reaches sonic conditions the velocity at the exit plane must equal the fluid sound velocity, and the mass flow rate is determined by the supply (stagnant) conditions and the area where the flow chokes.

### Rotordynamic Force Coefficients

The dynamic force coefficients for small amplitude motions about the centered seal position are obtained from the integration of the first order pressure field,

$$K_{\alpha\beta} + i\omega C_{\alpha\beta} = -\frac{(P_s - P_a)R^2}{c} \int_0^{L/R} \int_0^{2\pi} p_{\beta} h_{\alpha} d\theta d\bar{y} \quad (29)$$

where  $\alpha, \beta = X, Y$ , and  $h_x = \cos\theta$ ,  $h_y = \sin\theta$ . For concentric operation, equation (29) further reduces to:

$$\begin{Bmatrix} K_{XX} + i\omega C_{XX} \\ K_{XY} + i\omega C_{XY} \end{Bmatrix} = -\frac{(P_s - P_a)R^2}{c} \pi \int_0^{L/R} \begin{Bmatrix} p_c \\ p_s \end{Bmatrix} d\bar{y} \quad (30)$$

Additionally, for concentric seal operation,  $K_{xx} = K_{yy}$ ,  $K_{xy} = -K_{yx}$ ,  $C_{xx} = C_{yy}$ ,  $C_{xy} = -C_{yx}$ . The impedances, force-to-rotor displacement ratios, given in equations (30) do not follow the usual model presented in equation (1) with **constant** stiffness, damping and added mass rotordynamic coefficients. For compressible fluids and flow-mixtures, both stiffness and damping are functions of the excitation (whirl) frequency  $\omega$ .

## SUMMARY

A bulk-flow analysis for the prediction of the dynamic forced response of centered damper seals for cryogenic turbopumps operating under two-phase flow conditions is detailed. A "continuous vaporization" model is assumed, i.e. a liquid-vapor region exists when the fluid changes from liquid to vapor. The two-phase flow zone is regarded as a homogeneous mixture in thermodynamic equilibrium. The energy transport equation expressed in terms of fluid enthalpy then renders a single set of governing equations describing the flow in either the single or two-phase flow regions. Flow turbulence is accounted for through the use of turbulent shear stress parameters and Moody's friction factors. A model for mixture viscosity, including the increase of viscosity for low vapor content mixtures, as observed in several experimental studies, is also introduced.

Static and dynamic seal performance characteristics are obtained from a perturbation analysis. Small amplitude rotor motions about the centered position allow to express the governing equations in terms of zeroth and first order flow variables. Solution of the zeroth order equations provide the seal leakage, drag torque, and temperature, pressure, velocity, temperature and mixture composition fields. Stiffness and damping force coefficients as functions of an excitation frequency are obtained from integration of first order pressure fields.

Theoretical predictions and comparisons to experimental measurements in a liquid and gaseous nitrogen seal are presented in Part II (Arauz and San Andres., 1997). The effects of two-phase flow regimes on the static and dynamic force performance characteristics of an oxygen damper seal are also discussed in Part II.

## ACKNOWLEDGMENTS

The financial support of NASA Lewis Research Center through the grant NAG3-1434 is deeply acknowledged. Thanks to Mr. James Walker of NASA LeRC for his interest on this work.



## REFERENCES

- Arauz G., and San Andres, L., 1997, "Analysis of Two-phase Flow in Cryogenic Damper Seals. Part II: Model Validation and Predictions," submitted for review to the ASME Journal of Tribology.
- Beatty, P.A., and Hughes, W.F., 1987, "Turbulent Two-Phase Flow in Annular Seals," *ASLE Transactions*, Vol. 30, pp. 11-18.
- Beatty, P.A., and Hughes, W.F., 1990, "Stratified Two-Phase Flow in Annular Seals," *ASME Journal of Tribology*, Vol. 112, pp.372-381.
- Carey, V., 1992, *Liquid-Vapor Phase-Change Phenomena*, Taylor & Francis, Bristol, Pennsylvania, USA, pp. 416-417.
- Cicchitti, A., et al., 1960, "Two-Phase Cooling Experiments- Pressure Drop, Heat Transfer and Burnout Measurements," *Energia Nucleare*, Vol.7,6, pp. 407-425.
- Chamnirasart, K., 1992, "A Theoretical Model of Hydrodynamic Lubrication with Bubbly Oil," Ph.D. Dissertation, Department of Mechanical Engineering, University of Pittsburgh.
- Childs, D., 1993, *Turbomachinery Rotordynamics: Phenomena, Modeling, and Analysis*, John Wiley & Sons, Inc., New York, New York, pp. 40-71.
- Childs, D., and K., Hale, 1994, "A Test Apparatus and Facility to Identify the Rotordynamic Coefficients of High Speed Hydrostatic Bearings," *ASME Journal of Tribology*, Vol. 116, pp. 337-344.
- Dukler, A.E., Wicks, M.III, and Cleveland, R.G., 1964, "Pressure Drop and Hold-Up in Two-Phase Flow, Part A- A Comparison of Existing Correlations; and Part B- An Approach Through Similarity Analysis, *AIChE Journal*, Vol. 10, pp. 38-51.
- Hayward, A., 1961, "Viscosity of Bubbly Oil," *Fluids Report*, No 99, National Engineering Laboratory.
- Hendricks, R.C., 1987, "Straight Cylindrical Seals for High Performance Turbomachinery," NASA TP-1850.
- Hendricks, R.C., Braun, M.J., and Mullen, R.L., 1987, "Two-Phase Flows and Heat Transfer Within Systems with Ambient Pressure Above the Thermodynamic Critical Pressure," NASA TM-87228.
- Heshmat, H., 1991, "Investigation of Foil Bearings for Use in High-Thrust Liquid Rocket Engines," NASA Contractor Report CR-187099.
- Hughes, W.F., Winowich, N.S., Birchak, M.J., Kennedy, W.C., 1978, "Phase Change in Liquid Face Seals," *ASME Journal of Tribology*, Vol.100, pp. 74-80.
- Iwatsubo, T., and Nishino, T., 1993, "An Experimental Study on the Static and Dynamic Characteristics of Pump Annular Seals," *7th Workshop on Rotordynamic Instability Problems in High*

*Performance Turbomachinery*, held at Texas A&M University, College Station, Texas, May 10-12.

Look, D., Sauer, H., 1986, *Engineering Thermodynamics*, PWS Publishers, Boston, Massachusetts.

Mc Adams, W.H., Woods, W.K., and Heroman, L.C., Jr., 1942, "Vaporization Inside Horizontal Tubes- II -Benzene-Oil Mixtures," *ASME Transactions*, Vol. 64, p.193.

San Andres, L., 1991, "Analysis of Variable Fluid Properties, Turbulent Annular Seals," *ASME Journal of Tribology*, Vol. 113, pp. 694-702.

San Andres, L. 1995, "Thermohydrodynamic Analysis of Fluid Film Bearings for Cryogenic Applications," *Journal of Propulsion and Power*, Vol. 11,5, pp.964-972.

San Andres, L. 1996, "Angled Injection-Hydrostatic Bearings Analysis and Comparisons to Test Results," ASME Paper No. 96-TRIB-10.

Salhi, A., Rey, C., and Rosant, J.M., 1992, "Pressure Drop in Single-Phase and Two-Phase Couette-Poiseuille Flow," *ASME Journal of Fluids Engineering*, Vol. 114, pp.80-84.

Yang, Z., 1992, "Thermohydrodynamic Analysis of Product-Lubricated Hydrostatic Bearings in Turbulent Regime," Ph.D Dissertation, Mechanical Engineering Dept., Texas A&M University.

Yang, Z, San Andres, L, Childs, D., 1993, "Thermal Effects in Cryogenic Liquid Annular Seals - Part I: Theory and Approximate Solution, Part II: Numerical Solution and Results," *ASME Journal of Tribology*, Vol. 115, pp. 267-284.

Yasuna, J.A., Hughes, W.F., 1990, "A Continuous Boiling Model for Face Seals," *ASME Journal of Tribology*, Vol. 112, pp. 266-274.

Yasuna, J.A., Hughes, W.F., 1992, "Squeeze Film Dynamics of Two-Phase Seals," *ASME Journal of Tribology*, Vol. 114, pp. 236-247.

Zeidan, F.Y., Vance, J.M., 1990, "A Density Correlation for a Two Phase Lubricant and its Effect on the Pressure Distribution," *ALSE Transactions*, Vol. 33, pp. 641-647.

## APPENDIX 1. COEFFICIENTS FOR FIRST ORDER EQUATIONS

The following are the coefficients for equations (20) through (23).

### Circumferential Momentum

$$\begin{aligned}\Gamma_{uu} &= \gamma_{uu} - \text{Re}_p^* \bar{\rho}_o h_o \frac{du_o}{dy} \\ \Gamma_{up} &= \Gamma_{u\mu} \frac{\partial \bar{\mu}}{\partial p} \bigg|_{\bar{i}} + \Gamma_{u\rho} \frac{\partial \bar{\rho}}{\partial p} \bigg|_{\bar{i}} \quad (\text{a1}) \\ \Gamma_{ui} &= \Gamma_{u\mu} \frac{\partial \bar{\mu}}{\partial \bar{i}} \bigg|_p + \Gamma_{u\rho} \frac{\partial \bar{\rho}}{\partial \bar{i}} \bigg|_p\end{aligned}$$

### Axial Momentum

$$\begin{aligned}\Gamma_{vv} &= \gamma_{vv} - \text{Re}_p^* \bar{\rho}_o h_o \frac{dv_o}{dy} \\ \Gamma_{vp} &= \Gamma_{v\mu} \frac{\partial \bar{\mu}}{\partial p} \bigg|_{\bar{i}} + \Gamma_{v\rho} \frac{\partial \bar{\rho}}{\partial p} \bigg|_{\bar{i}} \quad (\text{a2}) \\ \Gamma_{vi} &= \Gamma_{v\mu} \frac{\partial \bar{\mu}}{\partial \bar{i}} \bigg|_p + \Gamma_{v\rho} \frac{\partial \bar{\rho}}{\partial \bar{i}} \bigg|_p\end{aligned}$$

### Energy

$$\begin{aligned}\Gamma_{ip} &= \gamma_{ip} - \text{Re}_p^* E_l v_o h_o \frac{di_o}{dy} \\ \Gamma_{iv} &= \gamma_{iv} + h_o \frac{dp_o}{dy} - \text{Re}_p^* E_l \bar{\rho}_o h_o \frac{di_o}{dy} \\ \Gamma_{ih} &= \gamma_{ih} + v_o \frac{dp_o}{dy} - \text{Re}_p^* E_l \bar{\rho}_o v_o \frac{di_o}{dy} \quad (\text{a3}) \\ \Gamma_{ip} &= i\sigma h_o + \Gamma_{i\mu} \frac{\partial \bar{\mu}}{\partial p} \bigg|_{\bar{i}} + \Gamma_{i\rho} \frac{\partial \bar{\rho}}{\partial p} \bigg|_{\bar{i}} \\ \Gamma_{ii} &= i\sigma \text{Re}_p^* E_l \bar{\rho}_o h_o + \Gamma_{i\mu} \frac{\partial \bar{\mu}}{\partial \bar{i}} \bigg|_p + \Gamma_{i\rho} \frac{\partial \bar{\rho}}{\partial \bar{i}} \bigg|_p\end{aligned}$$

### Shear Stress Coefficients

$$\begin{aligned}
 \gamma_{uu} &= -\bar{\mu}_o \left[ \frac{k_{xo}}{h_o} + f_{r1}(u_o - \Lambda)^2 + f_{s1}u_o^2 \right] \\
 \Gamma_{uv} &= -\bar{\mu}_o v_o [f_{r1}(u_o - \Lambda) + f_{s1}u_o] \\
 \Gamma_{uh} &= -\frac{\bar{\mu}_o}{h_o^2} \left[ u_o(-k_{xo} + C_{cr} + C_{cs}) - \Lambda \left( C_{cr} - \frac{k_{ro}}{2} \right) \right] \quad (\text{a4}) \\
 \Gamma_{u\rho} &= -\frac{\bar{\mu}_o b_m}{2h_o \bar{\rho}_o} [u_o(\gamma_r + \gamma_s) - \Lambda \gamma_r] + \frac{h_o}{\bar{\rho}_o} \frac{\partial p_o}{\partial \bar{x}} \\
 \Gamma_{u\mu} &= \frac{b_m}{2h_o} [u_o(\gamma_r + \gamma_s) - \Lambda \gamma_r]
 \end{aligned}$$

$$\begin{aligned}
 \gamma_{vv} &= -\bar{\mu}_o \left[ \frac{k_{yo}}{h_o} + (f_{r1} + f_{s1})v_o^2 \right] \\
 \Gamma_{vu} &= \Gamma_{uv} \\
 \Gamma_{vh} &= -\frac{\bar{\mu}_o v_o}{h_o^2} [-k_{yo} + C_{cr} + C_{cs}] \quad (\text{a5}) \\
 \Gamma_{v\rho} &= -\frac{\bar{\mu}_o b_m}{2h_o \bar{\rho}_o} [v_o(\gamma_r + \gamma_s)] + \frac{h_o}{\bar{\rho}_o} \frac{\partial p_o}{\partial \bar{y}} \\
 \Gamma_{v\mu} &= \frac{b_m}{2h_o} [v_o(\gamma_r + \gamma_s)]
 \end{aligned}$$

$$\begin{aligned}
 \Gamma_{iu} &= \frac{\bar{\mu}_o}{h_o} \left[ \left( 2u_o + \frac{\Lambda}{2} \right) k_{xo} - \Lambda k_{ro} \right] + \bar{\mu}_o [(u_{co} + 2u_{cl})(u_o - \Lambda)f_{r1} + u_{co}u_o f_{s1}] \\
 \gamma_{iv} &= \frac{\bar{\mu}_o}{h_o} (2v_o k_{xo}) + \bar{\mu}_o v_o [u_{co}(f_{r1} + f_{s1}) + 2u_{cl}f_{r1}] \\
 \gamma_{ih} &= \frac{\bar{\mu}_o}{h_o^2} [u_{co}(C_{cr} + C_{cs}) + 2u_{cl}C_{cr}] \quad (\text{a6}) \\
 \gamma_{i\rho} &= \frac{\bar{\mu}_o}{h_o \bar{\rho}_o} \left\{ u_{co} \left[ k_{xo} + \frac{b_m}{2} (\gamma_r + \gamma_s) \right] + u_{cl} (k_{ro} + b_m \gamma_r) \right\} \\
 \Gamma_{i\mu} &= -\frac{b_m}{h_o} \left[ \frac{u_{co}}{2} (\gamma_r + \gamma_s) + u_{cl} \gamma_r \right]
 \end{aligned}$$

here

$$C_{cr} = \frac{1}{2} (\text{Re}_{ro} C_r + b_m) \gamma_r \quad ; \quad C_{cs} = \frac{1}{2} (\text{Re}_{so} C_s + b_m) \gamma_s$$

$$C_r = c_m \frac{r_r}{h_o c} ; \quad C_s = c_m \frac{r_s}{h_o c}$$

$$\text{Re}_{ro} = \text{Re}_p \frac{h_o \bar{\rho}_o}{\bar{\mu}_o} \sqrt{(u_o - \Lambda)^2 + v_o^2} ; \quad \text{Re}_{so} = \text{Re}_p \frac{h_o \bar{\rho}_o}{\bar{\mu}_o} \sqrt{u_o^2 + v_o^2}$$

$$\gamma_r = \frac{-a_m e_m}{\left[ \frac{f_{ro}}{a_m} - 1 \right]^{\frac{1}{e_m} - 1}} ; \quad \gamma_s = \frac{-a_m e_m}{\left[ \frac{f_{so}}{a_m} - 1 \right]^{\frac{1}{e_m} - 1}}$$

$$f_{r1} = \frac{h_o}{2 \text{Re}_{ro}} \left( \frac{\text{Re}_p \bar{\rho}_o}{\bar{\mu}_o} \right)^2 \left[ f_{ro} + \frac{b_m}{\text{Re}_{ro}} \gamma_r \right] ; \quad f_{s1} = \frac{h_o}{2 \text{Re}_{so}} \left( \frac{\text{Re}_p \bar{\rho}_o}{\bar{\mu}_o} \right)^2 \left[ f_{so} + \frac{b_m}{\text{Re}_{so}} \gamma_s \right]$$

$$u_{co} = u_o^2 + v_o^2 + u_o \frac{\Lambda}{2} ; \quad u_{cl} = \frac{\Lambda^2}{4} - u_o \Lambda$$

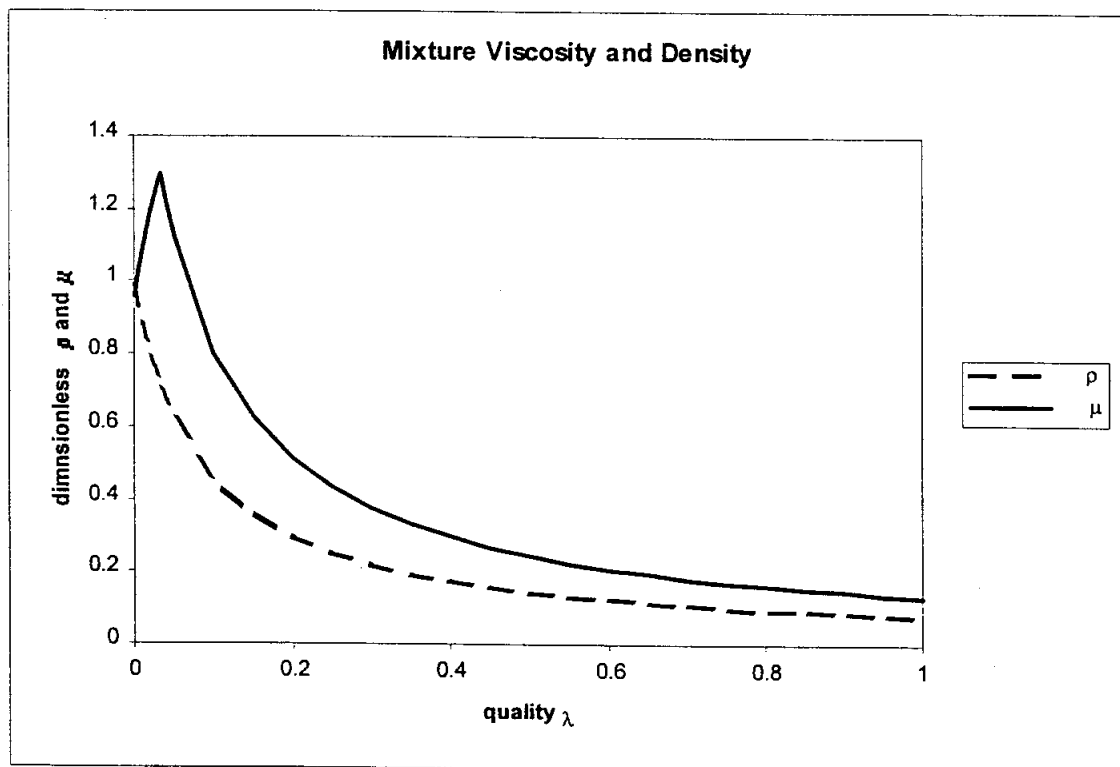
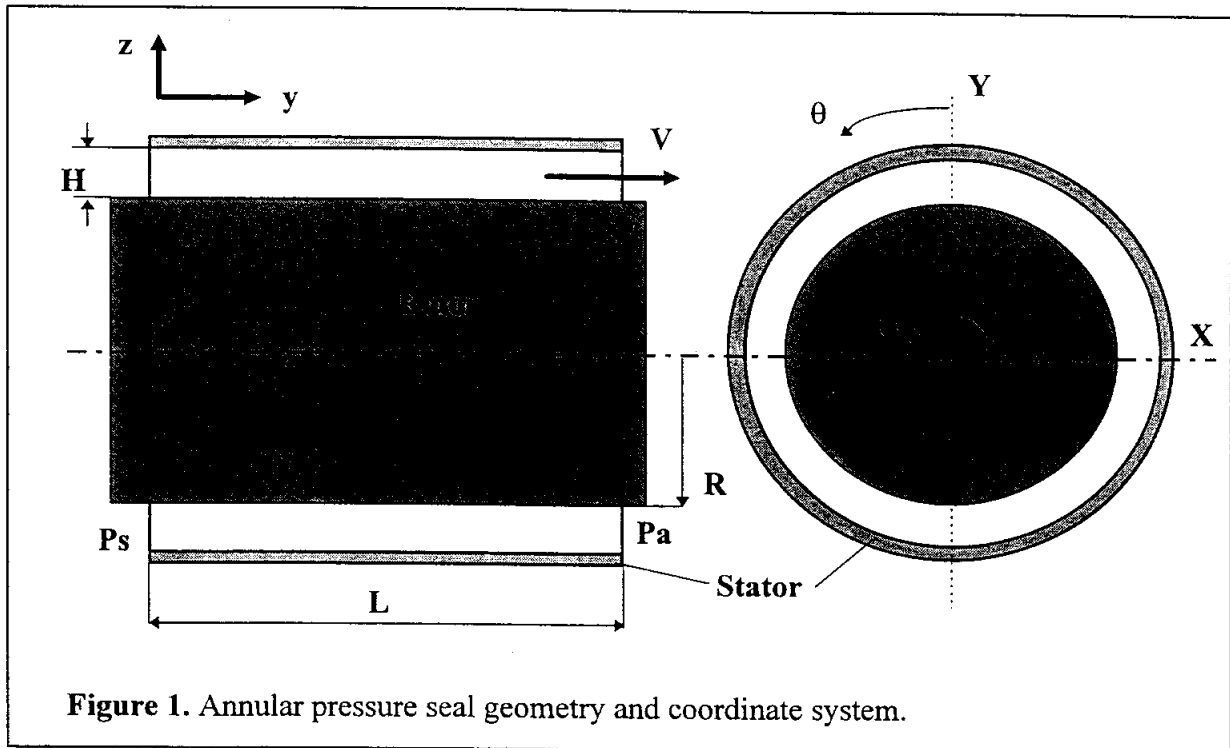


**Figure 2.** Variation of dimensionless mixture viscosity and density with quality for liquid oxygen (LOX) at  $P= 1.8 \text{ MPa}$  ( $T_{\text{sat}}=130.58 \text{ °K}$ ).

**16.** "Analysis of Two Phase Flow in Cryogenic Damper Seals. Part II: Model Validation and Predictions," 1996, Arauz, G., and L. San Andres, submitted for peer review to *ASME Journal of Tribology*, November.

# ANALYSIS OF TWO-PHASE FLOW IN CRYOGENIC DAMPER SEALS.

## PART II: MODEL VALIDATION AND PREDICTIONS<sup>1</sup>

Grigory L. Arauz  
Research Assistant  
Luis San Andres  
Associate Professor  
Mechanical Engineering Department  
Texas A&M University  
College Station, TX 77843-3123

11/96

### ABSTRACT

Cryogenic fluid damper seals operating close to the liquid-vapor region (near the critical point or slightly sub-cooled) are likely to develop a two-phase flow region and which affects the seal performance and reliability. An all-liquid, liquid-vapor, and all-vapor, i.e. a "continuous vaporization" bulk-flow model for prediction of the seal dynamic forced response is given in Part I. The numerical method of solution of the flow equations is here detailed. Theoretical predictions correlate well with test data from a gaseous nitrogen seal and liquid nitrogen seal with two-phase at the seal exit plane. The effects of two-phase flow regimes on the dynamic force coefficients and stability of an oxygen damper seal are discussed, and where fluid compressibility effects, particularly for mixtures with low mass content of vapor, are of utmost importance. Under these conditions, an increase on seal direct stiffness and reduction of whirl frequency ratio are shown to occur.

### NOMENCLATURE

- A: coefficient for flow variables in flow difference equations.  
c: radial clearance [m].  
D:  $2R$ , rotor diameter [m].  
i: fluid enthalpy [J/kg].  
 $K_{\alpha\beta}, C_{\alpha\beta}$ : stiffness and damping force coefficients [N/m, N.s/m].  $\alpha\beta=X,Y$   
L: seal length [m].  
P: fluid pressure [Pa].  
 $P_i$ : seal inlet pressure [Pa].  
 $P_s, P_a$ : supply and discharge pressure [Pa].  
p:  $(P-P_a)/(P_s-P_a)$ , dimensionless fluid pressure.  
Q:  $\rho V 2\pi R c$ , leakage [kg/s].  
R: rotor radius [m].  
 $r_r, r_s$ : mean roughness depth at rotor and stator surfaces [m].  
S: source term in discretized governing equations.  
T: fluid temperature [°K].  
WFR:  $K_{XY}/\Omega C_{XX}$ , whirl frequency ratio.  
X,Y: inertial coordinates for rotor center position within seal stator [m].  
 $\alpha$ : circumferential velocity entrance swirl factor.  
 $\Phi$ : represents flow primitive variables in equation (2).  
 $\lambda$ : vapor-to-mixture mass ratio (quality).  
 $\Omega$ : rotational speed of journal [rad/s].

<sup>1</sup> Research sponsored by NASA Lewis Research Center through grant NAG3-1434. Project "Thermohydrodynamic Analysis of Cryogenic Liquid Turbulent Flow Fluid Film Bearings".



$\omega$ : excitation whirl frequency [rad/s].  
 $\xi$ : empirical entrance loss coefficient.

**Subscripts:**

s: refers to seal external supply conditions  
sat: refers to fluid saturation conditions.

**Superscripts:**

N: refers to downstream (north) control volume.  
P: refers to current control volume.  
S: refers to upstream (south) control volume.

## INTRODUCTION

Cryogenic liquid damper seals operating close to the fluid critical point may develop a two-phase flow condition due the steep pressure variations within the seal (Hendricks et al., 1987, Yang et al., 1993). The transformation from a single- to a two-phase fluid brings considerable variations in the overall material properties, affecting the pressure and temperature gradients within the seal, and changing the overall performance of the sealing element. Part I (Arauz and San Andres, 1997) advances a bulk-flow analysis for the prediction of the dynamic forced response of damper seals operating under two-phase flow conditions. The relevant literature is there reviewed with detail. This second part outlines the numerical solution method and presents correlations of computed predictions with experimental flow rates and pressure drop measurements for a liquid nitrogen seal undergoing a phase change at the seal exit plane. A discussion of the effect of supply temperature on the computed force coefficients of an liquid and gas oxygen annular seal then follows.

## NUMERICAL MODEL

The numerical solution of the governing equations (15) through (23) presented in Part I (Arauz and San Andres, 1997) is obtained using the SIMPLEC finite difference scheme of Van Doormal and Raithby (1984). The accuracy and effectiveness of the algorithm for solving inertia dominated turbulent flow equations is documented by relevant comparisons to experimental data as given by San Andres (1992, 1996), Yang (1992), Yang et al. (1993) for liquid-hybrid journal bearings and seals.

The flow governing partial differential equations given in Part I are integrated over finite control volumes to render a set of non-linear algebraic difference equations with local mass conservation. The resulting equations are further simplified by means of two considerations. First, since the seal is assumed to operate concentric within the stator, the bulk flow is axi-symmetric, i.e. the flow variables do not change in the circumferential direction. Thus, all the primitive flow variables vary only in the axial direction. Second, the large pressure drop characteristic of annular pressure seals prevents any bulk-flow reversals.

Thus, the transport of momentum and energy from the downstream control volume within the seal are not important. With these considerations, the discrete difference equations have the following general form

$$A^P \Phi^P = A^S \Phi^S + S^P \quad (1)$$

where  $\Phi$  represents the fluid velocities (U,V), or the fluid enthalpy (i).  $A^P$  and  $A^S$  are the coefficients for the current (P) and the upstream (S) control volumes, respectively.  $S^P$  is the source term evaluated at the center of the control volume. The contribution of the downstream control volume cannot be neglected in the pressure correction equation (derived from mass conservation) which is given by an expression of the form:

$$-A^N p^N + A^P p^P - A^S p^S = S^P \quad (2)$$

where the superscript N denotes conditions downstream from the control volume. The discrete difference equations for momentum, enthalpy and pressure correction are given in full by Arauz (1997).

Integration of the first order governing equations (equations 19 to 23 in Part I) over the discrete control volumes renders a set of algebraic difference equations which reduce to the same form as (1) and (2), with the only difference that the first order variables are expressed as vectors in terms of their harmonic components (cosine and sine), i.e.  $\Phi = [\Phi_c, \Phi_s]^T$  and  $p = [p_c, p_s]^T$ . The coefficients A's and source terms are, of course, (2x2) matrices. Since these coefficients are functions of the calculated zeroth order flow variables the resulting discrete difference equations are linear. The complete first order difference equations for momentum, enthalpy and pressure are also presented in Arauz (1997).

Numerous simulations for different seal configurations and working fluids have shown the numerical algorithm to be stable and efficient. A grid independence study performed on the seal example introduced by Beatty and Hughes (1987) shows that the calculation of the static seal characteristics like leakage, drag torque, temperature rise and mixture composition (zeroth order solution) does not require fine meshes to achieve a grid independent solution. When the mesh is refined from a 14 node grid to a 28 node grid the maximum variation of the static seal parameters is 1.3%. If the grid is further refined to 56 nodes the maximum variation is 0.52%. Thus for the simulations requiring only static seal characteristics a mesh with 14 nodes along the seal length has been used. The dynamic force coefficients are quite sensitive to the extent of the two-phase region whose physical size does depend on the grid density. The finer the mesh, the more accurate prediction of the two-phase region extent. Thus, under two-phase flow conditions the maximum variation of the rotordynamic coefficients when comparing results from a 14 node and a 28 node grid is about 8%, and when the mesh is further refined to 56 nodes the variation is about 4%. Although these values are higher than those for the static seal characteristics they are still the same as observed in a

similar programs for gas annular seals (Yang et al., 1993). The predictions for seal rotordynamic force coefficients reported later are based on a 28 node mesh.

### Single phase fluid properties

Fluid properties for the cryogenic fluids ( $N_2$ ,  $O_2$  and  $H_2$ ) under single phase conditions are obtained using a NBS database (McCarty, 1986). The equilibrium properties are based on a 32-term modified Benedict-Webb-Rubin (MBWR) equation of state. A series of subprograms provide fluid properties such as enthalpy, entropy, internal energy, viscosity, density, sonic velocity, and saturation conditions using the pairs temperature and density, or temperature and pressure as known inputs. Since fluid enthalpy is used as primitive flow variable instead of temperature, an iterative method to calculate fluid temperature using known pressure and enthalpy as inputs was developed using the basic routines given in the NBS program.

## THEORETICAL PREDICTIONS

### Validation with Test Data from Hendricks (1987)

The scarce experimental data available for fluid film bearings used in cryogenic turbomachinery, and particularly for their operation near or at two-phase flow conditions, has limited the validation of the proposed model to the seal static characteristics, namely leakage and pressure drops. Hendricks (1987) presents experimental results for a smooth, uniform clearance seal working with liquid and gaseous nitrogen. The seal configuration, similar to the one proposed for the Space Shuttle Main Engine oxidizer turbopump (SSME-HPOTP) was tested under non-rotating conditions and for concentric and fully eccentric seal positions. The seal geometry and operating conditions are listed in Table 1. Fluid pressure was measured at seven axial locations, six within the seal and one beyond the seal exit. Predictions from the model are compared with the measurements within the seal. Experimental and theoretical predictions for several cases of liquid and gaseous nitrogen are detailed in Tables 2 and 3. Leakage flow rates and fluid pressure at the seal inlet ( $P_i$ ) are shown in the tables, along with deviation in percentage between model predictions and experiments. The predicted exit quality ( $\lambda_{exit}$ ) is also presented for the seal cases with liquid conditions at the inlet. These results are depicted in graphical form in Figure 2 where symbols represent the experiments and lines denote the theoretical predictions<sup>2</sup>.

---

<sup>2</sup> Table 2 also shows good agreement for runs 584-592. However, the exit quality presents an unusual behavior for the points with supply pressure near 5 MPa. This is due to the non-uniform variation of supply temperature in those runs.

Table 1. Seal Geometry and Operating Conditions for Hendricks (1987) seal example.

Diameter, D [m]	0.0842
Length, L [m]	0.0428
Radial Clearance, c [mm]	134.6
rotor and stator roughness, $r_r$ , $r_s$	0.0 (smooth)
Rotational Speed [rpm]	0
Supply Pressure, $P_s$ [MPa]	1 - 6
Supply temperature, $T_s$ [°K]	85 - 280
Discharge Pressure, $P_d$ [MPa]	0.1 - 1.2
Working fluid	Nitrogen (liquid and gaseous)

Table 2. Experimental and theoretical results for Liquid Nitrogen

run	$P_s$ [MPa]	$T_s$ [°K]	$leakage_{exp}$ [kg/s]	$leakage_{theo}$ [kg/s]	dev [%]	$\lambda_{exit}$ [%]	$P_{i,exp}$ [MPa]	$P_{i,theo}$ [MPa]	dev [%]
592	2.68	89.00	<b>0.943</b>	0.944	0.10	2.40	<b>2.18</b>	2.22	1.83
591	3.33	88.30	<b>1.083</b>	1.085	0.18	2.10	<b>2.71</b>	2.72	0.37
590	3.99	88.00	<b>1.215</b>	1.241	2.14	1.40	<b>3.27</b>	3.20	-2.14
589	4.58	87.90	<b>1.317</b>	1.348	2.35	1.30	<b>3.79</b>	3.65	-3.69
587	4.80	86.90	<b>1.354</b>	1.393	2.88	1.20	<b>3.99</b>	3.81	-4.51
586	4.91	86.70	<b>1.378</b>	1.424	3.34	1.04	<b>4.11</b>	3.88	-5.60
588	5.00	88.20	<b>1.357</b>	1.425	5.01	1.26	<b>4.08</b>	3.96	-2.94
585	5.08	86.40	<b>1.414</b>	1.440	1.84	1.16	<b>4.26</b>	4.03	-5.40
584	5.56	87.50	<b>1.455</b>	1.532	5.29	1.03	<b>4.59</b>	4.37	-4.79
615	1.22	92.30	<b>0.547</b>	0.531	-2.93	7.05	<b>0.98</b>	1.07	9.18
614	1.52	91.10	<b>0.648</b>	0.623	-3.86	5.64	<b>1.22</b>	1.31	7.38
613	1.98	88.90	<b>0.784</b>	0.754	-3.83	4.10	<b>1.57</b>	1.68	7.01
612	2.81	88.80	<b>0.964</b>	0.953	-1.14	3.10	<b>2.23</b>	2.34	4.93
611	3.51	88.50	<b>1.101</b>	1.111	0.91	2.20	<b>2.80</b>	2.87	2.50
610	4.06	88.40	<b>1.200</b>	1.232	2.67	1.70	<b>3.25</b>	3.28	0.92

**Table 3.** Experimental and theoretical results for Gaseous Nitrogen

run	$P_s$ [MPa]	$T_s$ [°K]	$leakage_{exp}$ [kg/s]	$leakage_{theo}$ [kg/s]	dev [%]	$P_{i,exp}$ [MPa]	$P_{i,theo}$ [MPa]	dev [%]
533	1.15	239.50	<b>0.064</b>	0.061	-4.38	<b>1.01</b>	1.05	4.36
532	1.36	239.80	<b>0.077</b>	0.074	-4.55	<b>1.23</b>	1.24	1.06
531	1.80	2.39	<b>0.107</b>	0.100	-6.54	<b>1.61</b>	1.64	1.68
530	2.51	245.00	<b>0.150</b>	0.141	-5.80	<b>2.28</b>	2.27	-0.39
529	3.51	254.90	<b>0.213</b>	0.198	-6.90	<b>3.15</b>	3.16	0.29
528	4.60	267.00	<b>0.279</b>	0.258	-7.63	<b>4.17</b>	4.12	-1.20

The comparisons of flow rate and seal inlet pressure ( $P_i$ ) show the present model to accurately predict the static conditions of the seal. Part of the deviations may be attributed to the fact that the experimental values referred as inlet and discharge pressures are slightly inside the seal (as also reported by Hendricks, 1987). Test and computed axial pressure distributions for selected liquid and gaseous seal test cases are depicted in Figure 3. The agreement between predictions and experiments is very good. The different character of the predicted pressures near the seal exit in the liquid nitrogen case arises from the discretization of the seal flow domain. The model assumes that entire last control volume element of the seal is under two-phase flow conditions when the actual transition from all-liquid to two-phase mixture may take place anywhere between the last two pressure nodes, or even just at the seal exit plane as Hendricks also explains. As the mesh is refined the extent of the two-phase region is predicted more accurately and the shape of the pressure curve approaches to that shown by the experimental results. This is illustrated by the second theoretical case shown in the Figure 3a in thin line ( $T_s = 86$  °K), where the phase change is predicted to occur just at the seal exit.

The discharge or exit plane is the most likely to present two-phase flow conditions due to the continuous drop in pressure across the seal. Depending on the supply conditions, the two-phase flow region then grows from the exit toward the seal entrance plane. Although a comprehensive treatment of the second law of thermodynamics for mixtures is not available, it is determined that, as a consequence of the continuous drop of pressure along the seal and the adiabatic character of the flow, the entropy is increasing along the seal in all the cases analyzed.

The bulk-flow model predicts two-phase flow conditions at the seal discharge for the liquid nitrogen cases as denoted by the values of mixture quality at the exit (see Table 1). This agrees with Hendricks observations that the changes in pressure between seal exit and the point downstream the seal discharge were similar to those found in two-phase choked flows in long tubes. The increase of the exit

quality( $\lambda$ ) with decreasing supply pressure ( $P_s$ ) is explained by the fact that as  $P_s$  is lowered a larger portion of the seal is operating close to saturation conditions and therefore the two-phase flow region extends. The quality can only increase as it approaches the seal exit since the mixture is assumed to be in thermodynamic equilibrium. Thus, the larger the two-phase region the higher the mixture quality at the seal discharge.

#### Oxygen Annular Seal Undergoing a Two-Phase Change - Regimes of Operation.

Predictions for the static and dynamic forced response of a liquid oxygen damper seal operating under two-phase flow conditions are detailed. Beatty and Hughes (1987) first introduced this seal case with a geometry similar to that of an application for the SSME HPOTP. The supply conditions are somewhat lower than normal in order to bring the seal operation close to the saturation region and to induce two-phase flow conditions throughout all the seal. Beatty and Hughes results include mass flow rate and pressure, temperature and mixture quality fields within the seal.

**Table 4.** Geometry and Operating Conditions for Beatty and Hughes (1987) seal example.

Diameter D [m]	0.065
Length L [m]	0.026
Radial clearance, c [mm]	174
Rotor and stator roughness, $r_r, r_s$	0.0 (smooth)
Rotational speed [rpm]	30,000 (3141 rad/s)
Supply pressure, $P_s$ [MPa]	2.79
Supply temperature, $T_s$ [°K]	139
Discharge pressure, $P_a$ [MPa]	1.8 ( $T_{sat}=129.5$ °K)
Entrance loss and swirl coefficients $\xi, \alpha$	0.5, 0.5
Working fluid	Oxygen

Numerical predictions are presented for supply temperatures ranging from 125 °K to 150 °K which bring a full range of flow conditions within the seal, i.e. all-liquid, liquid-mixture, all mixture, mixture-vapor, and all-vapor. At a supply temperature approximately equal to 129.5 °K a transition from liquid to a liquid-vapor mixture occurs just at the seal exit plane. The change from liquid to mixture along the entire seal occurs at the seal entrance for a supply temperature equal to 138.5 °K. Finally, the transition from flow mixture to all-vapor occurs at the seal entrance when the supply temperature is around 145 °K. The significance of these transition zones is illustrated in the following discussion.

### Static Seal Characteristics

Figure 4 shows the mass flow rate (leakage), torque, seal entrance pressure and mixture quality at the seal exit versus the supply temperature. When the fluid is fed to the seal as a mixture the supply temperature is equal to the saturation value (140 °K) at the corresponding supply pressure. Then, the mixture quality is varied to simulate different two-phase conditions at the supply. Note that a different physical property, such as enthalpy, is needed to uniquely identify the (apparently) multiple valued conditions shown at 140 °K in Figure 4 (see Arauz, 1997). The leakage, torque and exit quality agrees with the computed results of Beatty and Hughes (1987). Small deviations are due to the circumferential flow development and the use of a novel formulation of mixture viscosity (Arauz and San Andres, 1997).

Torque and leakage decrease from the all-liquid condition ( $T_s < 130$  °K) to the all-vapor condition ( $T_s > 145$  °K), while the mixture quality at the seal discharge increases between  $\lambda=0$  (all-liquid) to  $\lambda=1$  (all-vapor) in the same range. However, the pressure at the seal inlet ( $P_{in}$ ) presents a different behavior and its variation is not bounded by the all-liquid and all-vapor cases. Opposite variations with increasing supply temperature are observed in the liquid-mixture range ( $130 < T_s < 138.5$  °K) and all-mixture range ( $138.5 < T_s < 145$  °K) denoting the large change in the compressibility character of the flow at the seal entrance.

### Dynamic Force Coefficients

Predictions for dynamic stiffness ( $K_{ij}$ ) and damping ( $C_{ij}$ ) coefficients are presented for different supply conditions (temperature). The variation of the direct ( $K_{XX}=K_{YY}$ ) and cross-coupled dynamic stiffness ( $K_{XY}=-K_{YX}$ ) with supply temperature and for three levels of excitation frequency is presented in Figures 5a and 5b, respectively. The predictions for the lowest excitation frequency ( $\omega/\Omega=0.01$ ,  $\omega=5$ Hz) can be safely regarded as the static stiffness. Both stiffnesses ( $K_{XX}$  and  $K_{XY}$ ) appear to be unaffected by changes in supply conditions and excitation frequency on the all-vapor range ( $T_s > 145$  °K). The behavior within the all-liquid range ( $T_s < 130$  °K) is the typical of an incompressible fluid which includes a positive inertia or added mass coefficient. For two-phase flow conditions the stiffnesses present different behaviors depending on whether the flow has a liquid-mixture ( $130 < T_s < 138.5$  °K) or an all-mixture structure ( $138.5 < T_s < 145$  °K).

The direct dynamic stiffness ( $K_{XX}$ ) increases with increasing supply temperature in the liquid-mixture “regime” reaching values significantly larger than those predicted for the all-vapor case. This behavior denotes a continuous rise of the fluid mixture compressibility effects as the supply temperature increases. Direct stiffness seems to be independent of the excitation frequency at the supply conditions corresponding to 133 °K. From the transition point between liquid-mixture and all mixture ( $T_s=138.5$  °K),

as the mixture density drops to a value close to the vapor density, the direct dynamic stiffness decreases with increasing supply temperature until it reaches the all-vapor condition.

The cross-coupled dynamic stiffness ( $K_{XY}$ ) also decreases as the supply temperature increases in the all-mixture regime. However, the variation in the liquid-mixture regime shows a rather complex dependency of cross-coupled stiffness on excitation frequency and supply temperature with a minimum at around 137 °K. For the case with excitation frequency equal to 500 Hz ( $\omega/\Omega=1$ ), it even shows cross-coupled stiffnesses smaller than those predicted for the all-vapor case. Again this behavior is attributed to the rise in fluid compressibility effects mentioned above.

Figure 6 depicts the variation of direct ( $C_{XX}$ ) and cross-coupled ( $C_{XY}$ ) damping coefficients with supply temperature for three different excitation frequency ratios ( $\omega/\Omega$ ). The behavior in the all-liquid and all-vapor regimes is as expected for the single phase liquid and a gaseous seals, with little dependency on the excitation frequency and independent of the supply temperature for the all-vapor cases. The results under two-phase flow conditions show the direct damping to decrease as the excitation frequency increases. More importantly, an increment in direct damping with respect to its all-liquid value is observed when liquid and mixture are present along the seal. For high frequencies the direct damping shows the same type of dependency on frequency and temperature as the one shown by the cross-coupled stiffness. In the all-mixture regime the damping coefficients decrease steadily to reach the all-vapor values. The cross-coupled damping ( $C_{XY}$ ) shows a large drop in the liquid-mixture regime reaching even negative values of the same order of magnitude as those for the all-liquid conditions. When all the fluid within the seal is a mixture the cross-coupled damping increases steadily approaching the values for the all-vapor cases.

The whirl frequency ratio ( $WFR=K_{XY}/C_{XX}\Omega$ ) is a stability indicator defined as the ratio between destabilizing-to-stabilizing forces. A  $WFR=1$  denotes a system on the verge of instability at the operating speed, while a  $WFR=0$  denotes an inherently stable system. The typical WFR for damper seals without preswirl working with either liquid or gaseous fluids is approximately equal to 0.50, and which corresponds to the average tangential fluid velocity within the seal ( $0.5 R\Omega$ ).

When combining the variation of direct damping and cross-coupled stiffness a reduction of the whirl frequency ratio is predicted, as shown in Figure 7, implying a remarkable improvement on the seal stability. Iwatsubo et al. (1993) have found experimentally a similar result for a seal working with a mixture of water and air with void fractions (gas-to-mixture volume ratio) up to 70%. However, in this case, the mixture compositions in terms of quality (gas mass fraction) are just below 1%.

The dramatic changes in the variation of rotordynamic coefficients for cases where a liquid-mixture flow structure is present within the seal can be explained by the large compressibility exhibited by the



mixture, particularly for low vapor mass contents ( $\lambda \rightarrow 0$ ). This can be seen not only from the steep variation of mixture density in the transition from liquid to mixture as observed in Figure 8, but more clearly, by the dramatic changes in the derivative of mixture density with respect to pressure ( $\partial\rho/\partial P$ ), as shown in Figure 9, and which is several orders of magnitude larger for the cases *where liquid and two-phase mixture* coexist within the seal (131, 135, and 138 °K) than for the all-liquid case.

## CONCLUSIONS

A bulk-flow analysis for the prediction of the dynamic forced response of centered damper seals for cryogenic applications operating under two-phase flow conditions is detailed. A "continuous vaporization" model is assumed, i.e. a liquid-vapor region exists when the fluid changes from liquid to vapor. The two-phase flow region is regarded as a homogeneous mixture in thermodynamic equilibrium. A unique set of transport equations describes the flow in either single or two-phase flow conditions. Static and dynamic seal characteristics are obtained from a perturbation analysis for small amplitude rotor motions.

Computed predictions for leakage and pressure drop are validated by existing liquid nitrogen experimental results from Hendricks (1987) which show two-phase flow conditions at the seal exit. Flow rates and mixture quality predictions agree with the results of Beatty and Hughes (1987) for a liquid oxygen seal operating over a full range of two-phase flow conditions.

The most important effect of two-phase flow on the dynamic forced response of the seals studied occurs when the transition from liquid to mixture takes place within the seal. The large variations in fluid compressibility as this goes from a liquid to a low quality mixture within a short physical zone induce a significant change in the rotordynamic force coefficients, namely a rise in direct stiffness and a drop in cross-coupled stiffness. This notable phenomena has been observed experimentally in a seal with a of low gaseous mass content (Iwatsubo, 1993). <sup>mixture</sup>

## ACKNOWLEDGMENTS

The financial support of NASA Lewis Research Center through the grant NAG3-1434 is deeply acknowledged. Thanks to Mr. James Walker of NASA LeRC for his continued support and interest.

## REFERENCES

- Arauz, G., 1997, "Analysis of Two-Phase Flow in Damper Seals for Cryogenic Turbomachinery," Ph.D. dissertation, Mechanical Engineering Dept., Texas A&M University.
- Arauz G., and San Andres, L., 1997, "Analysis of Two-phase Flow in Cryogenic Damper Seals.

Part I: Theoretical Model," submitted for review to the ASME Journal of Tribology.

Beatty, P.A., and Hughes, W.F., 1987, "Turbulent Two-Phase Flow in Annular Seals," *ASLE Transactions*, Vol. 30, pp. 11-18.

Hendricks, R.C., 1987, "Straight Cylindrical Seals for High Performance Turbomachinery," NASA TP-1850.

Hendricks, R.C., Braun, M.J., and Mullen, R.L., 1987, "Two-Phase Flows and Heat Transfer Within Systems with Ambient Pressure Above the Thermodynamic Critical Pressure," NASA TM-87228.

Iwatsubo, T., and Nishino, T., 1993, "An Experimental Study on the Static and Dynamic Characteristics of Pump Annular Seals," *7th Workshop on Rotordynamic Instability Problems in High Performance Turbomachinery*, held at Texas A&M University, College Station, Texas, May 10-12.

McCarty, R.D., NBS Standard Reference Data Base 12, 1986, "Thermophysical Properties of Fluids, MIPROPS-86," Thermophysics Division, Center for Chemical Engineering, National Bureau of Standards, Colorado.

San Andres, L., 1992, "Analysis of Turbulent Hydrostatic Bearings with a Barotropic Cryogenic Fluid," *ASME Journal of Tribology*, Vol. 114, pp. 755-765.

San Andres, L. 1996, "Angled Injection-Hydrostatic Bearings Analysis and Comparisons to Test Results," ASME Paper No. 96-TRIB-10.

Van Doormaal, J.P., and Raithby, D., 1984, "Enhancements of the SIMPLE Method for Predicting Incompressible Fluid Flows," *Numerical Heat Transfer*, Vol. 7, pp.144-163.

Yang, Z., 1992, "Thermohydrodynamic Analysis of Product-Lubricated Hydrostatic Bearings in Turbulent Regime," Ph.D Dissertation, Mechanical Engineering Dept., Texas A&M University.

Yang, Z., San Andres, L, Childs, D., 1993, "Thermal Effects in Cryogenic Liquid Annular Seals - Part I: Theory and Approximate Solution, Part II: Numerical Solution and Results," *ASME Journal of Tribology*, Vol. 115, pp. 267-284.

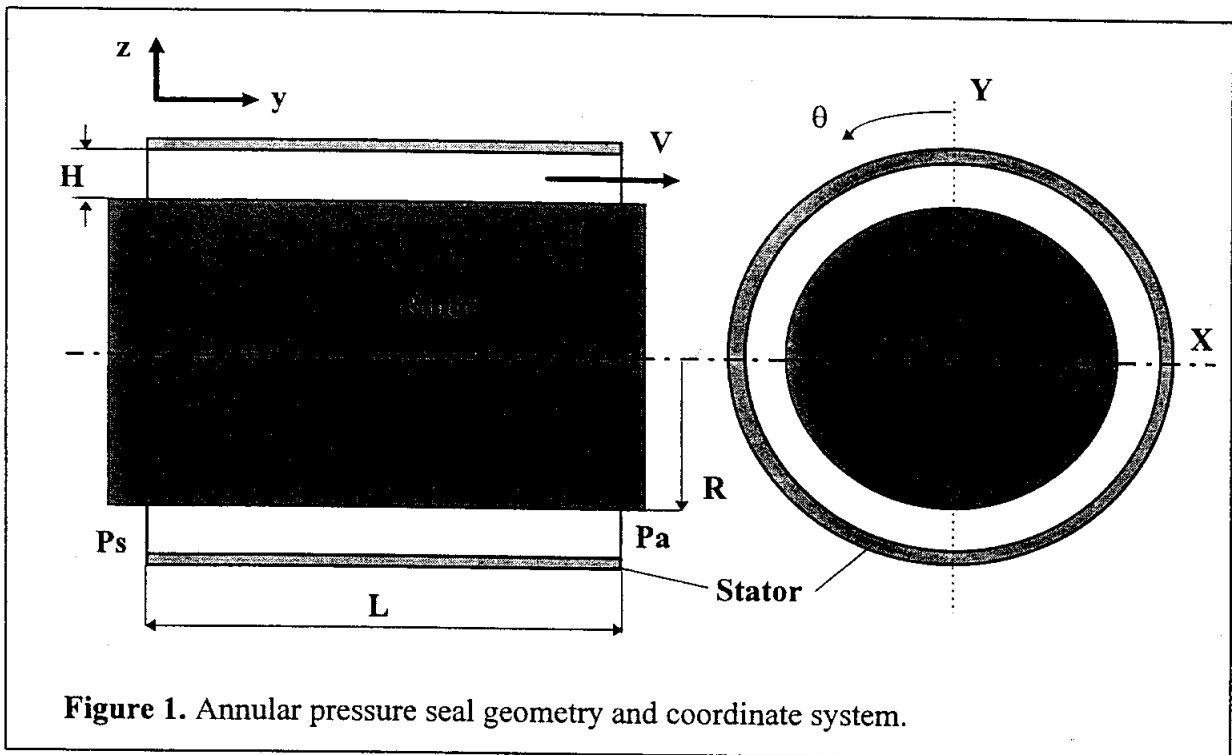
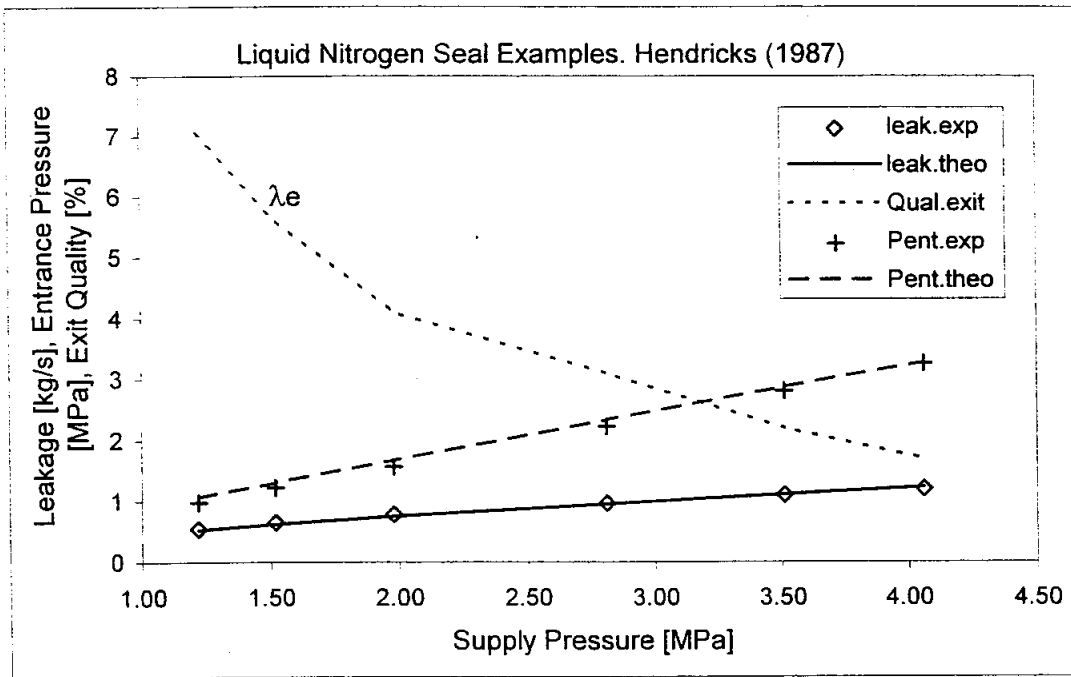
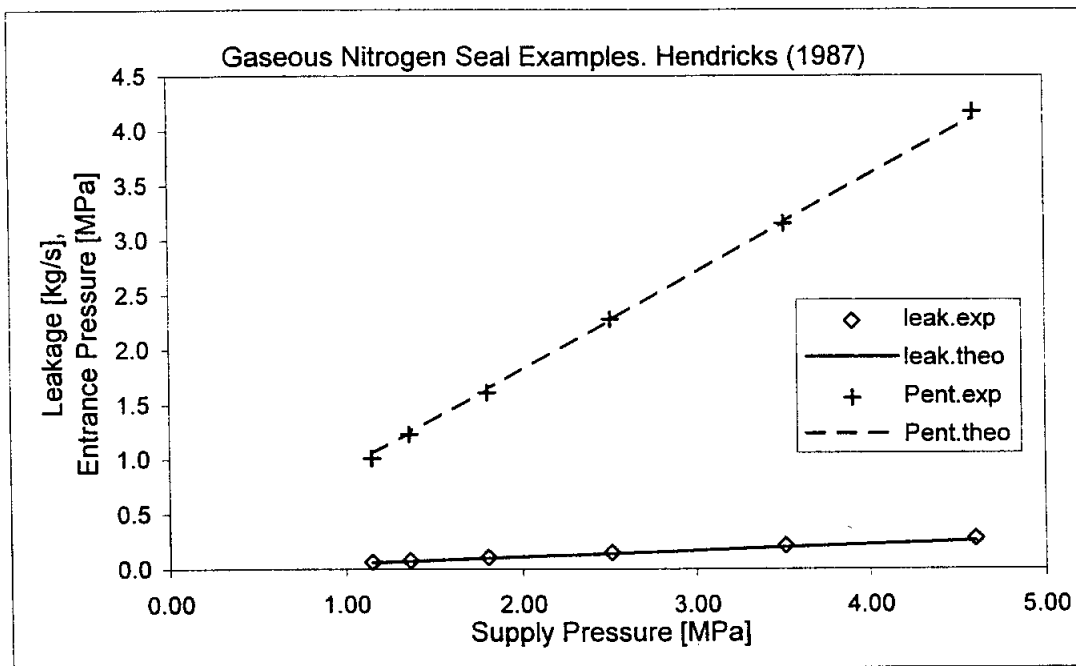


**Figure 1.** Annular pressure seal geometry and coordinate system.

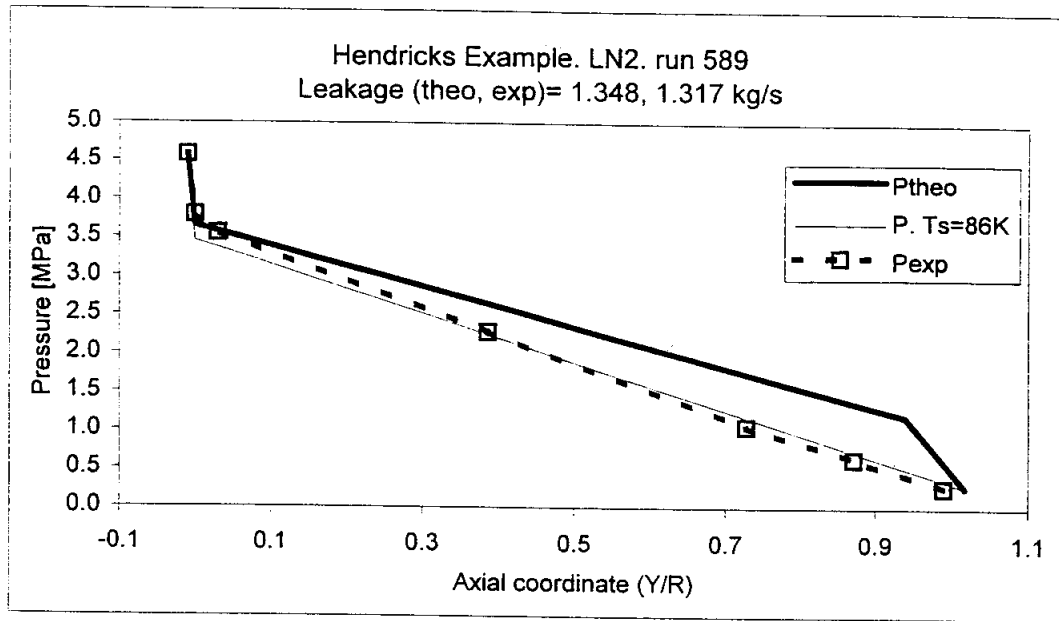


(a)

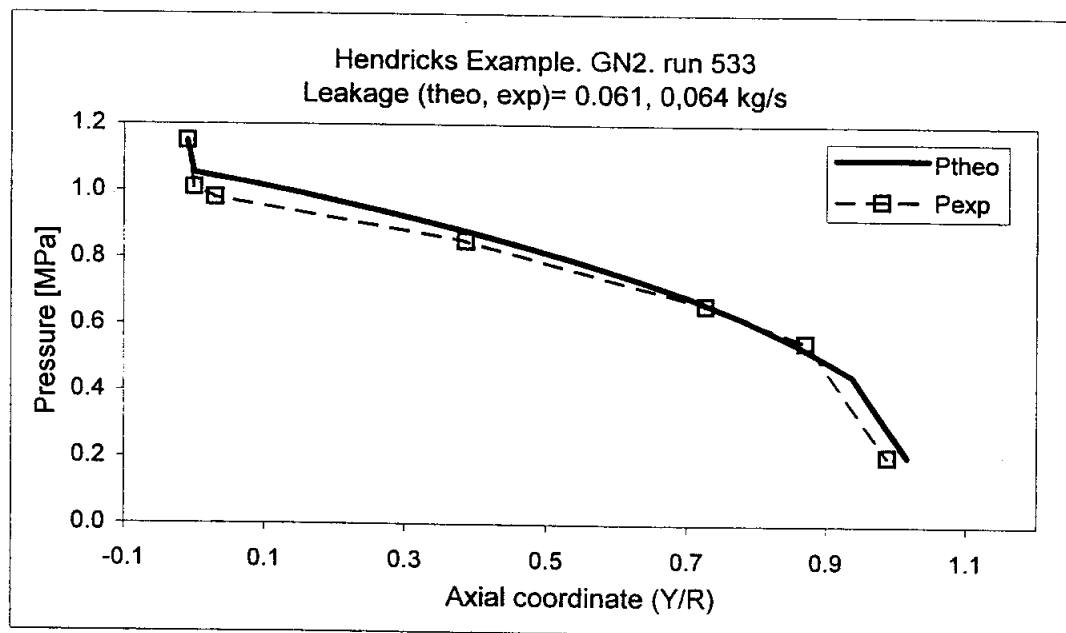


(b)

**Figure 2.** Comparison of theoretical predictions with experimental results from Hendricks (1987). (a) N2 Liquid  $T_s \sim 88$  K (b) N2 Gaseous  $T_s \sim 247$  K



(a)



(b)

**Figure 3.** Comparison of theoretical axial pressure drop with experiments from Hendricks (1987). (a) N2 Liquid  $T_s \sim 88$  K (b) N2 Gaseous  $T_s \sim 239$  K

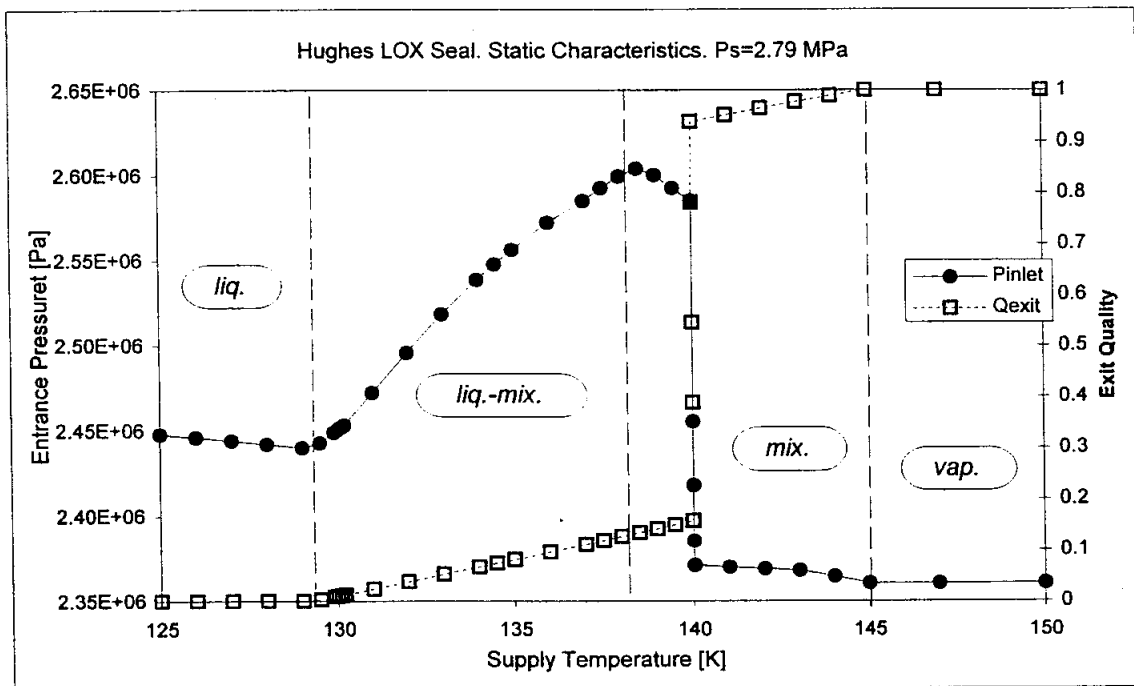
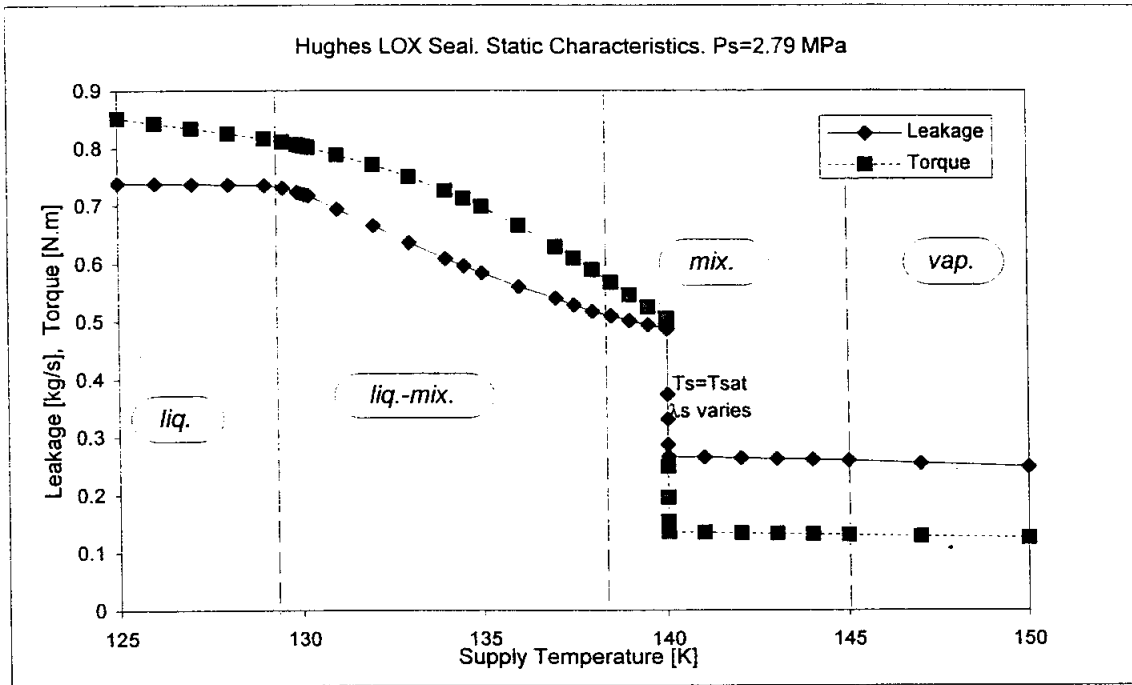
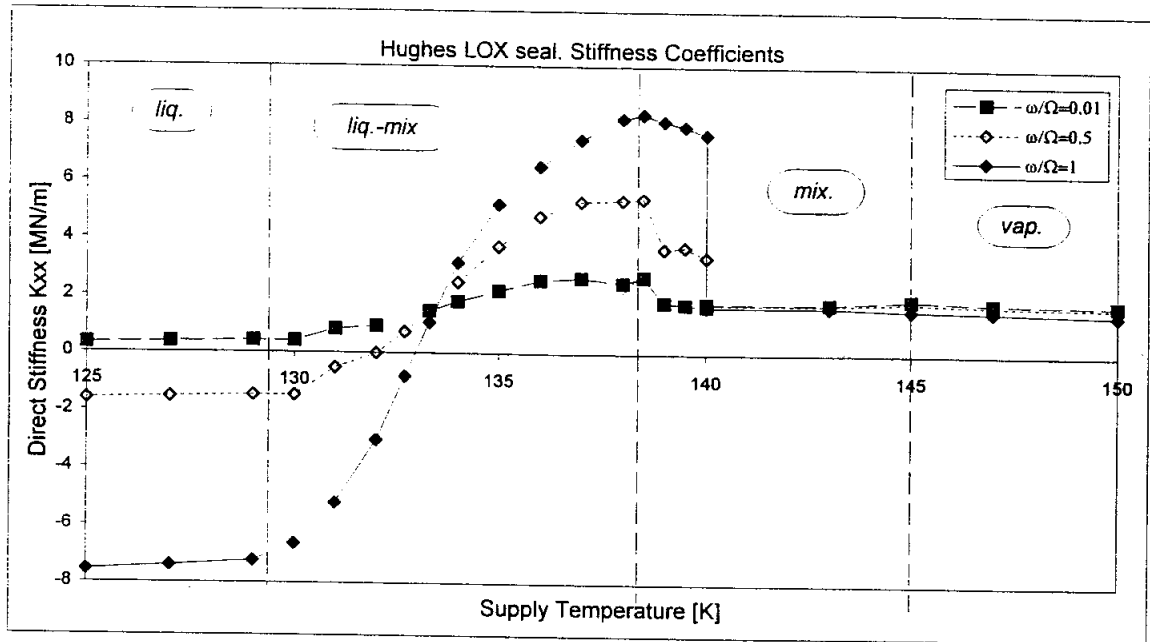
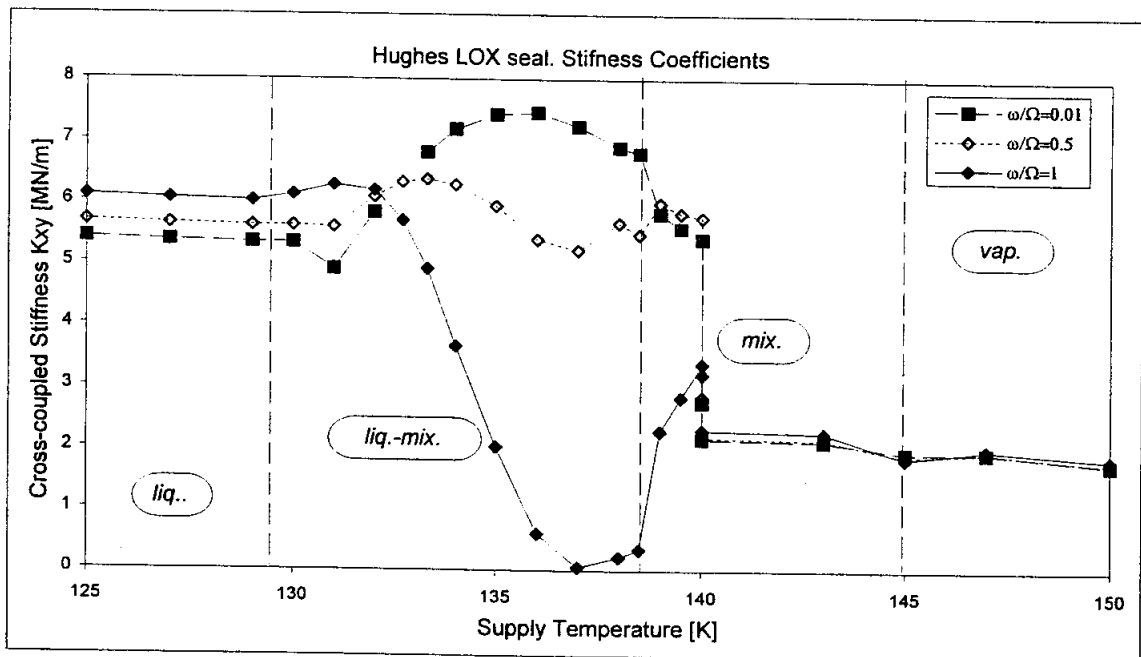


**Figure 4.** Leakage, torque, entrance pressure and exit quality for different supply temperatures.

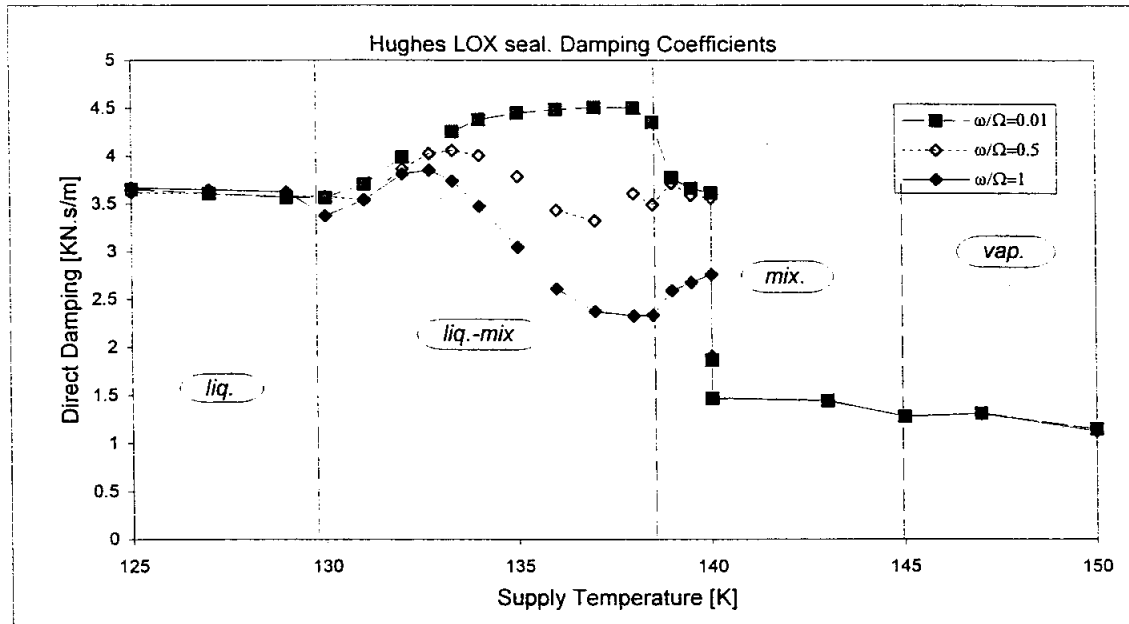


(a)

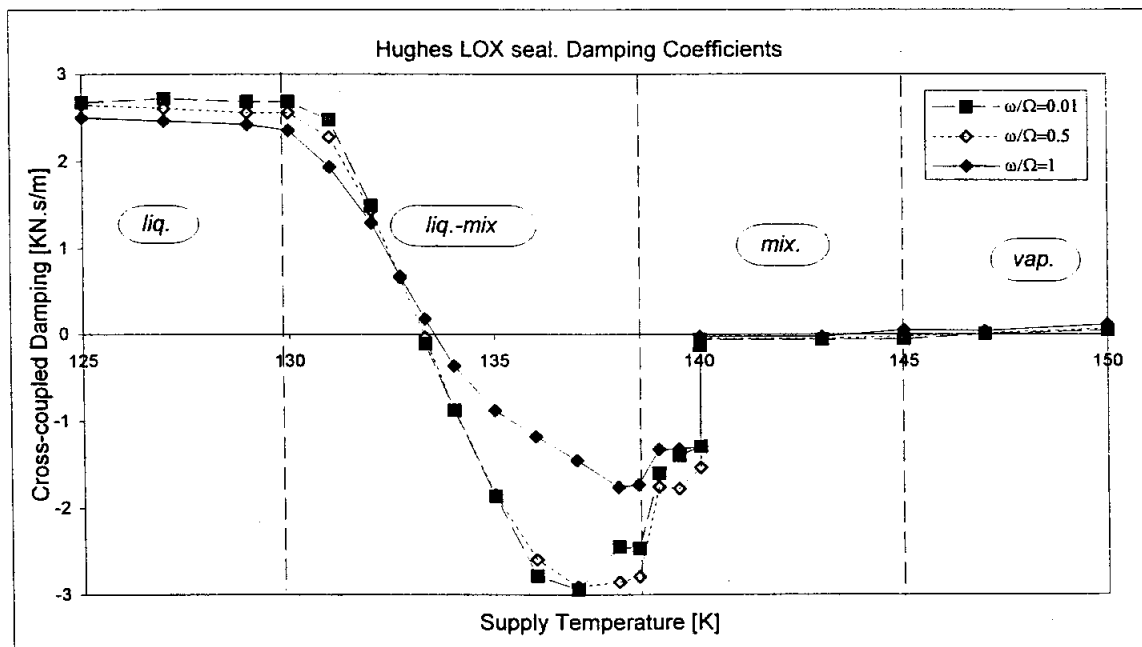


(b)

**Figure 5.** Variation of dynamic stiffness with supply temperature for different excitation frequencies.  
**(a)** Direct stiffness,  $K_{xx}$ . **(b)** Cross-coupled stiffness,  $K_{xy}$ .



(a)



(b)

**Figure 6.** Variation of damping with supply temperature for different excitation frequencies.  
**(a)** Direct damping,  $C_{xx}$ . **(b)** Cross-coupled damping,  $C_{xy}$ .



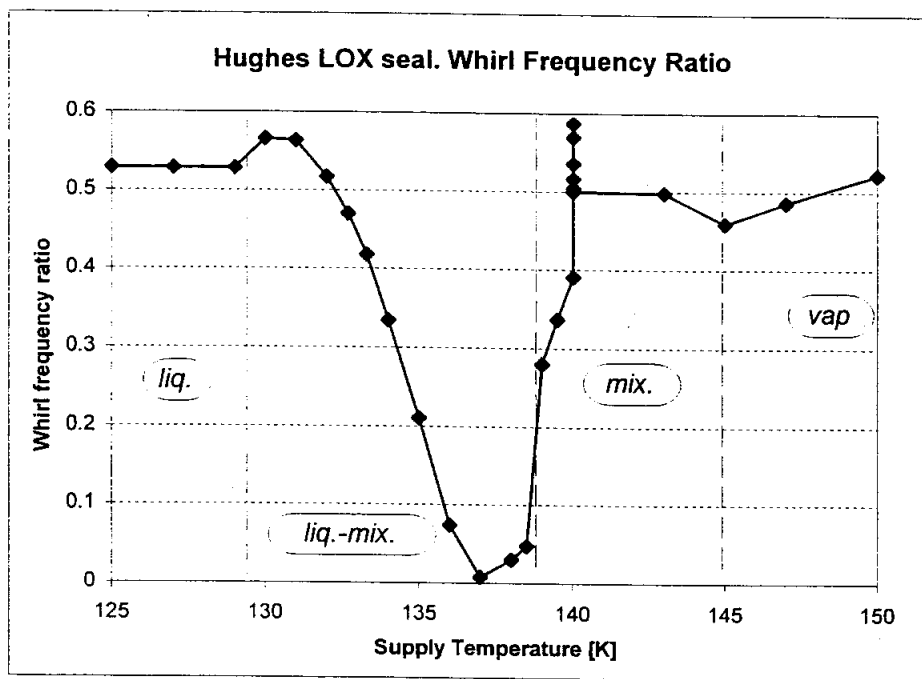


**Figure 7.** Variation of whirl frequency ratio with supply conditions.

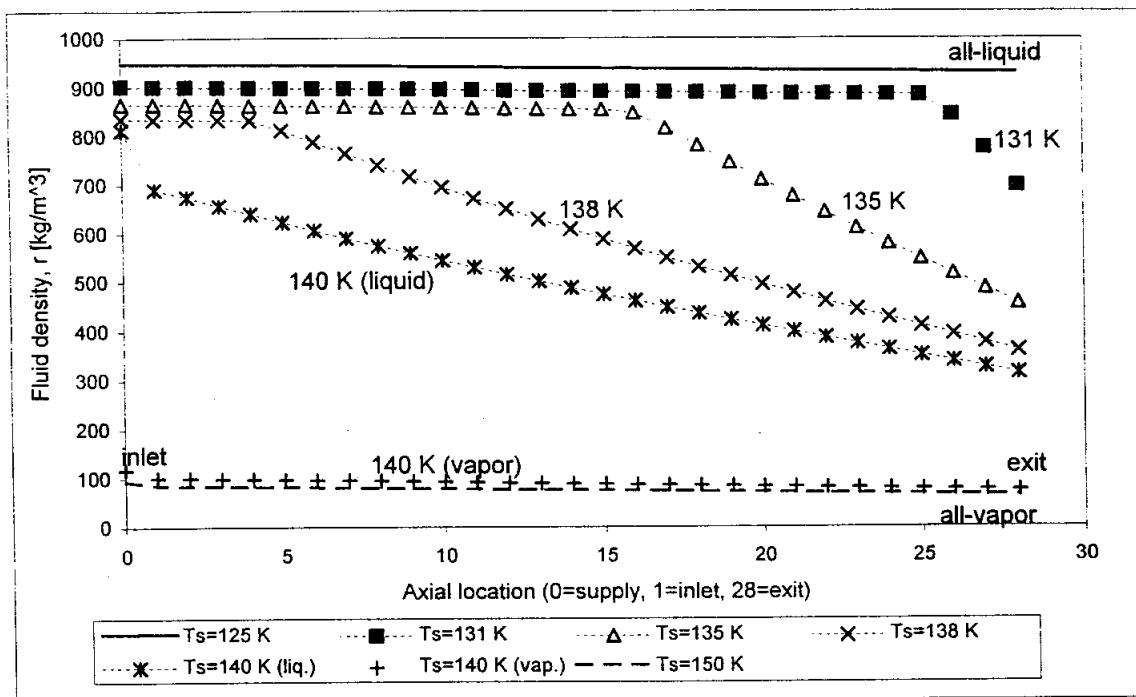


Figure 8. Variation of fluid density along the seal for different supply temperatures ( $T_s$ ).

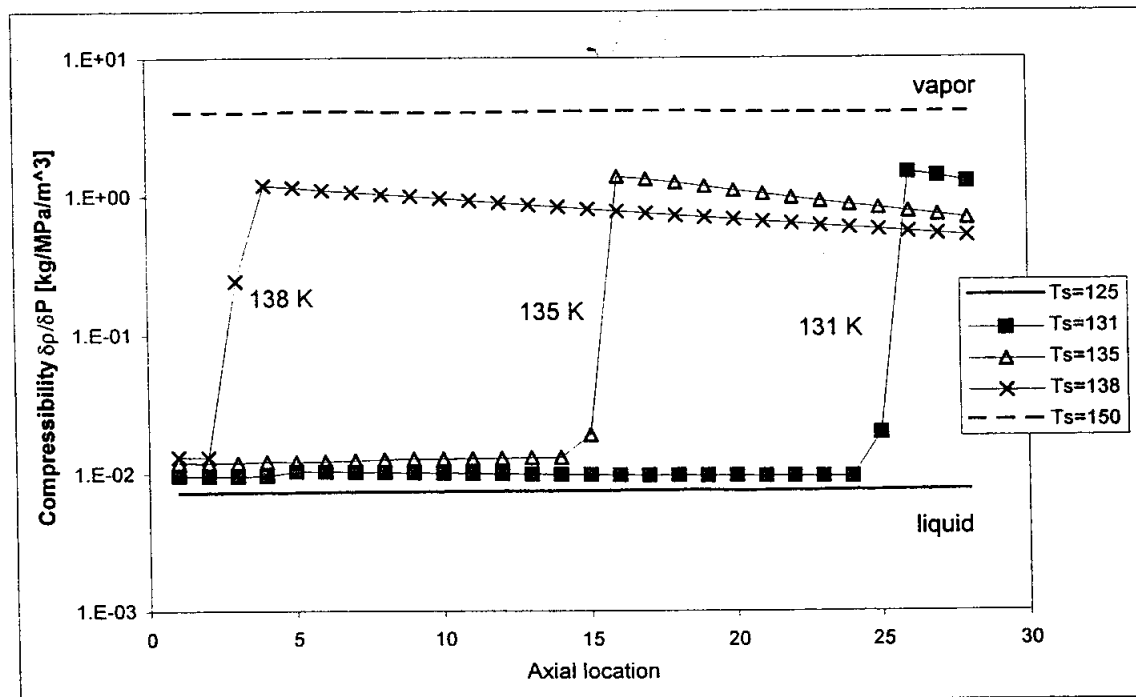


Figure 9. Variation of the derivative of density with respect to pressure along the seal for different supply temperatures ( $T_s$ ).

## LIST OF TABLES

**Table 1.** Seal Geometry and Operating Conditions for Hendricks (1987) seal example.

**Table 2.** Experimental and theoretical results for Liquid Nitrogen.

**Table 3.** Experimental and theoretical results for Gaseous Nitrogen

**Table 4.** Geometry and Operating Conditions for Beatty and Hughes (1987) seal example.

## LIST OF FIGURES

**Figure 1.** Annular pressure seal geometry and coordinate system.

**Figure 2.** Comparison of theoretical predictions with experimental results from Hendricks (1987). (a) N2 Liquid  $T_s \sim 88$  K. (b) N2 Gaseous  $T_s \sim 247$  K

**Figure 3.** Comparison of theoretical axial pressure drop with experiments from Hendricks (1987). (a) N2 Liquid  $T_s \sim 88$  K. (b) N2 Gaseous  $T_s \sim 239$  K

**Figure 4.** Leakage, torque, entrance pressure and exit quality for different supply temperatures.

**Figure 5.** Variation of dynamic stiffness with supply temperature for different excitation frequencies. (a) Direct stiffness,  $K_{xx}$ . (b) Cross-coupled stiffness,  $K_{xy}$ .

**Figure 6.** Variation of damping with supply temperature for different excitation frequencies. (a) Direct damping,  $C_{xx}$ . (b) Cross-coupled damping,  $C_{xy}$ .

**Figure 7.** Variation of whirl frequency ratio, WFR, with supply conditions.

**Figure 8.** Variation of fluid density along the seal for different supply temperatures ( $T_s$ ).

**Figure 9.** Variation of the derivative of density with respect to pressure along the seal for different supply temperatures ( $T_s$ ).